Unsteady Operation of the Francis Turbine

By

NG, Tzuu Bin, B.E. (Hons.)

School of Engineering

Submitted in fulfillment of the

requirements for the Degree of

Doctor of Philosophy

University of Tasmania

June 2007

Statement of originality and authority of access

This thesis contains no material that has been accepted for the award of a degree or a diploma by the University or any other institutions, except by way of background information and duly acknowledged in this thesis. To the author's best knowledge and belief, the thesis contains no material previously published or written by another person, except where due reference is made in the text.

This thesis may be made available for loan and limited copying in accordance with the *Copyright Act 1968*.

Tzuu Bin NG

16/6/2007

ABSTRACT

Increasing interconnection of individual power systems into major grids has imposed more stringent quality assurance requirements on the modelling of hydroelectric generating plant. This has provided the impetus for the present study in which existing industry models used to predict the transient behaviour of the Francis-turbine plants are reviewed. Quasi-steady flow models for single- and multiple-turbine plants developed in MATLAB Simulink are validated against field test results collected at Hydro Tasmania's Mackintosh and Trevallyn power stations. Nonlinear representation of the Francis-turbine characteristics, detailed calculation of the hydraulic model parameters, and inclusion of the hydraulic coupling effects for multiple-machine station are found to significantly improve the accuracy of predictions for transient operation. However, there remains a noticeable phase lag between measured and simulated power outputs that increases in magnitude with guide vane oscillation frequency. The convective lag effect in flow establishment through the Francis-turbine draft tube is suspected as a major contributor to this discrepancy, which is likely to be more important for hydro power stations with low operating head and short waterway conduits.

To further investigate these effects, the steady flow in a typical Francis-turbine draft tube without swirl is analysed computationally using the commercial finite volume code ANSYS CFX. Experimental studies of a scale model draft tube using air as the working medium are conducted to validate and optimise the numerical simulation. Surprisingly, numerical simulations with a standard k-ε turbulence model are found to better match experimental results than the steady-flow predictions of more advanced turbulence models. The streamwise pressure force on the draft tube is identified as a quantity not properly accounted for in current industry models of hydro power plant operation. Transient flow effects in the model draft tube following a sudden change in discharge are studied computationally using the grid resolution and turbulence model chosen for the steady-flow analysis. Results are compared with unsteady pressure and thermal anemometry measurements. The three-dimensional numerical analysis is shown to predict a longer response time than the one-dimensional hydraulic model currently used as the power industry standard. Convective lag effects and fluctuations in the draft tube pressure loss coefficient are shown to largely explain the remaining discrepancies in current quasi-steady predictions of transient hydro power plant operation.

ACKNOWLEGMENTS

The work described in this thesis was carried out at School of Engineering, University of Tasmania. This project has always been an interesting and challenging experience. The author has been accompanied and supported by many people and organizations throughout the process. In particular, the scholarship and financial support from University of Tasmania and Hydro Tasmania are gratefully acknowledged.

The author is highly indebted to Dr. G.J. Walker for being an excellent supervisor and outstanding professor. His constant support, frequent encouragement, and creative suggestions have made this work successful. It is amazing of how much the author can still learn from him after all these years of research. The author is very grateful to Dr. J.E. Sargison for her constructive comments, and for providing useful guidance during the experimental testing. The author wishes to express his gratitude to Dr. M.P. Kirkpatrick for sharing his knowledge and experience on CFD calculation of transient flow. The author would also like to thank his industrial advisors P. Rayner and K. Caney of Hydro Tasmania for their expert advice on technical matters and for offering opportunity to participate in their power plant testing. Many discussions and interactions with engineers from various departments of Hydro Tasmania had a direct impact on the final form and quality of this thesis.

The author would like to acknowledge all of the technical staff from the University (especially R. Le Fevre, N. Smith, P. Seward, J. McCulloch, B. Chenery, S. Avery, and G. Mayhew) who kindly spared their time to provide endless workshop support for preparing the experimental model in the laboratory. Special thanks are due to Dr. P.A. Brandner for sharing the equipment used for unsteady pressure measurements, F. Sainsbury for his excellent IT support, and A.D. Henderson for his friendship and frequent advice on the use of UNIX-based machines. The author wishes to acknowledge with appreciation the provision of academic licenses from ANSYS for CFX software.

On the home front, the author is deeply indebted to his parents and sisters for their love and support. Their confidence in the author's ability to overcome the many hurdles that the author had faced during his academic life had been a crucial driving force in the pursuit of his goals.

TABLE OF CONTENTS

LIST OF FIGURES

LIST OF TABLES

NOMENCLATURE

a	pressure wave speed / flow acceleration
A_G	guide-vane opening area
A_i	cross-sectional area of conduit section i
A_{IN}	cross-sectional area at the entrance of the waterway conduit
A_S	cross-sectional area of the surge tank
A_t	turbine gain factor
C	tuning parameter / calibration coefficient
$C_{d\text{-}o}$	surge tank discharge coefficient
C_D	turbine discharge coefficient
C_{Dyn}	head coefficient
C_f	skin friction coefficient
$C_{F\text{-}dt}$	draft tube static pressure force coefficient
C_H	dimensionless head coefficient
C_P	dimensionless power coefficient
C_{Pitch}	pitch coefficient
Cp_{ideal}	ideal static pressure coefficient
$Cp_{recovery}$	static pressure recovery factor
Cp_{static}	static pressure coefficient
Cs	surge tank storage constant
C_{Yaw}	yaw coefficient
C_Q	dimensionless flow coefficient
CFD	computational fluid dynamics
d	Pitot tube diameter
d_w	hot wire diameter
D	speed-damping factor (Chapter 4)
D_c	conduit diameter
D_{eq}	equivalent diameter for non-circular geometry
D_{in}	inlet diameter of the draft tube
D_{Turb}	turbine diameter
e	conduit wall thickness
E	Young's modulus of elasticity (Chapters 4 and 5)
E	fractional error of a grid (Chapters 6 and 7)

E_v	bulk modulus of elasticity of water (Chapters 4 and 5)
$E_{v\text{-}w}$	measured bridge voltage from the hotwire anemometer (Chapter 6)
f	friction factor (Chapters 4~7) / frequency of oscillation (Chapter 8)
f_{lt}	pressure loss coefficient for the lower tunnel
f_o	surge tank loss coefficient
f_q	quasi-steady part of the friction factor
f_P	pressure loss coefficient for the penstock
f_{ut}	pressure loss coefficient for the upper tunnel
f_v	valve oscillation frequency
F	static pressure force
F_s	support / safety factor
g	gravitational acceleration
G	guide vane position
GCI	grid convergence index
h_{rated}	rated head
H	static head at turbine admission or turbine net head / momentum shape factor
H_{all}	sum of the conduit head losses, inlet dynamic head and draft tube static head
H_{dt}	static head acting on the turbine draft tube
H_{eq}	equivalent head at penstock junction
H_f	conduit head losses due to friction and fittings
H_{IN}	inlet dynamic pressure head for the waterway conduit
H_{local}	local height of a draft tube section
H_o	static head between reservoir and tailrace
H_{outlet}	draft tube outlet height
H_{st}	static head in the surge tank
H_t	static head at the end of upper tunnel (Chapter 5)
H_{tot}	total available static head (Chapter 4)
I	turbulence intensity
$IEEE$	Institution of Electrical and Electronic Engineers
k	Brunone friction coefficient
k_f	air thermal conductivity
k_t	loss coefficient for individual component I
k_{loss}	total pressure loss coefficient of the draft tube
k_{nu}	factor accounting for flow non-uniformity
K_{dt}	factor accounting for inertia force on fluid in the turbine draft tube
K_{IN}	factor accounting for inlet dynamic pressure head

k_{Turb}	turbulence kinetic energy
l_p	inlet pipe length
L	average length of the draft tube
L_i	length of the conduit i
L_w	hot wire sensor length
m	mass of the fluid
N	turbine / fan rotational speed
N_s	specific speed
N_{rated}	rated turbine rotational speed
Nu	Nusselt number
p	order of convergence (Chapters 6 and 7) / static pressure (Chapter 8)
P	power output of the turbine (Chapters 4 and 5) / pressure (Chapters 7 and 8)
P_{atm}	atmospheric pressure
P_{Dyn}	dynamic pressure
P_m	electrical power output of a machine
P_M	mechanical power output of the turbine shaft
P_S	wall static pressure
P_{total}	total pressure
r	radial position from duct centre
r_{ij}	grid refinement ratio
R_{inlet}	radius of draft tube inlet
Re	Reynolds number
Re_{INLET}	Reynolds number based on draft tube inlet diameter
R_p	probe resistance of the hot wire
R_{pipe}	inlet pipe radius
R_t	total resistance of the hot wire
s	surface distance along a conduit
S_{in}	draft tube inlet swirl number
$Sscale$	scalling factor for the transmitter gain of turbine shaft
t	time
T	mechanical torque generated by turbine shaft
T_a	atmospheric temperature
T_{dt}	draft tube air temperature
T_e	elastic water time constant
T_m	mean flow temperature
T_{rated}	rated mechanical torque generated by turbine shaft
T_s	settling time

T_W	water starting time constant
Q	turbine flow rate
Q_{lt}	flow at the lower tunnel (Chapter 5)
Q_{nl}	no-load flow
Q_{peak}	flow at peak turbine efficiency
Q_{rated}	rated flow rate
Q_{st}	flow in the surge chamber (Chapter 5)
Q_{ut}	flow at the upper tunnel (Chapter 5)
U	flow velocity
y	main servo position
V_T	output signal from micromanometer
V_T	amplified signal from temperature transducer
W_H	dimensionless head coefficient
W_{Local}	local width for a draft tube section
W_T	dimensionless torque coefficient
z	elevation head
Z	hydraulic surge impedance
α	pitch angle
β	yaw angle
ε	surface roughness / grid error / turbulence dissipation rate
η_{Turb}	turbine efficiency
η_{Gen}	generator efficiency
μ	dynamic viscosity
μ_t	turbulent viscosity
ν	Poisson ratio
ν_a	air kinematic viscosity
ω	guide vane / valve oscillation frequency
δ	boundary layer thickness
δ^*	boundary layer displacement thickness
θ	angle of operating zone (Chapter 4) / valve position (Chapter 6)
θ	boundary layer momentum thickness (Chapter 7)
θ_R	mechanical torque angle of the rotor (Chapter 2)
ρ_a	air density
τ_d	convective time lag of the draft tube
$\tau_{falling}$	time interval between falling-edge pulses of the frequency transducer
$\tau_{1D\text{-}p}$	inertia time constant for inlet pipe

$\tau_{ID\text{-}dt}$	inertia time constant for draft tube
τ_w	wall shear stress
ω	speed or frequency

Superscript

–	per-unit quantity (Chapters 4 and 5) / mean value (Chapters 7 and 8)
∧	complex amplitude

Subscript

0	reference position / reference plane / initial state
a	axial direction / airflow / ambient condition
coarse	coarse mesh
dt	draft tube
fine	fine mesh
in	draft tube inlet
ini	initial condition
final	final condition
lt	lower tunnel
nl	no-load condition
peak	operating condition corresponding to peak efficiency
rated	rated condition
rms	root-mean-square
st	surge tank
t	turbine
tot	total
ut	upper tunnel
w	hotwire
BE	best efficiency condition
Dyn	dynamic
IN	inlet to waterway conduit (Chapters 4 and 5) / inlet to bellmouth nozzle (Chapter 7)
Gen	generator
Turb	turbine
∞	free stream condition

CHAPTER 1

INTRODUCTION

1.1 General Introduction of the Francis-Turbine Power Plant

Hydroelectricity has been widely used as a renewable energy source for decades. Mosonyi [83] provides a comprehensive introduction of the hydroelectric generating plant, including a brief historical survey from the first invention of the radial-outflow water wheel in 1827 to the establishment of the Francis turbines in 1850's as an accepted and reliable method of hydropower generation; and beyond to the recent hydropower developments around the world. Mosonyi [83] also discusses various types of power plant configurations and the design of various Francis turbine components to account for different geographic and economic constraints.

The number of Francis turbine units to be employed in the power plant depends on the operating cost, load fluctuation, and the flow availability in the reservoir [136]. In most cases, a hydro power plant with a single high-capacity machine has lower operating cost and higher efficiency than a station using multiple machines of smaller sizes. The multiple-machine configuration is required when the flow availability is subject to large variation (run-of-river type) or when the electricity demand is highly fluctuating [136]. The present work focuses on the study of transient operation for the Francis-turbine power plants. Particular attention will be given to unsteady flow effects in a single-machine station with a relatively short waterway conduit.

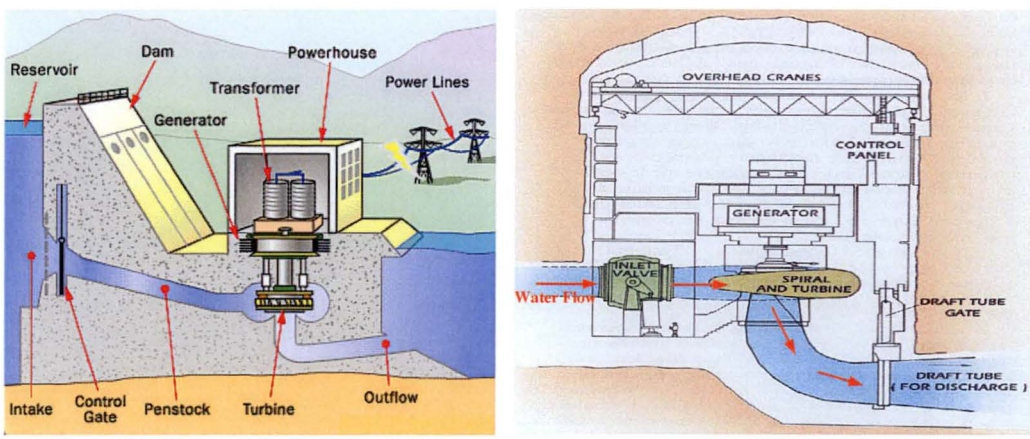

Figure 1.1: The schematic layout and the basic hydraulic components of a typical Francis turbine hydro power plant (adapted from references [17] and [112])

Figure 1.1 shows the basic layout of a typical hydroelectric generating plant with a single Francis turbine and a short waterway conduit. The water flow operating the Francis turbine is conveyed from an upper reservoir via a short water tunnel or a penstock. The water then flows through the Francis-turbine runner from a spiral casing, stay vanes and guide vanes (also known as wicket gates) before it finally discharges to the tailrace via an elbow draft tube. The electrical power is produced from a generator directly connected to the turbine shaft. The electricity is then transferred to the end user through the power systems. In general, a multiple-machine station operates in a similar manner to the single-machine station. To ensure the stability of the power system, a speed governor is often employed to monitor the frequency and the power output of an individual machine. The principles of governing Francis turbine operation will be reviewed in Chapter 2. A surge tank, which may be used to control water hammer in the conduit, is not shown in Figure 1.1. Travelling pressure wave effects are not significant in the short waterway conduit and are not the main concern of this study.

1.2 Motivation of the Investigations

The increasing interconnection of individual power systems into major grids has imposed more stringent quality assurance requirements on the modelling of the power plants. The hydraulic transient response of the hydroelectric generating plant must be accurately predicted to achieve stable operation of the power systems within specific tolerances. This is very important for the existing Tasmanian electrical power grid where most of the generating capacity comes from the hydraulic turbine plants. A review of the commonly used models for the hydraulic systems in the hydroelectric power plant is warranted to accurately identify and minimise transient stability problems. This work is motivated by several problems presented during the development of the turbine governor model for the design and study of the transient stability of the power plants.

Although most hydraulic turbines exhibit a nonlinear behaviour, linearised equations originally designed for implementation on the analogue computers are still widely used in the transient modelling of the Francis-turbine power plants. The linearised equations are only suitable for investigation of small power system perturbations or for first-swing

stability studies. The turbine characteristics vary nonlinearly with the speed, flow and the net head of the turbine. Such nonlinearities make the governing of the Francis turbine operation a nontrivial task, as the turbine governors designed for a particular operating condition may not work at all under other conditions. There is no guarantee that the closed-loop system will remain stable at all operating conditions and exhaustive stability analyses are needed if the linearised turbine models are utilised. However, simplifications of the nonlinear behaviour for the Francis turbines are no longer necessary with modern computing power. The present research seeks to improve the accuracy of existing industrial models for hydroelectric generating plant through the numerical and experimental flow modelling of the unsteady operation of the typical Francis-turbine draft tube, and more accurate representation of overall turbine performance characteristics. The hydraulic transient response of both single- and multiple-machine power plants will be analysed and described in detail in this thesis.

While extensive introduction on the steady-flow operation of the hydraulic turbines is currently available, relatively little is known about the transient-flow phenomena. The unsteady flow behaviour in the draft tube could easily affect the transient stability of the Francis-turbine power plant and modelling of the draft tube flow is therefore desirable in order to fully examine the dynamic behaviour of the hydro power plant. However, there remain great challenges in the simulation, visualization and analysis of the flow in the draft tube. The complex nature of the draft tube flow has hampered detailed flow investigations by both experimental measurement and numerical analysis. The swirl introduced at the draft tube inlet, streamline curvature, flow unsteadiness and separation, and the adverse pressure gradient caused by the diffusion and changing cross-sectional shape have complicated the study of draft tube flow behaviour. Each of these characteristics alone is known to be difficult to predict and measure accurately.

Although some recent publications [6, 7, 75, 92, 105, 107, 109, 118, 132] have started to investigate the unsteady-flow behaviour of the Francis-turbine draft tube, these studies are limited to the numerical simulations of the self-excited unsteadiness caused by the vortex rope and little effort has been applied to probe the externally-excited unsteadiness that results from the changes in the guide vane settings or the turbine operating conditions. Much effort is still needed to verify and validate the numerical solutions of the draft tube flow, even for a simpler steady-state calculation. This study

attempts to develop a more comprehensive data bank suitable for the analysis of the time-dependent draft tube flow near the best-efficiency operating condition. The prediction capacity of an existing commercial CFD (Computational Fluid Dynamics) code with different turbulence models will also be evaluated in this work. Attention is focused on the analysis of the transient fluid losses and the convective time lag in flow establishment through the draft tube, which are thought to be critical for the study of transient operation for the Francis-turbine power plants.

This research also aims to provide data for future plant refurbishments to improve the machine efficiency and the operating stability of a large number of ageing hydraulic turbine installations. The current refurbishment process that concentrates only on the redesign of the turbine guide vane and runner is insufficient, as unfavourable flow behaviour may occur if the new runner design and the draft tube are unsuitably matched. The deregulated energy market in Australia has called for the power plant operators to run their hydraulic machines more frequently at off-design conditions. The off-design performance of hydraulic turbines is strongly influenced by the unsteady flow behaviour of the draft tube. Although most hydraulic turbines are reasonably efficient, efficiency improvements of only a few tenths of a percent from the draft tube design can still generate substantially increased profits. This thesis therefore aims to gain further insights into the transient operation of the draft tube flow and its influence on the design and control of the hydro power plant.

1.3 Scope of the Study

This research commenced with an investigation of the deficiency in the existing industry model used to describe the hydraulic behaviour of Hydro Tasmania's Mackintosh power plant. Full scale measurement and computational modelling of the overall hydroelectric system were performed. The unsteady behaviour of the turbine draft tube and the pressure forces acting on it were later found to be the important factors affecting the accuracy of the existing model. To further examine this issue, a balanced approach consisting of both experimental and numerical modelling of the unsteady draft tube flow was carried out. Particular attention was paid to the transient operation of the single-machine station with a short waterway conduit. The improved plant model was developed based on transient analysis of the draft tube model, and was

validated against the Mackintosh test results. This single-machine model was also extended into multiple-machine model, which was validated against the full scale test results of the Hydro Tasmania's Trevallyn plant. This study had been bounded by several constraints, including:

- Modelling of Francis-turbine power plants in MATLAB Simulink [124] only. The complete analysis of the transient plant operation should incorporate both hydraulic and electrical models of the power plant and the results should be compared to various simulation codes in common industrial use. The full investigations of the entire power system and plant operation are performed by Hydro Tasmania and the study herein will only focus on the improvement in the hydraulic model of the Francis turbine plant.

- Experimental and numerical testing of the turbine draft tube only. The influences of the waterway conduit and the tailrace are not being considered in the modelling of the draft tube flow. Instead, the flow conditions without swirl are imposed at the draft tube inlet. Ideally the model should include the spiral case, stay vanes, guide vanes, and the runner as the impacts of the inlet swirl and the rotor-stator interactions could be essential for the analysis of the draft tube flow.

- Experimental and numerical testing of the draft tube with a predetermined geometry only. The chosen geometry models the Mackintosh power plant used in field studies. The effects of stiffening rib, the cross sectional shapes and the diffusing angle on the transient behaviour of the draft tube flow are not fully examined due to time constraints.

- Scaling effect of the model. Air is used as the working fluid in the experiments to facilitate measurements, but the model Reynolds number is about 100 times smaller than the full scale. Water model testing would have allowed operation at higher Reynolds numbers (around 12 times larger with similar flow rates) and given some indication of the magnitude of scale effects. The water models are required to observe cavitation effects in the draft tube, and also facilitate the observation of unsteady vortex rope phenomenon. However, logistical considerations and current resources preclude this.

- Limited computing resources. Approximately 12 million nodes are estimated to achieve the grid-independent solutions for the draft tube geometry used herein. This requires massive amounts of computing times and resources. Transient simulations with such numerical grids can easily take more than a month to finish, even though parallel solvers with multiple CPUs are adopted here. The majority of the computer simulations are therefore carried out with larger time steps and coarser grid.

1.3 Thesis Outline

The objectives and scope of the study have been stated earlier in this Chapter. A background survey of the literature relevant to this research is presented in Chapter 2. Transient operation of the Francis-turbine power plant is discussed and analysed in three separate Chapters. Chapter 3 details full-scale field testing of Francis-turbine power plants including the field-test procedures and the instruments used for both single- and multiple-machine tests. Chapter 4 examines the transient modelling of hydraulic components in a single-machine station. The computer model is validated against the full-scale test results conducted in the Mackintosh power station operated by Hydro Tasmania. Chapter 5 discusses the transient modelling of a hydro power plant with multiple machines in operation. The multiple-machine model is validated against the field test results collected in Hydro Tasmania's Trevallyn power station.

Phase lag problems identified in the above transient modelling exercises for Francis-turbine power plants have led to further detailed investigation of the unsteady flow effects of the turbine draft tube. Both experimental and numerical flow modelling of a Francis-turbine draft tube have been carried out. Chapter 6 summarises the experimental and numerical research methodologies used for the draft tube flow modelling. Experimental and numerical results are then presented in two separate Chapters. Chapter 7 contains the results of the steady-state operation that will be used as the initial conditions for the transient simulation of the draft tube flow. Chapter 8 gives the results of the unsteady draft tube flow under various transient operating conditions similar to the actual power plant operation at best efficiency with zero inlet swirl. Conclusions are drawn and recommendations for future studies are suggested in Chapter 9. Drawings of the experimental test rig can be found in the Appendix.

CHAPTER 2

LITERATURE REVIEW

2.1 Principles for Governing the Francis-Turbine Power Plant

Most electronic devices connected to an AC power system are sensitive to frequency variation. Precise control of the power plant operation is needed to fulfil safety and stability demands of the associated power system. To guarantee such requirements, the speed and pressure rises of Francis-turbine power plants must be regulated carefully. The speed governor is the usual means of controlling the operation of the hydro power plant. The main function of the governor is to change the generated power output and correct any error between the actual and the desired turbine speeds so that the system load is always in equilibrium with the generating unit output at the desired frequency (usually 50 or 60 Hz).

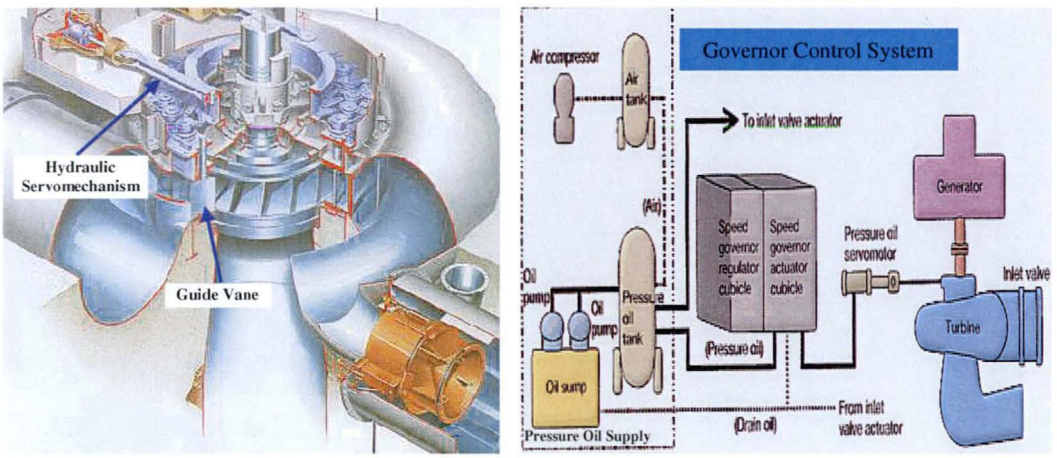

Figure 2.1: Hydraulic servomechanism and governor control systems of a typical Francis turbine hydro power plant (adapted from reference [86])

As illustrated in Figure 2.1, the governor uses a hydraulic servomechanism to control the guide vane movement, which in turn controls the amount of the water admitted to the turbine runner. In principle, the turbine speed tends to rise or drop when the electrical load is decreasing or increasing. The governor should respond to these changes by closing or opening the guide vanes (wicket gates) as fast as possible so that the mechanical torque generated from the turbine equals the torque offered by the electrical load on the generator, and the turbine should return to the desired generator synchronous speed within a specified time period.

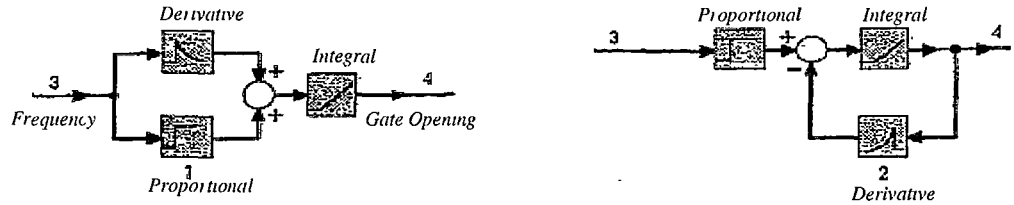

Figure 2.2. Simplified block diagrams showing typical stabilising elements of the turbine governors [45]

A good turbine governing system should be sensitive enough to deliver an acceptable speed of response for loading and unloading under normal synchronous operation. It must also be stiff enough to maintain a stable operation during system-islanding conditions or isolated operation. Speed governors for Francis-turbine power plants are generally of either mechanical-hydraulic or electro-hydraulic types. Both types consist of three basic elements [45]:

1. *Speed-sensing element* for detecting speed changes. To control the turbine speed, the governor must sense the system frequency and compare it to the standard (50Hz). For the mechanical-hydraulic governor, a flyball mechanism driven by a permanent magnet generator attached to the generator shaft is often employed to sense the change of the system frequency and correct it by adjusting the position of the flywheel mechanism. For an electronic-hydraulic governor, the system frequency is sensed directly from a potential transformer or an electrical amplifier attached to the generator and the frequency deviation is corrected via a transducer-operated valve.

2. *Power component* to operate the guide vanes and the speed control unit. As shown in Figure 2.1, the governor has a fluid-pressure-operated servomotor to move the guide vanes, a high-pressure oil supply to furnish the power for the action of the servomotor, and a distributor valve to regulate the oil pressure and flow of oil in the servomotor. The oil is pumped from the sump into an air-over-oil accumulator tank to maintain the required pressure. The pressure in the tank is controlled by the air compressor, which admits air into the tank to maintain the oil at the required level.

3. *Stabilising element* to prevent runaway speed in the turbine and hold the servomotor in a fixed position when the turbine output and the generator load are equal. Two stabilising methods are commonly used for the turbine governor. Figure 2.2 shows a simplified form of these two governor stabilising elements used for the control of

the hydro power plant. For the accelerometric governor, the servomotor is controlled both by an input proportional to the frequency deviation and by an input that is a measure of the turbine acceleration. These two inputs are summed and the acceleration signal is used to stabilise the control action. For the dashpot governor, the integrating pilot servomotor is controlled by a proportional frequency signal with an input of opposite sign that measures the time derivative of the guide vane movement. This input is used to damp and stabilise the control action. Theoretically, these two types of governors give exactly the same mathematical expressions for ratio between the gate deviation and the speed deviation [45]. However, the dashpot governor employs the "minor loop" stabilising principle, which is superior to the "series-equaliser" principle used by the accelerometric governor [45]. Hence many modern turbine governors are of the dashpot type.

To achieve optimal control performance of Francis-turbine power plant, proper tuning of the governor control parameters is needed. This can only be realised with an accurate model of hydraulic systems for the hydro power plant. Although a large body of proprietary information about the control and modelling of the Francis turbine operation exists, public domain knowledge on this topic is still very limited. The present study aims to address this shortcoming.

2.2 Transient Modelling of Francis-Turbine Power Plant

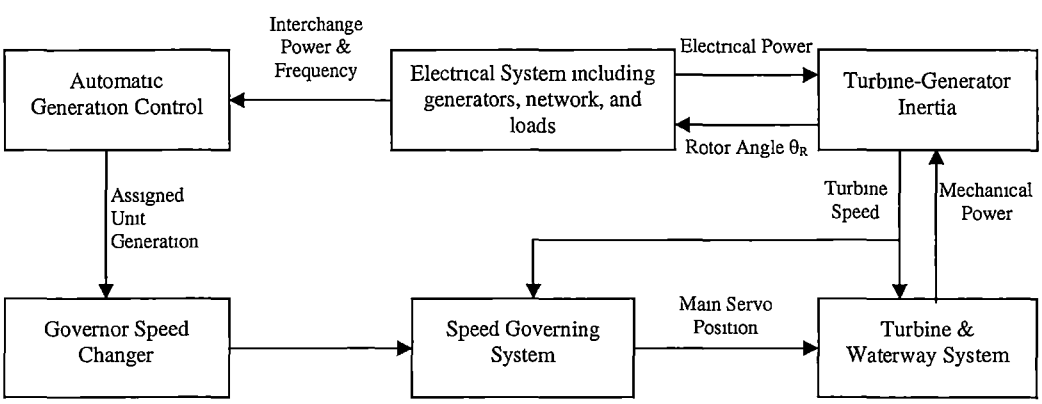

Figure 2.3: Functional block diagram showing the complete model of a hydroelectric power system

Figure 2.3 gives an overview of a complete power system utilising Francis-turbine plant. The dynamic model of the turbine and waterway system will be reviewed in detail here. Indeed, many different types of turbine and waterway models have been developed in the past to account for different applications. Some of the models consider

surge chamber effects or hydraulic coupling effects in multiple-turbine plants, others take into account either elastic or inelastic water columns, and many configurations include travelling pressure wave effects.

Chaudhry [21] and Streeter & Wylie [123] were among the first to develop a computer code simulating the hydraulic operation of a Francis-turbine power plant. The simplest hydraulic network (a turbine connecting to a reservoir via a pipe network) is modelled in their code but the electrical system is not considered in their models. The codes are designed only for a single case study and have not been thoroughly validated against the full turbine operation. Brekke and Li [18], on the other hand, use the structural matrix approach and a set of linearised equations to construct a more generalised model for a hydroelectric generating plant. This method has been used extensively for the investigation of small power system perturbations and has been applied to first swing stability studies (or frequency domain analysis). Ramey and Skooglund [96], 1973 IEEE Committee Report [47], Ye et al. [150], Malik et al. [71], and Kundur [59] investigate the dynamic behaviour of the hydro power plants with an ideal turbine and inelastic water columns. They all use the classical linearised turbine models, which relate the mechanical power deviation with the gate opening deviation at a particular operating condition, to represent the whole turbine performance. Sanathanan [111] develops an important method to obtain reduced order models for hydraulic turbines with long waterway conduits, and demonstrates that the first-order linearised turbine models are faulty, as they always show a stable and strongly damped transient behaviour even though the real system exhibits undesirable oscillations.

Jones [51] extends the application of the linearised model to the analysis of multiple-machine operation, concluding that single-machine operation has quite different hydraulic characteristics from the multiple-machine configuration. He suggests that the governor parameters must be tuned according to the number of operating machines in order to achieve the optimal control performance from a hydroelectric generating plant. The frequency response of the power station, which is important for the governor stability design, can be evaluated by injecting a sinusoidal signal into the transfer function of the linearised model [98]. The field test procedure designed to study the transient performance of such operation in the hydro power plant (Nyquist test) has been described in some detail by Rayner [99].

Although linearised models are widely used in the power industry, they are not applicable for time domain analysis, especially when the plant is subjected to a large frequency disturbance. Growing demand and competition for electric energy supplies has significantly increased the operating risk of power stations. The Tasmanian power plants, for instance, are nowadays operated closer to the capacity limits than in the past and a severe penalty is imposed on the power system operator if the generated power output fails to meet the fluctuating load demand. Hence, the transient modelling of the hydraulic systems in the power plant must be performed nonlinearly so that the plant performance can be accurately predicted. Linearised models were used in the past because of the lack of analytical tools to study the nonlinear equations, the absence of the control design tools for nonlinear systems, and the low computer power to implement the nonlinear models. These are no longer a problem with modern computer capacity and well-developed numerical methods to solve the nonlinear system.

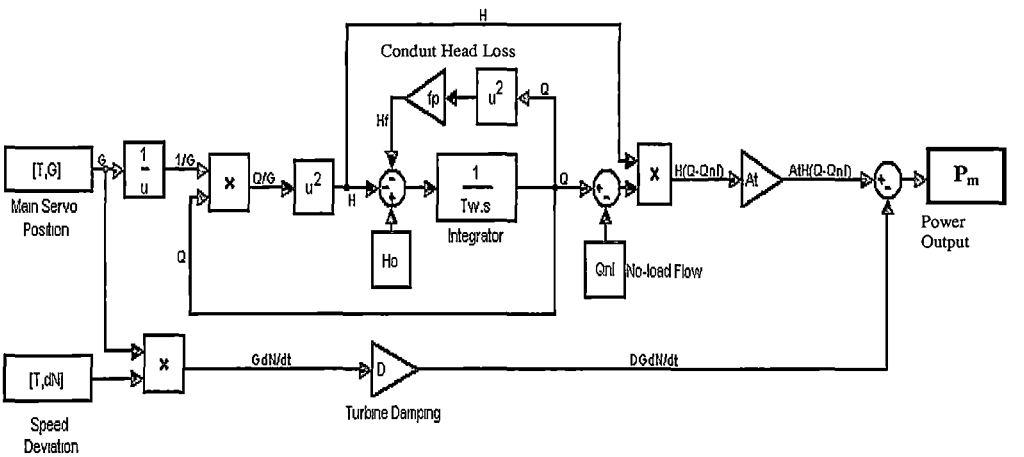

Figure 2.4: Simplified block diagram representing the 1992 nonlinear IEEE turbine and waterway model [141]

The development and derivation of simple nonlinear turbine and waterway models are presented in the 1992 IEEE (Institute of Electrical and Electronics Engineers) working group report [141]. The report presents both elastic and inelastic modelling of the hydraulic system in a hydroelectric generating plant. The formulation of this work is based on the application of one-dimensional Newton's second law and on the continuity equation. Many authors ([26], [58], [70], [138]) have used this IEEE model (see Figure 2.4) as a backbone for the simulation of the transient operation in the hydro power plant even though some serious drawbacks are found in this model. More discussion about the problems of this conventional model will be given in Chapters 4 and 5.

Nonlinear modelling is generally very useful for control and stability study of plant operation such as system islanding, excessive load shedding, and black start after power system restoration where large changes in power output or system frequency are expected [138]. Modelling of the electromechanical speed governor is usually well tested and is unlikely to cause any significant accuracy problem in the modelling of large system disturbance cases. Effective control of such operations will therefore rely heavily on the accuracy of the turbine and waterway model. Little information is available to validate this model, as large changes in the system rarely happen.

Nicolet et al. [85] indicate that the hydraulic model of Francis-turbine power plant can be improved by considering a pressure source driven by the hydraulic characteristic of the turbine instead of the pure resistance commonly used in the power-engineering domain to model turbine operation. The latest works of Nicolet et al. [85] attempt to include the unsteady vortex rope effect in the draft tube and the similitude of the pressure field along the draft tube extension in their in-house power plant simulation code SIMSEN. A linearised electrical analogy is still being used to illustrate the hydraulic components in their plant models. Two parameters are proposed to account for the wall deformation and water compressibility and for the vortex rope compliance [85]. Unfortunately, no simulation results have been given to validate this approach and more efforts are needed to evaluate the data transposed from scale model to prototype.

Up to the present time, no publications have considered the effects of unsteady turbine operation on the accuracy of the power system simulation. Although the influence of the unsteady flow behaviour has been recognised in the IEEE working group report [141], no further development has taken place to ensure the proper inclusion of this effect in the model. Vaughan [130] reports a significant phase lag between the simulated and measured power outputs from a single-machine power plant when the guide vane is oscillating at high speed. Travelling pressure wave effects should not be the cause of this observed phase lag since the waterway conduit is relatively short in this case. Instead, the transient flow behaviour of the Francis turbine is likely to be the source of this problem. The present work is the first step in an attempt to study the unsteady effects of the draft tube flow on the transient modelling of the Francis-turbine power plant using both experimental and computational fluid dynamic techniques.

2.3 Flow in the Francis-Turbine Draft Tube

The draft tube is the final passage of the Francis turbine where water is carried away from the turbine runner to the tailrace. The main function of the draft tube is to recover the kinetic energy in the flow and convert it to the pressure energy such that the overall efficiency of the Francis turbine can be improved. A brief history of the draft tube is given in references [37, 136]. Figure 2.5 shows the various types of draft tube being used in hydro power plant. The Francis turbine draft tube is usually of elbow type and consists of several sections that change its cross-sectional shape from circular to rectangular. It is generally beneficial for the diffusion and bending to take place over the shortest possible length simultaneously to avoid penalties in size and weight. It is also desirable to minimise the head losses in the draft tube and minimise the flow distortion at the exit to maximise the static pressure recovery. For highly efficient draft tubes, the cross-sectional areas are expanded in the streamwise direction such that the velocity is decreasing with minimum occurrence of vortices [136].

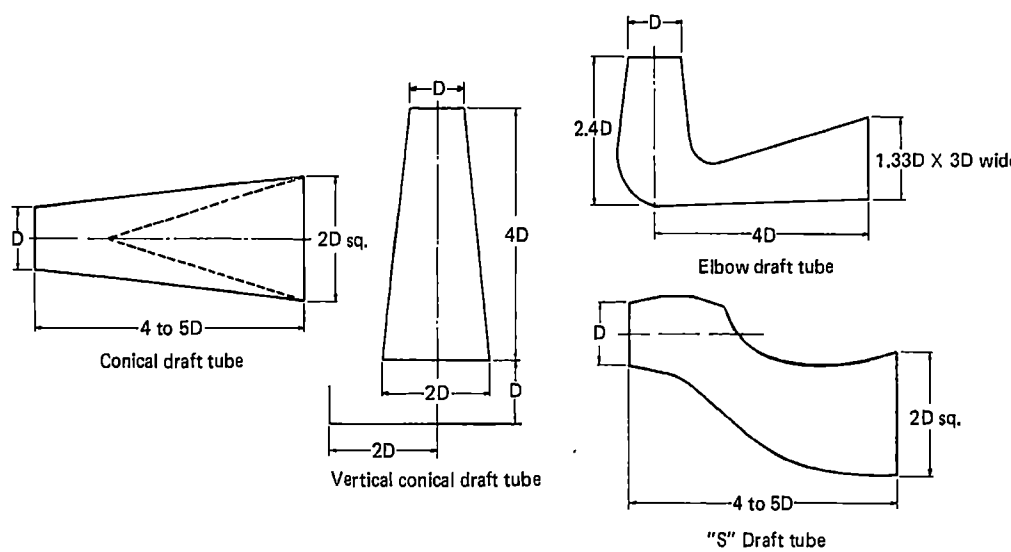

Figure 2.5· Different types of draft tube geometries used in the hydro power plants (adapted from reference [136])

DeSiervo and deLeva [27] provide some empirical formulas based on the specific speed and runner diameter to determine the leading dimensions of Francis turbine draft tubes. This can generally be used as a guideline for draft tube design but the final decision must be based on the detailed flow analysis in order to obtain the highest possible efficiency from the draft tube. Indeed, the flow in the draft tube is characterized by complex flow physics such as turbulence, separation, unsteadiness, swirl, backflow and

curved flow. All the flow phenomena present in the bend and straight diffuser will occur in the elbow draft tube, but will normally exist in a rather more extreme form [81]. Conversion of dynamic pressure to static pressure is therefore more difficult in an elbow draft tube than in a straight diffuser. An understanding of the draft tube flow physics will be helpful for the precise control and modelling of the power plant operation.

Fox and Kline [35] report a wide-ranging investigation of curved diffusing flow. The details of stall inception patterns for the axisymmetric curved diffuser are examined as a function of N/W_1 (axial length normalised on the throat width), β (turning angle) and 2θ (total wall divergence angle) [35]. Secondary flow in the form of a long helical roller is observed in curved diffusers with turning angles of more than 40°, and reasonable variations of the inlet velocity profile are found to have only a slight effect on the location of first appreciable stall [35]. The flow regime data of Fox and Kline [35] provide considerable insight into the fundamental problems associated with draft tube design, as the pressure recovery for the draft tube is closely related to its flow regime [35]. However, the effect of flow separation on the performance of curved diffuser is not detailed in this study.

Sagi and Johnston [110] present a systematic approach to the analysis of a two-dimensional diffusing bend. The streamline curvature is found to greatly affect the wall potential-flow velocity distribution and the existence of the secondary flow, as well as turbulent mixing near the wall (see also Parsons and Hill [93]). Sagi and Johnston [110] suggest that performance of a curved diffusing channel should be evaluated based on the potential-flow pressure distributions along the wall, since large changes in the secondary flow and turbulent mixing effects are usually difficult to obtain for a fixed geometry. A simple potential flow method is proposed for the design of a curved diffusing channel. Early designs of turbine draft tubes are mostly founded on the empirical data and findings given in Fox and Kline [35], and Sagi and Johnston [110].

The performance of a 90°-cascade diffusing bend with an area ratio of 1.45:1 for an aircraft duct system is studied in Friedman and Westphal [36]. Five different inlet boundary layers are used to examine the effect of inlet-boundary-layer shape and thickness on the performance of the diffusing bend [36]. Tests are made at Mach

numbers up to 0.41 and a cascade of airfoils are used to control the boundary layer at the bend. Results indicate that increasing the inlet boundary layer thickness will adversely affect the total pressure losses and static pressure recovery [36]. Increasing inlet Mach number is also shown to adversely affect the performance of the cascade in the diffusing bend. Vaned bends, however, are seldom used in water turbine draft tubes due to manufacturing difficulties, pressure forces and the possibility of cavitation in such applications.

The above publications neglect the strong curvature effects and the impacts of substantial variation in cross-sectional aspect ratio on the flow behaviour inside a diffusing bend. To understand the flow developments in such extreme geometry (which is the case for most draft tube geometries), Yaras [145, 146] has conducted a series of investigations for the strongly curved diffusing bend. Several aspects including the effect of flow turning on diffusion performance, the dominant structures influencing the flow development in such geometry and the effect of the inlet boundary conditions are examined [145]. The three-dimensional velocity distribution at the exit is found to be sensitive to circumferentially uniform alterations to the inlet boundary layer, while static-pressure recovery and total-pressure losses are observed to be relatively insensitive to variations of the inlet boundary layer [145].

Yaras [146] also mentions that the flow pattern within a strongly curved diffusing bend is similar to the one occurring in the constant-area bend. The secondary flows induced by a pair of counter-rotating vortices are found to reach maximum strength at about 30° into the diffusing bend and are significantly stronger for the case with a thinner boundary layer and lower free-stream turbulence intensity at inlet [146]. The difference between the actual and ideal static pressure distributions along the diffusing bend is primarily due to the total pressure losses with a thick inlet boundary layer, whereas the flow distortion and loss generation influence the streamwise static pressure distribution by comparable amounts for the thin boundary layer case [146].

Simonsen [119] performs a detailed flow survey in an axial-to-radial axisymmetric bend diffuser for a gas turbine system, concluding that the bend has an important influence on the flow in the diffuser and should not be neglected in the diffuser design as it can easily lead to poor performance or damage to the downstream equipment if not treated

properly. The boundary layer and the turbulent flow properties (particularly the development of Reynolds stress components) are examined in detail in Simonsen's research. The difference between the turbulence levels on the inner and outer wall perimeters is found to cause the wall normal mean velocity to be directed from the inner perimeter towards the outer perimeter of the diffuser [119]. This cross-stream flow is kept alive throughout most of the diffuser until turbulent diffusion has equalised the cross-sectional turbulence profiles [119]. The findings have been used to improve the boundary layer condition along inner perimeter so that flow separation is avoided. The flow in Simonsen's diffuser is generally less complex than that for Francis turbine draft tube because the flow is axisymmetric and the diffusion happens only after the bend.

Wahl [133] investigates experimentally the phenomenon of draft tube surge (see also Hosoi [44], Skotak [118]) and attempts to correlate the hill chart of the Francis turbine with different modes of draft tube vortex surging observed in experimental tests. The main objective is to identify the critical operating points where synchronous pressure pulsations, which cause severe vibrations, noise, fatigue failure and power swings in the power plants, may occur. A dimensionless swirl parameter ($\omega D_{Turb}/\rho Q^2$) has been used as an indicator for the existence of the twin vortex, which is an excitation source for the draft tube surging. However, Wahl [133] points out that the surge behaviour in the overload region is significantly different from that in part-load operation and the draft tube swirl parameter is still unable to fully explain the behaviour of the draft tube surge over the complete operating range of the Francis turbine.

Ruprecht et al. [108] examine numerically and experimentally the unsteady vortex rope behaviour in a draft tube under part load conditions. This causes oscillations in the waterway conduit and a discharge variation at the turbine admission (see also Dörfler [30], Vu et al. [132]). Dynamic behaviour of the waterway systems is taken into account using the one-dimensional method of characteristics [108]. Pressure at the draft tube inlet is averaged at each time step of the numerical simulation and this value is then fed into the one-dimensional model of the waterway system as a boundary condition [108]. The new discharge value obtained from the waterway model is used to update the inlet boundary condition of the draft tube in the numerical simulation [108]. Ruprecht et al. [108] indicate that a synchronous pressure oscillation of approximately 3% will cause about 1% variation in the turbine discharge. This case study assumes that the waterway

conduit is not in resonance with the draft tube surge. Otherwise, more severe pressure and velocity oscillations may result in the power plant [108].

Mauri [73, 75] explores the flow behaviour of a Francis-turbine draft tube from a different perspective. The mean flow field of the draft tube is analysed numerically and experimentally but the turbulence profiles are not fully examined. Mauri [73, 75] suggests using the topological structure of flow field to show the bifurcation with the flow rate as a parameter leading to a Werlé-Legendre separation, which can reduce the draft tube performance over an operating range [73]. The pressure recovery factor is found to be sensitive to the flow rate, which behaves in a similar way as the machine efficiency (i.e. the pressure recovery factor peaks at the full flow condition and then drops at overload operating conditions). A self-sustained time-dependent vortex shedding is observed numerically in some cases even though the boundary conditions remain unchanged. The mean flow field is not affected by this phenomenon [73].

At this stage, few studies have actually considered the unsteady flow effects at the draft tube. Mauri [75] presents a case of forced time-dependent draft tube flow where the fluctuations are caused by the runner rotation. A quick damping of the fluctuations, which is caused by an error in the prediction of the phase shift between velocity and pressure fluctuations, is observed numerically [75]. These fluctuations are however recognised to quickly disappear at the cone outlet during experiment. Similar statements are also made by Yang et al. [144]. Mauri [75] argues that computational error is mainly caused by the poor prediction of the flow unsteadiness and not the problems of turbulence modelling. This statement is questionable, since no detailed investigation is performed in his study to compare the turbulence quantities obtained from numerical calculations and experiments.

Yaras and Orsi [147, 149] conduct several tests to study the effects of the periodic-inflow unsteadiness on the flow development in a fishtail-shaped diffusing bend of strong curvature for gas turbine operation. When inflow oscillation condition is compared to the design operating condition, the time-averaged velocity field is found to be very similar to that obtained under steady inflow conditions with comparable inlet boundary-layer thickness [147]. A strong flow asymmetry caused by the difference in strengths of two counter-rotating streamwise vortices is also detected when the

frequency of the inflow velocity fluctuations is decreased. Furthermore, the transients in the ensemble-averaged velocity distribution at the diffuser exit are observed to decrease to negligible levels if a three- to fourfold increase in the frequency is imposed for the inflow unsteadiness [147, 149].

To the author's best knowledge, little or no study has been carried out on the unsteady flow effects of a Francis-turbine draft tube due to changes in flow operating condition. Most of the papers (including Mauri [75], Ruprecht et al. [108], Skotak [118], Vu et al. [132], Yaras & Orsi [147, 149]) that investigate the transient flow behaviour in the draft tube either concentrate on the self-excited unsteadiness caused by the turbulent motion, vortex shedding (Karman vortex street), and unsteady vortex rope in the draft tube, or focus on the externally forced unsteadiness resulting from changes of the inlet domain due to runner rotation. Although rotor-stator interactions in the turbine have been the subject of research for years, they are usually studied individually without taking the existence of draft tube into consideration. The moving-mesh technique for numerical computation is still at its early stage of development and is only usable when a very simple motion is applied on the geometry. Much effort is needed to make the solution more realistic. Applying transient boundary conditions is therefore the most effective method for such analysis. This thesis investigates numerically and experimentally the unsteady operations of the draft tube caused by changes of the turbine discharge. Emphasis is put on determining the time lag required to establish a new steady state in the draft tube after a change in inlet flow condition.

2.4 Experimental Testing

Although it has long been recognised that the flow in the hydraulic turbine is predominantly three-dimensional and unsteady, the approach to the design and development of Francis turbine power plant ignores most of these flow features. This approach is no longer appropriate for today's operating environments due to growing complexity of the power systems, which call for more precise control of the turbine operation. Such requirements can only be fulfilled through the more detailed flow modelling of the Francis turbine components. There are two basic approaches to model the unsteady flow effects in the Francis turbine draft tube, namely experimental testing and numerical modelling (CFD).

While numerical modelling offers the ability to study the evolution of the pressure and velocity fields inside the draft tube at less cost than the conventional experimental testing, experimental data for CFD validation is generally required. Mehta [77] defines validation as "an essential process of assessing the credibility of the simulation model, within its domain of applicability, by determining whether the right simulation model is developed and by estimating the degree to which the model is an accurate representation of reality...". Experimental testing may also reveal flow phenomena present in the actual flow for which the numerical model has no mechanism for prediction. Van Wie and Rice [129] also point out that "it becomes difficult to separate the validation of the measurement procedure from the validation of the analysis procedure. In this situation, the experimental and analytical techniques are intertwined in a single process".

Yaras [146, 147, 149] details the experimental model testing for a strongly curved diffusing bend (including both steady and unsteady flow measurements). The model with an area ratio of 3.42:1 is manufactured using CNC machining and an open-circuit wind tunnel provides the flow source for the tests. The boundary layer thickness at the inlet is established by adjusting the length of the entry pipe [146]. The steady-state flow field is measured via a miniature non-nulling seven-hole pressure probe (2.1 mm diameter) and a capacitive-type pressure transducer while the instantaneous velocity field is measured using a miniature hotwire probe with four tungsten sensors (of 1 mm long and 5 μm diameter) and a constant-temperature anemometer. A perforated plate mounted on a radial spoke in an alternating pattern is employed to generate the periodic inflow unsteadiness at various frequencies [147].

Simonsen [119] undertakes scaled model tests on an axisymmetric bend-diffuser geometry used for gas turbine operation. The model is made out of transparent plexiglass and the air is used as the working fluid in his experiments. Most of his measurements use the hotwire technique and the Reynolds number effects on the flow properties are investigated. The Reynolds stress components and the mean flow velocities at various sections of the diffuser are obtained using either 2.5 μm single-wire platinum-rhodium sensors or 5 μm cross-wire tungsten sensors. The static and total pressures are measured via linear response pressure transducers, while the skin friction measurements are performed using a surface Pitot tube. All the tests are accomplished at constant flow speed and no transient measurements are obtained in these experiments.

Andersson and Karlsson [2] discuss the experimental methods for the flow measurement in a 1:11 scale sharp-heel draft tube. Inlet boundary-layer control is not necessary in their case as the whole Kaplan runner is also included in the model. Water is used as the working fluid for the tests. The tangential and axial velocities at the draft tube inlet (and outlet) are obtained via Laser-Doppler Anemometry (LDA) but the radial velocity is not measured due to hardware limitations. The water is seeded with nylon particles to improve the LDA signal quality. The centreline wall pressures are obtained using a differential pressure gauge. Fluorescent dye is injected at various positions of the draft tube for flow visualisation. The model test results of Andersson [3] have been used extensively for CFD validation (Turbine 99 workshops [37]) but these do not include transient flow measurements.

Arpe and Avellan [6], Berca et al. [12], Vu et al. [132] and Mauri et al. [73] have investigated various aspects of the draft tube flow phenomena in the same Francis turbine model (1:10 scale) at the laboratory of EPFL. The model consists of stay vanes, guide vanes, runner and the draft tube (with transparent inlet cone). However, the waterway conduit and the tailrace are not included in their test facility. Laser-Doppler anemometry (LDA) and particle image velocimetry (PIV) are used to measure the velocity and turbulence fields at draft tube inlet and outlet. The water is seeded with spherical silver coated glass particles of 10 μm diameter to reduce the LDA acquisition time. A miniature five-hole pressure probe is employed for instantaneous velocity surveys at other locations of the draft tube. Unsteady wall pressure measurements are carried out using fast response pressure transducers (frequency response up to 51.2 kHz) while wall friction measurements are performed with a hot-film probe. Although unsteady flow measurements are conducted in their laboratory, the transient flow effects generated by the changes in the guide vane positions are not investigated at all and the tests are completed at fixed guide vane settings.

Wahl [133] tests a 1:40.3 scale model, consisting of the penstock, guide vanes, runner, draft tube and the tailrace. Although the complete hydraulic system is modelled in Wahl's experiments, no detailed pressure and velocity surveys are carried out in his tests. The amplitude and frequency of the pressure fluctuations at the draft tube inlet under different operating conditions are the only data being recorded [133]. The

analyses are centred on the visualisation of the vortices in the fibreglass draft tube. Wahl [133] points out that the results obtained from this water model are essentially identical to those from the air model (conducted by his predecessors). The study gives some fundamental insights into the complex nature of the draft tube flow and illustrates the difficulties in performing accurate measurements for such a large-scale facility.

Rayner [99] details the field test procedure (including the governor response test) to examine the transient behaviour in a full-scale Francis turbine power plant. The lack of suitable fast-response pressure transducers for the full-scale machine and the complexity involved in the installation of new pressure tappings on an existing draft tube preclude detailed flow surveys during the field tests. Although some wall pressure measurements at the draft tube inlet are recorded, the data may not be suitable for transient flow analysis as the frequency response of the pressure transducer used in the tests is quite low. Hence, the present study that employs wind-tunnel based experimentation using a scaled draft tube model and the pneumatically controlled vane systems are thought to be a more realistic and efficient approach to examine the unsteady flow effects in a Francis turbine power plant.

2.5 Computational Fluid Dynamics (CFD)

Computational Fluid Dynamics (CFD) methods have been widely used in the power generation industry for decades. Extensive literature on CFD studies of the hydraulic turbine draft tube can be found in numerous fluid mechanics publications (e.g. Avellan [9], Bergström [15], Drtina et al. [31], Engström et al. [33], Gebart et al. [37], Mauri [75], Rudolf and Skotak [105], Ruprecht [108], Shyy and Braaten [114], Vu et al. [132], Yang et al. [144] and Yuan and Schilling [151]). Large eddy simulation (LES) and Reynolds-averaged Navier-Stokes (RANS) code are two general numerical approaches used for such application. Three-dimensional viscous and turbulent solvers are often employed in these studies, as the potential flow analysis (or Euler codes) fail to fully describe the complex behaviour of the draft tube flow.

Gebart et al. [37] organised the first ERCOFTAC workshop to systematically investigate the limitations and the problems faced in the steady-flow simulation of a standard draft tube at a particular operating condition using different codes and

techniques. Many insights can be gained from this workshop, even though only the steady flow calculations are reported here. The experimental inlet velocity profiles (tangential and axial components) and the outlet wall pressures have been supplied as the boundary conditions for the simulation. The contributions to the workshop are based on simulations with nine different commercial and three different in-house CFD codes. The methods include finite element, structured multi-block finite-volume and unstructured finite-volume methods. Some useful findings from these simulations are summarised as follows:

- Bergström [15] uses the block-structured code CFX-4.2 with the Reynolds stress model for the simulation. The grid error is evaluated using the general Richardson extrapolation method (see also Avellan [9]) while the iterative error is assessed through the investigation of the residuals for all flow variables. However, the attempt to use pure Richardson extrapolation is unsuccessful in this case since the asymptotic range is not reached for the grid sequence used. The coarse grid and the poor iterative convergence for the Reynolds stress are thought to be the reasons for not reaching the asymptotic range. Bergström [15] recommends that a transient simulation should be carried out for further investigation and the unknown radial velocity (and its fluctuation) at the inlet should be resolved in order to get a more realistic solution.

- Kim et al. [54] and Lai and Patel [62] use the same grid with two different finite-volume codes (Fluent and U^2RANS) and they obtain almost identical results from the simulations. A mesh dependency test is performed through the visual inspection of the flow field at a particular section of the draft tube (after the bend) [62]. A mesh size of about 708000 cells is selected for the final calculation since no obvious changes in the flow features are observed for this mesh. The numerical results are found to be insensitive to the exit location. However, this is not always true as the outlet boundary location may affect the convergence and stability of a numerical solution when the strongly recirculating flow occurs at the outlet. No significant difference is found in the prediction of flow field inside the draft tube for both k-ε and k-ω turbulence models tested (except for slightly higher pressure recovery and energy losses predicted by k-ε turbulence model).

- Page and Giroux [91] find that the results generated from the finite element (FIDAP) and finite volume (CFX-TASCflow) codes are quite different even though the same turbulence model (standard k-ε) and the same grid size are applied in the simulation. The grid error is examined by comparing the centreline velocity profiles at different sections of the draft tube using two different mesh densities. The steady-flow solution is observed to be sensitive to the radial velocity distribution (which can increase the pressure recovery factor by 15% if included in the inlet boundary condition), while the turbulence dissipation at the inlet and the discretization scheme are found to affect the "shape" of the centreline velocity profile noticeably.

- Longatte et al. [67] compare results using the finite-element (N3S) and the finite-volume (Fluent-UNS) codes. Unstructured tetrahedral meshes with different grid sizes are employed (but a grid sensitivity test is not performed) and the predicted flow fields from these two codes are found to be quite different. The variation is thought to be caused by different approaches used for the near-wall treatment. Longatte et al. [67] also check the impacts of the outlet boundary location by adding a tank at the draft tube outlet, concluding that the outlet conditions have little influence on the steady-flow solution for the draft tube.

- Komminaho and Bard [57] perform unsteady calculations with different time steps using Fluent-5 and a realisable k-ε model, and conclude that an unsteady vortex in the inlet region can cause convergence problems in the steady-flow solution. Staubli and Meyer [122] conduct similar quasi-unsteady simulations using CFX-TASCflow and a standard k-ε model. Their attempt to study Reynolds number effects fails, as the inlet boundary layers of the prototype are different and not known in this case. The impacts of the unsteady flow behaviour on the draft tube performance are not discussed in detail in these papers and the transient simulation is conducted merely to explain the possible causes of the poor convergence in the solution when steady-flow solvers are used.

- Lörstad and Fuchs [68] estimate, based on physical arguments, the grid size necessary for a satisfactory LES simulation of the draft tube flow in a finite-element program SPECTRUM. A mesh size of about 4 million and a time step of around

0.002 second are necessary to properly resolve all length scales of LES [68]. However, no attempt has been made to perform a serious LES based on these estimates due to the lack of adequate computational resources. Three different combinations of inflow boundary conditions are tested and the Reynolds number dependency is investigated. However, no firm conclusions can be made at this stage due to large variations of the results, the unknown fluctuating part of the inflow boundary conditions and the relatively coarse mesh being applied in this analysis. Similar problems are reported by Yang et al. [144].

- Clerides and Jones [22], Grotjans [39], Komminaho and Bard [57], Kurosawa et al. [60], Lörstad and Fuchs [68], Ma et al. [69], Skotak [117], Skåre et al. [116], Staubli and Meyer [122] and Thakur et al. [125] discuss their results based on single-grid calculations. Although the importance of grid convergence is constantly cited in these papers, none actually undertake a grid sensitivity analysis. It is difficult to draw any general conclusions under such situation of what turbulence model is most suitable for draft tube simulation and which boundary condition is most stable when no proper grid sensitivity analysis has been carried out. Grid convergence study should be standard practice in all CFD analyses and are required, for instance, by ASME Journal of Fluids Engineering, International Journal for Numerical Methods in Fluids, and AIAA journals. It is no longer adequate to publish results performed on a single fixed grid (Wilcox [140], Roache [103]). Rumsey and Vatsa [106] state that "mesh refinement...can sometimes lead to dramatically different results, particularly for 3-D separated flow " (one of the important flow phenomena in the draft tube). Grid improvements are usually required to accurately model the surface shear stress, which is another important variable used to study the losses in a turbine draft tube.

- It has been demonstrated in the First ERCOFTAC workshop [37] that small alterations (especially the inlet boundary condition, turbulence model and the mesh density) in the numerical set-up could lead to large discrepancies in the final results. Different users solving the identical problem with the same numerical code can easily end up with varying results. User experience still plays an important role in the CFD simulation. A remark taken directly from Roache [103] is probably worth repeating here. "No one believes the CFD results except the one who performed the

calculation, and everyone believes the experimental results except the one who performed the experiment". This statement clearly emphasizes the need for extensive verification and validation for both numerical and experimental modelling of the draft tube flow.

To provide more consistent reporting of the results for numerical simulation of the draft tube flow, the grid and the material models are fixed in the second ERCOFTAC workshop organised by Engström et al. [33]. Several interesting findings from the workshop participants are listed below:

- Bélanger [11] uses the commercial code PowerFLOW for large eddy simulations. The approach is based on the kinetic energy of gases and the special discretization of the Boltzmann equation (instead of solving the RANS equations). The boundary condition at the wall is realised via a flux formulation according to the kinetic process while the RNG based k-ε model is used to represent the dynamics of sub-grid turbulence in the flow [11]. Simulations with two different grid sizes are performed but no details are given to show the grid convergent solution.

- Cervantes and Engström [20] employ the finite-volume code CFX-4 and the standard k-ε model to evaluate the influence and the interaction of the surface roughness, the inlet radial velocity and the inlet dissipation length scale on the important flow variables used for draft tube analysis. The inlet radial velocity distribution is found to be the most critical parameter influencing the pressure recovery and energy loss coefficient of the draft tube, while the dissipation rate at the inlet changes the flow variables only slightly. The surface roughness is observed to affect the total losses in the draft tube, but not the pressure recovery factor (22% change in the loss coefficient but only 3.3% for the pressure recovery factor if surface roughness increases from 0 to 200 μm). Hence, the near-wall flow should be carefully modelled to ensure an accurate prediction of draft tube losses.

- Jonzén et al. [50] use the unstructured finite-volume code Fluent 6 and the standard k-ε model to investigate the influence of wall adjacent cells (or Y^+ value) on the steady-flow calculations. A 1.8% variation of Y^+ value at the inlet wall is observed

to significantly increase the static pressure and wall shear stress at the inlet, but the effects are gradually decreased towards the outlet of the draft tube (and thereby generate a distinct pressure recovery factor). Apart from this, no major difference is found between the flow patterns for varying sizes of the wall adjacent cells used in the simulation.

- Shimmei et al. [115] compare the results of different turbulence models (standard k-ε model, Speziale's quadratic nonlinear k-ε model, Suga's cubic nonlinear k-ε model and LES) based on the single grid calculation. The nonlinear k-ε models are found to generate similar solutions if compared with the time-averaging results of LES, which is expected as the turbulence in the draft tube is highly anisotropic. However, it is impossible to tell if the numerical error is caused by the isotropic assumption of the turbulence models or insufficient grid resolution as a grid convergence study is not conducted in the simulation.

Hellström [43] use CFD to redesign the shape of an existing draft tube in order to improve the pressure recovery factor. Both steady and transient simulations are performed in CFX 5.7 with the standard k-ε and SST turbulence models. A maximum of 6.2 million unstructured tetrahedral cells generated by ICEM CFD is used for the numerical investigation. Computational analysis of the modified geometry by Hellström [43] indicates that the improvement in pressure recovery between the original and the modified geometry is small, which does not agree with experimental results. However, he points out that his grid quality is questionable (mesh sensitivity test are not performed) and the simulations using the Shear Stress Transport (SST) turbulence model are not converged even though many different numerical settings are tried. This is in line with the current author's experience for ICEM CFD and CFX 5.7. ICEM CFD employs an Octree unstructured meshing algorithm that does not work well with geometry having sliver surfaces and small angles, while the CFX mesher is unable to cope well with the "bumpy" surface mesh generated in this case. The use of unstructured hexahedral mesh should overcome this problem.

Rudolf and Skotak [105] conduct a numerical investigation of the unsteady self-excited vortex flow in an elbow draft tube using Fluent-5.4. Both inviscid and Reynolds stress

models have been used to examine the effect of dissipation on the draft tube vortex flow. The inviscid model is shown to predict the vortex rope dynamics fairly well in the region of inlet cone, but the solution becomes unrealistic downstream of the elbow due to the lack of the damping offered by the inviscid model. Hence, Rudolf and Skotak [105] comment that "using Reynolds stress model (RSM) appeared to be the best approach to simulation of turbulent unsteady flow in draft tube, although it was very time consuming". However, no details for verification of the calculations are given to show the effects of the varying boundary conditions and turbulence models. Time step and grid sensitivity tests are not mentioned at all in their works, which calls into question their statements that "the pressure pulsations at the draft tube inlet are not smooth sine waves but a superposition of two sine waves". Identical problems are also found in the work of Vu et al. [132]

Shyy and Braaten [114] examine numerically the effects of inlet swirl on draft tube performance, concluding that the strength of the inlet swirl will affect the overall pressure recovery factors and increase the non-uniformity of the exit velocity profiles. Two discretization schemes (hybrid and second-order upwind) are studied in detail with two different grid densities. Drtina et al. [31] employ a similar grid to investigate the impact of a stiffening rib in the draft tube. Although two different grid systems are used in the simulations, they do not discuss the influence of the grid densities at all, but only state that "many of the salient features observed on the fine grid system are smeared out on the coarse grid system". The lack of measurement data for turbulent quantities to validate the numerical calculations also limits the credibility of the results in this case.

Simonsen [119] undertakes both grid sensitivity analysis and experimental validation of numerical flow modelling for an axisymmetric curved diffuser using Fluent-6. The inlet and outlet boundary locations are extended some distances away from the original geometry to avoid the influence of the upstream bend effects and downstream reversed flow effects on the numerical solutions. Three different (hexahedral) grid densities are tested in conjunction with different turbulent models (Spalart-Almaras, standard k-ε, RNG based k-ε, realisable k-ε, and Reynolds stress models). A grid convergent solution is obtained via inspection of the variation of outlet velocity profiles caused by changing grid sizes. The Reynolds stress model is found to predict the pressure recovery factor and the turbulent kinetic energy most accurately but the model performs less well in the

predicting the skin friction distribution and the "shape" of the mean flow velocity profiles if compared to RNG based k-ε or realisable k-ε models. Simonsen [119] is unable to clearly explain the cause of this problem, but points out that the inlet boundary conditions (Reynolds stress components and the turbulence dissipation) and the near-wall treatment could well affect the accuracy of the Reynolds stress model.

Paik et al. [92] use an in-house CFD code to compare the solutions generated from unsteady Reynolds-averaged Navier-Stokes (URANS) simulations and detached-eddy simulations (DES). They conclude that the flow in the draft tube is highly unsteady even without imposing any kind of explicit unsteady forcing at the inlet. Significant discrepancies between the DES and URANS predictions of the turbulence statistics are observed in the straight downstream diffuser. Both URANS and DES predictions capture the onset of complex large-scale flow instabilities in the draft tube and yield mean velocity profiles in reasonable agreement with measurements. However, mesh dependency tests are not performed in their work and further detailed flow measurement is required to fully assess the performance of various unsteady statistical turbulence modelling strategies.

To the best of the present author's knowledge, no papers on the CFD analysis of draft tube flow have given a clear approach to the systematic refinement of near-wall elements. Most authors determine their grid independent solutions based on a fixed Y-plus value or a constant wall distance. Although Bergström [15] and Mauri [74, 75] have both utilized the Grid Convergence Index (CGI) and Richardson extrapolation methods to systematically refine the mesh and uniformly report the grid convergent solution, they do not detail the methods of refining the near-wall mesh when the wall function is also used in the simulation. In fact, the use of wall functions actually prevents the grid from being refined uniformly and systematically near the wall. The current study finds that refining the near-wall mesh can easily produce a huge difference in the solution and should therefore be considered in the grid sensitivity analysis.

In summary, CFD solutions of the draft tube flow are significantly affected by many factors such as boundary conditions, turbulence models, grid densities and the numerical approaches used in the flow modelling. The current study uses the total pressure rather than the experimentally derived velocity profiles (which have been

implemented by most of the papers found) as the inlet boundary condition in the numerical modelling of the draft tube flow. Extensive verification and validation must be performed before the results can be used with confidence in the design process. This is particularly true in the present work, as no papers have been found to address the issues of verification and validation for the transient flow simulation of the draft tube.

CHAPTER 3

FIELD TESTS FOR FRANCIS-TURBINE POWER PLANTS

3.1 Overview

A field test program was developed for the single-machine testing conducted at Hydro Tasmania's Mackintosh power station as well as the multiple-machine testing performed at Trevallyn power station. The main objective was to investigate experimentally the transient response of the Francis-turbine power plants when the system frequency or the electrical load is fluctuating. The tests provided useful data to validate the hydraulic models, to identify the model parameters for individual power plants, and to investigate the stability of a power plant. The major components of the field test program were steady-state measurement, frequency deviation tests and the Nyquist tests. This Chapter describes the general instrumentation and test procedures used for both single- and multiple-machine tests. Figure 3.1 shows a schematic of the locations and types of instrumentation used in the field tests of a Francis-turbine power plant. The analysis of test results and their comparison with simulation results generated from MATLAB Simulink will be covered in Chapters 4 and 5.

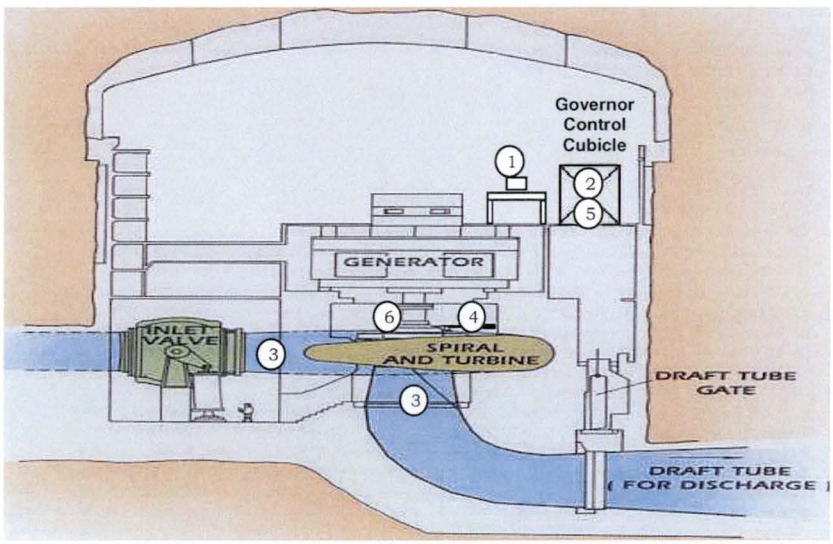

① Data Acquisition Tools
② Generator Frequency Transducer
③ Pressure Transducer
④ Servomotor Position Feedback
⑤ Three-phase Wattmeter
⑥ Strain-Gauge Torque Sensor

Figure 3.1: Locations and types of instrumentation used in the field tests of a Francis-turbine power plant

3.2 Instrumentation

3.2.1 Data Acquisition

Data acquisition tools varied slightly depending on the number of channels needed to record the test results. Field test data were acquired automatically and simultaneously via the commercial software package, LABVIEW 6 running on an IBM-compatible laptop computer interfaced with a PCMCIA National Instruments data acquisition card. Since simultaneous sampling of more than 10 data channels was required for multiple-machine testing, an Iotech WaveBook high-speed data acquisition system (see Figure 3.2) was also used during the tests. The WaveBook system consists of a WBK16 8-channel, 16 bit signal-conditioning module and two WBK10A 8-channel analogue expansion modules. The gain amplification, high-pass AC coupling and low-pass noise rejection filtering of each channel were configured via the built-in software WaveView (version 7.1.2.5). The strain gauge bridge of the signal conditioner was balanced automatically to remove the static portion of the strain load and the inputs were zeroed to compensate for any input drift to the system. Typical sampling rate was 2~10 Hz.

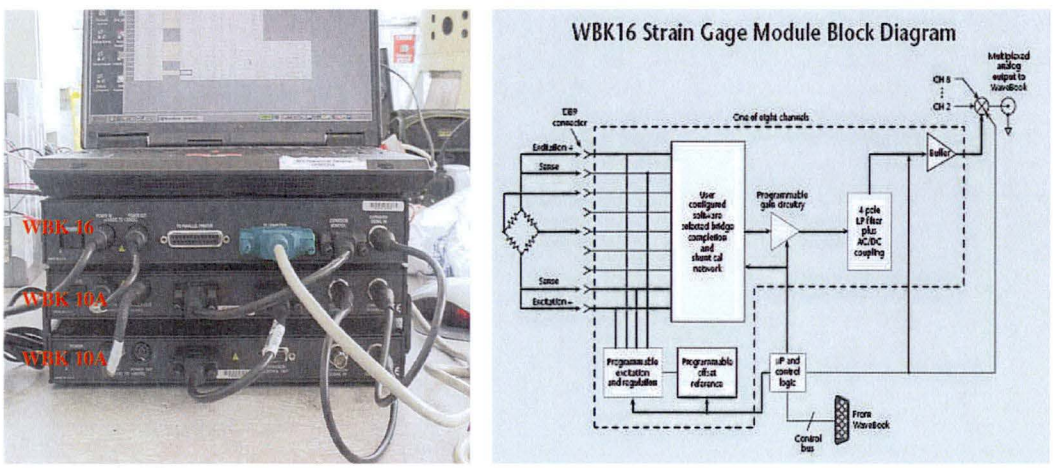

Figure 3.2: WaveBook data acquisition system (one WBK16 signal conditioning model and two WBK10A analogue expansion modules) used for simultaneous data sampling at Trevallyn power station

3.2.2 Water Temperature

A CENTER-305 portable data logger with a K-type temperature sensor was used to monitor the water temperature in a Francis turbine. The manufacturer's specified accuracy of this unit is ±0.2%+1°C. The temperature was recorded manually by taking a few samples from the piezometer tap located at the draft tube and the spiral case. The variation of water temperature was found to be insignificant during the tests.

3.2.3 Turbine Rotational Speed

A DATAFORTH DSCA45 frequency input module was used to monitor the turbine rotational speed. The generator frequency was measured instead of the actual rotational speed of the turbine runner since the generator magnet attached to the turbine shaft rotated at exactly the same speed as the turbine runner. To improve signal integrity, DSCA45 isolates the zero-crossing voltage signals from generator during the test and converts these signals to an industry standard current output (4~20 mA). The block diagram of DSCA45 is shown in Figure 3.3. For recording purposes, the current output is converted to an analogue voltage output (0.8~4 V) using a 200 Ω precision resistor. The DSCA45 unit has a special input circuit that protects the system against accidental connection of power-line voltages up to 480 VAC and reduces the transient events as defined by ANSI/IEEE C37.90.1. The DSCA45 also has excellent stability over time and does not require frequent recalibration, which makes it ideal for complex field tests of hydro power plant. The manufacturer's specified accuracy of DSCA45 is ±0.05% of span, including nonlinearity, hysteresis, and repeatability.

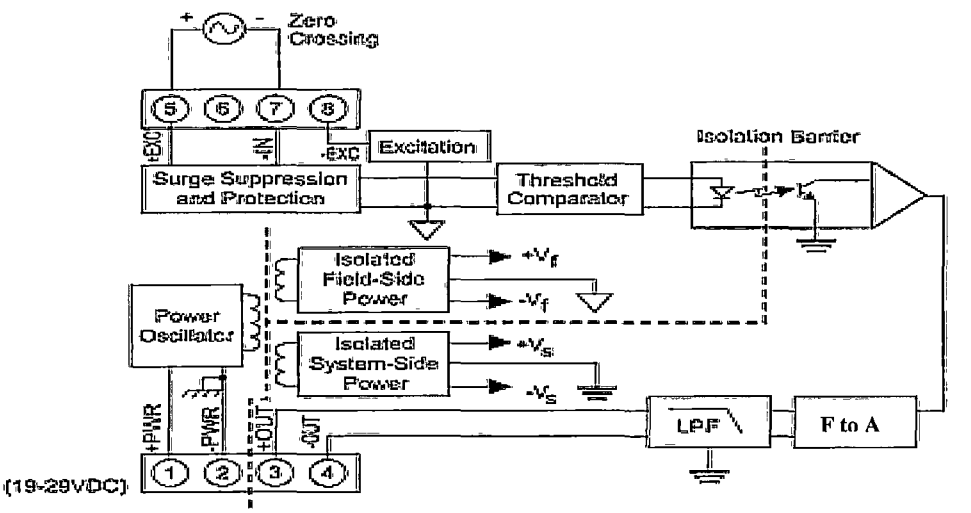

Figure 3.3: Block diagram of the DATAFORTH DSCA45 frequency input module connected to a generator bus-bias at Trevallyn power station. The current output from DSCA45 will then be converted to an analogue voltage signal using a 200Ω precision resistor

3.2.4 Static Pressure

The static pressure at the spiral case entry (to determine the net turbine head) was measured using a DRUCK PTX1400 gauge pressure transducer (pressure rating>12.5 Bar). The static pressure at the draft tube inlet was monitored with a DRUCK PTX1400

absolute pressure transducer (pressure rating>2Bar). Typical accuracy of the PTX1400 is ±0.15%, including nonlinearity, hysteresis and repeatability. Each transducer provides a 2-wire 4-to-20 mA current output proportional to applied pressure. 100 Ω precision resistors are used to convert the current output to analogue voltage output (0.4~2 V) for recording purposes. All pressure transducers were calibrated against a dead-weight calibrator. Zero readings were recorded at the start and the end of each test to minimise errors from thermal drift in the electronics.

Figure 3.4: Druck PTX industrial pressure sensor used to measure the static pressure at entry of the spiral case and draft tube of a Francis turbine

3.2.5 Main Servo Position

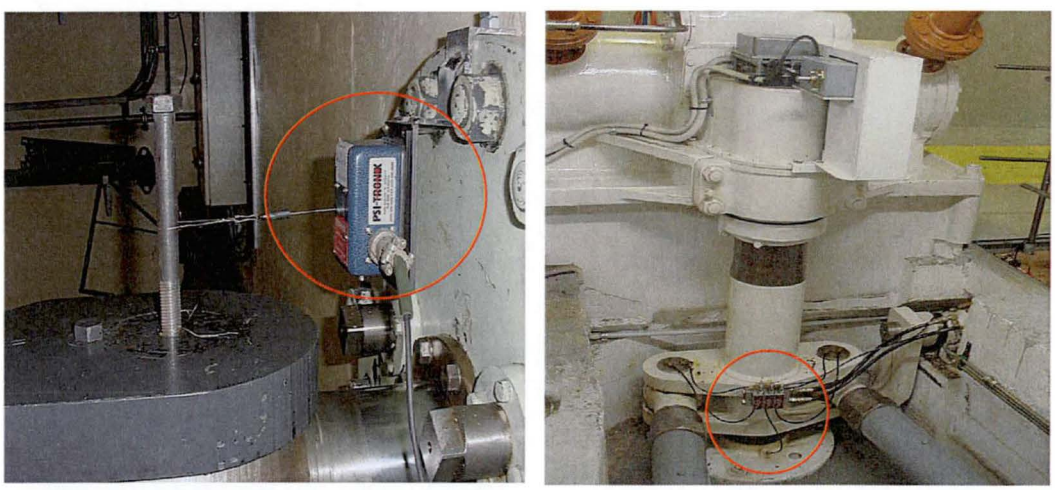

Figure 3.5: PSI-Tronix displacement transducer (left) and GEC-Alston C651B servomotor position feedback transducer (right) used to measure the position of the main servo that control the opening of turbine guide vanes

The main servo position determines the amount of guide vane opening for a Francis turbine. A PSI-Tronix DT420-10 string transducer attached to the servomotor piston rod was used to sense the main servo position for the single-machine station. Four GEC-Alston C651B servomotor position feedback transducers were employed for the

multiple-machine station. Different transducers were used for the multiple-machine testing because they were already installed in the power plant and could easily be connected to the data acquisition system. Standard accuracy of the displacement transducer is ±0.1% F.S. The servomotor stroke was calibrated over the entire operating range from markings on the main servo connecting rod before the field tests commenced. In general, the fully closed position of main servo can be defined in several ways:

- Penstock is empty, governor actuator is fully closed, but no governor "close" signal applied.
- Penstock is empty, governor actuator is fully closed, and with governor "close" signal.
- Penstock is full, governor actuator is fully closed, but no governor "close" signal applied.
- Penstock is full, governor actuator is fully closed, and governor "close" signal is applied.
- Indicator on main servo link reads "0".
- Governor actuator dial reads "0%".

There is no significant difference between these definitions. To prevent confusion, the first statement was always used to describe the fully closed position. The fully open position of the main servo was defined in a similar way. When the governor actuator is fully open and the penstock is empty, the actuator dial reads "97%"; this position is defined as 97% open.

3.2.6 Electrical Power

The active power output of generating unit was measured by a high accuracy three-phase wattmeter, consisting of an AC voltage transducer and an AC current transducer in the same box. The wattmeter was connected to a station telemetry circuit. Larger current signals of 4000 A were stepped down to approximately 5 A through a current transformer, while larger voltage signals of 11000 V were stepped down to about 110 V via a voltage transformer. The transformed voltage and current signals of all three phases were input to the wattmeter to determine the active power. To record the signal, a standard 4-to-20 mA current output was produced from wattmeter and converted to an analogue voltage output (0.4~2 V) using a 100 Ω precision resistor. Wattmeters were calibrated on site and all wire connections were checked carefully prior to the tests.

3.2.7 Mechanical Power

It is important to measure the mechanical torque (and power) variations of the turbine shaft when the machine is in a transient state due to starting-up or load rejection/ acceptance. This is done to identify the impacts of the electrical components on the transient response of the Francis-turbine power plant. The measurements of mechanical power were conducted at one of the machines in Trevallyn power plant, using a TorqueTrak TT9000 strain gauge system [16]. A simplified block diagram of this system is illustrated in Figure 3.6. This approach overcomes problems with traditional methods such as slip rings or inline torque sensors, which can be cumbersome and costly. Bonding a torsion-sensitive strain gauge to the existing shaft eliminates the cut-and-fit requirements of an inline torque sensor and should be used whenever possible.

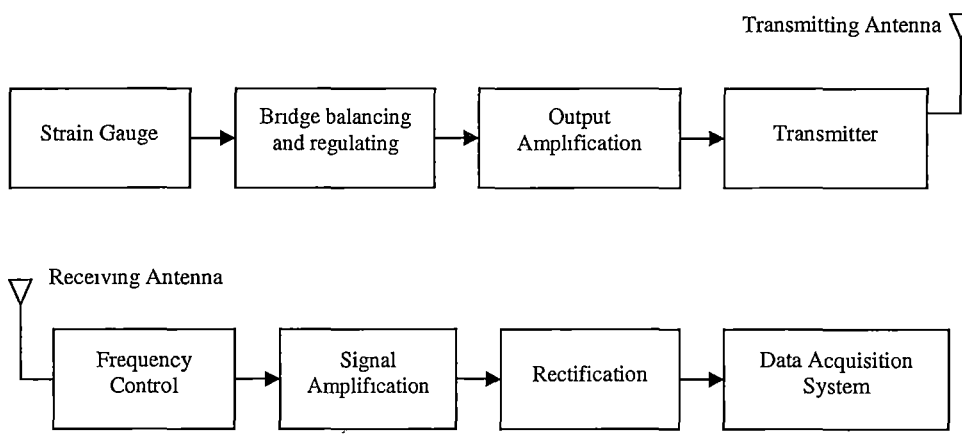

Figure 3.6: Simplified block diagram of TorqueTrak TT9000 strain gauge system used to measure the mechanical power generated from a Francis turbine. The system consists of a transmitting circuit and a receiving circuit [16]

As illustrated in Figure 3.7, a battery-powered digital radio telemetry transmitter strapped on the shaft transmitted the millivolt data signal wirelessly from the strain gauge to the data receiver, which was placed at about 2m away from the strain gauge. The voltage outputs from the strain gauge were then recorded by the data acquisition system. No machine disassembly was required. A single strain gauge (full bridge, 4 active arms) was used as the torque sensor. Mounting procedures of the strain gauge are well documented in TorqueTrak system manual [16]. The calibration of the strain gauge system was verified against a traceable voltmeter prior to the tests. The maximum frequency response of this system is 250 Hz and the manufacturer's specified accuracy is ±0.2% F.S.

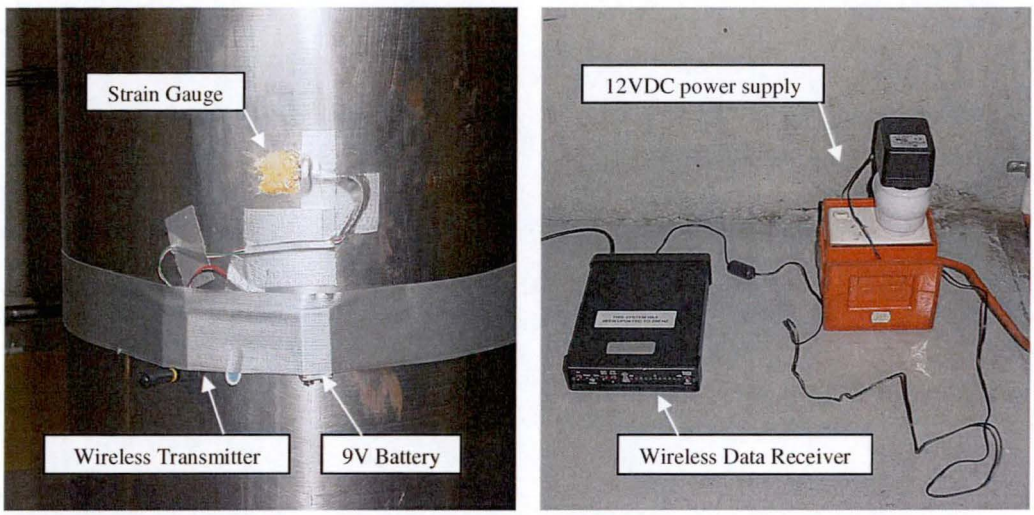

Figure 3.7: Strain gauge is bonded to the turbine shaft of machine no.3 at Trevallyn power station and it is connected to the transmitter via a cable. The battery-powered digital radio telemetry transmitter strapped on the shaft transmits the millivolt data signal wirelessly from the strain gauge to the data receiver

Equation 3.1 shows the relationship between millivolt output signal of the strain gauge system and the mechanical power. The calculations are based on material properties and diameter of the turbine shaft, sensor parameter (such as gauge factor), and transmitter gain setting. The values of the material properties for the Trevallyn turbine shafts were obtained from the previous tensile test results (Certificate C.12300 from Hydro Tasmania).

$$P_M = \frac{TN}{10^6} = \left(\frac{E}{1+\nu}\right)\left(\frac{\pi D_s^3}{16}\right)\left(\frac{Sscale \times V \times N}{10^6}\right) \tag{3.1}$$

where E = Young's modulus of elasticity of the shaft (GPa)

ν = Poisson ratio of the shaft

D_s = diameter of the shaft (m)

$Sscale$ = scaling factor for the transmitter (±250 for a transmitter gain of 4000)

V = millivolt data transmitted from strain gauge (mV)

T = mechanical torque of the shaft (Nm)

N = shaft speed (rad/s, obtained from frequency input module)

P_M = mechanical power output of the shaft (MW)

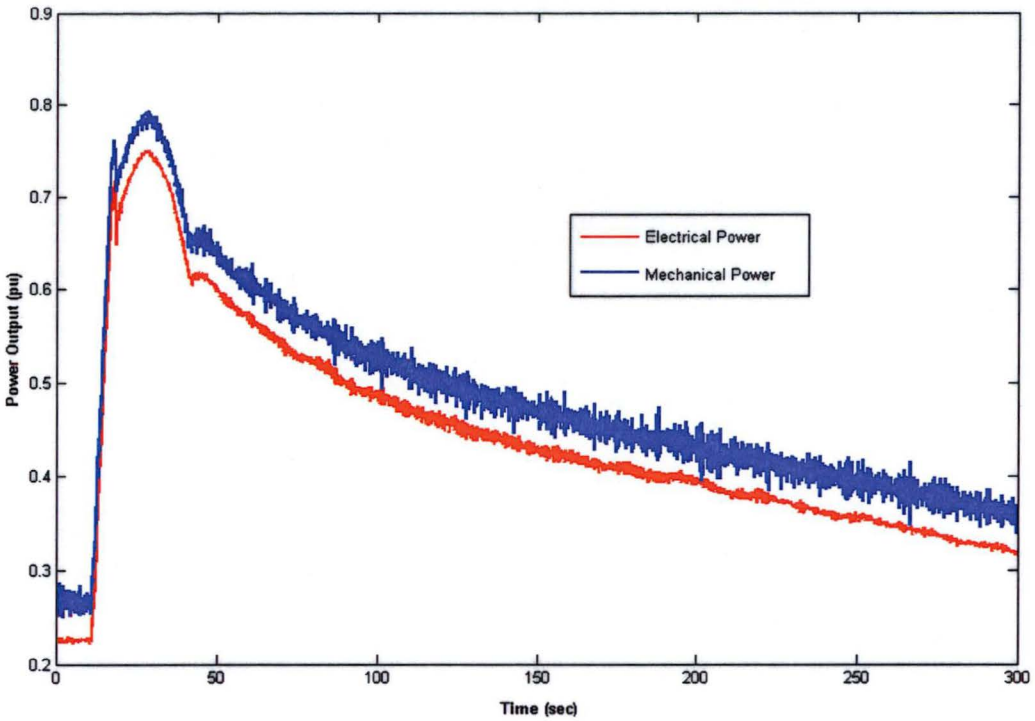

Figure 3.8: Comparison of mechanical and electrical power outputs generated from machine 3 at Trevallyn power plant during a load acceptance. The mechanical output is measured by the strain gauge while the electrical power is measured by the wattmeter connected to the generator bus (All values are normalised by rated values)

It is easily observed in Figure 3.8 that the mechanical output power exceeds the electrical power. The difference is expected due to mechanical and electrical losses in the alternator. Hence the conventional approach of lumping the performance curves of both electrical and hydraulic components into a single curve is inappropriate and insufficient to describe the entire operating characteristics of a Francis-turbine power plant. The mathematical details will be discussed in Chapter 4. Although there is uncertainty about the shaft properties like the exact value of Young's modulus of elasticity and Poisson ratio, the argument is still valid within an uncertainty of 10%. The noise in the strain gauge measurement could be largely due to the vibration of the shaft, as this phenomenon is notable when the machine is operating at high load. No noticeable signal noise was observed when the turbine was stationary. Overall, the test gives some useful indications about the difference between the behaviour of the mechanical and electrical systems of hydro power plant, and a similar test procedure is recommended for future site testing.

3.2.8 Control of the Main Servo Position

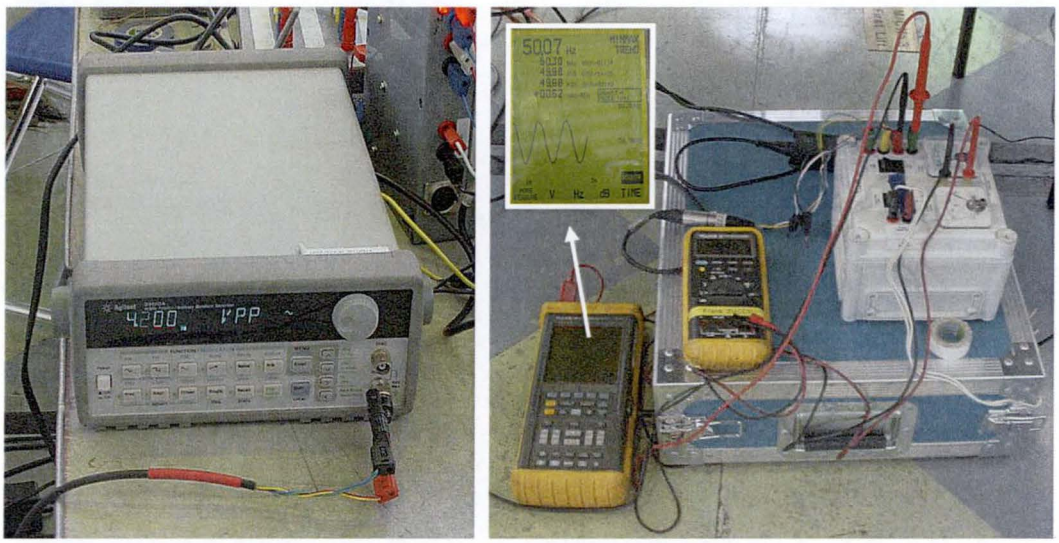

Figure 3.9: HP33120A waveform generator (left), a power amplifier, and a 1:2 transformer (right) used to produce a 50 Hz 110 V AC injected frequency signal to the turbine governor that control the motion of the main servo link. A handheld oscilloscope is used to check the frequency signal from HP33120A

In normal service, a turbine changes its operating condition only when there is a load or frequency change in the power system. One way to reproduce this type of events, and to study the resulting behaviour of a hydro power plant, is to manually control the main servo and guide vane positions of the turbine during field tests. The guide-vane control circuit built in the governor is only suitable for steady-state measurement, and therefore cannot be applied to the dynamic testing of power plant. The tasks are usually achieved by injecting an analogue signal (in place of generator feedback signal) proportional to turbine speed or generated power frequency, which then initiates the required movement of the main servo link and turbine guide vanes.

An HP33120A waveform generator was used to supply such an artificial signal (either a step or an oscillatory input signal) to the governor control system. The HP33120A uses a direct digital-synthesis technique to create a 2 V peak-to-peak voltage signal, which then passes through a power amplifier and a 1:2 transformer to generate a standard 50 Hz 110 V analogue signal to the governor. A changeover switch was installed in the governor circuit to select between the power amplifier output and the generator signal. The governor moves the guide vane to a new steady state operating condition when its control system detects the injected frequency input signal. This frequency input signal was monitored on site by a hand-held oscilloscope connected to the waveform generator. The typical accuracy of the HP33120A is ±2% at a setting of + 2 mV.

3.3 Staged Tests of the Francis-Turbine Power Plants

Full-scale field tests were carried out to provide information for verifying mathematical models of power plant operation and to identify key model parameter values. The hydraulic system tests were always combined with governor response tests because of the close interaction between turbine and governor performance. All tests were designed to minimise interruption to plant and system operation, allow ease of simulation of staged tests, and to reduce the complexity of the parameter derivation problem by limiting the number of parameters significantly affecting an individual test. Technical information such as turbine characteristics, equipment drawings, plant layouts, and previous commissioning test reports were collected and studied before the actual tests. Measurements of water levels at the upper and lower reservoirs were obtained from the system control data and recorded regularly during the tests.

The turbine was unresponsive to the system frequency disturbances during the field tests, since the functions of the guide vanes and governor had been switched to manual mode. However, the plant and generator protection system remained intact all the time. An interlock circuit was installed on the machine under test. If the machine circuit breaker were accidentally tripped, the governor solenoid will be tripped to limit the machine speed rise. Plant operators were present during the test to assist the control of the guide vane operation. System dispatchers were also informed when the tests were to start. No operator adjustments were performed during data recording. The field tests typically took about a week to finish, including instrumentation set up.

The sequence of test program was carefully designed to facilitate parameter identification and model verification in a logical order. All tests requiring the turbine to be in a particular mode of operation were finished before proceeding to the tests demanding a different mode of operation. The first stage of the tests involved measuring the steady-state responses of the turbine. This information was used to identify parameter values that are associated with steady-state operation. The second phase of tests involved observing the hydraulic transient response of the plant subjected to various types of disturbances. Step and sinusoidal changes of guide vane position (Frequency deviation and Nyquist tests) were performed at different loading conditions during this stage, and the responses were recorded for later analysis.

3.3.1 Steady-State Measurement

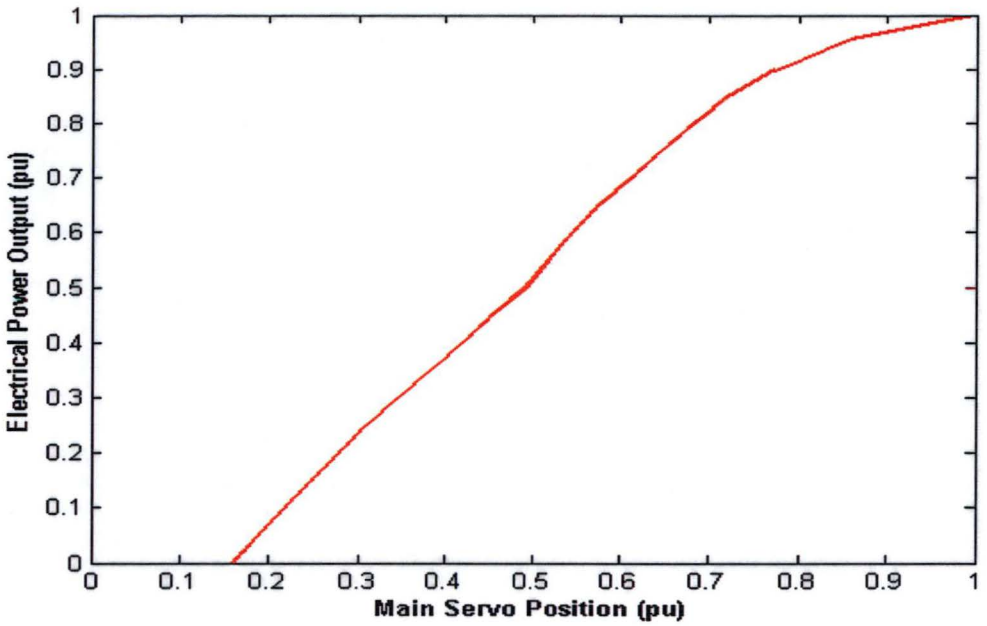

Figure 3.10: Typical test result of a steady-state measurement conducted at a Francis-turbine power plant (All units expressed in the diagram are normalised by the rated values when the machine is running at full output)

Steady-state measurements are useful for determining steady-state relationships between main servo position, electrical output power, and static pressure of the waterway conduit during steady-state operating condition of a Francis turbine. Measurements are taken online with the turbine connected to an electrical network. The machine under test is initially run at a minimum load. The load is then increased in 10% increments until it reaches the full output. This is done by feeding a control signal to the guide-vane control limiter, or by injecting a small step signal from the waveform generator to the governor control system. A delay time is set in the acquisition system to allow the machine to settle at a steady-state output after a change in main servo position. Electrical power output and main servo position, as well as the static pressures at the spiral case inlet and draft tube entrance are sampled for 500 seconds at 2 Hz. An average value is taken to represent the steady-state condition of the turbine at a particular operating point. Typical measurement results are summarised in graphical form in Figure 3.10. As shown, the steady-state power output of the machine is increased with increasing main-servo position. However, the rate of power rise is reduced when the main-servo position is more than 75% of the full stroke, which demonstrates the nonlinear response characteristic of a Francis-turbine power plant even if the machine is running at steady-state condition.

3.3.2 Frequency Deviation Tests

Frequency deviation tests provide a step disturbance to a generating unit in order to excite the machine under test. The dynamic performance of a machine subjected to a large guide vane movement, as would be present in a real situation following a significant system frequency disturbance, is measured and assessed during the tests. The field tests demonstrate the ability of a turbine to instantly shed or accept an electrical load without tripping. Transient response of a Francis turbine exposed to a step disturbance has a great influence on the short-term frequency deviation, the distribution of transient power between units, and the ability of a machine to supply an isolated network. The usual approach to study such plant behaviour is to conduct a series of load rejection and load acceptance tests with the unit initially carrying a partial load.

A step change in the guide vane position is applied to simulate the action of accelerating or decelerating torque on a Francis turbine when the electrical load is changing. This is accomplished either by altering the generator load set point for the machine under test or by injecting a step frequency signal directly to the turbine governor. The second approach is used in the tests described here. The machine is run online with frequency feedback signal supplied by an isolated load simulator (signals generated from an HP33120A unit as described in Section 3.2.8) and a power amplifier. The isolated load simulator is operated in a pass-through mode. Electrical power output, main servo position, and static pressures along the waterway conduit are sampled and recorded at 10Hz for more than 300 seconds. The test procedure is repeated for at least four different initial load settings and for different disturbance types.

Opening the machine circuit breaker or losing a major industrial load may trigger a load rejection in the power plant. Frequency deviation tests verify if a machine is capable of operating continuously and uninterruptedly during a partial load rejection (or load acceptance) that occurs within 10 seconds. Figure 3.11 shows a typical plant response for a given load rejection. The electrical power output of the machine drops when the main servo position is closed. However, initial static head at the turbine admission rises, as the flow does not change instantaneously with the guide vane opening. A new steady-state operating condition is established once the injected frequency deviation at the governor is cancelled.

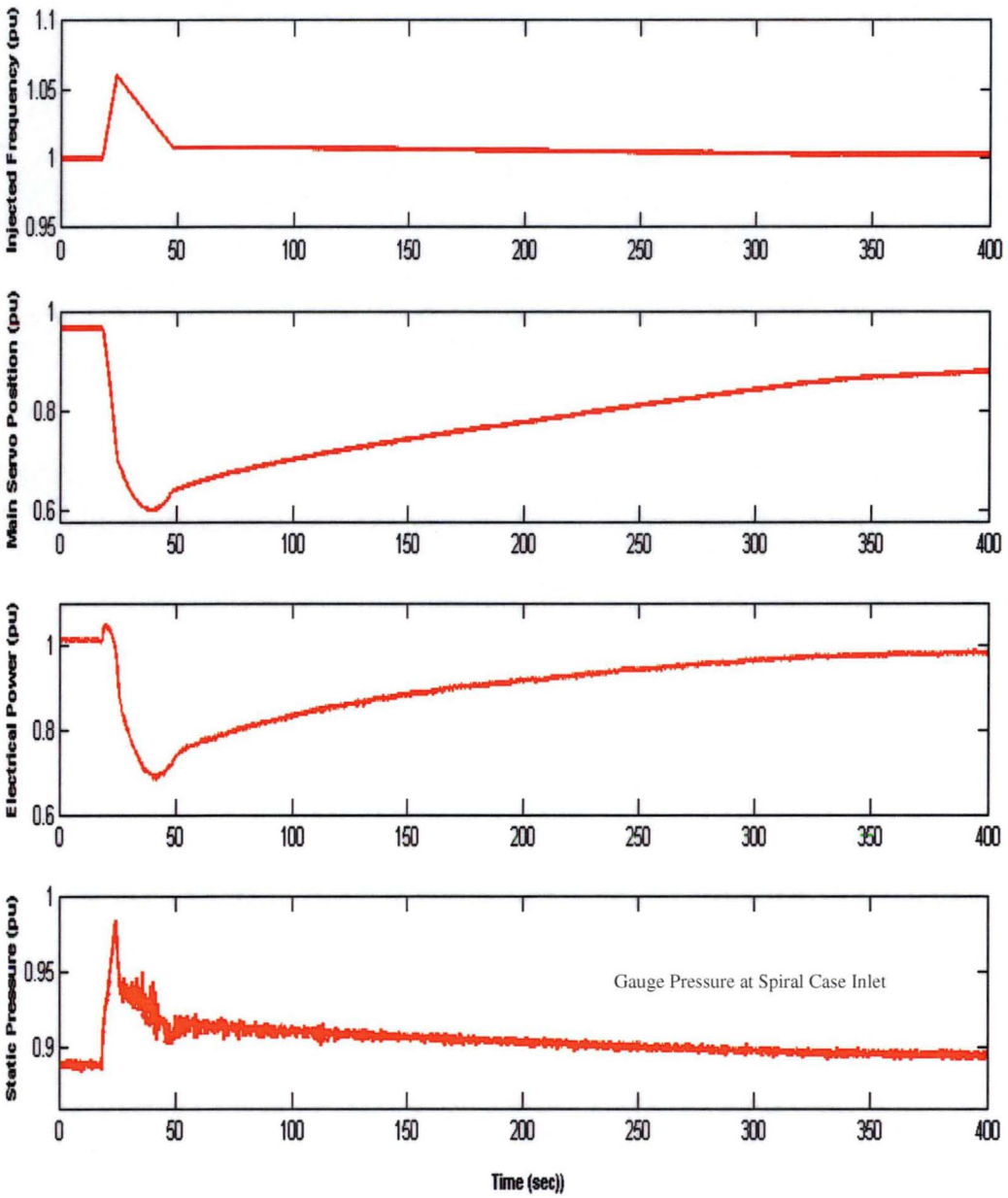

Figure 3.11: Typical frequency-deviation test result for a Francis-turbine power plant subjected to a load rejection (All units expressed in the diagram are normalised by the rated values)

Figure 3.12 gives another example showing the behaviour of a generating unit under a load acceptance case. The guide vane of the generating unit is opened to increase the power output but the initial static pressure at turbine entrance reduces due to the sudden increase of the main servo position.

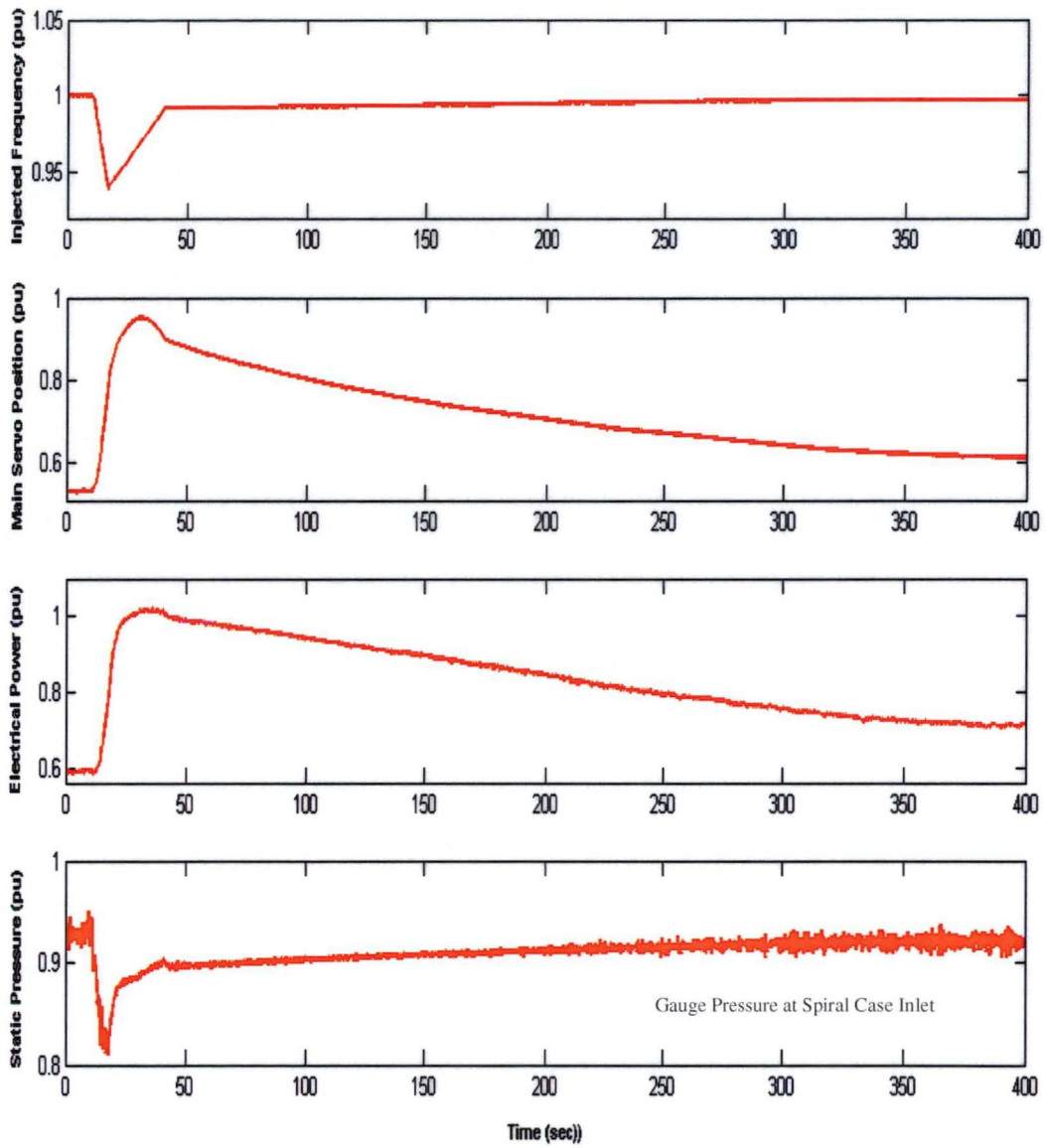

Figure 3.12: Typical frequency-deviation test result for a Francis-turbine power plant under a load acceptance case (All units expressed in the diagram are normalised by the rated values)

3.3.3 Nyquist Tests

Nyquist tests are also known as frequency-response tests. They are carried out to investigate the frequency-response of a Francis-turbine power plant subjected to a sinusoidal input signal, which is very important for a stable isolated operation. The stability of the control system for the power plant can be evaluated directly by use of the Nyquist test data and a linear system approach without the need to derive a mathematical model for the power plant. The effects of undesirable noise are often negligible using this method.

Results of Nyquist tests enable one to assess the dynamic performance of a speed governing system in terms of amplitude ratio and phase displacement between the sinusoidally varying main servo position and the corresponding electrical output power, as a function of test frequency. To examine the characteristics of a turbine governor in the frequency domain for a simulated isolated operation, the generator is synchronised and run steadily at a certain load level prior to the tests. The governor parameters are set as specified for normal operation. Frequency feedback from generator is then disconnected and replaced by an external speed signal, which is an artificial speed signal synthesized by means of an HP33120A signal generator. The injected sine wave is superimposed onto the synthesized speed signal during the tests. This speed input signal is made to vary sinusoidally about a given average value so that the servomotor piston will move sinusoidally about a given average position as well.

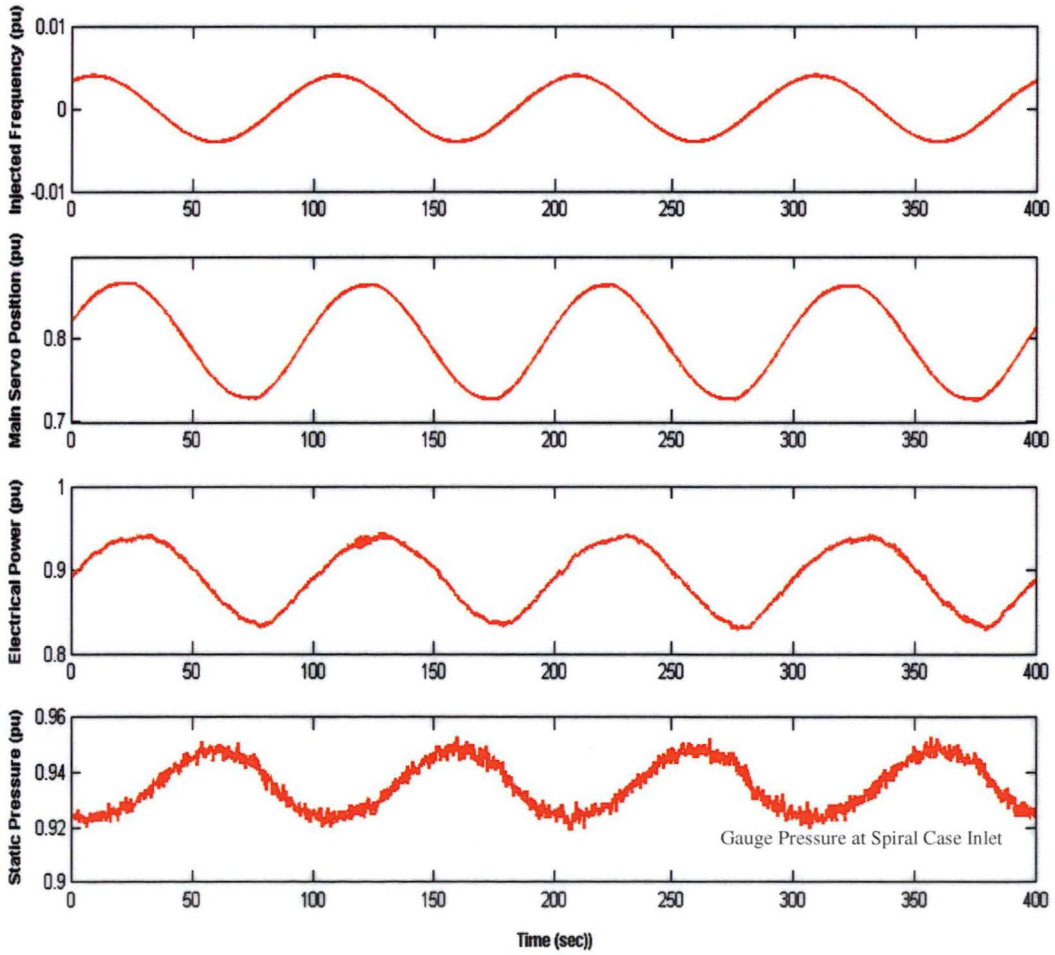

Figure 3.13: Typical Nyquist test result for a Francis-turbine power plant with guide vanes operated sinusoidally at the lowest test frequency of 0.01 Hz (All units expressed in the diagram are normalised by the rated values)

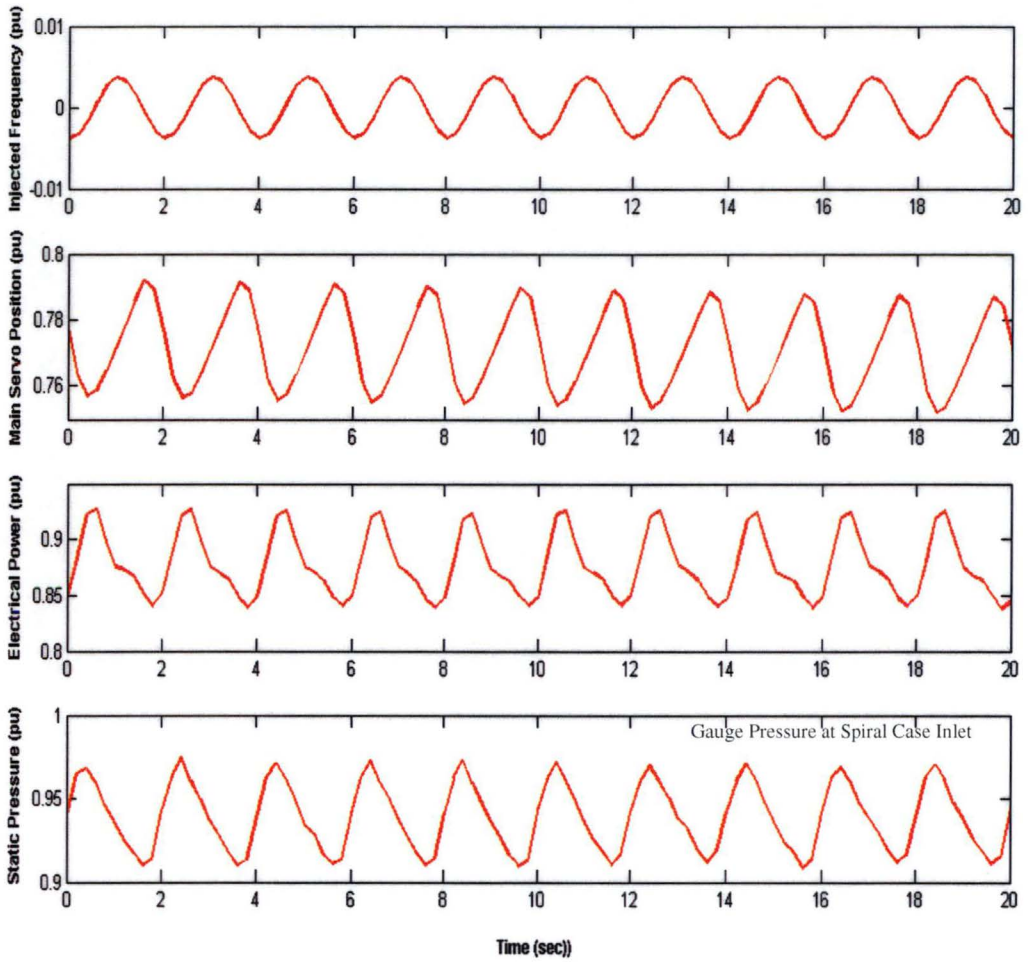

Figure 3.14: Typical Nyquist test result for a Francis-turbine power plant with guide vanes operated sinusoidally at the highest test frequency of 0.5 Hz (All units expressed in the diagram are normalised by the rated values)

The main servo position, electrical power output, and static pressures of the waterway conduit are sampled and recorded for at least five cycles of the injected speed signal once the power swings have stabilised. The tests are repeated by gradually increasing the frequencies of the sinusoidal signal until they cover the entire frequency domain of interest. To allow more in-depth investigations of the machine stability, Nyquist tests are also conducted at two different load levels and with different combinations of machines in operation for the case of multiple machine station. Figures 3.13 and 3.14 shows typical results of the Nyquist test when the turbine guide vanes are oscillating at the lowest and highest test frequencies. The magnitude of the injected signal causes peak-to-peak power swings of approximately 20% of the maximum power for the lowest test frequency.

It is critical to ensure that the sinusoidal signal is reasonably free from harmonics and distortion. The amplitude of this sinusoidal signal should be such that the corresponding movement of the main servo link and electrical power output are as near sinusoidal as possible, taking care to avoid nonlinear characteristics of dead band and rate limits [98]. The magnitude of the power swing is reduced at higher guide-vane oscillating frequencies to avoid relief valve operation. However, exact sinusoidal movement of servomotor piston is difficult to achieve at high oscillation frequency due to nonlinear characteristics of the hydraulic servomechanism and possible hydraulic valve cavitation. The application of Nyquist test results in the stability analysis of a Francis-turbine power plant will be discussed in Section 3.5.1.

3.4 Multiple-Machine Tests

Multiple-machine tests carried out at Hydro Tasmania's Trevallyn power station were identical to those of the single-machine station, except that the transducer installations were duplicated on other machines of the plant, and the procedures for frequency deviation and Nyquist tests were repeated with different combinations of machines in operation. The main objective was to investigate the hydraulic coupling effects between individual machines sharing a common waterway conduit. The basic approach of the tests is to change the operating condition of a machine while running the other units at a constant load according to the plan listed in Table 3.1. In other words, only the guide vane of one machine is varied during the tests while the guide vanes of the other machines are either locked in a fixed position or totally closed.

Test Case	*Machines Dispatched*
A	Only machine under test and the remaining units are shut down
B	Machine under test plus one other running at fixed guide vane position
C	Machine under test plus two others running at fixed guide vane positions
D	Machine under test plus three units operating at fixed guide vane positions

Table 3.1: Combinations of machine operation during the field tests conducted at Trevallyn power station

In general, the rate of change in flow at a machine is zero at steady-state operation, making each unit turbine head equal to the static head less losses. In steady-state operation, the flow going through each turbine is established independently from the other units. However, the transient operating conditions of a multiple-machine station are quite different from those in steady-state operation (refer to Chapter 5).

Figure 3.15 presents the typical result of a partial load rejection test conducted at Trevallyn plant. The case involves four turbine units, each supplying a constant load connected to an infinite bus, and the shedding of load at one of the units (Machine 3 as quoted in Figure 3.15). This was accomplished through an injected frequency change to the governor of the machine 3, causing the gate on that unit to be ramped down. The gate positions of the other units in the plant remained stationary, since they were locked in a fixed position by use of guide vane control circuit built in the governors.

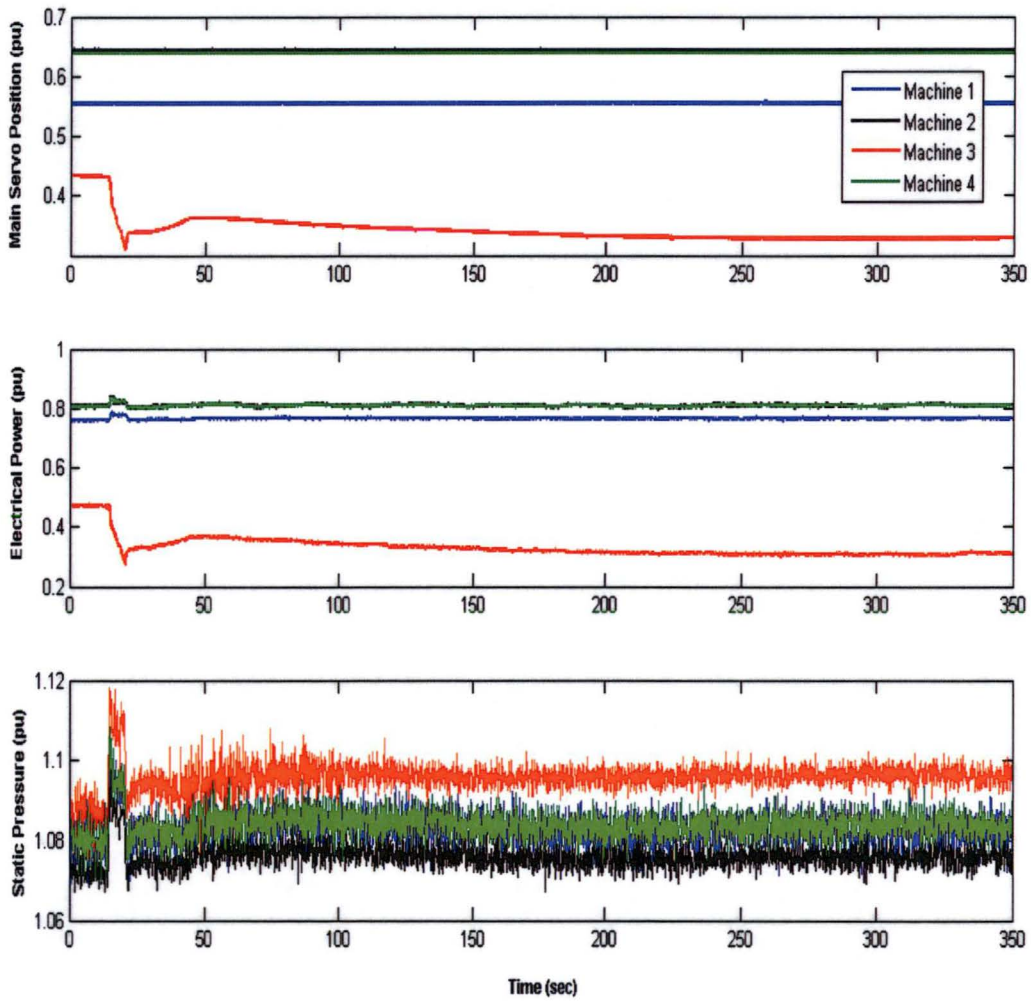

Figure 3.15: Typical field test results collected at Trevallyn power station, showing four machines supplying a constant load and the event of shedding the power output at one of the units (All units expressed in the diagram are normalised by the rated values)

Although the machines were unresponsive to the real system frequency disturbance during the tests, the effects and the risks were acceptably small, as the system to which the units are connected was very large. When the load is rejected at unit 3, the turbine

head rises, as the guide vane opening is reduced. The initial rise in the turbine head of this unit results in a decreased flow and at the same time produces an increase in flows to the other units because the total flow in the common tunnel cannot be changed instantaneously. For this reason, the power output of the other machines rises initially when the guide vane opening of unit 3 is reduced. The effect gradually disappears when the final flow conditions reach a new steady state. Similar behaviours are observed in the Nyquist tests and for step load changes with two and three machines in operation. The multiple-machine site testing generally confirmed the expected nonlinear and multivariable behaviour of this type of power plant. Although this did not constitute a system verification of the mathematical model for the power plant, it did provide good evidence for its authenticity and emphasise the importance of considering the hydraulic coupling effects in modelling a multiple-machine station.

3.5 Discussion

3.5.1 Estimation of Instantaneous Flow Rate

Precise measurement of flow through a Francis turbine is desirable for more detailed verification of the hydraulic models developed for both single- and multiple-machine stations. However, factors such as cost, complexity and time involved in the equipment installation, or the accuracy of the measuring techniques for a large flow rate have precluded the measurement of instantaneous turbine flow in the current field tests. The instantaneous flow in the system model (see Chapters 4 and 5) is derived from the instantaneous turbine head via the orifice head-flow relationship. The system verification will therefore rely on the measurement of instantaneous power output, which is proportional to the product of the instantaneous head and flow. It is worthwhile in this section to review some commonly used measuring techniques that have been tried successfully by others in the steady-state performance testing of a full-scale Francis turbine. These techniques may be applied in the future site testing, if time and budget allow, which will permit direct verification of the instantaneous flow modelling:

- *The current-meter method* uses a number of propeller-type current meters placed in turbine inlets or penstocks to measure the local mean velocities simultaneously. The turbine discharge is estimated by integrating the flow velocities over the conduit cross section. The method is recommended by IEC publication 41 and

other codes for measuring flow in a hydraulic turbine [80]. However, to get an acceptable accuracy, this approach requires a uniform and rectilinear flow over the cross section of the measuring plane to obtain a favourable velocity distribution. The penstock must also be emptied for installation of the instrumentation support frame and related work. This is difficult to implement, particularly when a Francis turbine is tested in a transient state, and must be operated continuously for economic purposes. Thus, this method was not applied in the current site testing.

- *The Gilson pressure-time method* determines the turbine flow indirectly from the pressure rise between two sections of the penstock during an interruption of flow caused by closing the turbine guide vanes. The distance between two measurement sections should be at least 9m or two times the conduit diameter. Moreover, this method relies on piezometer taps that have been installed during construction of the power plant [32]. Installing a new pressure taps in existing concrete penstocks is costly and time consuming. Hence, this method is not being used for transient flow measurement of the Francis turbine.

- *The salt dilution tracer method* [32] measures the flow rate by observing the concentration of a solution of sodium dichromate injected into the main water flow at points evenly distributed over the cross section of the penstock. The flow must be perfectly turbulent so that the salt solution is evenly distributed in the conduit. To get a meaningful result, extreme care is needed when injecting the salt solution to the water. This is difficult to apply in the typical operating environment of a hydraulic turbine. Nor does the method guarantee acceptable accuracy when the machine is running at a transient state. Hence, it is not useful for dynamic testing of a turbine plant.

- *The Pitot tube gauging approach* [32] obtains the turbine discharge from local measurements of flow velocity over the penstock cross section. Although this method is simple in principle, it is not suitable for large diameter conduits with relatively high velocities due to stiffness problems of the tube support. The difficulty of retrofitting tube access ports in existing conduits is also a problem.

- *The acoustic method* utilises two acoustic transducers installed in a steel penstock over a distance of about one-half of the penstock diameter. The transducer

measures the travel time of an acoustic wave in and against the flow direction, and relates these two travel times to the mean velocity of the water along the acoustic path. The discharge is determined by integrating the profile of mean velocities numerically. This approach has the advantages that the transducers can be installed without the penstock emptied and that it is not necessary to cause a sudden variation in flow in order to measure it. Dubé and Martin [32] report a high repeatability and an accuracy of 0.5% using the acoustic method in a crossed plane. The drawback of this approach is that an acoustic transducer is always expensive.

- *The relative discharge method* [32] determines the "relative" turbine flow by means of Winter-Kennedy pressure taps located in the turning section of the spiral case or through the head loss measurement between two sets of pressure taps. The discharge is found through the pressure differential caused by different locations of the pressure taps in the measurement section and due to the centrifugal forces of the water. The measurement accuracy depends on the accuracy of the pressure transducer. If the knowledge of absolute flow is required, an index test must be performed simultaneously; or alternatively, calibration data may be obtained from model tests. This approach should be tried in the future for stations where Winter-Kennedy pressure taps are already installed in the spiral case.

3.5.2 Transmission Time Lag

The transmission lag of a measuring system is critical in unsteady flow measurements. The lag can be caused either by the dynamic characteristics of equipment or by communication delay between Graphical User Interfaces (GUIs) used in the LABVIEW data acquisition program. The time lag generated by a transducer is minimised by use of an electrical current for signal transmission since the state of change of an electrical signal occurs with virtually no time losses. The transmission lag due to acquisition software is reduced by using an external triggering device to make sure that all signals are send without significant delay. The oscillation period of the pressure wave in the pressure tubes is estimated to be two order of magnitude less than that of the fastest oscillation encountered in the Nyquist test and the actual plant verification. Hence, the pressure wave in the cavity tube is quite unlikely to affect the system measurement here.

3.5.3 Stability Analysis of a Hydro Power Plant

Knowledge of the signal form and amplitude is essential in understanding the behaviour of a nonlinear control system for a hydro power plant. In the frequency-response method, the sinusoidal input signal to a turbine governor is varied over a frequency range of interest, and the resulting response is analysed to determine if the plant operation is stable for a given set of governor control parameters. The Bode plot is a powerful tool for stability analysis of the control system used in a Francis-turbine power plant. This method is characterised by the variations in amplitude ratio and phase angle between the main servo position and the electrical output power with guide vane oscillating frequency. In general, the Bode stability criterion states that:

"A closed-loop system is stable if the open-loop system is stable and the frequency response of the open-loop transfer function has an amplitude ratio of less than unity at all frequencies corresponding to a phase angle of –180 °– 360n °where n=0,1,2..."

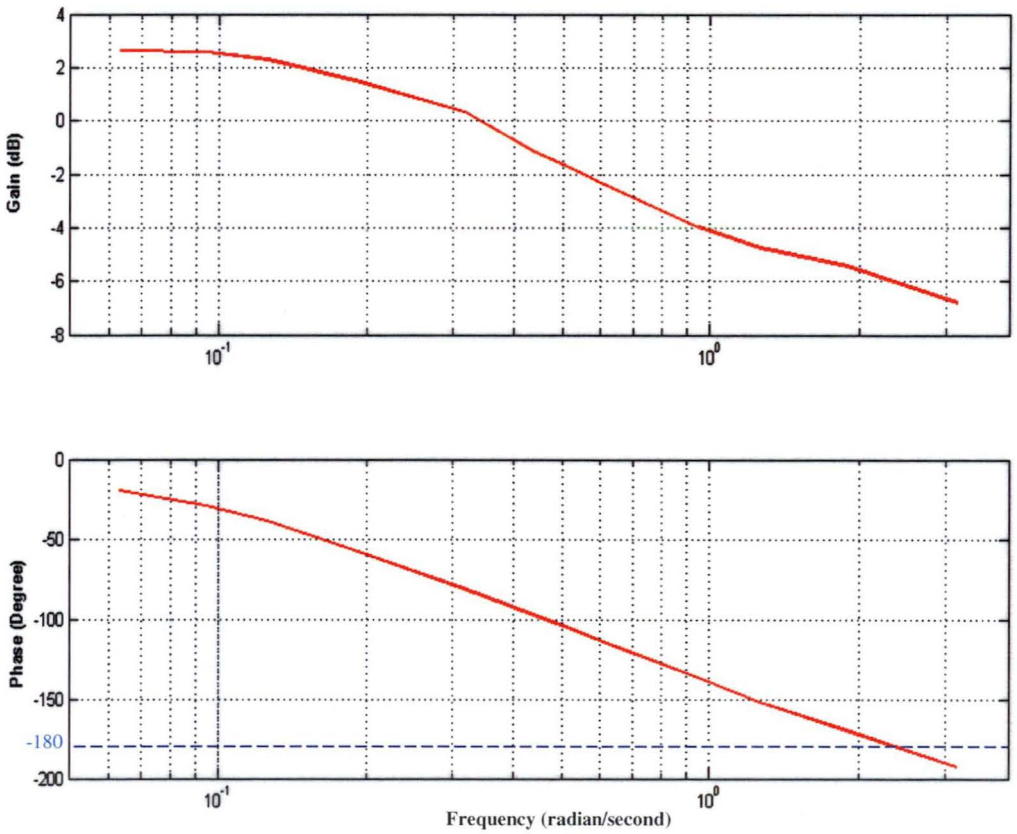

Figure 3.16: Bode diagram of the Mackintosh power station. Open-loop frequency-response characteristics of the plant are obtained from Nyquist test data where guide vane is oscillating at high initial load

The open-loop frequency-response characteristics of the power plant are obtained directly from Nyquist test data described previously. This is convenient because it often happens that the mathematical expressions or transfer functions of the hydraulic systems in the power plant are not known exactly, and only the frequency-response data are available. Figure 3.16 shows a Bode diagram for the Mackintosh power station. The machine is operated at high initial load throughout the Nyquist tests. As mentioned in Section 3.3.3, an exact sinusoidal movement of servomotor piston is difficult to achieve when the guide-vane is oscillating at high frequency. Hence, a curve fitting approach (Equation 3.2) is employed to approximate input and output signals at higher test frequencies, as linear stability analysis requires that both signals are perfectly sinusoidal. To minimise the normalised root-mean-square error, the optimal solution of the curve fitting equation is obtained using a structural matrix approach and least square error method.

$$BestFit = a\ sin\ (\omega t) + b\ cos\ (\omega t) + ct + d \tag{3.2}$$

where a = sine coefficient

b = cosine coefficient

c = diagonal offset coefficient

d = vertical offset

ω = guide-vane oscillating frequency

t = time (Second)

As illustrated in Figure 3.16, the electrical power output follows the sinusoidal movement of the guide vanes faithfully at low frequencies. However, as the oscillating frequency of the guide vanes is increased, the power can no longer follow the movement of the guide vanes. A certain amount of time is required for the system to build up the magnitude, and so the system becomes slow in responding at higher frequencies. The amplitude of the power output is reduced and the phase lag approaches 180° at higher frequencies.

If a fast speed of response is required for a power plant, excessive phase lag should be avoided in designing and tuning of the turbine speed governor. It is shown in this test that Mackintosh power station possess a gain margin of 5.95dB and a phase margin of

73°. For a given set of governor parameters, positive gain and phase margins means the system is stable. IEEE recommends a margin of 9dB and 30° for satisfactory performance [98]. The gain and phase margins represent the amount of gain and phase that can be increased before the system becomes unstable and exhibits sustained oscillations. It should be noted that either gain margin alone or phase margin alone does not give a sufficient indication of relative stability. Both gain and phase margins must be positive for the system to be stable.

Figure 3.17 gives a bode diagram for the Trevallyn power station. In this case, only one of the four machines in the power plant is tested and the Nyquist tests are conducted at both high and low initial loads. Although both test results indicate a stable system, significant difference is observed between the high and low load open-loop frequency responses of the machine under test. Rayner and Ho [98] obtained similar results during the Devil's Gate TEC compliance test. However, in their case, a Nyquist test at high load indicated a stable system while test at low load implied an unstable operation.

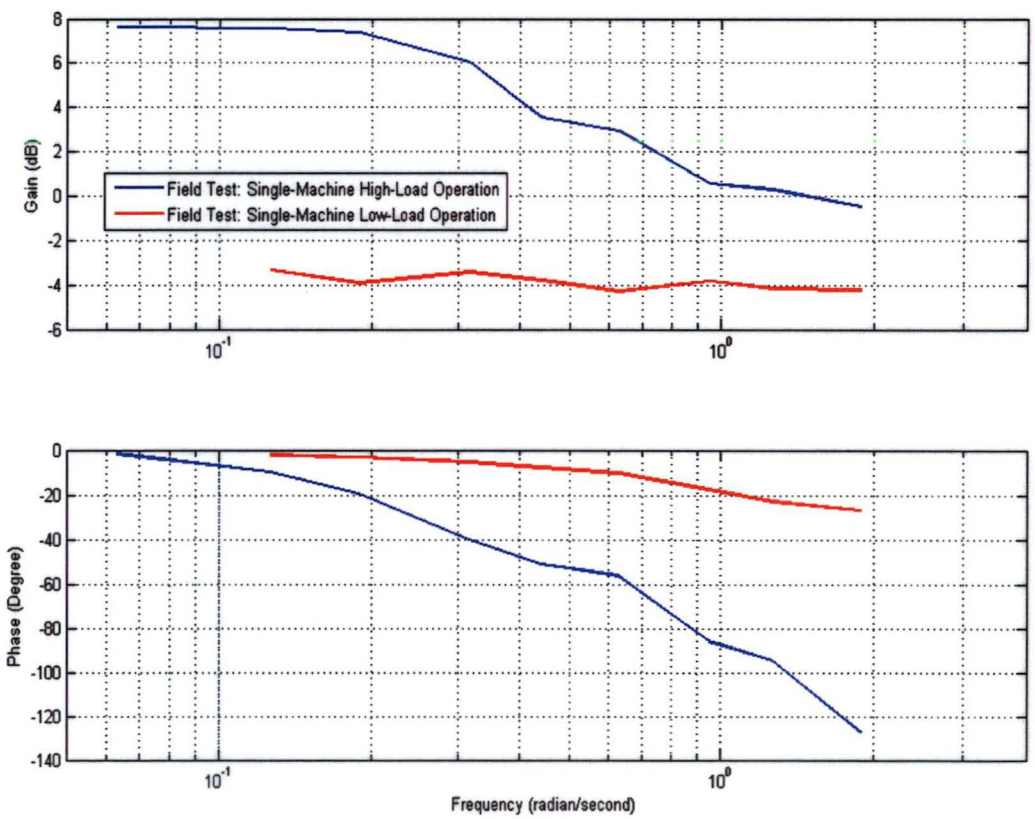

Figure 3.17: Bode diagram for Machine 3 at Trevallyn power station, comparing the open-loop frequency-response characteristics of the machine running at high and low initial loads

Figure 3.18 compares the frequency responses of a Trevallyn machine when running in single- and multiple-machine modes. It is apparent that the number of machines in operation has little impact on the phase characteristics of the Trevallyn machine 3. However, the gain for single-machine operation is more sensitive to the guide-vane oscillation frequency if compared with the multiple-machine operation. It should be noted that the observation is made based on the conditions that the power outputs of the other machines are not varying significantly during multiple-machine testings. Hydraulic coupling could in fact introduce further instability to the operation of an individual machine. Nevertheless, frequency-domain analyses confirm that Nyquist tests conducted at a certain load level or machine configuration are unable to describe the machine stability over the entire operating conditions of the power plant. Hence, governor tuning should not be based solely on a single set of test data.

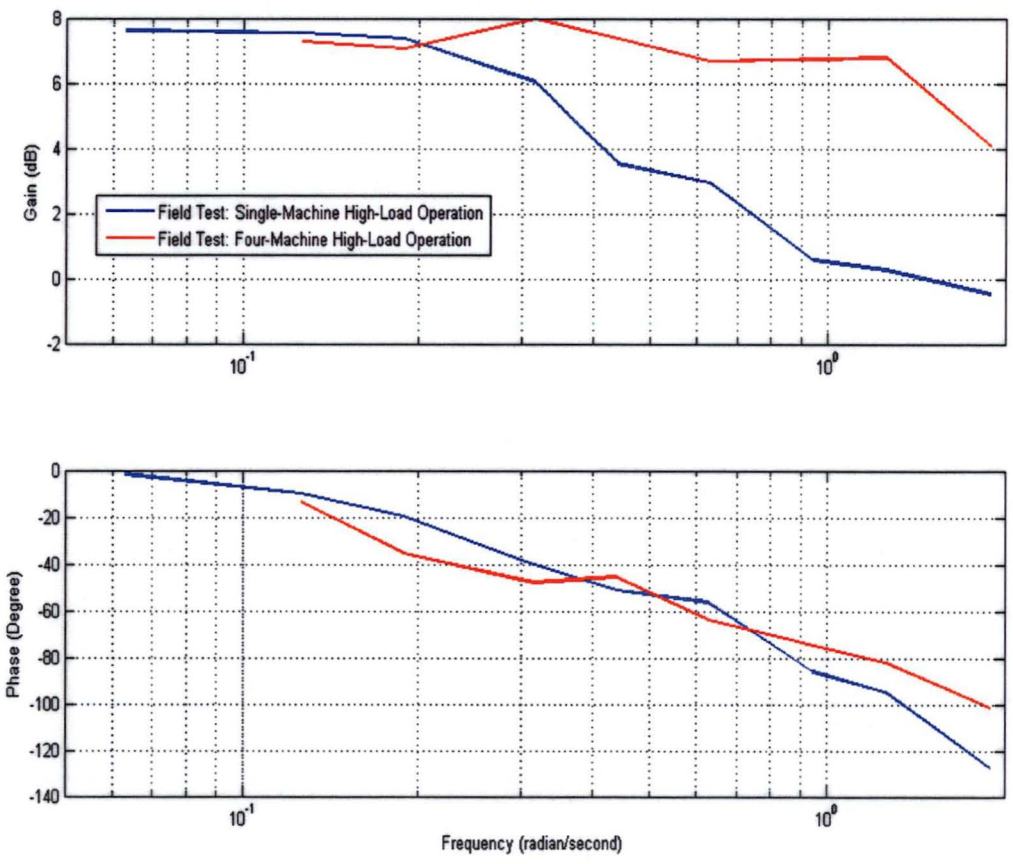

Figure 3.18: Bode diagram for Machine 3 of the Trevallyn power station, showing the open-loop frequency-responses of the machine when running in single- or multiple-machine modes

Although Nyquist tests have been used to determine the stability margins for generators with Francis turbines, the appropriateness of the test on generators with other types of turbines is not fully explored. Some tests have been conducted by Hydro Tasmania on a generator with a Pelton turbine but the test outcome was not encouraging [98]. The deflector action and the opening (or closing) rate of the spear generate nonlinearities in power output of the Pelton turbine that invalidate the linear stability analysis of the power plant. The accuracy of the Nyquist test approach is also greatly affected by the characteristics of the instrumentation used. The frequency response of the measuring equipment must have a nearly flat magnitude-versus-frequency curve. Frequency characteristics of the test instruments used in the current field tests were not fully calibrated due to time constraints, but they were assumed to behave according to their manufacturer's specifications.

3.6 Conclusions

A field-test program has been successfully carried out to investigate the dynamic behaviour of both single- and multiple-machine stations. The techniques and instrumentation used for field testings are discussed in detail here. The test results show that the operating characteristics of Francis-turbine power plants are highly nonlinear. Stability analyses using the Bode diagram indicate that a turbine governor should not be tuned based solely on a single set of Nyquist test results. Nyquist tests at different loading conditions and machine configurations must be performed in order to optimise the governor tuning parameters and to achieve stable operation over the entire operating range of a power plant. However, this would generally require more time and money to be invested into the field-testing. Computer simulation provides a low-cost alternative for predicting the dynamic behaviour of a Francis-turbine power plant. The development of computer models for hydraulic systems in the Mackintosh and Trevallyn power plants will be presented in the Chapters 4 and 5 to assist the stability analysis of these power plants.

CHAPTER 4

HYDRAULIC MODELLING OF SINGLE-MACHINE POWER PLANT

4.1 Overview

Computer simulation is a powerful and inexpensive tool for system planning and development, as well as for optimising the performance of a hydropower plant. For a typical Francis-turbine installation, transient simulation and analysis are essential, as the system looping and service connections of the power plant's waterway systems may amplify hydraulic transient effects and complicate flow control operations of the Francis turbine. The existing industry model employed for a single-machine power plant is usually the manufacturer-supplied model or the standard *IEEE* (Institution of Electrical & Electronic Engineers) model that has not been thoroughly verified by field tests (see Chapter 3). An accurate hydraulic modelling can increase the overall power-transfer capability of a hydraulic turbine plant, whereas an inaccurate simulation model could result in the power plant being allowed to operate beyond safe margins.

This Chapter presents a case study of modelling the transient behaviour of a single-machine power plant with the commercial simulation package MATLAB Simulink [124]. Hydro Tasmania's Mackintosh power station was chosen for this transient analysis due to its relatively simple configuration. The Chapter begins with a brief introduction of the hydraulic circuit for Mackintosh power station. Nonlinear modelling of the waterway conduit and Francis turbine are presented in Sections 4.3 and 4.4. The mathematical assumptions and limitations of the inelastic waterway models will be discussed in some detail here. The drawbacks of linearising the nonlinear plant model are then investigated; the need of a nonlinear model to correctly represent the Francis turbine characteristics is emphasised in Section 4.5. The basic structures and formulation of the nonlinear Simulink model, as well as identifications of the hydraulic model parameters, are summarised in Section 4.6. The mathematical model is validated against field test results previously collected at Mackintosh power station. Possible sources of errors in modelling the transient operation of the single-machine power plant are reviewed in Section 4.7.

4.2 Basic Arrangement of the Studied Power Station

Transient behaviour of the Hydro Tasmania's Mackintosh power station is described in this Chapter. The water for power generation is supplied by one of the largest rivers in Tasmania, the Pieman, and its two major tributaries, the Murchison and the Mackintosh. Lake Mackintosh, which has a maximum volume of about 2.7×10^8 m^3, is the main storage for the Mackintosh power station (see Figure 4.1). The rectangular intake structure, as shown in Figure 4.2, is designed to eliminate the creation of vortices and streamline the water flow into the pressure tunnel. Two sets of gates are located at the start of the tunnel for maintenance work and emergency access. They are raised during normal plant operation. The water is conveyed from intake structure to power station via a 5.2 m-diameter pressure tunnel, providing a net head of about 61 m. The first 149 m of the pressure tunnel is lined with concrete while the remaining 75 m is constructed with stainless steel. The plant is equipped with a single 79.9 MW Francis turbine. The water passing through the Francis turbine discharges into Lake Rosebery via an elbow draft tube. The maximum flow rate from the turbine is 150 m^3/s.

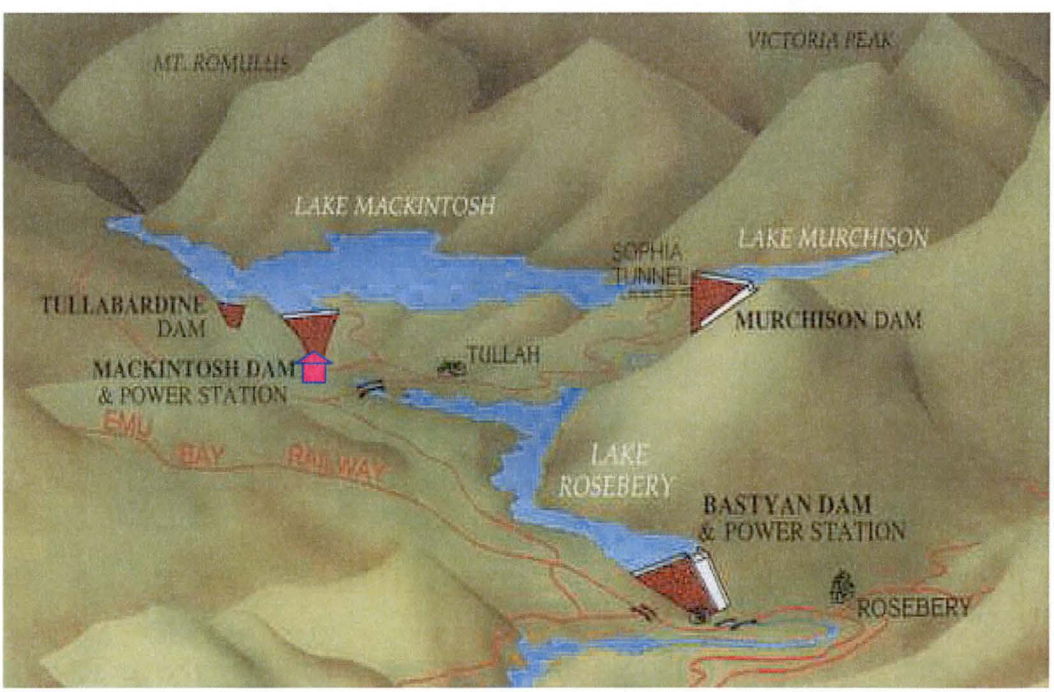

Figure 4.1: Geographical location of the Mackintosh power station (adapted from reference [112]). The plant has been operated by Hydro Tasmania since 1982

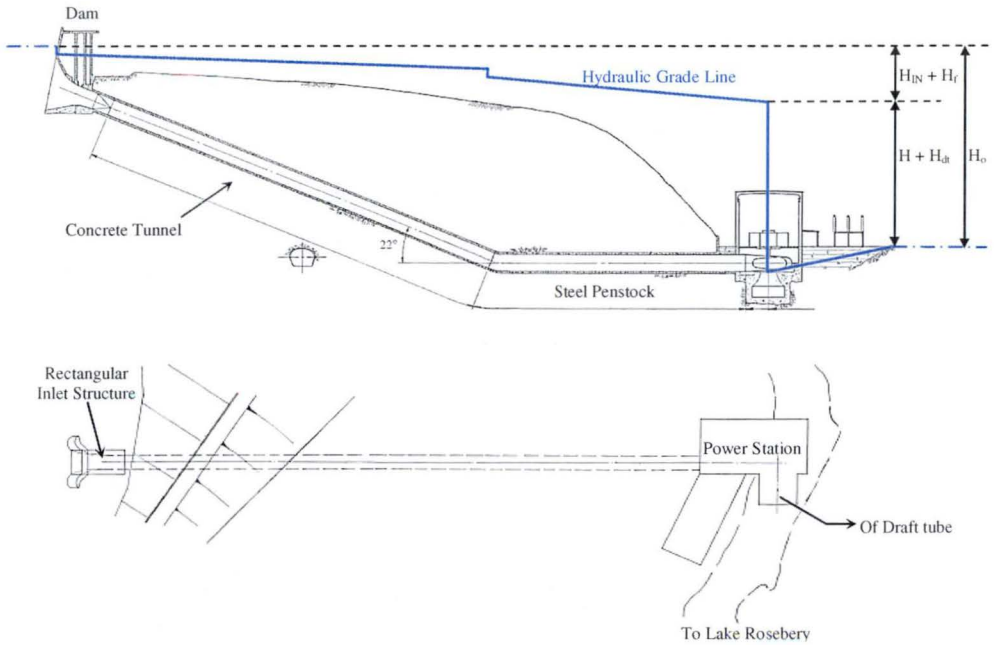

Figure 4.2: Schematic layout of the Hydro Tasmania's Mackintosh power station (Source: Hydro Tasmania Inc.)

The difference in elevation of the hydraulic grade line (shown in Figure 4.2) between the two ends of the waterway conduit indicates the head necessary to overcome the flow resistance of a waterway system and the inertia forces in the conduit.

4.3 Nonlinear Modelling of the Power Plant's Waterway Conduit

Transient performance of a Francis-turbine power plant depends heavily on the characteristics of its waterway conduit that carries water from upper reservoir to the power station. Water inertia, fluid compressibility, and elasticity of the conduit wall are the major concerns in such analysis. When the guide vane positions are changing in a hydraulic turbine plant, the flow momentum in the waterway conduit varies, and a hydraulic transient is generated. This hydraulic transient can be analysed mathematically by solving the flow and pressure head equations for a well-defined elevation profile of the system, given certain initial and boundary conditions determined by the guide vane operation.

One-dimensional continuity and momentum equations are employed for computation of flow and pressure in a power plant's waterway system. Solving these equations produces a theoretical result that usually reflects actual measurements if the data and assumptions used to build the numerical model are valid. Transient results that are not

comparable with field measurements are generally caused by inappropriate system data or improper assumptions. In general, hydraulic transients can be examined using either inelastic or elastic models. The model assumptions and limitations will be discussed next. Selection criteria between these two models are presented in Section 4.3.3.

4.3.1 Inelastic Waterway Model

The inelastic waterway model takes into account the inertia effect of the water column, which causes a lag between changes in turbine flow and guide vane opening. The model assumes that the waterway conduit is non-deformable and the flow inside the conduit is always incompressible. Guide-vane control operation will only affect the inertia and hydraulic losses of the transient flow. In other words, flow control operation will generate an instantaneous flow change throughout the system. The water will travel as a single mass inside the conduit, causing mass oscillation when the positions of turbine guide vanes are varied. The water density is assumed constant, and instantaneous velocity and pressure are the same over given cross sections of the waterway conduit according to the one-dimensional model [139]. For a simple turbine system such as Mackintosh, the inelastic waterway model can be established for each time instant of the transient period using a normalised unsteady momentum equation [141]:

$$\overline{H}_o - \overline{H}_f - \overline{H} = T_w \frac{d\overline{Q}}{dt} \tag{4.1}$$

where Q = turbine flow

$\overline{Q}$ = per-unit turbine flow = Q/Q_{rated}

$\overline{H}_o$ = per-unit static head between reservoir and tailrace = H_o/h_{rated}

$\overline{H}_f$ = per-unit conduit head losses due to friction and fittings = $f_p\overline{Q}^2$

$\overline{H}$ = per-unit static head at turbine admission

f_p = pressure loss coefficient

T_W = water starting time constant = $\sum Q_{rated} L_i / gA_i h_{rated}$

L_i = length of conduit section i

A_i = area of conduit section i

g = gravitational acceleration

Q_{rated} = rated flow rate

h_{rated} = rated head

Equation 4.1 represents a conventional inelastic waterway model that has been reported by Institute of Electrical & Electronics (IEEE) and is constantly used in the power industry to describe the hydraulic transient of the waterway system in a hydroelectric generating plant with a single turbine and penstock, unrestricted headrace and tailrace, and no surge tank [141]. The normalised or "per-unit" values of the flow and head (see also section 4.6.2.1) in Equation 4.1 are obtained by dividing the dimensional flow and head values by the rated flow and head values, respectively.

This conventional model contains some significant drawbacks. Conduit head losses in the conventional model are often ignored for simplicity (either linear or nonlinear models). This simplification is no longer necessary with today's modern computing power. In fact, conduit losses (modelled as a constant pressure loss coefficient times flow squared) could easily amount to around 5% of the total available head at rated flow and are not always constant, even for a simple hydro power plant such as Mackintosh. Hence the inclusion of the conduit losses is considered desirable and will be carefully evaluated here.

Another deficiency of the conventional model is that the dynamic pressure at entrance to the pressure tunnel is neglected. This will cause an overestimate of the flow changes in the system, and in turn over-predict the transient power output of a hydro power plant if the guide vane position is changed. To resolve this issue, inlet dynamic pressure head should be included and modelled in the similar manner to the conduit head losses. Calculation of the inlet dynamic pressure head and conduit head losses will be summarised in Sections 4.6.2.4 and 4.6.2.5.

The conventional model also assumes that the flow inside the conduit is one-dimensional and the velocity is uniformly distributed over the cross section of the waterway conduit. For a hydraulic turbine plant where the flow is always viscous and non-uniform, the effect of flow non-uniformity could be significant, depending on the flow profile at the given operating condition. At least 5% difference in acceleration (or deceleration) can be expected between flows with uniform and non-uniform velocity distributions. A simple analysis to investigate the effect of flow non-uniformity on transient behaviour of the Francis-turbine operation is discussed in Chapter 8.

The conventional inelastic model calculates the inertia forces only up the point where the flow exits the runner. The static pressure force generated by the turbine draft tube and the inertia of fluid within it is often overlooked. A realistic waterway model for a Francis-turbine plant should consider every hydraulic component of the system through which the water flows through the turbine draft tube will recover some of the kinetic energy at the runner exit and failure to include the static pressure force of the draft tube in the calculation will cause an over-prediction of the flow and power output for a given operating condition. Hence, a dimensionless force coefficient should be included here to account for the effect of the draft tube static pressure force. The value for this force coefficient can be estimated through CFD simulation of the draft tube flow. More details will be presented in Chapters 7 and 8.

The static pressure head at the turbine admission is determined using an additional head-flow relation for the turbine. In the generic model, Francis turbine is depicted as an orifice with constant discharge coefficient for a particular guide vane setting. A simple dimensionless orifice flow relation for the Francis turbine [141] is given by:

$$\overline{Q} = \overline{G}\sqrt{\overline{H}} \tag{4.2}$$

The guide vane function $\overline{G}$ in the conventional model is assumed to vary linearly as a function of guide vane opening only; it takes a value of unity at the base flow where $\overline{Q} = 1$. In reality, the slope of this function $d\overline{G}/dt$ varies with discharge coefficient and Reynolds number over the full range of turbine operations. This is evidenced in model test results for the Mackintosh turbine [128]. A nonlinear function should be used to represent such a relation. The nonlinear treatment of the guide vane function in the power plant model will be discussed in more detail in Section 4.6.2.8.

Overall, the accuracy of the conventional inelastic model (Equation 4.2) can be improved by adding extra terms to account for the effects of flow non-uniformity, inlet dynamic head, and static pressure force caused by the turbine draft tube.

The improved model leads to the modified unsteady momentum equations:

$$\overline{H}_o - \overline{H}_f - \overline{H}_{IN} - \overline{H} - \overline{H}_{dt} = k_{nu} \times T_w \frac{d\overline{Q}}{dt} \tag{4.3}$$

where $\overline{H}_{IN}$ = per-unit inlet dynamic head = $K_{IN}\overline{Q}^2$

$\overline{H}_{dt}$ = per-unit static head caused by turbine draft tube = $K_{dt}\overline{Q}^2$

k_{nu} = factor accounting for flow non-uniformity

K_{IN} = factor accounting for inlet dynamic pressure head

K_{dt} = factor accounting for inertia force on fluid in the turbine draft tube

Initial conditions for Equation 4.3 can be obtained by considering a steady flow case where the change of flow with time is zero. For this condition, Equation 4.3 can be simplified as follows:

$$\because \overline{H}_o - \overline{H}_f - \overline{H}_{IN} - \overline{H} - \overline{H}_{dt} = 0$$

(4.4)

$$\therefore \overline{Q}_{ini} = \sqrt{\frac{\overline{H}_o}{\left(f_p + K_{IN} + K_{dt}\right) + \frac{1}{\overline{G}_{ini}^2}}}$$

where $\overline{Q}_{ini}$ = per-unit initial turbine flow

$\overline{G}_{ini}$ = per-unit initial guide vane position

Practical applications of the inelastic model have been confined to the analysis of hydraulic surge or slow-flow transients, because the equation does not accurately account for the physical phenomenon of pressure wave propagation caused by rapid guide vane operations [142]. The predicted head change is often excessive for instantaneous flow changes due to the instantaneous guide vane movements. Therefore, the inelastic model is not realistic for analysing rapid system changes. However, this is not an issue for the current study as the guide vane operations are performed over a period that is longer than the system characteristic time. Reasons for using the inelastic waterway model in this analysis will be further illustrated in Section 4.3.3.

4.3.2 Elastic Waterway Model

Transient analysis of a hydraulic turbine plant is incomplete without considering the option of an elastic waterway model. This model assumes that changing the momentum of the water causes compression of the fluid (also known as water hammer effect) and deformations in the conduit. Flow in the conduit is assumed one-dimensional with velocity and pressure uniform at each cross section. The pressure tunnel is assumed to remain full with no column separation during the transient. Water density will change for strong and fast pressure disturbances in the waterway conduit if there is no gradual pressure relief or kinetic energy transfer. The free gas content in the water is assumed small enough to have no influence on the pressure wave speed. Pressure wave propagation occurring under these conditions will have a finite velocity that depends on the elasticity of the conduit and of the water. This differs from the rigid water column model, which assumes an infinite pressure wave speed and a simultaneous displacement of all water molecules when one of the water molecules in the system is moved. For transient flow operation, the steady flow continues to enter the conduit at the upstream end of the pressure tunnel and the mass of the water will be accommodated through the expansion of the waterway conduit caused by elasticity properties of the conduit and fluid compressibility.

Derivation of complete elastic equations for transient analysis is beyond the scope of this thesis, but details can be easily found in most classical fluid mechanics textbooks like Wylie and Streeter [142]. The elastic waterway model is characterised by one-dimensional unsteady water hammer equations, including continuity and momentum equations:

$$\begin{cases} \dfrac{\partial H_{tot}}{\partial t} + U\dfrac{\partial H_{tot}}{\partial s} - U\sin\theta + \dfrac{a^2}{g}\dfrac{\partial U}{\partial s} = 0 \\ g\dfrac{\partial H_{tot}}{\partial s} + \dfrac{\partial U}{\partial t} + U\dfrac{\partial U}{\partial s} = 0 \end{cases} \tag{4.5}$$

where H_{tot} = total available static head

U = flow velocity

a = pressure wave speed

s = distance along waterway conduit

For hydraulic engineering practice, the convective terms $U\partial H/\partial s$, $U\partial U/\partial s$, and $U\sin\theta$ are very small compared to the other terms and can be neglected in power plant modelling. A simplified version of Equation 4.5 using discharge $Q = UA$ instead of flow velocity U can be expressed as:

$$\begin{cases} \dfrac{\partial H_{tot}}{\partial t} + \dfrac{a^2}{gA}\dfrac{\partial Q}{\partial s} = 0 \\ \\ \dfrac{\partial H_{tot}}{\partial s} + \dfrac{1}{gA}\dfrac{\partial Q}{\partial t} = 0 \end{cases} \tag{4.6}$$

Transient modelling of an elastic waterway conduit essentially consists of solving Equations 4.6 for various boundary conditions and system topologies. These equations, however, cannot be analytically solved and approximate methods are needed to calculate flow and pressure head at a given time instant. The graphical method, method of characteristics, finite difference implicit method, linear impedance method, and perturbation method are some of the most popular methods for solving these equations [142].

The linear impedance method will be introduced in this Section because the formula can be easily constructed in block diagram form in MATLAB Simulink [124]. The algorithms are identical to those used in linear vibration theory or electrical transmission-line theory [142]. The method assumes the existence of a periodic oscillatory motion, with any initial transients dying out immediately in the waterway system.

The general solution of Equations 4.6, normalised by rated head and flow, is as follows:

$$\begin{cases} \overline{H}_2 = \overline{H}_1 \sec h(T_e s) - \overline{Z}\overline{Q}_2 \tanh(T_e s) - \overline{H}_{all} \\ \overline{Q}_1 = \overline{Q}_2 \cosh(T_e s) + \frac{1}{\overline{Z}} \overline{H}_2 \sinh(T_e s) \end{cases} \tag{4.7}$$

where $\overline{H}_2$ = per-unit static head at turbine admission

$\overline{H}_1$ = per-unit static head at upper reservoir

$\overline{Q}_2$ = per-unit turbine flow

$\overline{Q}_1$ = per-unit flow at upper reservoir

$\overline{H}_{all}$ = sum of the per-unit conduit head losses, inlet dynamic pressure head, and draft tube static pressure head = $K_{sum}\overline{Q}^2 = (f_p + K_{IN} + K_{dt})\overline{Q}^2$

$\overline{Z}$ = normalised hydraulic surge impedance = T_w / T_e

T_e = elastic water time constant = $\dfrac{\text{conduit length}}{\text{wave speed}} = \dfrac{\sum L_t}{a}$

T_w = inelastic water starting time constant as defined previously

a = pressure wave speed = $\sqrt{\dfrac{E_V / \rho}{1 + D_c E_V F_s / eE}}$ for $D_c / e > 40$

ρ = water density

E_V = bulk modulus of elasticity of the water

E = young modulus of elasticity of the waterway conduit

D_c = conduit diameter

e = conduit wall thickness

F_s = support factor that depends on Poisson's ratio and conduit characteristics

For a station with a single turbine and penstock, unrestricted headrace and tailrace, and no surge tank, Equation 4.7 can be further simplified to:

$$\overline{H}_2 = -\overline{Z}\overline{Q}_2 \tanh(T_e s) - (f_p + K_{IN} + K_{dt})\overline{Q}_2^2 \tag{4.8}$$

Despite its ability to simulate the pressure wave travelling effect, the elastic waterway model obviously requires a lot more computing power than the inelastic waterway

model, even for a calculation utilising a simplified water hammer equation (Equation 4.8). Vaughan [130] points out that the travelling wave velocity affects only the "shape" of the time domain response, but not the frequency domain phase response. For power system stability analyses where more than one turbine plant is usually involved in the simulation and many different scenarios have to be investigated, computations using the elastic waterway model may require excessive amounts of computing time and resources. Clearly, the types of models used in a simulation must been chosen carefully to achieve a practical balance between the accuracy achieved and the computing time required.

4.3.3 Model Comparison and Selection

The distinction between elastic and inelastic models can be observed by examining the pressure changes calculated by each model in an ideal inviscid flow case:

$$\frac{dP_{inelastic}}{dP_{elastic}} \propto \frac{L\dfrac{dQ}{dt}}{adQ} \tag{4.9}$$

where $dP_{inelastic}$ = pressure change calculated by inelastic waterway model

$dP_{elastic}$ = pressure change calculated by elastic waterway model

As illustrated by Equation 4.9, the guide-vane control movements over a time interval dt that cause a flow change dQ in the waterway conduit will have significant effect on the ratio of pressure changes computed using inelastic and elastic waterway models. In the elastic waterway model, pressure changes depend on the opening or closure time of the guide vanes (compared to the system characteristic time). When a rapid guide vane movement occurs ($dt \to 0$), head changes calculated by inelastic model will be excessive and will increase with conduit length L, even for small flow changes. Both models produce similar results only when $dQ \to 0$ or $dt \to \infty$, which corresponds to a steady-flow or a very slow transient flow conditions.

The system characteristic time (T_s) for the power plant's waterway conduit, which defined as $2L/a$, is the most important criterion used to classify the relative speed of a guide vane movement and to determine which model is best suited for evaluating a

particular hydraulic transient flow case. Guide-vane control operation is "rapid" when it generates a flow change dQ in a time interval (T_{op}) less than the system characteristic time (T_C). On the other hand, guide vane movement is considered "slow" when the operation is carried out over a period longer than the system characteristic time.

While the inelastic waterway model can reasonably predict the pressure variation in slow transient conditions ($T_C << T_{op}$), it generally fails to adequately predict the discharge when the flow conditions are rapidly varying. The inelastic model is derived by assuming that the wave speeds of a pressure pulse are infinite. In reality the wave speeds are always finite, and therefore application of inelastic waterway models is restricted to hydraulic transients that do not cause significant water compression and conduit deformation. For the Mackintosh power plant, the highest frequency of guide vane movement utilised during field test was about 0.5 Hz ($T_{op} \approx 2$ seconds). This execution time is 30% larger than the system characteristic time ($T_C \approx 1.4$ seconds). For normal operation, the guide vanes are usually moving at a slower rate of around 0.1 Hz. Hence, the inelastic waterway model is expected to give reasonably accurate results for the power plant simulation in the present study. Another important consideration is that the computational time for an inelastic model is about 4 times faster than the one employing elastic model (using a desktop computer with Pentium IV 1.6 GHz and 256 MB RAM). For these reasons, the inelastic waterway model has been used for transient modelling of Francis-turbine power plant throughout this project.

4.4 Nonlinear Modelling of Francis Turbine Characteristics

The Francis turbine is a more complicated element to model than the waterway conduit. Accuracy of the Francis turbine model is the key of the nonlinear simulation of turbine governing system. The performance of the Francis turbine is affected by many physical variables including head (H), flow (Q), power output (P), rotational speed (N), turbine diameter (D_{Turb}), water density (ρ), and viscosity (μ). Consequently, the accurate modelling of Francis turbine performance over the whole range of possible operating conditions is a complex and challenging task.

The 1992 IEEE committee report [141] suggests the use of a simple linearised equation to evaluate the turbine characteristics and power output:

$$\overline{P}_m = A_t \overline{H}\left(\overline{Q} - \overline{Q}_{nl}\right) - D\overline{G}(\overline{N} - \overline{N}_{rated}) \tag{4.10}$$

where $\overline{P}_m$ = per-unit electrical power output of a machine
A_t = turbine gain factor
$\overline{Q}_{nl}$ = per-unit no-load flow
D = speed-damping factor
$\overline{N}$ = per-unit turbine rotational speed
$\overline{N}_{rated}$ = per-unit rated turbine rotational speed

The no-load flow $\overline{Q}_{nl}$ is used to allow for bearing friction and windage losses in both the turbine and generator. The turbine gain factor A_t allows for other internal flow losses. Separation of losses into two components is not rational. Nor is the assumption that the turbine characteristic representing by a gain factor A_t is constant with guide vane opening, which is quite incorrect for large load disturbances.

The damping factor D is introduced in the IEEE model to allow for efficiency changes resulting from varied operating conditions. A constant value of $D = 0.5$ is employed for Francis turbine modelling. The basis for choosing this value as the speed-damping factor is not explained in the IEEE report [141]. The use of this speed-damping factor is unrealistic for Francis turbine operation and could lead to significant error when the change in turbine operating conditions is large. In fact, this equation is incorrect for a power plant that is governed to maintain a constant runner speed in order to keep the AC frequency constant within the electrical power grid, in which case the dimensionless turbine flow coefficient ($C_Q = Q / ND^3_{Turb}$) must vary with turbine net head for a fixed guide vane position. Besides, the power and efficiency changes with speed could be positive or negative depending on the guide vane position, and their rates of change may also vary with guide vane position.

Damping effects due to head changes are also completely neglected in Equation 4.10. As the net head decreases, the Francis turbine becomes relatively more inefficient at part loads. Changing the turbine net head will change the flow rate of the machine. At a

constant turbine speed, this also changes the flow coefficient $C_Q \propto Q/N$ and moves to a different turbine operating point and efficiency. The probable magnitude of the damping due to head changes is similar to the speed damping effect and must be taken into account in the simulation. Vaughan [130] suggests multiplying the turbine gain by a factor of $(H / h_{rated})^{3/2}$ to correct for damping effects due to head changes. This is incorrect, as it will result in power output being factored by $H^{9/4}$ through the related dependence of flow on $H^{1/2}$. Altering the turbine net head while maintaining constant turbine speed results in a change in flow coefficient, making an exact $H^{3/2}$ dependence of power output impossible.

The only feasible way to correctly represent a Francis turbine characteristic is to use a dimensionless turbine performance curve. This is done by utilising the model test information of a scaled down unit and incorporating the empirical data into the real turbine unit. Dimensional analysis is often employed to handle and extrapolate these empirical data to the full-scale machine. Four dimensionless groups can be specified using this approach: flow coefficient ($C_Q = Q / ND_{Turb}^3$), head coefficient ($C_H = gH / N^2 D_{Turb}^2$), power coefficient ($C_P = P / \rho N^3 D_{Turb}^5$), and Reynolds number ($\mathrm{Re} = \rho N D_{Turb}^2 / \mu$). These dimensionless quantities however are not all independent, as power coefficient is the product of head and flow coefficients. Ramos and Almeida [97] use a rather different set of parameters (known as Suter parameters) to characterise the dynamic behaviour of a Francis turbine. This approach assumes a homologous relationship between turbines and pumps. Two parameters can be obtained as follows:

$$W_H(\theta) = \frac{H/H_{rated}}{(N/N_{rated})^2 + (Q/Q_{rated})^2}$$

$$W_T(\theta) = \frac{T/T_{rated}}{(N/N_{rated})^2 + (Q/Q_{rated})^2} \qquad (4.11)$$

where W_H = dimensionless head coefficient

W_T = dimensionless torque coefficient

T = mechanical torque generated by Francis turbine

T_{rated} = rated mechanical torque generated by Francis turbine

θ = angle of operating zone = $\tan^{-1}(N/Q)$

The Suter parameters described in Equation 4.11 require an enormous effort to recalculate various parameters listed in the model test report [128] for the Mackintosh turbine. Two independent variables N and Q are needed to work out a particular turbine operating condition. Hydraulic turbine engineers always work with the head and power coefficients, as the flow and mechanical torque are difficult to measure in full-scale prototype. It should be noted that exact similarities (geometric, kinematic, and dynamic) in the operation of Francis turbine installations must be achieved so that model test data can be used correctly for the full-scale turbine. To satisfy geometric similarity, the turbine model should be tested with identical guide vane settings, same runner design, and similar draft tube geometry. As meridional velocity v_m in the Francis turbine is proportional to Q / D_{Turb}^2 , and the peripheral speed of the turbine runner u is proportional to ND_{Turb}, it can be seen that kinematic similarity (v_m / u) requires the flow coefficient C_Q to be constant in order to ensure similar flow patterns or velocity diagrams at the turbine. Dynamic similarity requires all force components in the same ratio for both model and prototype, which implies that the head coefficient C_H and Reynolds number must be the same for both installations.

For an incompressible and non-cavitating flow, the turbine operation is accurately described by the following relation:

$$C_H = f(C_Q, Re) \text{ or } C_P = f(C_Q, Re) \tag{4.12}$$

Changes in turbine performance with Reynolds number are relatively slow, and for small variations in Reynolds number, the Francis turbine performance can be approximated by:

$$C_H = f(C_Q) \text{ or } C_P = f(C_Q) \tag{4.13}$$

In real cases, the turbine net head will vary due to transients or long period changes in the supply head. Similar operating conditions (C_Q, C_H constant) with varying speed require that $Q \propto N$, $H \propto N^2$, and $P \propto N^3$ or alternatively $N \propto H^{0.5}$, $Q \propto H^{0.5}$, and $P \propto H^{1.5}$.

Model test data for the Francis turbine are usually presented in a hill chart or in a series of tables. Finding efficiency data over the whole ranges of turbine operating conditions is difficult. This is particularly true for an ageing turbine plant. Turbine manufacturers

regard such information as proprietary and often publish efficiency data as relative with a peak relative efficiency for runner set at unity. Nearly all published efficiency data for full-scale turbines are provided as a curve of efficiency plotted against power. For the Mackintosh power station, the model test data is published in terms of pseudo-dimensionless groups: unit speed ($N_{11} = ND_{Turb} / H^{0.5}$), unit discharge ($Q_{11} = Q / H^{0.5} D_{Turb}^2$), and unit power ($P_{11} = P / H^{1.5} D_{Turb}^2$). However, only data near the best-efficiency operating conditions are presented in the chart. Information regarding off-design conditions is not available.

Gordon [38] has developed a generic formula based on empirical data from eight different Francis turbines to describe the shape of the turbine efficiency curve:

$$\eta_q = \eta_{peak} - \Delta\eta_{peak} \tag{4.14}$$

where η_q = turbine efficiency at flow Q

η_{peak} = peak turbine efficiency

$$= 0.9187 - [(1998 - y)/187]^3 - [(N_s - 52)/292]^{1.017} + d_{size}$$

$\Delta\eta_{peak}$ = change from peak turbine efficiency

$$= \eta_{peak}\left[\left(1 - \frac{Q}{Q_{peak}}\right)\Big/\left(1 - \frac{Q_{nl}}{Q_{peak}}\right)\right]^{3.94 - 0.0195 N_s} \quad \text{for } Q < Q_{peak}$$

$$= \left[\left(\frac{1998 - y_c}{100}\right)^2 + 0.4\right]\left(\frac{Q}{Q_{peak}} - 1\right)^{1.5} \quad \text{for } Q > Q_{peak}$$

y_c = year when unit was commissioned

d_{size} = factor accounting for different size of Francis turbine diameter

N_s = specific speed = $NQ_{rated}^{0.5} h_{rated}^{-0.75}$

Q_{peak} = flow at peak turbine efficiency

From an engineering viewpoint, the shape of efficiency curve is approximated by a parabola with the apex at peak efficiency. Equation 4.14 takes into account three important characteristics of the Francis turbine's efficiency curve: the peak efficiency flow (Q_{peak}) relative to the rated flow (Q_{rated}) changes as the specific speed changes; the shape of efficiency curve becomes flatter as the specific speed decreases; and the no-load flow relative to rated flow position decreases as the specific speed decreases. The

age of the Francis turbine is also being considered in the equation. Higher efficiency values are expected if the unit has recently been commissioned.

For the Mackintosh power station, a combined technique utilising full-scale steady-state test data, Gordon's empirical formula, simulations, and turbine model test results is adopted to form the complete efficiency curve for the Francis turbine. A nonlinear relation can then be established to calculate the per-unit electrical power output generated in a hydro power plant:

$$\overline{P_m} = \overline{\eta}_{Turb}\,\overline{\eta}_{Gen}\,\overline{HQ} \quad \& \quad \overline{\eta}_{Turb} = f(C_Q) \tag{4.15}$$

No further correction for variation from rated head is required with this arrangement. More details about the turbine performance curve will be presented in Section 4.6.2.7.

4.5 Linearised Model of the Single-Machine Power Plant

Linearised models originally designed for implementation on analogue computers are still widely used in the power industry. They are useful only for investigation of small power system perturbations or for first swing stability studies. The linearised plant model using inelastic waterway column theory can be obtained by rearranging the basic equations for waterway and turbine system (Equations 4.2, 4.3 and 4.10). The formulation is based on small perturbations in flow, head, guide vane opening, and power output during the operation. To ease the calculation, the linearised model always assumes that the turbine is ideal, hydraulic losses in the conduit are negligible, flow is uniform, and other flow effects are minimal for a small change in guide vane position. The resulting model is expressed by:

$$\frac{\Delta\overline{P}_m}{\Delta\overline{G}} = \frac{1 - T_{Wt}s}{1 + 0.5T_{Wt}s} \tag{4.16}$$

Readers are referred to Kundur [59] for full derivations of this linearised model. Equation 4.16 represents a typical "non-minimum phase" system since its zero is located in the right half of the s-plane[1]. In other words, the system will always behave

[1] A two-dimensional complex space defined by a real-number axis and imaginary-number axis. It is used in control theory to visualise the roots of equation describing a system's behaviour. This equation is normally expressed as a polynomial in parameter 's' of the Laplace transform, and hence named s-plane.

stably. When knowledge of the frequency response of such a system is required, both the phase and magnitude of the system must be investigated as it does not possess a minimum amount of phase shift for a given magnitude plot. This is important if the system is to manoeuvre at the highest frequency possible. The water starting time constant T_{Wi} in this case corresponds to the turbine nominal operating condition rather than the rated condition and must therefore be adjusted according to the variation of the guide vane opening ($\overline{G}_{ini}$) if the initial operating conditions are changed, according to:

$$T_{Wi} \cong \overline{G}_{ini} \cdot T_W \tag{4.17}$$

The complete time response of the linearised plant model can be examined by taking the inverse Laplace transform of Equation 4.16:

$$\Delta\overline{P}_m(t) = \left(1 - 3e^{-\frac{2t}{T_{Wi}}}\right)\Delta\overline{G}(t) \tag{4.18}$$

For an ideal turbine with a given step increase in guide vane opening, the normalised power output is bounded within values of [-2, 1]. The initial power surge will be opposite to the direction of change in guide vane position because of the inertia effect of the waterway conduit. Applying an elastic waterway model and still assuming an ideal turbine leads to:

$$\frac{\Delta\overline{P}_m}{\Delta\overline{G}} = \frac{1 - \overline{Z}\tanh(T_e s)}{1 + 0.5\overline{Z}\tanh(T_e s)} \tag{4.19}$$

Although simplified, Equation 4.19 is still difficult to solve analytically and a reduced-order approach is needed to approximate the hyperbolic tangent:

$$\tanh(T_e s) = \frac{1 - e^{-2T_e s}}{1 + e^{-2T_e s}} = \frac{sT_e \sum_{n=1}^{\infty}\left[1 + \left(\frac{T_e s}{n\pi}\right)^2\right]}{\sum_{n=1}^{\infty}\left[1 + \left(\frac{2T_e s}{(2n-1)\pi}\right)^2\right]} \tag{4.20}$$

The number of terms to be retained in the series expansion depends on the purpose of study and the accuracy required. However, the model may become unstable and results will be useless for system stability studies if higher-than-four order series expansion is employed. Kundur [59] shows that the linearised plant model using inelastic waterway conduit theory has a phase characteristic that is valid up to about 0.1 Hz while the linearised plant model assuming elastic waterway column (with n = 1 in Equation 4.20) is valid up to about 1.0 Hz.

Figure 4.3 shows a typical load acceptance test case for the Mackintosh station. The performances of the linearised and nonlinear plant models (applying inelastic water column theory) are compared here. For this large load disturbance, it is easily seen that nonlinear model outperforms linearised model in predicting the transient behaviour of the plant. The linearised model fails in the sense that it predicts a much lower power fluctuation when the guide vane position has changed significantly. This is expected, as the linearised model is inadequate for studies involving large variations in power output [59]. Hence, nonlinear modelling of Francis-turbine operation is highly recommended for large-signal time-domain simulation.

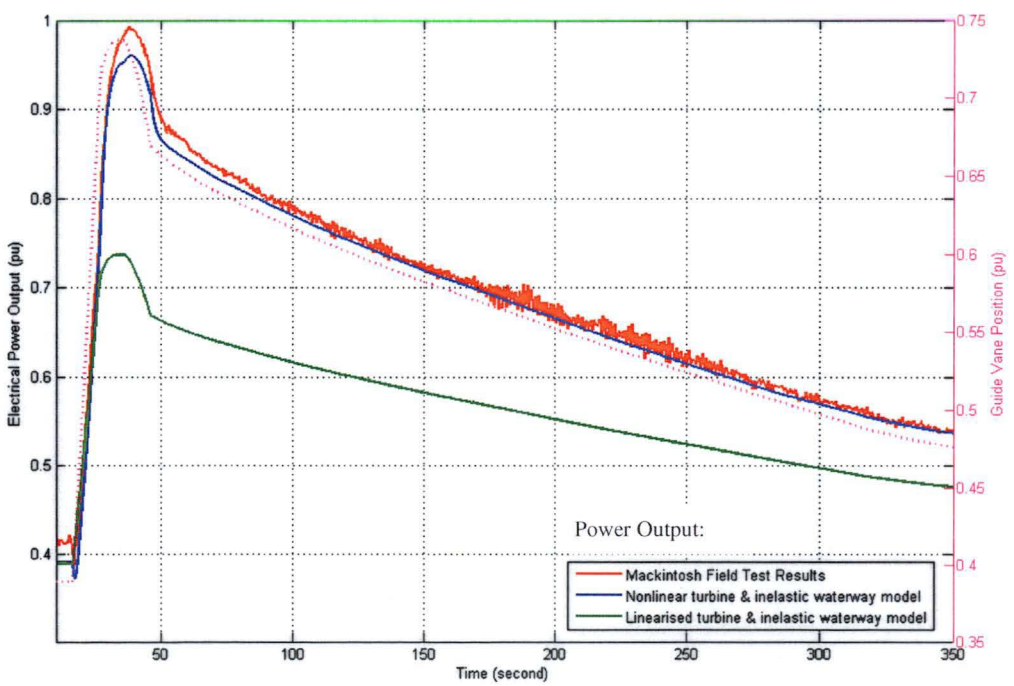

Figure 4.3: Comparison between linearised and nonlinear plant models using inelastic waterway column theory for a given load acceptance in Mackintosh station (Dotted line indicates main servo position and solid lines represent power output of the machine)

4.6 Transient Analysis of the Single-Machine Power Plant

4.6.1 Model Structure and Formulation

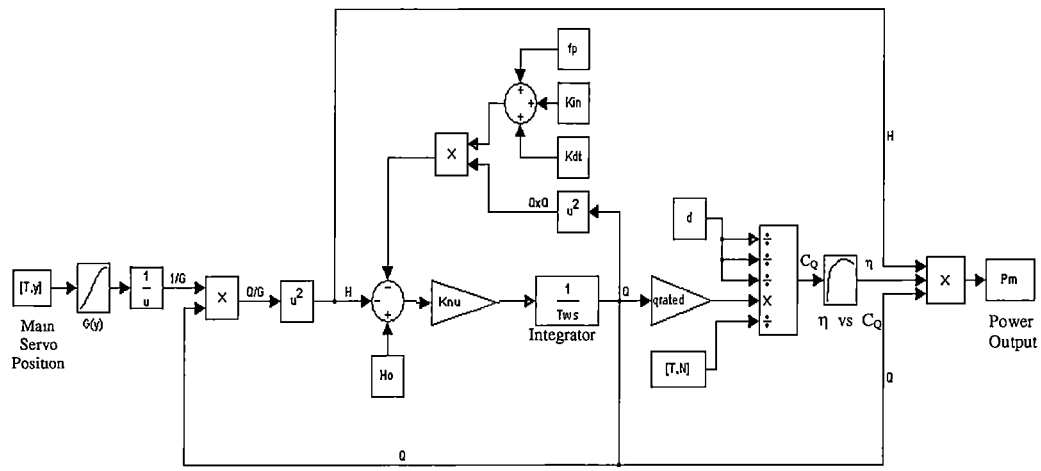

Figure 4.4: Simulink block diagram showing the nonlinear turbine and inelastic waterway model for Mackintosh power plant

A one-dimensional nonlinear power plant model has been used in the transient analysis of the Mackintosh power station. The model is formulated on the basis of inelastic water column theory and nonlinear representation of the Francis turbine characteristics. MATLAB Simulink is employed to solve these normalised equations (Equations 4.2, 4.3, and 4.15) for each main servo position and time instant simultaneously. The Simulink block diagram is shown in Figure 4.4. Main-servo position $y(t)$ and turbine rotational speed $N(t)$ are two main inputs to the power plant model, while the power output from the machine $P_m(t)$ is the only output variable from the model. The computed head and flow from the inelastic waterway model is fed into the turbine model, which is used to determine the transient output of the power plant. Determination of the nonlinear guide vane function, calculation of the water starting time constant, identification of various hydraulic parameters such as conduit loss coefficients, draft tube force coefficient and inlet dynamic pressure head coefficient, as well as the construction of turbine characteristic curve for the Simulink model, will be discussed in Section 4.6.2.

The default solver *ode45* [124] is used in the Simulink model to numerically integrate the linear momentum equation and calculate the per-unit turbine flow rate. It is a one-

step solver based on the 4/5-order Runge-Kutta formula, the Dormand-Prince pair, which is designed to handle the initial value problem for systems of differential equations with the form of $y' = f(y, t)$. The solver imposes the initial conditions at the beginning of a calculation and returns the solution evaluated at every integration step. Only the solution from the immediately preceding time point is needed for each integration step. This solver algorithm is recommended for power plant simulation because it requires the smallest number of function evaluations, the minimal number of floating-point operations, and the least amount of numerical steps to get a converged solution compared to other solver algorithms built in the MATLAB Simulink [124]. Overall, the model is set up in the way that no algebraic loop will occur in the simulation. The implications of algebraic loops and the need to avoid them are well explained in MATLAB user manual [124].

When the guide vanes of a turbine become almost closed and the associated flow rate in the conduit decreases, the numerical integration of the ordinary differential equation becomes more difficult due to the assumption of inelastic water column. If the turbine guide vanes are shut off at some small discharge Q, the value of this turbine flow will be replaced discontinuously by zero. In this case, the flow rate Q will become less than a small value ΔQ and the mass continuity at the upstream and downstream ends of the conduit can no longer hold. In fact, the jump in flow rates is incompatible with a strictly applied inelastic water column assumption. To resolve this issue, a decision block is added to the model to overcome the discontinuity problem and ensure that simulation runs smoothly when the guide vanes are almost closed.

4.6.2 Evaluation of Hydraulic Model Parameters

The parameter identification and evaluation process for the Francis-turbine plant model requires numerous simulations to examine the effects of changing one model parameter on the overall plant response. For each parameter change, a comparison is made between response of the model and that recorded from the field tests. This traditional methodology is highly dependent on the skills of the experienced engineers applying their knowledge to select the best-suited parameters, perform calculations using those parameters, and adjust the parameters manually based on difference between measured and calculated values to improve the fit between model and real-plant response. The

task becomes even more tedious if non-linear dynamic interactions are involved in the power plant modelling. Various important hydraulic model parameters for Simulink model of the Mackintosh power station will be thoroughly assessed and discussed in the following subsections.

4.6.2.1 Rated Parameters Used in the Per-Unit System

It is common practice in time-domain simulations of power plant to express the resulting head, flow rate and the power output of a machine in a normalised way or a per-unit (pu) base. The advantages of the per-unit system are that it:

- imposes proper scaling, which is good for numerical solution;
- yields valuable relative magnitude information; and
- simplifies searching of erroneous data since the parameters tend to fall in relatively narrow numerical ranges.

For the Mackintosh power plant, the rated flow of the Francis turbine, which corresponds to the turbine flow when guide vanes are fully opened, is chosen as the base flow value in the calculation. The base value for static pressure head is defined as the elevation difference between water levels at Lake Mackintosh and Lake Rosebery when the machine is operating at the design condition; but the rated power output is related to the amount of electrical power generated by the machine under the base flow and head values. The rated turbine efficiency is obtained by dividing the actual turbine output with the hydraulic power input (ρgHQ) of the machine. However, the choices of these base values are not restricted. Users are free to choose any set of base quantities for power, head, and flow in the model as long as they are consistent throughout the calculations. The values of rated parameters used in the present modelling of Mackintosh power plant are listed in Table 4.1.

Rated Parameters Used in Per-Unit System	*Base Values*
Rated Speed (rpm)	166.7
Rated Head (m)	61
Rated Flow Rate (m^3/s)	149.7
Rated Power Output (MW)	79.9
Rated Guide Vane Opening (%)	100
Rated Turbine Efficiency (%)	89.2
Rated Generator Efficiency (%)	97

Table 4.1: Rated parameters used in the per-unit based simulation of transient operations of the Mackintosh station

4.6.2.2 Total Available Static Pressure Head

The total available static head H_o is defined as the elevation difference between head and tail water levels. For the Mackintosh power station, the average water levels at Lake Mackintosh and Lake Rosebery are measured and recorded daily. The full storage level of Lake Mackintosh is 228.6 m above sea level while the minimum operating level of Lake Mackintosh is 218.8 m above sea level. The average water level at Lake Rosebery is 159.3 m above sea level, and is essentially independent of the station flow (only ±0.4 m variation between full- and no-flow operating conditions). The normal operating head of the Mackintosh power station is approximately 61 m. However, the total static head increased from 60 to 65 m during the field tests because of the significant rainfall at that time. The variation of the total available static head must be taken into account in the transient simulation of the Francis-turbine power plant, as it will affect the accuracy of the computed turbine flow from the waterway model.

4.6.2.3 Water Starting Time Constant

The water starting time constant T_W is defined as the amount of time required to accelerate the flow from zero to the rated flow under the base head or rated head (Mansoor [70]). The time constant calculation is based on the geometry of the waterway system when the machine is operating at rated conditions. Unlike the linearised model where instantaneous flow and head values are employed, the water starting time of the nonlinear waterway model does not need to be updated in successive iterations for a simulation. However, it is essential to ensure that consistent values of rated flow and rated head are used in the calculation of water starting time constant. For an inelastic waterway conduit with varying geometries and irregular cross-sectional areas, the water starting time constant is computed from:

$$T_W = \sum \left(\frac{L_i}{A_i} \right) \times \frac{Q_{rated}}{g h_{rated}} \tag{4.21}$$

The computation of the water starting time constant for Mackintosh station includes the entire waterway column from the reservoir to the tailrace, which also incorporates the flow passage through the Francis turbine and draft tube components. A constant starting time of 3.17 seconds is used in the modelling of transient operation for Mackintosh

power plant. Vaughan [130] examined the effects of varying the water starting times of the model based on simplified and detailed waterway columns. Detailed calculation of the water starting time was found to greatly improve the predicted time-domain response of the power plant, and to reduce the magnitude of differences between the measured and simulated results [135]. However, significant phase error is still reported in Vaughan's simulations.

4.6.2.4 Head Loss Coefficient

The flow in the waterway system is turbulent and highly complex. A portion of the energy has to be spent to overcome the forces of hydraulic resistance in the conduit. This analysis is restricted to the computation of steady-flow head loss coefficient. As little information is available on the flow structure during transients, the quasi-steady flow assumption has to be made so that the steady-flow loss coefficients can be used. The overall pressure or head loss can be found by summing the pressure losses of all individual components along the waterway conduit [81]. This includes head losses due to friction and other minor losses due to geometrical transitions and turbulence within the bulk fluid. The formula for conduit head losses on a per unit base is:

$$\overline{H}_f = f_P \overline{Q}^2 \quad \text{where} \quad f_P = \sum \left(\frac{k_t}{A_t^2} \right) \left(\frac{Q_{rated}^2}{2gh_{rated}} \right) \tag{4.22}$$

The k_t values in Equation 4.22 represent the loss coefficients of individual components that are determined from given empirical charts or tables. The calculating procedures of the loss coefficients are well documented in Miller [81] and Idelchik [46].

Friction losses in the conduit are normally represented by a factor depending on the dimensions and surface roughness of the conduit, fluid viscosity, and flow speed. The effects of joints, local resistance, blockages, formation of wall deposits, and other complicating factors may increase the friction losses in the pressure tunnel. In fact, friction calculations involve an element of judgement in selecting roughness values [46]. It is assumed in the current study that the concrete tunnel has good surface finish and average joints, while the steel penstock is smooth and without any significant deterioration on the walls. Numerous formulae are available to relate the friction factor

(f) to the Reynolds number (Re) of the flow and the relative roughness (ε) of the conduit. One of the most popular formulae is Colebrook-White equation [139]:

$$\frac{1}{\sqrt{f}} = -2\log_{10}\left(\frac{\varepsilon}{3.7D_{eq}} + \frac{2.51}{\mathrm{Re}\sqrt{f}}\right) \tag{4.23}$$

The equivalent diameter $D_{eq} = A / P$ is used to account for non-circular cross-section geometry. Equation 4.23 is solved by iterating through assumed values of friction factor f until both sides are equal. A quick solution of friction factor can be obtained graphically from Moody diagram.

For the rectangular intake structure, minor energy losses occur in the entrance and contraction zone. The entrance loss coefficient is a measure of the efficiency of the inlet structure to smoothly transport the water flow from the upstream reservoir into the pressure tunnel; although it does vary with flow, a constant value corresponding to the full flow condition is used here. The "wing-wall" build at the entrance has the effect of streamlining the flow into the tunnel and hence can minimise the energy losses. Moreover, a converging section with a contraction length ratio of 7 is employed to provide a gradual change in the area and velocity, which has a positive impact on minimising losses at the inlet.

A 22° bend at the end of the concrete-lined tunnel (see Figure 4.2) will cause a diffuser effect at the outer (bottom) wall and a bellmouth effect at the inner wall. This generates a secondary flow along the bend and may lead to flow separation in the penstock. The bend loss is strongly dependent on the bend curvature, flow Reynolds number, surface roughness, and the geometry of the connecting tunnels at both ends.

Transition losses for the elbow draft tube are also included in the head loss calculation. Losses due to the combined turning and diffusion in the draft tube are highly dependent on the inlet-outlet area ratio, inlet boundary layer thickness, bend angle, and the outlet conditions. The kinetic energy of flow at exit from the draft tube is always lost to the system. It is assumed that the exit flow is discharged into an infinitely large reservoir and therefore the downstream effect will be minimal in this case. More details about the

flow behaviour inside the turbine draft tube will be presented in Chapters 7 and 8. Table 4.2 summarises the values of head loss coefficients for the Mackintosh simulations.

Component i	*Loss Type*	*Loss Coefficient, k_i*	*Normalised Loss Coefficient, f_{Pi}*
Intake Structure	*Entrance*	0.100	2.55×10^{-7}
	Contraction	0.100	2.55×10^{-7}
	Head Gates	0.100	2.55×10^{-7}
	Friction	0.027	6.89×10^{-8}
Concrete Tunnel	*Friction*	0.292	3.30×10^{-5}
	Bend	0.051	5.76×10^{-6}
Steel Penstock	*Friction*	0.148	1.67×10^{-5}
Draft tube	*Friction*	0.059	1.78×10^{-5}
	Transition	0.150	4.53×10^{-5}
	Exit	1.000	1.16×10^{-5}
		Σ	1.31×10^{-4}

Table 4.2: Steady-flow head loss coefficients for Mackintosh hydraulic system (Loss coefficients are expressed in per-unit base)

4.6.2.5 Inlet Dynamic Pressure Head Coefficient

The conversion of pressure energy to kinetic energy in the tunnel inlet will cause a drop in the total available static pressure. This effect cannot be ignored, especially if the machine is operating at high flow rates. Dynamic pressure at inlet can be expressed in the similar way as the conduit head losses. A normalised equation for dynamic pressure head can be established as below:

$$\overline{H}_{IN} = K_{IN}\overline{Q}^2 \quad \& \quad K_{IN} = \frac{Q_{rated}^2}{2gA_{IN}^2 h_{rated}} = 2.552\times10^{-6} \tag{4.24}$$

The cross-sectional area at the entrance of the rectangular intake structure is used in the calculation of this head coefficient. Dynamic pressure head (i.e. inlet velocity head) will increase as the guide vane opening or the turbine flow rate is increased.

4.6.2.6 Draft Tube Static Pressure Force Coefficient

The static pressure force acting on the turbine draft tube must be included in the linear momentum equation because the inertia effect of the entire waterway column is also being considered in the calculation of water starting time. The static pressure force depends on the turbine flow and is expressed in a dimensionless force coefficient $C_{F\text{-}dt}$.

The value of this coefficient has been determined through steady-flow CFD simulation of draft tube flow (see Chapters 7 and 8). A constant value of $C_{F\text{-}dt} = 1.15$ is currently employed in the simulation for simplicity. Discussions about transient effects of the draft tube flow on power plant simulation will be presented later in Chapter 8. The normalised static pressure force at draft tube is represented in the Equation 4.25, in which A_{IN} corresponds to the inlet cross-sectional area of the draft tube:

$$\overline{H}_{dt} = K_{dt}\overline{Q}^2 \quad \& \quad K_{dt} = \frac{C_{F-dt}Q_{rated}^2}{2gA_{IN}h_{rated}} = 4.5\times10^{-3} \tag{4.25}$$

4.6.2.7 Turbine Characteristics

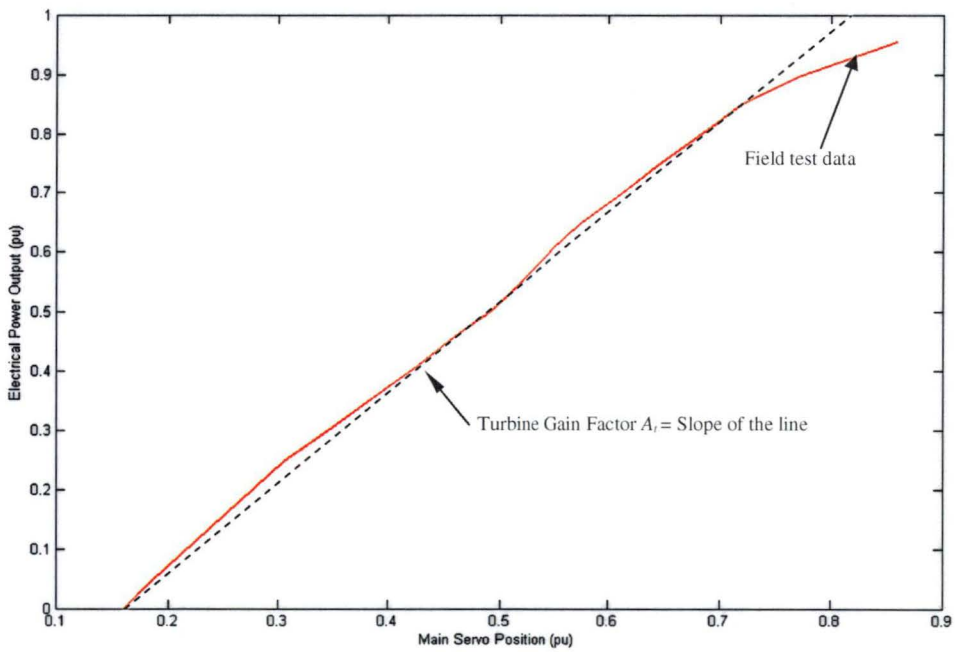

Figure 4.5: Steady-state measurement of Mackintosh power plant to characterise the Francis-turbine performance ($H \approx 60$ m)

The conventional IEEE turbine model (see Equation 4.10) uses site test results to describe the turbine performance [34, 141]. It is based solely on the steady-state measurements relating electrical power output with the main-servo position. Turbine performance is assumed to depend only on the main servo position or guide vane opening. Figure 4.5 shows a typical test result for steady-state measurements at Mackintosh station. These tests are carried out at a constant speed and without significant head variation. The turbine gain factor A_t is determined via the slope of a

straight line fit between the no-load and best-efficiency operating conditions. The formula for the gain factor is:

$$A_t = \frac{\overline{P}_{m-BE} - \overline{P}_{m-nl}}{\overline{y}_{BE} - \overline{y}_{nl}} \tag{4.26}$$

where $\overline{P}_{m-BE}$ = per-unit electrical power output at best-efficiency condition
$\overline{P}_{m-nl}$ = per-unit electrical power output at no-load condition
$\overline{y}_{BE}$ = per-unit main servo position at best-efficiency condition
$\overline{y}_{nl}$ = per-unit main servo position at no-load condition

The no-load condition is denoted as the operating point where turbine efficiency is zero. Per-unit no-load flow is about 0.16 and the turbine gain factor is 1.48 for Mackintosh station. This method is easy to apply but it does not allow for the efficiency variations (or damping effects in power engineering nomenclature) due to speed and head changes.

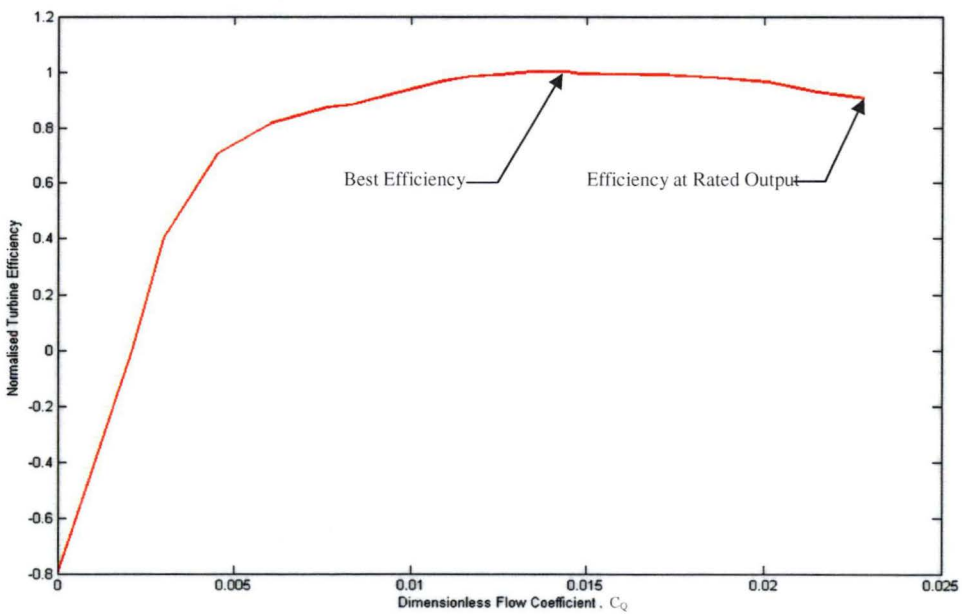

Figure 4.6: Turbine characteristic curve relating normalised turbine efficiency η_{Turb} /$\eta_{Turb\text{-}rated}$ to the dimensionless flow coefficient C_Q

Instead of using this standard approach, it is more accurate to use the relationship between turbine efficiency and dimensionless flow coefficient to derive the actual power output of the machine. The instantaneous flow coefficient C_Q is calculated using instantaneous values of turbine net head (H) and rotational speed (N) as well as the runner diameter (D_{Turb}). The characteristic curve shown in Figure 4.6 is obtained using a combination of data from full-scale steady state tests, Gordon's formula, simulations

and model test results. This approach will automatically take in to account the efficiency variations due to *both* speed and head changes, and therefore no further damping correction for variation from rated head is required. Direct effects of head change are also incorporated in this method.

Model test results and full-scale measurements of the Mackintosh turbine show that the efficiency does not vary greatly with the net head. However, only data with flow coefficient above 0.0048 are presented in the hill chart of the turbine model. To fill the gap, Gordon's empirical formula, simulation, and steady-state test results were used to determine the turbine efficiency where the flow coefficient is below 0.0048 (i.e. the first five data points). The negative efficiency in the curve implies that the power is supplied to the generator in order to synchronise the machine. The generator is assumed to work at a constant efficiency of 97% (or 1 in per-unit system) as no relevant information on the generator efficiency is available in the Hydro Tasmania's database.

4.6.2.8 Nonlinear Guide Vane Function

The guide vane function is the key parameter relating the water flow and the net head of the Francis turbine. The working principle is very similar to a nozzle orifice. However, the resulting flow pattern for the Francis turbine is more complicated than the flow in an orifice meter; and secondary flow, separation, and turbulence effects are more severe inside a Francis turbine. The amount of head drop across the turbine depends on the guide vane opening. The head drop decreases as the guide vanes close. The guide vane function is defined as [26, 76]:

$$\overline{G} = \frac{C_D A_G}{C_{D0} A_{G0}} \quad \& \quad A_G = f(y) \tag{4.27}$$

$$\begin{cases} \overline{G} = 0 & \text{if guide vanes are fully closed} \\ \overline{G} = 1 & \text{if guide vanes are fully open} \end{cases}$$

where C_D = instantaneous discharge coefficient at the given guide-vane opening area A_G

C_{D0} = reference discharge coefficient at full guide-vane opening area A_{G0}

y = instantaneous main servo position

Precise values of discharge coefficient depend on the specific turbine geometry, flow and Reynolds number. Overall, the guide vane function consists of two nonlinear relationships:

- The guide-vane opening area varies nonlinearly with main servo position.
- The discharge coefficient varies nonlinearly with guide-vane opening area.

Nonlinear relations for the guide-vane opening area and the main servo position can be obtained directly by measuring the opening area of the guide vanes with increasing main servo stroke from the fully closed position. Eleven data points are determined based on the geometry of the guide vanes and main servo linkages for Mackintosh turbine. A 3-order polynomial curve fit has been applied for these data.

For nonlinear variation of the discharge coefficient, a quadratic approximation is used in the parameter identification process [26]. An optimising algorithm using a simple quadratic equation is employed in the MATLAB program. As shown in Equation 4.28, the discharge coefficient is a function of guide-vane opening area A_G [76]. Only one parameter C needs to be identified.

$$C_D = A_G - C + 4C(A_G - 0.5)^2 \tag{4.28}$$

The tuning process starts with an initial guess of the parameter C. The value of C is then tuned until the variations between the simulated and measured results are minimised. A constant value of $C = -0.285$ is found to best fit the simulated results with the field data.

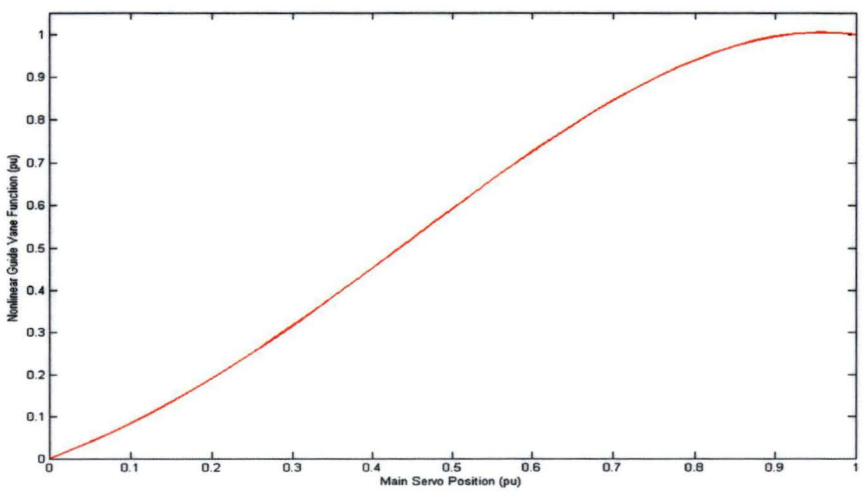

Figure 4.7: Characteristic curve showing nonlinear guide vane function versus main servo position for Mackintosh power plant

Figure 4.7 shows the nonlinear guide vane function used in the Simulink model. This guide vane function combines both effects of nonlinear discharge coefficient and nonlinear guide-vane opening area. Weber [138] and De Jaeger et al. implement a similar parameter optimising procedure for hydro plant modelling. They report a very good agreement between the measured and simulated dynamic transients. Thus, the quadratic form of Equation 4.28 appears satisfactory here but in any case, there is insufficient information available to justify a more complex curve fit at present. A higher-order term could be used in the identification process when more data are available in the future.

4.6.2.9 Coefficient for Flow Non-uniformity

The velocity distribution in the waterway conduit has some impacts on flow acceleration or deceleration. Analysis of the transient flow in the draft tube shows that flow with a non-uniform axial velocity profile at inlet has faster response time than flow with a uniform velocity profile for a given initial flow rate and static pressure fluctuation. This effect is expected to vary nonlinearly with the turbine operating conditions and will be more significant for conditions where flow separation causes greater flow non-uniformity. This will be discussed in more details in Chapter 8. Due to a lack of further information for Mackintosh station, a constant coefficient of k_{nn} = 1.05 is currently used to account for the effect of axial velocity non-uniformity in the turbine and waterway system.

4.6.3 Simulation of Time Response for Single-Machine Station

The time response of a single-machine station subjected to a large frequency disturbance is simulated and analysed here. The main servo position and the turbine rotational speed measured during field tests are used as the inputs to the Simulink model. The total available static head for Mackintosh station is set at a level of 65 m. Simulated electrical power outputs are compared with the site test results. The performances of the conventional IEEE (Figure 2.4) and the improved (Figure 4.4) models are investigated. Load acceptance cases with different initial power outputs are illustrated in Figures 4.8 to 4.12. These results show that the new model is more capable of reproducing the transient behaviour of the Mackintosh power station despite some under-prediction of the magnitude of the transient power at high load. The errors are largely explained by the transient behaviour of the draft tube flow, and these will later be discussed in detail in Chapter 8.

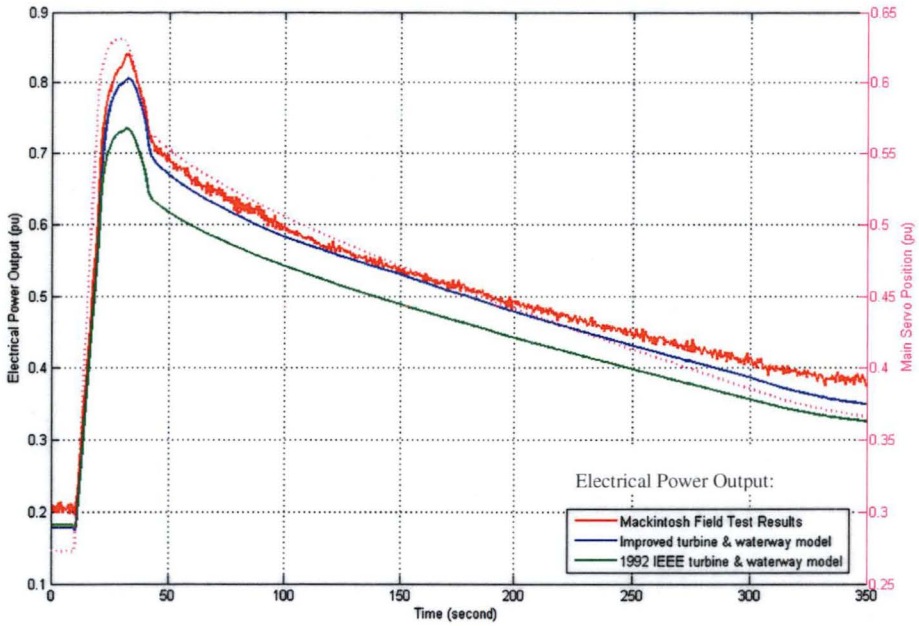

Figure 4.8: Comparison of the simulated and measured power outputs when the machine is operated at an initial load of 0.2 p.u. (Dotted line indicates main servo position and solid lines represent power output of the machine)

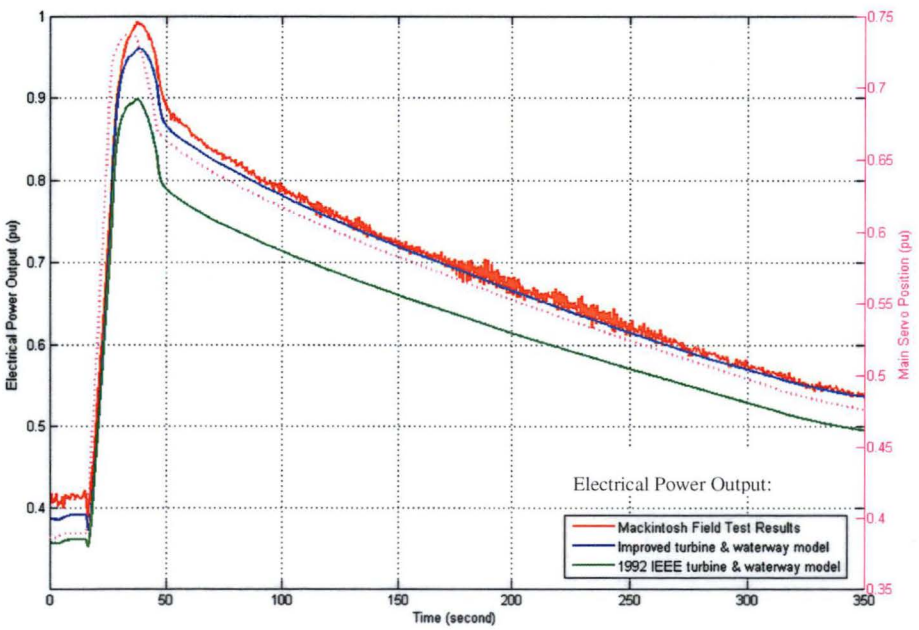

Figure 4.9: Comparison of the simulated and measured power outputs when the machine is operated at an initial load of 0.4 p.u. (Dotted line indicates main servo position and solid lines represent power output of the machine)

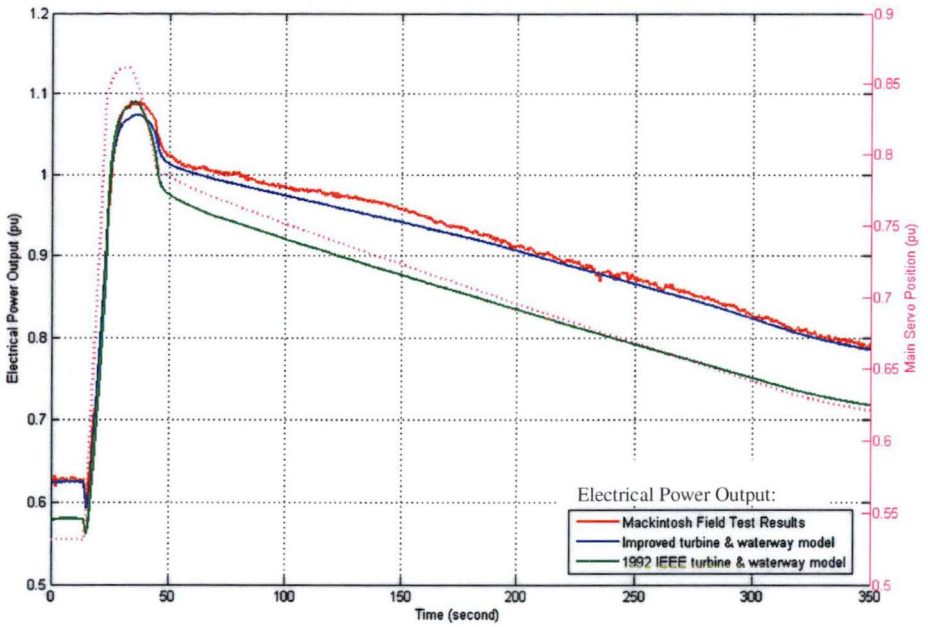

Figure 4.10: Comparison of the simulated and measured power outputs when the machine is operated at an initial load of 0.6 p.u. (Dotted line indicates main servo position and solid lines represent power output of the machine)

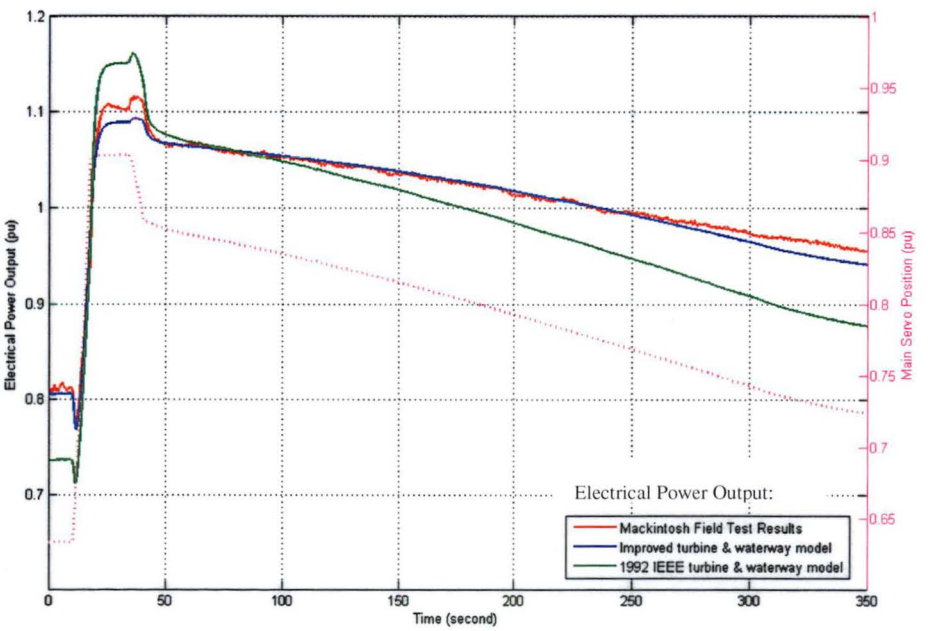

Figure 4.11: Comparison of the simulated and measured power outputs when the machine is operated at an initial load of 0.8 p.u. (Dotted line indicates main servo position and solid lines represent power output of the machine)

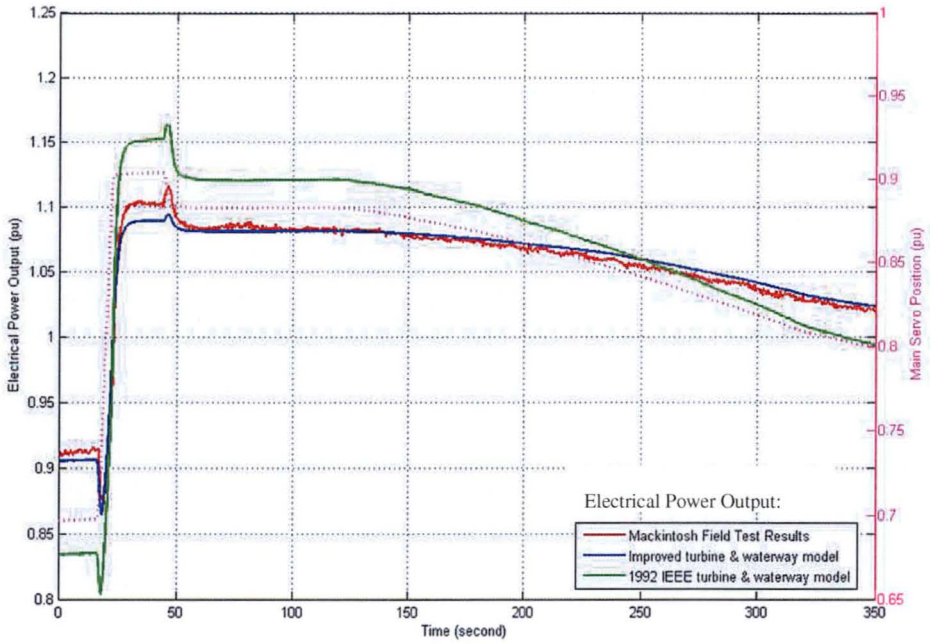

Figure 4.12: Comparison of the simulated and measured power outputs when the machine is operated at an initial load of 0.9 p.u. (Dotted line indicates main servo position and solid lines represent power output of the machine)

4.6.4 Simulation of Frequency Response for Single-Machine Station

Frequency responses of the single-machine power plant are simulated and analysed through a series of Nyquist tests performed at various guide-vane oscillation frequencies (0.01~0.5 Hz). The gain factor A_t for the IEEE model [141] was retuned to 1.15 during the simulations as the turbine is operating outside the linear range. Figures 4.13 to 4.20 compare the simulated and measured power fluctuations at high initial load. The new model better simulates the repetitive power fluctuations for higher test frequencies, but the magnitude of the power fluctuations at lower test frequencies is still not predicted correctly. The error is expected as the quadratic guide vane function does not work well at higher load. The resulting Bode plot is presented in Figure 4.21. The new model gives a more accurate prediction of the phase characteristics, but it fails to show any sign of instability for the range of frequencies covered in the field tests (i.e. predicted phase angle does not cross –180° at highest frequency of 0.5 Hz). There remain some retraceable phase lags between the measured and simulated power outputs, which increase in magnitude with guide vane oscillation frequency. This phase information must be predicted accurately, as it is critical in establishing secure limits for the system operations and identifying operational problems for the power plant.

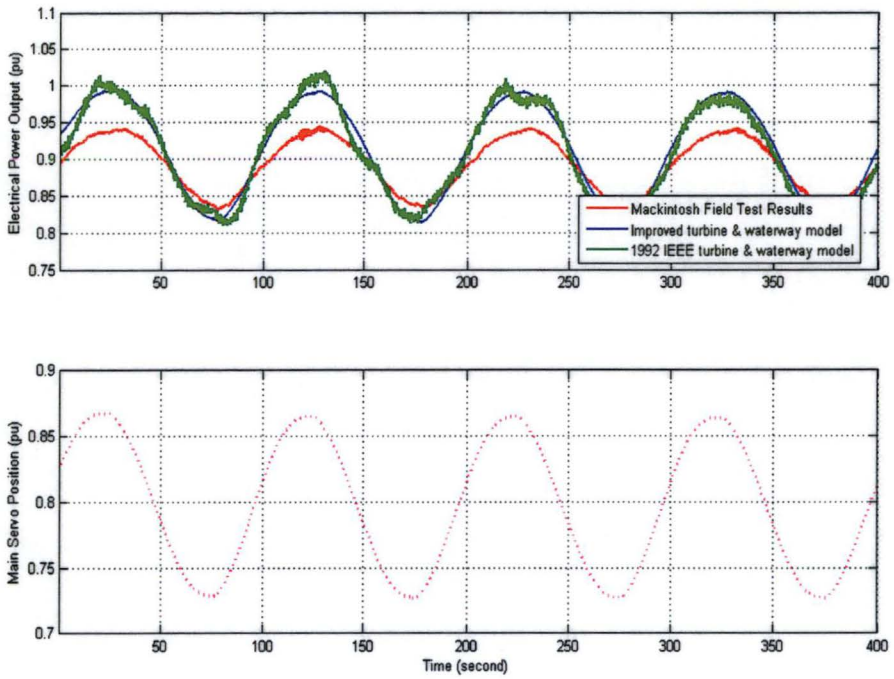

Figure 4.13: Comparison of the simulated and measured power outputs when the turbine guide vanes are oscillating at a test frequency of 0.01 Hz for a given high initial load

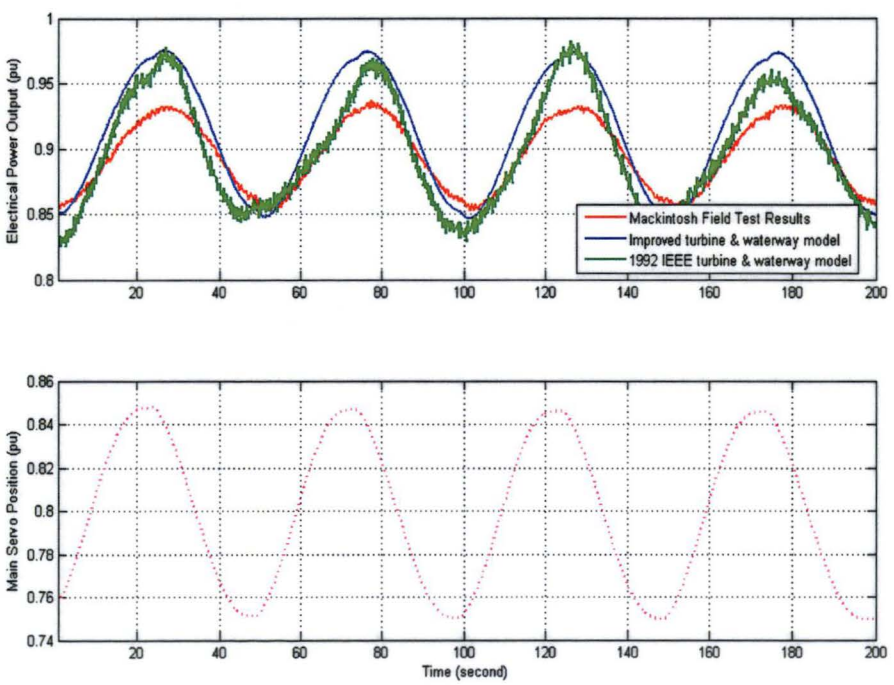

Figure 4.14: Comparison of the simulated and measured power outputs when the turbine guide vanes are oscillating at a test frequency of 0.02 Hz for a given high initial load

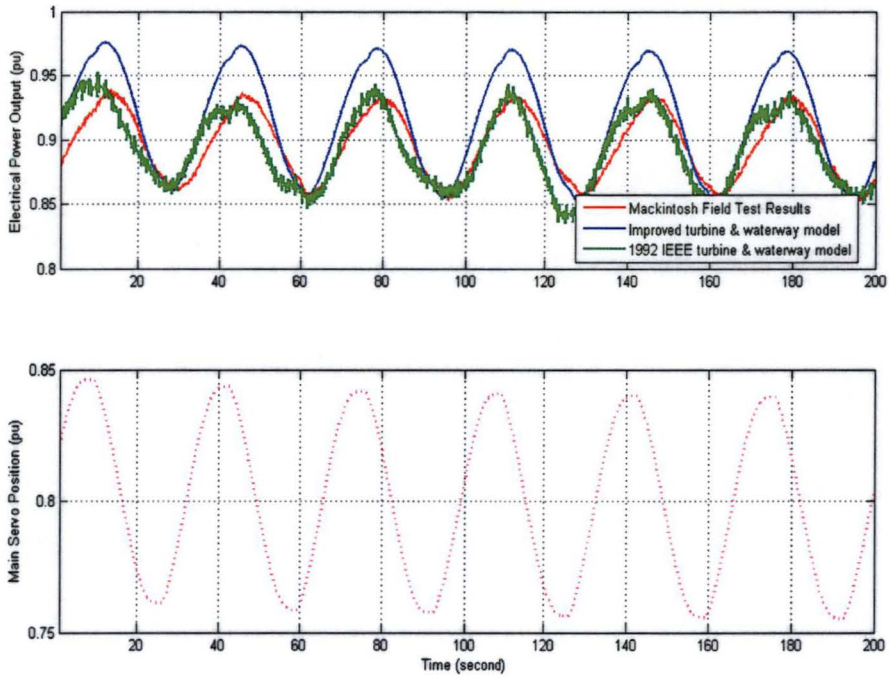

Figure 4.15: Comparison of the simulated and measured power outputs when the turbine guide vanes are oscillating at a test frequency of 0.03 Hz for a given high initial load

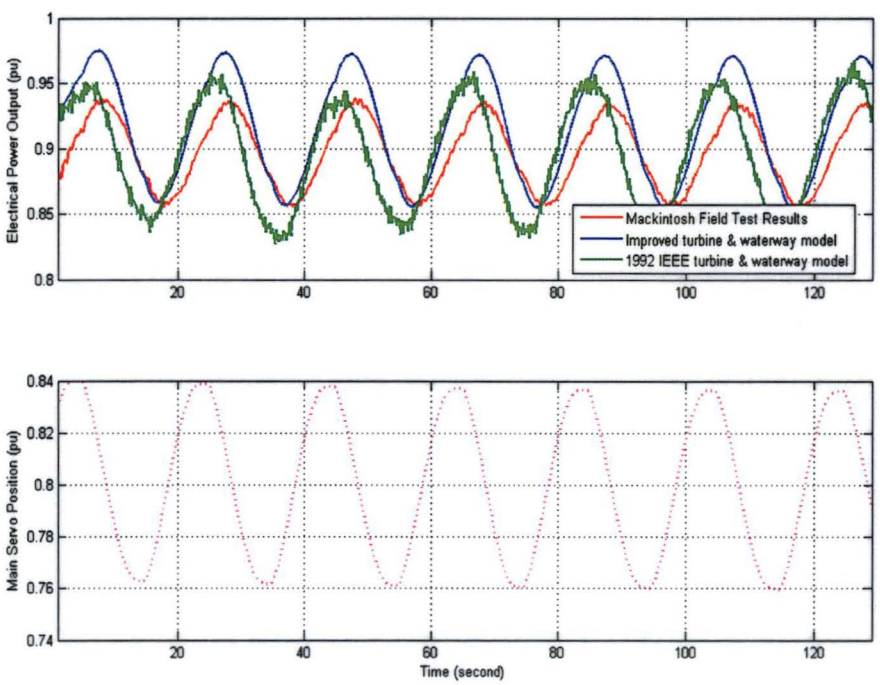

Figure 4.16: Comparison of the simulated and measured power outputs when the turbine guide vanes are oscillating at a test frequency of 0.05 Hz for a given high initial load

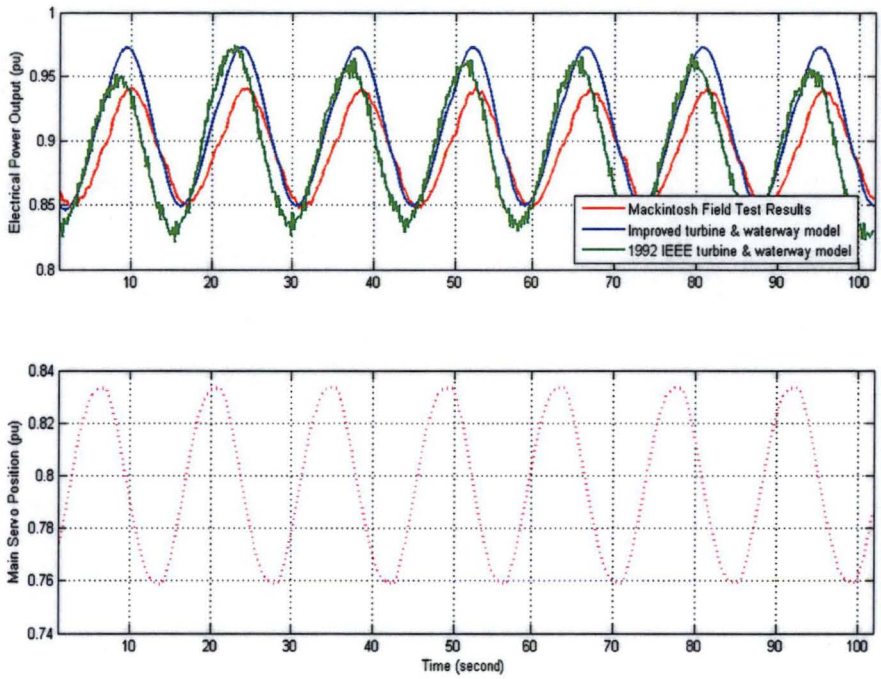

Figure 4.17: Comparison of the simulated and measured power outputs when the turbine guide vanes are oscillating at a test frequency of 0.07 Hz for a given high initial load

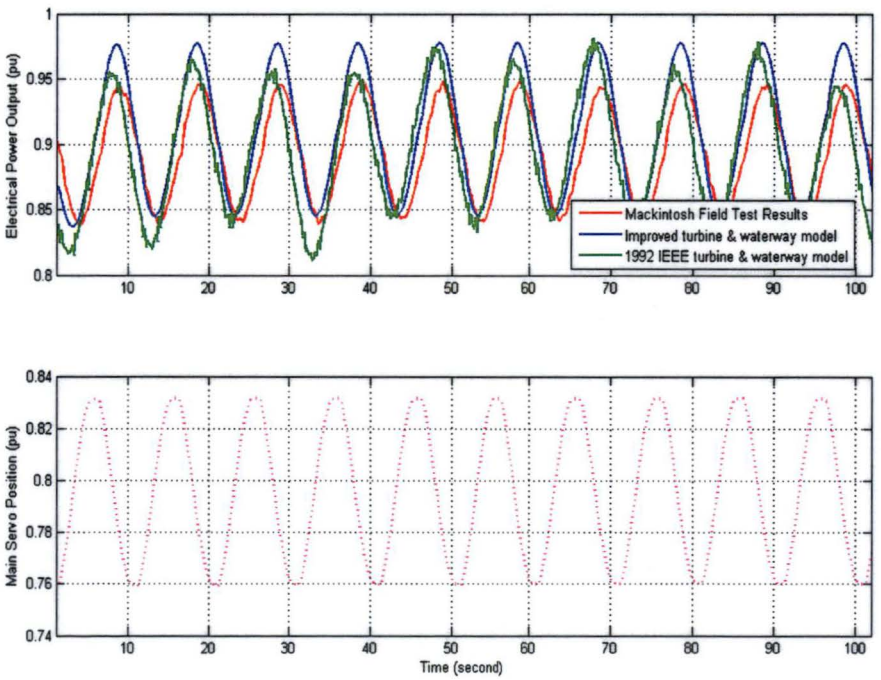

Figure 4.18: Comparison of the simulated and measured power outputs when the turbine guide vanes are oscillating at a test frequency of 0.10 Hz for a given high initial load

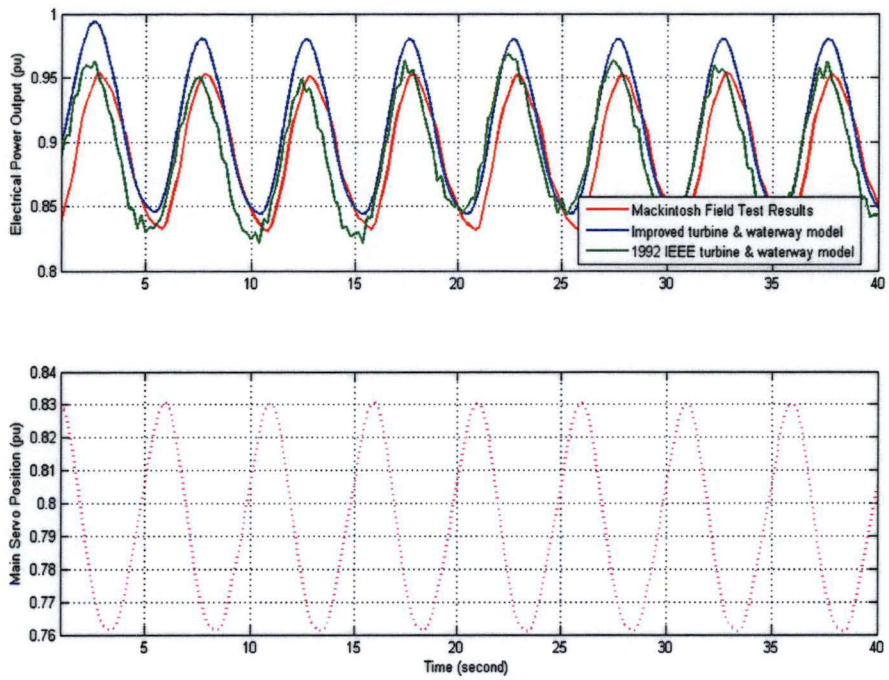

Figure 4.19: Comparison of the simulated and measured power outputs when the turbine guide vanes are oscillating at a test frequency of 0.20 Hz for a given high initial load

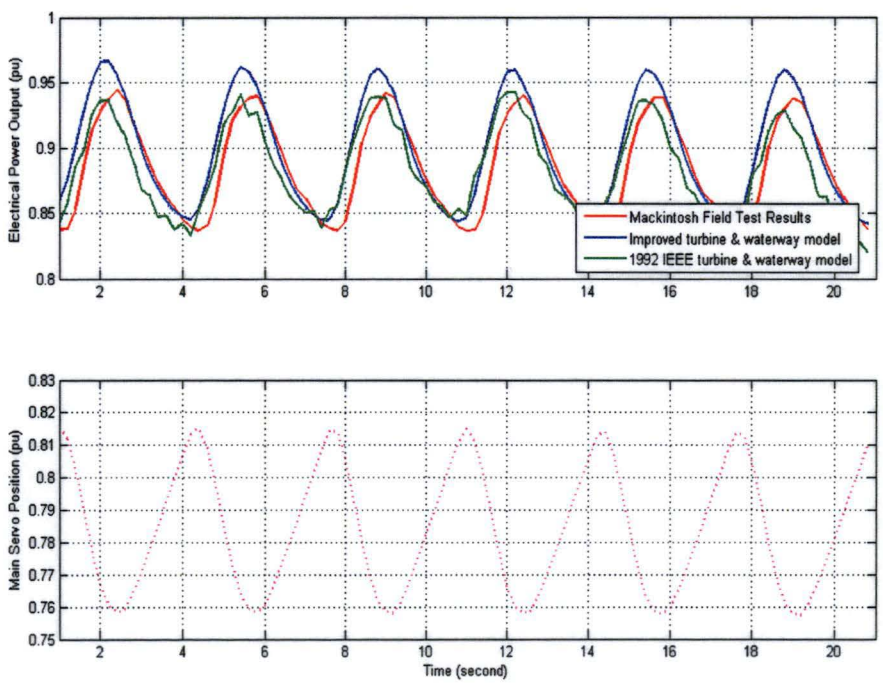

Figure 4.20: Comparison of the simulated and measured power outputs when the turbine guide vanes are oscillating at a test frequency of 0.30 Hz for a given high initial load

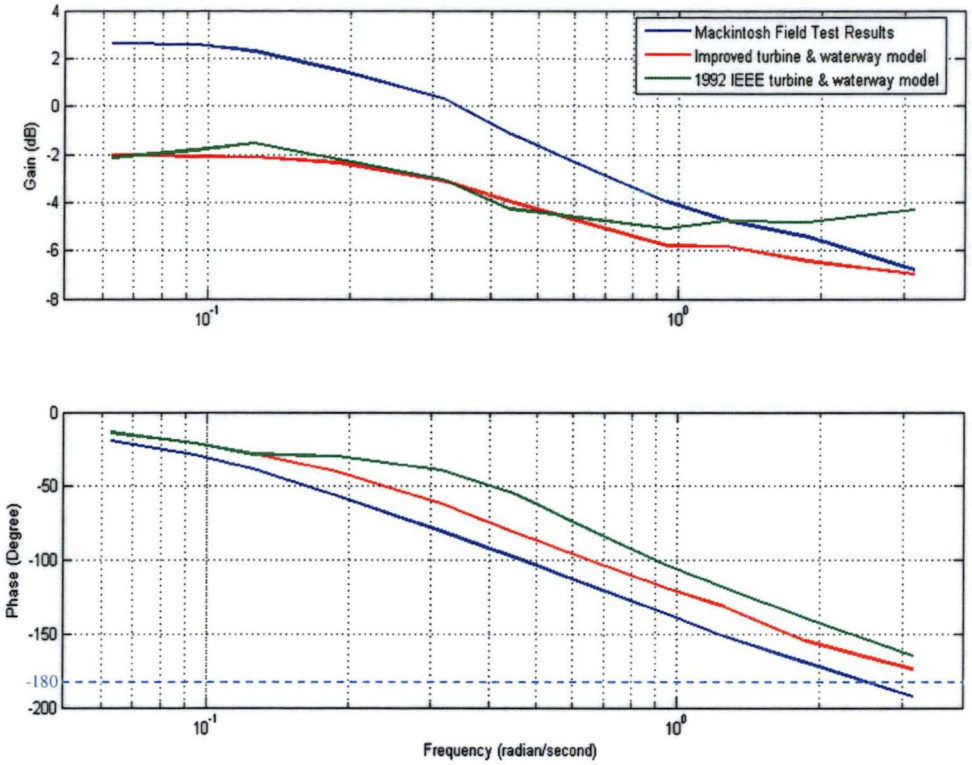

Figure 4.21: Bode plot showing the simulated and measured frequency response of the Mackintosh power plant

4.7 Discussion and Conclusions

Accurate simulation models for hydro power plants and their controls are essential for predicting plant and system performance under various conditions and contingencies. The models are used extensively in planning power system enhancements and designing protection systems including generation rejection and load shedding schemes. Increasing risks of power system blackouts in Tasmania have highlighted the need for more accurate simulation models. Hence, an improved nonlinear turbine and waterway model suitable for Francis turbine operation of a single-machine station has been developed here. Comparisons between simulation and full-scale test results have demonstrated significant improvements in accuracy. However, there remain some frequency-dependent discrepancies for this short penstock installation that appear to be associated with unsteady flow within the turbine. In general, model inaccuracies can be caused by either steady state or transient errors. The possible sources of errors are:

- The quasi-steady-flow simulation always fails to describe unsteady flow behaviour when the guide vane is suddenly closed or opened. This phenomenon is

well known in the simulation of hydroelectric systems. Pressure changes during the transient operation will propagate at sonic velocity and pass almost instantaneously through the machine, but the vortical flow that convects through the machine at through-flow velocity is a much slower process and therefore the time lag of the flow establishment in the turbine can be significant for a station with a relatively short penstock. A constant force coefficient used to represent the pressure force on the turbine draft tube can also generate some errors, since unsteady flow effects in the draft tube could be significant for large variations in the turbine flow condition.

- The turbine characteristic curve used for simulations relies heavily on the model test data. No change in the turbine design (exact geometric similarity) is assumed in this case. Turbine efficiency can increase or decrease if a new runner or other components have been modified or replaced in recent years. A maximum of 2% of uncertainty due to this factor is expected in the calculations.

- Generator efficiency is assumed independent of the turbine flow conditions. A constant efficiency of 97% is used for the Mackintosh generators due to a lack of detailed information. This can be misleading as the generator efficiency may vary nonlinearly with the machine output. Although the variation could be small, 0.5% difference in generator efficiency may cause an uncertainty of ±0.5MW for Mackintosh station. Hence, a steady state variation of 1~2% may occur due to this assumption.

- The quadratic guide vane function may not give a true representation of the flow characteristic, especially if machine is running at high load. It is known from observation that the flow will usually increase very slowly at or near the full gate opening. The quadratic flow relation may not work very well at this operating condition and so a larger steady-state error is expected for units initially operating near or at the full load. This effect, however, can be minimised when more data are available for tuning in the future.

- Constant water levels are assumed for both upper and lower reservoirs. The available static head may increase or decrease if the reservoir conditions are changed. This effect must be considered when the simulation is to be carried out

over a long period. However, its impact on the current simulation is minimal because each simulation test case is run for a few minutes only.

- A less severe flow non-uniformity is assumed in the current simulation. This applies fairly well for conditions near the best-efficiency point. However, flow non-uniformity could be greater when the machine is operating at off-design condition. More detailed flow surveys are needed to investigate and confirm this issue.

- A quasi-steady friction term is used in the present model. This assumption is satisfactory for very slow transients where wall shear stress has a quasi-steady behaviour. However, for rapid transients, a significant discrepancy in the attenuation and phase shift of the pressure trace is observed in many published studies when computational results are compared with measurement data [13]. This is caused by differences in the velocity profile and turbulence effects. Bergant et al. [13] applied an unsteady friction model and reported a significant improvement in modelling both the magnitude and the phase shift of the pressure head for the transient turbulent pipe flow. The unsteady friction model used by Bergant et al. [13] is:

$$f = f_q + \frac{kD_{eq}A}{Q|Q|}\left(\frac{DQ}{Dt}\right) \tag{4.29}$$

where f_q = quasi-steady part of the friction factor

A = cross-sectional area of the conduit

D_{eq} = equivalent diameter of the conduit

k = Brunone friction coefficient $= 1.361 \times \left[\mathrm{Re}^{\log(14.3/\mathrm{Re}^{0.05})} \right]^{0.5}$

Re = flow Reynolds number based on D_{eq}

CHAPTER 5

HYDRAULIC MODELLING OF A MUTIPLE-MACHINE POWER PLANT

5.1 Overview

Large system disturbances impose a serious threat to the stability of power systems. Many power plant analyses are devoted to improving the defence mechanisms and preventing disasters caused by large disturbances. Increased competition in the electricity supply industry, stricter market rules, and the structural changes in generation capacity have put more pressure on power system security. Accurate modelling of power plants with a multiple-machine configuration, which is the most common design for modern power stations, has played a critical role in ensuring satisfactory plant and system performance. In Chapter 4, a new model for the waterway system and turbine of a single-machine hydro plant without a shared waterway conduit was developed. This Chapter will focus on the modelling of transient operations for plants with more than one turbine unit. In contrast to a single-machine station, the case of a multiple-machine power plant with a common tunnel supplying a manifold from which individual penstocks branch out to each turbine will introduce hydraulic coupling effects.

This Chapter extends the application of the inelastic waterway model and nonlinear turbine characteristics discussed previously into multiple-machine modelling. The transient behaviour of Hydro Tasmania's Trevallyn power station will be used as a case study. The hydraulic configuration of the Trevallyn plant is briefly introduced in Section 5.2. Nonlinear modelling of flow in turbine and waterway conduits with multiple penstocks is presented in Section 5.3, while modelling of surge tank dynamics is discussed in Section 5.4. The mathematical assumptions of these models will be explained in some detail there. The structure of the nonlinear model constructed in MATLAB Simulink and the parameter evaluations of this hydraulic model are described in Section 5.5. The mathematical model will be validated against field test results previously collected at Trevallyn power station. The implication of hydraulic coupling effects on governor tuning, influence of travelling pressure waves, and possible sources of model inaccuracies for a multiple-machine station are reviewed in Section 5.6.

5.2 Basic Arrangement of the Studied Power Plant

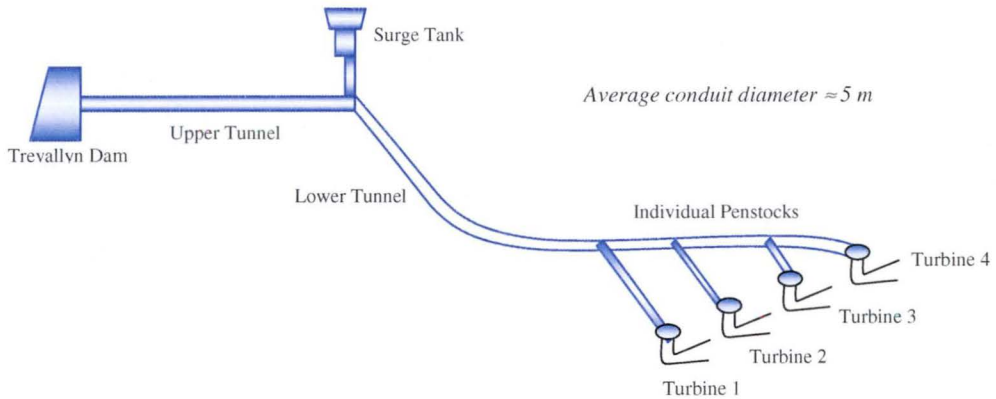

Figure 5.1: Simplified layout of the Trevallyn waterway system (Not to scale). The water is drawn from the Trevallyn Lake and discharged into the Tamar River through a tailrace (see reference [112])

Trevallyn power station is located at 5 km away from the centre of Launceston, Tasmania (see Figure 5.2). It is a run-of-the-river station that consists of four identical 20.9 MW Francis turbines and operates on an average head of 112 m. The maximum flow rate for individual turbine units is approximately 21.5 m^3/s. The discharge operating these turbines is conveyed from the Trevallyn Lake through a 2.5 km upper concrete tunnel and an 800 m lower concrete tunnel. The lower tunnel later splits into four 110 m steel penstocks, each supplying a Francis turbine. A surge tank is built at the end of the upper tunnel to minimise water hammer effects in the conduit. The surge tank consists of a surface reservoir 24.4 m in diameter and 4.3 m deep, a shaft 13.1 m and 13.7 m in diameter and 45.4 m deep, and a gallery leading to the main tunnel. A simplified version of the layout for Trevallyn plant is shown in Figure 5.1 while the geographical location of the power station is illustrated in Figure 5.2.

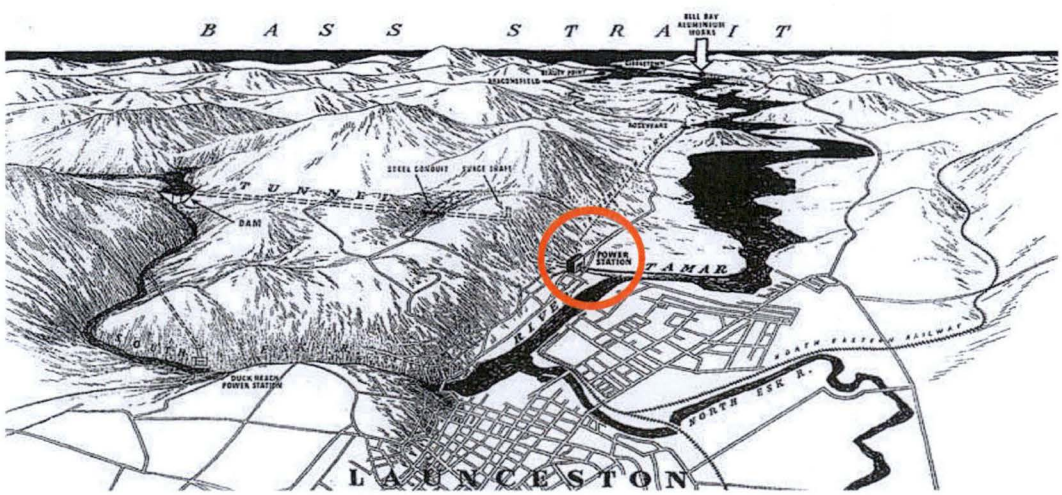

Figure 5.2: Location of the Trevallyn power station and its waterway conduits (Source: Hydro Tasmania Inc.)

5.3 Modelling of a Turbine & Waterway System with Multiple Penstocks

This Section gives an overview of the formulae used to simulate the turbine and waterway system of a multiple-machine station with four individual machines and separate penstocks, unrestricted head and tail races, and a surge chamber at the common tunnel. One-dimensional continuity and momentum equations, as well as the inelastic water column theory, are employed in this case. The formulation is identical to that of the single-machine model, except that the waterway conduit is now being divided into three separate parts: upper tunnel, lower tunnel, and penstocks. Hydraulic transients are described by the linear momentum equations applied from the reservoir to the end of the upper tunnel; from the end of the upper tunnel (or the start of the lower tunnel) to the end of the lower tunnel (or penstock junction); and from the end of the lower tunnel to each individual machine:

$$\begin{cases} \overline{H}_o - \overline{H}_{f-ut} - \overline{H}_t - \overline{H}_{IN} = k_{nu-ut} \times T_{Wut} \dfrac{d\overline{Q}_{ut}}{dt} \\ \overline{H}_t - \overline{H}_{f-lt} - \overline{H}_{eq} = k_{nu-lt} \times T_{Wlt} \dfrac{d\overline{Q}_{lt}}{dt} \\ \overline{H}_{eq} - \overline{H}_{f-i} - \overline{H}_i - \overline{H}_{dt-i} = k_{nu-i} \times T_{Wi} \dfrac{d\overline{Q}_i}{dt} \end{cases} \tag{5.1}$$

where $\overline{Q}$ = per-unit flow at the upper tunnel (*ut*), lower tunnel (*lt*), and penstock (*i*)

$\overline{H}_o$ = per-unit static head between reservoir and tailrace

$\overline{H}_t$ = per-unit static head at the end of the upper tunnel

$\overline{H}_{eq}$ = per-unit equivalent static head at the penstock junction

$\overline{H}_i$ = per-unit static head at the turbine admission

$\overline{H}_{IN}$ = per-unit inlet dynamic head = $K_{IN}\overline{Q}_{ut}^2$

$\overline{H}_{f-ut}$ = per-unit head loss at the upper tunnel = $f_{ut}\overline{Q}_{ut}^2$

$\overline{H}_{f-lt}$ = per-unit head loss at the lower tunnel = $f_{lt}\overline{Q}_{lt}^2$

$\overline{H}_{f-i}$ = per-unit head loss at the individual penstock i = $f_i\overline{Q}_i^2$

$\overline{H}_{dt-i}$ = per-unit static head caused by draft tube of machine i = $K_{dt-i}\overline{Q}_i^2$

T_W = water starting time for upper tunnel (*ut*), lower tunnel (*lt*), and penstock (*i*)

k_{nu} = flow nonuniformity factor for upper tunnel (*ut*), lower tunnel (*lt*), and penstock (*i*)

Flow in the upper tunnel, lower tunnel, and the individual penstocks are related by assuming flow continuity at the end of the upper tunnel and at the penstock junction (see Figure 5.3):

$$\begin{cases} \overline{Q}_{ut} = \overline{Q}_{st} + \overline{Q}_{lt} \\ \overline{Q}_{lt} = \sum \overline{Q}_i \end{cases} \tag{5.2}$$

It is noted that part of the flow in the upper tunnel will be diverted to the surge chamber in order to reduce excessive water-hammer pressure during hydraulic transients. $\overline{Q}_{st}$ in Equation 5.2 is therefore defined as the per-unit flow being diverted to the surge tank. More discussion about the surge tank dynamics will be given in Section 5.4.

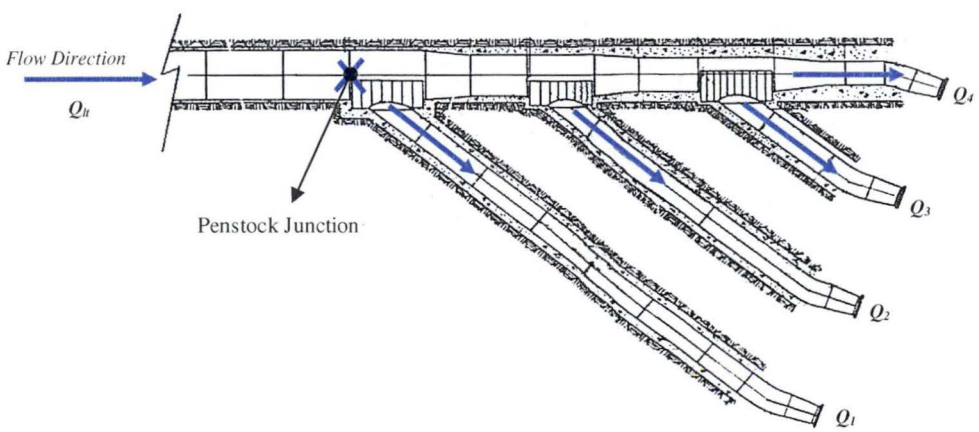

Figure 5.3: Common tunnel supplying a manifold from which individual penstocks branch out to each turbine

The equivalent head $\overline{H}_{eq}$ at the penstock junction can be found by taking the derivative of the Equation 5.2 (assuming flow in each penstock is independent of the others) and then substituting Equations 5.1 into this equation. The resulting formula is:

$$\overline{H}_{eq} = \frac{1}{\dfrac{1}{T_{Wlt}} + \sum_{i=1}^{4} \dfrac{1}{T_{Wi}}} \left\{ \frac{1}{T_{Wlt}} \left(\overline{H}_t - f_{lt} \overline{Q}_{lt}^2 \right) + \sum_{i=1}^{4} \left[\frac{1}{T_{Wi}} \left(\overline{H}_i - f_i \overline{Q}_i^2 - K_{dt-i} \overline{Q}_i^2 \right) \right] \right\} \tag{5.3}$$

The equivalent head will depend on the number of machines in operation. Equation 5.3, which assumes four machines are currently operating, can be easily modified to model cases with two or three machines in operation.

Nonlinear modelling of the Francis turbine characteristics is essentially the same as in the single-machine model:

$$\begin{cases} \overline{P}_{mi} = \overline{\eta}_{Gen-i}\overline{\eta}_{Turb-i}\overline{H}_i\overline{Q}_i \\ \overline{Q}_i = \overline{G}_i(\overline{y}_i)\sqrt{\overline{H}_i} \\ \overline{\eta}_{Turb-i} = f(C_{Q-i}) \end{cases} \tag{5.4}$$

where $\overline{\eta}_{Turb-i}$ = per-unit turbine efficiency for machine $I = \eta_{Turb-i} / \eta_{Turb-rated}$

$\overline{\eta}_{Gen-i}$ = per-unit turbine efficiency for machine $i = \eta_{Gen-i} / \eta_{Gen-rated}$

$\overline{y}_i$ = per-unit main servo position for machine i

C_{Q-i} = flow coefficient for machine i

Evaluation of the nonlinear guide vane functions $\overline{G}_i$ and efficiency curves for each Trevallyn machine will be presented in detail in Section 5.5. Initial values for numerical integration of head and flow in the waterway system are obtained by setting the rate of flow changes to zero (assuming four Trevallyn machines are operating simultaneously).

$$\begin{cases} \overline{Q}_{1\_ini} = \sqrt{\overline{H}_o \Big/ \left[(f_{lt} + f_{ut} + K_{IN})(1 + A + B + C)^2 + 1/\overline{G}_{1\_ini}^2 + f_{P1} + K_{dt-1}\right]} \\ Q_{2\_ini} = A \cdot \overline{Q}_{1\_ini} \\ \overline{Q}_{3\_ini} = B \cdot \overline{Q}_{1\_ini} \\ \overline{Q}_{4\_ini} = C \cdot \overline{Q}_{1\_ini} \\ \overline{H}_{t\_ini} = \overline{H}_o - f_{ut}\overline{Q}_{ut\_ini}^2 \end{cases} \tag{5.5}$$

where $A = \sqrt{(1/\overline{G}_{1\_ini}^2 + f_{P1})/(1/\overline{G}_{2\_ini}^2 + f_{P2} + K_{dt-2})}$

$B = \sqrt{(1/\overline{G}_{1\_ini}^2 + f_{P1})/(1/\overline{G}_{3\_ini}^2 + f_{P3} + K_{dt-3})}$

$C = \sqrt{(1/\overline{G}_{1\_ini}^2 + f_{P1})/(1/\overline{G}_{4\_ini}^2 + f_{P4} + K_{dt-4})}$

5.4 Nonlinear Modelling of Surge Tank

Numerous methods have been developed in the past to control the magnitude of the hydraulic transients and to prevent the objectionably high and low pressures resulting from rapid guide vane movement, turbine failure, or column separation. A surge tank is the most effective device for this purpose, and is commonly used in the hydro plants with long waterway conduits. Its main function is to compensate for the mass oscillation of the water flow in the pressure tunnel when the operating conditions or the loads of the turbines are changing. A surge tank will act as a temporary storage for excess water in the upper tunnel to reduce traveling pressure waves. It will also act as a water supply to the lower tunnel when more fluid is needed to prevent excessive flow deceleration in the penstocks. In other words, the surge tank will provide flow stabilization to the turbines, pressure regulation, and improvement in speed control [137]. As a result, the mass oscillation and water hammer effects can be treated and studied separately. The travelling pressure wave effect in the presence of surge tank is a very complicated phenomenon and is not the subject of interest for this study. Excellent descriptions of this problem are provided by Mosonyi and Seth [82], Wylie and Streeter [142], and Watters [137].

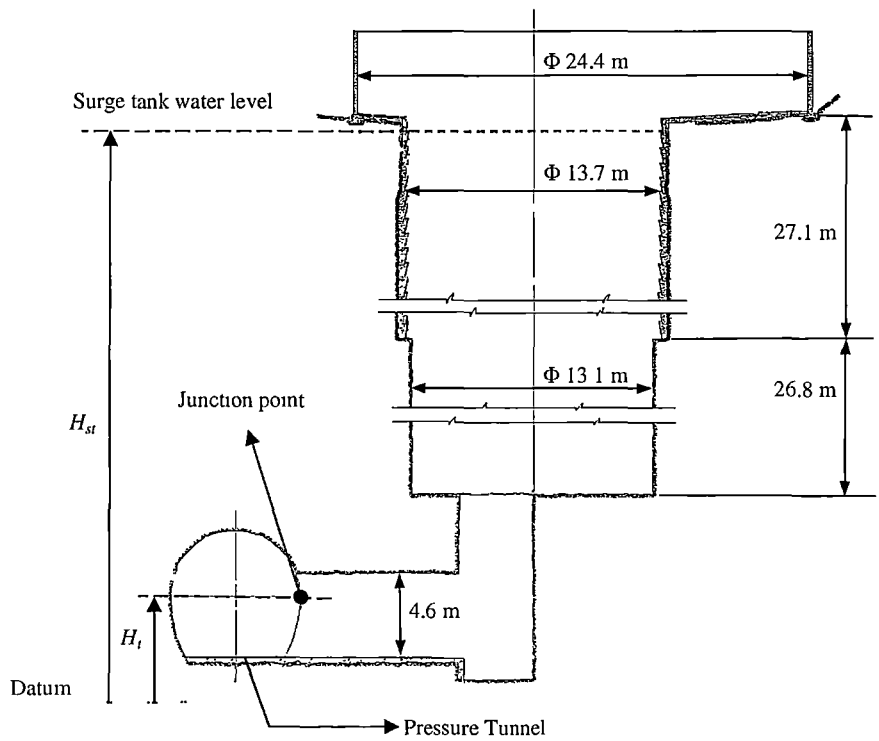

Figure 5.4: Simplified geometry of the surge tank used for Trevallyn power station

A simplified view of the surge chamber used in the Trevallyn plant is shown in Figure 5.4. The surge tank is a restricted orifice type. Flow in this type of surge tank can be obtained by keeping track of the elevation of water surface in the surge tank above the tunnel through:

$$\overline{Q}_{st} = C_s \frac{d\overline{H}_{st}}{dt} \quad \& \quad C_s = f(A_s) \tag{5.6}$$

where $\overline{H}_{st}$ = per-unit static head in the surge tank
C_s = storage constant of the surge tank
A_s = cross-sectional area of the surge tank

The flow in the surge tank can then be linked to the static head at the main tunnel by rearranging and substituting Equation 5.6 into Equation 5.7. This relation is based on the assumption that the pressure head at entry to the surge tank, and the upper or lower tunnel endpoints is the same at any instant. The mass is conserved and the velocity distribution over the cross section of each conduit at the junction is assumed uniform [139]. The primary and reflected pressure waves emanating from the junction are also assumed plane-fronted.

$$\overline{H}_t = \overline{H}_{st} - \overline{H}_{f-o} = \frac{1}{C_s}\int d\overline{Q}_{st}\,dt - f_o\overline{Q}_{st}^2 \tag{5.7}$$

where $\overline{H}_{f-o}$ = per-unit head losses in the surge tank
f_o = head loss coefficient due to restricted orifice

A restricted orifice, like many diaphragms, causes concentrated local losses. This head loss is modelled as the steady-flow loss coefficient times flow squared in the simulation. An initial value for numerical integration of the surge tank flow can be obtained by assuming a steady flow conditions at the start of the simulation. The variation of flow with respect to time will be equal to zero in this case (assuming four Trevallyn machines in operation):

$$\overline{Q}_{st\_ini} = \overline{Q}_{1\_ini} + \overline{Q}_{2\_ini} + \overline{Q}_{3\_ini} + \overline{Q}_{4\_ini} \tag{5.8}$$

The inclusion of surge tank effects is warranted in cases where transient performance of the plant is being analysed over a few minutes of "real" time. The surge tank causes a long-period damped oscillation of flow in the tunnel between the reservoir and the tank [70]. The oscillation period of the Trevallyn surge tank is 305 seconds, which is about the total length of simulation time. Hence, adding Equations 5.6 and 5.7 to the model is expected to generate a more accurate result.

5.5 Transient Analysis of a Multiple-Machine Power Plant

5.5.1 Model Structure and Formulation

The approach used to implement the multiple-machine system is similar to the one used for the single-machine model, except that the multiple-machine model is now broken down into smaller subsystems. The system complexity prevents the hydraulic system from being represented as a single subsystem, and this applies to the electrical system too [70]. Therefore, three subsystems have been created in MATLAB Simulink for the following elements:

- individual penstock and turbine;
- upper tunnel, lower tunnel and surge tank; and
- equivalent head.

The first two subsystems of the model are depicted by inelastic water column theory where conservation of momentum and continuity of flow at the surge chamber junction apply. The inelastic model is used as it is relatively easy to construct and more efficient in terms of computational time and resources used. The surge tank alleviates the travelling wave effects in the lower tunnel. Thus, the use of the inelastic model is expected to give the accuracy needed for the current power system design process. Figures 5.5 to 5.8 show the resulting Simulink block diagram of the multiple-machine model where four units are assumed operating at the same time.

In addition, the multiple-machine model for the Trevallyn plant assumes the lower tunnel branches into four at one point and models the inertia of the resulting five segments accordingly. These five pipeline segments are the lower tunnel and the four branches to each individual machine. In reality, the portion downstream of the surge

tank consists of a common tunnel with successive off-takes to each machine (see Figure 5.3). Private communication with Hydro Tasmania's consultant, P. Rayner, indicates that this portion can be represented more accurately by considering the inertia of seven segments, which are: the lower tunnel; four individual pipes to each machine; a common section between pipe to first machine and pipe to second machine; a common section between pipe to second machine and pipe to third machine. However, this approach requires a more complex hydraulic model, which implies a more complicated and time-consuming process for the simulation. The improvement of simulation accuracy due to this effect would be relatively insignificant in the present case, as the water starting time constants of the branches are small in the Trevallyn system.

Although the steady-state losses have been calculated in detail, they do not represent the true nature of the hydraulic system under transient flow conditions. The errors in estimating the transient flow losses from a quasi-steady model may be more significant than the errors due to the model topology simplification. The Simulink model presented in this Section is therefore recommended as providing a good compromise between modelling accuracy and computational time required.

The effects of hydraulic coupling between the individual machines will be taken into account in the computation of equivalent head at the penstock junction. As illustrated in Section 5.3, the formula is based on continuity relations for the flow in the tunnel and the penstocks. This computed head value is fed back to the models of individual penstocks and machines (see Figure 5.5).

For gate positions at or near total closure, the inelastic simulations of the turbine head and penstock flows are no longer applicable, and are replaced by a steady-state algebraic solution of the penstock. This method is currently used in the simulation to account for conditions when a machine is operated below 5% of the total guide vane opening.

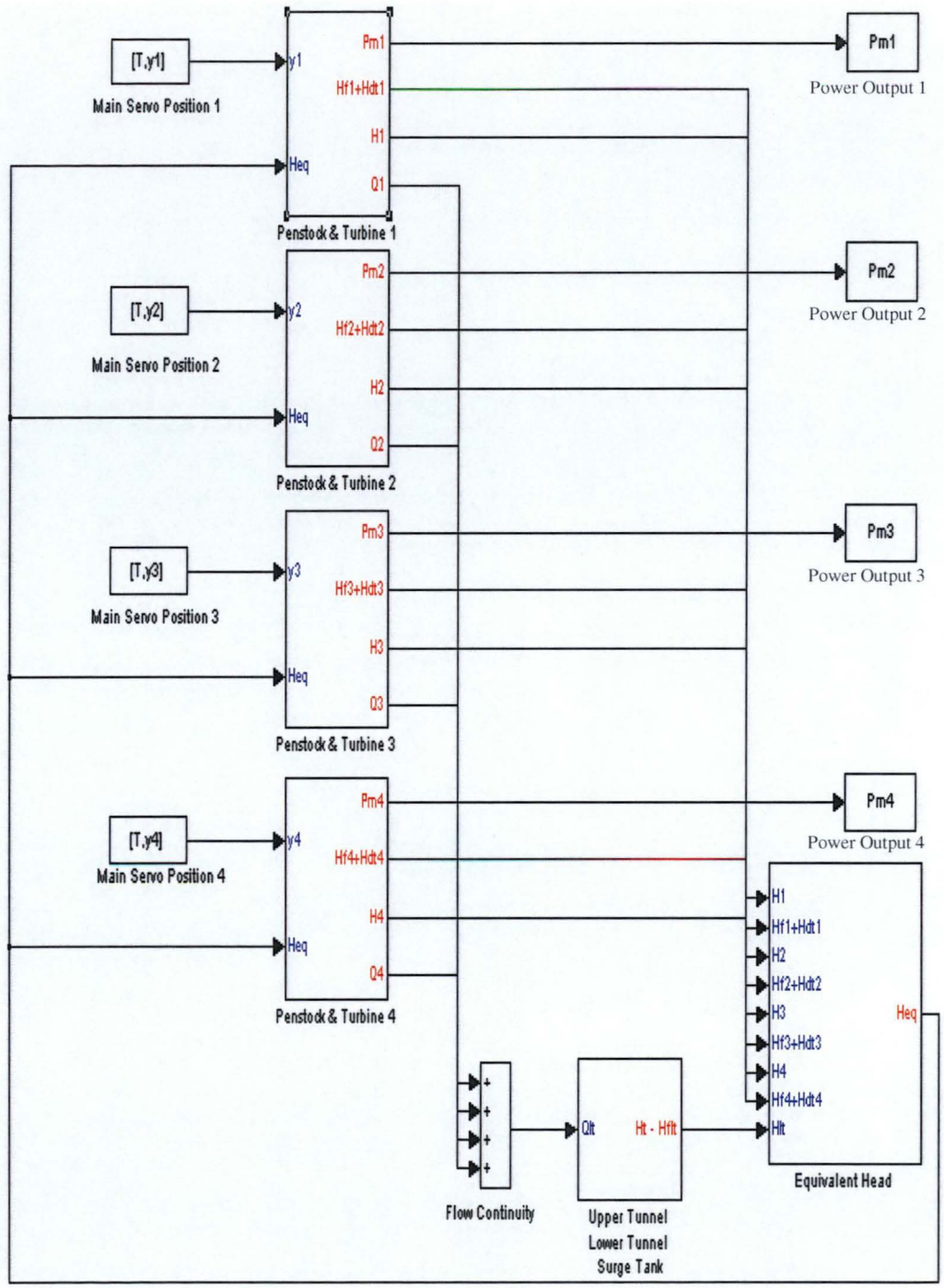

Figure 5.5: Main block diagram of the four-machine hydraulic model for Trevallyn multiple-machine plant

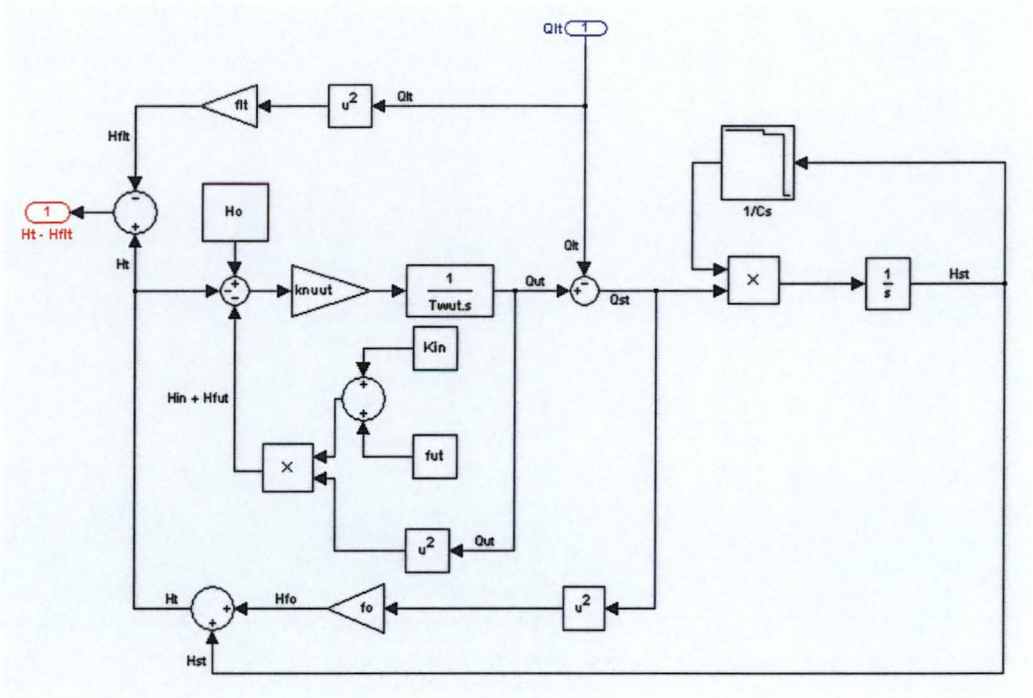

Figure 5.6: Details of the "Upper Tunnel, Lower Tunnel & Surge Tank" block in Figure 5.5

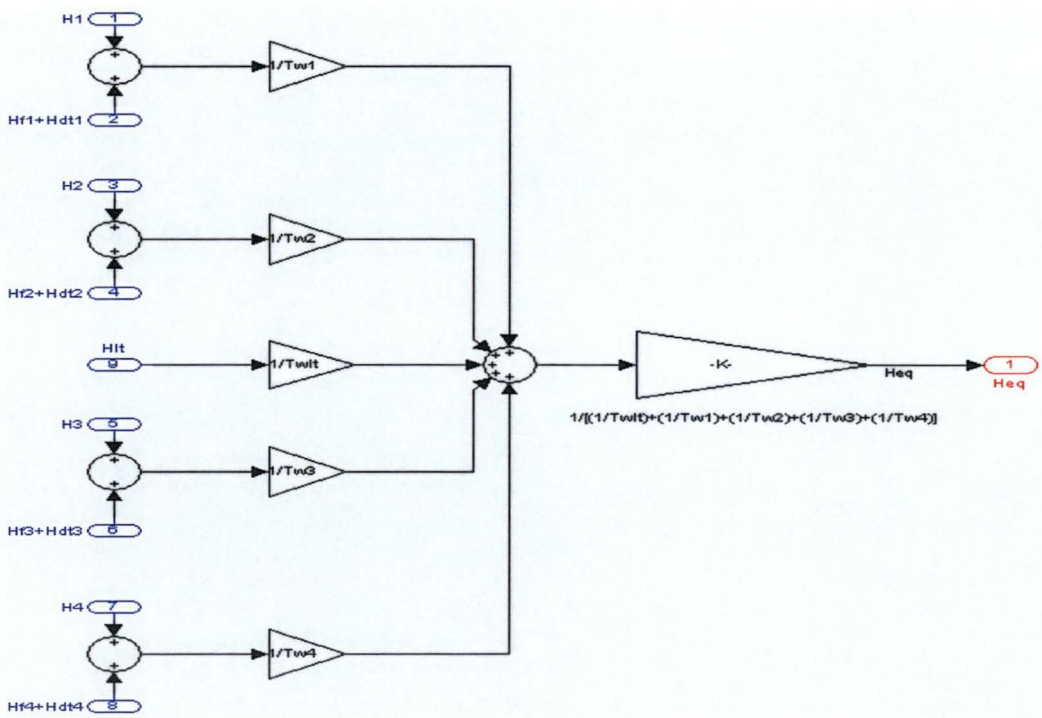

Figure 5.7: Details of the "Equivalent Head" block in Figure 5.5. Note that the value of K will change as the number of units online changes. A decision block will be added to cater for this change

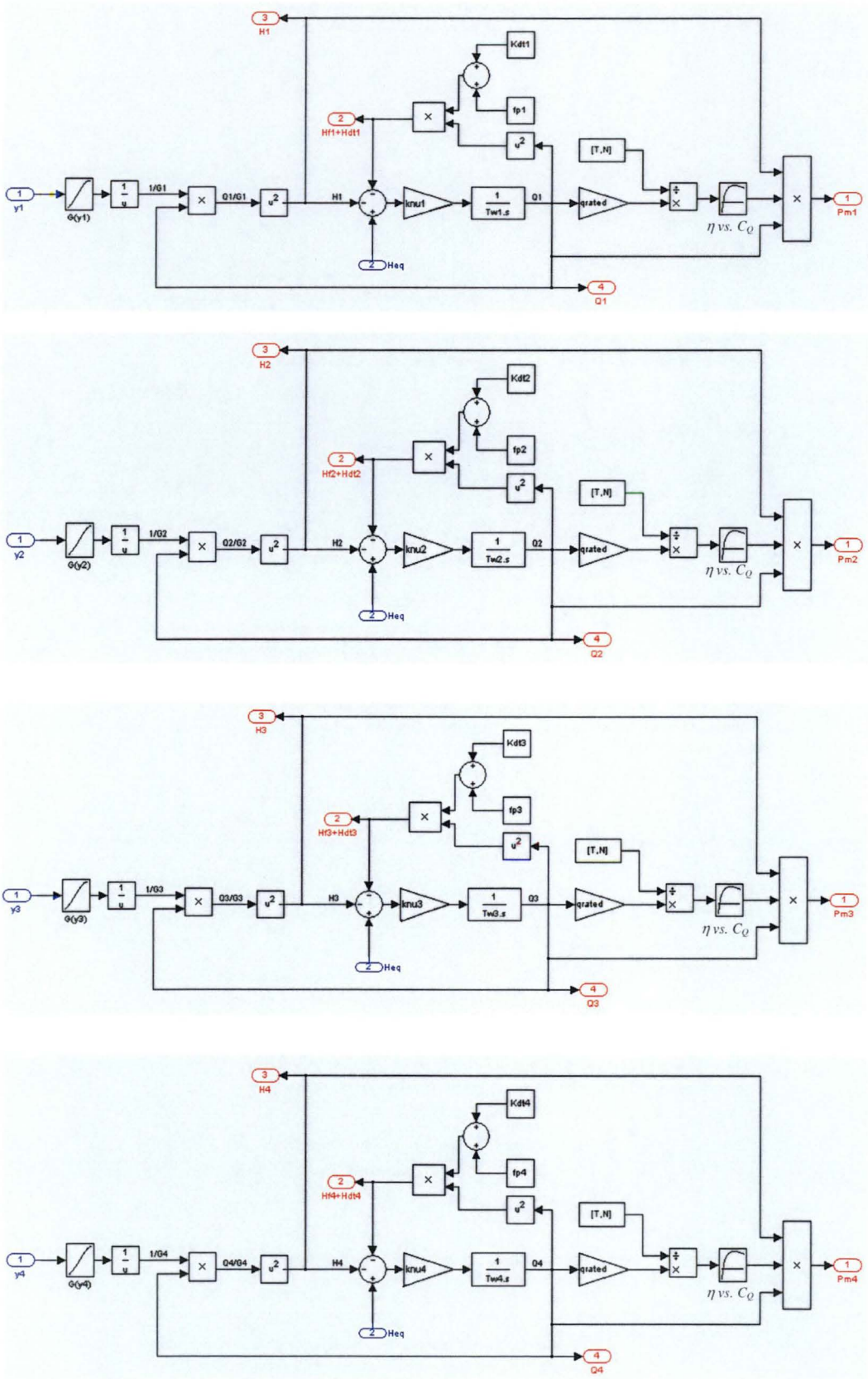

Figure 5.8: Details of the "Penstock & Turbine 1–4" blocks as shown in Figure 5.5

5.5.2 Evaluation of Hydraulic Model Parameters

5.5.2.1 Rated Parameters used in Per-Unit System

The rated parameters used for the multiple-machine station are defined in the same manner as those for the single-machine station. For the Trevallyn plant, the rated flow for each unit is chosen as the base value in order to maintain the convention that has been used for the single-machine model. This provides the same transformation between electrical power output and flow. Taking the flow of the common tunnel as the base value would require redefining the transformation of the electrical power from its flow expressed on a different per-unit system [42]. However, the choice of the rated flow will have little influence on the nonlinear hydraulic model as long as it is consistent throughout the simulations. Table 5.1 shows the values of the rated parameters used in the modelling of Trevallyn plant.

Rated Parameters Used in Per-Unit System	*Base Values*
Rated Speed (rpm)	375
Rated Head (m)	112.78
Rated Flow Rate (m^3/s)	21.446
Rated Power Output (MW)	20.88
Rated Gate Opening (%)	100
Rated Turbine Efficiency (%)	88
Rated Generator Efficiency (%)	97

Table 5.1: The rated parameters used in the per-unit based simulation of Trevallyn multiple-machine station

5.5.2.2 Total Available Static Pressure Head

Total available head for Trevallyn station is defined as the water level at the Trevallyn dam with reference to the tailwater level. This hydrological information is obtained from the Hydro Tasmania's ECS database. In general, the water level at the upper reservoir did not change greatly (± 2% of the net head) during testing and therefore an average value of 126 m (relative to the mean sea level at Bass Strait) can be employed in the simulation for simplicity. The Trevallyn tailwater level, on the other hand, is independent of the station flow but it will depend on the level of the Tamar River. The Tamar River level at the station outlet is subjected to daily tidal effects and to upstream pickup, which includes spill from the Trevallyn Dam. A provision should be made to

include tidal information in modelling the Trevallyn tail water level. However, it should be noted that the tidal effect is generally very hard to model accurately as the tide level can easily be influenced by many factors such as the barometric pressure, wind effects, and solar or lunar effects. Private communication with Hydro Tasmania's consultant, P. Rayner indicates that the use of general tidal information predicted by the National Tidal Facility Australia [153] will give sufficient accuracy for the power system simulation. The mean sea water level in Bass Strait (see Figure 5.2) is currently used as the tail water level in the simulation for simplicity.

5.5.2.3 Water Starting Time Constant

Computation of the water starting time constant for Trevallyn is based on the total water column from the Trevallyn Lake to the tailrace. The basic definition of the water starting time can be found in Section 4.6.2.3. For the Trevallyn plant, the calculation has been divided into three separate parts (i.e. the water time constants for the upper tunnel, lower tunnel and penstock) to account for the inclusion of the surge chamber effects and the distributing piping downstream of the waterway conduit. The geometric data used for the calculation were supplied by the Hydraulic Department of Hydro Tasmania.

There are two ways of representing the water starting time for a multiple-machine station. One approach is to develop a model in which a matrix of water time constants is used for the penstock dynamics [141]. Another method is to use a separate model for the penstock, but vary the water time constant according to the number of units that are online [42]. The latter approach has been adopted here. In either case, a nonlinear model should be employed, as the linearized penstock model will require different values of water time constant when the initial operating conditions are changed [42].

Table 5.2 shows the values of water starting times when various numbers of machines are in operation. The water time constant for the upper tunnel varies from 2.19 to 8.77 seconds, while the water time constant for the lower tunnel changes from 0.74 to 2.95 seconds as the number of units online varies from one to four. This change is mainly due to the increase of flow rates when the number of units online is increased.

Water Starting Time Constant	*1 unit*	*2 units*	*3 units*	*4 units*
Upper Tunnel, Tw_{ut} (second)	2.192	4.385	6.577	8.770
Lower Tunnel, Tw_{lt} (second)	0.736	1.472	2.209	2.946
Penstock and Turbine, $Tw_{i,\ i=1\ to\ 4}$ (second)	0.448	0.448	0.448	0.448

Table 5.2: The water starting time for the Trevallyn power station. Note that the water time constant at the upper tunnel and the lower tunnel increase as the number of machines in operation increases

5.5.2.4 Head Loss Coefficients

For the Trevallyn case, the head loss coefficients are divided into six elements for modelling purposes. These elements are the loss coefficients for the upper tunnel (f_{ut}), lower tunnel (f_{lt}), and the individual penstocks (f_{P1}, f_{P2}, f_{P3} and f_{P4}). The calculation of loss coefficients of individual components at the Trevallyn station is based on the same approach employed for the single-machine model. Table 5.3 summarises the values of head loss coefficients used in the Trevallyn simulation.

Head Loss Coefficient	*Value (-)*
Upper Tunnel, f_{ut}	0.004714
Lower Tunnel, f_{lt}	0.001876
Machine 1, f_{P1}	0.010012
Machine 2, f_{P2}	0.007736
Machine 3, f_{P3}	0.005975
Machine 4, f_{P4}	0.004311

Table 5.3: Steady-flow head loss coefficient for the Trevallyn hydraulic system. Note that the head loss is expressed in the per-unit base and the branch loss for the individual penstocks is assumed positive for all machines

The total hydraulic loss increases with the number of units running, as the flow in the common tunnel depends upon the number of units dispatched [141]. For the Trevallyn power station, additional complexity arises from the interaction between closely spaced components in the waterway system involving a departure from simple summing of the individual component losses. Knoblauch et al. [56] report an interesting interaction effect for flow at the penstock junction. A negative branch loss coefficient was found in the model test for a well-developed turbulent flow. The causes of this phenomenon are explained in detail in the relevant literature [56]. Generally, it is due to the interaction among the branches connected in series in a distribution system and results from asymmetry of the velocity profile behind the junction.

Neglecting the interaction effects among the branches may result in the overall losses at the individual penstocks being slightly overestimated or underestimated. Hence, a steady-state offset error between the simulated and the measured results may occur. A computational study could be carried out in the future to investigate this interaction effect in the distributing system. However, in the absence of any better information at present, the branch losses are currently assumed positive and the values used in the simulation are the same for all four machines.

5.5.2.5 Inlet Dynamic Pressure Head Coefficient

The definition previously applied for the single-machine model is employed in the multiple-machine modelling. For the Trevallyn plant, the cross-sectional area at entrance to the upper tunnel is 29.2 m^2, which gives a value of the inlet dynamic head coefficient $K_{IN} = 2.31 \times 10^{-4}$.

5.5.2.6 Draft tube Static Pressure Force Coefficient

A provision is made in the model to include the static pressure force generated by the flow in the draft tube and the tailrace water tunnel. However, the values of these force coefficients are not known exactly at this stage, as the steady-flow CFD simulations were not conducted for the draft tubes of the Trevallyn station. For this reason, the coefficients are currently set to zero. This will have little impacts on the overall accuracy of the model, as the flow through each turbine is relatively small compared to that of the Mackintosh station.

5.5.2.7 Coefficient for flow non-uniformity

The factor accounting for flow non-uniformity in the Trevallyn waterway system is based on the assumption of a fully developed turbulent velocity profile. The non-uniformity effects are expected to be more significant in the common tunnel as the flow rate is greater in the tunnel than the penstock. Nevertheless, a constant coefficient value of 1.05 is used for both common tunnel and penstocks, as no information is currently available to distinguish the effects of flow non-uniformity in these conduits.

5.5.2.8 *Turbine Characteristics*

An identical turbine characteristic curve is used for all the Trevallyn machines. Information on the turbine efficiency at 112 m and 128 m net head was obtained from the field test data previously collected at Trevallyn station. Figure 5.9 shows that the normalised efficiency (η_{Turb} / $\eta_{Turb\text{-}rated}$) does not vary greatly with these values of net head. However, only data with flow rate above 7.5 m^3/s are available. To resolve this issue, both simulation and steady-state test results were used to determine the turbine efficiency where the flow rate is below 7.5 m^3/s (i.e. the first five data points). The negative efficiency in the first data point implies that the power is supplied to the generator in order to synchronise the machine. The generator is currently assumed to work at a constant efficiency of 97% (or 1 in per unit system) as no detailed information on the generator efficiency is found in the model test report.

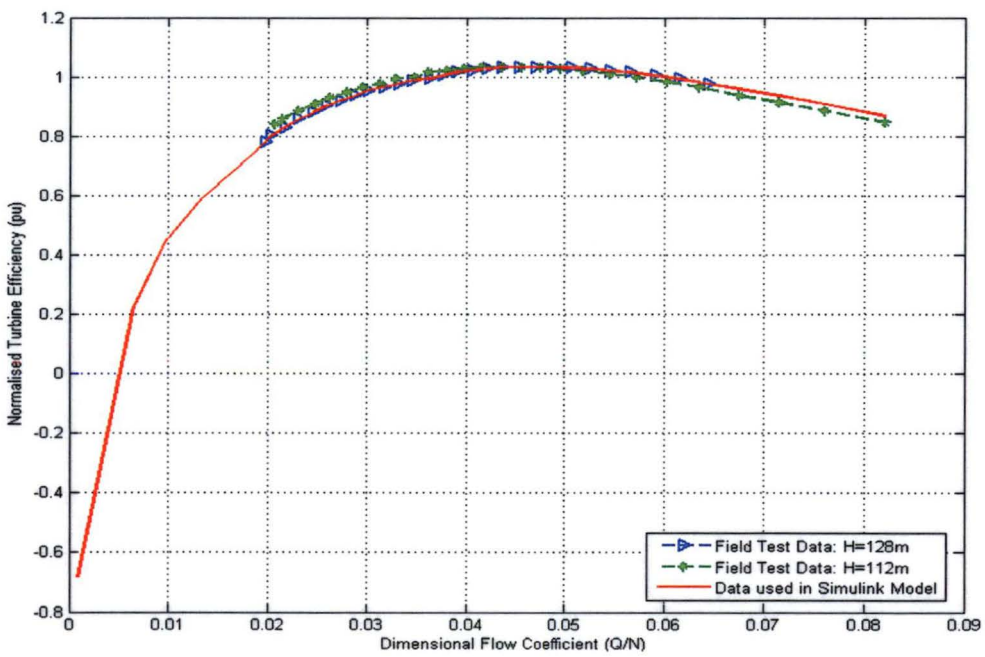

Figure 5.9: Turbine characteristic curve relating the normalised efficiency to the dimensional flow coefficient of Trevallyn station

5.5.2.9 *Nonlinear Guide Vane Function*

The nonlinear guide vane function takes into account the nonlinearities of both the guide-vane opening area and the discharge coefficient. This relationship can be found in the similar way to the single-machine model (see Section 4.6.2.8). Three methods are

proposed in this Section to determine the nonlinear discharge coefficient relation for the Trevallyn machines:

- *Using the hill chart data for Trevallyn station.* The relationship is found by processing the head and flow coefficients of the model turbine at different guide vane positions. The discharge coefficient will be a function of these two variables. It is assumed that the machines will normally operate well above a head coefficient of 0.25, and therefore the guide vane function should be insensitive to variations in the head coefficient. Unfortunately, there is some doubt about the values of unit speed and unit flow rate presented in the hill chart. Private communication with K. Caney of Hydro Tasmania indicates that it would be quite difficult to trace the errors due to lack of detailed documentation for the Trevallyn station. Thus, this method is not being used here.

- *Using pressure measurement data from site tests.* P. Rayner of Hydro Tasmania suggests the use of steady-state test results to establish the nonlinear guide vane function. The values can be found by processing pressure data at the turbine spiral case and subsequently calculating the corresponding head drop from the no-flow static head condition. However, due to the equipment limitations, only the pressure readings of one machine were recorded during the Trevallyn site tests. Analysis of the test data indicates that each Trevallyn machine may have a slightly different characteristic, and so the use of one machine characteristic to represent all may not be appropriate here.

- *Using a quadratic approximation to identify the nonlinear guide vane function.* A quadratic relation is used for parameter identification because only one parameter C_i needs to be tuned in the equation. The identified parameters for each machine are listed in Table 5.4 and the resulting nonlinear guide vane functions are presented in Figure 5.10.

$G_i = A_{G\text{-}i} - C_i + 4C_i(A_{G\text{-}i} - 0.5)^2$	*Identified Value for Machine i*
Machine 1, C_1	-0.310
Machine 2, C_2	-0.220
Machine 3, C_3	-0.253
Machine 4, C_4	-0.220

Table 5.4: Identified parameters (C_i) used to determine the nonlinear guide vane functions for the Trevallyn machines

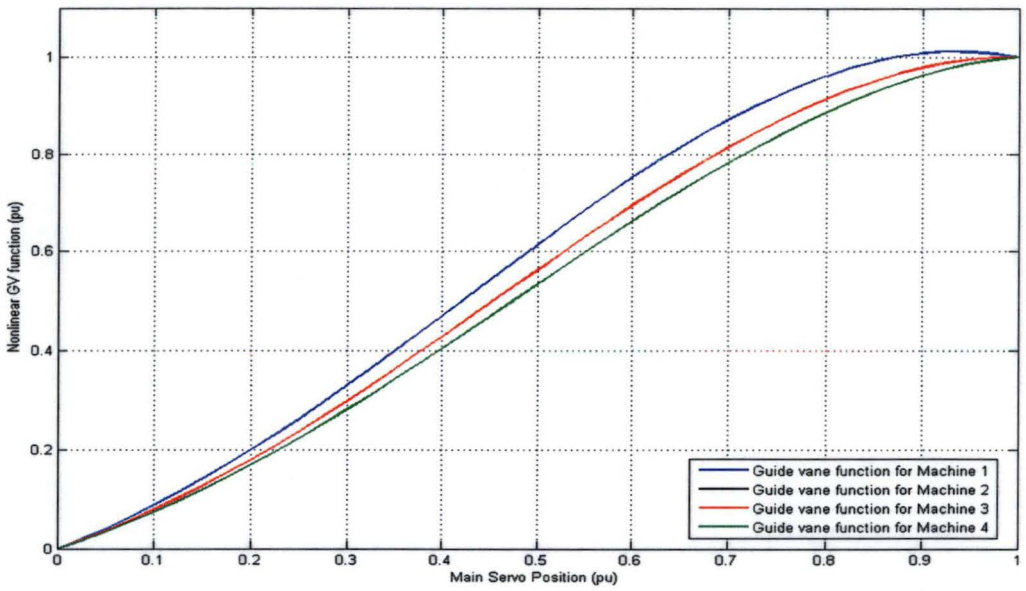

Figure 5.10: The nonlinear GV characteristic curves for the machines at Trevallyn power station (the machine number follows the arrangement as shown in Figure 5.1)

5.5.2.10 Storage Constant and Orifice Loss Coefficient of Surge Tank

For a complex hydro plant like Trevallyn, the "high frequency" oscillations resulting from pendulum action between the surge chamber and the speed governor may interfere with the governor's speed regulating loop [82]. To eliminate this problem, the surge chamber effect is being modelled in the power system simulation. As illustrated in Section 5.4, the surge tank at Trevallyn is treated as a restricted orifice (throttled) type and the orifice flow equation is applied here. Two parameters must be determined as a result of this flow equation (see Equation 5.7). The first parameter, the storage time constant of the surge chamber (C_S), is a function of the cross-sectional area of the tank (A_S). It is defined in per-unit system as:

$$C_S(A_S) = \frac{A_S h_{rated}}{Q_{rated}} \text{ seconds} \tag{5.9}$$

The Trevallyn surge tank has three different cross-sectional areas at different elevations, and thus the storage time constant changes with the water level in the surge chamber. The values of storage constant are listed in Table 5.5 and a look-up table is constructed in the Simulink model to represent this effect.

Surge Tank Level, H_{st} (ft above MSL)	*323*	*418*	*418.001*	*471.12*	*471.1201*	*486*
Cross Sectional Area, A_s (m^2)	134.9	134.9	141.3	141.3	467.0	467.0
Storage Constant, C_S (second)	709.5	709.5	742.9	742.9	2455.7	2455.7

Table 5.5: The storage time constant of the surge tank at Trevallyn power station. The mean sea water level (MSL) at Bass Strait is set as the reference in measuring the surge tank level

The second parameter, loss coefficient (f_o), assumes a two-dimensional shard-edged orifice and a constant discharge coefficient $C_{d\text{-}o}$ = 0.68. The loss coefficient can therefore be established from:

$$f_o = \frac{Q_{Rated}^2}{2gh_{rated}C_{d-o}^2A_o^2} \tag{5.10}$$

The validity of applying this steady-flow loss coefficient to the case where the flow is unsteady and rapidly fluctuating is questionable. However, the error involved in making this assumption is on the safe side as far as the transmission of travelling pressure waves is concerned, because the head loss reduces when the flow through the orifice is decreasing with time.

5.5.3 Time Response Simulation of the Multiple-Machine Station

The dynamic performance of the Trevallyn station is now investigated. The time response of the plant when subjected to a large disturbance is the principle interest in this study. The main servo positions for the individual machines are input to the Simulink model and the simulated electrical power outputs are compared with the site test results. As the testing time was limited, only events of varying the load at one of the four Trevallyn units (Machine 3 as named in Figure 5.1) are examined in the multiple-machine operation. This analysis proves that the model is capable of reproducing the hydraulic coupling effects for multiple-machine operation. It can be seen from the simulation that the phase lag between the simulated and measured power outputs is insignificant. The magnitude of error in power fluctuations is quite small despite some power offset caused by steady-state errors. For machine 3, the predicted phase lag is 0.1 second and the maximum magnitude error is 0.03 p.u. However, the errors are greater for the other machines due to unsteady flow effects in the turbine and waterway conduit as well as uncertainties in the actual turbine characteristics. The maximum phase error for these machines is 0.3 second and the greatest magnitude error is 0.04 p.u.

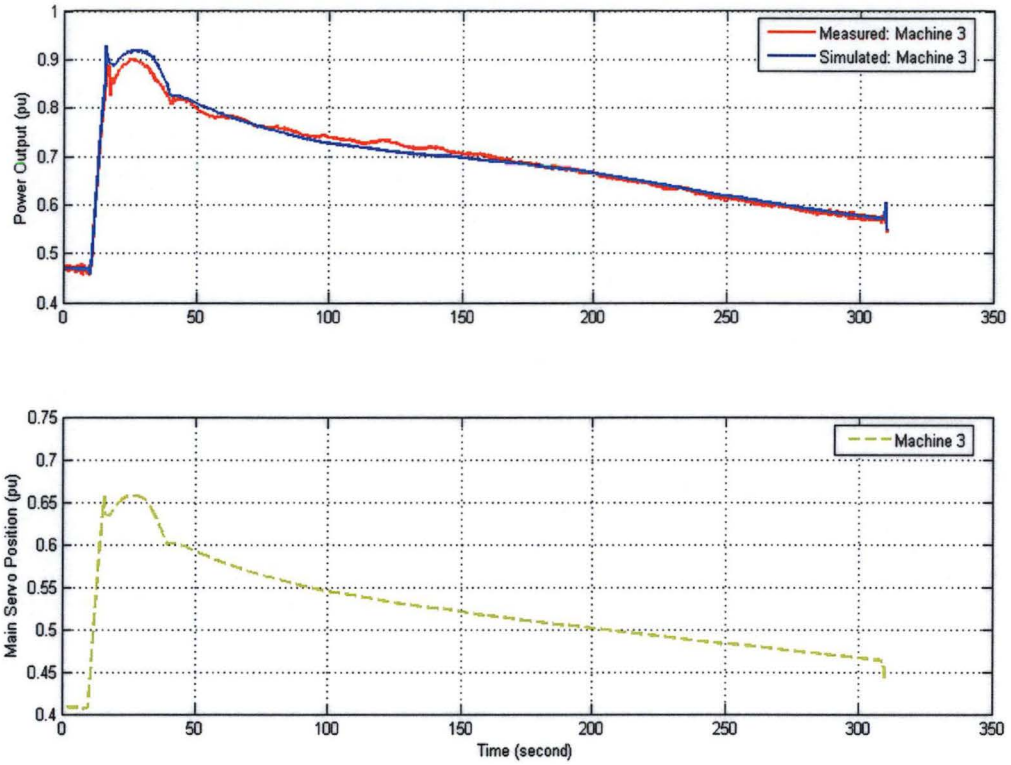

Figure 5.11: Worst-case comparison between single-machine model and the measured outputs for Trevallyn machine 3

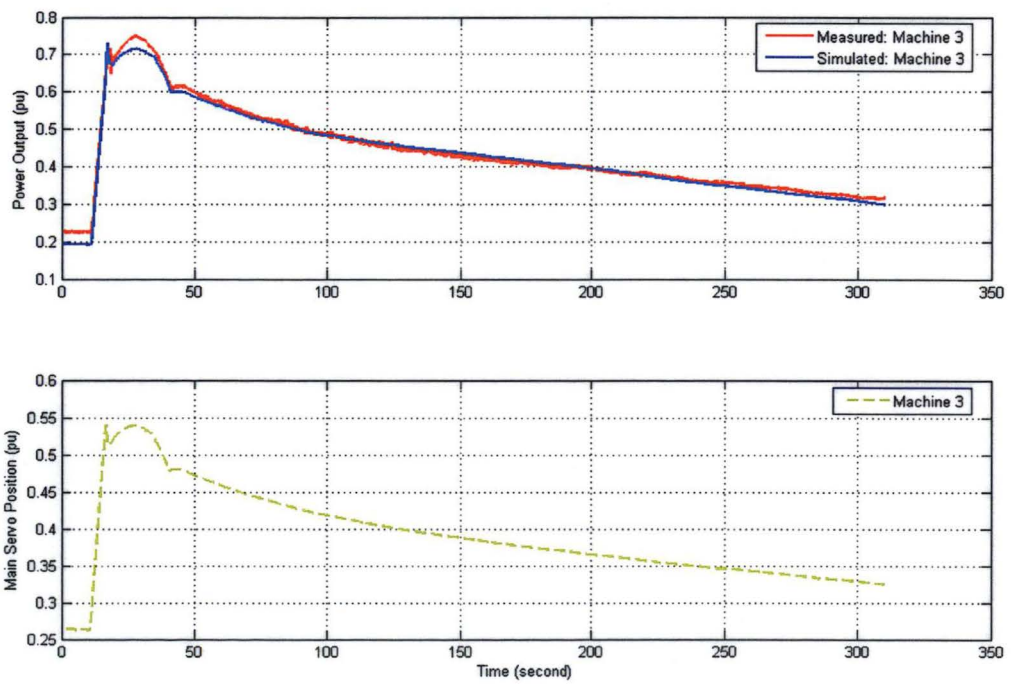

Figure 5.12: Best-case comparison between single-machine model and the measured outputs for Trevallyn machine 3

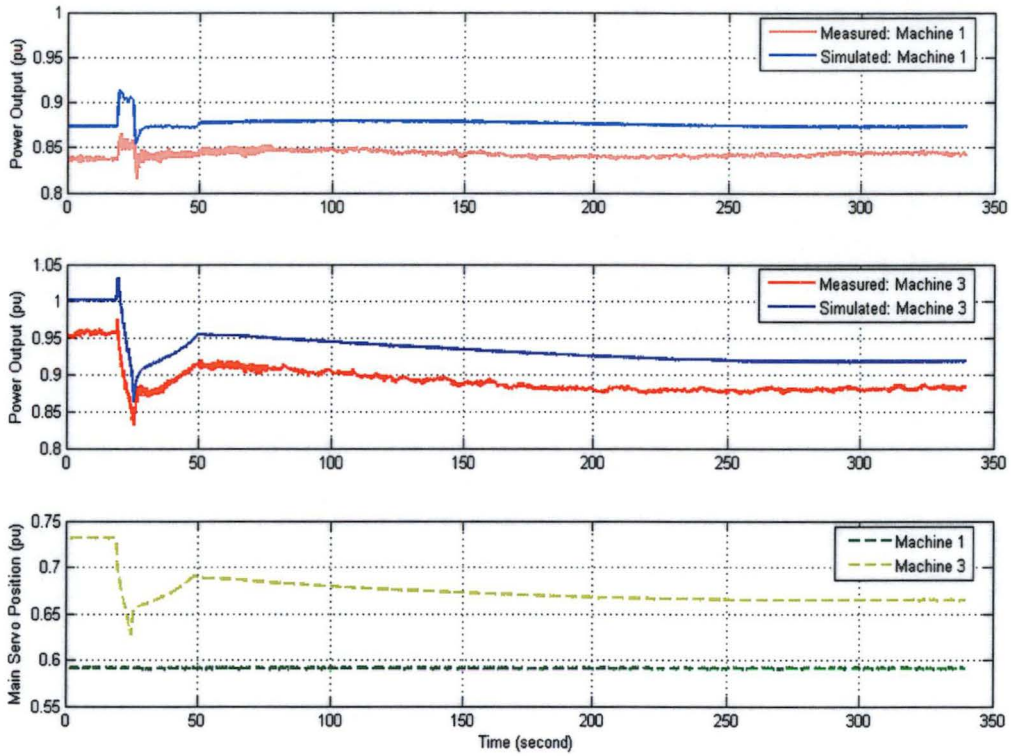

Figure 5.13: Worst-case comparison between two-machine model and the measured outputs for Trevallyn machines 1 and 3

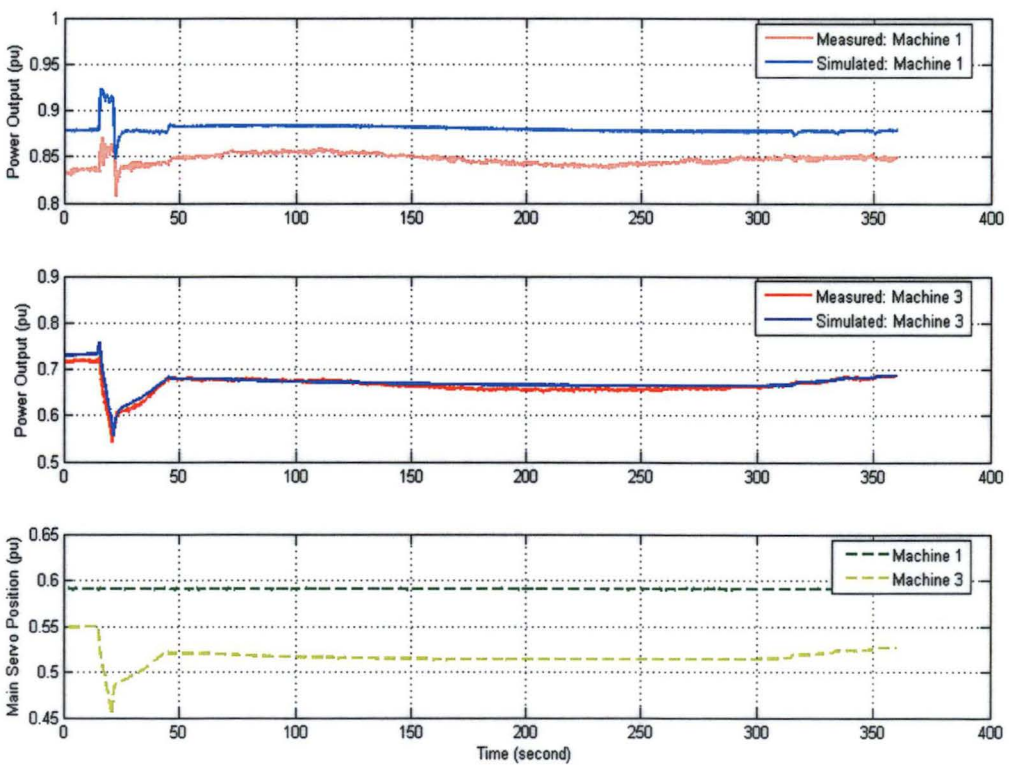

Figure 5.14: Best-case comparison between two-machine model and the measured outputs for Trevallyn machines 1 and 3

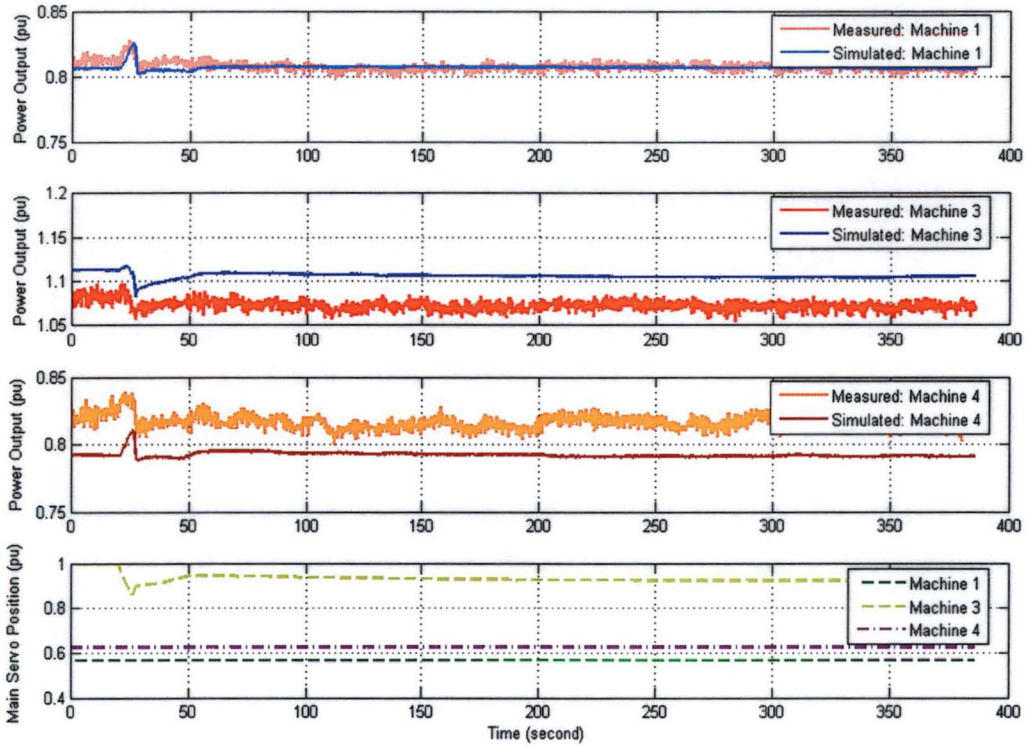

Figure 5.15: Worst-case comparison between three-machine model and the measured outputs for Trevallyn machines 1, 3, and 4

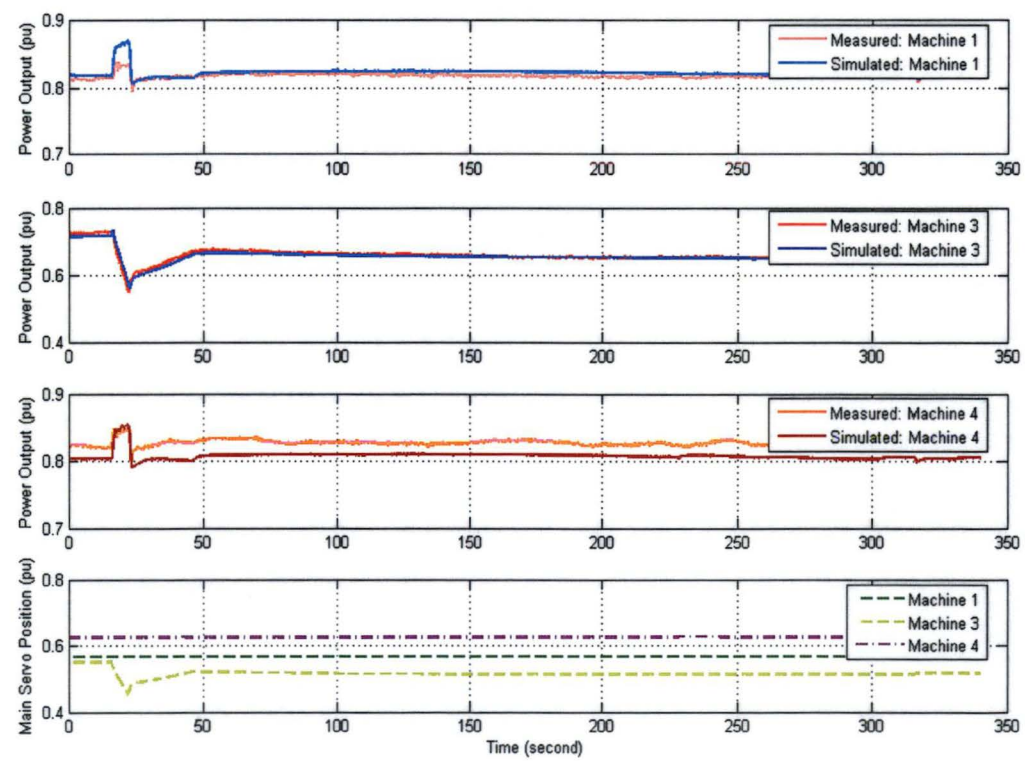

Figure 5.16: Best-case comparison between three-machine model and the measured outputs for Trevallyn machines 1, 3, and 4

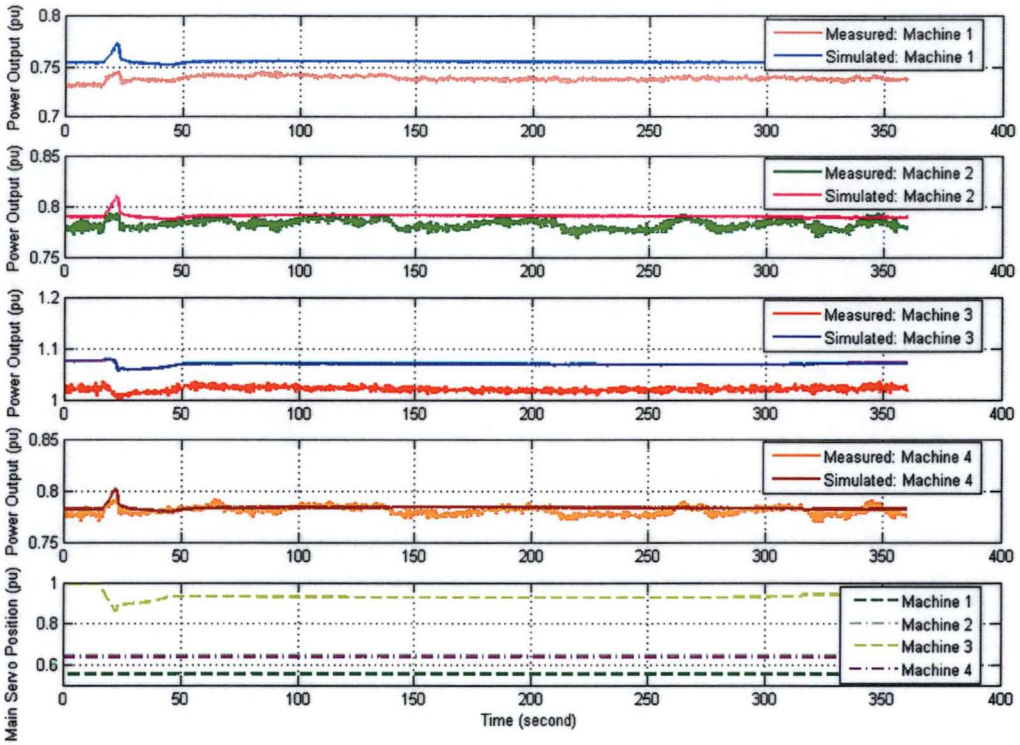

Figure 5.17: Worst-case comparison between four-machine model and the measured outputs for Trevallyn machines 1, 2, 3, and 4

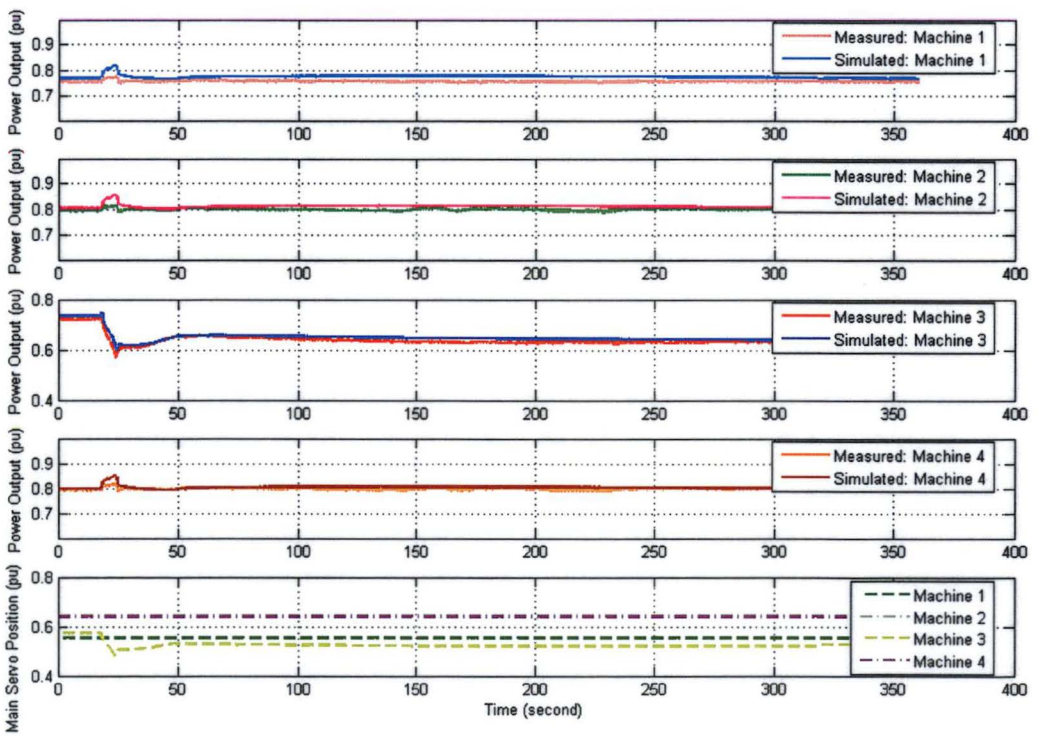

Figure 5.18: Best-case comparison between four-machine model and the measured outputs for Trevallyn machines 1, 2, 3, and 4

5.5.4 Frequency Response Simulation of the Multiple-Machine Station

The frequency responses of the multiple-machine Trevallyn station were studied through a series of Nyquist tests performed at different guide-vane oscillation frequencies. This information is very useful in deriving an optimal set of governor parameters for improving the plant and system performances. The Nyquist criterion, in general, guarantees the closed loop stability. However, the use of Nyquist tuning rules to determine the governor parameters in a nonlinear system is still controversial as the theory is derived mainly for use in the linear systems.

For Mackintosh station, where the waterway conduit is relatively short, a significant error is found in simulating both the phase and the magnitude of the power output when the guide vanes are moving at high frequencies. The error is thought to be caused by the unsteady flow effects in the Francis turbine. This unsteady flow effect, however, is not a significant problem for the Trevallyn power station. The contradictory result is not surprising since Trevallyn has a long waterway conduit and its water inertia is relatively high. Therefore, the inertia effect of the water column is expected to overwhelm the unsteady flow effects of the Francis turbine operation here.

Figures 5.19 to 5.26 show several Nyquist test cases where the power outputs of machine 3 are varying at two different initial load levels. To save space, only the results of the highest test frequency are shown here. The offset between simulated and measured power outputs is a consequence of the steady-state errors and thus it is not the main concern for frequency-domain analysis here. Spikes in the high-frequency power output are observed in both simulation and measurement. They are mainly caused by the cavitation of machine oil in the control valve of the main servo system. This effect becomes more obvious, as the guide vanes oscillation frequency is increased. The presence of this non-sinusoidal power output signals complicates the frequency-domain analysis, and greater errors for the system gain are expected at high guide-vane oscillation frequencies. The resulting Bode diagrams are presented in Figures 5.27 and 5.28. As illustrated, the phase and magnitude of the oscillating power outputs are simulated quite well for Trevallyn station. The phase characteristic of machine 3 is greatly affected by the initial operating condition, but it is insensitive to the number of machines in operation if power outputs of the other machines are not fluctuating significantly.

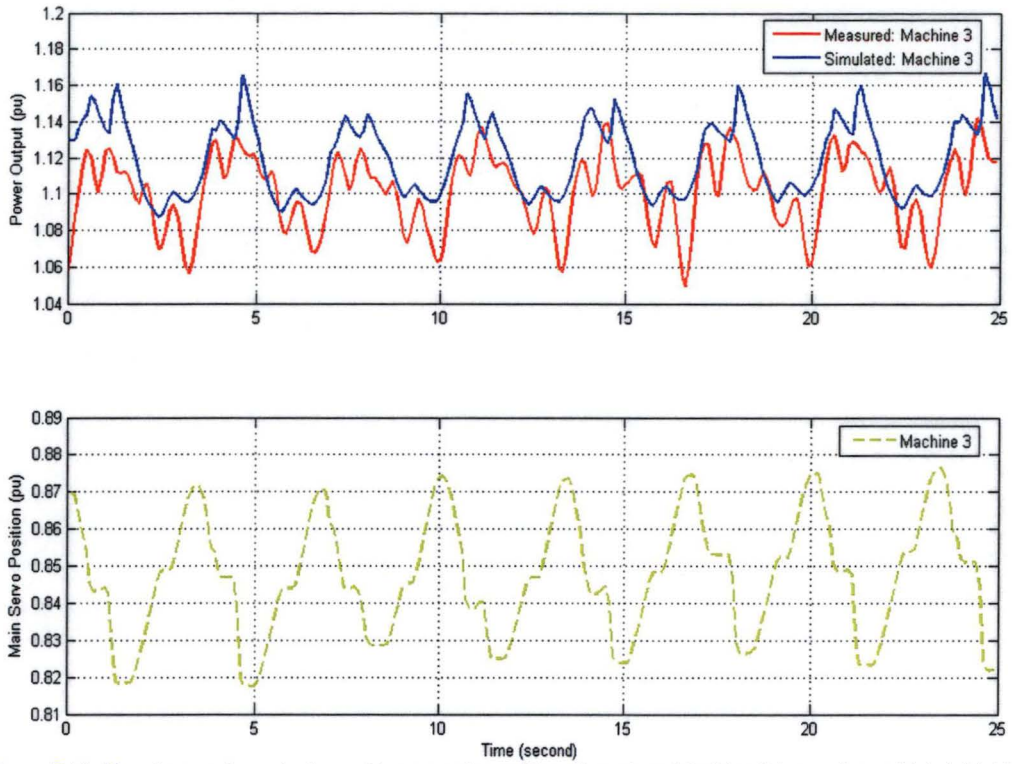

Figure 5.19: Nyquist-test for a single machine operating at Trevallyn plant. Machine 3 is running at high initial load and its guide vanes are moving at the highest test frequency of 0.3 Hz

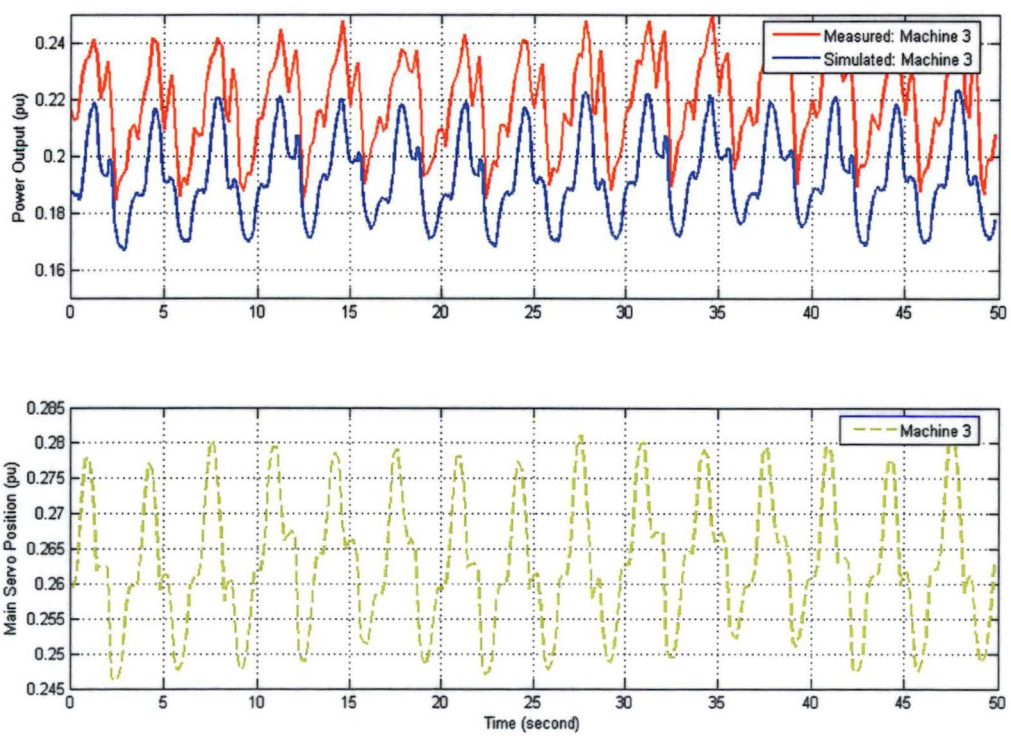

Figure 5.20: Nyquist-test for a single machine operating at Trevallyn plant. Machine 3 is running at low initial load and its guide vanes are moving at the highest test frequency of 0.3 Hz

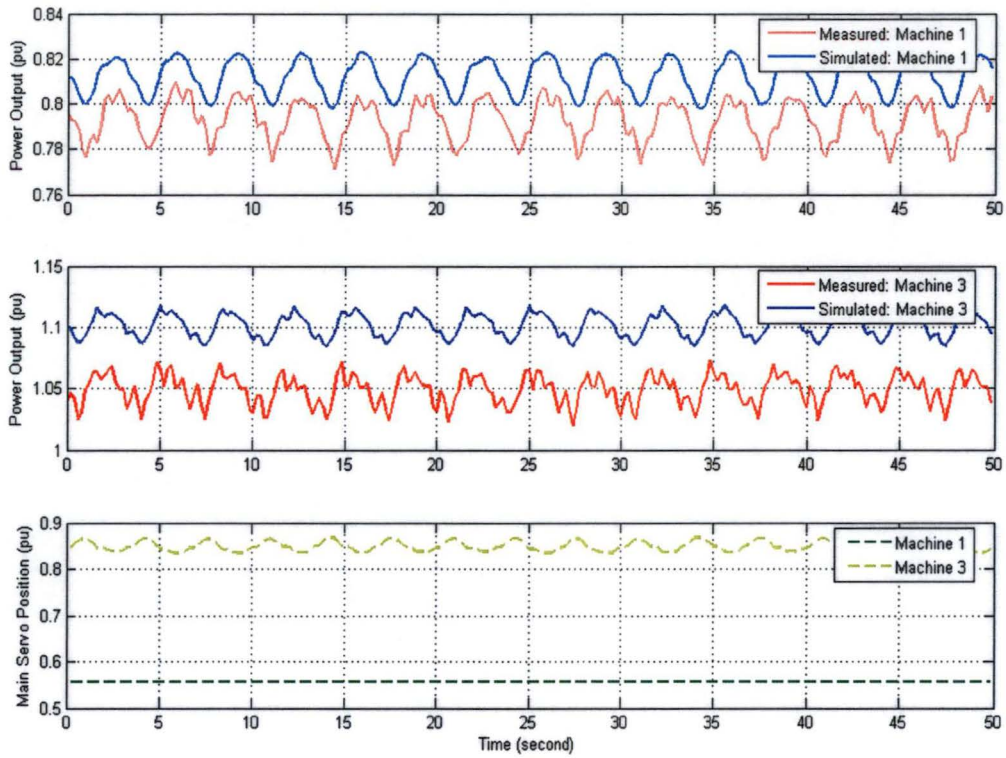

Figure 5.21: Nyquist-test for two machines operating at Trevallyn plant. Machine 3 is running at high initial load and its guide vanes are moving at the highest test frequency of 0.3 Hz

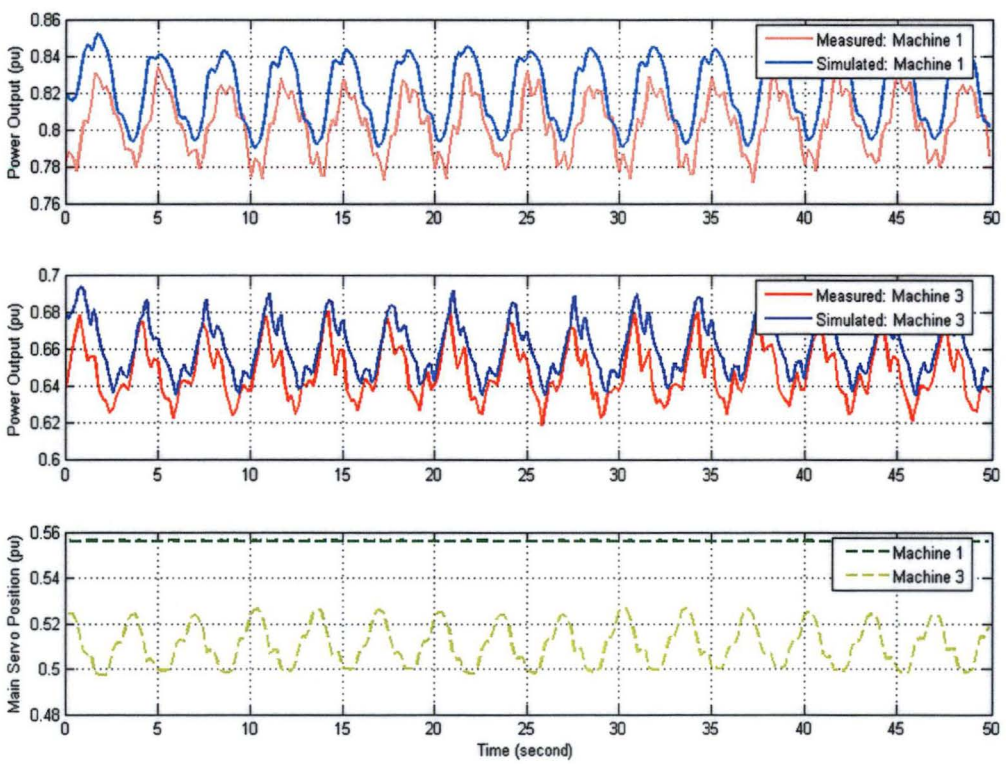

Figure 5.22: Nyquist-test for two machines operating at Trevallyn plant. Machine 3 is running at low initial load and its guide vanes are moving at the highest test frequency of 0.3 Hz

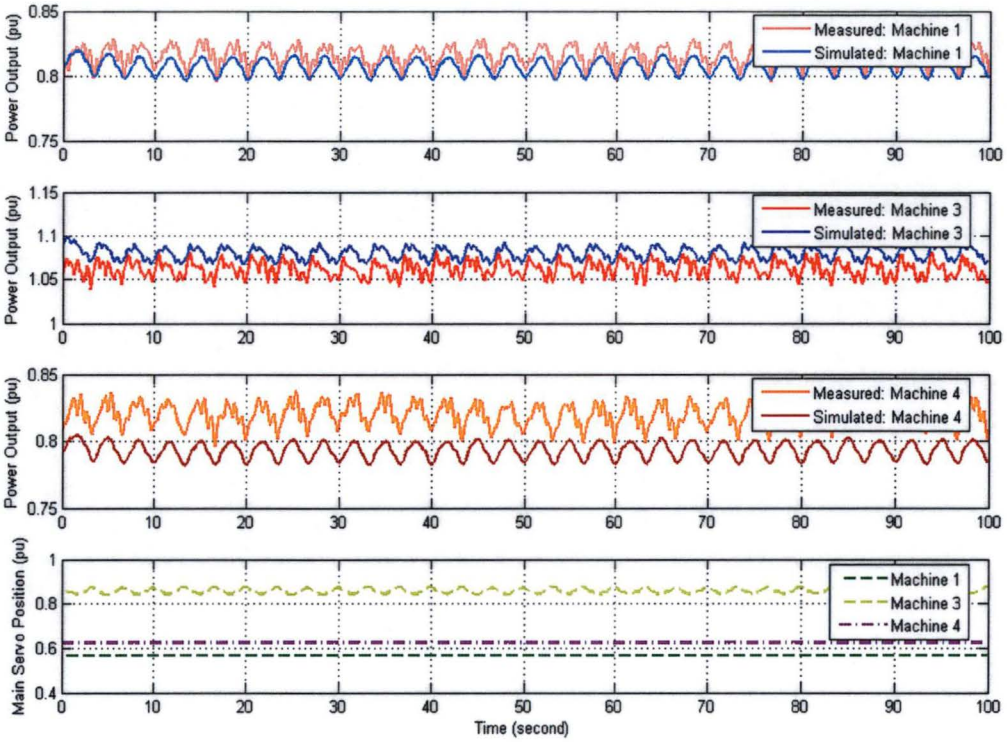

Figure 5.23: Nyquist-test for three machines operating at Trevallyn plant. Machine 3 is running at high initial load and its guide vanes are moving at the highest test frequency of 0.3 Hz

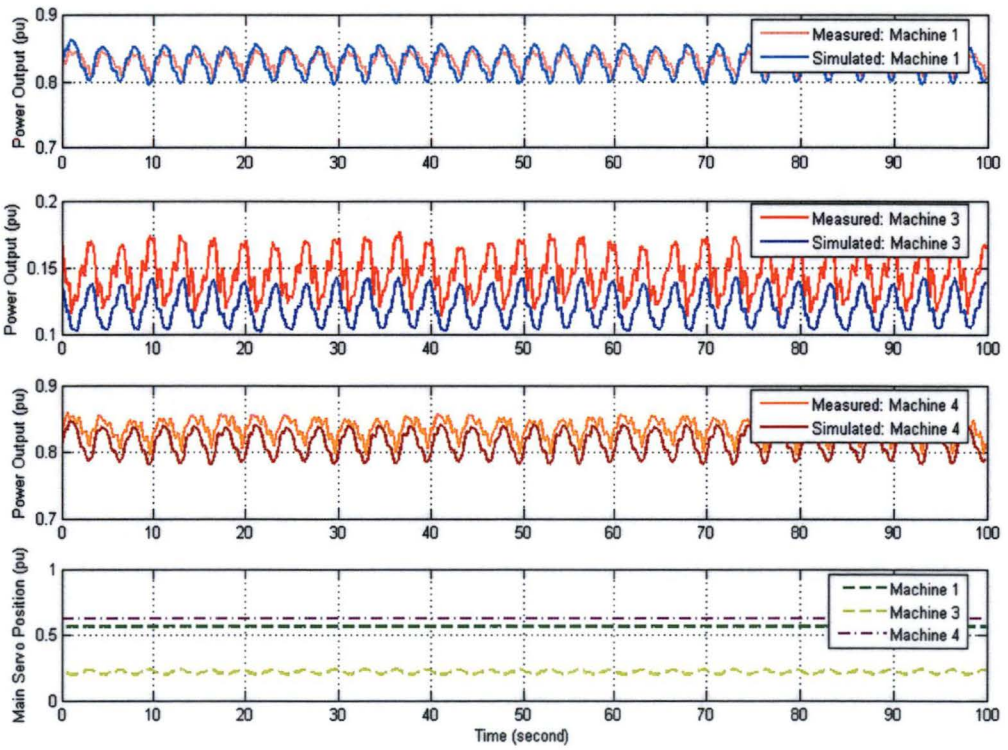

Figure 5.24: Nyquist-test for three machines operating at Trevallyn plant. Machine 3 is running at low initial load and its guide vanes are moving at the highest test frequency of 0.3 Hz

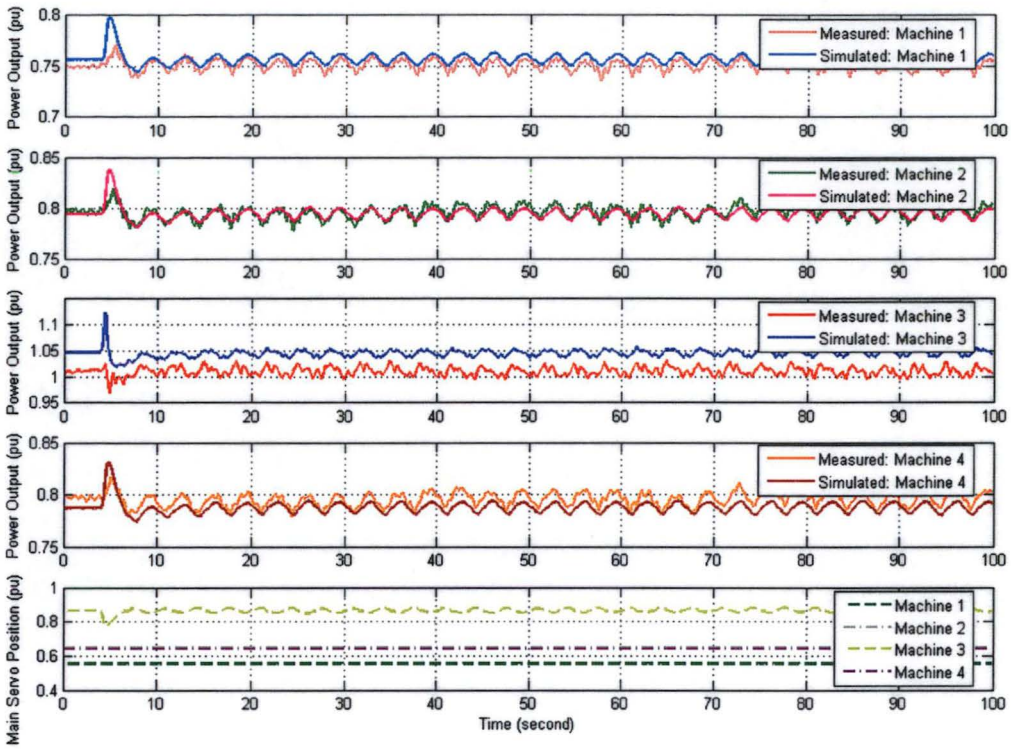

Figure 5.25: Nyquist-test for four machines operating at Trevallyn plant. Machine 3 is running at high initial load and its guide vanes are moving at the highest test frequency of 0.3 Hz

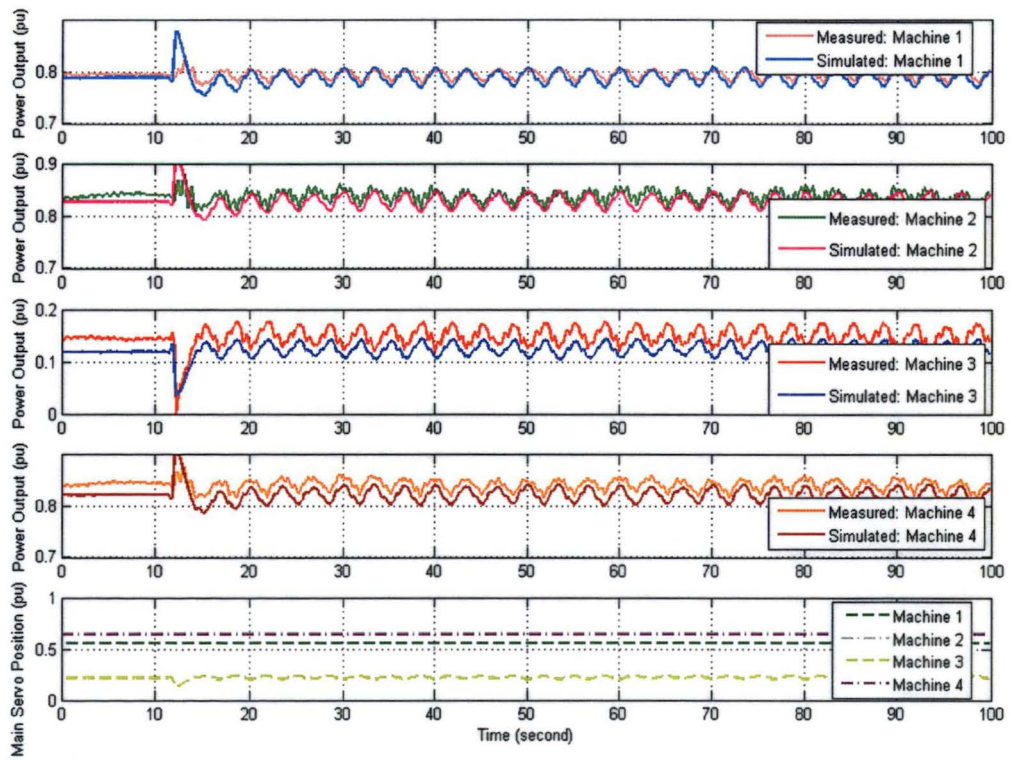

Figure 5.26: Nyquist-test for four machines operating at Trevallyn plant. Machine 3 is running at low initial load and its guide vanes are moving at the highest test frequency of 0.3 Hz

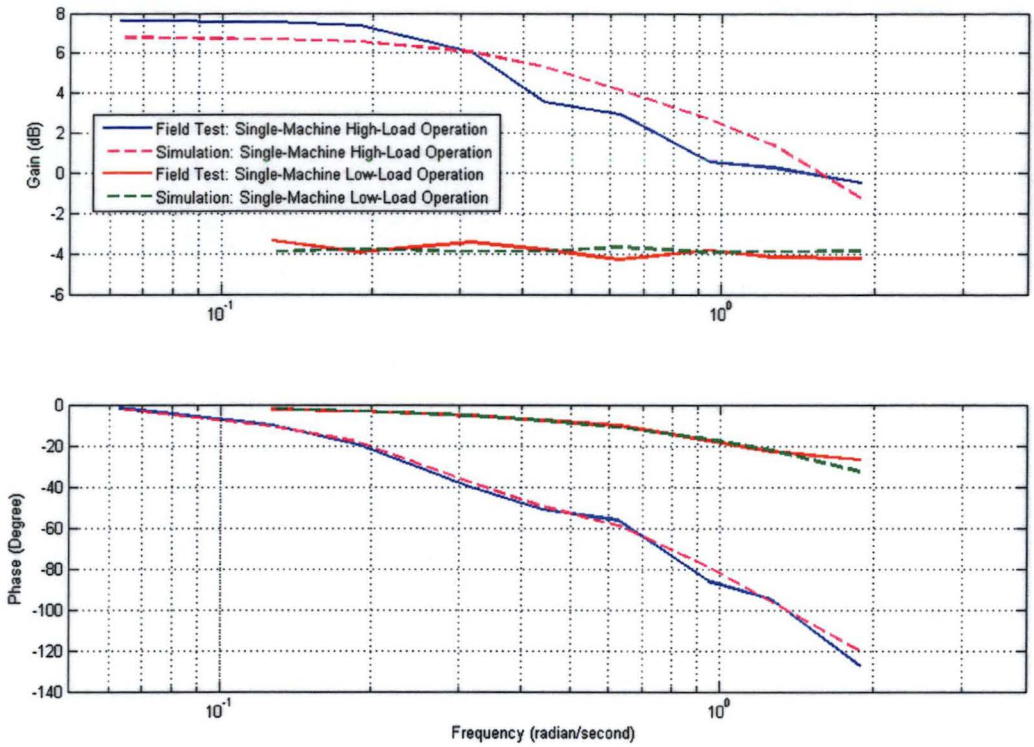

Figure 5.27: Bode plot showing the frequency characteristics of the Trevallyn machine 3 when it is running at low and high initial loads

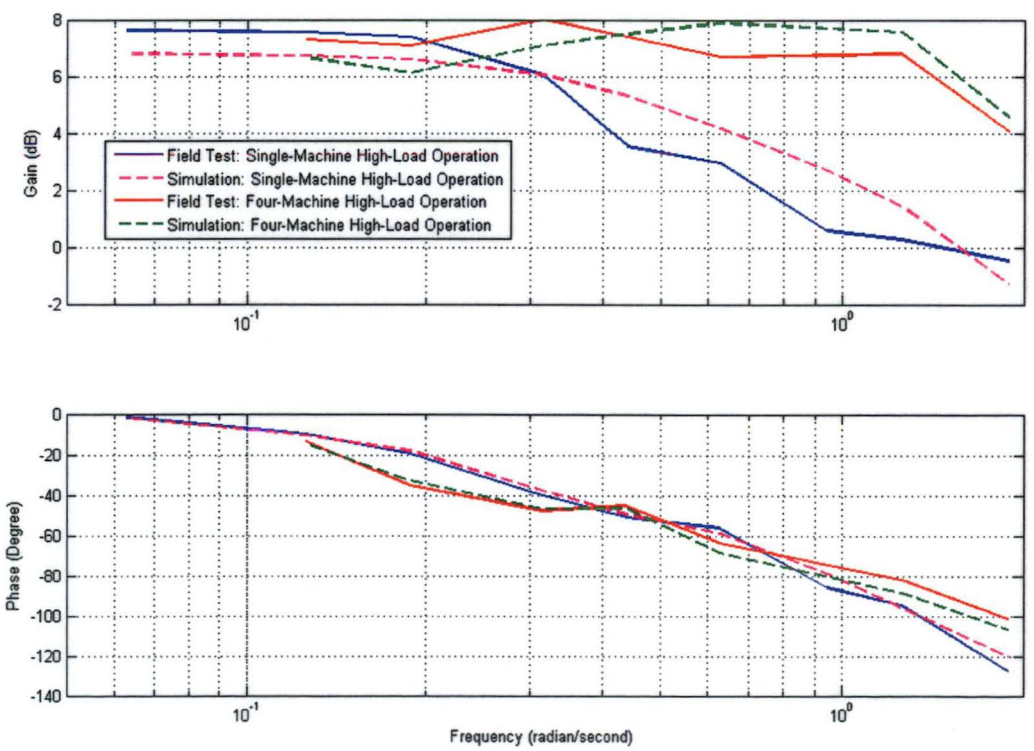

Figure 5.28: Bode plot showing the frequency characteristics of the Trevallyn machine 3 when it is running in a single- and multiple-machine mode

5.6 Discussion

5.6.1 Influence of Hydraulic Coupling Effects on Control Stability

Hydraulic coupling in the water supply column is a very well known effect for a multiple-machine plant [141]. A plant subjected to a large external disturbance has been studied in this Chapter. The phenomenon is quite important in the governor tuning to ensure the stable response of the plant for all conditions. Using simplified models that neglect such effects can lead to errors in control tuning leading to unstable operation under certain operating scenarios. When an individual unit is tuned through field tests to verify the adequacy of the governor settings, one may be misled by the testing results. In fact, a well-tuned response obtained from testing an individual unit does not necessarily guarantee a well-tuned or even stable response for the entire plant [42]. This scenario is even more critical when units of various sizes are sharing a common waterway conduit [42].

Although little analysis is done on a plant like Trevallyn where units of identical sizes are used, care must be taken when applying standard tuning rules such as Hovey's criteria to set the governor parameters. It is easy to foresee that a counteracting control of the guide vane is required to reduce the effect of the perturbation caused by any change in the operating condition of the machines. For stability under islanding or black start conditions, the governor tuning criteria must be based on the set of units or the hydro plant as a whole rather than on individual operating units [42].

While certain control tuning parameters may be acceptable under open circuit conditions or when connected to a large system, the case of isolated load operation or black start under unusual system restoration conditions may be limiting. More conservative turbine/governor parameters are needed here ([42], [51]). As conservative setting of the parameters may result in sluggish plant response under normal conditions, it is wiser to compute in advance the appropriate values for the tuning parameters and establish a procedure for implementing them when isolated operation or black start scenarios occur [70]. However, the nature of hydro plant together with the costs, and indeed risks, associated with carrying out tests on all the machines means that it is not practical to carry out site testing at the detailed level required to establish the optimum governor settings over the full range of system and station conditions [70]. Hence, an accurate turbine and waterway model that captures the hydraulic coupling effects will play an essential role in the overall system stability study.

5.6.2 Travelling Wave Effects of Waterway Conduit

An inelastic waterway model was utilised in this study, as the fastest guide-vane execution time (3.33 seconds) is longer than the system characteristic time (1.6 second). Although modelling of hydraulic systems using inelastic water column theory seems to be adequate in the simulation of Trevallyn plant, the consequences of neglecting travelling pressure waves or water hammer effects must be carefully investigated to ensure the stability of the plant under all operating conditions.

Water hammer is the result of flow deceleration or acceleration caused by the sudden closing or opening of the guide vanes. This phenomenon is characterised by a series of positive and negative pressure waves, which travel back and forth in the conduit until they are damped out by friction. The difference between elastic and inelastic solutions is generally negligible, except for some transient high frequency effects [70].

Even with a throttled surge tank installed in the waterway system, the travelling pressure wave effects still merit full attention. It would be a dangerous illusion to think that the surge tank will stop any type of pressure wave. Indeed, it is an established fact that pressure tunnels have been severely damaged by water hammer in spite of ample protection provided by the surge tank (Monsonyi & Seth [82]).

Besides, the ability of inelastic model to simulate the total load rejection of a hydro plant remains in question. No tests have been carried out so far in the Trevallyn station to investigate the plant behaviour when total load rejection of all four machines occurs. The costs and the risks of performing such an experiment have prevented it from being carried out. The effect of travelling waves could be significant here, and there is no guarantee of the model accuracy or system stability under this circumstance. Hence, readers must be aware of the assumptions made in the inelastic theory before applying the model to the power system design.

5.6.3 Model Inaccuracies

It is necessary to confirm that the simulated response agrees with the real plant behaviour before using a simulation to investigate the transient operation of the hydroelectric generating plant. Simulations using the MATLAB Simulink program reveal a worst-case accuracy of about 4 percent for the Trevallyn power outputs. The model inaccuracies are caused by either steady-state or transient errors. The possible sources of errors are:

- Identical turbine characteristic curves being used to simulate the machine behaviour at Trevallyn power station. This could have significant impacts because the efficiency of individual turbines may differ depending on the conditions of the mechanical parts being used for that unit. The guide vanes of two machines at the Trevallyn had been replaced just before the field tests, and the guide vanes of another machine were found badly pitted during the tests. Neglecting these factors may result in steady-state errors or an offset between the simulated and measured power outputs.

- Generator efficiency being assumed independent of the turbine flow conditions, due to lack of any detailed information. A constant efficiency of 97% was used for the Trevallyn generators. This could be misleading, as the generator efficiency will vary slightly with the machine output. A steady state variation of 1 or 2% may occur.

- The quadratic guide vane function may not be a true representation of the Trevallyn flow characteristic. A larger steady-state error is expected for units initially operating near or at the full load.

- Daily tidal effects will have some impacts on the Trevallyn tail water level. It will change the turbine net head from time to time, which in turn may generate some steady state errors for the power output simulation if an incorrect value is being used. This effect must be considered when the testing is to be carried out over a longer period. The tail water level at the Trevallyn outlet ranges between sea level +1.8 m and –2.6 m as the tide varies in the Tamar River [154]. The magnitude of

this error is still an unknown, as it can either be compensated or amplified by the errors made in the lake water level measurement. Nevertheless, its impact on the transient behaviour of the plant is minimal because the simulation is usually run for a few minutes only.

- A one-dimensional quasi-steady-flow simulation does not capture any unsteady or three-dimensional flow effects in the Francis turbine. Errors of this type are generated because of the unsteady Francis turbine operation and the convective time lag in establishing a new flow pattern in turbine runner and draft tube after altering the guide vane position.

- A quasi-steady friction term is used in the model. For the Trevallyn plant, the friction loss is relatively large in magnitude due to its long waterway conduit and thus an unsteady friction model should be considered to improve accuracy.

5.7 Conclusions

This Chapter has emphasised the contributions made by the multiple-machine simulation to improving the accuracy of governor tuning and power system design. The multiple-machine model successfully captured hydraulic coupling effects observed in the field tests that parallel single-machine models were unable to predict accurately. Unsteady flow effects were found to be insignificant for the Trevallyn station, as the inertia effect of the water column dominated the unsteady flow effects of the Francis turbine operation. Hence, the unsteady flow studies presented in the later part of this thesis will focus on operations at power plants with relatively short waterway conduits.

CHAPTER 6

RESEARCH METHODOLOGIES FOR MODELLING OF THE DRAFT TUBE FLOW

6.1 Overview

Quasi-steady flow analysis for Mackintosh power station reveals that unsteady flow behaviour in the runner and draft tube could easily affect the operations of a Francis turbine. The transient effects are thought to be more significant in stations with relatively short waterway conduits. This has motivated further investigation of unsteady flow effects in the Francis turbine. Due to time constraints and limited resources, the current study will only focus on the modelling of the flow inside the Mackintosh's draft tube with zero inlet swirl. The flow behaviour in the turbine draft tube actually merits even greater attention, as the stability of a hydraulic power plant is influenced and restricted by the presence of complex draft tube flow phenomena when the turbine is operating at off-design conditions. Experimental and numerical procedures for modelling both steady and transient flow behaviour of the draft tube flow are presented in details in the following subsections.

6.2 Experimental Model Testing

The experimental program was based on a 1:27.1 scale plexiglass model of the draft tube component employed in Mackintosh power plant. All experimental tests were carried out in the Aerodynamics Laboratory of the University of Tasmania. The airflow in the model was supplied by a centrifugal fan and controlled via a pneumatic-actuated butterfly valve. Flow visualisation, velocity and turbulence traverses, static pressure surveys, and skin friction measurements were the main components of the steady-flow investigations; the transient-flow study involved measurements of instantaneous velocity at inlet and instantaneous static pressure at outlet. The experimental scale model and the flow control system are described in Section 6.2.1, while the instruments and techniques used for the experimental testing are detailed in Sections 6.2.2 and 6.2.3 respectively. The main objectives of this experimental program were to provide an insight into the physical flow processes of an elbow draft tube; provide quantitative

assessment of the transient flow effects in the draft tube following a change in the turbine discharge; and supply data for validation of Computational Fluid Dynamics (CFD) modelling as well as the Simulink plant model.

6.2.1 Experimental Model

Figure 6.1 shows the experimental test rig used for the present study. The scale model draft tube was mounted on a steel support frame and arranged in an open-circuit configuration where air was extracted at the outlet of the draft tube model and expelled back to the atmosphere via a ten-blade centrifugal fan (driven by a 4 kW AC motor with 2840 rpm rated speed). The fan motor was run at a constant frequency of 35 Hz, corresponding to a speed of 2070 rpm under steady conditions. An Xtravert variable frequency digital speed controller was used to monitor the fan speed. A rotating valve mounted on a computer-controlled swivel actuator (manufactured by Festo AG & Co.) at the fan exit was used to control the flow rate inside the draft tube model. A standard BS1024 bellmouth nozzle was employed at the inlet pipe to measure the flow rate and the average throughflow velocity.

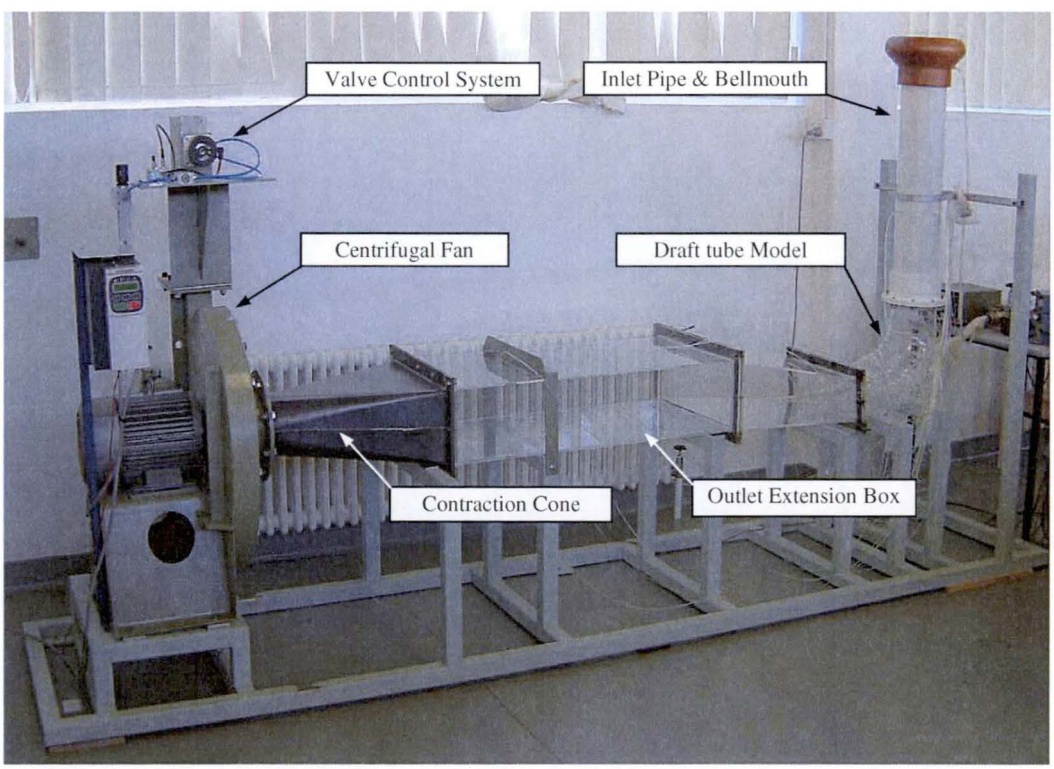

Figure 6.1: General view of the experimental test rig. Airflow in the system is supplied by the centrifugal fan system and the flow rate is controlled by a pneumatic actuated butterfly valve at outlet

6.2.1.1 Draft Tube Model Specification

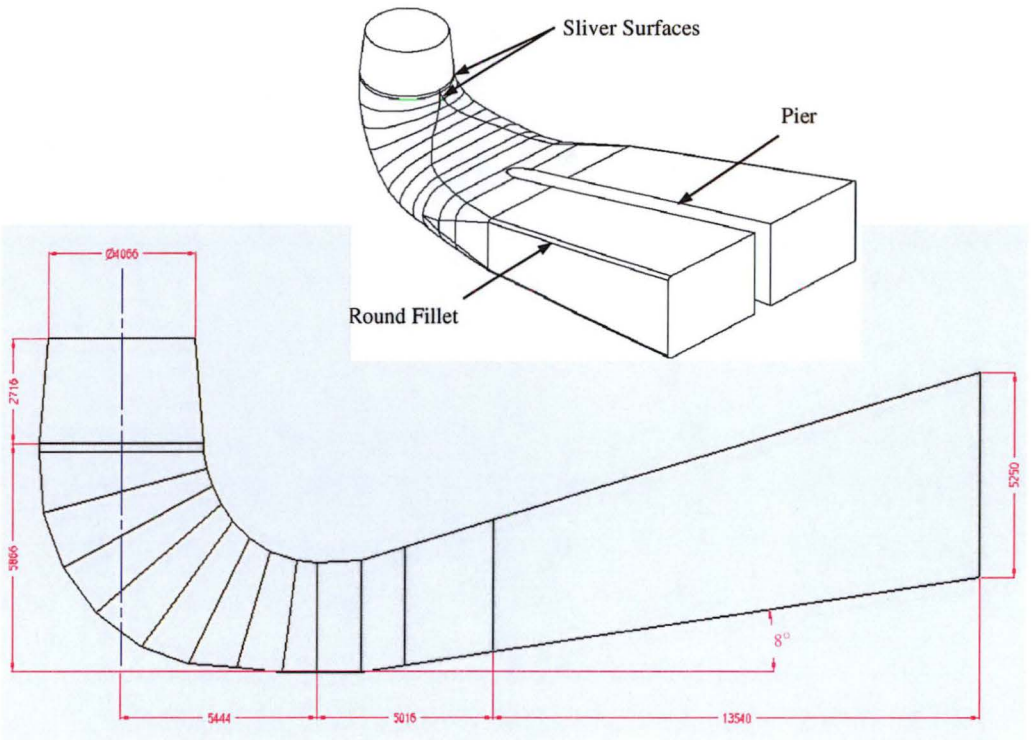

Figure 6.2: Geometry characteristics and centreline profile of the full-scale draft tube employed in the Mackintosh power plant (All Dimensions in mm)

A 1:27.1 scale model was hand-constructed in acrylic by Plastic Fabrications Pty Ltd. Plexiglass was chosen as the material for the model construction because of its easy machinability, lighter weight than like-substitutes, and high transparency. The model is closely geometrically similar to the Francis-turbine draft tube currently employed in the Mackintosh power plant (see Figure 6.2) despite some model imperfections due to manufacturing difficulties. The model has a circular-to-rectangular cross-sectional transition with a 90° diffusing-bend (see Figure 6.3). It is attached to a PVC pipe (with 151 mm diameter and 750 mm length) at the inlet and a rectangular box (with 968 mm length and a cross-sectional aspect ratio of 2.4) at the outlet. The model is fitted with 124 static pressure tappings (internal diameter 1.0 mm) distributed on the surface of the model. They were used mainly for observations of the static pressure distributions.

Generally, the flow path in the draft tube model approximates the so-called fishtail diffuser. The first section provides a conical flow path with an inlet diameter of 151 mm and an included angle of 5.3°. The flow then turns by 90° along the centreline. In the

subsequent sections along the bend, the cross-sections of the flow path become increasingly oblong with the downstream distance and the cross-sectional areas continuing to expand until they reach a size that is 5.1 times the inlet area of the draft tube model. The step-and-groove design of the flanges provides for the alignment of the adjacent sections and helps to prevent leakage. The flow cross sections are constant in the inlet pipe and the outlet extension box. The airflow is guided through a steel contraction cone with 5:1 contraction ratio at the exit of from the extension box before finally discharging to atmosphere through a centrifugal fan.

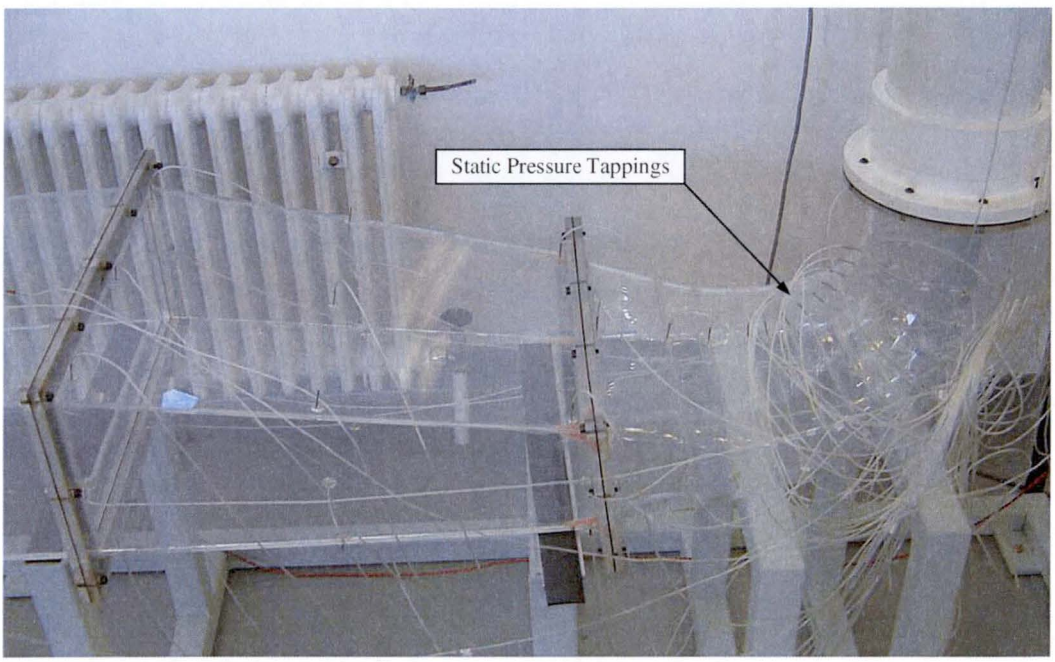

Figure 6.3: Close-up view of the draft tube scale model used for experimental testing in the laboratory

There are some slight differences between the geometry of the full-scale prototype and the experimental model. The round fillets near the model outlet have been squared off to simplify the geometry, while the sliver surfaces below the inlet cone have been smoothed to simplify the model construction. The tilt angle for the diffuser box downstream of the model (right after the bend) has been reduced to about 4° (if compared to the full-scale tilt angle of 8°) due to manufacturing difficulties. These modifications are expected to have minimal effect on the overall bulk flow behaviour of the draft tube. Figure 6.4 illustrates the difference between the designed and the actual centreline profiles for the draft tube model. A compromise had to be made in order to maintain the cross-sectional profile of the each section and the streamwise curvature of the model as close to the prototype as possible.

The support pier downstream of the Mackintosh's draft tube (see Figure 6.2) was not modelled due to concerns that its presence might complicate the flow and cause some measuring problems at the draft tube outlet. The exclusion of the support pier created some structural and vibrational problems in the model especially when the flow was changing rapidly. These were overcome by increasing the thickness of the downstream diffusing box to about 20 mm to stiffen the model.

The elbow of the model is made up of 12 different sections. Tiny depressions of about 2 mm were found between these section joints as constructed. This geometrical misalignment, although small, might have retarded the flow in the model and promoted flow separation within the diffusing bend. This is detrimental to the overall performance of the draft tube. To resolve this problem, the surface depressions were covered with the transparent tape.

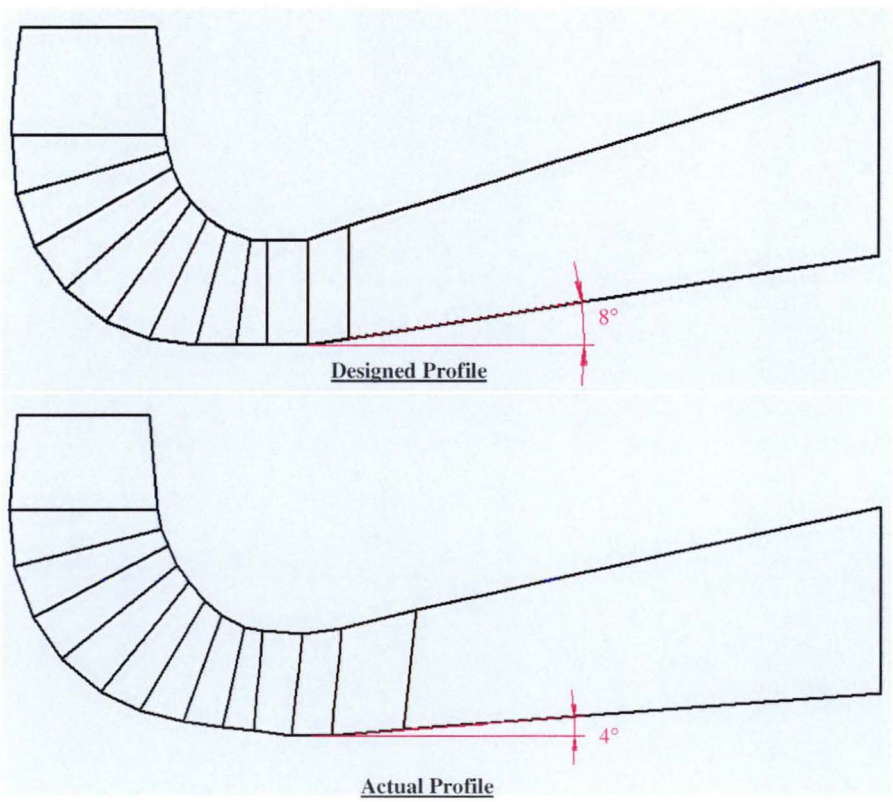

Figure 6.4: Comparison of the designed and actual centreline profiles for the experimental draft tube scale model

The Francis turbine and the waterway conduit were not modelled in these experiments in order to simplify the whole testing process. The runner and guide valves are expected to further increase the inlet flow distortion and losses in a complete Francis-turbine installation. This fact has already been mentioned in Chapter 2. Apart from the design constraints stated above, the geometric misalignments of the draft tube model are not fully examined and they are thought to be insignificant in the experiments. The effect of inlet swirl were not examined: it will become apparent that convective time lag effects in the meridional flow account for the majority of transient effects observed in the full-scale plant tests.

6.2.1.2 General Description of the Air Flow Control Systems

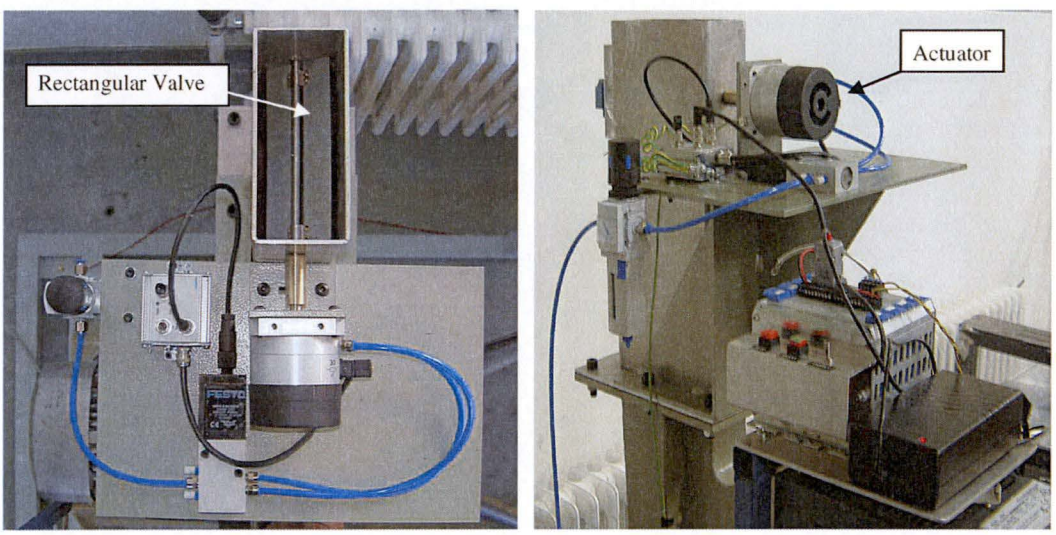

Figure 6.5: Overview of the pneumatic-actuated valve system used to control the flow rates of the draft tube

As illustrated in Figure 6.5, the flow rates of the draft tube are controlled by a pneumatic-actuated butterfly valve located at the exit of the centrifugal fan. The pneumatic actuator was chosen for these experiments because of its compact design and the ability to operate at high frequency (up to 2 Hz). The rectangular steel valve (of 185×75 mm^2) is mounted firmly on a Festo DSMI swivel actuator. The relationship between the amount of valve opening and the average inlet flow velocity measured by bellmouth nozzle is shown in Figure 6.6.

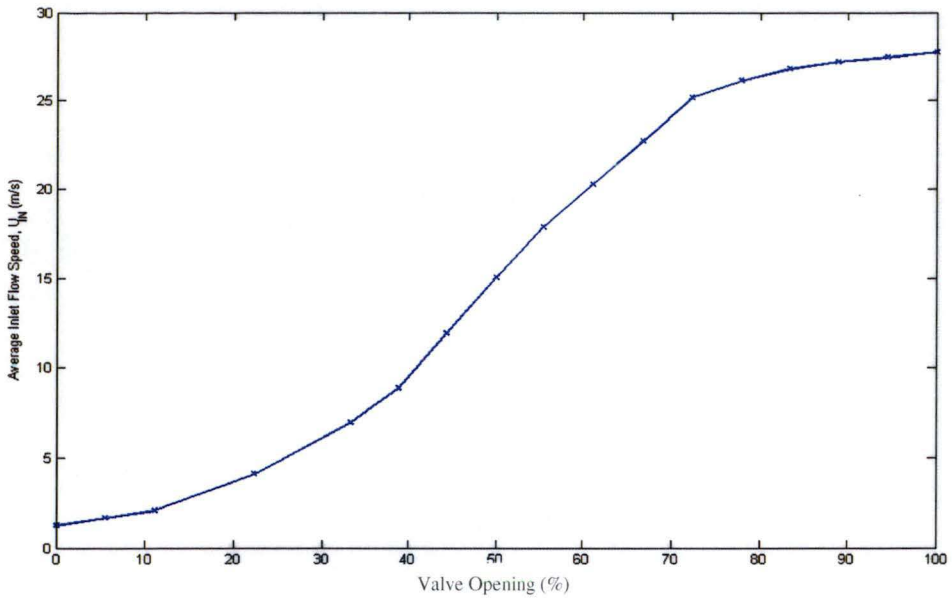

Figure 6.6: Valve characteristic curve showing the relationship between the amount of valve opening and the average inlet flow velocity measured by the bellmouth nozzle

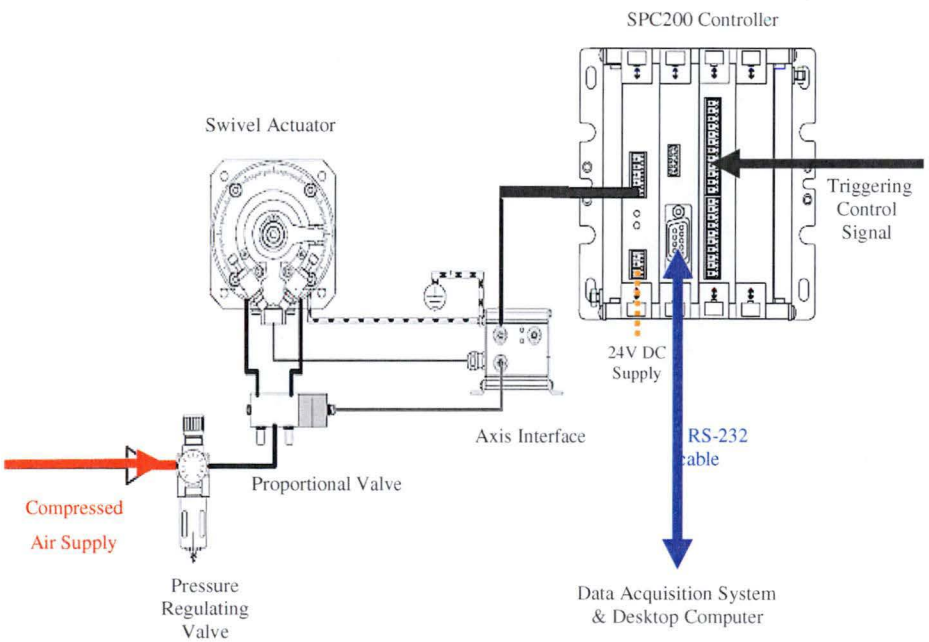

Figure 6.7: Basic layout of the Festo positioning control system used to monitor the flow rate inside the model

Figure 6.7 shows the basic layout and connection of the Festo SPC200 positioning system. The controller has a power supply module, a diagnostics module, and an I/O module. The axis interface, controller, valve, pneumatic actuator, and measuring system are connected with each other to form a closed-loop control circuit. The measuring

system registers continuously the position of the valve and passes this on to the axis interface in the form of an electrical signal. The measured values are then passed on from the axis interface to the SPC200 positioning controller. SPC200 compares the nominal position with the current position and subsequently calculates the positioning signal for the 5/2-way proportional directional control valve. The valve drives the actuator by pressurizing one drive chamber and exhausting the other.

High quality of the compressed air and power supply is essential to maintain good positioning behaviour of the valve during its operation. The use of a pressure-regulating valve with 5 μm filter guaranteed a stable supply of the clean compressed air and prevented any sudden change in the valve pressure that could lead to uncontrolled actuator movement or damage to the entire system. The compressed air tubing was also made as short as possible to maximise the dynamic response of the system. Overall, the compressed air pressure was kept at 6 Bar and the power supply for the controller was regulated at 24 Vdc throughout the tests. The controller was linked to data acquisition computer via a RS-232 null cable.

The commercial software WINPISA (Version 4.31) designed by Festo AG & Co. was used to configure the actuator settings, tune the control parameters, and program the motion for the pneumatic actuator. The controller could store up to 100 programs and 2000 commands at a time. Each program had to be compiled before uploading it to the controller. The following lists summarise the important quality-assurance procedures for the valve control system carried out prior to usage:

- Static and dynamic system identification processes were carried out to optimise the parameters of the actuator. Characteristic system values such as friction, hysteresis, acceleration and braking ability were ascertained and saved automatically during these identification processes.

- The measuring system was calibrated and checked regularly to compensate for system-induced differences between the estimated and actual positions. The calibration allowed the correction of the slope and tuning of the measuring system to actual measurements so that the absolute positioning accuracy could be improved.

- Controller parameters such as gain factor, damping factor, signal filter factor and positioning timeout were optimised using a trial-and-error approach. The mass moment of inertia of the valve system was unknown and needed to be tuned such that no swinging or oscillation around a position occurred while keeping the overshoot error for the valve position following a step change below 1°. The typical rise time of the valve setting from the fully opening to the fully closed position was about 0.15 second.

- All devices were tightly screwed to the support frame to minimise vibration. The actuator and the valve were earthed to ensure that they functioned correctly during the operation.

6.2.2 Instrumentation

6.2.2.1 Data Acquisition

Several methods were used to collect information in the present work. The pressure and temperature calibration data were recorded manually from instruments like thermometer or barometer. All critical experimental data were acquired automatically via the commercial software package LABVIEW (Version 8) running on an IBM compatible Pentium-IV 1.7 GHz desktop computer interfaced with a National Instruments (NI) PCI 6025E 12-bit data acquisition (DAQ) card and an United Electronic Industries (UEI) PCI 12-bit multifunctional board (PD2-MFS-4-1M/12). As most of the readings fluctuated markedly during the tests, proper averaging of the data points and observation of trends were essential to obtain reasonable results.

6.2.2.2 Ambient Condition Monitoring

A Vaisala PA11A digital barometer, interfaced to the data acquisition computer via a RS232 link, measured the atmospheric pressure. A Vaisala HMP 45A temperature and humidity probe acquired the ambient temperature using a resistive platinum sensor and the relative humidity through a capacitive thin film polymer sensor. The manufacturer's specified accuracies of PA11A were ±0.18 hPa; HMP 45A ±2% for relative humidity and ±0.2°C for temperature.

6.2.2.3 Draft Tube Temperature Measurement

A Temtrol T-type 316SS-inconel thermocouple (1.5 mm sheath diameter) was used to measure the draft tube air temperature. This thermocouple was placed just below the top surface of the downstream extension box (700 mm away from the draft tube outlet) to minimise any interference to the flow. The sensor was connected to an amplifier circuit and calibrated against a JOFRA D55SE temperature bath and calibrator (uncertainty less than ±0.1°C, Calibration Certificate T06727). The calibration relationship (see also Figure 6.8) was established via a second-order polynomial curve fit:

$$T_{dt} = C_1 \times V_T^2 + C_2 \times V_T + C_3 \tag{6.1}$$

where T_{dt} = draft tube air temperature (°C)

V_T = amplified transducer output signal (V)

C_1, C_2, C_3 = calibration coefficients for thermocouple

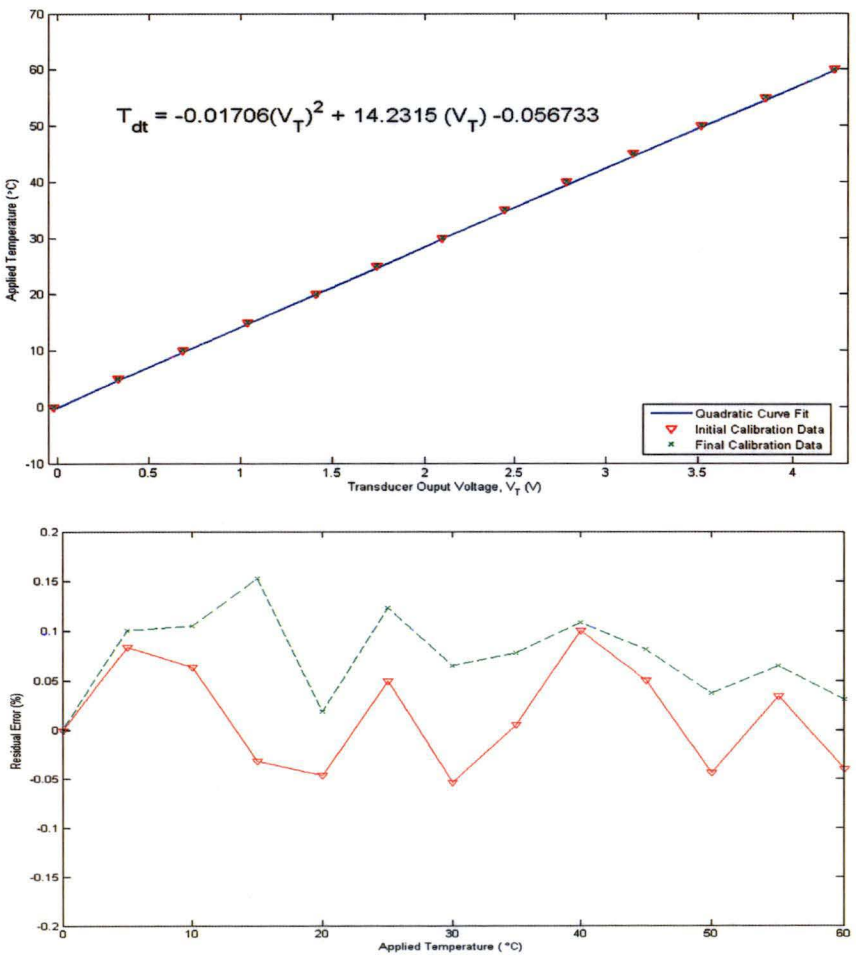

Figure 6.8: Calibration curve and residual plot of Temtrol thermocouple for draft tube temperature measurement

6.2.2.4 Steady-Flow Measurement

6.2.2.4.1 Micromanometer and Scanivalve

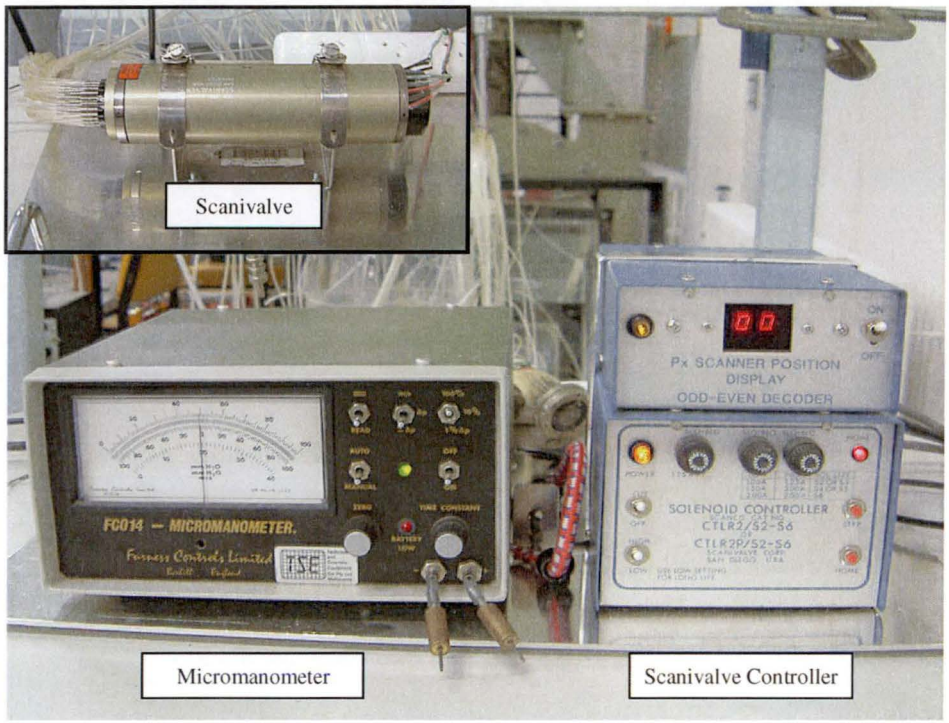

Figure 6.9: Furness Controls micromanometer and the computer-controlled 48J9 Scanivalve for static pressure measurements

A Furness Controls FC014 analogue micromanometer (range ±199.9 Pa while operating at 100% ΔP) with a computer-controlled 48J9 Scanivalve measured the differential pressures in the draft tube model. No other external pressure signal conditioning was applied for steady-flow pressure measurements. 5000 pressure samples were typically acquired at 1 kHz and five replicates were taken. The delay time after each pressure switch was set at 1 second to ensure the stability of the pressure readings. Five replicates were chosen as a compromise between testing time and maximising the likelihood of statistically reliable results. The typical variation was 0.25% (standard deviation normalised by mean) with the exclusion of statistical outliers.

The micromanometer is calibrated dynamically against a Betz-type projection micromanometer (S/N 7582) manufactured by Van Essen (readability ±0.01 mm water). The pressure differential at the draft tube inlet (with respect to atmospheric pressure) was chosen as the calibration pressure source; its value was changed by altering the fan

speed. The calibration curve is shown in Figure 6.10. The micromanometer was calibrated several times during the tests and no obvious change was observed for the calibration coefficients. A second-order polynomial curve-fitting method was employed to relate the measured voltage to the static pressure differential:

$$P_i - P_{atm} = C_4 \times V_{mm}^2 + C_5 \times V_{mm} + C_6 \tag{6.2}$$

where $P_i - P_{atm}$ = pressure differential with respect to atmospheric pressure (Pa)

V_{mm} = micromanometer output signal (V)

C_4, C_5, C_6 = calibration coefficients for micromanometer

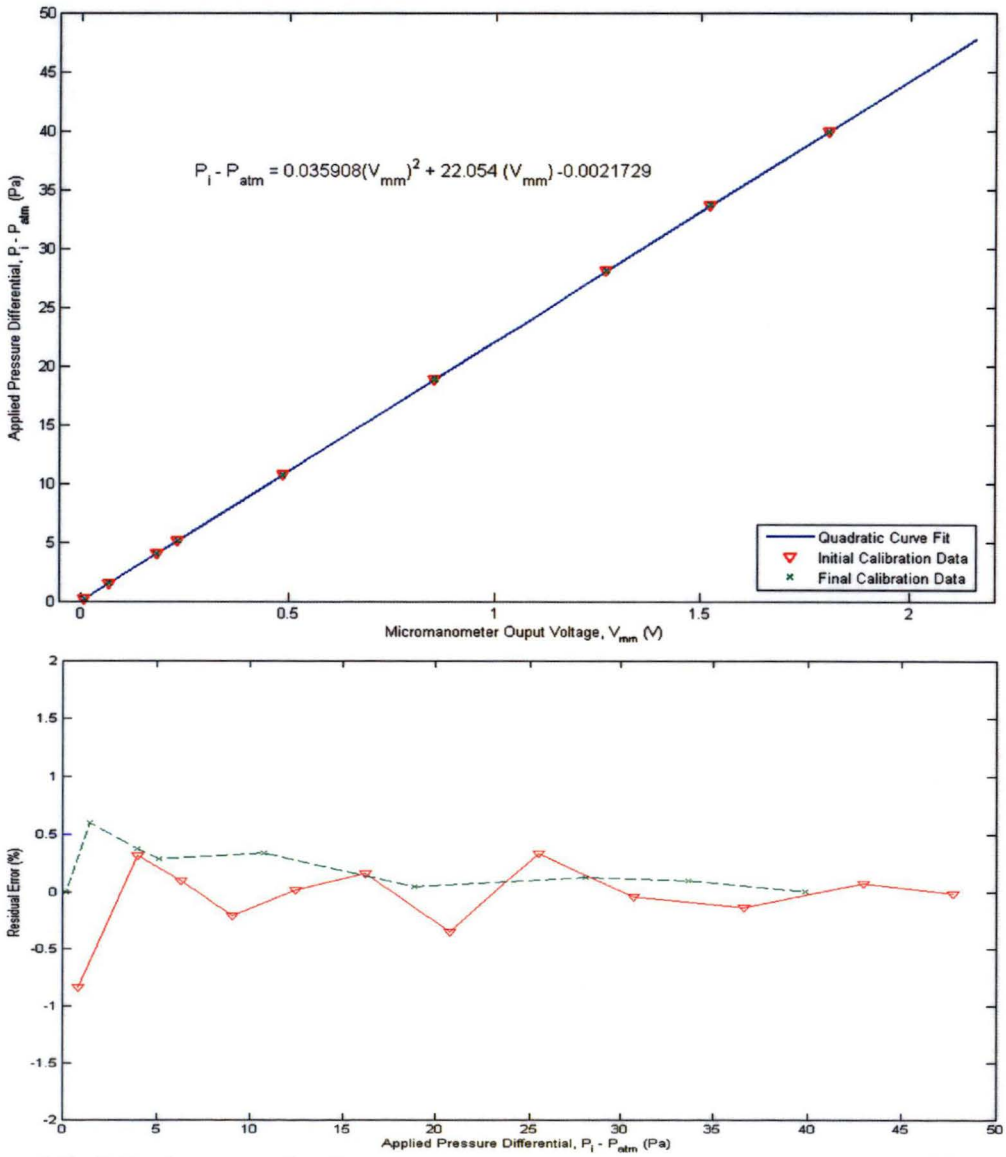

Figure 6.10: Calibration curve and residual error plot of Furness Control FC014 micromanometer used for static pressure measurements

6.2.2.4.2 Four-Hole Probe

An accurate knowledge of the velocity and its direction is very important for the study of draft tube flow. A four-hole pyramid probe (probe h3) constructed by the University of Oxford was employed to check the velocity measured by hotwire anemometry. As illustrated in Figure 6.11, the sensing head contains a central hole surrounded by three holes in plane sloping side faces. The sensing probe is supported by a stainless-steel tube of 10 mm diameter. The pressure holes are labelled A to D with the centre hole labelled A. Two flow angles (yaw and pitch) can be obtained using the four-hole probe.

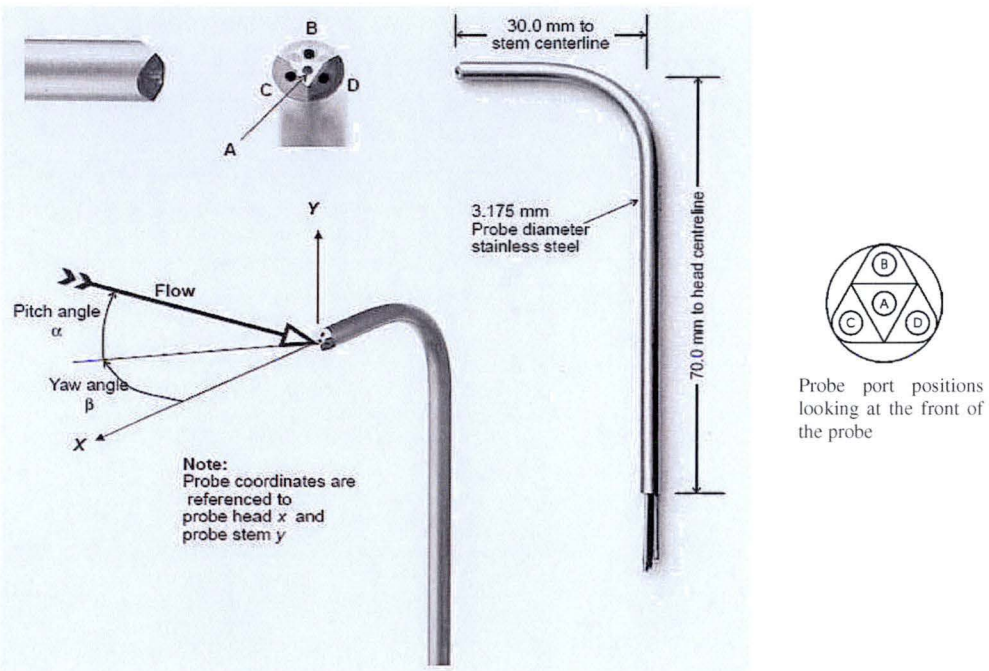

Figure 6.11: The geometry and the associated dimensions of the Oxford four-hole pyramid probe (reference [127])

The four-hole probe was connected to the Furness Controls FC014 micromanometer via the computer-controlled 48J9 Scanivalve. The sampling strategy was identical to the one used for static pressure measurements. This probe was designed primarily for application in low Mach number, incompressible flow. Hence, the probe coefficients defined in Equations 6.3 are assumed independent of the Mach number. They were computed using an average value of 250 pressure measurements at each probe position [127] and the calibration results are plotted in Figure 6.12. These calibration data were supplied by the University of Oxford. The procedure was not checked due to the lack of

proper pitch angle control in the available calibration facility. Overall, the probe is usable to an angle of about 30° from the probe axis.

$$\begin{cases} C_{Pitch} = \dfrac{P_B - 0.5(P_C + P_D)}{P_A - \overline{P}} \\ C_{Yaw} = \dfrac{P_C - P_D}{P_A - \overline{P}} \\ C_{Dyn} = \dfrac{P_{Dyn}}{P_A - \overline{P}} \end{cases} \tag{6.3}$$

where C_{Pitch} = pitch coefficient for four-hole probe

C_{Yaw} = yaw coefficient for four-hole probe

C_{Dyn} = head coefficient for four-hole probe

$P_{A,\,B,\,C,\,D}$ = static pressure from pressure tubes A to D as shown in Figure 6.4

P_{Dyn} = dynamic pressure obtained from calibration tunnel or measurement

$\overline{P}$ = average static pressure $= (P_B + P_C + P_D) / 3$

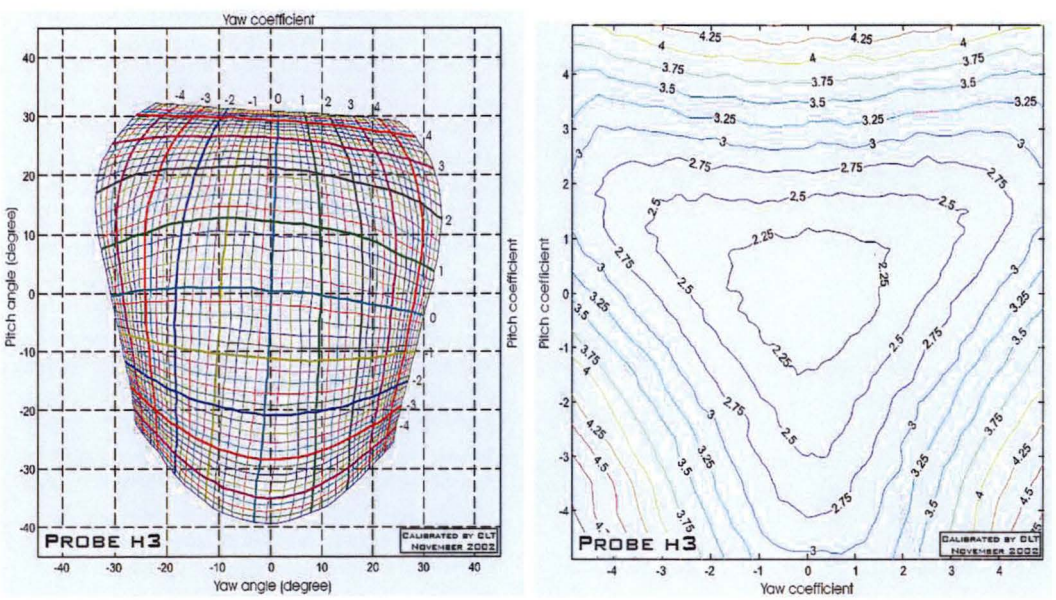

Figure 6.12: Calibration results of the Oxford four-hole pyramid probe (calibrated by Tsang, University of Oxford, UK, November 2002). Left picture: variations of yaw and pitch angles with pitch and yaw coefficients. Right picture: variation of head coefficient with pitch and yaw coefficients (reference [127])

6.2.2.4.3 Hot-Wire Anemometry

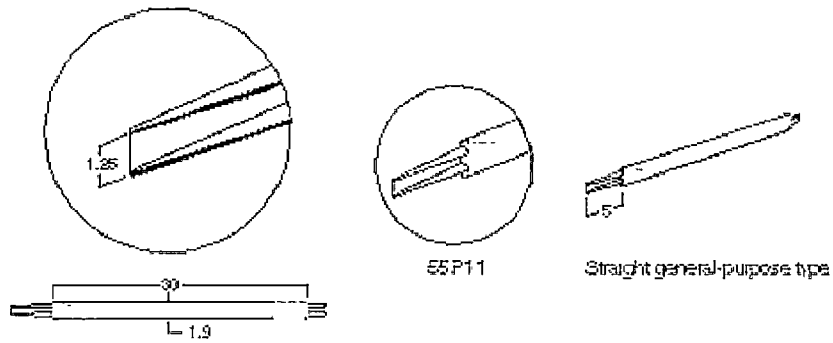

Figure 6.13. Dantec 55P11 single-sensor hotwire probe used in the current investigation

A 55P11 single-sensor hotwire probe (manufactured by Dantec Dynamics) with 5 μm diameter and 1.25 mm sensing length (see Figure 6.13) was employed to measure the velocity distribution and the turbulent intensities of the flow inside the draft tube model. The sensing wire is platinum-plated tungsten. Typical sensing element resistance at 20°C is 3.5 Ω with the wire temperature coefficient of resistance $\alpha_{20} = 0.36$ % per °C. An overheat ratio of, 1.6 was used for all hotwire measurements, giving a film temperature (T_m) of around 190 °C.

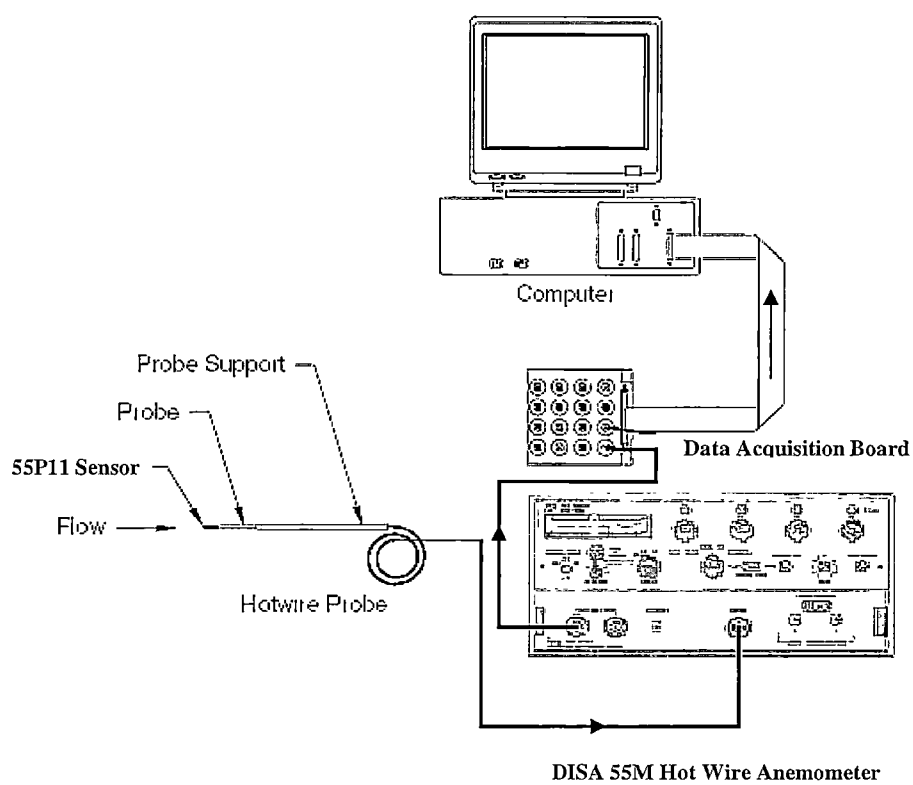

Figure 6.14: Overview of the DISA 55M10 constant temperature anemometer system

As illustrated in Figure 6.14, the signals from 55P11 hotwire sensor are transferred to the DISA 55M Constant Temperature Anemometer (CTA) via a coaxial cable. The system consists of a 55M05 power pack, 55M01 main unit, and 55M10 standard bridge. The power pack contains circuits to rectify and smooth out AC line voltage as well as voltage limiting and short-circuit protection [28]. The high output voltage at low current was selected as the default setting for this application. The main unit includes amplifiers, filter, square-wave generator, decade resistance, and probe protection circuits [28]. No other external signal conditioner was employed for these measurements. The bridge circuit operates at a bridge ratio of 1:20 and a ratio resistance of 50 Ω in the active arm of the bridge [28]. The resistance measurement accuracy is estimated to be 0.1% ± 0.01. Details of the calibration procedures and measurement accuracy of the hotwire probe are given in Section 6.2.3.3.

6.2.2.4.4 Preston Tube

A 2 mm-diameter Preston tube was used to measure the surface shear stress or skin friction. The tube was connected to a Furness Controls FC014 micromanometer and the pressure reading is acquired via NI PCI 6025E 12-bit data acquisition (DAQ) card. The measurement techniques are presented in Section 6.2.3.4.

6.2.2.5 Transient Flow Measurement

6.2.2.5.1 Unsteady Wall Pressure Transducer

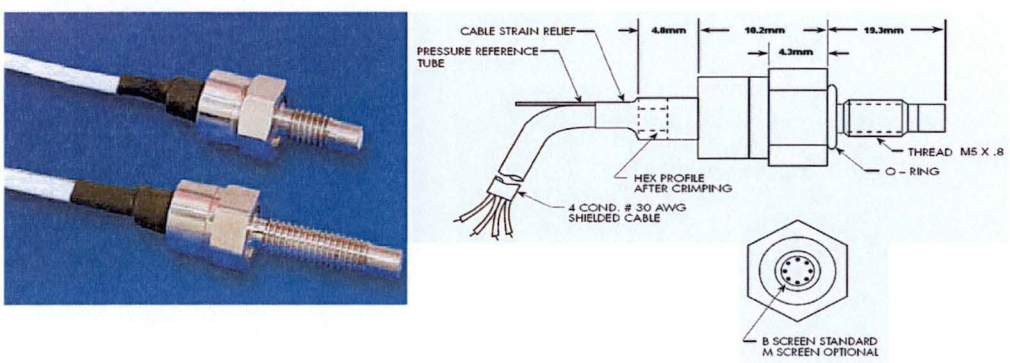

Figure 6.15: Kulite XCS-190 differential pressure transducer

A miniature high sensitivity IS® piezoresistive transducer XCS-190 (manufactured by Kulite Semiconductor Products Inc.) was used for unsteady measurements of static

pressure at the draft tube outlet. This differential pressure transducer has a maximum sensing range of 34.5 kPa and a nominal full-scale output (FSO) of 150 mV for operation with a fixed excitation voltage of 10 Vdc. The silicon sensing-chip is mounted at the front of the transducer with a standard B-screen designed to protect the sensing surface (see Figure 6.15). This transducer is highly insensitive to the acceleration inputs. The manufacturer certifies frequency response up to 300 kHz. The millivolt output from pressure transducer was fed into a VISHAY signal conditioner. The system consisted of a full-bridge strain gauge with a maximum amplifier gain of 2100. The amplifier output was transferred to the UEI acquisition board for data recording.

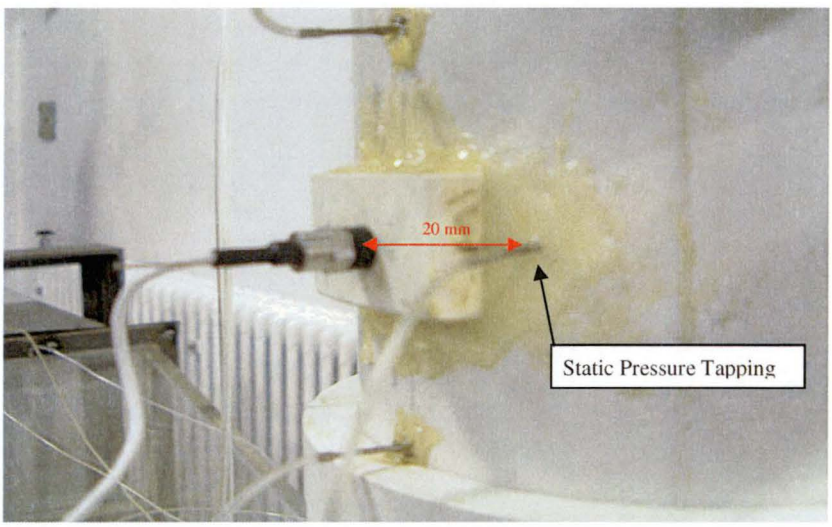

Figure 6.16: Location of the Kulite XCS-190 pressure transducer and the static pressure tapping used for calibration

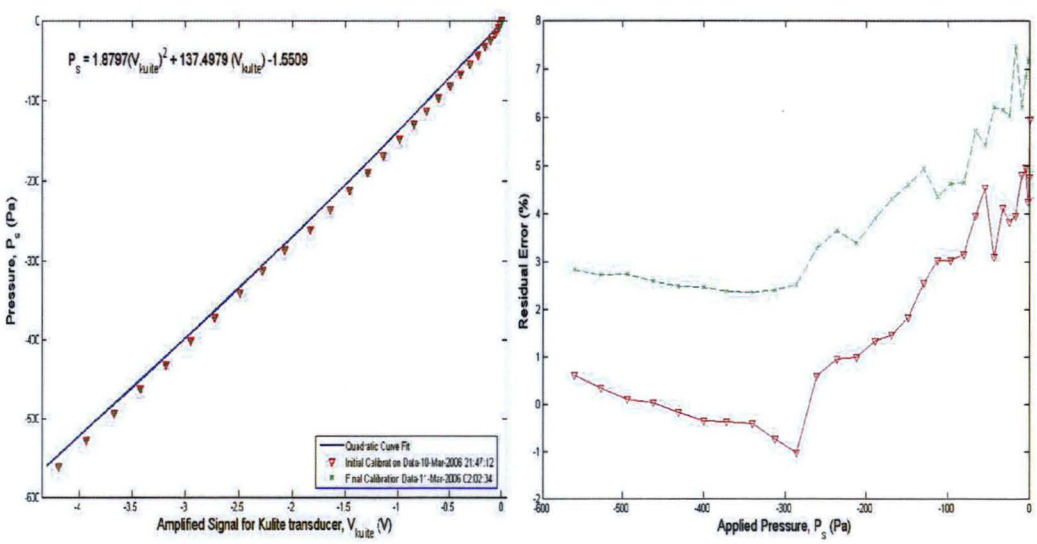

Figure 6.17: Calibration curve showing relationship between amplified signal and applied static pressure

The voltage output from the signal conditioner was calibrated against the micromanometer readings with the transducer positioned at the sidewall of the inlet pipe (150 mm above the inlet of the draft tube model) and a reference static pressure tapping placed 20 mm apart (see Figure 6.16). The zero offset was manually adjusted by observing the readings from the voltmeter connected to the conditioner prior to the tests. The calibration curve shown in Figure 6.17 was checked regularly during the tests to ensure no change in the relationship had occurred.

6.2.2.5.2 Hot Wire Anemometry

The Dantec 55P11 single-sensor hotwire probe (which was also used for time-mean velocity and turbulence traverses at steady-flow operation) was used to measure the variations of instantaneous velocity during transient operation of the draft tube model. The experimental methods used for the unsteady velocity measurements will be described in Section 6.2.3.5.

6.2.2.5.3 Optical Encoder

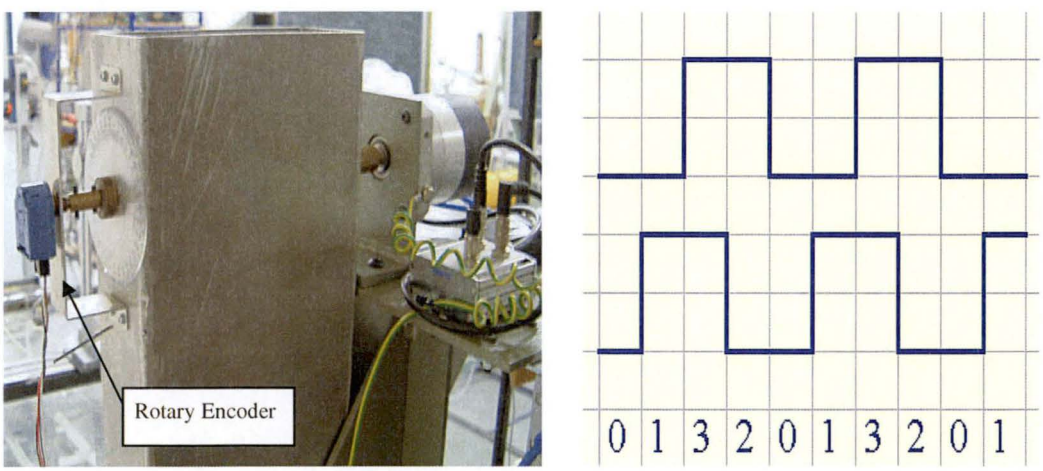

Figure 6.18: Location of the HP rotary encoder and its output signals used to determine the direction of rotation

An HP HEDS5701-A00 rotary encoder connected to the NI PCI 7334 motion control card was used to monitor the valve position at the fan outlet. Figure 6.18 shows its mounting location. The encoder has 500 steps per revolution and produces square wave output signals that are 90° out of phase and the leading phase of these waves determines

the direction of the rotation. Turning the valve clockwise generates a signal pattern of 0-1-3-2-0, while rotating the valve counter-clockwise produces a pattern of 0-2-3-1-0. The encoder compares the old value with the new value to decide the direction of the valve. An externally mounted protractor reading to 1° was used to establish the fully valve position.

6.2.2.5.4 Motor Frequency Transducer

A magnetic pickup sensor was placed 15 mm in front of the motor cooling blades to measure the variation of motor speed during a transient. Four magnets were embedded into the cooling fan blades 90° apart from each other so that four falling-edge pulses could be detected in a complete motor revolution. The transducer signal was fed into the built-in counter of the NI 6025 acquisition card, where the inverse of the time interval between pulses ($1/4\tau_{falling}$) was determined to give the motor speed.

6.2.3 Experimental Techniques

6.2.3.1 Inlet Boundary Layer Measurement

Inlet conditions greatly affect the draft tube performance. Hence, the boundary layer properties at the entrance of the draft tube model were thoroughly investigated to guarantee identical inflow conditions for both experimental and numerical models. All boundary layer measurements were carried out within the inlet pipe (of 151 mm diameter). The measuring procedures were repeated at two longitudinal positions located 560 mm and 750 mm above the entrance of the draft tube model. For each location, data were collected for two different operating conditions: 78% and 44% of the maximum valve opening. A Pitot tube (of 2 mm diameter) with wall tapping in the same plane was used to measure the time-mean boundary layer velocity profile. The tube was inserted from the opposite wall of the inlet pipe pointing into the oncoming flow. Initial measurement was taken with the tube tip in contact with pipe wall.

As shown in Figure 6.19, the Pitot tube was secured to a Mitutoyo height gauge adopted as a traversing rig. This was clamped on the pipe wall, and measurements were taken by traversing the tube gradually from the wall position to the centre of the inlet pipe. An identical profile was assumed on the opposite wall. The Pitot tube was connected to the

Furness Controls FC014 micromanometer and the NI 6025 data acquisition system. These devices have already been discussed in Sections 6.2.2.1 and 6.2.2.4.1. As the boundary layer flow is turbulent, the pressure readings fluctuated rapidly near the wall position. A long data acquisition time (120 seconds at 1 kHz sampling frequency) was needed to ensure that statistically reliable results are obtained. For the case with 78% valve opening, the boundary layer profiles were measured at intervals of 1 mm up to 15 mm from the wall, 2 mm up to 35 mm from the wall, and 5 mm thereafter. When the draft tube was operated at 44% valve opening, the profiles were measured at intervals of 1 mm up to 15 mm from the wall, 5 mm up to 35 mm from the wall, and 10 mm thereafter. The boundary layer displacement and momentum thicknesses were computed by numerically integration (using the trapezoidal rule).

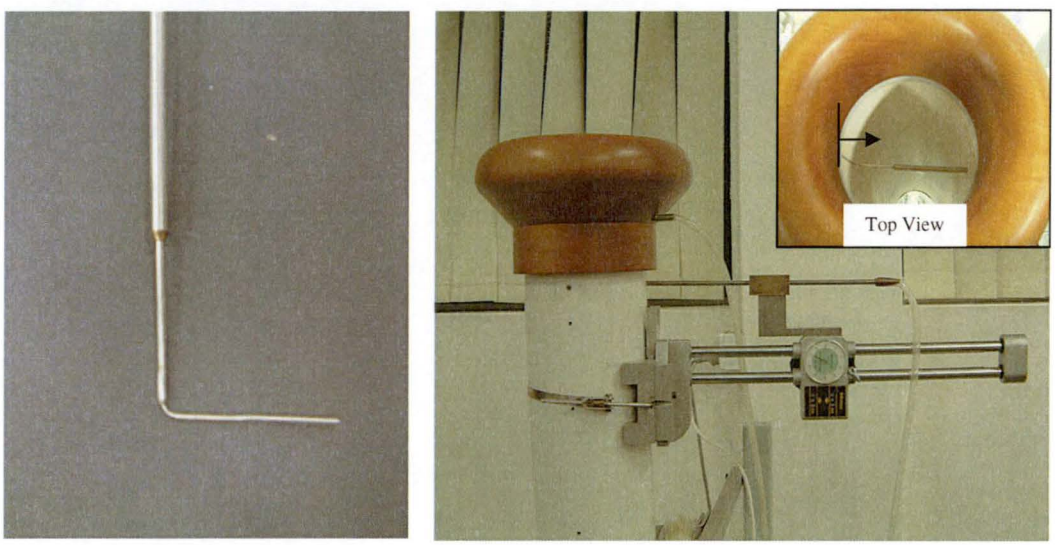

Figure 6.20: 2 mm-diameter Pitot tube used to measure the velocity profiles and boundary layers at the inlet pipe

The velocity profiles at the start of the inlet pipe exhibited some instability. This was most likely due to the motion of air in the laboratory that is caused by a range of factors such as movement of people, conditioning air flow in and out of the laboratory, or the air motion in the laboratory due to thermal gradients.

The main factors influencing the accuracy of these boundary layer measurements were:

- *Turbulence effects:* Fluid turbulence generates unsteadiness and fluctuating velocity components in the boundary layer. Pitot tube measurements within turbulent flows are not reliable because velocity fluctuations in the flow produce random pressure fluctuations, which would not occur in absence of the tube. In

addition, turbulence may also change the level of static pressure across the pipe. However, its contribution to the wall pressure measurements represents only a small correction at high frequency and can always be approximated as constant [87]. The effect is not corrected in the present study, as the turbulence intensity was quite low in the inlet pipe. However, turbulence effects were more severe inside the draft tube model and accurate boundary layer measurements were not possible in that case. Hence, boundary layer analysis was only performed for the inlet pipe.

- *Velocity gradient effect:* The effective measurement location is about 65% of the tube diameter from the low velocity side of the tube. Hence, the smallest distance from the wall that a 2 mm-diameter tube can effectively reach is 1.4 mm from wall.

- *Blockage effect:* The presence of Pitot tube in a pipe creates both solid and wake blockages. These effects may generate some small errors in the measurements. The effect of solid blockage may be examined by treating the tube as a doublet in a two-dimensional flow. Wake blockage effect, on the other hand, may be approximated based on the known drag coefficient for a circular cylinder in uniform flow. The maximum estimated total blockage correction for the 2 mm-diameter Pitot tube used in these tests was 1.3%.

6.2.3.2 Static Pressure Survey

The static pressure distribution represents one of the most important flow characteristics of the draft tube, as the performance of the draft tube is closely related to its ability to recover the kinetic energy at the runner exit by conversion into pressure energy. 124 wall static pressure taps were installed by drilling holes on the model surface and inserting stainless steel tube (of 1 mm diameter) into the holes, with the tubing subsequently connected to the Scanivalve and micromanometer. Electrical circuits for pressure devices were energised and allowed to warm up for long enough to ensure stability of operation after setting up the transducer and making the electrical connections. Zero readings were recorded before and after each pressure scan to account for thermal drift during the tests. To reduce the uncertainty, all pressure results were expressed in terms of pressure coefficients and statistical outliers were excluded from the data averaging.

A tube size of 1 mm diameter was chosen for the wall pressure taps as a compromise between the acquisition time and measurement accuracy. Errors due to the dimensions of the static pressure tappings are well documented in reference [8]. Better results are always obtained for static pressure tappings with smaller diameters. Hole diameters below 0.5 mm result in large response times, and the holes are easily blocked by dust; measurements with larger holes are less accurate due to the amount of distortion introduced into the flow field [8]. For 1 mm-diameter pressure holes, the estimated uncertainty is about 0.6% of the dynamic head. To reduce the effects of pressure gradients and surface curvature, the static pressure tapping holes were made as perpendicular to the surface as possible.

The surface adjacent to each pressure tap was smoothed and squared off to ensure no disturbance was generated due to surface undulations. Any visible burrs protruding into the airstream were carefully checked for and removed from the surface. This is critical because the failure to remove any burrs resulting from drilling a hole onto the surface may generate a negative error of around 15~20% of the dynamic head [8]. Dirt collected at the edge of the static pressure hole can have similar effect to burrs. A burr with height as small as 1/30 of the hole diameter can easily produce errors of about 1% of dynamic pressure [8]. To eliminate this problem, the inner surface of the model was thoroughly cleaned prior to the tests.

Eddies developing in the pressure tapping cavity and fluid turbulence may cause additional problems in the wall pressure measurement. The shear stress of the boundary layer passing over the static pressure tap induces recirculating flows in the tube, which in turn entrains relatively high momentum fluid from the free stream into the static pressure tap [8]. This results in a static pressure in the tube that is higher than the actual pressure on the surface. A short tube would have minimised this error, but the tube length is limited by the thickness of the model. An uncertainty of around 3~5% of the local dynamic pressure can occur due to this effect. The influence of fluid turbulence, on the other hand, mainly results from fluctuations of the velocity component perpendicular to the wall. Irreversibility and nonlinearity of the energy exchange with the pressure tap may produce an error of around 0.5% of the dynamic head. However, the error due to turbulence disappears when the hole diameter is smaller than the length

scale of the turbulent fluctuations [8], which is likely to be the case in this study. Hence, no correction for turbulence was applied here.

Finally, any air leaks around the pressure tappings were identified by spraying detergent liquid on the model surface and then observing bubble development due to flow being drawn into the model. Any leaks identified were eliminated by applying glue or rubber tape. Blockages in the pressure tubing were checked for by blowing the air through the tube. Pressure tubing leaks were identified by blocking the air in the tube and then connecting it to the micromanometer to observe whether a constant pressure was maintained. Vacuum grease was applied to all tube connections to reduce leakage problems.

6.2.3.3 Hot-Wire Anemometry

Velocity and turbulence profiles for steady-flow operation were measured using the hotwire technique. The probe was traversed horizontally and vertically in several different planes of the model. The exact measurement positions will be defined later in Section 7.2.3. For transient-flow operations, the instantaneous velocity at the inlet was acquired using the same hotwire anemometry techniques. The unsteady flow measurements will be discussed in Section 6.2.3.7. The following operating procedure was carried out during the initial set up of the test gear:

- The probe cables were carefully tested to ensure they functioned properly. All plug-and-socket connections for the hotwire probe were secured tightly to the anemometer to ensure no change in the probe resistance during the tests. The condition of the hotwire sensor was investigated using a zoom telescope. Any dirt on the wire was removed by cleaning before measurements were taken.

- The equipment was continuously powered until all measurements were taken. This minimised temperature drift in the system and reduced calibration curve shifts during the tests.

- The overheat ratio of the 55P11 probe was set to 1.6 after proper allowance for the lead and probe support resistances.

- The frequency response of the hotwire is optimised via square wave tests. The probe was exposed to a constant flow velocity and the response of the system subjected to a square wave test current was monitored on an oscilloscope. For optimal and stable performance, the square wave test should produce an oscilloscope pattern showing the shortest possible impulse response without superimposed oscillation. Such response can be achieved by tuning the amplifier gain or adjusting the setting of the bridge-T filter in the anemometer. Generally, the frequency response of the probe is faster when the flow speed is increasing. The typical frequency response obtained from the 55P11 probe under the above operating conditions was around 15 kHz. Figure 6.20 shows the result of the square wave test from a digital oscilloscope.

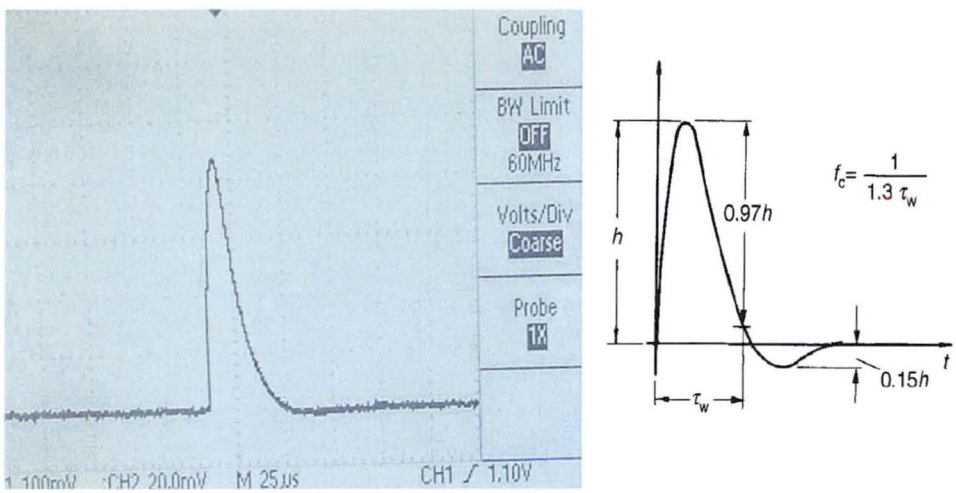

Figure 6.20: Digital oscilloscope output showing the result of a square wave test used to determine the frequency response of a DISA 55P11 probe. The right picture shows the typical optimised response of the square wave test

6.2.3.3.1 Hot-Wire Calibration

The hotwire probe was calibrated in-situ in the inlet pipe of the experimental model. The calibration velocities were measured with a 4 mm-diameter Pitot-static tube placed 560 mm above the draft tube inlet. The pipe centre was taken as the reference position. The hotwire probe was subsequently positioned in exactly the same location as the Pitot-static tube. The spot was selected for several reasons. First, the turbulence intensity in the inlet pipe is quite low (< 3%). Second, the average velocity measured at this location is steady (1.8% variation) and is not affected by the downstream bend curvature. Third, the probe blockage effect is small (approximately 2%) in the inlet pipe. Calibration at this position could cover the entire velocity range of interest for the

highest Reynolds number experiments. Fourth, the risks involved in transferring the fragile probe to another calibration facility outweigh any inaccuracies caused by the in-situ calibration. All calibrations were performed by gradually increasing the valve opening at the fan exit from the fully closed to the fully open position to vary the air velocity.

The calibration procedure of Walker [134] has been employed in this study. It is a modification of the method of Collis and Williams [25]. A quadratic term was added to the equation in order to improve the calibration at low velocities. The theory is based on the heat loss generated from an infinitely long heated cylinder in a cross flow. A non-dimensional data fit was established using Equation 6.4 with the coefficients C_7, C_8, and C_9 being determined by the method of least squares.

$$Nu\left(\frac{T_m}{T_a}\right)^{-0.17} = C_7 \times \left(\mathrm{Re}_w^{0.45}\right)^2 + C_8 \times \mathrm{Re}_w^{0.45} + C_9 \tag{6.4}$$

where Nu = Nusselt number = $\dfrac{E_{V-w}^2 R_p}{\pi L_w \Delta T k_f R_t^2}$

Re_w = wire Reynolds number = $\dfrac{U d_w}{\nu_a}$

$E_{v\text{-}w}$ = measured bridge voltage (V)

R_p = probe resistance (Ω)

L_w = hotwire sensor length (m)

ΔT = temperature difference = $T_m - T_a$ (°C)

T_a = air temperature (°C)

T_w = wire temperature (°C)

T_m = mean flow temperature = $0.5(T_w + T_a)$ (°C)

k_f = air thermal conductivity = $0.0001423 \times (\mathrm{T_m}+273.15)^{0.9138}$ (W/m.K)

R_t = total resistance including resistances for lead, cable, probe, and bridge (Ω)

U = mean velocity measured by Pitot-static tube (m/s)

d_w = hotwire diameter (m)

ν_a = air kinematic viscosity (m^2/s)

This type of data fit automatically eliminates the effects of thermal drift in the model and atmospheric condition changes over long data collection runs. Non-dimensional parameters used in this approach appear to better compensate for thermal drift than the correction to anemometer output voltage method used in Jørgensen [52]. A typical calibration curve is shown in Figure 6.21. Once the probe was calibrated, it was periodically recalibrated with no electrical contacts being broken. For each measurement location, the traversing rig for hotwire probe was carefully aligned using a level. Positioning of the probe relative to the wall was performed with the fan operating, because the model was moving in the order of ±2 mm due to vibrational effects.

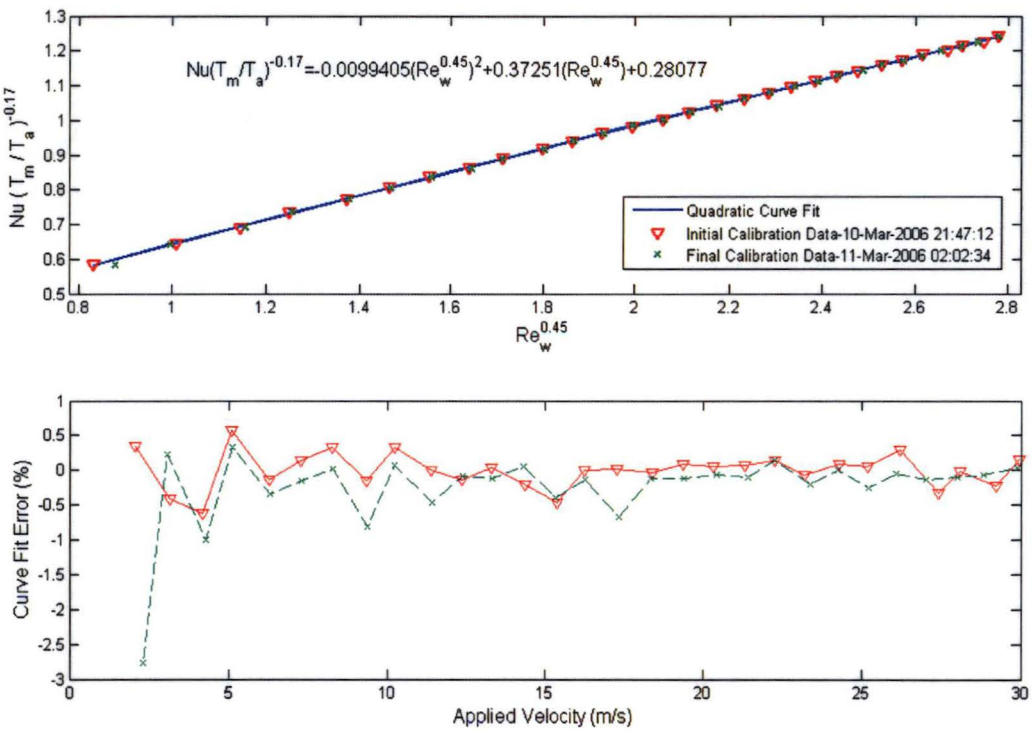

Figure 6.21: In-situ calibration of a Dantec 55P11 hotwire probe (Probe is located 560mm above the draft tube inlet)

6.2.3.3.2 Hot-Wire Mounting

Vibrational problems and electrical noise were noticed when using hotwire probe with the Mitutoyo traversing rig. The effect was more severe when the model was operating at high Reynolds number. A Brüel & Kjær accelerometer (Type 4368) connected to a conditioning amplifier (Type 2626) was used to investigate the probe vibration. Two frequencies (21.9 Hz and 34.5 Hz) were identified from spectral analysis of the accelerometer output signal when the draft tube was operating at the highest average inlet velocity of around 27 m/s. These frequencies seemed to correspond to the blade

passing frequency of the fan. The natural frequency of the probe support was estimated using Rayleigh's formula and treating the support as a stepped cantilever. The calculated natural frequency of the support was around 32 Hz, which was quite close to the problematic frequency zone identified by the accelerometer. These vibrational problems were overcome by reducing the length of the probe support and making the traversing rig as close to the measurement location as possible. This shifted the probe out of the observed vibrational mode. The support frame was stiffened by replacing the metal stand with a heavier stainless steel bar (using an added mass approach). A cushioning plate was also added between the support frame and the traversing rig in order to dampen any vibrations.

In addition to the vibrational effects, some significant electrical noise was initially observed in the hotwire signal when a metal structure was used for the traversing rig. Subsequent investigation indicated that this noise arose from the ground loop problems. These were eliminated by employing rubber plates and plastic bolts to isolate the traversing rig from the ground, and ensuring that all the electrical loops returned to the ground connection of the anemometer.

6.2.3.3.3 Hot-Wire Accuracy

Hot-wire measurement is challenging for the current model geometry, as the uncertainties are difficult to quantify in a highly unsteady and turbulent flow possessing many small turbulent scales and high velocity gradient. The major factors affecting the accuracy of the hotwire measurements are summarised as follows:

- *Calibration error:* Accuracy of the calibration velocities is largely affected by the pressure readings obtained from Pitot-static tube. The maximum uncertainties resulting from the Pitot-static tube measurement is around 3%. Five replicates are taken for bridge voltages at each calibration point, giving an average error of 0.08%. The error due to analogue-to-digital conversion is negligible if compared to the noise on the data acquisition channel. The temperature measurement error is around ± 0.1 °C, producing an uncertainty of less than 0.3% in Nusselt number.

- *Probe orientation:* Although extreme care was taken to minimise misalignment of the probe, variations in sensor orientation of up to ±4° may have occurred when moving between different measuring locations.

- *Nonlinear cooling effect:* Simonsen [119] indicated that this effect was caused by mean velocity gradients in the flow. Little information is available in the present study about its impact on the mean velocity distribution. It is believed that a negative error in mean velocity will occur when measuring in a high velocity gradient flow.

- *Turbulence effect:* For regions with high turbulence intensities, truncation errors arise from ignoring the effect of non-measurable velocity components normal to the probe axis [119]. Moreover, the inability of a hotwire probe to determine the flow direction will cause rectification errors. This error is significant at the outlet of the draft tube model, as a strong velocity fluctuation and intermittent flow reversal can be clearly seen in this region. More details about the velocity and turbulence distributions will be given in Chapter 7. High measuring accuracy cannot be expected in these locations.

- *Electrical noise:* White noise is usually related to the 50 Hz line power in the area and cannot be reduced except by decreasing the amplifier gain. Electrical noise was regularly checked during the tests by momentarily turning off the excitation source and observing the output from the conditioner. Shielded or twisted multi-conductor wire was used for all electrical connections, with the shields grounded at the input connector and insulated against accidental grounding at the bridge end to minimise inductive effects. All metal structures were electrically connected to a common good ground and wiring was kept well clear of magnetic fields caused by the electric motor.

- *Probe support blockage effect:* Blockage effects due to the presence of hotwire probe support may have caused an error of up to 2%. This estimation is based on the approach described in Section 6.2.3.1.

6.2.3.4 Four-Hole Probe Measurement

The major problem of the single-sensor hotwire anemometer described in the previous Section is the impossibility of detecting the sense of velocity vector [8]. This is of particular concern when measurements are to be taken in a highly turbulent flow. Although many solutions to this problem have been suggested, they always lead to a very complicated probe design that would be extremely difficult to apply in the present draft tube geometry. Only non-intrusive measurement techniques such Laser-Doppler Velocimetry (LDV) and Particle Image Velocimetry (PIV) may provide valid alternatives for this application [48]; but these facilities were not available. A simpler approach utilising a four-hole pressure probe was therefore implemented at several locations of the model to double-check the validity of the hotwire measurements. The four-hole probe is preferred for three-dimensional measurements because no redundant data is gained and smaller flow disturbance can be achieved due to its more compact probe size (compared to five- or seven-hole probes).

No precise yaw nulling procedure is needed for the four-hole probe measurements. The probe was simply oriented with reference to its bottom surface for vertical traverses or with respect to its side surface for horizontal traverses. The tip was pointed towards the incoming flow. Only half the flow passage could be traversed with the probe inserted from the sidewall because of the limited probe support length. The measurement grid will be shown later in Section 7.2.3. Pressures from the four ports were sampled and stored sequentially during the experiments. Any statistical outliers were excluded from averaging.

The flow velocity and angularity were deduced from the probe pressure coefficients (see Equation 6.3) using calibration lookup tables established by Tsang and Oldfield [127]. Since all calibration data are arranged in matrix form, a simple program is constructed in MATLAB to linearly interpolate and interpret the measurement data into pitch angle (α), yaw angle (β), and dynamic pressure (P_{Dyn}). For each measurement position, the axial velocity (U_a) perpendicular to the model cross section is computed from:

$$U_a = \sqrt{\frac{2P_{Dyn}}{\rho_a}} \cos\alpha \cos\beta \tag{6.5}$$

The uncertainties of the total pressure, yaw angle, and pitch angle are 5 Pa, 0.8°, and 1.2° respectively. This gives an uncertainty of 0.6 m/s in the velocity magnitude. Overall, four-hole probe measurements suffer from problems caused by dynamic stall or vortex shedding effects as well as the limitations of probe geometry. These problems are significant for an inherently unsteady and turbulent flow fields [8]. Erroneous measurement data were obtained at several locations along the centreline plane of the model because the flow angle was unsteady and occasionally fell outside the usable measurement range of the probe. Rotating the probe into different orientations could have improved the flow angle measurement, but the procedure would have been tedious without an automatic probe traversing device and would have required large access slots in the model walls. Besides, such approach cannot guarantee accurate result if the velocity profile is highly unsteady.

Reynolds number effects were neglected, due to the pressure coefficients being weakly dependent on velocity or Reynolds number. Wall proximity effects were also insignificant for the four-hole probe due to the absence of near-wall measurements as well as the relatively flat response of the pressure coefficients to wall proximities greater than 7 mm. The probe diameter and the radiused support bend restricted the probe from measuring nearer than 20 mm from the wall. Despite its shortcomings, four-hole probe can provide valuable information on measurement locations for which the hotwire data should be interpreted more cautiously and conservatively.

6.2.3.5 Skin Friction Measurement

Various direct and indirect methods exist for skin friction measurement. Direct techniques based on floating elements, oil films, and liquid crystal layers have been developed to measure both magnitude and direction of the local wall shear stress [19]. These methods avoid any assumptions regarding the nature of the boundary layer responsible for the skin friction. Although powerful, their accuracies are strong affected by several aspects like sensor alignment, pressure gradient, and head gap effects. Hence, indirect approaches are still widely employed. These methods are based on measured parameters such as surface heat flux or impact pressure near the surface, and the assumed relations between these measured parameters and the skin friction. The Preston tube is the most popular and inexpensive technique to indirectly determine the local skin

friction. The attractiveness of the Preston tube lies in its simplicity and manoeuvrability within the boundary layer and across the wall surface. The dynamic pressure measured by a simple Pitot tube resting on the surface and facing the flow is correlated with the boundary shear stress using the law of wall for the boundary layer velocity distribution.

The Preston tube measures the impact pressure imparted by the air across the mouth of the tube (with diameter d) while a static pressure measurement is simultaneously taken by an adjacent static pressure tapping. The wall shear stress (τ_w) is then calculated from the pressure differential (ΔP_d) measured by the Preston tube and static pressure tapping using:

$$\frac{\tau_w d^2}{\rho_a v_a^2} = f\left(\frac{\Delta P_d d^2}{\rho_a v_a^2}\right) \tag{6.6}$$

The applicability and accuracy of the Preston tube deteriorates in flows with severe pressure gradients because of the break down of the standard logarithmic velocity law on which the Preston tube calibration depends. Such shortcomings are exacerbated in three-dimensional flows. For smooth boundary surfaces, Patel [94] correlates the errors in the inferred skin friction using a pressure gradient parameter ΔP:

$$\Delta P = \left(\frac{\nu_a}{\rho_a u_T^3}\right)\frac{dp}{ds} \quad \text{where} \quad u_T = \sqrt{\frac{\tau_w}{\rho_a}} \tag{6.7}$$

For the current investigation, 6~10% uncertainty in the Preston tube measurement is indicated by the Patel correlation. However, this value should be viewed conservatively as Patel's results are derived from a rather simple geometry where three-dimensional flow effects may not be significant. The error for Preston tube measurements can easily exceed 10% because of the intrusive nature of the probe and the fluctuating flow direction caused by three-dimensional unsteady flow effects in the draft tube.

6.2.3.6 Flow Visualisation

The tuft probe technique provides an effective, inexpensive, and fast means of visualising the flow direction for low speed testing with models of moderate size. A light and flexible tuft attached to a stainless steel probe (of 2 mm diameter) was used in

the present experiment. The probe had a torque-free hinge at its tip and the mini-tuft consisted of two polyester sewing threads (of 0.2 mm diameter and 40 mm length) that were glued to the hinge. A red colour was chosen for the tuft material because it gave excellent visibility inside the plexiglass model. Effects of flow disruption due to the probe insertion are considered to have been minimal. This technique is very flexible and does not need any glueing of tufts on the surface, which are always difficult to remove cleanly when no longer required.

The tuft probe was inserted into the model at various measurement locations when the fan was operating. Airflow speeds higher than 2 m/s were required to avoid undue errors arising from stiffness of the tuft and gravitational effects. The flow direction could be interpreted from the tuft behaviour, as the tuft responds to the flow within a layer approximately the same thickness as the thread. Streamwise vortices were indicated by the tuft spinning about its hinge and forming a narrow cone with axis nearly parallel with the wall. In regions of separating flow, the tuft oscillated and reversed direction periodically.

Video recording of the tuft behaviour was attempted via a digital video camera but the tuft images were blurry due to the relatively low resolution and limited zoom function of the available camera. A more efficient recording technique should be developed in the future. Due to limited time and resources, these tuft images were not retaken and they are not shown in this thesis. However, valuable insights about the flow processes in the draft tube were gained, and the accuracy of the hotwire measurements was better assessed with the help of these mini-tuft flow visualisations.

6.2.3.7 Unsteady Flow Measurement

Unsteady flow measurements were carried out to study the time evolution of the transient velocity and pressure fields in the model draft tube. The flow responses of the draft tube model when subjected to an impulsive change of pressure force were measured and analysed in this experiment. Transients were created by varying the amount of valve opening at the outlet of the centrifugal fan. The fan motor frequency was maintained at a constant value of 35 Hz throughout the tests. The fan speed for steady operations was about 2070 rpm. Only a slight change of fan speed (±30 rpm) was detected when the transients occurred.

Both step and oscillatory valve motions were investigated in this experiment. For the step response, the valve position was varied by increasing or decreasing the valve opening between 44% and 78% of the full opening. A complete opening or closure of the valve was not carried out because the flow has a rather flat response when the valve position was less than 40% or greater than 80% of the full opening. The step motion was usually completed within 0.1 second after the valve started moving. For oscillatory response, the valve position was changed periodically between 44% and 78% of the full opening in a roughly sinusoidal manner. Five cycles were recorded at two different oscillatory frequencies: 0.6 Hz and 1.2 Hz, which corresponded to the full-scale power plant frequencies of 0.013 Hz and 0.027 Hz respectively. Although motion with a maximum frequency of 2 Hz was possible for the pneumatic actuator, this frequency was not used because it would have required retuning of the control parameters to obtain stable valve operation.

For each transient measurement, the DISA 55M hotwire anemometry system was used to measure the instantaneous velocity while a Kulite transducer was applied to trace the instantaneous wall static pressure. The hotwire probe was inserted at the centre of the inlet pipe 560 mm above the draft tube inlet. The probe was calibrated periodically at the same location during the tests. Risks of breaking the hotwire were thereby minimised, as the probe remained fixed in position. Reasons for choosing this measurement location have already been discussed in Section 6.2.3.3.1. Procedures to set up the hotwire system are detailed in Section 6.2.3.3.

The Kulite transducer was flush-mounted on a surface that had been carefully cleaned to ensure no visible burrs were present to corrupt the pressure readings. A rubber fixture was attached on the transducer so that it could be easily positioned and screwed tightly to the model. The manner of transducer mounting did not influence its response. Transient wall pressures at various locations were monitored by systematically moving the pressure transducer from one location to another.

Techniques for reducing hotwire errors are discussed in Section 6.2.3.3.3. For the pressure transducer, the major source of errors is the white noise. The low-voltage unsteady pressure signal was very sensitive to contamination from electric ground loops

and radio frequencies. The signal conditioner was therefore put as close to the measuring location as possible. All possible precautions were taken to eliminate ground loops and properly shield all signal carrying wires. A ground return structure to the amplifier bridge circuit was provided, and asymmetry of the ground returns for the inputs was checked thoroughly to prevent any significant fluctuations in the amplifier output. The bias current was insignificant for the pressure transducer due to its low source impedance and it could always be offset with the amplifier zero control. Vibrations of the model had little or no impact on the accuracy of the pressure signal, as the Kulite transducer is insensitive to the acceleration. Pressure fluctuation errors due to acceleration effects were checked by placing a Brüel & Kjær accelerometer on the wall near the pressure transducer as shown in Figure 6.22. As illustrated in Figure 6.23, the maximum pressure fluctuation (using manufacturer supplied data of 1.5×10^{-3} % FS/g) was less than 1% of the static pressure measured at outlet (± 1.5 Pa).

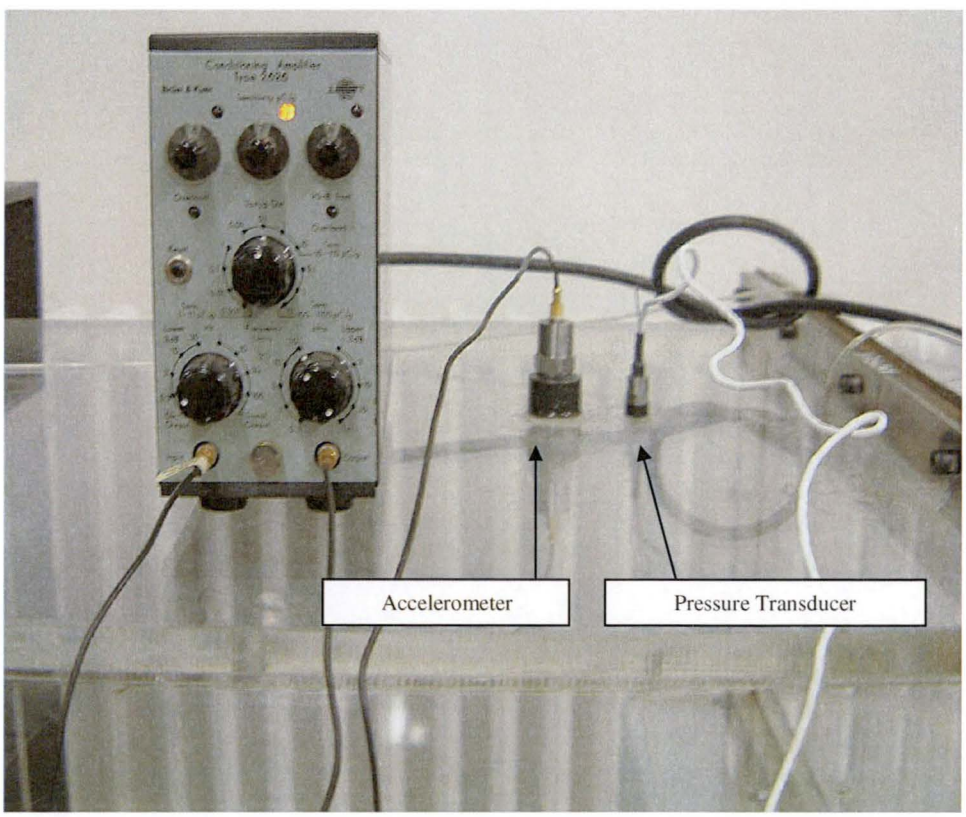

Figure 6.22: Brüel & Kjær accelerometer used to check the vibrational effect on the pressure transducer output signal

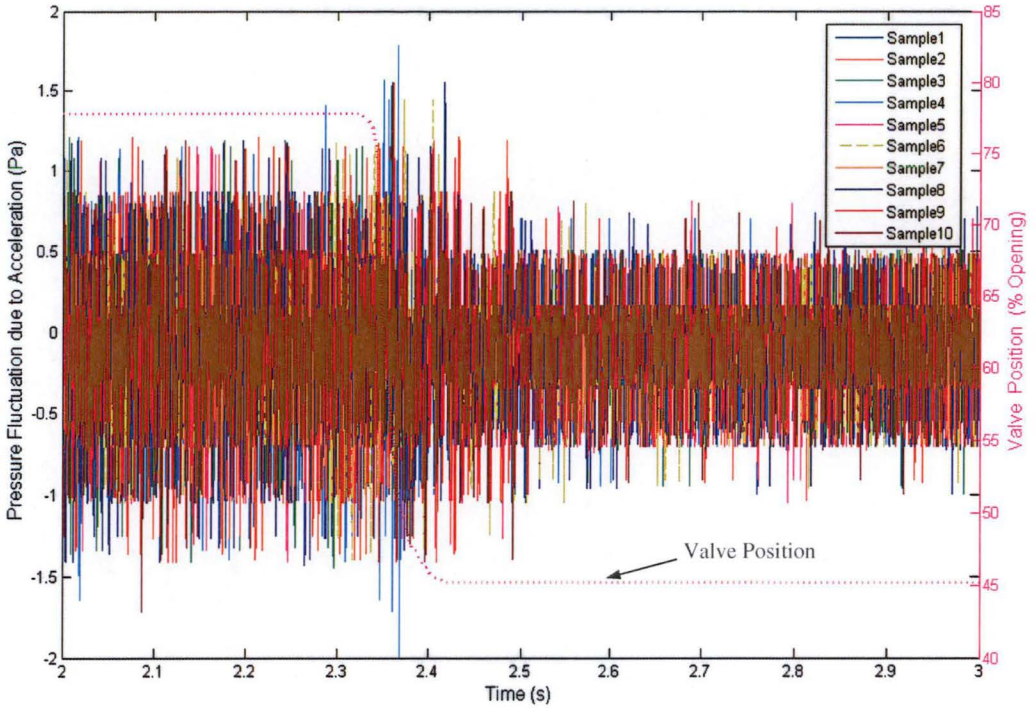

Figure 6.23: Pressure fluctuations due to acceleration effects of the Kulite transducer during a transient

Signals from the pressure transducer, hotwire probe, optical positioning encoder, and the fan speed sensor were monitored and recorded simultaneously using a Labview data acquisition program. The valve movement and data acquisition were triggered by the same digital signal. A 2-second delay time was set for the actuator system to ensure a steady state condition before the valve moved. Although the transients were expected to damp out within a second, some effects were still observed for about 10 seconds after the valve finished the required motion. Ten replicates were taken as a compromise between acquisition time and the accuracy required. The pressure and hotwire signals were acquired at a sampling frequency of 10 kHz, while the fan speed and valve position were recorded at lower sampling rate due to the limitations of the sensors and the motion control card. The data reduction process can be summarised as follows:

- *Signal conversion:* Pressure and hotwire readings were digitised and recorded as voltage levels. Raw voltage data were stored in a binary-formatted file. Calibration data collected at the start and the end of each measurement were used to convert these voltage signals into the relevant physical variables. The time histories of the pressure and velocity were subsequently saved in a text-formatted file for later analysis.

- *Zero drift correction:* Zero readings were recorded for both hotwire and pressure transducer at the start and the end of each measurement. Zero drift may be different from the calibration data and care must be taken to eliminate these zero errors that cause an offset in the readings. The DISA hotwire anemometer was very stable over a long period of data acquisition, but the pressure signal conditioner was more sensitive to zero drift and required manually tuning at the beginning of each measurement.

- *Time averaging:* Ten replications of the valve manoeuvre were performed for each measurement to check the repeatability of the flow response. Instantaneous values of the inlet velocity (U_{IN}), wall static pressure (p), valve position (θ), and fan speed (N) were ensemble averaged to reduce random noise in the unsteady measurements. Standard deviations of the variables were calculated at each time instant. The transient data were highly repeatable in most cases, as the standard deviations of the ensemble-averaged values are shown to be at least an order of magnitude smaller than the average values. Outliers were determined from the student's t-distribution where $t = 1.83$ was chosen for 9 degrees of freedom with 90% confidence level. Statistical outliers were excluded from the data averaging as illustrated in Equation 6.8. Typical effects of ensemble averaging of the transient data are shown in Figure 6.24.

$$\begin{cases} U_{IN}(t) = \dfrac{\sum_{i=1}^{10} U_{IN-i}(t)}{10 - n_{outlier}} \\ p(t) = \dfrac{\sum_{i=1}^{10} p_i(t)}{10 - n_{outlier}} \\ \theta(t) = \dfrac{\sum_{i=1}^{10} \theta_i(t)}{10 - n_{outlier}} \\ N(t) = \dfrac{\sum_{i=1}^{10} N_i(t)}{10 - n_{outlier}} \end{cases} \tag{6.8}$$

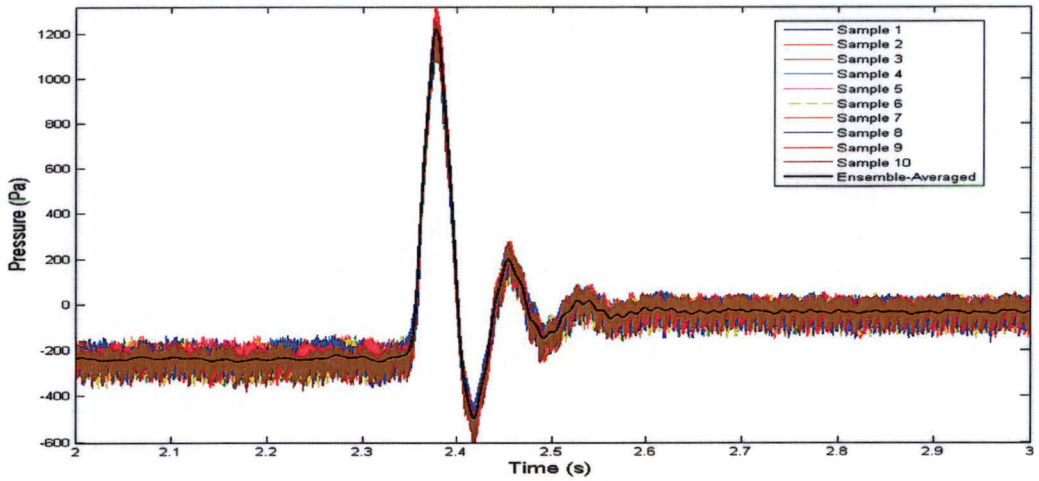

Figure 6.24: Typical effect of ensemble averaging to reduce the random noise in unsteady pressure data

- *Data smoothing:* High-frequency pressure fluctuations of around ±25 Pa were still observed in the ensemble-averaged data. These fluctuations were not the critical to the analyses and were filtered out to better interpret the transient results. Savitzky-Golay filtering was applied to digitally smooth both pressure and velocity data. The filter coefficients were derived from a fourth-order polynomial least square fit, and a frame size of 451 was used for data averaging. The filter was optimal in the sense that it minimised the least-square error in fitting a polynomial to each frame of noisy data. This approach was preferred to the standard moving averaging technique because it was very effective in preserving the pertinent components of the signal as well as producing a minimum phase error for the time-dependent data. A typical effect of this filtering process for the pressure data is shown in Figure 6.25.

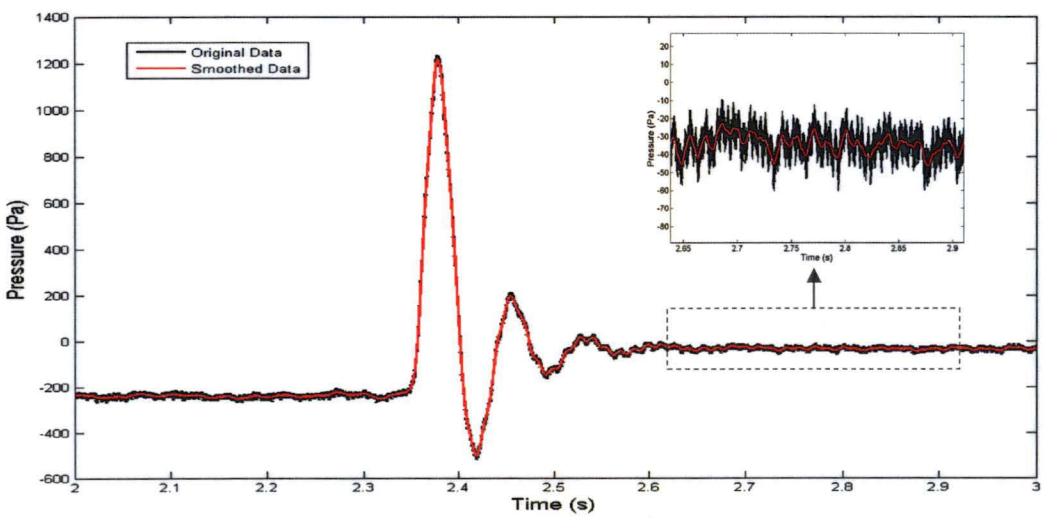

Figure 6.25: Typical effect of the Savitzky-Golay approach for smoothing out noisy signals measured by the Kulite pressure transducer

6.3 Numerical Flow Modelling

The three-dimensional flow modelling of the draft tube geometry using Computational Fluid Dynamics (CFD) techniques is presented here. The Section includes a brief description of the commercial finite-volume code ANSYS CFX. Issues involved in the simplification of flow domains, meshing of physical geometry, modelling of fluid turbulence, selection of appropriate boundary condition, and modelling of transient flow are discussed in detail. Grid resolution and turbulence models chosen from the best steady-flow predictions will also be applied in the transient-flow simulations. Steady-flow results for the draft tube model will be given in Chapter 7, while the transient-flow results will be presented in Chapter 8. CFD solutions for the transient flow operations will also be evaluated against simple models based on the one-dimensional momentum equation and two-dimensional unsteady stall analysis.

6.3.1 Code Description

The commercial finite-volume code ANSYS CFX 10 was used to model the draft tube flow. ANSYS CFX employs an unstructured, coupled implicit, pressure-based numerical solution strategy. The flow domain is discretised into finite control volumes and all relevant quantities in the governing equations are integrated and conserved over each control volume. Rhie and Chow [156] interpolation is applied to overcome the problem of checkerboard oscillations when the pressure and velocity are collocated. The diffusion terms in the governing equations are calculated based on an element shape function, whereas the convection terms are computed using a second-order upwind differencing scheme. In the unsteady flow simulation, transient terms are approximated using a fully implicit, second-order backward Euler scheme. The resulting coupled and non-linear equations are linearised and assembled into a solution matrix using a fully implicit approach. To improve the convergence rate, the linearised equations are solved iteratively using an algebraic multi-grid (AMG) accelerated Incomplete Lower Upper (ILU) factorisation technique. The convergence of the solution is judged from the normalized residual of each solution variable [4].

All simulations were run in parallel via the Message Passing Interface (MPI) on a multiple-processor SGI machine. Turbulence closure was achieved by applying the

simple eddy-viscosity or more sophisticated Reynolds stress models. First-order approximation is used for the time derivative of turbulence quantities to ensure bounded solution for all turbulence quantities. Scalable wall functions and an automatic near-wall treatment that allows for a smooth shift from low-Reynolds number form to the wall function formulation were employed to model the flow near walls.

6.3.2 Geometry and Flow Domain

The flow domain for the current CFD study is based on the 1:27.1-scale laboratory model, and the geometric shape of which is closely similar to the existing draft tube used in the Mackintosh power plant. Modelling of the turbine draft tube at full-scale Reynolds numbers was not practical for this analysis due to large amounts of computational time and resources required to get reliable and consistent results. The difficulty in obtaining detailed measurement data to validate the CFD model in the full-scale field tests was another major reason for employing laboratory-size model in the CFD simulation. Apart from the scale effects, there are some slight differences between the shapes of the full-scale prototype and CFD model. The tiny corner fillets in the rectangular section of the draft tube and the sliver surfaces below the inlet cone were not modelled due to meshing difficulties. The support pier downstream of the draft tube was also excluded for simplicity. The flow domain has been rotated 4° about the inlet plane to make it identical to the laboratory model. Reasons for this modification we previously stated in Section 6.2.1.1.

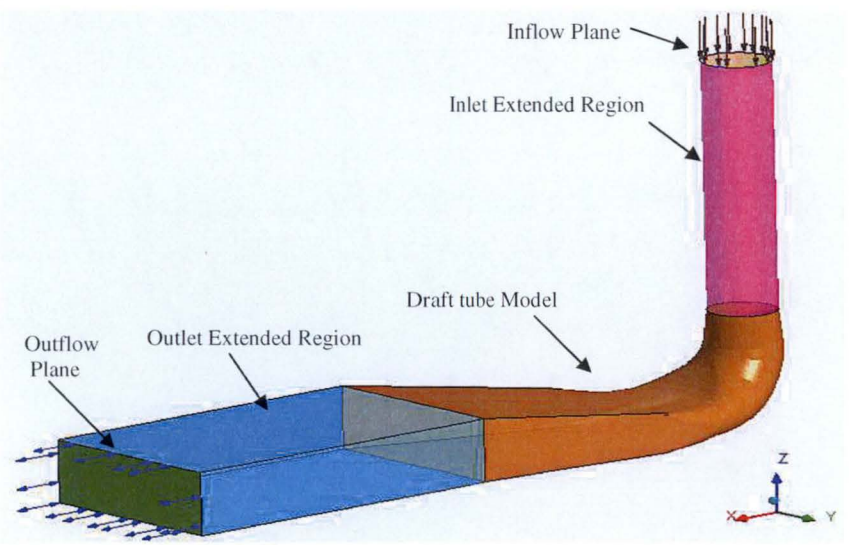

Figure 6.26: Flow domain of the draft tube model used in the CFD simulations (image is obtained from ANSYS CFX-Pre)

As shown in Figure 6.26, the inlet and outlet planes of the draft tube have been extended to the parallel planes of 5-inlet diameters and 5-outlet heights away from their original locations to minimise the influence of boundary locations on the solution. The meshing issues that arose from these boundary extensions are discussed in the next Section. The entire flow field was calculated even though the physical geometry is symmetrical about its half plane. This was done to account for any possible flow asymmetry due to the transient operations or the unsteady flow physics of the draft tube.

6.3.3 Mesh Generation

Mesh generation is an essential first step in numerical flow solutions. A poor quality mesh can adversely affect the stability and accuracy achieved. Detailed descriptions of the most popular meshing technologies and their numerical implementations are given in the books of Liseikin [66] and Thompson et al. [126]. A survey of the recent development in the mesh generation technologies is presented in references [90, 155].

Significant problems were encountered in the meshing phase of the CFD simulations, and three different commercial mesh generation packages (ANSYS CFX-Mesher version 10.0, ICEM CFD version 10.0.1, and Pointwise Gridgen version 15.02) were tested as a result. ICEM CFD was finally chosen because of its ability to quickly produce a hexahedral mesh using multi-block strategy and its compatibility with the current unstructured ANSYS CFX solver code. The integration of CFD analyses with the present complex geometric model proved a time-consuming and challenging task.

Overall, the meshing problems faced in this work are caused by the complex geometry and the limitations of the wall distance imposed by ANSYS CFX as part of its turbulence modelling and near-wall treatment. A three-dimensional model was first created in the CAD modelling package (Solid Edge version 15) and then imported to ICEM CFD through an IGES translator. This required extensive geometry cleanups before a mesh could be created. Sliver surfaces with strong curvature, filleting around the corners, and the large streamwise variation of the draft tube cross-sectional aspect ratio create a geometry that is difficult to mesh. Many of the strategies tried for meshing this flow region were found to be problematic.

Bergström [15] reports similar meshing problem for a Kaplan-turbine draft tube when dealing with IGES-based CAD geometry. The restructuring and grouping of the internal solids into a single block may eliminate this problem. However, this approach was difficult to apply in the current study due to the complexity of the geometry and the lack of direct translation between the CAD and meshing software. The built-in geometry creation tools in the current version of ICEM CFD and ANSYS CFX Mesher are still insufficient for an accurate solid modelling of the three-dimensional geometry. Besides, it is essential to divide the domain into several sections in order to correctly capture the important geometric feature of each draft tube section.

The use of proper wall element size is vitally important for the turbulent flow studied here. The wall elements may fail to work correctly if their sizes are either too large or too small. The turbulence model, flow operating conditions, and the availability of the computational resources all significantly influence the size of the wall elements to be used in the CFD simulation. The wall element size can be examined via a dimensionless wall distance Y+ and the value is obtained using trial-and-error approach. To correctly resolve the boundary layer flow and the wall shear stress, relatively thin wall elements are required.

The extension of the draft tube inlet and outlet planes resulted in a large number (approximately half) of the elements being placed outside the draft tube. To improve computational efficiency, the number of extension nodes was reduced by gradually increasing the mesh sizes through an exponential growth function when the elements were located away from the inlet and outlet regions. The element volume ratio was kept below 5 as a compromise between the number of nodes used (computational time is proportional to the square of the number of nodes) and the stability of the numerical solution [4].

6.3.3.1 Mesh Type and Topology

Unlike some simple linear geometries, the strong curvature of the draft tube can incur more adverse pressure gradients in which flow separation may occur. Mesh resolution will play an important role in correctly modelling the scale of this geometry. Accurate simulation of the flow phenomena in the draft tube requires computational grids that simultaneously capture the geometric curvature and discontinuities in the solution [15]. Element type and mesh topology can have a considerable impact on coarse grid solutions, and may affect the mesh resolution required to achieve a grid-independent solution [103].

A non-uniform hexahedral mesh generated by ICEM CFD was used for the current simulations because it is best suited for adequately resolving the near-wall region of the flow field. Phillipson [95] performed a CFD validation check on the CFX solver using various mesh types and found that about 4 times as many elements are required to achieve the same accuracy when a tetrahedral mesh is employed. The discretisation error is larger for tetrahedral elements because the grid is highly non-orthogonal and the equations need extra terms for tetrahedral mesh. A non-uniform mesh was also found to outperform a uniform mesh in terms of the computer resources needed to obtain solutions of the same accuracy [95]. Better results are generally obtained for internal flow problems when the elements are more distributed around the walls than in the centre of the flow passage.

Hexahedral elements do not present any significant problem for meshing a non-manifold geometric domain that has small angles on the surfaces. Although a tetrahedral mesh is relatively easier to generate for a complex geometry than a hexahedral mesh, it does not always mesh well domains with small angles, especially if these domains are non-manifold (irrespective of whether Delaunay, Advancing Front, or Octree methods are used) [113]. In fact, no meshing algorithm up to date can guarantee a triangulation of a domain without creating any small angles that are not already present in the input domain [113]. To achieve accurate solutions and good convergence properties on tetrahedral meshes, special discretisation techniques and a large number of cells are needed. None of these remedies is optimal. A code is more complicated and difficult to

maintain, and the memory and computing time requirements for the simulations are increased, with the use of tetrahedral meshes.

The Octree meshing method [90] adopted by ICEM CFD tends to deteriorate the tetrahedral mesh quality when the boundaries are approached. Further mesh smoothing does not seem to improve the quality, even though many smoothing steps have been assigned. The advancing front and Delaunay meshing algorithms used in the ANSYS CFX-Mesher are unable to distribute the nodes uniformly across the non-manifold surfaces. Thousands of nodes are placed on the smaller surface, and little control has been offered in the current package to resolve this problem. Another drawback is that mesh refinement studies cannot be properly conducted for unstructured tetrahedral meshes because the refined elements are not nested subdivisions of the coarsest mesh (a property that cannot be guaranteed for meshes generated using unstructured tetrahedral meshing methods). These limitations resulted in a hexahedral mesh being used for the current research.

A good blocking strategy is essential for the creation of a hexahedral mesh [152]. A multi-block O-grid topology was used to map the elements onto curved sections of the geometry because it provided optimal skew angles for control volumes around the wall boundary. The use of multi-block grid arrangement improved the orthogonality of the hexahedral elements near the curved diffusing bend. Skewed elements must be avoided as they always cause convergence difficulties and induce errors in the solution. Zhu et al. [152] identified various issues about blocking strategies for CFD simulations and concluded that the number of iterations needed for a multi-block grid to converge is essentially the same as that for single block. The thickness of the near-wall grid was also found to have significant impact on the solution convergence rate[1].

[1] Only one paper was found in literature search that discusses the issues of blocking strategy, but the examiner comments that *"The finding of Zhu et al. [152] is not a general observation. Slower convergence has been observed by the examiner's research group when a multi-block grid is used in place of a single-block grid, provided that the geometry of the computational domain is such that the use of a single block instead of multiple blocks does not adversely affect the skewness of the grid elements. While the computations are typically implicit within each block, the algorithm is explicit at the block level in that the blocks are computed separately (within each outer iteration) before data exchange amongst the blocks at the block interfaces is performed. This explicitness tends to reduce the convergence rate."*

6.3.3.2 Mesh Quality

Areas of poor mesh can have a detrimental effect on the overall solution [41]. Quality assessment of the hexahedral grid is a relatively straightforward task, and two different methods can be used [10]. The easiest way is to visually inspect the plots of the hexahedral mesh on the boundary surface or at various cross-sectional planes, as shown in Figures 6.27 and 6.28. Regions of poor mesh quality can be identified and corrected by manually adjusting the vertices of the control volumes.

Figure 6.27: Visualisation of surface mesh elements for the draft tube geometry (image extracted from ANSYS CFX-Post with medium mesh size as specified in Table 6.1)

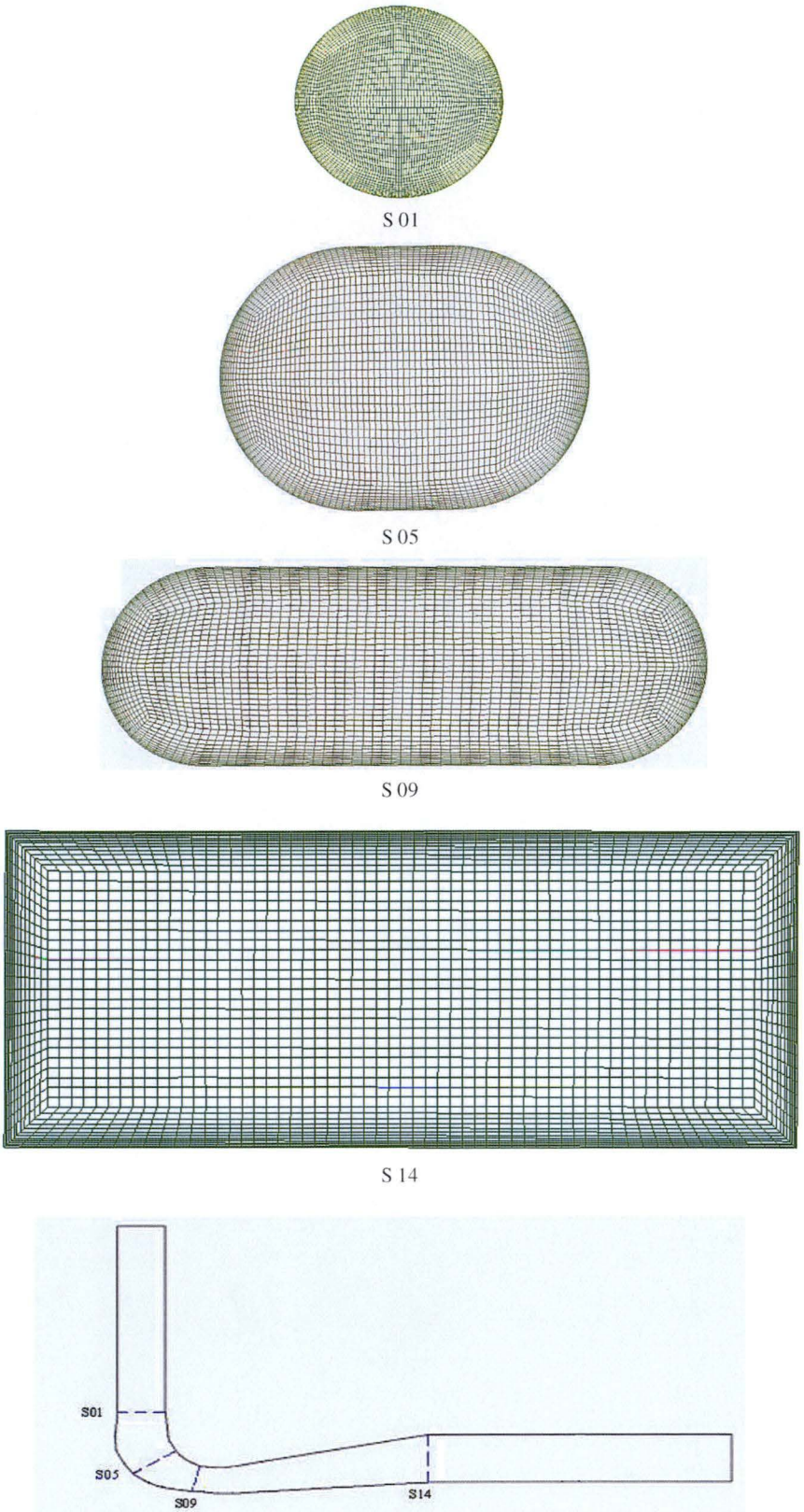

Figure 6.28: Visualisation of hexahedral mesh elements on various cross-sectional planes along the draft tube geometry (image taken from ICEM CFD 10 with medium mesh size as specified in Table 6.1)

Alternatively, the quality of a three-dimensional mesh can be assessed via histograms of suitable element quality measures (including Jacobian determinant, warp, skewness, aspect ratio, internal angle, distortion and parallelism of the hexahedral elements). As illustrated in Table 6.1, the meshes used in the current study meet the grid quality requirement specified by ANSYS CFX solver. Although this procedure can inform the user where a region of poor quality mesh exists, it can do little to aid in understanding why the mesh is bad and how to improve it.

Criteria	*Code Requirement* [4]	*Coarse Mesh*	*Medum Mesh*	*Fine Mesh*
Number of Nodes	–	638400	1176000	2207724
Edge length ratio	< 100	≤ 44.25	≤ 37.83	≤ 82.87
Minimum face angle	> 10°	≥ 41 33°	≥ 41 38°	≥ 42 47°
Element Volume Ratio	< 5	≤ 3 68	≤ 3.89	≤ 3.19
Connectivity Number	< 24	2 ~ 8	2 ~ 8	2 ~ 8
Jacobian Determinant	> 0 3	≥ 0.71	> 0.73	≥ 0.74
Eriksson Skewness	> 0.5	≥ 0 58	≥ 0.53	≥ 0.53

Table 6 1: Quality criteria of the hexahedral meshes (3 grid resolutions) employed for CFD simulations

The quality of the near-wall mesh can be assessed through the dimensionless wall distance Y+. This Y+ value was sensitive to flow rate of the draft tube and was evaluated at the highest flow rate being applied in the current simulations. The use of wall functions requires Y+ values of the first node from the wall to remain within the range of 30 and 500. However, the wall functions based on the law of the wall do not apply to separated flow in this study. Nevertheless, the dimensionless wall distance can still provide some useful information about the grid resolution. For the current geometry, the Y+ value was kept within 70 for more than 85% of the wall area.

6.3.3.3 Grid Convergence Study

The identification of discretisation errors is crucial for CFD calculations. A grid convergence test must be carried out to evaluate the numerical errors due to finite discretisation of the problem. A single calculation in a fixed grid is generally not acceptable as it is impossible to infer an accuracy estimate from such a calculation [103]. Hardware limitations are no longer an excuse for not performing a mesh sensitivity analysis. Excellent reviews of the methods for identifying and estimating the discretisation error from a numerical calculation are given by Roache [103].

The systematic grid convergence study carried out in this project involved performing simulations on three successively finer grids and then quantifying the discretisation errors based on the generalised Richardson extrapolation. The doubling of grid points in each coordinate direction was not necessary, and a non-integer grid refinement was performed for the non-uniform hexahedral mesh with generalised Richardson extrapolation [103]. The wall spacings normal to the walls were chosen as the reference for refinement and the same ratio was applied to these spacings when the mesh was refined. The mesh refinement ratio $r_{3i} = (N_{finest\ mesh-3} / N_{mesh-i})^{1/3}$ was maintained above 1.1 to allow the discretisation error to be differentiated from other error sources. If a p^{th} order accurate solution scheme is used, the estimated fractional error E of the coarse-grid solution f_{mesh-i} can be defined by:

$$E_{i3} = \frac{\varepsilon_{i3}}{r^p - 1} \quad \text{where} \quad \varepsilon_{i3} = \frac{f_{mesh-i} - f_{finest\ mesh-3}}{f_{finest\ mesh-3}} \tag{6.9}$$

However, an error estimator based on Richardson extrapolation does not assure the maintenance of conservation properties. Roache [103] proposes the use of a more conservative Grid Convergence Index (GCI) with a safety factor of 1.25 to uniformly report the results of grid convergence studies. The GCI is a measure of the percentage the computed value is away from the value of the asymptotic value, and it indicates how much a solution will change with a further refinement of the grid. A small value of GCI implies that the computation is within the asymptotic range [103]. The GCI for a grid is defined by:

$$GCI_i = \frac{F_s|\varepsilon_{i3}|}{r_{3i}^p - 1} \quad \text{where} \quad F_s = 1.25 \tag{6.10}$$

Three levels of mesh refinement were applied here to ensure an accurate estimate of the order of convergence and to check that the solutions were within the asymptotic range of convergence. This approach is recommended by Roache [103] for use whether or not Richardson extrapolation is actually used to improve the accuracy, and in some cases even if the conditions for the theory do not strictly hold. The objective is to provide a measure of uncertainty or an error band of the grid convergence. The draft tube pressure recovery factor and energy loss coefficient obtained with three meshes were compared for the steady flow case with a Reynolds number based on inlet diameter $Re_{INLET} \approx 2.51\times10^5$. The results for these mesh dependency tests will be presented in Chapter 7.

All three meshes used in these tests had the same topology but the grid refinement was not uniform in space. Different meshing strategies could well produce different results, although a truly grid independent solution would be independent of both grid density and meshing strategy [103]. Difficulties in meshing the physical geometry restricted the computational fluid dynamics study to one meshing topology with different mesh densities tested. In general, it is difficult to quantify what constitutes a good mesh for a given flow geometry. This is still very much an "art form" and requires user expertise with similar geometry [103].

Although solution-adaptive mesh refinement is less inexpensive to implement than systematic grid refinement, it was not employed for the present simulations because the unstructured mesh adaptation algorithm used in ANSYS CFX caused undesired stalling in the solution convergence due to large number of tetrahedral and prismatic elements being added to the hexahedral-element based flow domain. Roache [103] also points out that the solution-adaptive grid generation algorithm is unable to produce any useful error measure to quantify the uncertainty for a final calculation, and the increase in the number of nodes based on the use of an adaptation method does not always mean that the solution accuracy is improved.

6.3.4 Boundary Condition Modelling

Transient flow calculations for the elbow draft tube rely heavily on the precision of the appropriate boundary conditions. Information on the dependent flow variables at the domain boundaries must be properly specified in order to obtain a unique solution for the problem. Poorly defined boundary conditions can have a significant impact on the accuracy of the CFD solution, no matter how fine the discretisation or how sensible a turbulence model is. This is particularly true for the present study since only the draft tube component of the Francis turbine is examined here. The integration domain was cut off at the runner outlet, and the tail-water conditions were not being considered at all. The approach essentially ignores all variability outside the truncated integration flow domain. To get a realistic solution, experimental data is still needed to determine the inlet and outlet boundary conditions for the draft tube flow. The boundary conditions have been carefully determined here to prevent the over-specifying or under-specifying of the problem, which could result in a non-physical solution or failure of the solution to converge [4]. All boundary conditions for the CFD model were set up through the built-in pre-processing tool, ANSYS CFX-Pre.

6.3.4.1 Inflow Plane

The boundary treatment used for the inflow plane is the so-called "capacitive boundary condition". An experimental profile for the total pressure was specified at the inlet to account for the boundary layer effects. Flow angle normal to the boundary surface is employed because the inlet swirl is not modelled in this project. For transient operations, the same shape of the inlet velocity profile is assumed in order to evaluate the instantaneous total pressure distribution at the inlet. The total pressure specification requires an initial calculation of static pressure. The velocity is determined after the static pressure at the inlet is known. The inlet static pressure is a primitive variable and a function of the interior unknowns. It is computed by extrapolating the information propagated from the interior towards the boundary of the computational domain [4]. The assumption of isothermal and incompressible flow conditions eliminated the temperature and density gradient effects.

A constant turbulence intensity of I = 2.6% was applied at the inlet. The turbulence kinetic energy (k_{Turb}) was calculated from this specified intensity via the relationship $k_{Turb} = 1.5I^2U^2$ for isotropic conditions. The turbulence dissipation rate (ε) was approximated via the relationship $\varepsilon = k_{Turb}^{3/2} / 0.3D_h$ where D_h is the hydraulic diameter of the inlet. The turbulent length scale is determined automatically by the code. The approach of determining the dissipation rate based on experimental results was not used here because of the large variation and limited published data available for draft tube analysis. When the Reynolds stress model was used, the stress tensor at the inlet was extracted using the computed value of turbulence kinetic energy and assuming the inlet boundary to be isotropic with respect to Reynolds stresses. Diffusion flows at the inlet were equated to zero, as they were small compared to the advection [4].

6.3.4.2 Outflow Plane

The boundary treatment used at the outlet is closely related to the boundary conditions specified at the inflow plane. The outlet condition must be carefully defined, as the disturbances introduced at an outflow boundary can propagate upstream and have an effect on the entire computational region. Total pressure cannot be used to specify the outflow condition, as it is unconditionally unstable when the air flows out of the domain

[4]. The vorticity is transported downstream by advection, and so the only physical process that can transfer information upstream is static pressure. Hence, static pressure was applied as the outflow boundary condition for both steady and transient simulations.

For steady-flow operation, a constant static pressure boundary condition was established from the circumferentially averaged value at the draft tube outlet recorded during an experiment. The pressure loss in the outlet extended region was taken into account when calculating the outflow static pressure, but the buoyancy effects were neglected as they played no significant role in the current problem. The outlet flow direction was left unspecified, and to be determined by the local velocity field computation. The other flow variables on the outlet boundary surface were extrapolated from the interior by the computation. For unsteady-flow simulations, the outlet static pressure was imposed as a function of time, with values obtained from the experimental observations using a fast response pressure transducer flush-mounted on the surface of the outlet extension box. This outlet boundary is only assumed spatially constant at any instant. Wave reflections will largely occur within the draft tube where large change in area occurs. Hence, the pressure variations in the outlet box will be relatively small and should not pose a major problem when the time varying static pressure is used to describe the outflow condition.

As mentioned previously, the outlet was extended further downstream to a distance five times the outlet height away from its actual location. The flow profile is not changing significantly at this distance. This approach was used to eliminate the stability problems caused by the inflow at the real outlet plane due to recirculation close to the boundary. ANSYS CFX will enforce a temporary wall on the boundary to prevent inflow occurring at the outlet, which in turn can cause serious convergence problems if no pressure level is felt by the code when the full outlet is walled off [4]. To prevent this numerical problem, the opening boundary condition that allows for simultaneous inflow and outflow at an outlet was also applied [4]. The extended region cannot be eliminated, even though the opening boundary condition is used because the opening does not provide exact approximation of the flow behaviour outside the boundary. Turbulence conditions at outlet boundaries are always unknown, and Neumann boundary conditions are imposed such that the turbulence quantities are assumed to have a zero normal gradient at the outlet.

6.3.4.3 Wall Boundary

A smooth wall boundary condition was applied at the surfaces of the inlet extension pipe, draft tube and the outlet extension box. A non-slip adiabatic heat transfer flow condition was imposed at the wall. The flow immediately next to the wall assumes the zero wall velocity. The effect of surface roughness was not studied here, even though it may have some influence on the loss mechanism and the efficiency of the full-scale draft tube. A logarithmic wall function relating the tangential velocity to the wall shear stress was employed if using the ε-based model for turbulence simulation. The automatic near-wall treatment in ANSYS CFX was used when an ω-based turbulence model was applied. Discussion of the near wall flow treatment associated with different turbulence models will be presented in Section 6.3.5.3.

6.3.5 Turbulence and Near Wall Modelling

Turbulent fluctuations in the draft tube are always three-dimensional and unsteady, and consist of eddying motion with a wide range of length scales. To predict the effects of turbulence, the Reynolds Averaged Navier-Stokes (RANS) equations are solved together with the suitable statistical turbulence models. These models are needed to resolve the Reynolds stresses resulting from the time-averaging procedure. The use of turbulence models significantly reduces the amount of computational effort compared to Direct Numerical Simulation (DNS). Although Large Eddy Simulation (LES) model and Detached Eddy Simulation (DES) model are also provided in ANSYS CFX, they were not used in the present study because of the considerable amount of computing resources required to get reliable results for high Reynolds number flow and uncertainties in the fluctuating component of the inflow boundary condition [68]. The statistical turbulence models in ANSYS CFX can be classified into two categories: eddy-viscosity models and differential Reynolds stress models. Mathematical details of various turbulence models can be easily found in references [4, 63, 78, 79, 104, 121, 131, 140]. The following subsections briefly highlight some important features of the turbulence models used in the current simulations.

6.3.5.1 Eddy-Viscosity Model

Eddy-viscosity models are based on the assumption that the Reynolds stresses can be related to the mean velocity gradients and the turbulent viscosity (μ_t) by the gradient diffusion (Boussinesq) hypothesis [4]. The eddy-viscosity models used in the present study are of the two-equation type where two separate scalar-transport equations are solved for velocity and length scale in order to obtain information about the turbulent viscosity of the flow [4]. The zero-equation model was not considered here because the simple algebraic expression for the mixing length is not feasible for recirculating flow (with strong convection and diffusion).

Eddy-viscosity models are widely used in the industry because they are relatively easy and inexpensive to implement in the viscous solver. The extra viscosity aids stability in the numerical algorithms. However, the anisotropy (i.e. normal stresses are different in nature) and history effects are always neglected. Only one Reynolds stress can be represented accurately in this type of model. The standard k-ε model [4], RNG k-ε model [4], Wilcox's k-ω model [140], and Menter's Shear-Stress-Transport (SST) model [78] were all examined in the present study. These models were employed in their standard configurations, with various empirical constants set to values proposed by their respective developers.

The **standard k-ε model** assumes that the turbulent viscosity is linked to the turbulence kinetic energy k and turbulence dissipation rate ε. This model describes the mechanisms that affect the turbulence kinetic energy of the flow. The values of k and ε are obtained directly by solving the differential transport equations for the turbulence kinetic energy and turbulence dissipation rate. A large dissipation rate always occurs when the production of the turbulence kinetic energy is high. The model has been extensively validated in CFD simulations and is capable of predicting broad features of the draft tube flow reasonably well [4]. However, care must be taken while using the k-ε model as it is well known for its erroneous predictions of the turbulence production in strong strain fields and its inability due to isotropic assumption to predict secondary motions that are driven by the difference between the normal stresses [4, 79].

The **RNG k-ε model**, which is based on renormalisation group analysis of the Navier-Stokes equations, was proposed to overcome the over-predictions of turbulence production in the standard k-ε model. The transport equations for turbulence production and dissipation are the same as those for standard k-ε model, but the model constants are different [4, 5]. This modification dramatically increases the turbulence dissipation for rapid distortions, which yields lower levels of turbulence in complex geometries. The RNG k-ε model often actually underestimates the turbulence kinetic energy (less viscous), but this will sometimes result in more realistic flow features. The trend is in the right direction but for entirely wrong reasons [5]. It is the production of turbulence kinetic energy that is overestimated by standard k-ε model, and not the level of dissipation underestimated. However, the changes should indeed be made for better representation of anisotropy, and essentially of the normal stresses [4, 5, 106].

The **Wilcox's k-ω model** assumes that the turbulence viscosity is related to the turbulence kinetic energy k and the turbulence frequency ω. This model is also known as the low Reynolds number model. The details associated with its near-wall treatment method will be discussed in Section 6.3.5.3. The values of k and ω are obtained via the transport equations for turbulence kinetic energy and turbulence frequency. In some cases, the k-ω model is superior to the k-ε model in near wall layers because it does not involve the complex non-linear damping functions required for the k-ε model [4, 5, 78]. However, the Wilcox model is very sensitive to free-stream conditions and suffers from a problematic wall boundary condition (where ω tends to infinity) [140]. The solution may vary greatly with changes in turbulent frequency specified at the inlet.

The **Menter's Shear Stress Transport (SST) k-ω model** was developed in an attempt to resolve the sensitivity problem of the ω-equation by blending the k-ω model near the surface with the k-ε model in the outer region [4, 78]. The blending functions used in this model are critical to the success of the method and their formulation is based on the distance to the nearest surface and on the flow variables [4]. The distances of the nodes to the nearest wall for performing blending between k-ω and k-ε models are determined via the wall-scale equation. Overall, the model has taken into account the transport of the turbulent shear stress and may give a more accurate prediction of the onset and amount of flow separation under strong adverse pressure gradients [78, 79]. Detailed discussion of the SST turbulence model is given in Menter et al. [79].

Nonlinear eddy-viscosity models [5] such as the cubic k-ε model have also been developed to reduce the model deficiency caused by isotropic assumptions, and are expected to improve the accuracy of predictions for swirling flow. Unfortunately, ANSYS CFX does not currently include any non-linear eddy-viscosity models, and so they are not discussed further here.

6.3.5.2 Differential Reynolds Stress Model

The differential Reynolds stress model in ANSYS CFX uses individual differential transport equations for the Reynolds stresses (rather than the turbulence kinetic energy) and one transport equation for the turbulence dissipation (which is similar to the one used for k-ε model). The turbulence transport equation for the Reynolds stress has a term to describe the rate of change of the Reynolds stress, an advection term, a diffusion term, a production term that creates energy from the mean flow, a dissipation term due to viscosity acting on fluctuating velocity gradient, and a redistribution (pressure-strain) term to transfer energy between stresses via pressure fluctuations [5]. The model does not use an eddy-viscosity hypothesis, but has included the history-dependent non-local effects of the flow through convection and viscous diffusion of the Reynolds stresses [5]. As such, the model contains more turbulence physics, because the rate of production of Reynolds stresses, advection and production terms are exact in the equations.

The production term is a function of stress-strain products, which are sensitive to anisotropy in the flow field (and essential for proper modelling of the streamline curvature effects, impingement and rotation in the flow) [121]. The diffusion term is modelled using a General Gradient Diffusion Hypothesis that assumes the rate of Reynolds stress transport by diffusion is proportional to the gradient of the Reynolds stress [5]. The assumption of local isotropy is used for the dissipation of the Reynolds stresses. The model chosen for the pressure-strain correlation can either be the linear Launder, Reece and Rodi (LRR) model [63] or the quadratic Speziale, Sarkar and Gatski (SSG) model [121]. The wall reflection part of the pressure-strain correlation has a net effect in the direction normal to a wall by damping the fluctuations only [5]. However, the application of a wall reflection term into a general complex geometry is

difficult, as it includes normal distances to walls. For this reason, the wall reflection term is omitted in the CFX form of the LRR-model because the published results have not always shown an improvement of these relatively small contributions; they sometimes cause a degradation of the model performance [4, 5].

Although the Reynolds stress model contains several important features of turbulence physics, it is seldom used in industry because it is very expensive computationally (as six stress-transport equations and an equation for turbulence dissipation rate must be solved). The strong nonlinearities and the lack of a turbulent viscosity in the differential stress transport equation may degrade the numerical stability and lead to solver failure. Many important terms in the equations (such as redistribution and dissipation of turbulence) still require extensive modelling. Furthermore, the Reynolds stress model is not as widely validated as the eddy-viscosity models and more research is needed to overcome several modelling issues as stated above. ANSYS CFX also provides ω-based Reynolds stress models but they are not considered here due to very fine meshes required and the inherent numerical instability.

6.3.5.3 Near-Wall Treatment

Near-wall treatment is crucial for modelling the turbulent flow in the draft tube. Non-slip boundary condition is required at the solid surface so that both mean and fluctuating velocities vanish. This generates a very large flow gradient near the wall and suppresses the wall-normal fluctuations in high Reynolds number flow. The viscous and turbulent stresses are of comparable magnitude in this region. The common approach to overcome turbulent flow problems near the wall surfaces is to use either a wall function or a low-Reynolds-number turbulence model [4].

For turbulence models using an ε-equation, the wall function approach is usually implemented. The wall function in ANSYS CFX follows the method of Launder and Spalding [139] by assuming a logarithmic profile between near-wall nodes and the boundary [4]. This function is based on the local equilibrium of fluid turbulence. In other words, the production and dissipation of turbulence are always assumed balanced. This approach works well if the equilibrium assumption is reasonable, but fails in highly non-equilibrium regions such as the recirculating flow. The standard wall

function is sensitive to the near-wall meshing, and the near-wall node should optimally be placed in the region of $30<Y^{+}<500$. Refining a near-wall mesh with a standard wall function being used will not guarantee a unique solution of increasing accuracy, as the function is not compatible with the systematic grid refinement technique [103]. For turbulence models using ω-equations, the wall problem is tackled by solving the turbulence transport equation right up to the boundary. The effects of molecular viscosity are included in the coefficients of the eddy-viscosity formula and dissipation transport equations. However, full resolution of the flow requires the near-wall node to satisfy the condition of $Y^{+} \leq 1$. The low Reynolds number model is therefore very computationally demanding, particularly for high-Reynolds-number flows [4].

Hence, several improvements are made in ANSYS CFX to overcome the potential problems of both the wall function and low-Reynolds-number models [4]. A scalable wall function is employed to replace the standard wall function for all turbulence models using ε-equation. The basic idea behind this approach is to limit the value of dimensionless wall distance Y+ used in the logarithmic formulation to 11.06 so that all mesh points are outside the viscous sub-layer and all fine mesh inconsistencies are avoided [4]. At least 10 nodes are placed in the boundary layer and the upper limit for dimensionless wall distance is kept below 100 in all cases [4]. For the low-Reynolds-number model, an automatic near-wall treatment is used in the code to automatically switch the low-Reynolds-number formulation to the wall function mode, depending on the grid resolution [4].

6.3.6 Initial Condition Modelling

A good initial guess can improve the convergence of a CFD solution. Initial values for all solved variables were set as "automatic with value" in the ANSYS CFX-Pre (pre-processing tool) before starting the solver. The ANSYS CFX solver automatically reads the initial conditions from the initial value file or uses the specified value during the course of solution. For the steady-flow calculation, the initial variable values give the solver a flow field from which to start its computation [4]. Although the convergence of the solution is more rapidly achieved if sensible initial guesses are supplied, the converged results are not affected by the initialisation [4]. For transient-flow simulation, the initial values provide the actual flow field at the instant when the CFD calculation

starts. It is essential to apply a proper initial condition for a transient simulation, as the error may propagate in successive time steps and cause the divergence of a solution. Hence, validated and converged steady-state solutions were used to provide initial conditions for the transient simulations. The values specified should be the actual flow field present at the beginning of the time of the simulation [4].

An automatic linearly varying initial condition was used to specify the velocity field in the draft tube domain. It was generated using a weighted average of boundary condition information from the inlet and outlet. The magnitude of the velocity was set lower than the inlet velocity, as the flow was decelerating in the draft tube. The initial guess for the turbulent kinetic energy was obtained using the turbulent intensity of 2.6% and the initial velocity guess. To prevent zero turbulence kinetic energy in the domain, a minimum clipping velocity of 0.01 m/s was employed whenever a zero initial velocity value was found [4]. The static pressure was initialised in the same way as the velocity, but the inlet and outlet pressure values were decreased and increased respectively by 10% of the range of values to avoid creation of walls at the domain inlet and outlet [4]. The pressure values were set as the average of the highest value of pressure specified on the outlet boundary and the lowest value of pressure specified at inlet boundary. This approach can reduce the likelihood of unrealistic spurious inflow at outlet or outflow at inlet, which may cause the solver to fail [4].

6.3.7 Transient Flow Modelling

Transient characteristics of the draft tube flow were analysed through transient simulations that required real time information to determine the time intervals at which the ANSYS CFX solver calculated the flow field. Transient flow behaviour of the draft tube is caused by the inherently unsteady nature of the flow and the changing boundary conditions when the turbine operating condition varies. The boundary conditions used for transient modelling have already been discussed in Section 6.3.4. Turbulence model and grid resolution choices were guided by the verification and validation of steady-flow results presented in Chapter 7. In ANSYS CFX, the transient term is discretised via a first- or second-order Backward Euler scheme. The first-order approach suffers from the numerical diffusion and the code developer does not recommend the use of a first-order scheme for production runs [4]. Hence, a second-order method was used in this study. This approach is a fully implicit time-stepping scheme and it is second-order accurate. However, the transient scheme for turbulence quantities remains first-order

accurate regardless of the types of transient schemes chosen because the second-order approach is not monotonic and is unsuitable for calculations of turbulence quantities that must be bounded in the calculations for stability reasons.

For transient simulations, the time step size and the maximum number of iterations within a time step are two important variables that must be set properly in order to get an accurate result within an acceptable time frame. ANSYS CFX will perform several coefficient iterations until it reaches the specified maximum number of 5 iterations or the predefined maximum residual tolerance of 5×10^{-5} at each simulation time instant. The solver will continue to compute the solutions until the desired simulation time is reached [4]. Setting an appropriate time step size is very challenging for transient analyses, as no precise procedure has been established for this practice.

The code supplies information on the Courant number ($CFL = U_{local}\Delta t/\Delta x$ where Δt represents the time step size and Δx represents the characteristic computational grid spacing) at each simulation time to help determine if the current time step size is good enough for the simulation. The Courant number describes the time step size relative to the spatial discretisation and compares the time step in a calculation to the characteristic time of moving a fluid element across a control volume. It should be noted that stability of the transient scheme is not restricted by the Courant number, as the code is fully implicit. A Courant number greater than unity may be applied in the simulation. Nevertheless, a time-step dependency test was carried out to check the effect of the time step size on the accuracy of the results. The simulations were repeated at three different time steps: 0.005 second, 0.001 second, and 0.0002 second, which in turn gave the maximum Courant numbers of 4.8, 12.2, and 60.9 for a typical run. Generally, the solutions were found insensitive to Courant number and so the time step of 0.001 second was used in the transient analyses to ensure the solutions would converge within five coefficient iterations for any time instant. More details of the transient flow results will be presented in Chapter 8.

6.3.8 Convergence Criteria for a Simulation

Many factors can affect the convergence of a CFD solution. The preceding discussion has described efforts to reduce numerical instabilities arising from ill-posed boundary conditions, poor quality meshes, and inappropriate solver settings. ANSYS CFX uses the normalised residuals of solution variables to judge convergence. Converging

residuals imply a decreasing imbalance in the conservation equations being solved [4]. If the problem is well defined, the solver will run until the specified levels of residuals are met. Normalised maximum residuals of $1\sim5\times10^{-5}$ were set as the convergence criteria for the present simulations. It should be noted that the residual level for the turbulence transport equations does not constitute part of the convergence criteria in ANSYS CFX [4]. Global imbalances for the conservation equations were checked at the end of a simulation to ensure that they were well below 1% for the hydrodynamic equations in all cases.

For steady simulations, oscillatory convergence behaviour was occasionally observed when more advanced turbulence models were used. This could not be eliminated even though a damping factor or steady-state time step control was applied in the calculations. The root-mean-square (RMS) residual was found to be about 100 times smaller than maximum residuals for most of steady simulations. This implies that unstable flow behaviour such as separation and reattachment of the flow may occur in the draft tube, even though the boundary condition does not vary [4]. Running these simulations in transient considerably reduced the residual levels of the solution. Figure 6.29 shows the typical residual plots of the simulations where the solutions are considered converged.

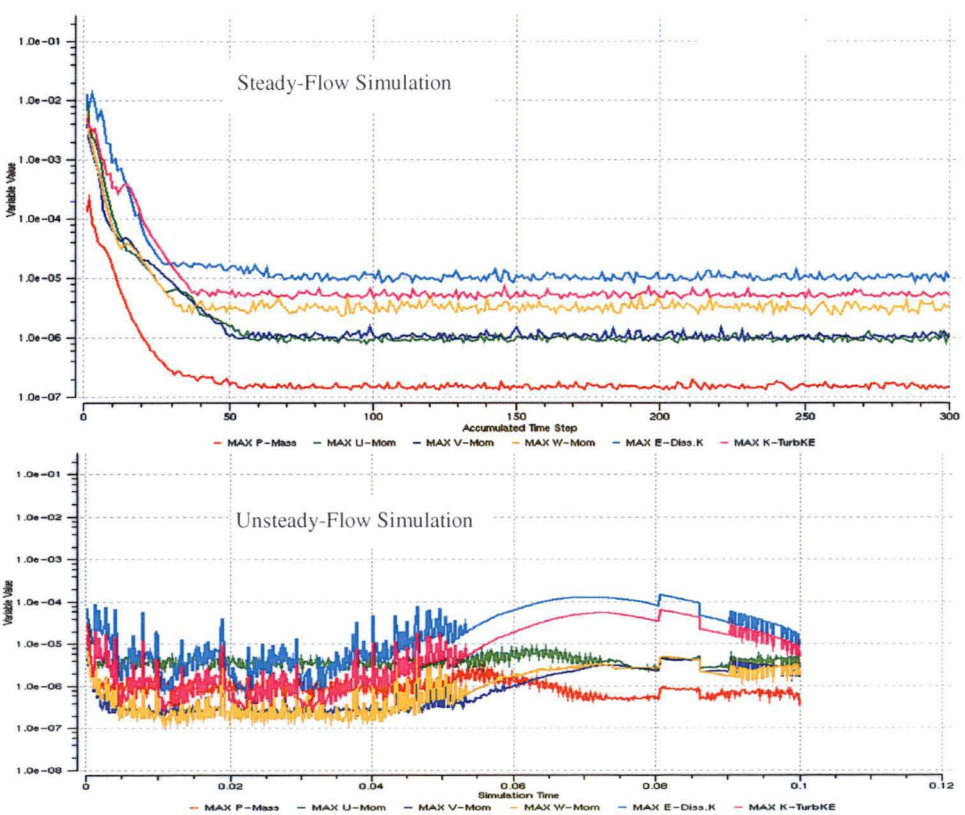

Figure 6.29: Residual plots of typical steady and transient simulations showing "good" converging behaviour of a calculation (image extracted from ANSYS CFX-Solver Manager)

6.3.9 Post Processing

The majority of post-processing jobs were carried out using the built-in post-processing tool ANSYS CFX-Post. The area-averaged velocity, area-averaged static pressure coefficient, and the mass-flow-averaged total pressure coefficient were computed using the macro function provided in the software. The area averages of the velocity and static pressure are calculated by integrating the local pressure or velocity values multiplied by the associated elemental area and divided by the total area over the region. A spatially dominant quantity will have the greatest impact on an area-averaged result. The mass-flow averaged total pressure, on the other hand, is obtained by integrating the total pressure value times absolute mass flow divided by the total absolute mass flow over the region. Mass averaging returns the value that is dominant in the mean flow, and was applied for the total pressure because that quantity is not spatially conserved. The absolute value of the mass flow was employed to minimise adverse effects of flow recirculation on the averaging process.

For steady-flow analyses, velocity contour and vector plots at different sections of the draft tube were constructed by specifying the coordinates of the planes and the ranges of the velocities to be shown in the graph. Hybrid variable values were chosen in these plots so that the velocities at the wall node were set to their true values of zero, and not the values averaged over the control volumes at the boundaries. The flow topology was examined via skin friction lines created using the Runge-Kutta method of vector variable integration with variable time step control [4]. The lines start at nodes uniformly distributed over the entire wall surface of the model. Two-dimensional plots used for CFD validation were generated in MATLAB, as the experimental results were also processed and presented using the MATLAB program. For transient-flow studies, the pressure and velocity values for each time step at a specified location were evaluated and exported to a text-formatted file using the CFX Command Language (CCL). The CCL syntaxes are borrowed directly from the programming language PERL. Structures such as looping or I/O processing can be easily added to the program to extract the transient information automatically from a large result file. All transient data were analysed in MATLAB.

CHAPTER 7

STEADY-FLOW ANALYSES OF THE DRAFT TUBE MODEL

7.1 Overview

Procedures for experimental model testing and numerical simulation of the draft tube flow have already been discussed in Chapter 6. In this Chapter, the experimental and computational results for steady-state operation of the scale model draft tube are presented. The model is geometrically similar to the one used in Hydro Tasmania's Mackintosh power station. No significant Reynolds number dependency is observed over the limited range of the Reynolds numbers tested. Section 7.2 summarises the experimental results for steady-flow operation. These include inlet boundary layer analysis, static pressure surveys, turbulence and velocity traverses, skin friction measurements, and tuft flow visualisation. Section 7.3 covers the verification and validation of the CFD simulations. Meshing issues, turbulence models, and boundary conditions are examined and verified in detail. The numerical solutions are also validated against the experimental results collected at two different Reynolds numbers: 2.51×10^5 and 1.06×10^5. Several important phenomena for the draft tube flow are reviewed in Section 7.4. The discussion includes Reynolds number effects, flow separation, inlet swirl, flow asymmetry, flow unsteadiness, and effects of the stiffening pier. The validated steady-flow results will be used as the initial conditions for the transient-flow analyses presented in Chapter 8.

7.2 Experiments

7.2.1 Inlet Boundary Layer Analysis

The initial boundary layer thickness has a major influence on the flow development within the elbow of a draft tube. In this analysis, the boundary layer is assumed turbulent from the start of the inlet pipe. For an equilibrium turbulent boundary layer, the local value of the pressure gradient parameter at separation is $(\theta/U)(dU/ds) \approx -0.004$ where θ is the local boundary layer momentum thickness and dU/ds is the local free-

stream velocity gradient [139]. Boundary layer development in an elbow draft tube is greatly influenced by the curvature due to increasing static pressure and decreasing turbulent mixing on the convex wall of the draft tube model. The combined effect of the adverse pressure gradient and reduced turbulence mixing is very unhealthy, as it may induce flow separation along the bend. Even with an initially subcritical value of the pressure gradient parameter, the boundary layer growth and local pressure gradient in the draft tube may subsequently lead to separation. A draft tube that operates satisfactorily with a particular value of inlet boundary layer thickness could still separate if the inlet boundary layer thickness is increased. Equations 7.1 define the important boundary layer parameters used in this analysis. The trapezoidal rule was used for numerical evaluation of the momentum and displacement thicknesses from the experimental data.

$$\theta = \text{momentum thickness} = \int_0^\infty \frac{u}{U_\infty}\left(1-\frac{u}{U_\infty}\right) dy$$

$$\delta^* = \text{displacement thickness} = \int_0^\infty \left(1-\frac{u}{U_\infty}\right) dy \qquad (7.1)$$

$$H = \text{momentum shape factor} = \frac{\delta^*}{\theta}$$

The momentum shape factor H is a crude indicator of flow separation in a turbulent boundary layer: the value of H at separation ($H_{sep} \approx 3$) depends on both the Reynolds number and the upstream history of the boundary layer. The value of H at the inlet to the draft tube model is well below the value for separation, because the pressure gradient at the inlet pipe is close to zero. However, this starting value of H does not indicate whether the flow will separate inside the draft tube.

The local values of H at the positions inside the draft tube have to be measured in order to determine the locations of local flow separation. Boundary layer measurements inside the draft tube were not obtained in this experiment because the flow was highly fluctuating and the boundary layer along the bend was unsteady. Figure 7.1 shows the total pressure profiles measured by a Pitot tube at two different locations along the inlet

pipe for two valve positions: 78% and 44% of the valve opening, which correspond to the inlet Reynolds numbers of 2.51×10^5 and 1.06×10^5 respectively. The experimental technique for these boundary layer measurements had been summarised in Section 6.2.3.1. The resulting velocity profiles are presented in Figure 7.2, while the boundary layer properties are summarised in Table 7.1. The velocity profile is axisymmetric because the upstream influence of the bend was minimal at these measuring locations.

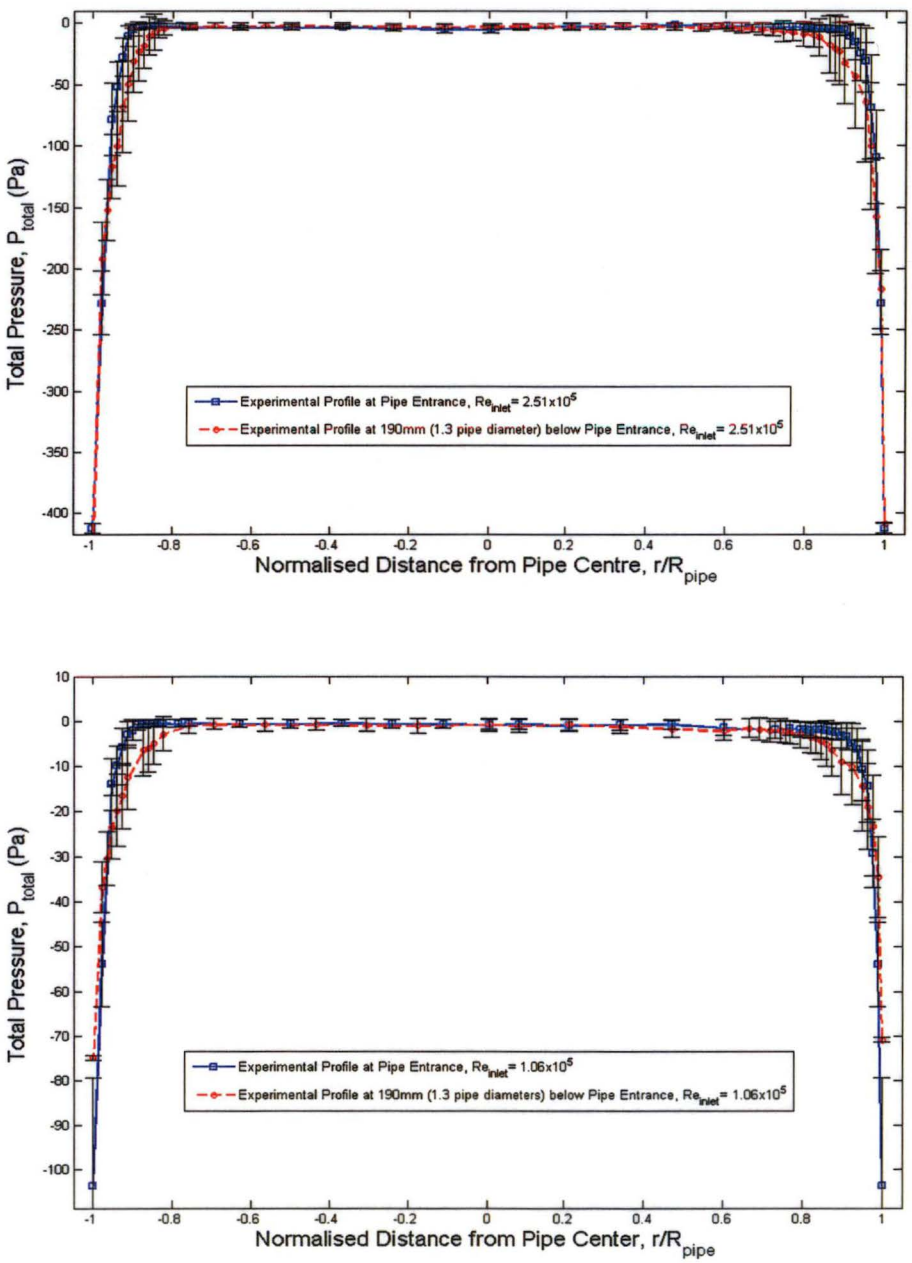

Figure 7.1: Total pressure profiles measured by Pitot tube at the pipe inlet and 190 mm (1.3 pipe diameters) below pipe entrance for two valve positions: 78% (top) and 44% (bottom) of the valve opening. Error bars show the root-mean-square variations of the total pressures

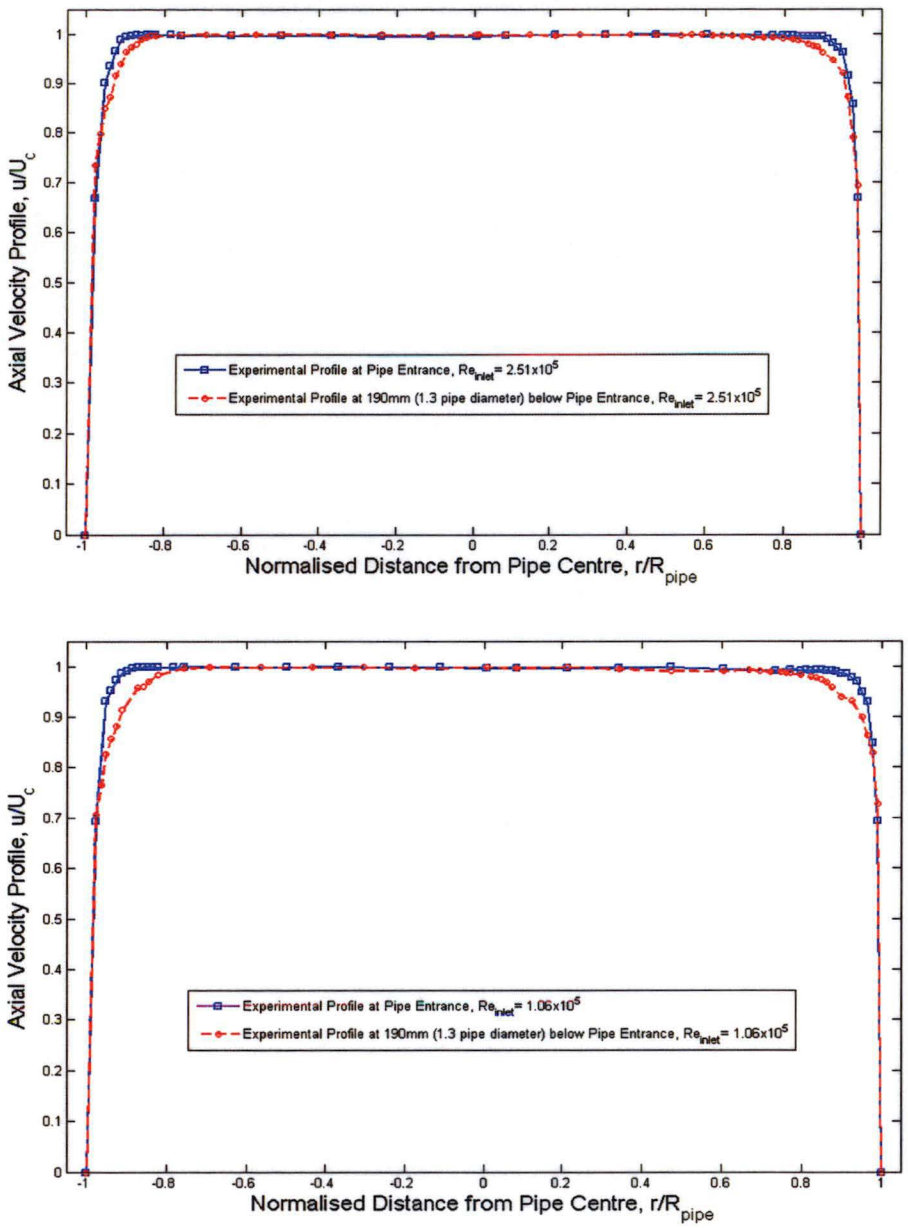

Figure 7.2: Velocity profiles at the pipe inlet and 190 mm (1.3 pipe diameters) below pipe entrance for two valve positions: 78% (top) and 44% (bottom) of the valve opening

Location	δ (*mm*)	δ^* (*mm*)	θ (*mm*)	δ^* / δ	*H*
At Pipe Entrance (78% Valve Opening)	7.6	0.81	0.54	0.106	1.61
190 mm below Pipe Entrance (78% Valve Opening)	13.5	1.44	0.88	0.106	1.63
At Pipe Entrance (44% Valve Opening)	8.6	0.89	0.63	0.103	1.42
190 mm below Pipe Entrance (44% Valve Opening)	15.4	1.57	1.10	0.102	1.44

Table 7.1: Measured boundary layer properties at the pipe inlet and 190 mm (1.3 pipe diameters) below pipe entrance for two valve positions: 78% and 44% of the valve opening

7.2.2 Static Pressure Distributions

Wall static pressures were measured along the model centrelines. Figure 7.3 defines the locations of the centrelines along the top, bottom, left, and right wall of the draft tube model. 81 static pressure taps were distributed along these centrelines, and the pressure values are presented in the form of dimensionless static pressure coefficient as follows:

$$Cp_{static-i} = \text{static pressure coefficient at location } i = \frac{P_i - P_{atm}}{0.5\rho_a U_{IN}^2} \tag{7.2}$$

where $P_i - P_{atm}$ = static pressure at location i relative to the atmospheric pressure (Pa)

U_{IN} = average inlet velocity measured by the bellmouth nozzle (m/s)

Figures 7.4 and 7.5 show the static pressure distributions along the top and bottom centrelines of the model, while Figure 7.6 illustrates the evolution of wall static pressures along the left and right centrelines of the model. The difference in the static pressure distributions along the top and bottom surfaces is mainly caused by the effects of longitudinal curvature. Although the model is symmetrical about its centre plane, some small discrepancies are observed for centreline static pressure distributions on the left and right sides of the model. The sources of flow asymmetry will be discussed later in Section 7.4.4. The circumferential wall static pressure distributions at the inlet and outlet planes of the draft tube model are presented in Figure 7.7. Variations of circumferential wall static pressures are greater at the inlet planes because of the downstream curvature effect. The effect gradually decays towards the outlet of draft tube. The circumferentially averaged static pressures at the draft tube inlet and outlet ($\overline{P}_{dt-in}$ and $\overline{P}_{dt-out}$) are used to calculate the pressure recovery factor. The pressure recovery factor commonly used to assess the performance of a diffusing channel is defined as follows:

$$Cp_{recovery} = \frac{\overline{P}_{dt-out} - \overline{P}_{dt-in}}{0.5\rho_a U_{IN}^2} = \overline{Cp}_{dt-out} - \overline{Cp}_{dt-in} \tag{7.3}$$

The measured static pressure recovery factors for various inlet Reynolds numbers are listed in Table 7.2. The measured values of $Cp_{recovery}$ are well below the ideal pressure recovery factor of $Cp_{ideal} = 1 - AR^2 \approx 0.96$ for an inlet-to-outlet area ratio, $AR \approx 1/5$.

This is expected, as the flow in the draft tube is complex and the momentum loss will further reduce the amount of energy being converted to the static pressure rise in the draft tube.

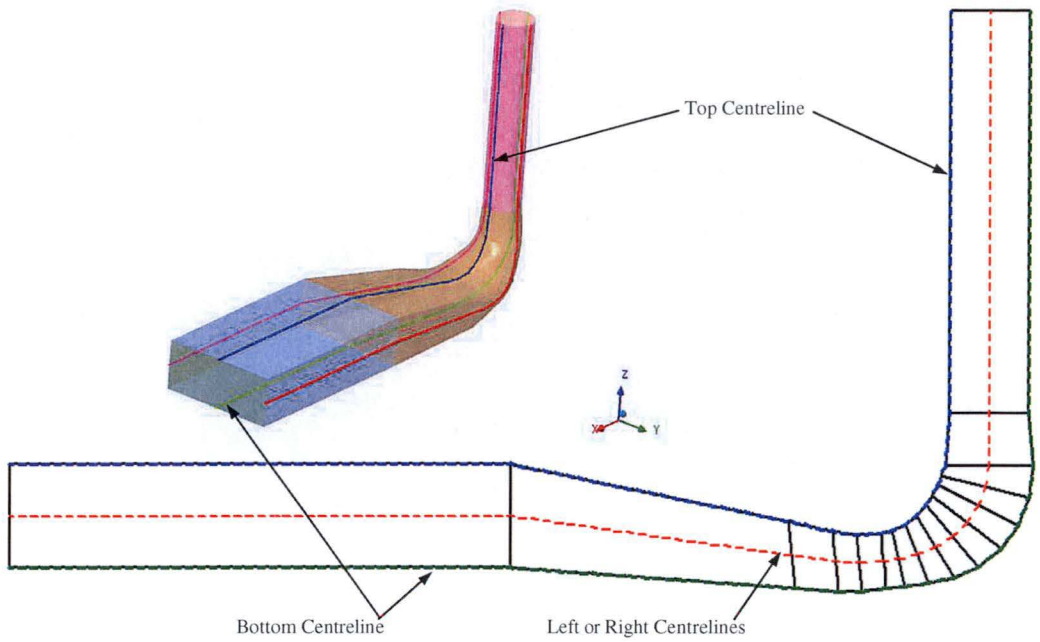

Figure 7.3: Definitions and locations of the top, bottom, left, and right centrelines on the draft tube model

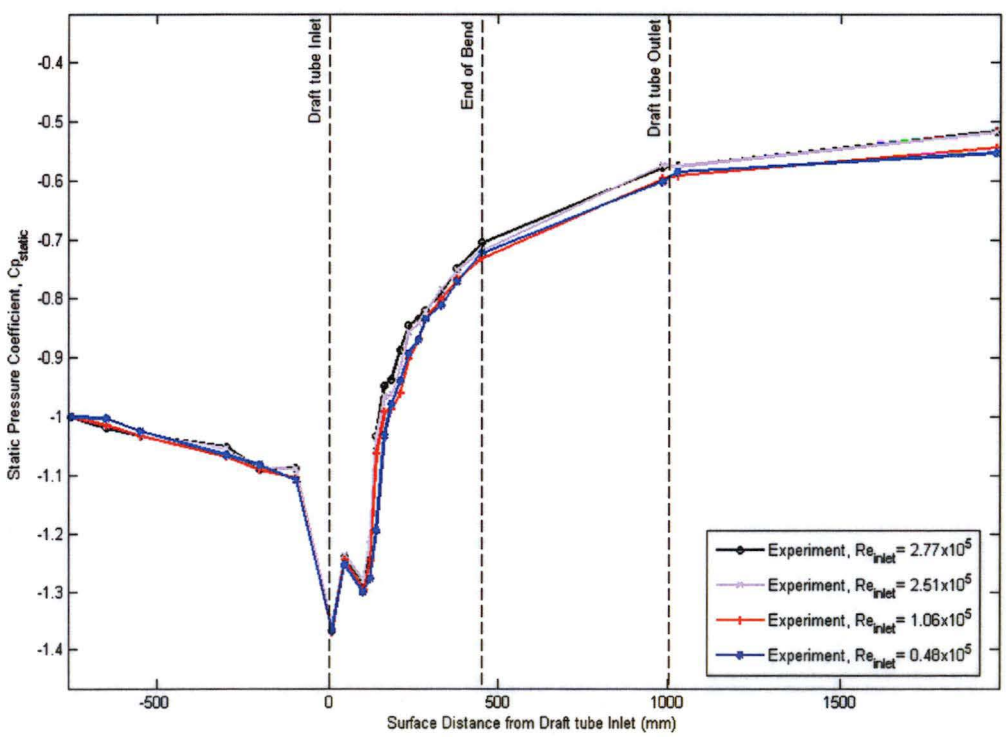

Figure 7.4: Wall static pressure distributions for various Reynolds numbers along the top centreline of the model

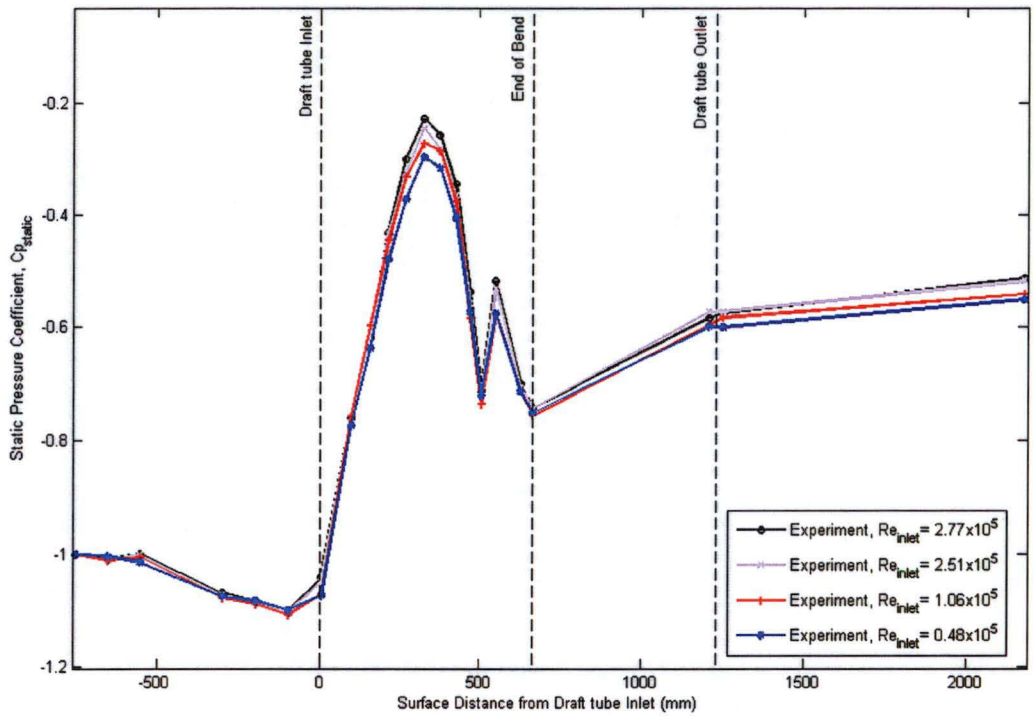

Figure 7.5: Wall static pressure distributions for various Reynolds numbers along the bottom centreline of the model

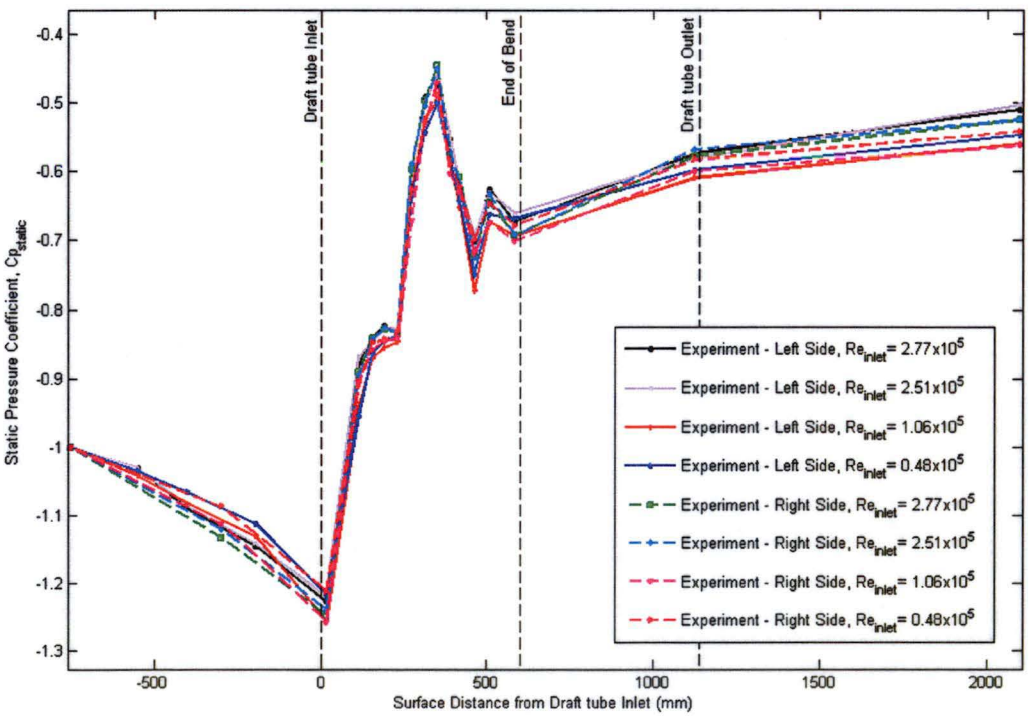

Figure 7.6: Wall static pressure distributions for various Reynolds numbers along the left and right centrelines of the model

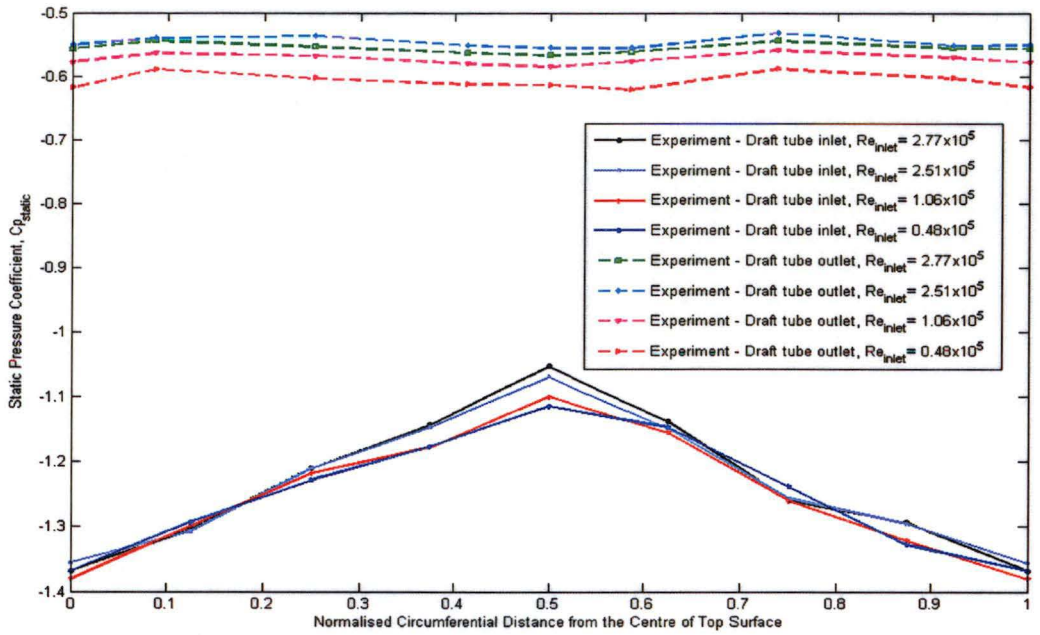

Figure 7.7: Circumferential wall static pressure distributions for various Reynolds numbers at the draft tube inlet and outlet

Valve Opening (%)	*Inlet Reynolds Number, Re_{INLET}*	*Static Pressure Recovery Factor, $Cp_{recovery}$*
100	2.77×10^5	0.671
78	2.51×10^5	0.681
44	1.06×10^5	0.681
22	0.48×10^5	0.666

Table 7.2: Measured static pressure recovery factors for various valve positions. The evaluation is based on the circumferentially averaged static pressures measured from the wall pressure tappings installed at the inlet and outlet planes of the draft tube model

7.2.3 Mean Velocity Distributions

The mean velocity was measured using a hotwire probe traversed across different cross-sections of the model as illustrated in Figure 7.8. The probe was traversed either vertically from the bottom to the top surface or horizontally from the sidewall towards the duct centre. Experimental techniques for mean velocity measurements were discussed in detail in Sections 6.2.3.3 and 6.2.3.4. Hotwire results for two different Reynolds numbers ($Re_{INLET} = 2.51 \times 10^5$ and 1.06×10^5) are presented in Figures 7.9~7.12. As the hotwire probe was incapable of sensing the flow direction in the draft tube, the four-hole probe was also employed to measure the mean velocity. The hotwire measurements are compared against the four-hole probe data in Figures 7.13~7.16. Both measurements agree fairly well with each other. However, the four-hole probe data

reveal that an unsteady backflow region may occur at Stations V2c and V3c as the probe fails to measure the flow angles there.

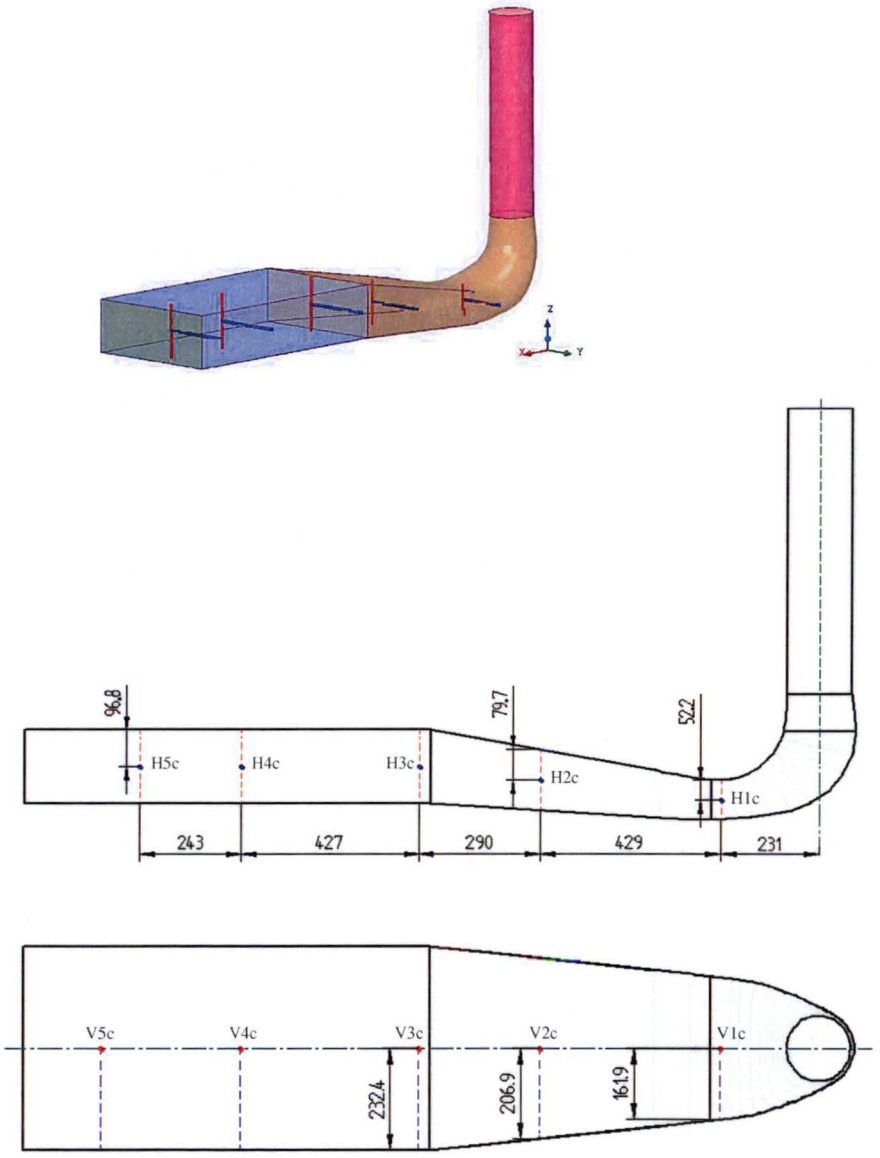

Figure 7.8: Measurement locations of the mean velocity profiles for both hotwire and four-hole pressure probes. All dimensions are in mm (blue lines indicate the extent of horizontal probe traverses, red lines define the extent of vertical probe traverses, blue dots represent the Stations for horizontal probe traverses, red dots represent the Stations for vertical probe traverses)

For the horizontal traverse, velocity profiles downstream of the bend are similar in shape. Velocity peaks at locations near the wall and gradually decreases towards the centre of the duct where secondary flows cause accumulation of low energy fluid (see Figures 7.11 and 7.12). The magnitude of this near-wall velocity peak is decreasing as the flow travels further downstream. The secondary motion is expected to persist downstream of the bend but it will slowly disappear in the flow direction. The flow becomes more uniform due to increasing turbulent mixing. The viscous effect is only

significant for flow near the wall. It is easily seen from these experimental results that the secondary flows cause the high momentum fluid on the bottom wall at the bend exit to move towards the sidewall and onto the top of the diffusing passage. This produces the somewhat unexpected result (later confirmed by CFD in Section 7.3.1.2) that the peak velocity at the draft tube exit occurs on the top of the duct.

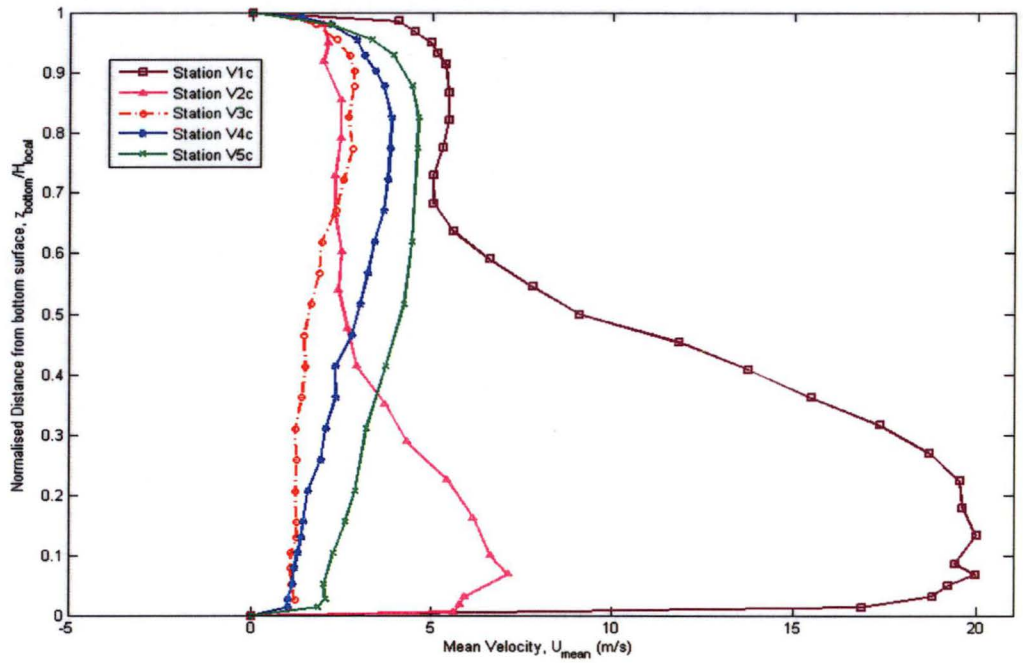

Figure 7.9: Vertical hotwire traverse for mean velocity profiles at various locations of the draft tube ($Re_{INLET} = 2.51 \times 10^5$)

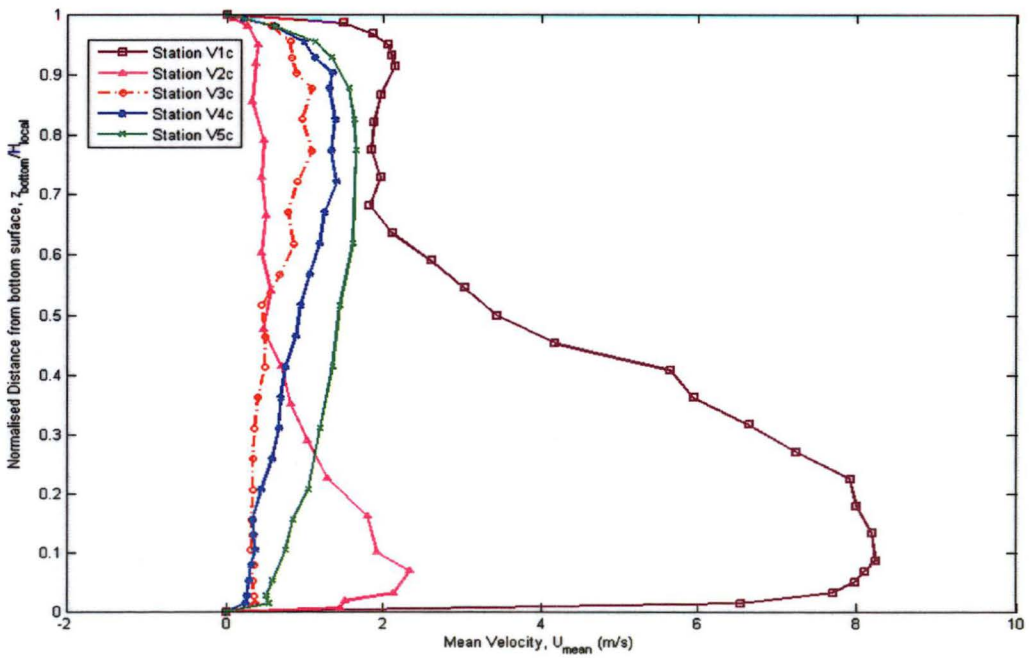

Figure 7.10: Vertical hotwire traverse for mean velocity profiles at various locations of the draft tube ($Re_{INLET} = 1.06 \times 10^5$)

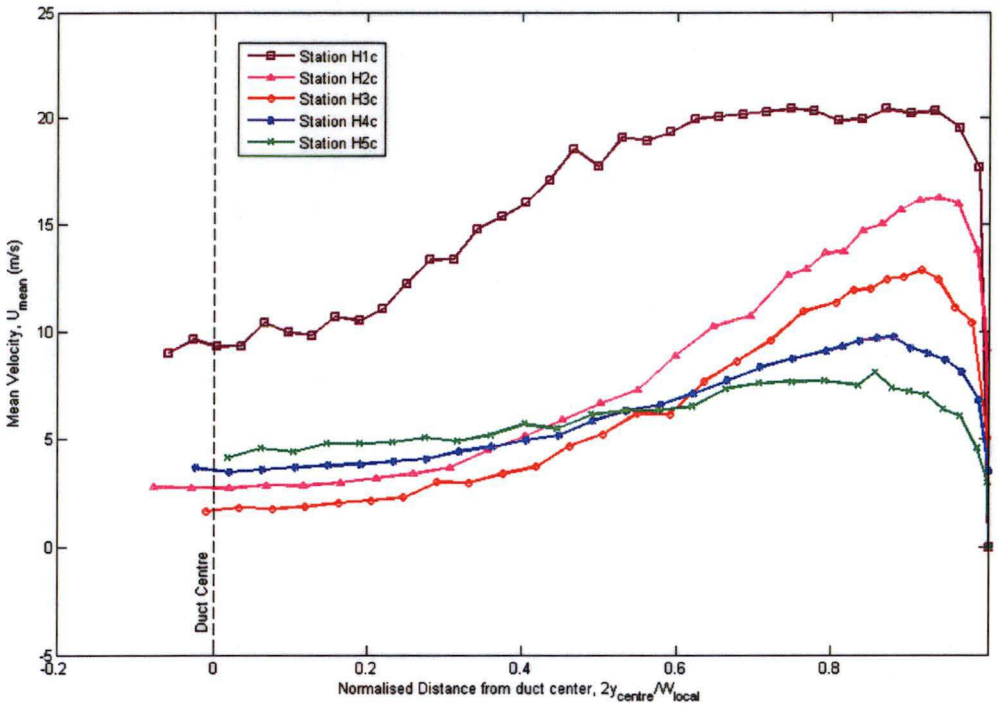

Figure 7.11: Horizontal hotwire traverse for mean velocity profiles at various locations of the draft tube ($Re_{INLET} = 2.51 \times 10^5$)

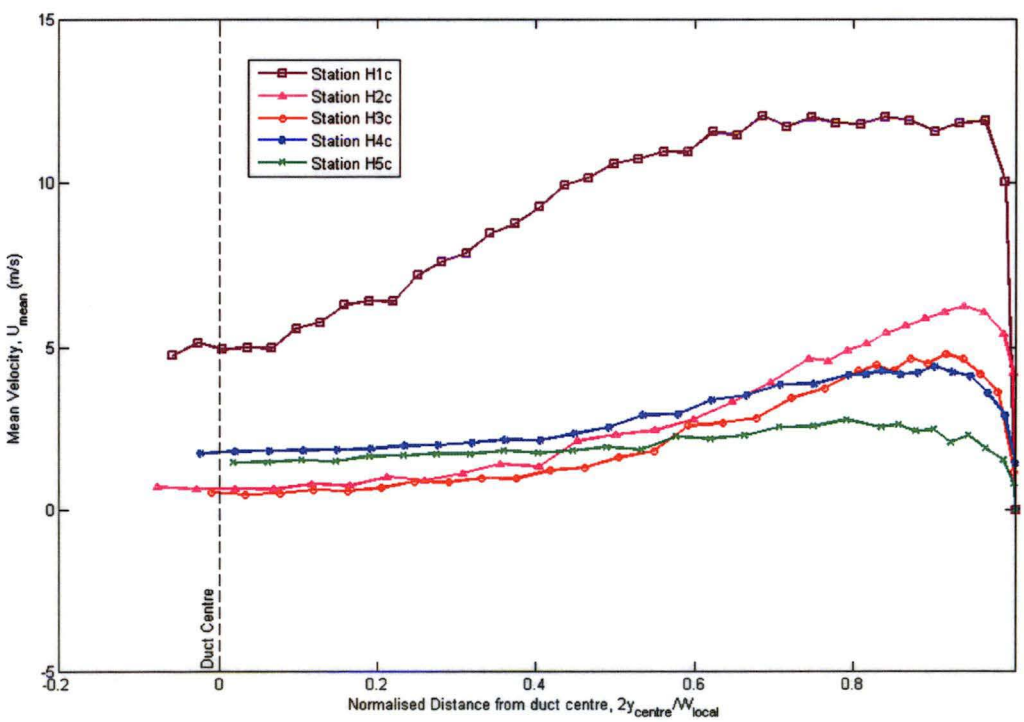

Figure 7.12: Horizontal hotwire traverse for mean velocity profiles at various locations of the draft tube ($Re_{INLET} = 1.06 \times 10^5$)

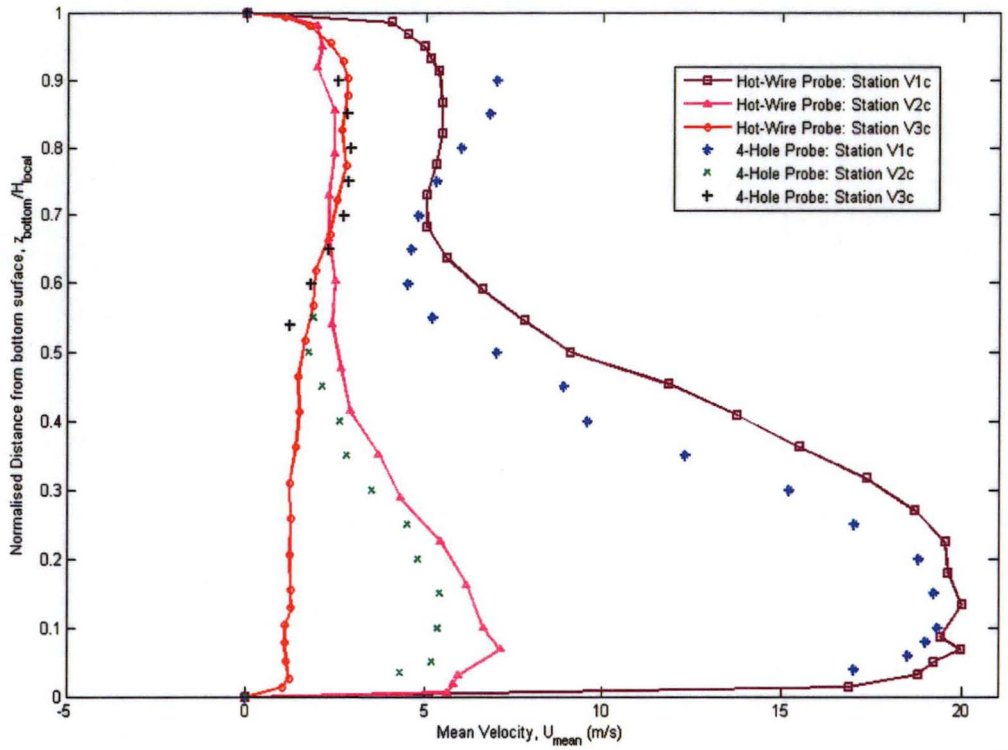

Figure 7.13: Comparisons of the hotwire and four-hole probe measurements for vertical probe traverse at various locations of the draft tube model ($Re_{INLET} = 2.51 \times 10^5$)

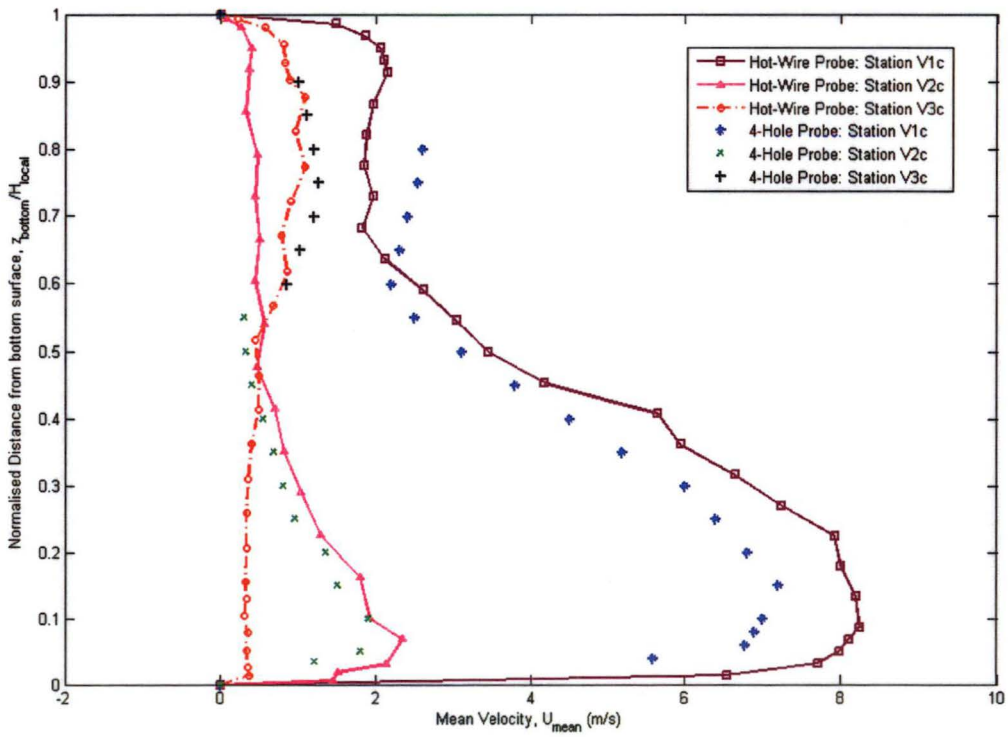

Figure 7.14: Comparisons of the hotwire and four-hole probe measurements for vertical probe traverse at various locations of the draft tube model ($Re_{INLET} = 1.06 \times 10^5$)

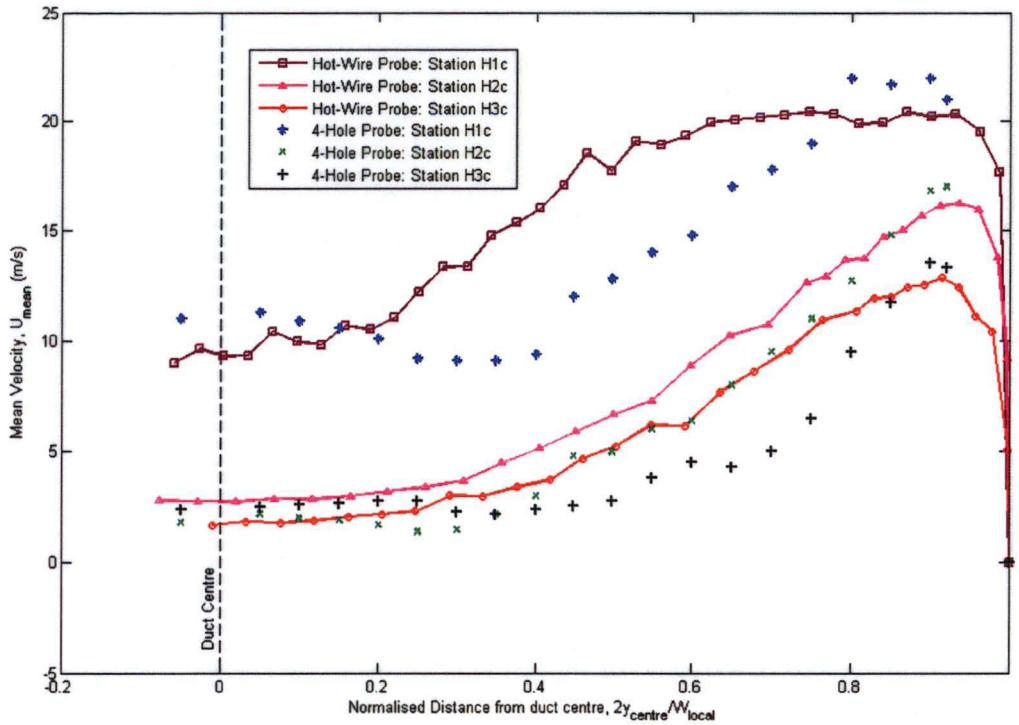

Figure 7.15: Comparisons of the hotwire and four-hole probe measurements for horizontal probe traverse at various locations of the draft tube model ($Re_{INLET} = 2.51 \times 10^5$)

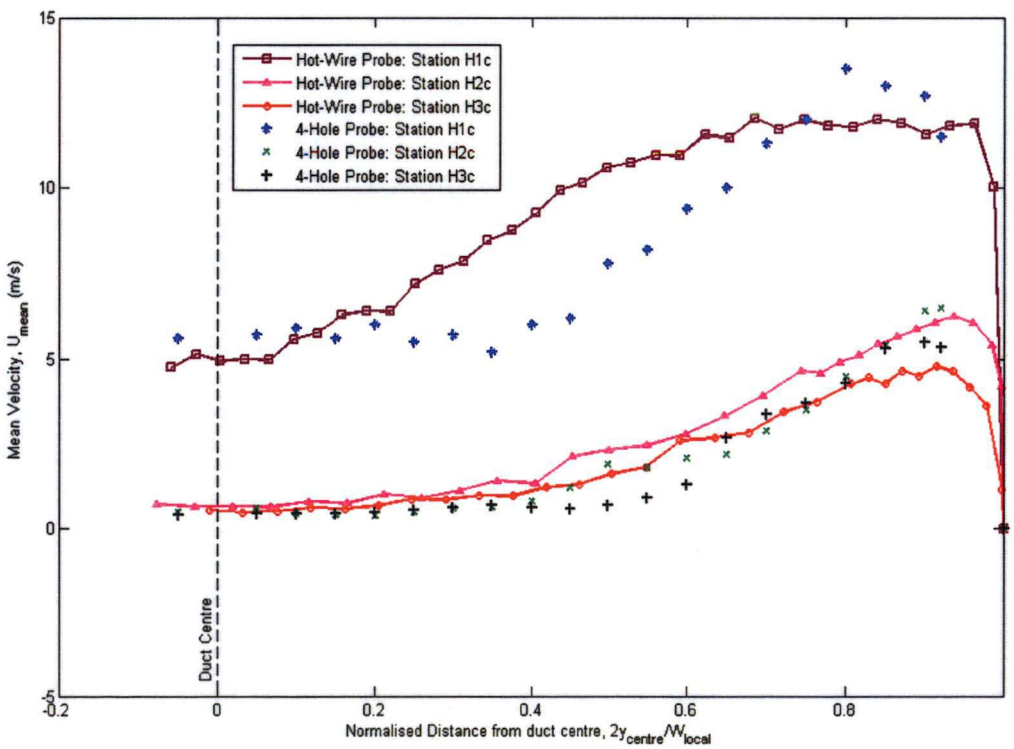

Figure 7.16: Comparisons of the hotwire and four-hole probe measurements for horizontal probe traverse at various locations of the draft tube model ($Re_{INLET} = 1.06 \times 10^5$)

7.2.4 Turbulence Profiles

Figures 7.17~7.18 show the development of turbulence profiles inside the draft tube model as measured by the single-sensor hotwire probe. The turbulence intensity is determined by dividing the local fluctuating velocity component from the hotwire signal (u_{rms}) with the local mean hotwire velocity (U_{mean}). The study is not intended to provide detailed investigation of the turbulence quantities in the draft tube, but to provide additional data for validating the turbulence model in CFD simulations. The retardation of the mean flow may enhance the production of normal turbulent stress in the draft tube. Decreasing mean velocity magnitude with streamwise distance will also increase the turbulence intensity. Hence, it is not surprising that relative turbulence intensity grows significantly after the bend.

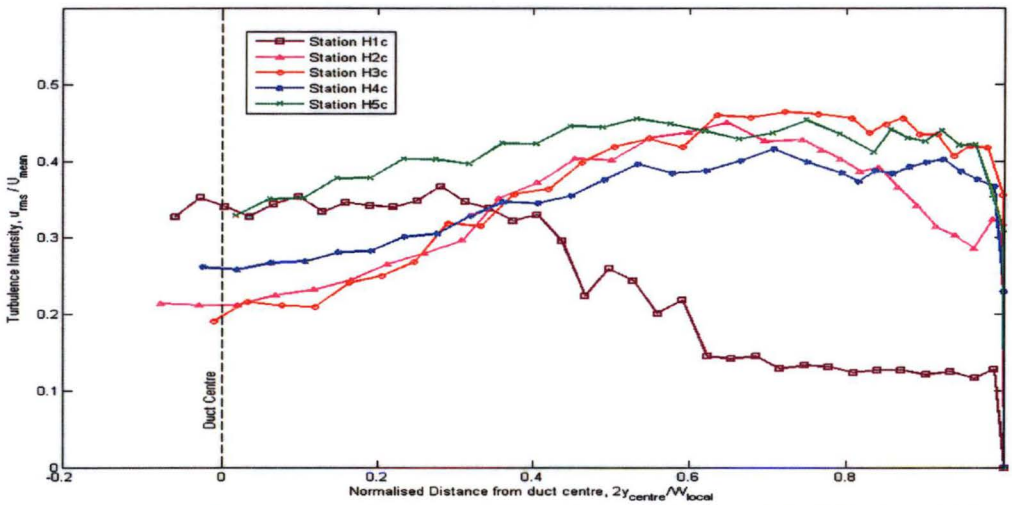

Figure 7.17: Horizontal hotwire traverse for turbulence profiles at various locations of the draft tube model ($Re_{INLET} = 2.51 \times 10^5$)

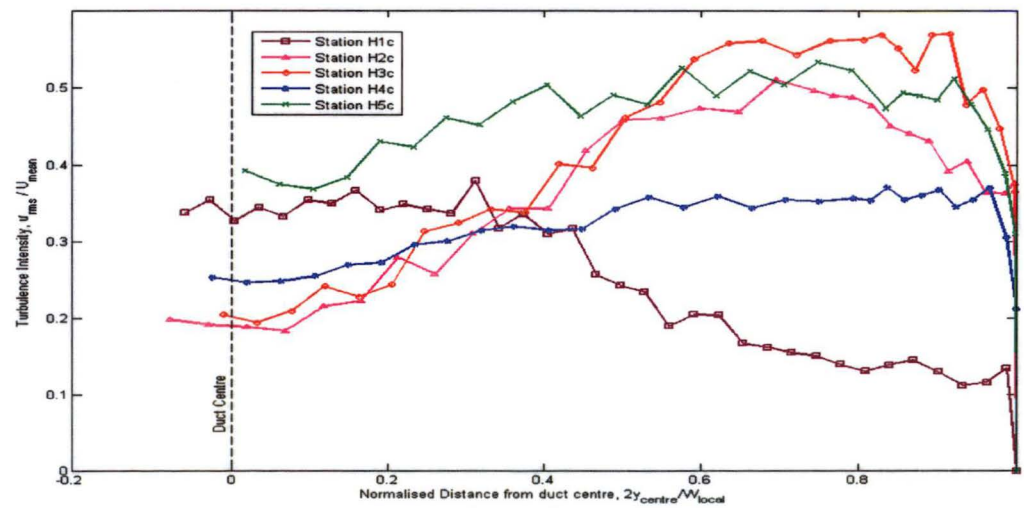

Figure 7.18: Horizontal hotwire traverse for turbulence profiles at various locations of the draft tube model ($Re_{INLET} = 1.06 \times 10^5$)

7.2.5 Skin Friction Distributions

Accurate determination of skin friction inside the draft tube is a challenging task. No measurements were taken along the bend due to difficulties of probe insertion. Figures 7.19 and 7.20 show the results of skin friction distributions along the bottom and the side walls of the model at three different inlet Reynolds numbers. The skin friction coefficient is defined by:

$$C_{f\text{-}i} = \text{local skin friction coefficient at position } i = \frac{\tau_W}{0.5\rho_a U_{IN}^2} \tag{7.4}$$

As illustrated in these Figures, local skin friction coefficients decrease sharply at the inlet cone of the draft tube. This trend is observed at both the bottom and the side walls of the model, which indicates an increasing risk of boundary layer separation at the start of bend. Although the skin friction coefficients are also reducing in the downstream rectangular diffusing section, there is no obvious sign of boundary layer separation at this region. It should be noted that the flow inside the draft tube is three-dimensional and a positive value of skin friction does not guarantee the absence of three-dimensional separation.

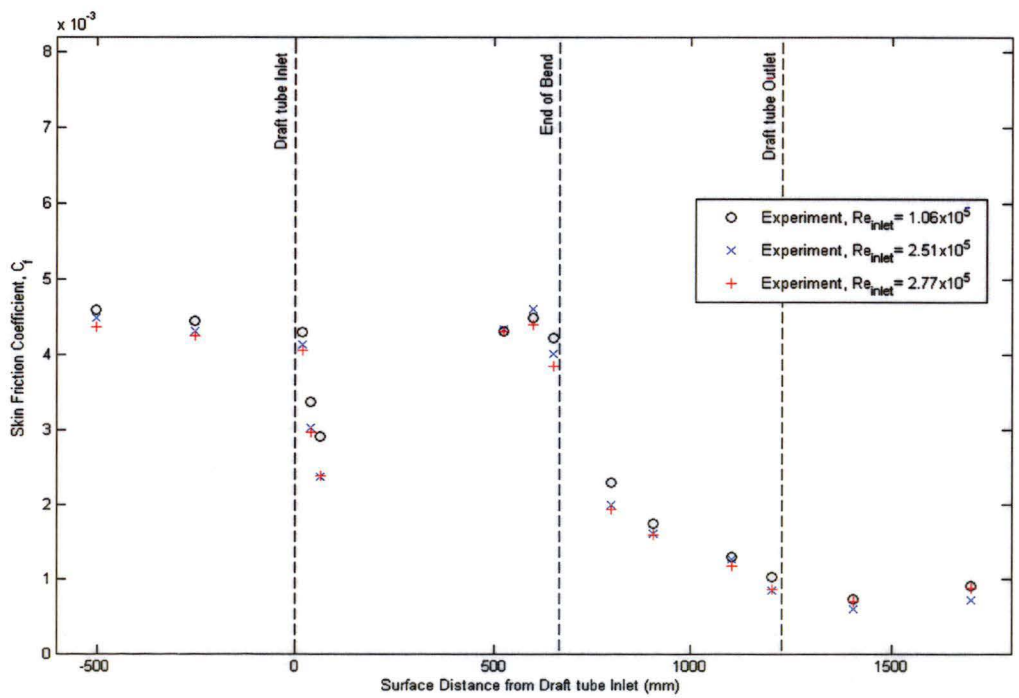

Figure 7.19: Skin friction distribution for various inlet Reynolds numbers along the bottom centreline of the draft tube model

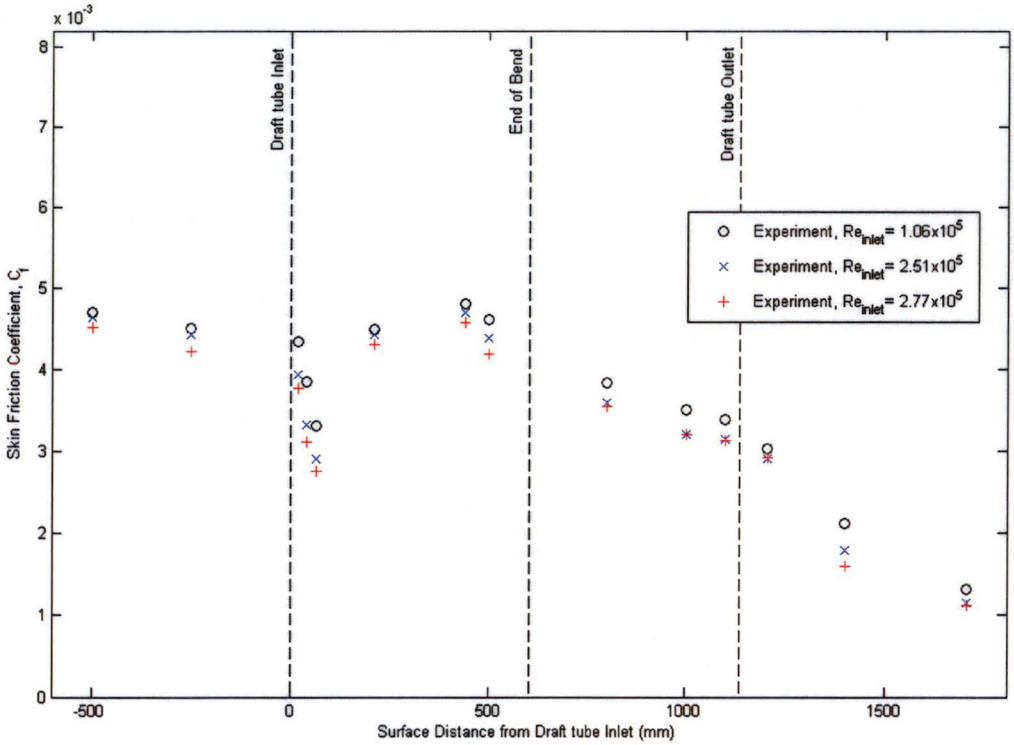

Figure 7.20: Skin friction distribution for various inlet Reynolds numbers along the right centreline of the draft tube model

7.2.6 Flow Visualisation

Tuft flow visualisation was used to locate backflow regions and the streamwise vortices inside the draft tube. The experimental technique had been discussed in Section 6.2.3.6. The tuft spun about its hinge forming a narrow cone with axis nearly parallel to the wall when placed inside the bend. This indicated the existence of a strong streamwise vortex generated by the bend. However, the strength of rotation weakened, as the tuft was moved further downstream of the bend. Curvature effects seemed to dampen quickly within the downstream rectangular diffusing box. The tuft was observed to reverse its direction at the centre plane near the end of the bend and at the outlet of the draft tube. While the tuft generally pointed upstream at these locations, it flickered rapidly at a frequency of several Hertz. The back flow region was highly unsteady even though the inflow was maintained at approximately the same condition. The reversal in tuft direction indicates the presence of essentially two-dimensional separation. The separation region at the centre plane did not seem to reattach until the draft tube exit. This explains why the velocity inside the draft tube was extremely difficult to measure accurately with hotwire and four-hole pressure probes.

7.3 Computational Fluid Dynamics (CFD)

7.3.1 Verification

Verification of a CFD simulation involves the process of determining if a computational model is the correct representation of the conceptual model and if the resulting approach or the model assumptions can be used for the relevant flow analysis. The main objective is to identify and estimate the errors due to the implementation of the particular grid resolution, turbulence model, and boundary conditions. In other words, verification of a CFD calculation aims to "solve the equations right" by evaluating the accuracy of the solutions generated by the CFD code [103]. To save space, only the CFD solution for an inlet Reynolds number of 2.51×10^5 is presented here.

7.3.1.1 Mesh Resolution

Examination of spatial convergence for a simulation is the basic approach for determining the discretisation error of a CFD simulation. The method involves performing the simulation on two successively finer grids. Three different mesh sizes (mesh1: 638400 nodes, mesh2: 1176000 nodes, and mesh 3: 2207724 nodes) are applied in this analysis. As the number of nodes in the flow domain increases, the spatial discretisation errors should asymptotically converge to the computer round-off errors. Preliminary analysis based on the static pressure recovery factor $Cp_{recovery}$ and the total pressure loss coefficient k_{loss} confirms that the CFD solutions are within the asymptotic range of convergence. Methods for evaluating the spatial convergence of the CFD simulations were discussed in Section 6.3.3.3.

The choice of the turbulence model inevitably affects the grid independence of a CFD solution because of the various assumptions made by the different turbulence models. It is not possible to separate the grid errors and the numerical errors generated by a particular turbulence model. Hence, the grid convergence is investigated together with turbulence models in this study. The order of convergence (p) based on three mesh sizes and assuming a constant grid refinement is found to be within the range of 1.78~1.84, which is quite close to the theoretical value of 2. Hence, $p = 2$ is applied in the computation of fractional error E and Grid Convergence Index (GCI) for consistency. The finest grid size used in the analysis does not produce a grid independent solution. Approximately 12 million nodes would be needed to achieve the grid independent solution. This would require a huge amount of computational time and resources, which is unrealistic for the current study. The mesh resolution of 1176000 nodes was adopted

as a good compromise between the solution accuracy and the computational resources required. The solution for zero grid scale can be estimated using the Richardson extrapolation method, based on the following formulae:

$$\begin{cases} Cp_{recovery-est} = \dfrac{r_{32}^2 Cp_{recovery-mesh3} - Cp_{recovery-mesh2}}{r_{32}^2 - 1} \\ k_{loss-est} = \dfrac{r_{32}^2 k_{loss-mesh3} - k_{loss-mesh2}}{r_{32}^2 - 1} \text{ where } k_{loss} = \dfrac{\overline{P}_{total-inlet} - \overline{P}_{total-outlet}}{0.5\rho_a U_{JN}^2} \end{cases} \tag{7.5}$$

Results of the grid convergence study are summarised in Table 7.3. The estimated values of the pressure recovery factor ($Cp_{recovery}$) and the loss coefficient (k_{loss}) at zero grid scale are listed in Table 7.4. It should be noted that the static pressures used to compute the $Cp_{recovery}$ in CFD are area-averaged while the total pressures used to predict the k_{loss} in CFD are mass-flow-averaged over the inlet or the outlet planes of the draft tube. Hence, the predicted $Cp_{recovery}$ is expected to be lower than the measured $Cp_{recovery}$, which is calculated based on the circumferentially averaged wall static pressures measured at the draft tube inlet or outlet. Figure 7.21 shows the predicted streamline pattern along the geometric symmetry plane of the draft tube model. As shown in this Figure, SST k-ω model and Reynolds Stress model are very sensitive to the number of computational nodes applied in the flow domain.

Turbulence Model	*Number of Nodes,* N_{mesh-i}	*Refinement Ratio,* r_{3i}	*Static Pressure Recovery Factor*			*Total Pressure Loss Coefficient*		
			$Cp_{recovery}$	$E_{p=2}$	$GCI_{p=2}$	k_{loss}	$E_{p=2}$	$GCI_{p=2}$
Standard k-ε	638400	1.51	0.548	– 0.056	0.070	0.219	0.135	0.169
	1176000	1.23	0.581	– 0.031	0.039	0.194	0.075	0.094
	2207724	1.00	0.590	–	–	0.187	–	–
RNG k-ε	638400	1.51	0.490	– 0.124	0.155	0.273	0.213	0.266
	1176000	1.23	0.562	– 0.069	0.086	0.228	0.119	0.149
	2207724	1.00	0.582	–	–	0.215	–	–
Wilcox k-ω	638400	1.51	0.600	0.092	0.115	0.115	– 0.311	0.388
	1176000	1.23	0.551	0.051	0.064	0.174	– 0.174	0.217
	2207724	1.00	0.537	–	–	0.191	–	–
SST k-ω	638400	1.51	0.552	0.233	0.291	0.203	– 0.246	0.307
	1176000	1.23	0.454	0.130	0.162	0.276	– 0.138	0.172
	2207724	1.00	0.426	–	–	0.296	–	–
LRR Reynolds Stress	638400	1.51	0.483	– 0.091	0.114	0.388	0.159	0.198
	1176000	1.23	0.532	– 0.051	0.063	0.337	0.088	0.110
	2207724	1.00	0.547	–	–	0.322	–	–
SSG Reynolds Stress	638400	1.51	0.467	– 0.087	0.109	0.404	0.141	0.177
	1176000	1.23	0.513	– 0.039	0.049	0.356	0.079	0.099
	2207724	1.00	0.526	–	–	0.342	–	–

Table 7.3: Grid convergence studies showing results of various turbulence models applied for a CFD calculation with identical boundary conditions and convergence criteria

Turbulence Model	*Estimated Value for* $Cp_{recovery}$	*Estimated Value for* k_{loss}
Standard k-ε	0.609 ± 0.02	0.173 ± 0.02
RNG k-ε	0.623 ± 0.05	0.189 ± 0.03
Wilcox k-ω	0.510 ± 0.03	0.224 ± 0.05
SST k-ω	0.371 ± 0.06	0.337 ± 0.06
LRR Reynolds Stress	0.574 ± 0.04	0.294 ± 0.03
SSG Reynolds Stress	0.552 ± 0.03	0.315 ± 0.03
Experiment	0.681 ± 0.08	–

Table 7.4: Estimated values of pressure recovery factor and loss coefficient at zero grid scale (within 90% confidence level)

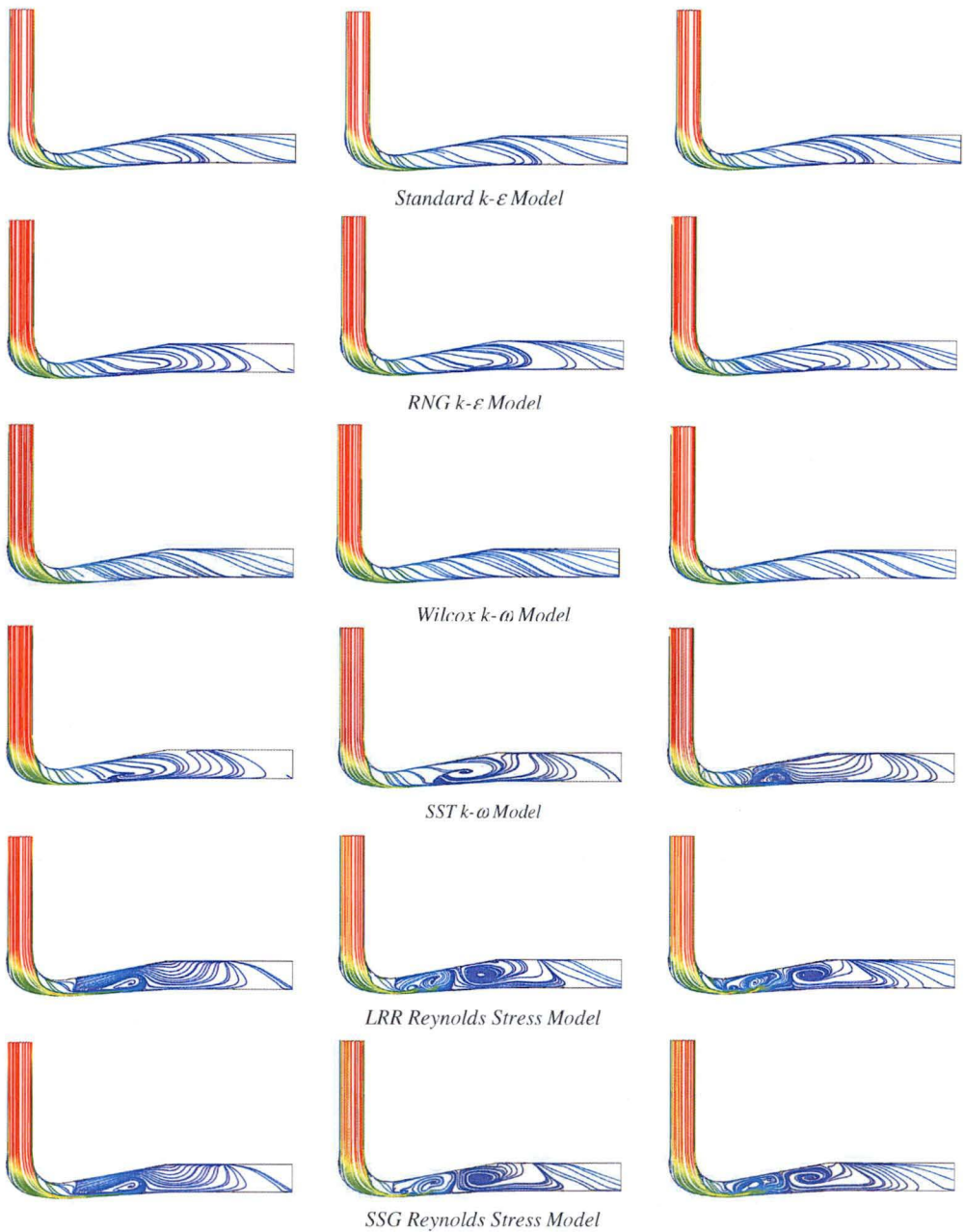

Figure 7.21: Predicted streamline pattern along the geometric symmetry plane of the draft tube model using different grid sizes and turbulence models (left: coarse-mesh solution, middle: medium-mesh solution, right: fine-mesh solution)

7.3.1.2 Turbulence Models

As noted by Roache [103], "a fundamental difficulty associated with the validation and verification of turbulence modelling is the essential lack of a universal turbulence model". Various important features of the turbulence models and the near-wall treatments employed in ANSYS CFX were discussed in Section 6.3.5. Figures 7.22~7.27 show the axial velocity contours (U_a) and the secondary flow velocity vectors (U_t) predicted by different turbulence models at various cross-sections of the draft tube model. All CFD solutions presented here are based on the mesh size of 1176000 nodes.

Overall, the predicted flow feature in the draft tube is characterised by a pair of counter-rotating vortices, a feature that is well known in studies of flow in bends. The fluid that possesses the highest streamwise momentum at the bottom wall will migrate toward the top surface. Streamwise momentum of the fluid along the bottom wall diminishes with increasing distance from the wall. These broad features are predicted by all turbulence models, although differences appear for the engineering quantities. This flow structure is mainly caused by the well-known imbalance between the centrifugal force and the radial pressure gradient acting on the relatively slow-moving fluid. A weak radial cross flow generated in the region along the symmetry plane will carry the fluid toward the stalled region on the top surface.

Although a similar flow structure is predicted by all turbulence models, some significant differences can still be observed between the solutions. First, the strength of the vortex pair computed via the eddy-viscosity model is weaker than the one for Reynolds stress model, which yields a broader low-momentum region at the outlet and a larger pressure loss. Second, the streamwise momentum is observed to decay and dissipate more slowly if the eddy-viscosity model is used; this results in a higher peak velocity predicted inside the draft tube. Third, the Reynolds stress models capture unsteady flow phenomena that are not predicted by the eddy-viscosity models. The flow asymmetries found in solutions of the Reynolds stress models are direct consequences of the flow unsteadiness. Solutions of the eddy-viscosity models are stable even if the unsteady simulations are performed. The longer detached shear layers predicted by eddy-viscosity models stabilise the recirculating flow inside the draft tube. This explains why the CFD simulations using eddy-viscosity models are numerically stable in most cases.

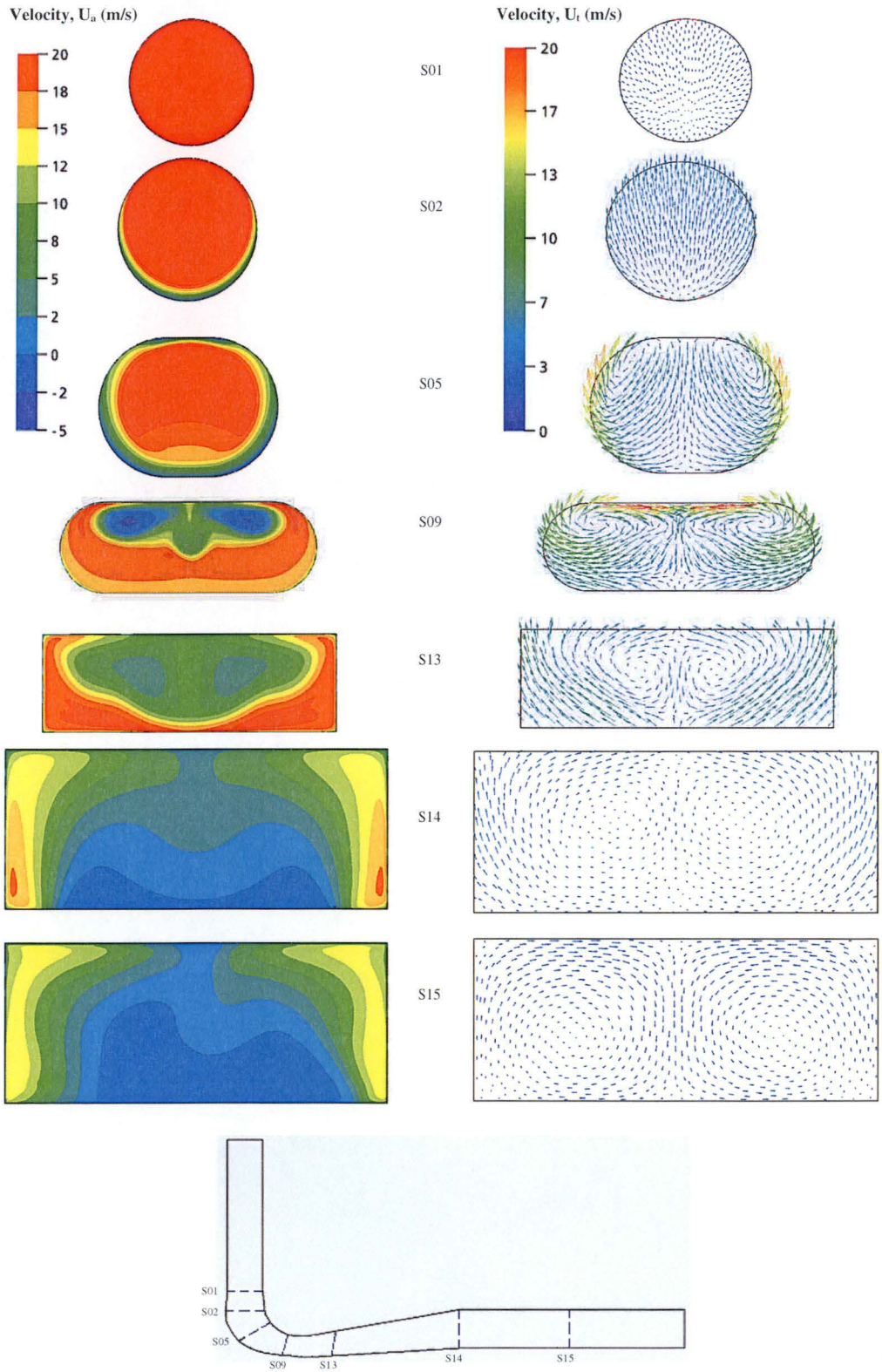

Figure 7.22: CFD Result for standard k-ε model and a mesh size of 1176000 nodes (Left: Axial Velocity Contours, Right: Secondary Velocity Vectors)

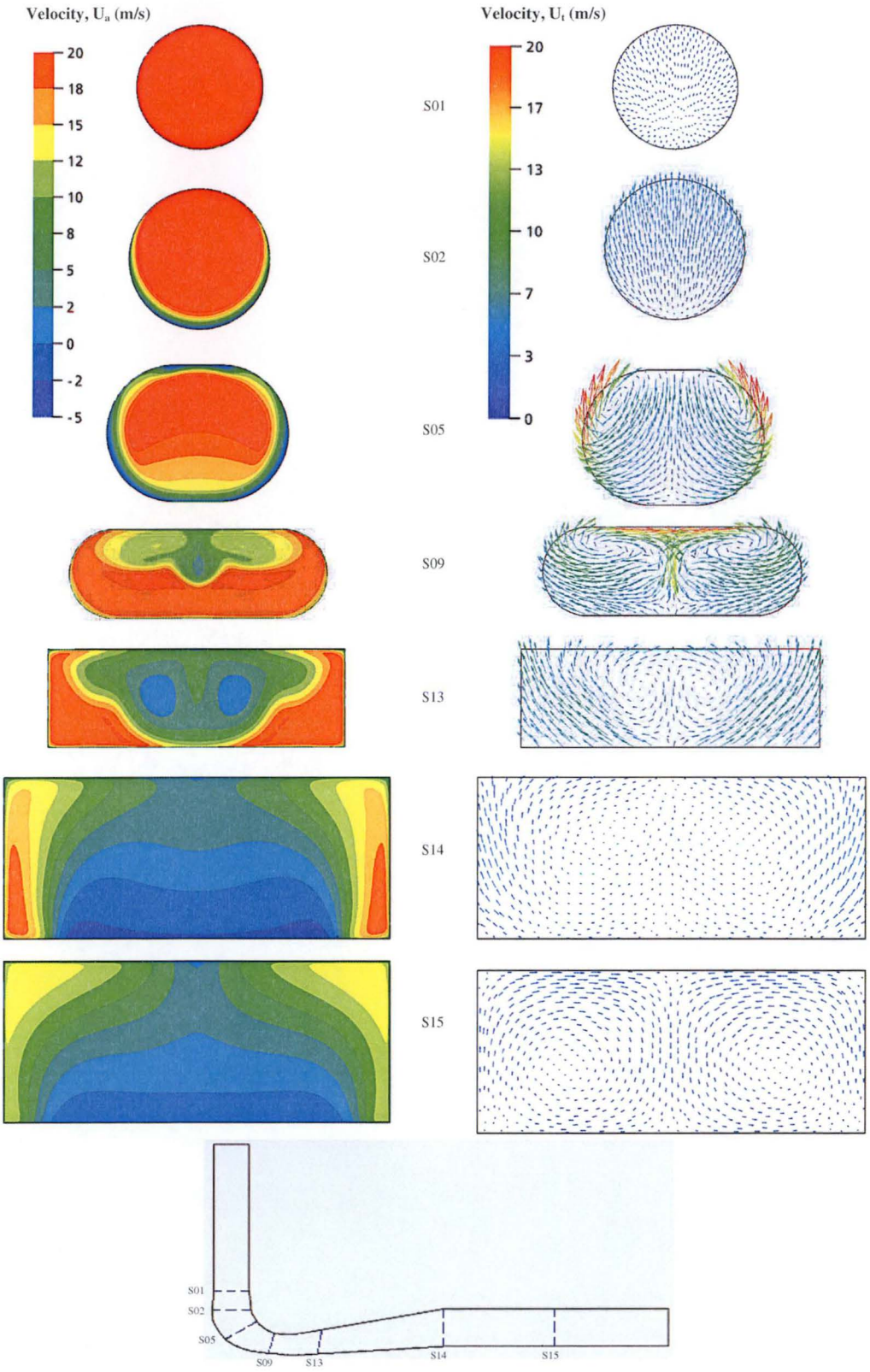

Figure 7.23: CFD Result for RNG k-ε model and a mesh size of 1176000 nodes (Left: Axial Velocity Contours, Right: Secondary Velocity Vectors)

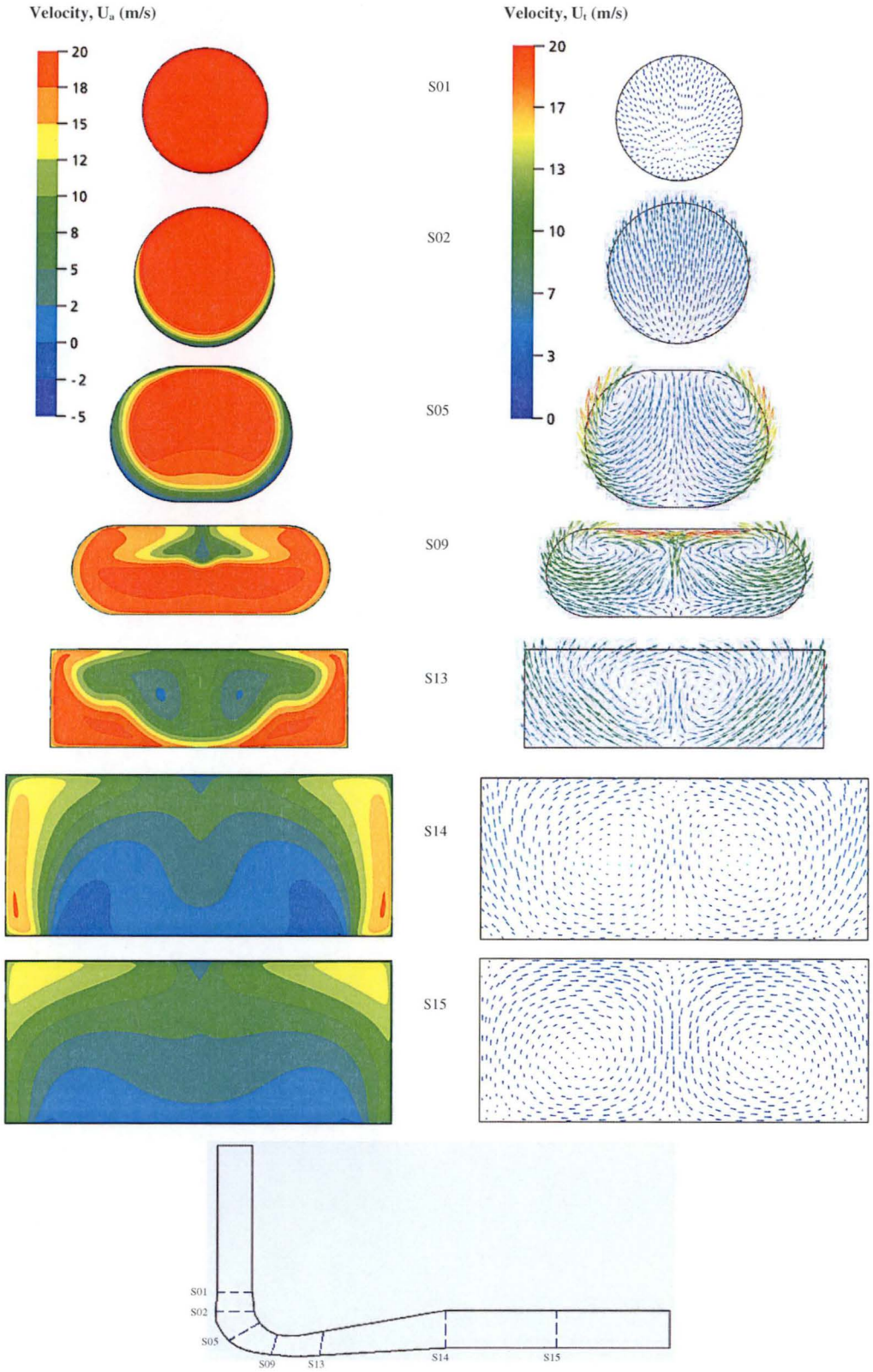

Figure 7.24: CFD Result for Wilcox's k-ω model and a mesh size of 1176000 nodes (Left: Axial Velocity Contours, Right: Secondary Velocity Vectors)

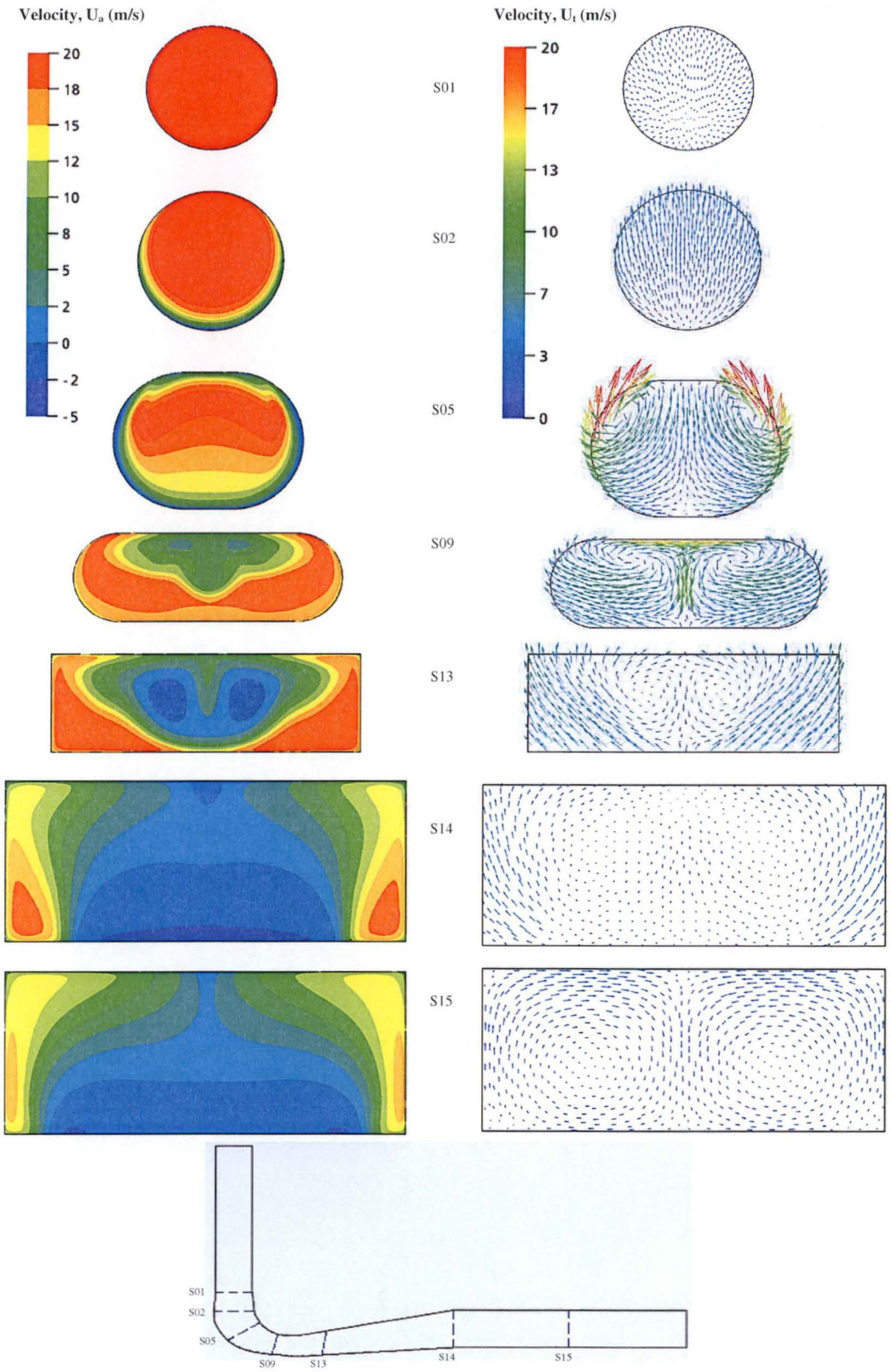

Figure 7.25: CFD Result for SST k-ω model and a mesh size of 1176000 nodes (Left: Axial Velocity Contours, Right: Secondary Velocity Vectors)

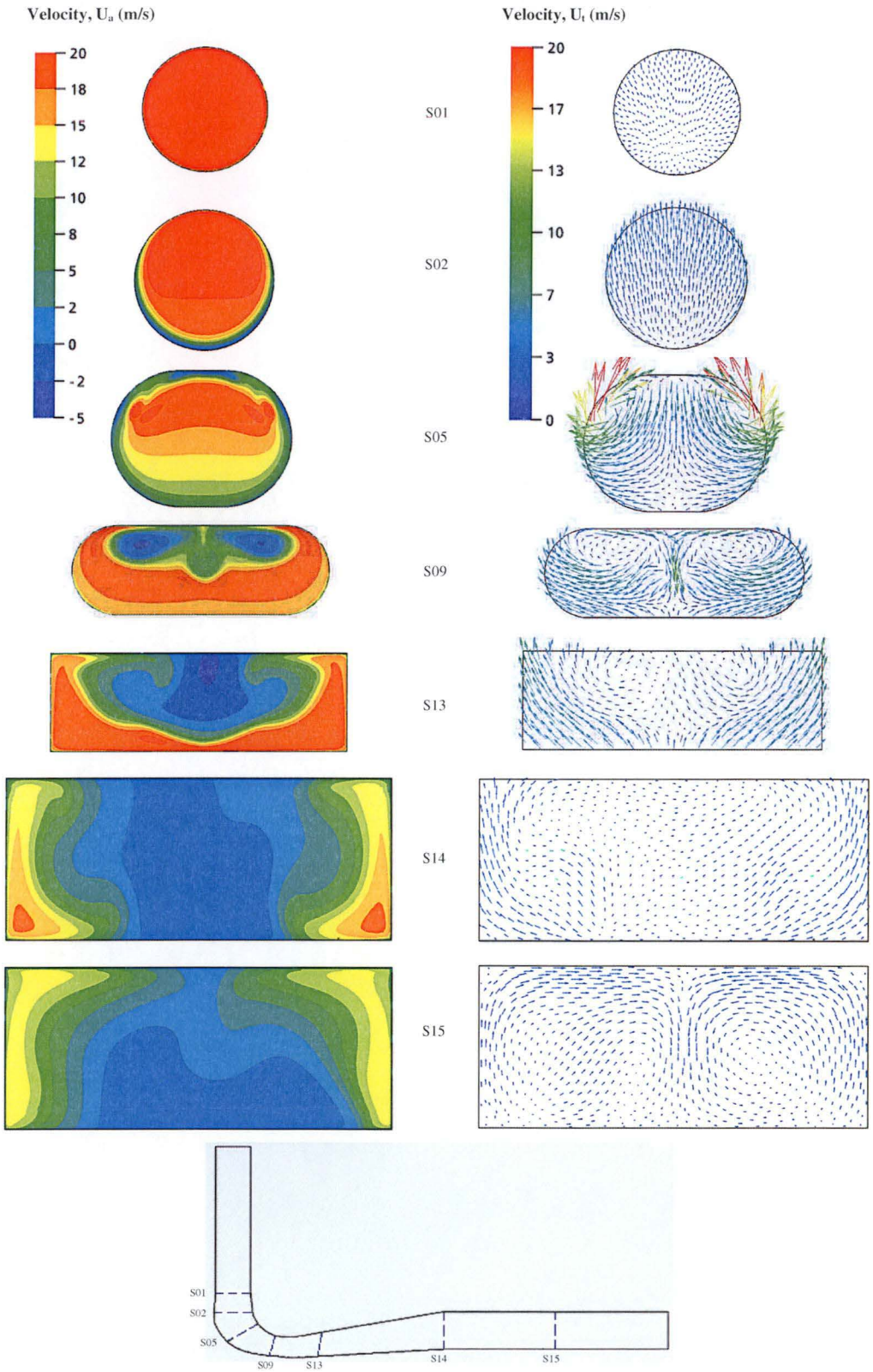

Figure 7.26: CFD Result for LRR Reynolds Stress model and a mesh size of 1176000 nodes (Left: Axial Velocity Contours, Right: Secondary Velocity Vectors)

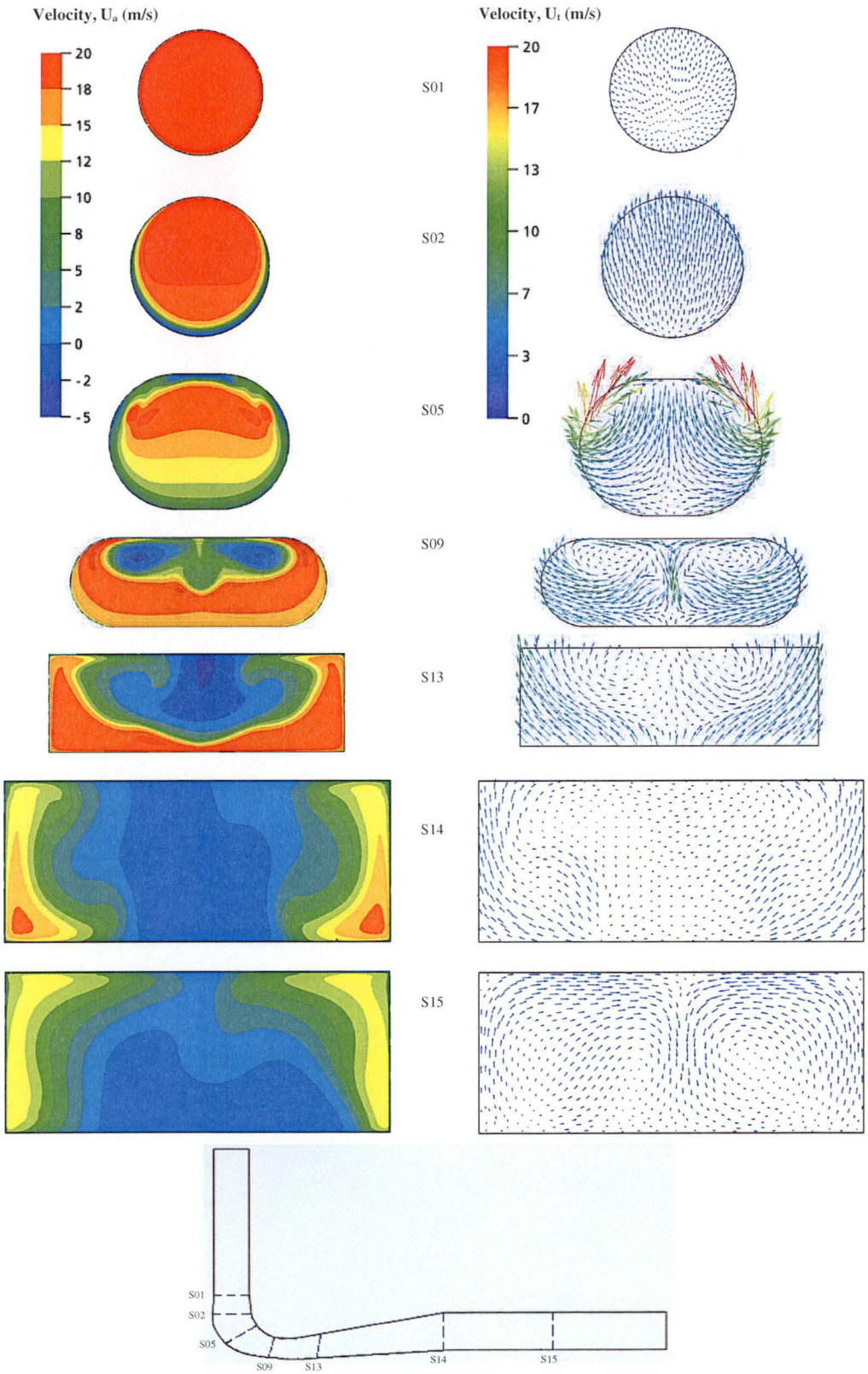

Figure 7.27: CFD Result for SSG Reynolds Stress model and a mesh size of 1176000 nodes (Left: Axial Velocity Contours, Right: Secondary Velocity Vectors)

7.3.1.3 Inlet Boundary Condition

The inlet boundary condition greatly affects the stability and accuracy of a simulation. Numerical solutions usually generate some fluctuations in static pressure near the inflow boundary. The common practice of specifying the measured velocity at the inflow boundary may result in the predicted total pressure distribution being incompatible with the actual values. This total pressure discrepancy will only be diffused slowly due to viscous effects and it can propagate throughout the solution space. This may produce faulty solutions and cause numerical instability. Hence, using the total pressure profile instead of the velocity distribution at the inlet boundary allows better control of the total pressure distribution inside the draft tube model. Other details about the boundary treatment of the inflow plane were given in Section 6.3.4.1.

Figures 7.28~7.29 shows the development of velocity profiles in the inlet pipe computed from various turbulence models. The solutions are compared with the experimental velocity profiles measured at the pipe entrance and 1.3 pipe diameters below the pipe entrance for the inlet Reynolds number of 2.51×10^5. The boundary layer properties at these two locations are presented in Tables 7.5 and 7.6. The predicted boundary layer parameters and the velocity profiles are the same for different Reynolds number cases because the same total pressure profile was used as the inlet boundary condition in the simulations. The calculated momentum and displacement thicknesses at both inlet pipe measurement stations match closely with the measured values if the eddy-viscosity turbulence models are applied. The Reynolds stress models predict a fuller velocity profile and a smaller momentum thickness at both inlet pipe stations if compared to experiment. This is surprising as Reynolds stress models are physically more realistic than the eddy viscosity models. Shape factor of around 1.8 for Reynolds stress models (refer to Table 7.6) suggests the occurrence of transitional flow at the inlet pipe. This may be due to the low Reynolds number effect at the inlet region.

The inlet turbulence level has an insignificant influence on the flow field and the draft tube performance. For a straight diffuser, increasing turbulence at the inlet generally enhances the static pressure recovery [55]. Increased free-stream turbulence promotes mixing and reduces boundary layer growth on the walls. This in turn delays the flow separation and reduces the outlet blockage, which yields improved pressure recovery. For an elbow draft tube, the effect of turbulence is likely to be diminished because of the dominating effect of the secondary flows generated by the bend [146]. The turbulence length scale at the inlet may affect the solution by altering the turbulence

dissipation rate inside the draft tube. An average turbulence length scale of 0.003 m at inlet was used in the current simulations. This value was determined automatically by the code due to lack of other information. A sensitivity analysis revealed that increasing this turbulence length scale by a factor of 10 only increased the pressure recovery factor by about 2%, and did not considerably alter the flow structure.

Turbulence Model	δ (*mm*)	δ^* (*mm*)	θ (*mm*)	δ^* / δ	*H*
Standard k-ε	6.95	0.80	0.57	0.115	1.403
RNG k-ε	6.95	0.89	0.60	0.129	1.485
Wilcox k-ω	6.65	0.74	0.54	0.112	1.375
SST k-ω	6.50	0.98	0.58	0.151	1.709
LRR Reynolds Stress	3.17	0.31	0.22	0.096	1.679
SSG Reynolds Stress	3.18	0.31	0.22	0.096	1.679
Experiment ($Re_{INLET} = 2.51 \times 10^5$)	7.64	0.81	0.54	0.106	1.612

Table 7.5: Predicted boundary layer properties at entrance to the inlet pipe. Results of various turbulence models using the same mesh with 1176000 nodes are presented

Turbulence Model	δ (*mm*)	δ^* (*mm*)	θ (*mm*)	δ^* / δ	*H*
Standard k-ε	11.40	1.30	0.85	0.114	1.525
RNG k-ε	10.45	1.33	0.85	0.127	1.556
Wilcox k-ω	11.56	1.30	0.89	0.112	1.449
SST k-ω	8.50	1.28	0.94	0.151	1.366
LRR Reynolds Stress	7.36	0.70	0.53	0.095	1.806
SSG Reynolds Stress	7.35	0.70	0.53	0.095	1.806
Experiment ($Re_{INLET} = 2.51 \times 10^5$)	13.50	1.44	0.88	0.106	1.632

Table 7.6: Predicted boundary layer properties at 1.3 pipe diameters below the pipe entrance. Results of various turbulence models using the same mesh with 1176000 nodes are presented

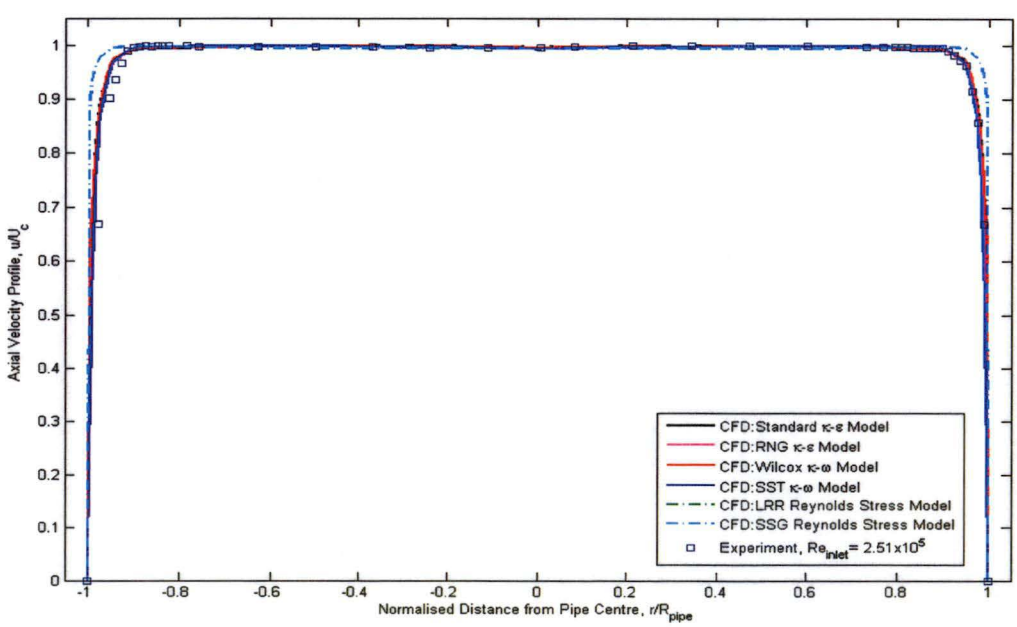

Figure 7.28: Comparisons of the experimental and computed velocity profiles at pipe entrance

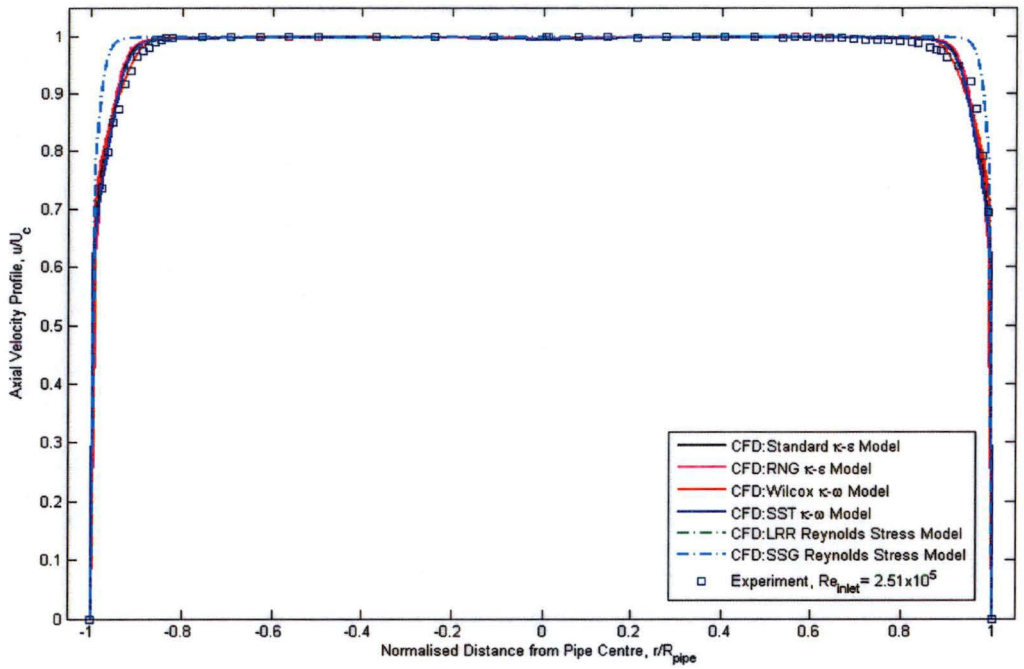

Figure 7.29: Comparisons of the experimental and computed velocity profiles at 1.3 pipe diameters below pipe entrance

7.3.1.4 Outlet Boundary Condition

As mentioned in Section 6.3.4.2, an extension of the outlet boundary was necessary in the CFD computation. RANS equations may behave elliptically and so the flow at the draft tube exit may significantly affect the flow inside the draft tube. A conventional approach that does not allow for information exchange at the outlet could lead to numerical instabilities. Elongation of the computational volume in the downstream direction was found to improve the convergence. This modification moves the outflow boundary downstream to a position where an assumption of zero gradients and constant static pressure is more realistic. The standard outflow boundary condition with zero diffusion fluxes for all flow variables cannot be used directly at the draft tube outlet, due to the existence of normal gradients of variables and possible back flow.

Mauri [75] investigated the effects of different geometrical treatments (simple box and cylindrical tank) for the draft tube outlet condition and found that the shape of the outlet channel did not affect the flow field inside the draft tube. Hence, the current study uses a simple rectangular box that has the same cross-sectional area as the draft tube outlet to resolve the outflow boundary condition. Table 7.7 shows the effect of extending the

outlet region to a distance L from the exit. For simplicity, only the solutions of the standard k-ε model are presented here. The convergence of the solutions is significantly improved when the outlet boundary is placed at a distance of about 5 times the outlet height (H_{outlet}) of the draft tube model. Further elongation does not affect the convergence rate or change the flow quantities of the draft tube, but only increases the computational time and resources required.

Distance of Elongation from Draft Tube Exit, L	*Maximum Residual Level after 200 Iteration Loops*	*Static Pressure Recovery Factor, $Cp_{recovery}$*	*Total Pressure Loss Coefficient, k_{loss}*
$0.5 \times H_{outlet}$	5.45×10^{-3}	0.5843	0.1992
$1.0 \times H_{outlet}$	3.21×10^{-3}	0.5835	0.1989
$2.0 \times H_{outlet}$	1.07×10^{-3}	0.5827	0.1973
$4.0 \times H_{outlet}$	2.86×10^{-4}	0.5814	0.1938
$5.0 \times H_{outlet}$	1.06×10^{-5}	0.5810	0.1937
$6.5 \times H_{outlet}$	1.05×10^{-5}	0.5809	0.1937
$8.0 \times H_{outlet}$	1.04×10^{-5}	0.5809	0.1937
$10.0 \times H_{outlet}$	1.05×10^{-5}	0.5809	0.1937

Table 7.7: Effect of the distance of passage elongation (L) from the draft tube exit. The solution is based on the standard k-ε model and identical mesh size within the draft tube

7.3.2 Validations

Validation of a CFD simulation consists of the process of determining the extent to which a computational model can accurately describe the real flow behaviour in a particular application. Validation of a CFD calculation aims to "solve the right equations" by comparing it to the experimental data [103]. The main objective is to identify and assess the difference between the experimental and numerical results. Experimental data collected at the inlet Reynolds numbers of 2.51×10^5 and 1.06×10^5 are used for validation of the steady-state CFD solutions herein.

The CFD simulations are all based on a mesh size of 1176000 nodes. Solutions of different turbulence models will be presented in the following subsections. It should be noted that the experimental techniques (see Section 6.2) used in the current analysis are also imperfect, and it makes no sense to expect or even look for computational agreement finer than this experimental uncertainty [1]. The estimated errors for experimental measurements were discussed in Section 6.2, while details of the commercial package ANSYS CFX used for CFD simulations were given in Section 6.3.

7.3.2.1 Static Pressure Distributions

Figure 7.30~7.35 shows the centreline static pressure distributions on the top, bottom, and side walls of the draft tube model. The standard k-ε, RNG k-ε, and Wilcox k-ω models all underestimate the amount of static pressure drop near the end of the bend. The static pressure rise on the top centreline after the inlet cone of the draft tube is over-predicted by all eddy-viscosity models. Over-prediction of the static pressure in the separated zone is common for the eddy-viscosity models. Reynolds stress models compute the magnitude of static pressures along the bend quite close to the experimental values. All models except the standard k-ε and Wilcox k-ω predict a bump in the static pressure distribution on the top centreline that is not seen in the measurements. Surface smoothness and geometry imperfection may have caused some perturbation in the experimental values. It is also observed that the Reynolds stress models are very sensitive to the changes of the inflow and outflow conditions. The same total pressure profile and constant outlet static pressure does not work well in low Reynolds number cases for both LRR and SSG Reynolds stress models. This emphasises the need of detailed boundary conditions to get reasonable predictions from the differential Reynolds stress models.

7.3.2.2 Velocity Traverses

Figures 7.36~7.47 compare the CFD solutions with the hotwire velocity measurements. Overall, the standard k-ε model seems to predict the time-averaged velocity profile reasonably close to the hotwire results, given the uncertainty in the hotwire data.

For Station V1c, the standard k-ε and Wilcox k-ω models predict the magnitude and the shape of the velocity profile closest to the experimental velocity distribution. Other turbulence models calculate a steeper velocity gradient and a faster drop in the velocity peak near the bottom wall. The SST k-ω and Reynolds stress models also predict a high peak in the velocity near the top wall, which is not detected by the hotwire and four-hole probe. For Stations V2c~V5c, solutions of the standard k-ε model still match reasonably well with the hotwire results, although the model predicts a small flow reversal at the outlet. Flow reversal is a phenomenon that the hotwire probe is unable to resolve in the experiment. The SST k-ω and Reynolds stress models predict a larger backflow region at Stations V2c and V3c. Four-hole probe data indicate that the flow angles are highly fluctuating in these measurement locations. It is therefore not surprising that different turbulence models generate very different velocity distributions

at these positions. For Station H1c, all turbulence models predict a similar flow distribution to the hotwire measurements. Velocity peaks at a location near the sidewall and slowly decays towards the duct centre. However, solutions of RNG k-ε, Wilcox k-ω, and Reynolds stress models show some peaks in velocity halfway through or near the duct centre. This flow phenomenon is not captured by the hotwire. The standard k-ε and SST k-ω models, on the other hand, predict a smoother decay in the velocity towards the duct centre. For Stations H2c~H5c, the predicted locations of the velocity peaks are closer to the sidewall for all turbulence models than in the hotwire data. All models successfully predict a drop in the magnitude of the velocity peaks as the flow travels further downstream. However, the Reynolds stress models also predict some flow asymmetries around the centre of the duct. The hotwire data cannot confirm this, as only half the duct was traversed in the experiment. It is possible that flow asymmetries may exist, as tuft visualisation showed unsteady flow angles at these locations.

7.3.2.3 Turbulence Profiles

Figures 7.48~7.53 compare the turbulence profiles derived from the computational models with the hotwire measurements. Eddy-viscosity models do not calculate the normal stresses directly. As isotropic turbulence is assumed in these models, the local turbulence intensity (I) of the CFD solutions can be determined via the relationship:

$$I = \frac{u_{rms}}{U_{mean}} = \frac{2\sqrt{k_{Turb}}}{3U_{mean}} \tag{7.6}$$

where k_{Turb} = turbulence kinetic energy (m^2/s^2)

For Reynolds stress models, the turbulence intensity can be obtained directly from the solution since all Reynolds stress components are being modelled in this case. The eddy-viscosity models compute the turbulence intensity surprisingly well. The Reynolds stress models underestimate the amount of fluid turbulence at the location immediately after the bend (Station H1c) as well as slightly over-predicting the magnitude of turbulence intensity further downstream compared to the hotwire results. The difference is expected, as eddy-viscosity models generally predict a higher turbulence levels in the flows. The sources of discrepancies between the numerical and experimental profiles of streamwise turbulence intensity cannot be identified, due to the lack of information on other turbulent stress components.

7.3.2.4 Skin Friction Distributions

Figures 7.54~7.57 show the comparisons of skin friction measurements with the computed values at the bottom and right centrelines of the draft tube model. The skin friction values predicted by all turbulence models are generally lower than the values measured by the Preston tube. However, all models capture the general pattern of the measured skin friction distributions. For the bottom centreline, skin friction values drop sharply near the inlet cone region of the draft tube but gradually rise towards the end of the bend. A large portion of the pressure loss is therefore expected to occur within the bend. After a peak in the magnitude of skin friction near the end of the bend, the values decrease again in the rectangular diffusing section of the draft tube.

A nearly zero skin friction is predicted by all turbulence models along the bottom centreline, which implies that the local flow separation may occur on the bottom surface. The first location of zero skin friction predicted by different turbulence models varies between 120~160 mm from draft tube inlet. This first location of separation is important for the draft tube flow because it may induce flow instabilities further downstream. However, the Preston tube measurements are not able to confirm these findings due to the limited amount of data collected during the experiments and the inherent drawbacks of the Preston tube for measuring skin friction in three-dimensional flows.

For the right centreline, the trends of the skin friction in the bend vary significantly with the different turbulence models used. Solutions of the SST k-ω and Reynolds stress models show a very high jump in the skin friction, while others predict a relatively small peak in magnitude of the skin frictions along the bend. The values of skin friction at the sidewalls are well above zero, which suggests a lower likelihood of flow separation at these locations.

Berca et al. [12] argue that the classical log-law approach is not valid for the turbine draft tube, as the measured boundary layer on the cone wall does not agree well with the results derived from von Karman-Prandtl universal logarithmic law. Three-dimensional boundary layer, adverse pressure gradient, and the unsteady nature of the sheared flow may significantly affect the accuracy of log-law approach and therefore the prediction of skin friction using the wall function approach inside the draft tube is questionable. The experimental skin friction values are similarly questionable, as the Preston tube calibration is also based on the assumptions of logarithmic similarity in the wall layer.

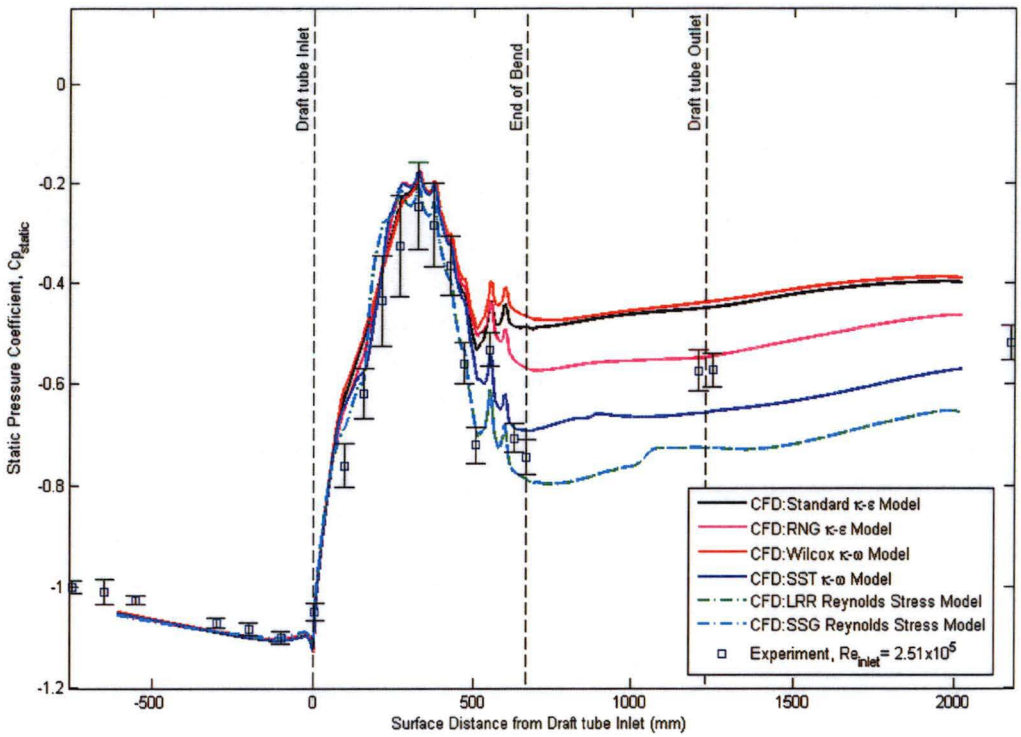

Figure 7.30: Comparison of experimental measurement and CFD prediction of wall static pressure distribution along the bottom centreline of the model at inlet Reynolds number of 2.51×10^5 (mesh size: 1176000 nodes)

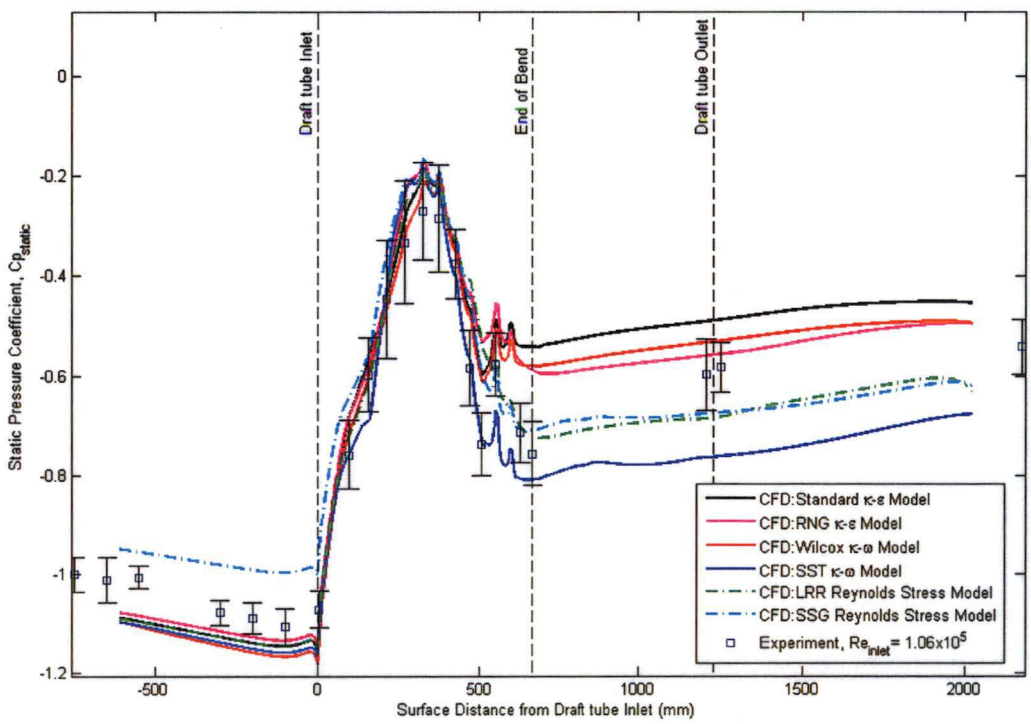

Figure 7.31: Comparison of experimental measurement and CFD prediction of wall static pressure distribution along the bottom centreline of the model at inlet Reynolds number of 1.06×10^5 (mesh size: 1176000 nodes)

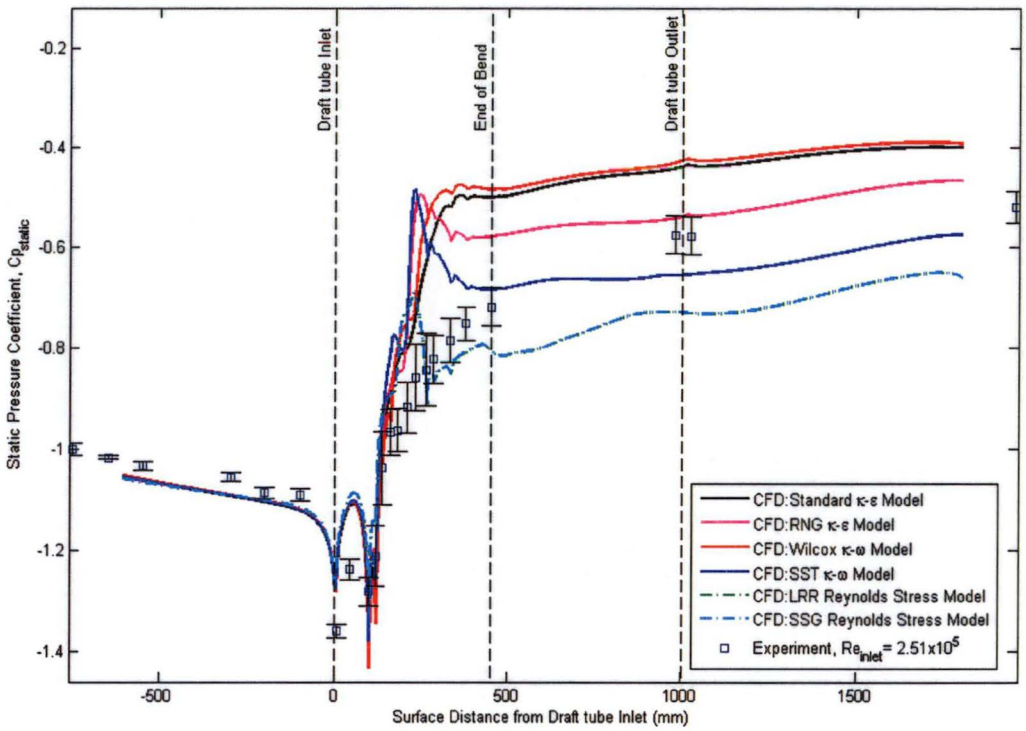

Figure 7.32: Comparison of experimental measurement and CFD prediction of wall static pressure distribution along the top centreline of the model at inlet Reynolds number of 2.51×10^5 (mesh size: 1176000 nodes)

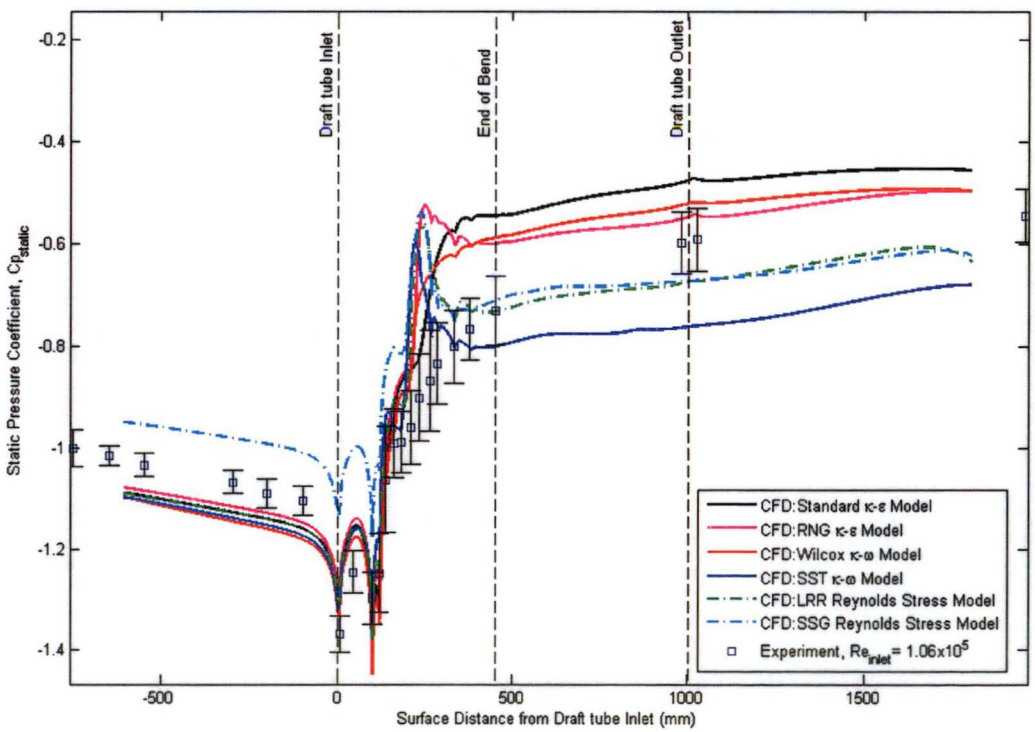

Figure 7.33: Comparison of experimental measurement and CFD prediction of wall static pressure distribution along the top centreline of the model at inlet Reynolds number of 1.06×10^5 (mesh size: 1176000 nodes)

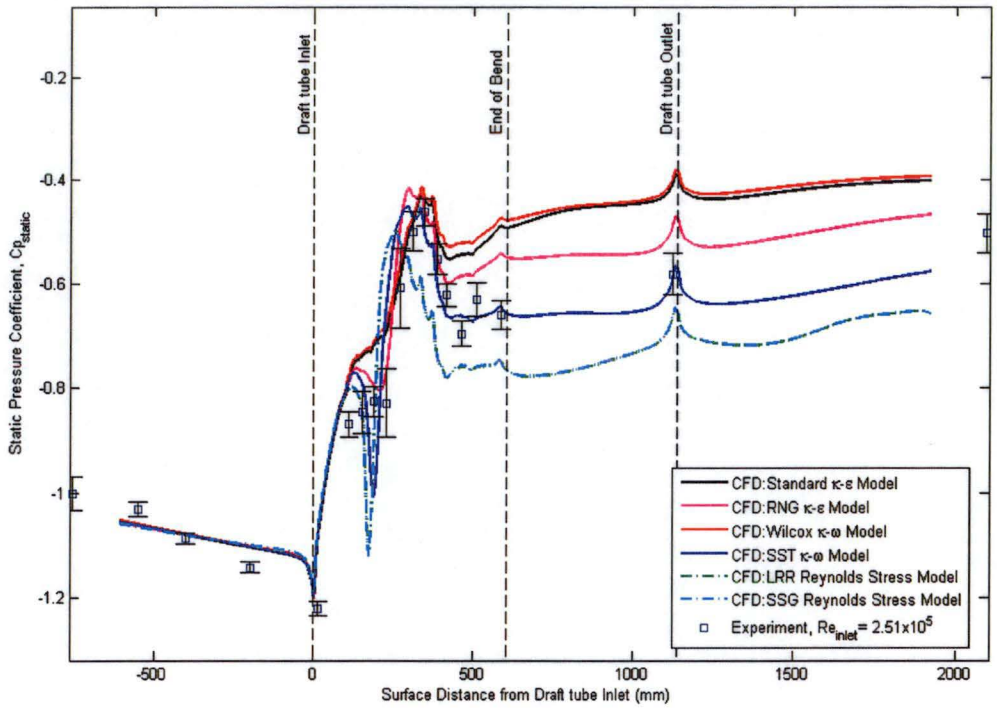

Figure 7.34: Comparison of experimental measurement and CFD prediction of wall static pressure distribution along the right/left centreline of the model at inlet Reynolds number of 2.51×10^5 (mesh size: 1176000 nodes)

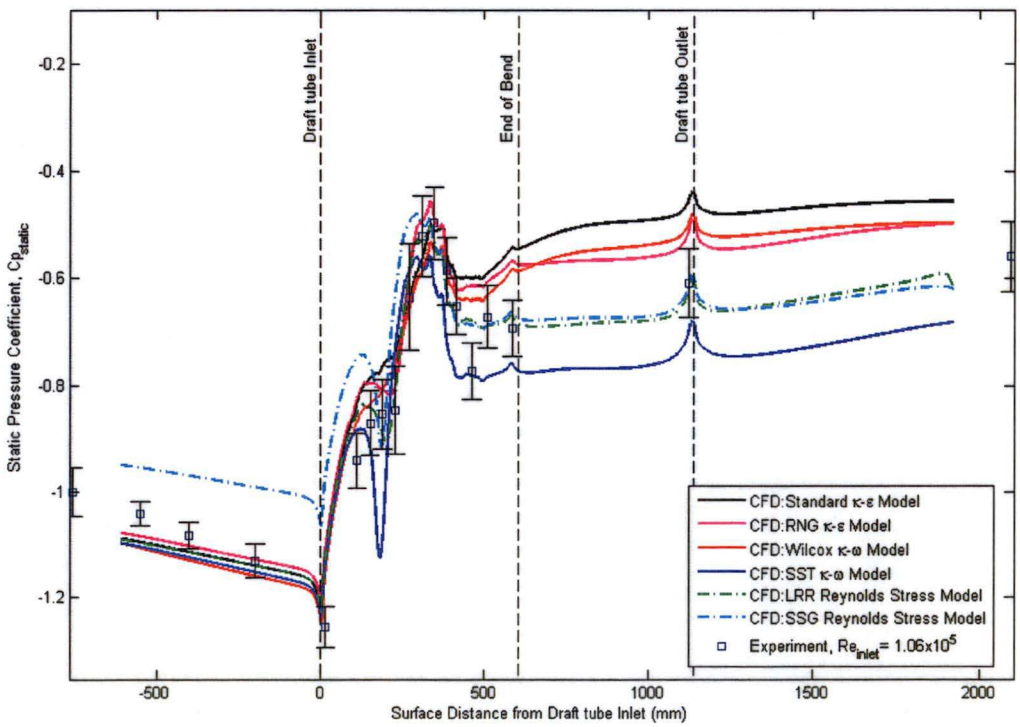

Figure 7.35: Comparison of experimental measurement and CFD prediction of wall static pressure distribution along the right/left centreline of the model at inlet Reynolds number of 1.06×10^5 (mesh size: 1176000 nodes)

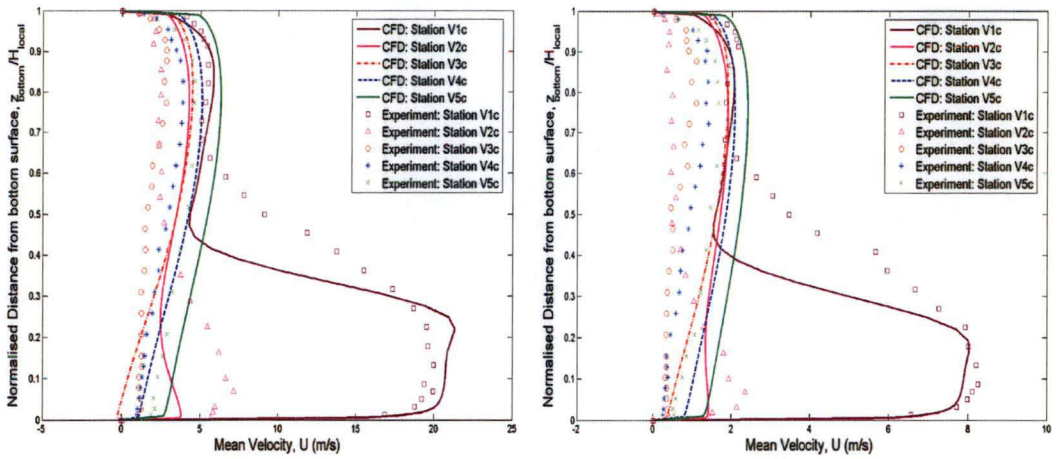

Figure 7.36: Comparison of experimental and predicted velocity profiles for vertical traverse along the centre plane of the model at inlet Reynolds numbers of 2.51×10^5 (left) and 1.06×10^5 (right) (mesh size: 1176000 nodes, turbulence model: *standard k-ε Model*)

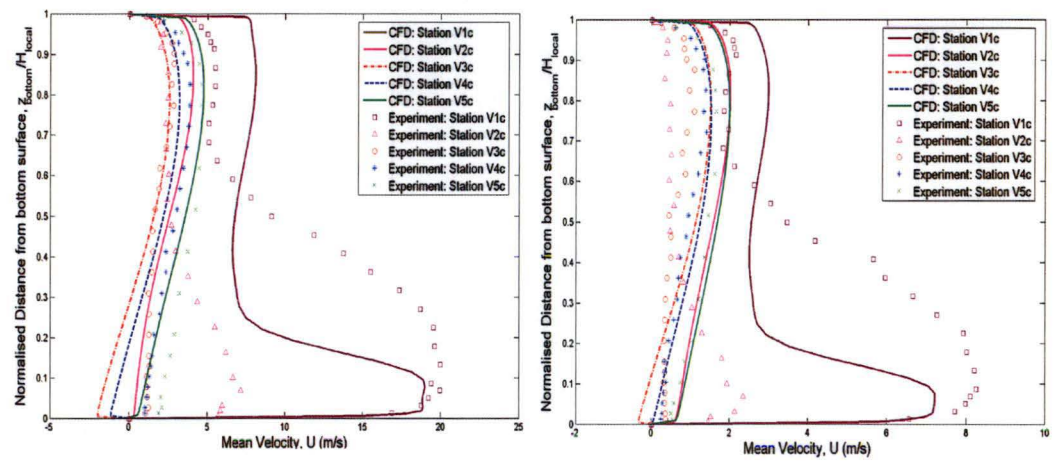

Figure 7.37: Comparison of experimental and predicted velocity profiles for vertical traverse along the centre plane of the model at inlet Reynolds numbers of 2.51×10^5 (left) and 1.06×10^5 (right) (mesh size: 1176000 nodes, turbulence model: *RNG k-ε Model*)

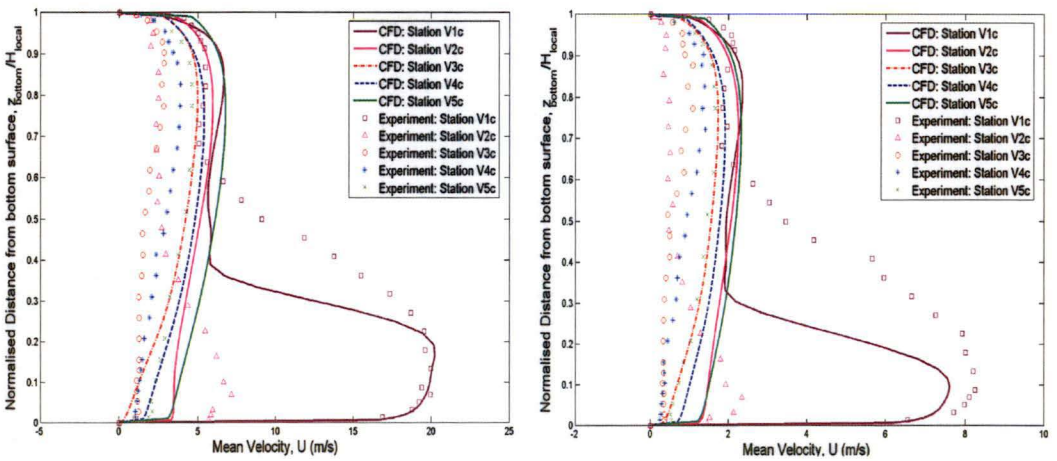

Figure 7.38: Comparison of experimental and predicted velocity profiles for vertical traverse along the centre plane of the model at inlet Reynolds numbers of 2.51×10^5 (left) and 1.06×10^5 (right) (mesh size: 1176000 nodes, turbulence model: *Wilcox k-ω Model*)

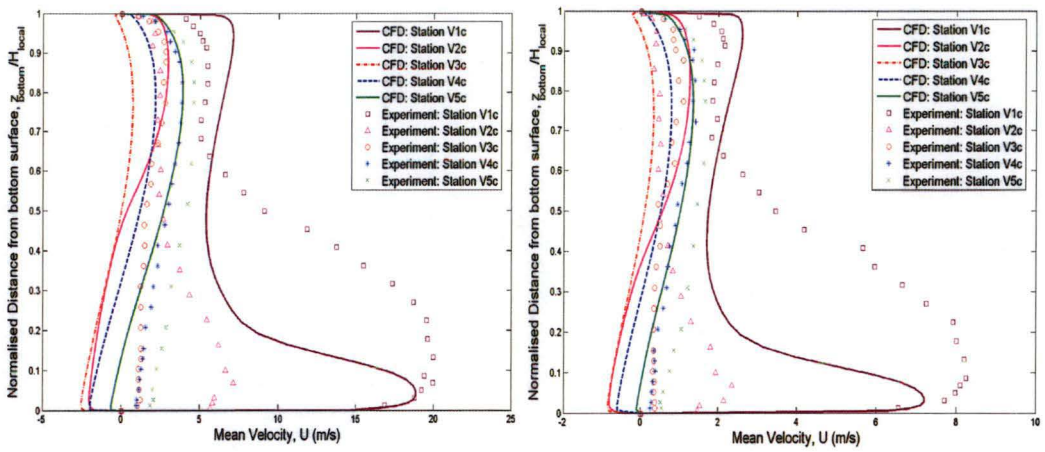

Figure 7.39: Comparison of experimental and predicted velocity profiles for vertical traverse along the centre plane of the model at inlet Reynolds numbers of 2.51×10^5 (left) and 1.06×10^5 (right) (mesh size: 1176000 nodes, turbulence model: *SST k-ω Model*)

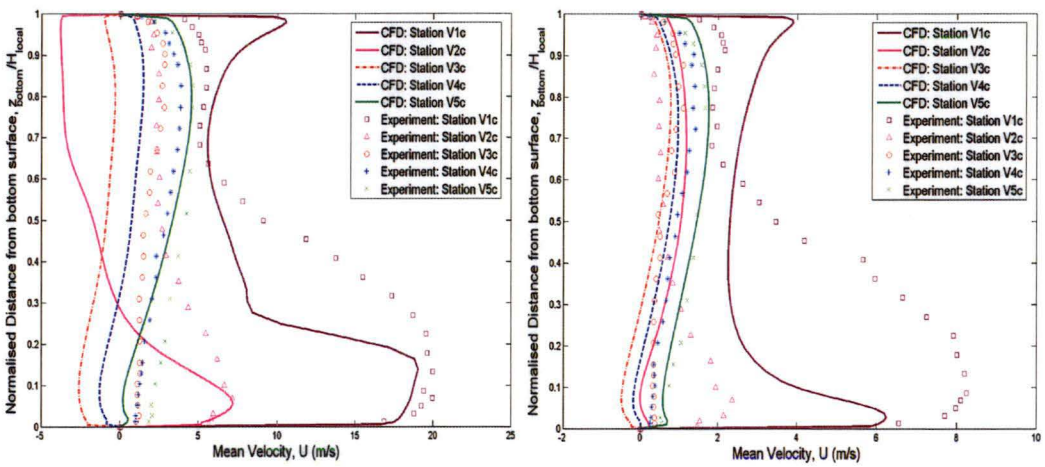

Figure 7.40: Comparison of experimental and predicted velocity profiles for vertical traverse along the centre plane of the model at inlet Reynolds numbers of 2.51×10^5 (left) and 1.06×10^5 (right) (mesh size: 1176000 nodes, turbulence model: *LRR Reynolds Stress Model*)

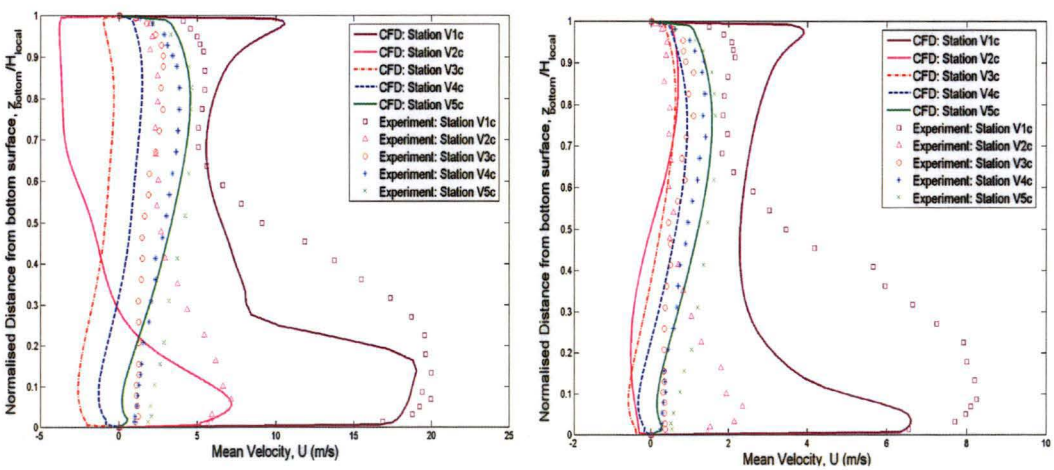

Figure 7.41: Comparison of experimental and predicted velocity profiles for vertical traverse along the centre plane of the model at inlet Reynolds numbers of 2.51×10^5 (left) and 1.06×10^5 (right) (mesh size: 1176000 nodes, turbulence model: *SSG Reynolds Stress Model*)

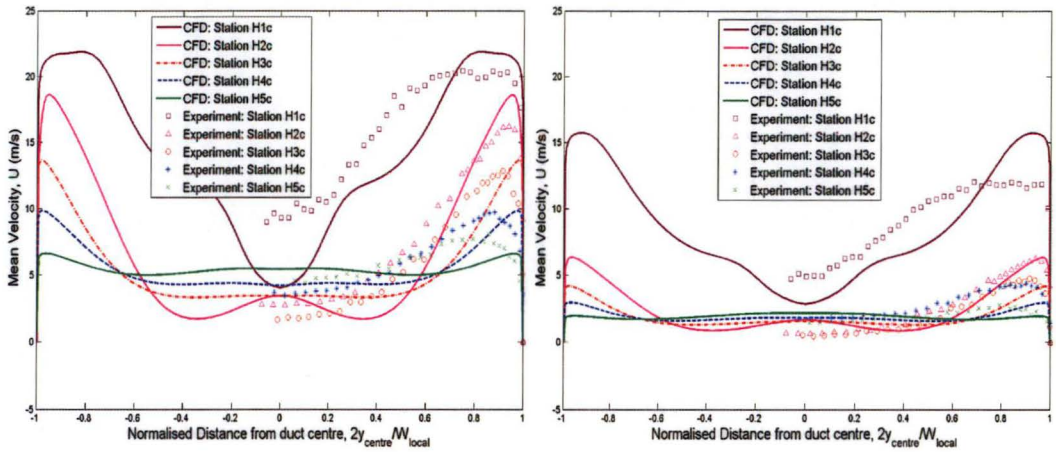

Figure 7.42: Comparison of experimental and predicted velocity profiles for horizontal traverse along the duct centre at inlet Reynolds numbers of 2.51×10^5 (left) and 1.06×10^5 (right) (mesh size: 1176000 nodes, turbulence model: *standard k-ε Model*)

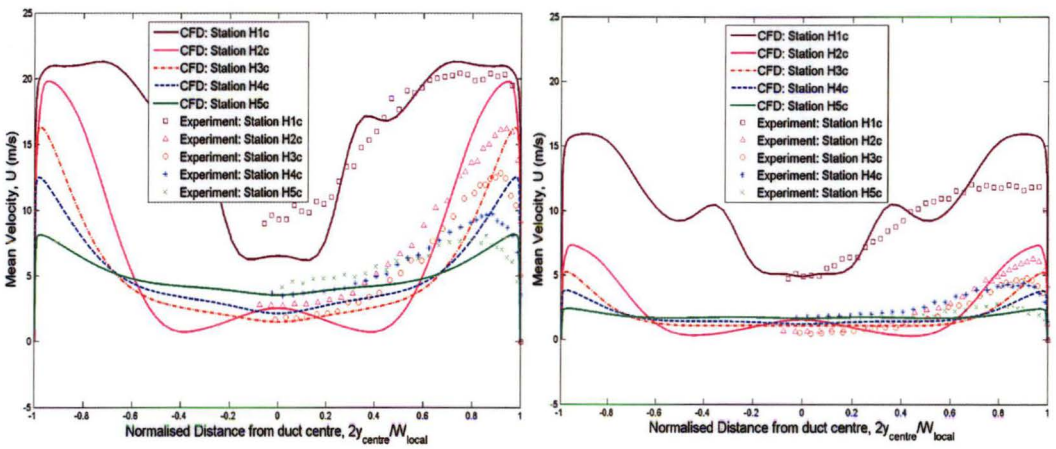

Figure 7.43: Comparison of experimental and predicted velocity profiles for horizontal traverse along the duct centre at inlet Reynolds numbers of 2.51×10^5 (left) and 1.06×10^5 (right) (mesh size: 1176000 nodes, turbulence model: *RNG k-ε Model*)

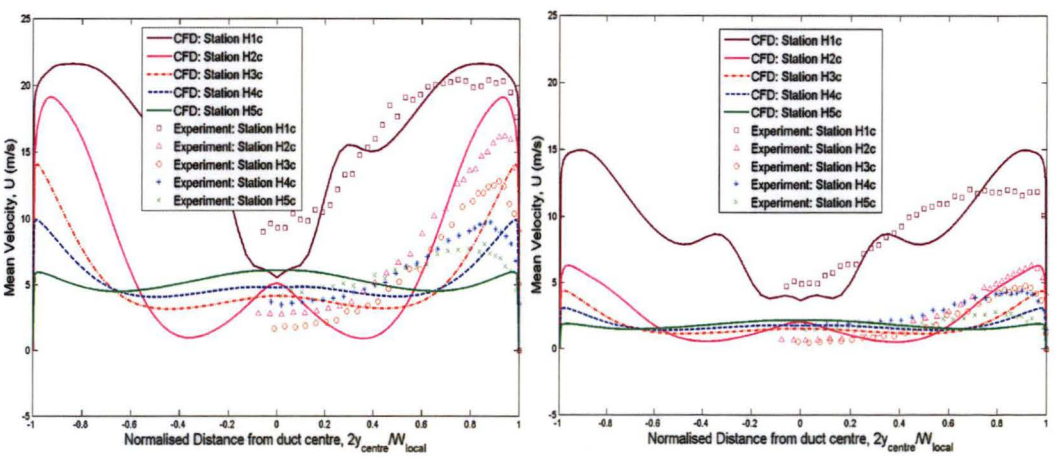

Figure 7.44: Comparison of experimental and predicted velocity profiles for horizontal traverse along the duct centre at inlet Reynolds numbers of 2.51×10^5 (left) and 1.06×10^5 (right) (mesh size: 1176000 nodes, turbulence model: *Wilcox k-ω Model*)

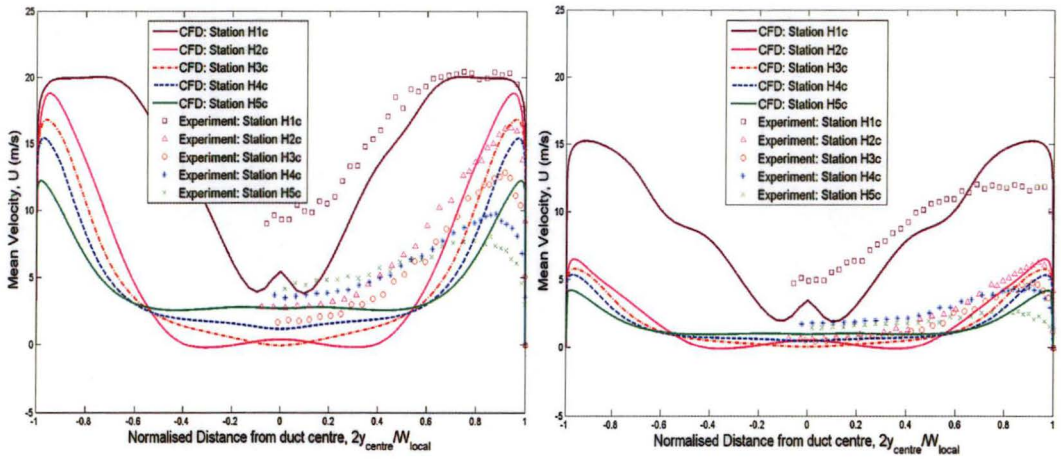

Figure 7.45: Comparison of experimental and predicted velocity profiles for horizontal traverse along the duct centre at inlet Reynolds numbers of 2.51×10^5 (left) and 1.06×10^5 (right) (mesh size: 1176000 nodes, turbulence model: *SST k-ω Model*)

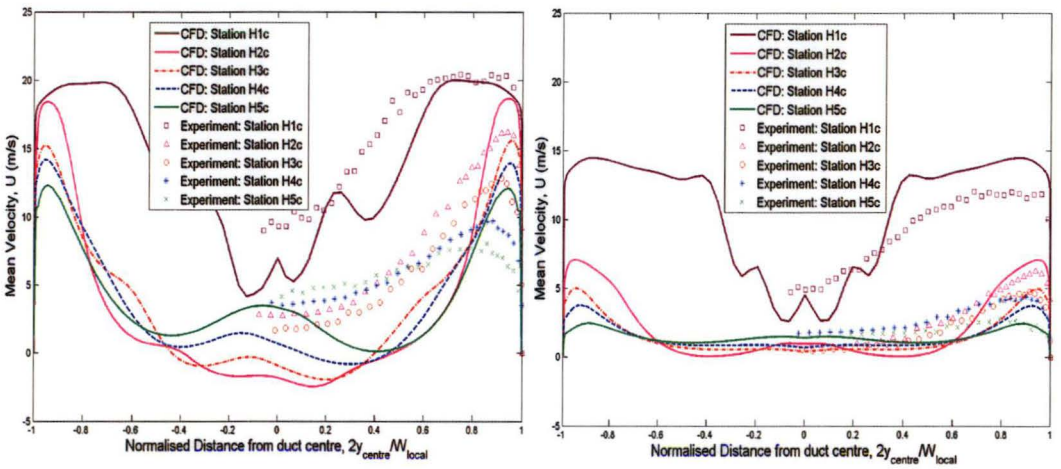

Figure 7.46: Comparison of experimental and predicted velocity profiles for horizontal traverse along the duct centre at inlet Reynolds numbers of 2.51×10^5 (left) and 1.06×10^5 (right) (mesh size: 1176000 nodes, turbulence model: *LRR Reynolds Stress Model*)

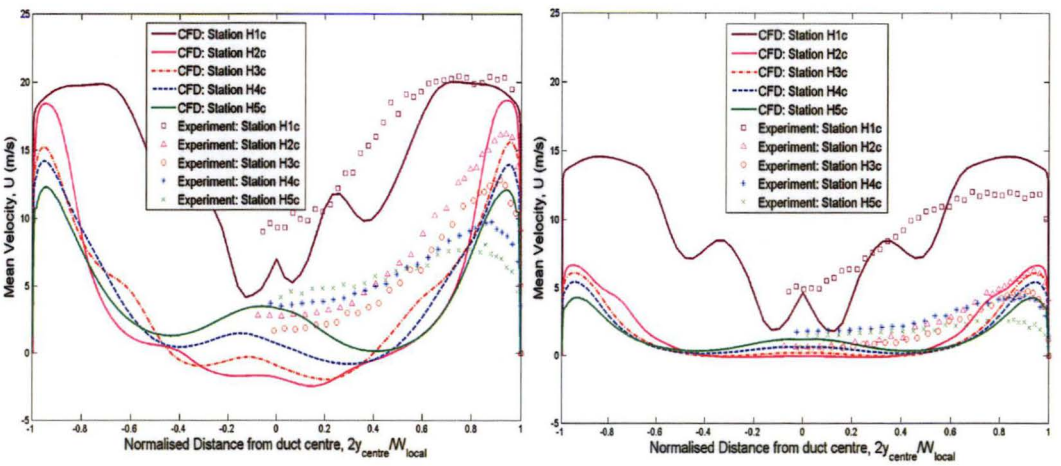

Figure 7.47: Comparison of experimental and predicted velocity profiles for horizontal traverse along the duct centre at inlet Reynolds numbers of 2.51×10^5 (left) and 1.06×10^5 (right) (mesh size: 1176000 nodes, turbulence model: *SSG Reynolds Stress Model*)

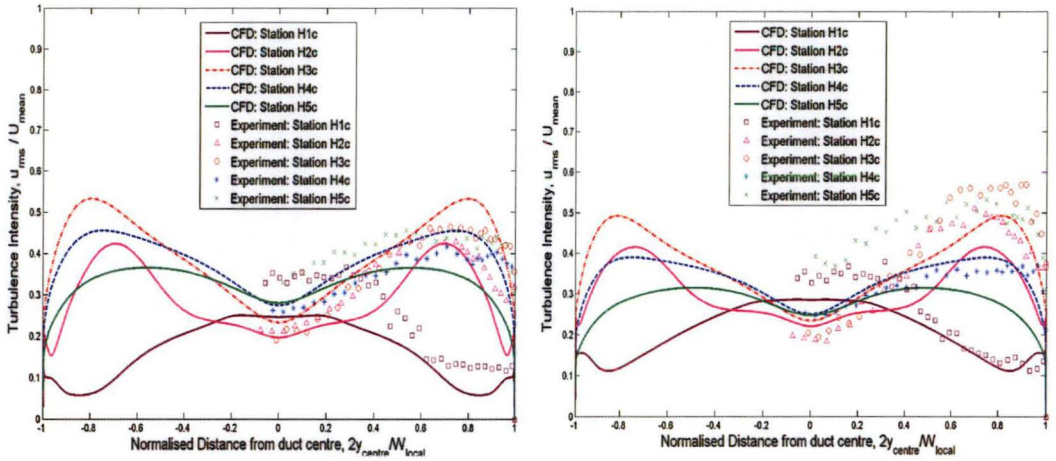

Figure 7.48: Comparison of experimental and predicted turbulence (normal stress) profiles for horizontal traverse along the duct centre at inlet Reynolds numbers of 2.51×10^5 (left) and 1.06×10^5 (right) (mesh size: 1176000 nodes, turbulence model: *standard k-ε Model*)

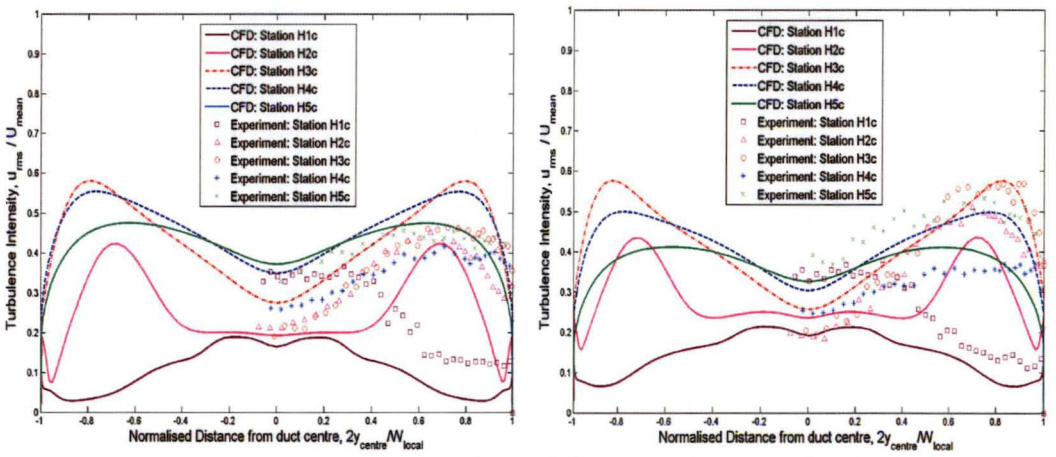

Figure 7.49: Comparison of experimental and predicted turbulence (normal stress) profiles for horizontal traverse along the duct centre at inlet Reynolds numbers of 2.51×10^5 (left) and 1.06×10^5 (right) (mesh size: 1176000 nodes, turbulence model: *RNG k-ε Model*)

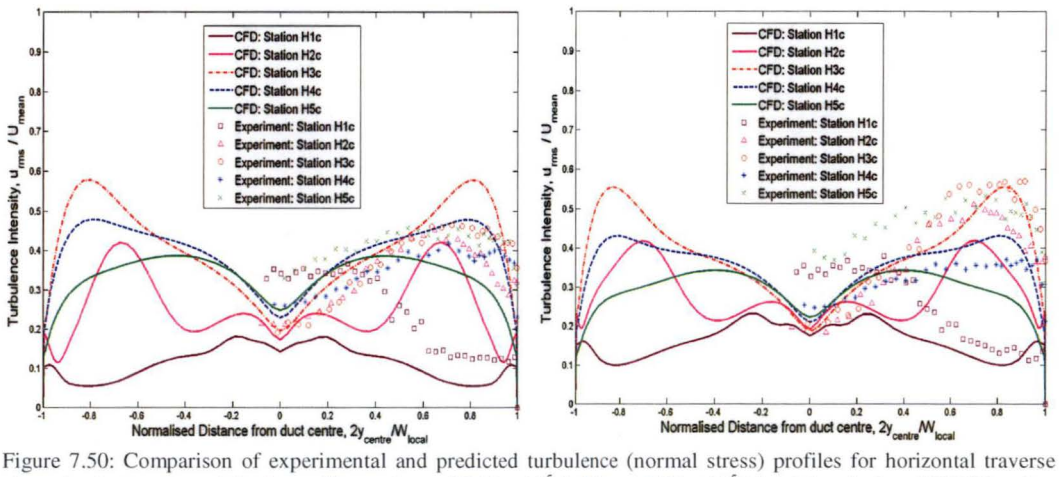

Figure 7.50: Comparison of experimental and predicted turbulence (normal stress) profiles for horizontal traverse along the duct centre at inlet Reynolds numbers of 2.51×10^5 (left) and 1.06×10^5 (right) (mesh size: 1176000 nodes, turbulence model: *Wilcox k-ω Model*)

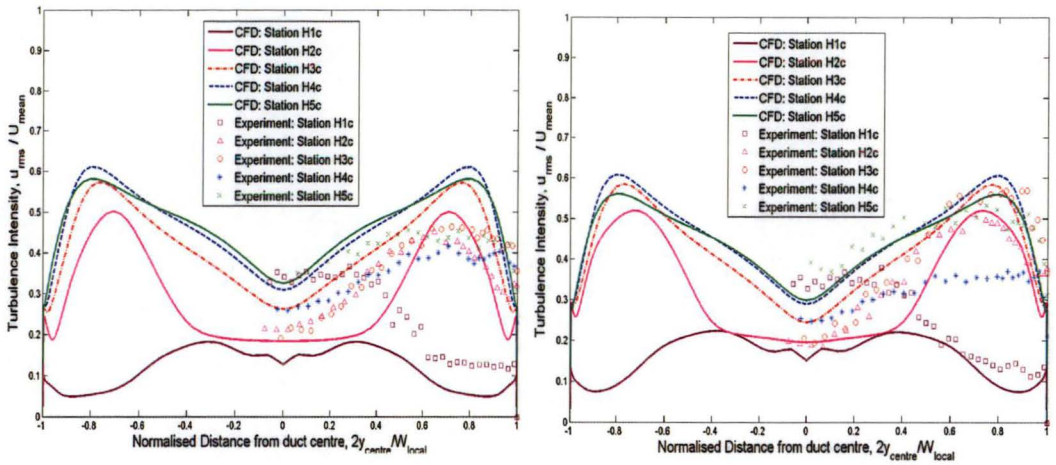

Figure 7.51: Comparison of experimental and predicted turbulence (normal stress) profiles for horizontal traverse along the duct centre at inlet Reynolds numbers of 2.51×10^5 (left) and 1.06×10^5 (right) (mesh size: 1176000 nodes, turbulence model: *SST k-ω Model*)

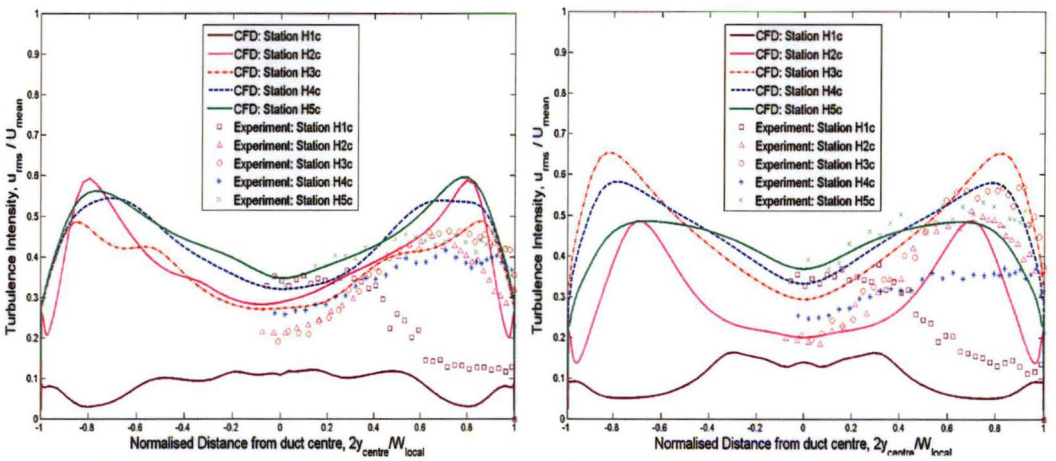

Figure 7.52: Comparison of experimental and predicted turbulence (normal stress) profiles for horizontal traverse along the duct centre at inlet Reynolds numbers of 2.51×10^5 (left) and 1.06×10^5 (right) (mesh size: 1176000 nodes, turbulence model: *LRR Reynolds Stress Model*)

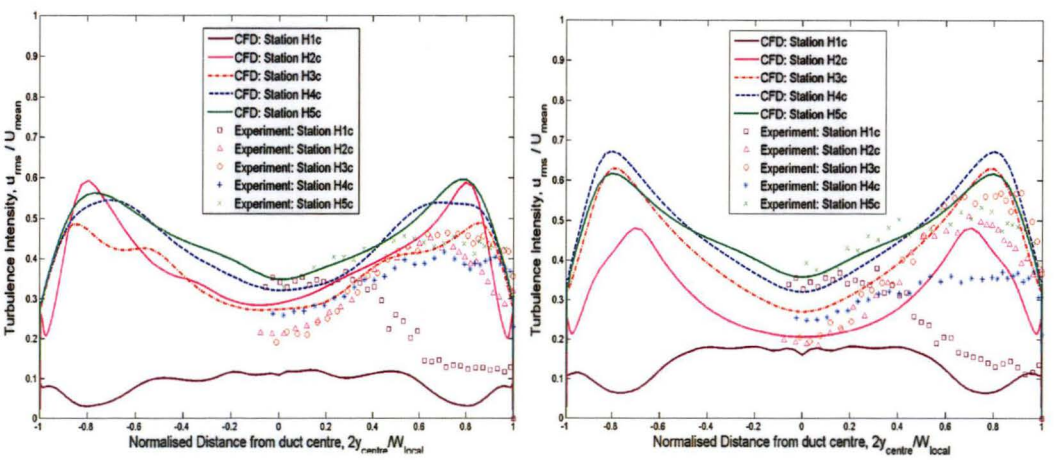

Figure 7.53: Comparison of experimental and predicted turbulence (normal stress) profiles for horizontal traverse along the duct centre at inlet Reynolds numbers of 2.51×10^5 (left) and 1.06×10^5 (right) (mesh size: 1176000 nodes, turbulence model: *SSG Reynolds Stress Model*)

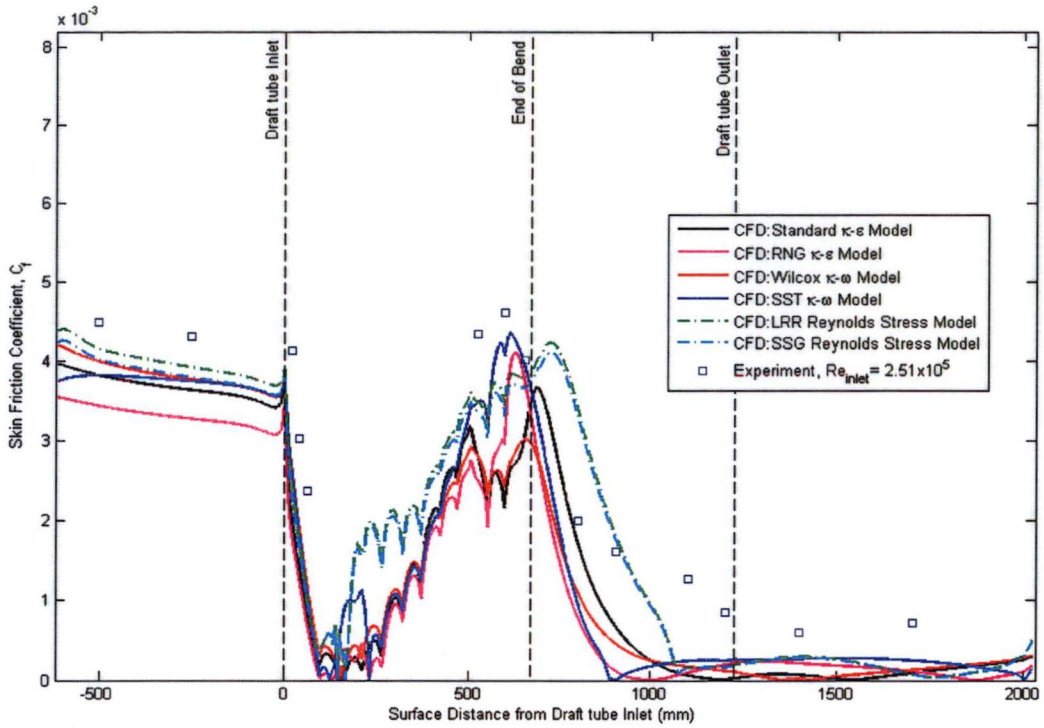

Figure 7.54: Comparison of experimental measurement and CFD prediction of skin friction distribution along the bottom centreline of the model at inlet Reynolds number of 2.51×10^5 (mesh size: 1176000 nodes)

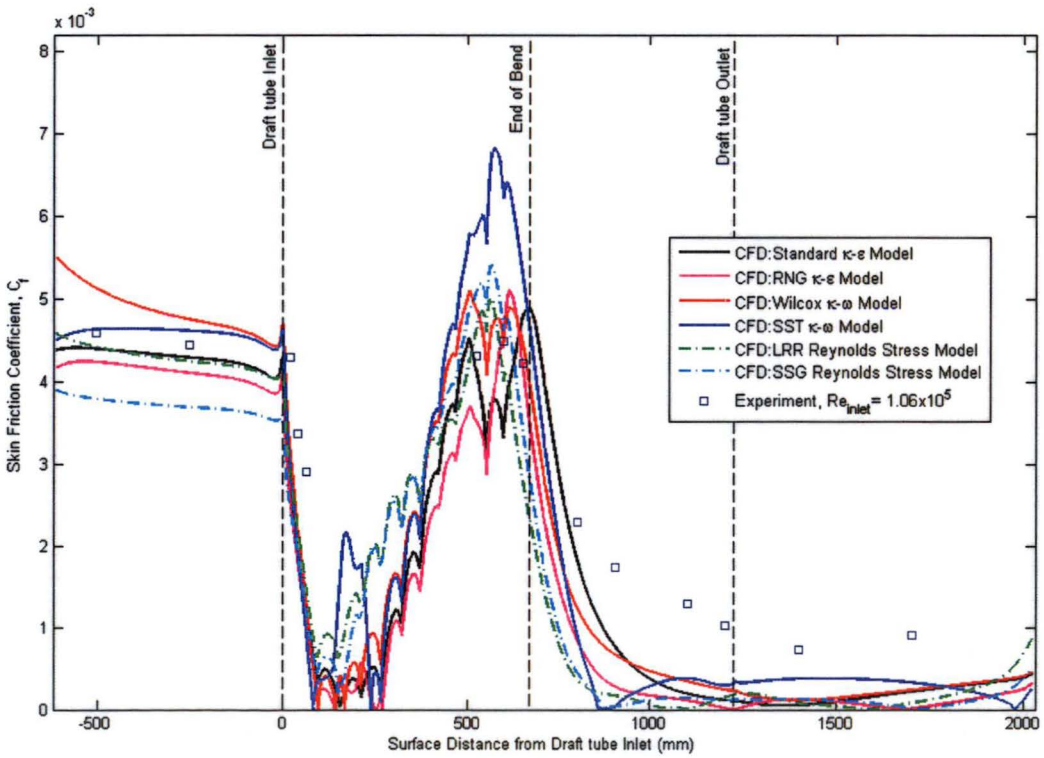

Figure 7.55: Comparison of experimental measurement and CFD prediction of skin friction distribution along the bottom centreline of the model at inlet Reynolds number of 1.06×10^5 (mesh size: 1176000 nodes)

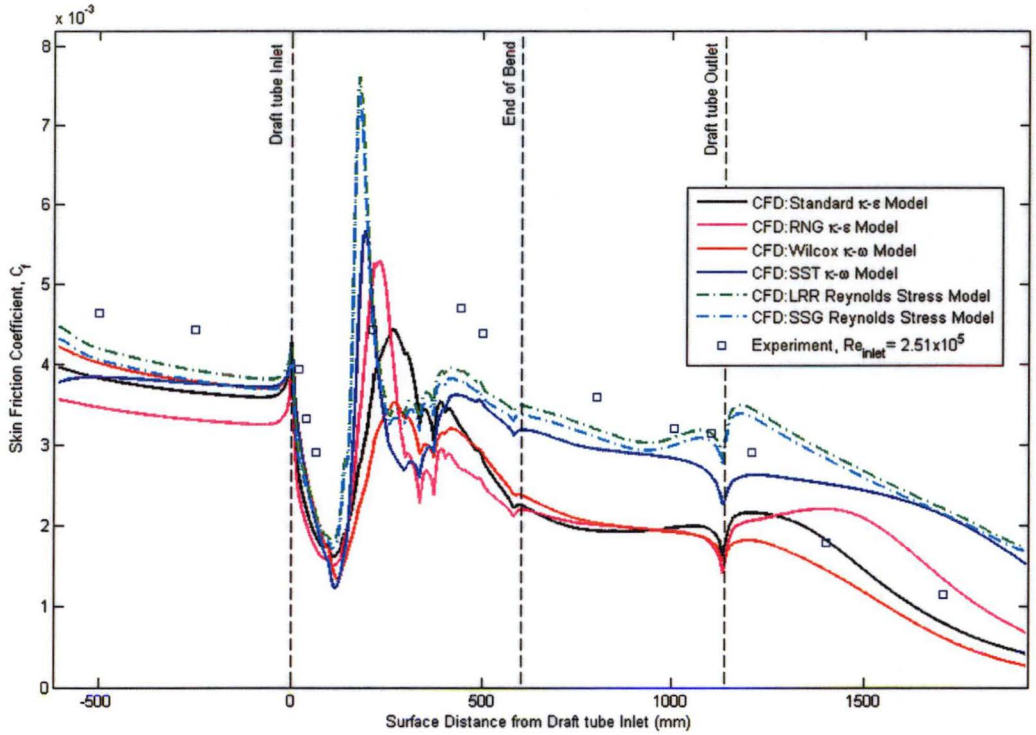

Figure 7.56: Comparison of experimental measurement and CFD prediction of skin friction distribution along the right centreline of the model at inlet Reynolds number of 2.51×10^5 (mesh size: 1176000 nodes)

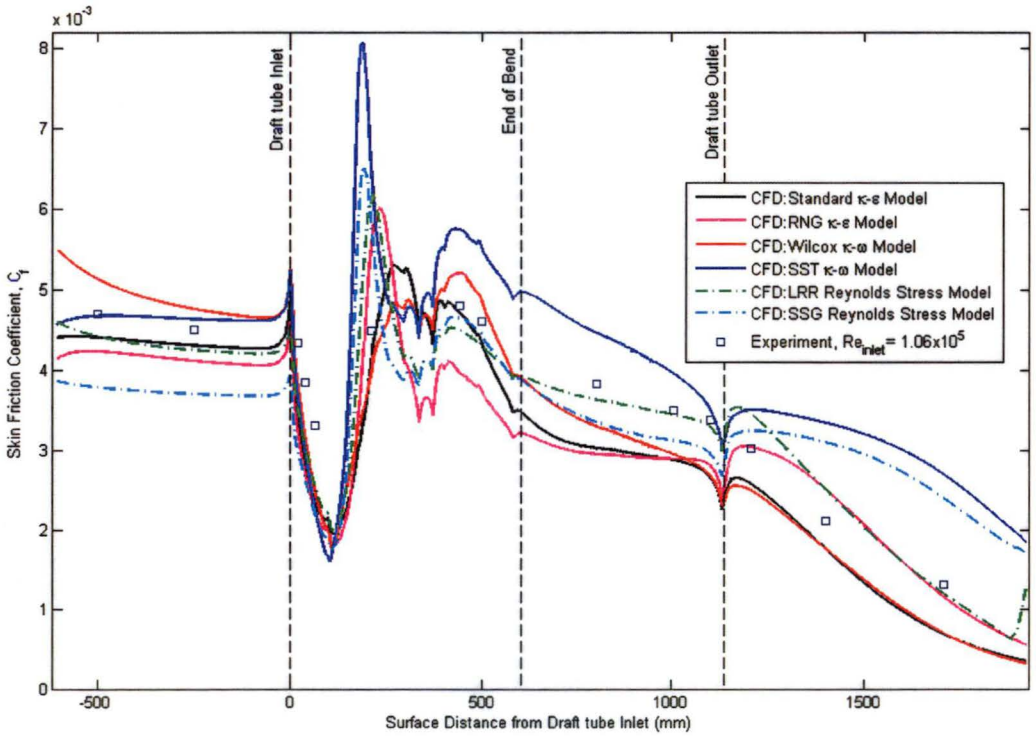

Figure 7.57: Comparison of experimental measurement and CFD prediction of skin friction distribution along the right centreline of the model at inlet Reynolds number of 1.06×10^5 (mesh size: 1176000 nodes)

7.4 Discussion

7.4.1 Reynolds Number Effects

Investigation of Reynolds number effects is essential for this analysis because the flow of the Mackintosh Francis-turbine draft tube will operate at Reynolds numbers of about 100 times larger than these in the present experiments or simulations. For the limited Reynolds numbers tested, no obvious Reynolds number dependency was observed for the measured wall static pressure distribution along the draft tube. There was a very weak drop in the pressure recovery with decreasing Reynolds number that could be explained by the increasing boundary layer momentum thickness at the draft tube entry as the Reynolds number reduces. The flow losses increased weakly with increasing Reynolds number but all of the foregoing changes were within the experimental uncertainty.

For the mean velocity profiles in the draft tube, the Reynolds number effects are generated by the Reynolds number dependency of the velocity normal to the wall emerging from the bend [119]. This unmeasurable velocity component enhances the boundary layer growth on the top wall but delays the boundary layer growth on the bottom surface. The shift in the peak of the velocity profile towards the top surface as the flow travels further downstream also supports this argument. This effect will not change the shapes of the mean velocity profiles substantially. For turbulence intensity, the Reynolds number effect is also insignificant when the local velocity is used for scaling. Some differences in behaviour are found at the draft tube exit, where increasing Reynolds number reduces the turbulence intensity. This behaviour may be related to the unsteady flow in the recirculation region or the stronger pressure gradients occurring at lower Reynolds number, which increase the production of normal turbulent stress.

The values of skin friction coefficient in the draft tube generally reduce with increasing Reynolds number. Larger differences are found near the inlet cone region of the draft tube, where the skin friction coefficients at low Reynolds number are about twice as large as the ones at high Reynolds number.

7.4.2 Flow Separation

Flow separation is crucial for the analysis of draft tube flow, as it will reduce the kinetic energy recovery by introducing a blockage in the flow passage. Specification of separation by means of a reverse flow or vanishing wall shear stress is usually inadequate in three-dimensional flow. Three-dimensional separation is very different from the two-dimensional separation: a two-dimensional separation is always accompanied by an abrupt breakaway of flow from the surface with no opportunity for lateral relief. The mainstream flow is deflected away from the wall and a backflow is created to supply the flow entrained by the separated shear layer. Three-dimensional separation, on the other hand, shows no such breakaway. The wall-limiting streamlines bend towards the separation line and the mainstream will remain unaffected [139]. A universal definition of three-dimensional flow separation is still a subject of debate.

Mauri [73, 75] argues that the necessary condition for the occurrence of flow separation is the convergence of the skin friction lines onto a separation line. Skin friction lines are identical to the streamlines in the sense that they cannot cross each other, except at stagnation points where the length of the skin friction vector is zero. The three-dimensional separation is characterized by the onset on the surface of a focus accompanied with a saddle point (see Figure 7.58). The focus on the wall extends into the fluid as a concentrated vortex filament, while the surface rolls up around the filament [75]. This flow behaviour is also known as Werlé-Legendre separation. Table 7.8 summarises the CFD predictions and the experimental observations of the starting location of flow separation along the top centreline of the model for the inlet Reynolds number of 2.51×10^5. CFD prediction is based on the diminishing wall shear stress on the surface while the experimental observation relies on the response of the tuft. The tuft will oscillate and reverse its direction periodically at a point of two-dimensional turbulent separation. As illustrated in Figure 7.58, the separating flow on the top surface is also evidenced by numerical flow visualisation of skin friction lines.

Turbulence Model	*Starting Location of Flow Separation (mm from Draft Tube Entry)*
Standard k-ε	160
RNG k-ε	134
Wilcox k-ω	151
SST k-ω	126
LRR Reynolds Stress	147
SSG Reynolds Stress	147
Experimental Observation	153

Table 7.8: Starting location of the flow separation along the top centreline of the model for inlet Reynolds number of 2.51×10^5: CFD predictions based on diminishing wall shear stress and experimental observations based on mini-tuft flow visualisation

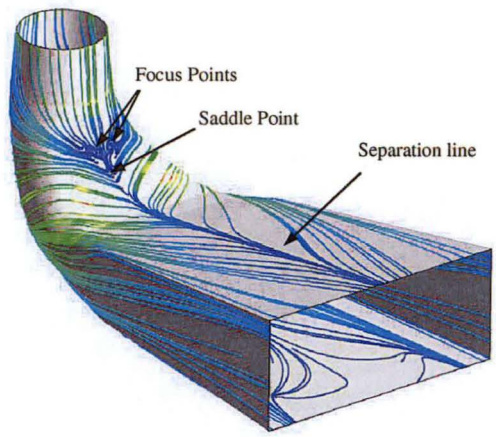

Standard k-ε model

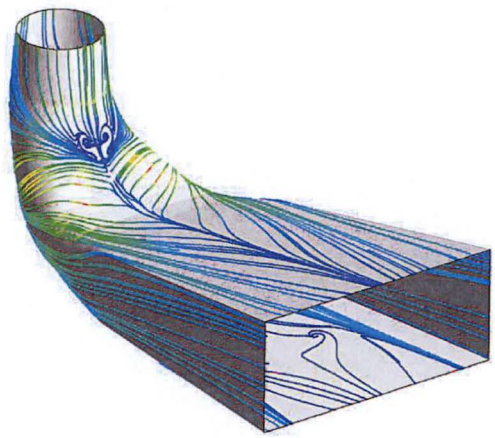

RNG k-ε model

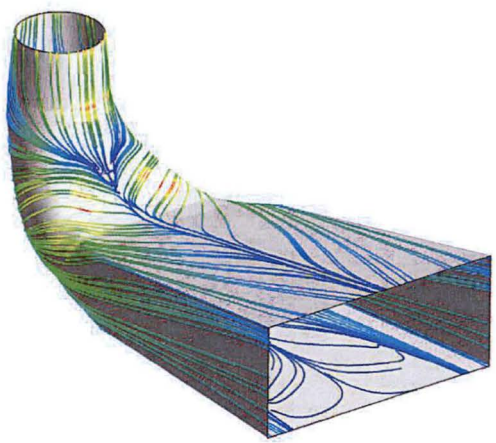

Wilcox k-ω model

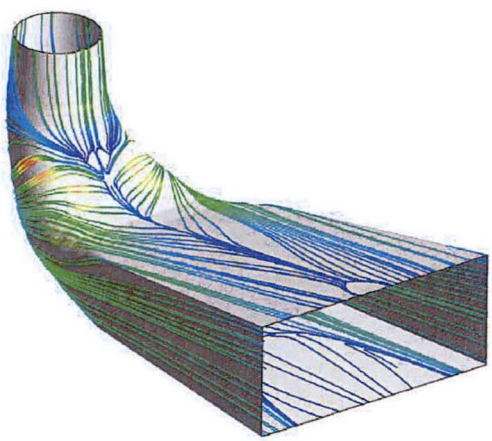

SST k-ω model

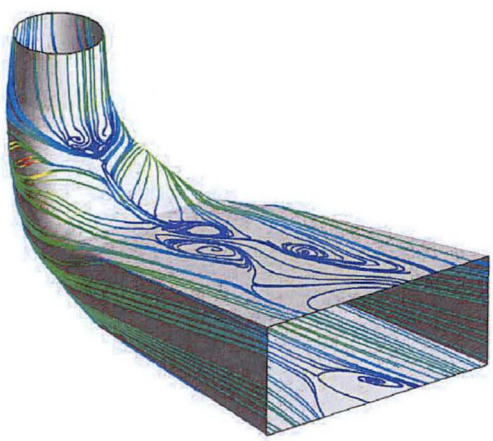

LRR Reynolds Stress model

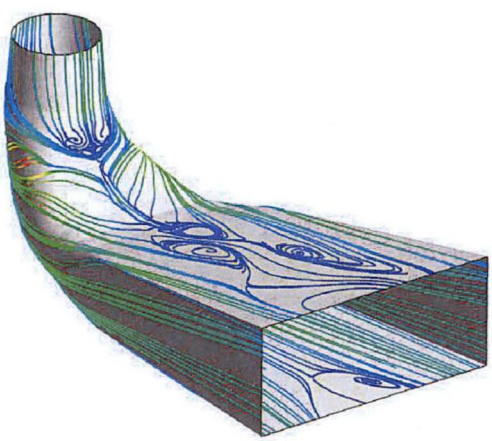

SSG Reynolds Stress model

Figure 7.58: Numerical flow visualisation of skin friction lines predicted by various turbulence models at inlet Reynolds number of 2.51×10^5 (example of the saddle point and the focus points are shown in the top left diagram)

7.4.3 Inlet Swirl

Flow into a draft tube has very little swirl when the turbine is operating near the best-efficiency point. However, the inlet swirl becomes stronger when the turbine is operating away from this design condition. The swirling flow at draft tube inlet can be represented by superimposing the three distinct vortices to the uniform circumferential and axial velocity profiles at the turbine exit, as described by Resiga et al. [101]. The vortical flow consists of a rigid body rotation motion, a counter-rotating and co-flowing Batchelor vortex with large core radius, and a co-rotating and counter-flowing Batchelor vortex with small vortex core. The strength of the inlet swirl is always represented by a dimensionless swirl number (S_{in}) in the draft tube flow analysis (Equation 7.7). The induced vortex is similar to a forced vortex at low swirl numbers and a Rankine vortex at higher swirl numbers. A radial variation of the circumferential velocity must be accompanied by a variation in axial velocity. The axial velocity inside the vortex core increases when a Rankine vortex circumferential velocity is induced by viscous effects in the boundary layer of the runners or guide vanes [101].

$$S_{in} = \frac{\text{axial flux of swirl momentum}}{\text{axial flux of axial momentum}} = \frac{\int \rho_a U_{a-in} U_{t-in} r dA}{R_{inlet} \int \rho_a U_{a-in}^2 dA} \tag{7.7}$$

Where $U_{a\text{-}in}$ = local axial velocity at draft tube inlet
$U_{t\text{-}in}$ = local circumferential velocity at draft tube inlet
R_{inlet} = radius of the draft tube inlet
r = radial position from the duct centre

The Francis-turbine draft tube benefits from the swirl at runner outlet, which helps to prevent the flow detachment in the cone; but it suffers from flow instabilities leading to the pressure fluctuations and draft tube surge or power swings.

To examine the likely effect of inlet swirl in the present draft tube model, a new calculation is performed by imposing a uniform clockwise-rotating circumferential velocity (6 m/s) to the draft tube inlet. Other boundary conditions remain unchanged as previous calculations. As summarised in Table 7.9, solutions using the standard k-ε model indicate that inlet swirl increases the total pressure losses. Inlet swirl may help the draft tube to perform better as it will re-energise the boundary layer, but it will also result in the flow being suddenly unbalanced as part of the draft tube flow is completely

separated and a strong backflow occurs at the outlet region. The convergence of the solutions is improved with the introduction of inlet swirl. Swirling flow seems to have some stabilising effect on the simulation of draft tube flow.

Figures 7.59~7.60 show that inlet swirl at the draft tube causes flow asymmetry. The inlet swirl attenuates the co-rotating vortices and enhances the counter-rotating vortices. Further increase of swirl will gradually damp all the vortices induced by the bend of the draft tube. The gyroscopic effects force the core of the swirling flow towards one side of the draft tube and result in a stronger gradient there. The presence of strong gradients close to the wall will increase the dissipation of energy. This explains why the performance of the draft tube drops when the inlet swirl is introduced (see Table 7.9). The inlet swirl considerably widens the range of profiles that can give rise to absolute instability of the draft tube [75]. Only a slight amount of counter flow is necessary to trigger the instability. Detailed analysis is therefore needed in the future to examine the influence of swirling flow to the overall instabilities of the power plant operations.

Criteria	*With Inlet Swirl*	*Without Inlet Swirl*
Inlet Swirl Number	0.13	0.0
Area-Averaged Circumferential Velocity at inlet	6	0.0
Area-Averaged Axial Velocity at inlet	29	29
Static Pressure Recovery Factor	0.578	0.581
Total Pressure Loss Coefficient	0.225	0.194
Maximum Residual after 170 iteration loops	8.02×10^{-6}	3.01×10^{-5}

Table 7.9: Effects of adding a constant swirl (rotating in clockwise direction) at the draft tube inlet. Solutions are based on the standard k-ε model and the identical mesh size of 1176000 nodes

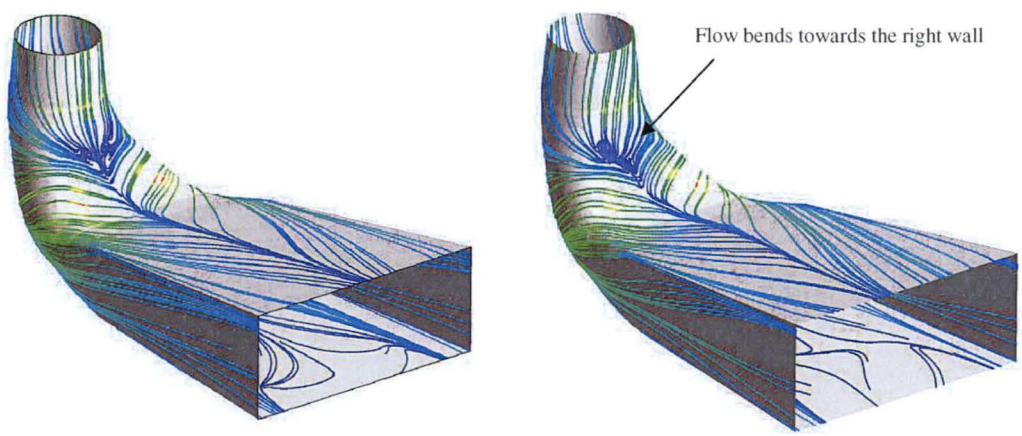

Figure 7.59: Numerical flow visualisation of skin friction lines predicted by standard k-ε model and the identical mesh size of 1176000 nodes for cases with and without inlet swirl

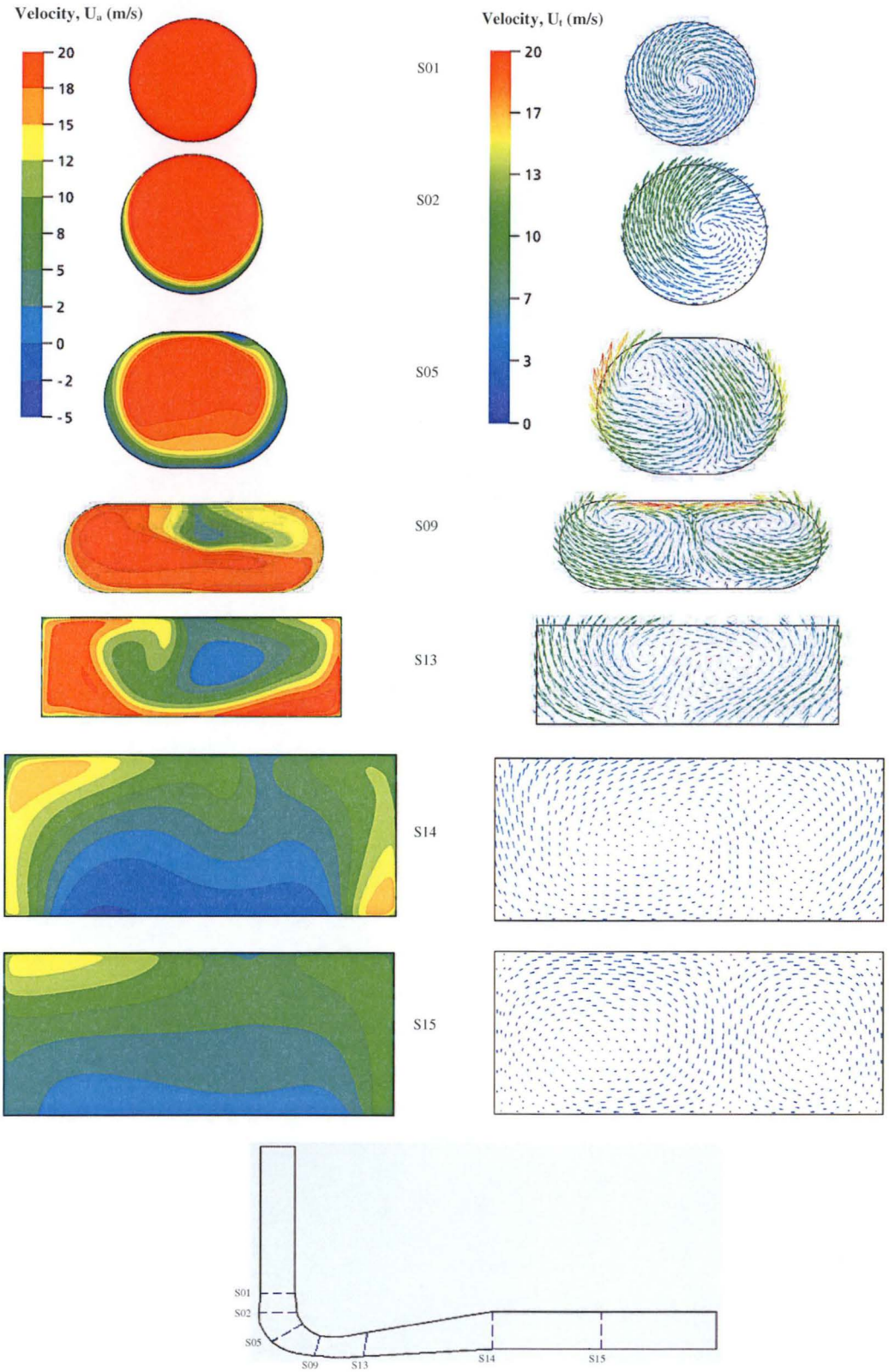

Figure 7.60: CFD Result for standard k-ε model with swirling flow at draft tube inlet. see Figure 7.22 for comparions of the case without inlet swirl (Left: Axial Velocity Contours, Right: Secondary Velocity Vectors)

7.4.4 Flow Asymmetries

The experimental wall static pressure distributions at the left and right centrelines of the model show slight asymmetry. Sotiropoulos and Ventikos [120] suggest that flow asymmetry observed in an internal flow system is the result of the outer disturbances from some small but finite imperfections of a non-ideal environment. The flow asymmetry in the experiments could be caused by many factors such as noise and vibrations, thermal gradients, model imperfections, proximity of the inlet to a wall, or small asymmetries at the boundaries. These problems are also common in real turbine plants. Although asymmetry does not generally emerge from imperfections at the wall, it is still impossible to exclude this randomness from reality [40]. The experimental model was placed quite close to the wall due to limited space in the laboratory. The measured surface temperature close to the wall side was usually about 0.5~1°C above the temperature of the opposite surface. Temperature gradients through the thermal boundary layer may induce a density driven down-flow near the wall and generate some small discrepancies in the flow behaviour. The presence of the wall (one diameter away from the draft tube model) may cause asymmetry of the inlet flow and the introduction of a streamwise vortex originating from the wall surface ("ground vortex").

For numerical simulations, the use of a symmetrical total pressure profile at inlet would suggest that the solution should also be symmetrical. Although symmetrical solutions may exist, they will probably never be obtained in the real flow due to unstable properties of the three-dimensional physics. In general, flow asymmetry in a simulation may arise from the round-off errors of the coordinates of the nodes as well as the asymmetries in grid structure, block topology, or CAD geometry. These effects should be relatively insignificant in the present case, as flow asymmetry is only observed in the solutions of Reynolds stress models where the unsteady flow behaviour near duct centre is predicted. Instead, the asymmetric behaviour is thought to be caused by the instabilities of the symmetric mode that gives rise to an oscillating wave in the flow and the periodic pressure fluctuations in the draft tube [40]. Flow asymmetry is one of the possible solutions of the nonlinear problem expressed by the unsteady Navier-Stokes equations. Separated or recirculating flow may break the symmetry of the precedent flow, adopting a form of lesser symmetry in which dissipative structures arise to absorb just the amount of excess available energy that the more symmetrical flow can no longer be able to absorb [40].

7.4.5 Flow Unsteadiness

Flow in a draft tube is known to be highly unsteady even though the boundary conditions remain constant. In the backflow region, an inflection point may occur in the velocity profile due to recirculating flow. This triggers the Kelvin-Helmholtz type of unstable flow mechanism in the draft tube. Such a mechanism is quite insensitive to external noise and acts as a self-sustained hydrodynamic oscillator. Although Kelvin-Helmholtz instability theory is derived based on two-dimensional flow, some qualitative indications of the unsteady mechanism can still be gained in the draft tube flow [75]. Figure 6.61 shows the time varying pressure recovery factor predicted by the SSG Reynolds stress model over a period of 0.1 second. Table 7.10 summarises the instantaneous value of the pressure recovery factor at various time instants. The resulting skin friction lines on the model surface and the streamline pattern at the centre plane are presented in Figures 6.62~6.64. The solution captures the periodic unsteadiness of the flow, as all Reynolds stress components are modelled. This self-excited unsteadiness is usually of low frequency (about 17~20 Hz as observed in Figure 7.61). The separated flow recirculates back to the upstream, meets the incoming flow, and forms a saddle point of separation. As the flow is structurally unstable, the convergence of the solution towards the steady state is difficult in the simulation. The focus point moves along the separation line in the downstream direction, modifying the surrounding flow field and giving rise to interactions with the upstream saddle point. This interaction leads to periodic vortex shedding in the recirculating region.

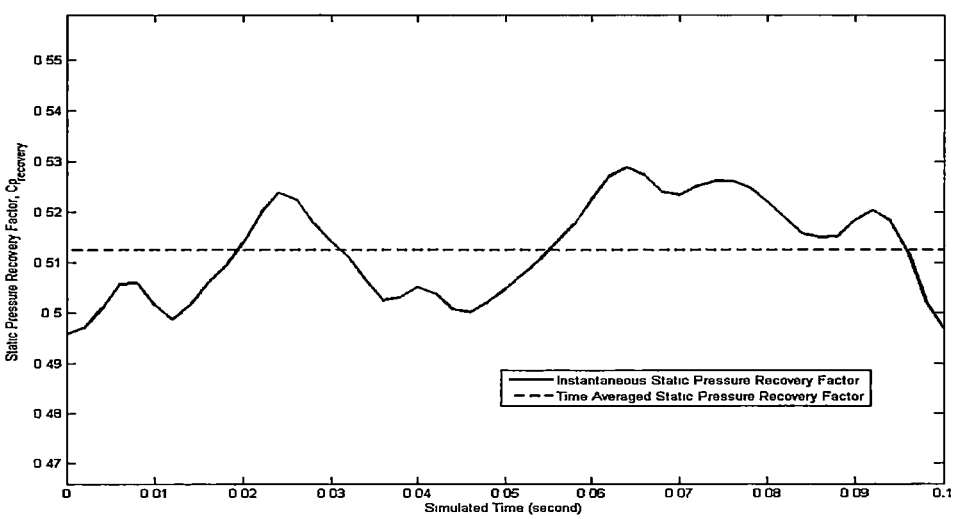

Figure 7.61: Instantaneous static pressure recovery factor predicted by unsteady RANS simulation using SSG Reynolds stress model and the mesh size of 1176000 nodes. Boundary conditions remain unchanged during the simulation

Simulation Time (second)	*Instantaneous Static Pressure Recovery Factor*
0.012	0.4988
0.016	0.5061
0.022	0.5200
0.032	0.5112
0.056	0.5141
0.070	0.5234

Table 7.10: Predicted instantaneous static pressure recovery factor at various time instant. Unsteady RANS simulation is run over a period of 0.1 second and the solutions are based on the SSG Reynolds stress model and the mesh size of 1176000 nodes

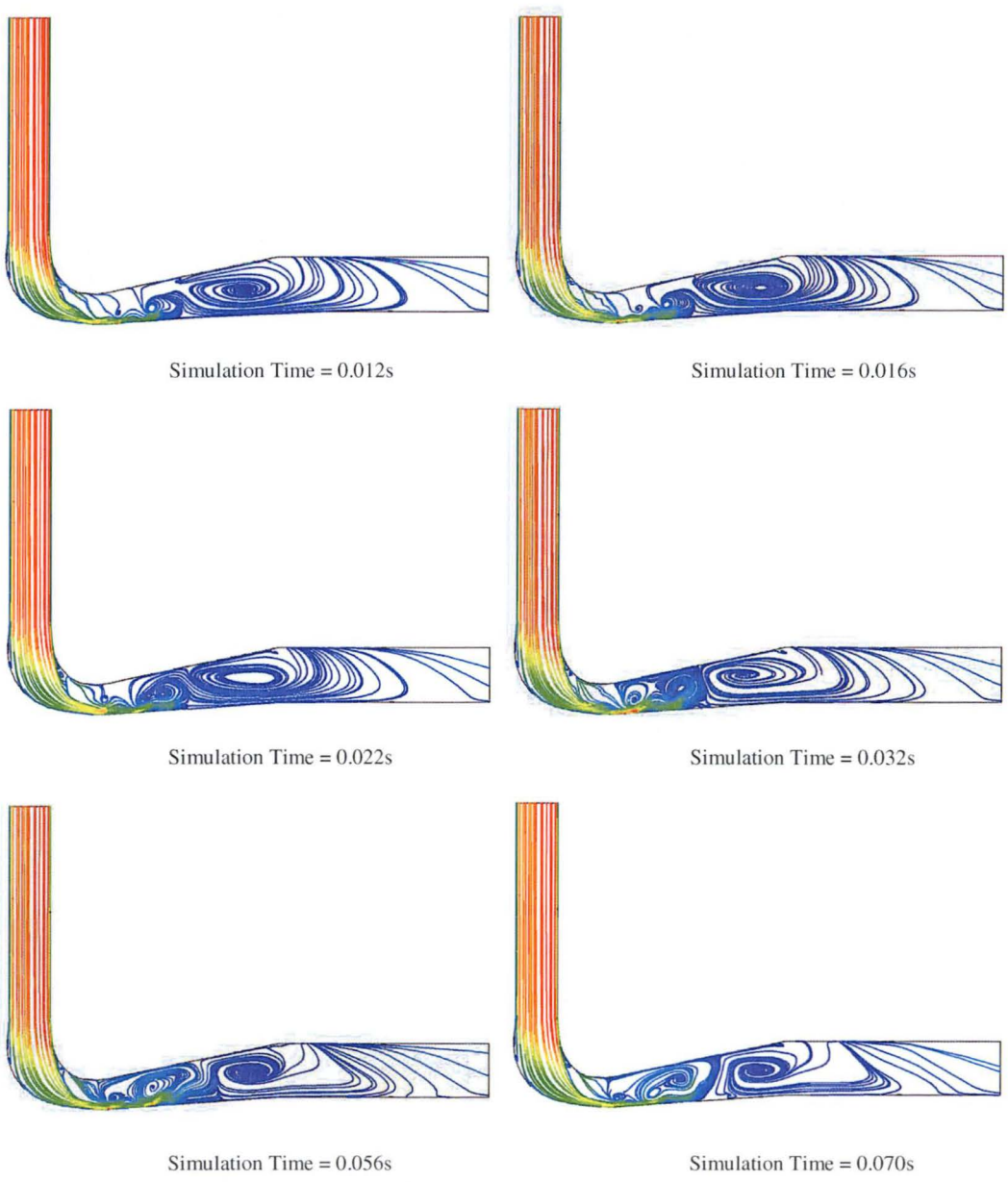

Figure 7.62: Instantaneous streamline pattern on the centre plane of the draft tube model. Unsteady RANS simulation is run over a period of 0.1 second and the solution is based on the SSG Reynolds stress model and the mesh size of 1176000 nodes

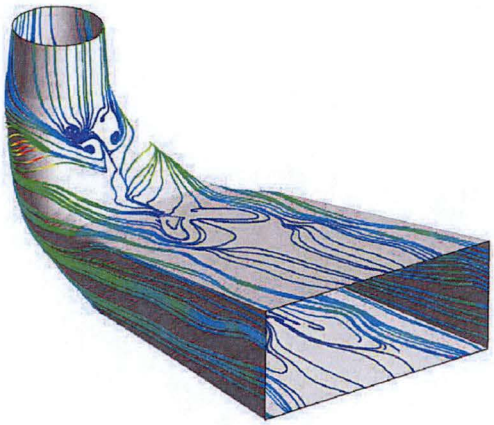

Simulation Time = 0.012s

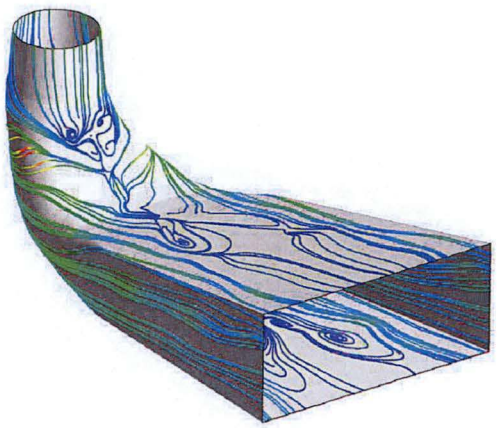

Simulation Time = 0.016s

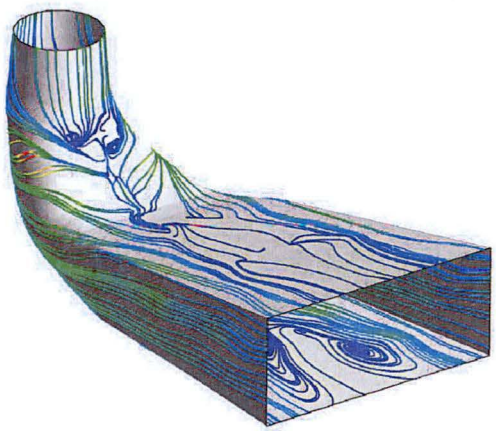

Simulation Time = 0.022s

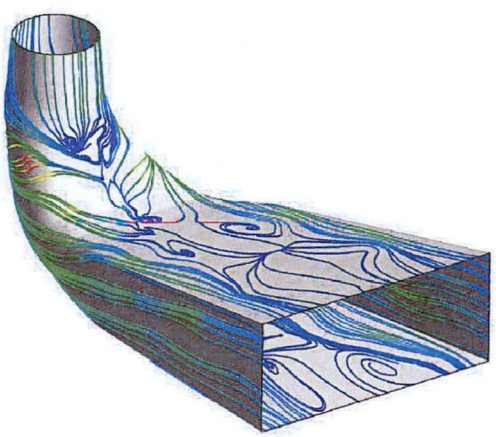

Simulation Time = 0.032s

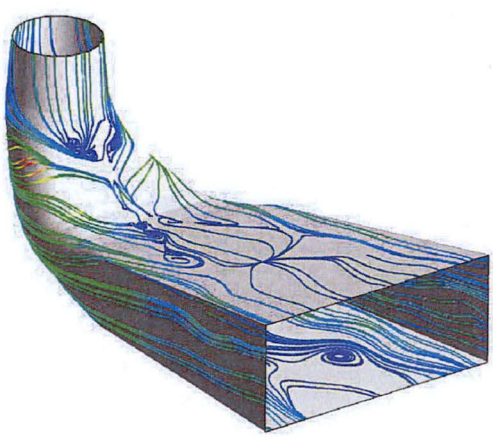

Simulation Time = 0.056s

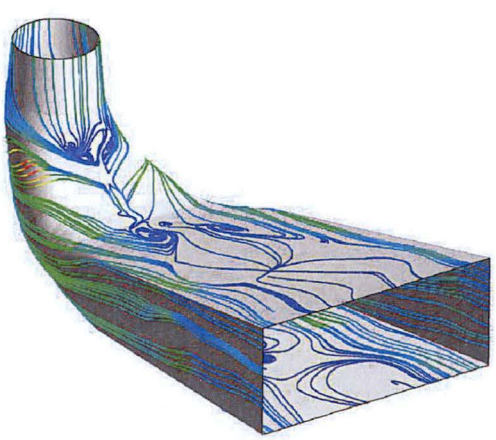

Simulation Time = 0.070s

Figure 7.63: Skin Friction lines viewing from the topside of the draft tube model. Unsteady RANS simulation is run over a period of 0.1 second and the solution is based on the SSG Reynolds stress model and the mesh size of 1176000 nodes

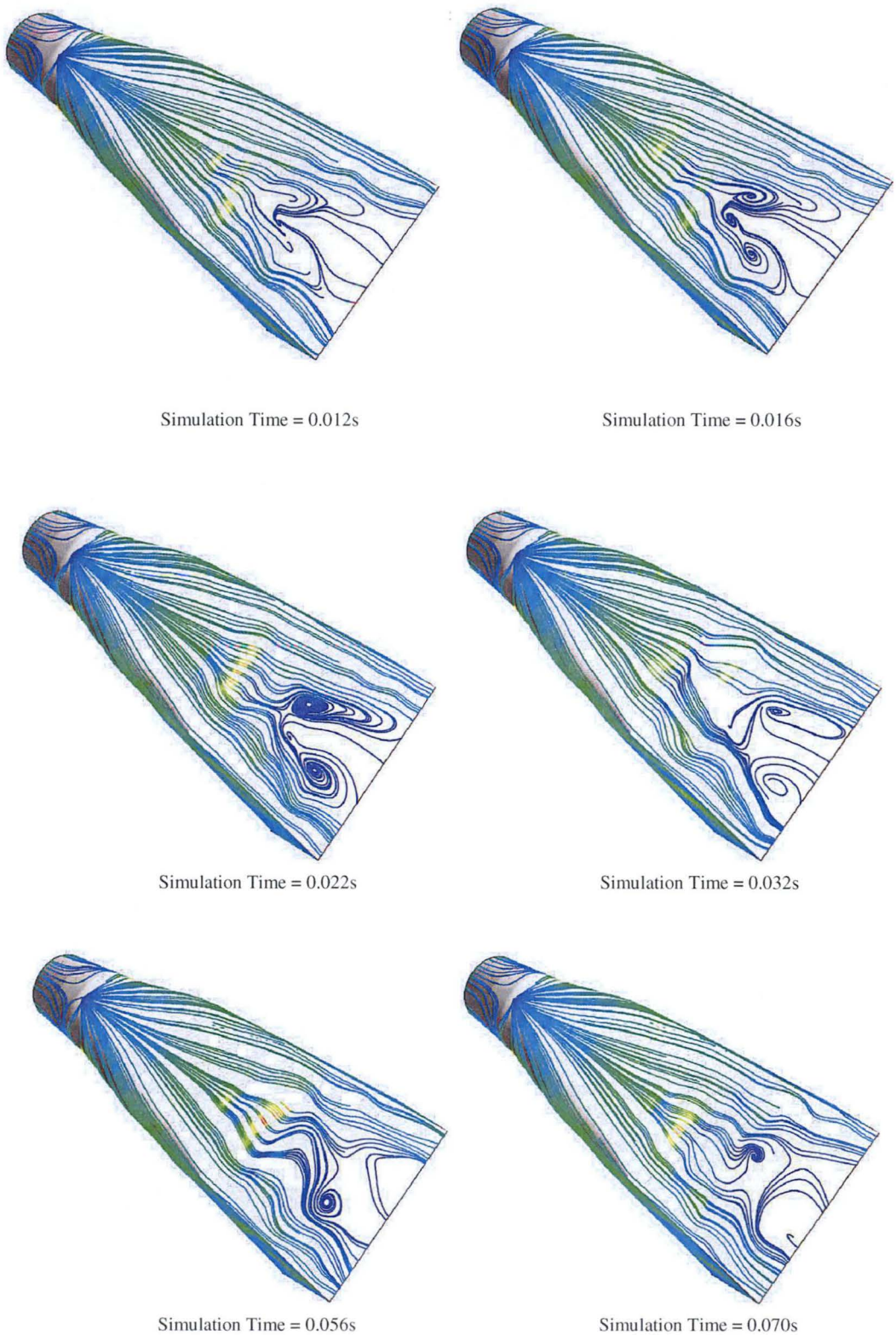

Figure 7.64: Skin Friction lines viewing from the bottom side of the draft tube model. Unsteady RANS simulation is run over a period of 0.1 second and the solution is based on the SSG Reynolds stress model and the mesh size of 1176000 nodes

7.4.6 Effects of the Stiffening Pier

The stiffening pier downstream of the draft tube was not modelled in the current study. However, for structural requirement, a stiffening pier is always present in a turbine draft tube with larger flow capacity. The leading edge of the pier is usually streamlined and is located at the exit section of the elbow. The flow will stagnate at the leading edge of the stiffening pier, which has a small radius of curvature that induces losses. The blockage of a stiffening pier in the draft tube increases the flow velocity, which increases the hydraulic losses due to friction and reduces the overall turbine efficiency. Reductions in the turbine efficiency generally increase with increasing number of piers and their thickness. The impacts of stiffening piers on the turbine efficiency also increases with increasing volumetric flow through the draft tube [136] Drtina et al. [31] studied the flow field of a draft tube with and without the stiffening pier. They argue that the pier does not affect the upstream flow field substantially, but it will relocate the vortices into two separate channels and cause a strong mass flow imbalance at the draft tube exit.

7.5 Conclusions

For complete flow modelling of a hydroelectric generating plant, the governing differential equations have to be integrated over an infinite flow domain, which considers all the components in the waterway system such as dam, water tunnel and the whole Francis turbine. However, this approach requires a huge amount of computing power and still does not eliminate the uncertainties in specification of boundary conditions. The current study has been focussed on the individual draft tube component to make it practicable. Extensive verification and validation of the steady-flow CFD simulations were performed. A mesh size of 1176000 nodes was found to provide a good compromise between accuracy and computational time required. It is difficult to draw any firm conclusions at this stage about the accuracy of the turbulence models due to limited amount of experimental data available for validating the CFD solutions. However, preliminary analysis indicates that simulations using standard k-ε turbulence model and an outlet extension length equivalent to five times the outlet height of the draft tube produce reasonably accurate results. The use of more advanced turbulence models does not seem to improve the agreement with the experiments. The validated steady-flow results will be used as an initial condition for the unsteady flow simulations that will be presented in the Chapter 8.

CHAPTER 8

TRANSIENT-FLOW ANALYSES OF THE DRAFT TUBE MODEL

8.1 Overview

Comparisons between simulations and full-scale test results for the Hydro Tasmania's Mackintosh station show some frequency-dependent discrepancies that appear to be associated with the transient flow within the Francis turbine. To probe the unsteady effects, flows in a model draft tube following a sudden change in discharge are studied experimentally and numerically. The model draft tube employed in this analysis is geometrically similar to the one used for Mackintosh power plant but the inlet swirl of the draft tube is not being modelled here. Section 8.2 presents the experimental results for different types of valve motions. Section 8.3 describes the mathematical models of various complexities including the three-dimensional CFD model, two-dimensional unsteady stall model, and one-dimensional momentum theory. The experimental data will be used for validating the transient solutions of the CFD model. Convective lag responses of the draft tube flow are investigated in Section 8.4 while the transient force and pressure loss coefficients for the draft tube are examined in Section 8.5. The effects of transient draft tube forces on the power plant modelling and the influence of inlet swirl on the transient behaviour of the draft tube flow are discussed in Section 8.6.

8.2 Experiments

Transient measurements are carried out primarily for validating the solutions of the mathematical models. The system layout for the experimental model has been described in Section 6.2, while the unsteady measurement technique are discussed in Section 6.2.3.7. The transient wall static pressures are measured at 8 different locations along the centrelines of the top and side walls of the draft tube model, whereas the unsteady velocities are acquired at the centre of the inlet pipe. The transient static pressures convey almost instantaneously throughout the draft tube. The measurement locations are defined in Figure 8.1.

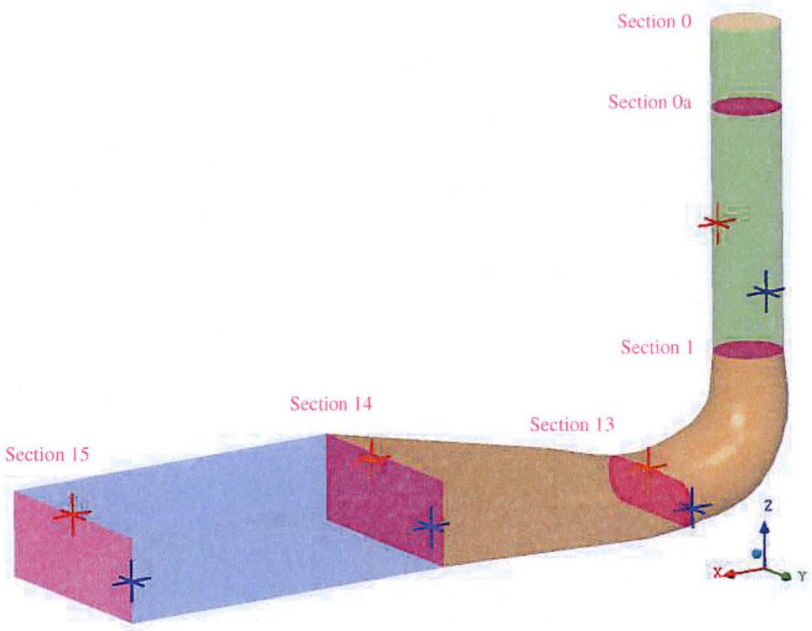

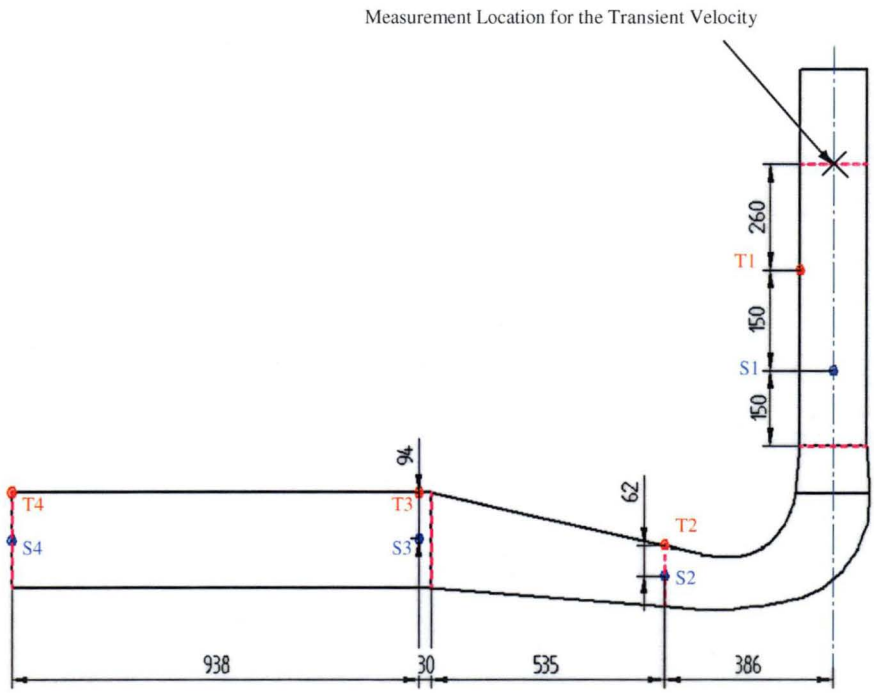

Figure 8.1: Measurement locations of the transient wall static pressures and velocity for the model draft tube (Blue dots represent stations for transient pressure measurements along the sidewall of the model while red dots indicate stations for transient pressure measurements along the top wall of the model)

Two types of valve operations are investigated during the tests: the step and sinusoidal valve motions. Figures 8.2~8.3 present the results of a given step increase or decrease in the draft tube flow (within 0.1 second) while Figures 8.4~8.6 show the effects of sinusoidally varying the discharge in the draft tube model. Two oscillation frequencies are tested in this experiment: 0.6 and 1.2 Hz, which are equivalent to the full-scale frequencies of around 0.013 and 0.027 Hz. The relationship between the model and full-scale frequencies is established in Equation 8.1.

$$\left(\frac{f_v D_{in}}{U_{in}}\right)_{\text{model}} = \left(\frac{f_v D_{in}}{U_{in}}\right)_{\text{prototype}} \tag{8.1}$$

where f_v = oscillation frequency of the pressure signals at the draft tube outlet

U_{in} = averaged velocity at draft tube inlet = $0.5\times(U_{initial} + U_{final})$

D_{in} = diameter of the draft tube inlet

Sinusoidal valve motions are very difficult to perform in this case due to the nonlinear resistance of the pneumatic valve, limitations of the valve controller, and the Helmholtz resonance of the draft tube model. This Helmholtz resonance is associated with compressibility of the air in the draft tube outlet plenum, and this effect would not be present in the hydraulic system with water as the working fluid. Although the signals are not perfectly sinusoidal, rough estimates of the phase and gain between the outlet static pressure and the inlet flow speed can still be obtained from this analysis. As shown in Table 8.1, the phase and gain increase with increasing oscillation frequency.

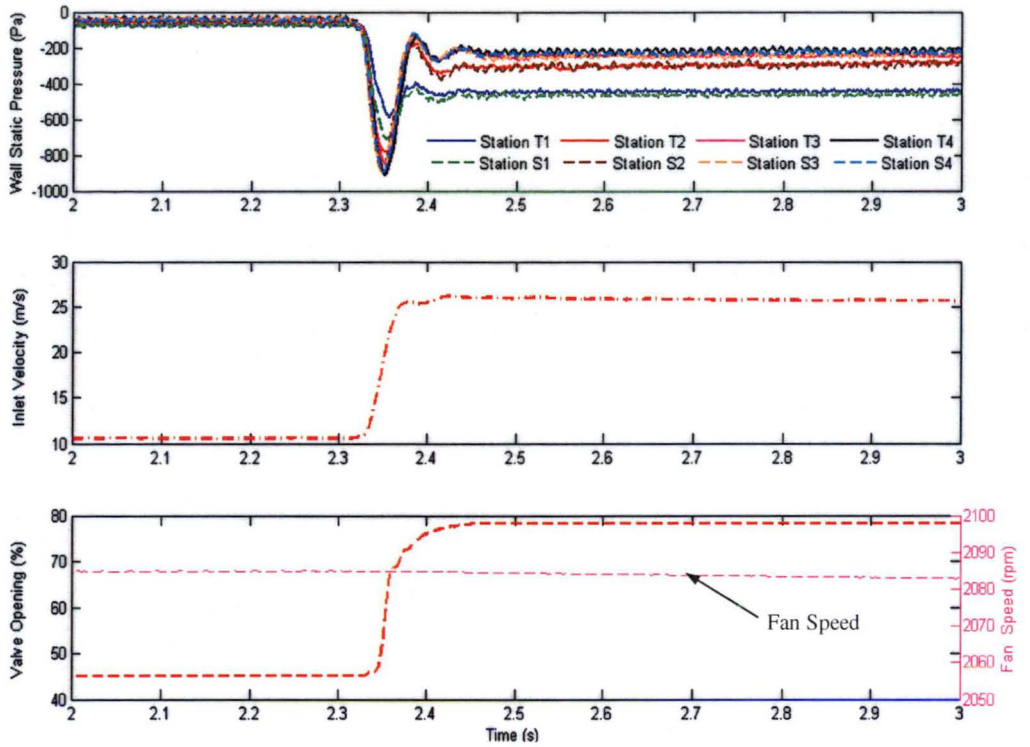

Figure 8.2: Experimental result of the transient flow in the draft tube for a step increase in the valve position (from 44% to 78% valve opening)

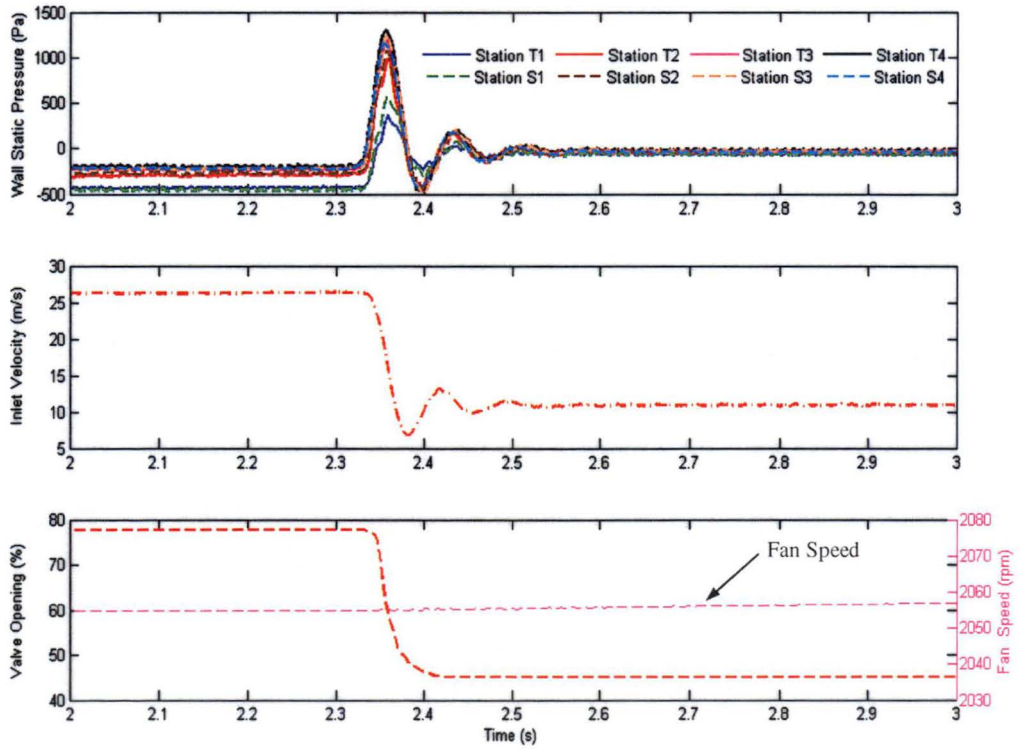

Figure 8.3: Experimental result of the transient flow in the draft tube for a step decrease in the valve position (from 78% to 44% valve opening)

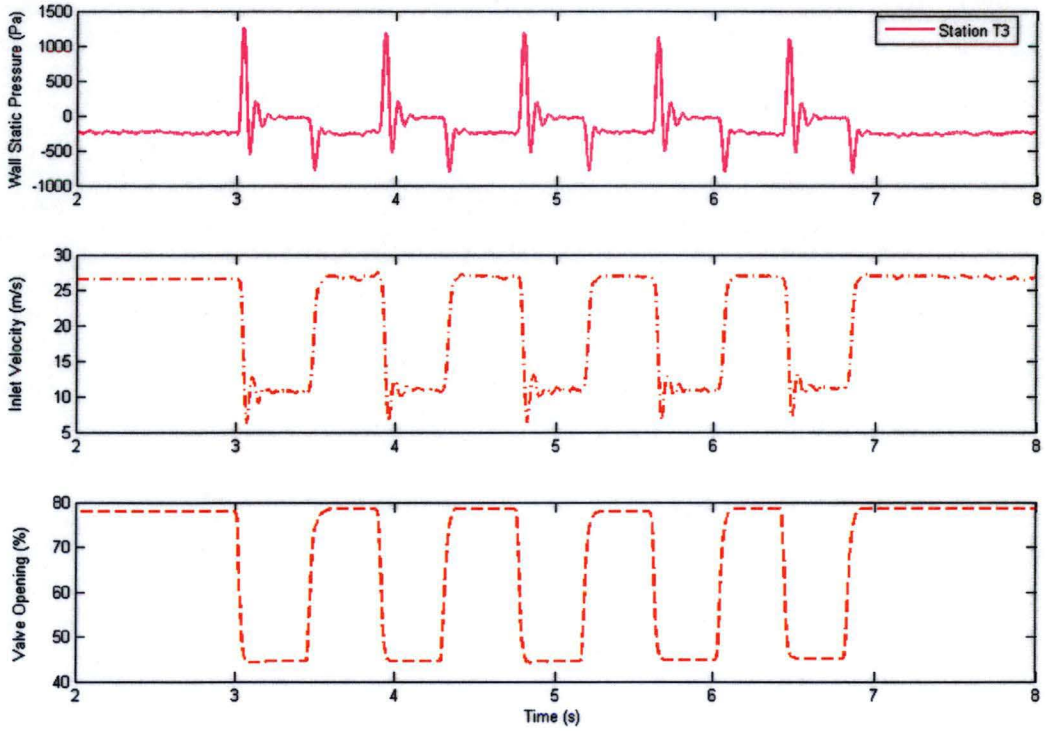

Figure 8.4: Experimental result of the transient flow in the draft tube following a sinusoidal valve movement (between 78% and 44% valve opening) conducted at the oscillation frequency of 1.2 Hz

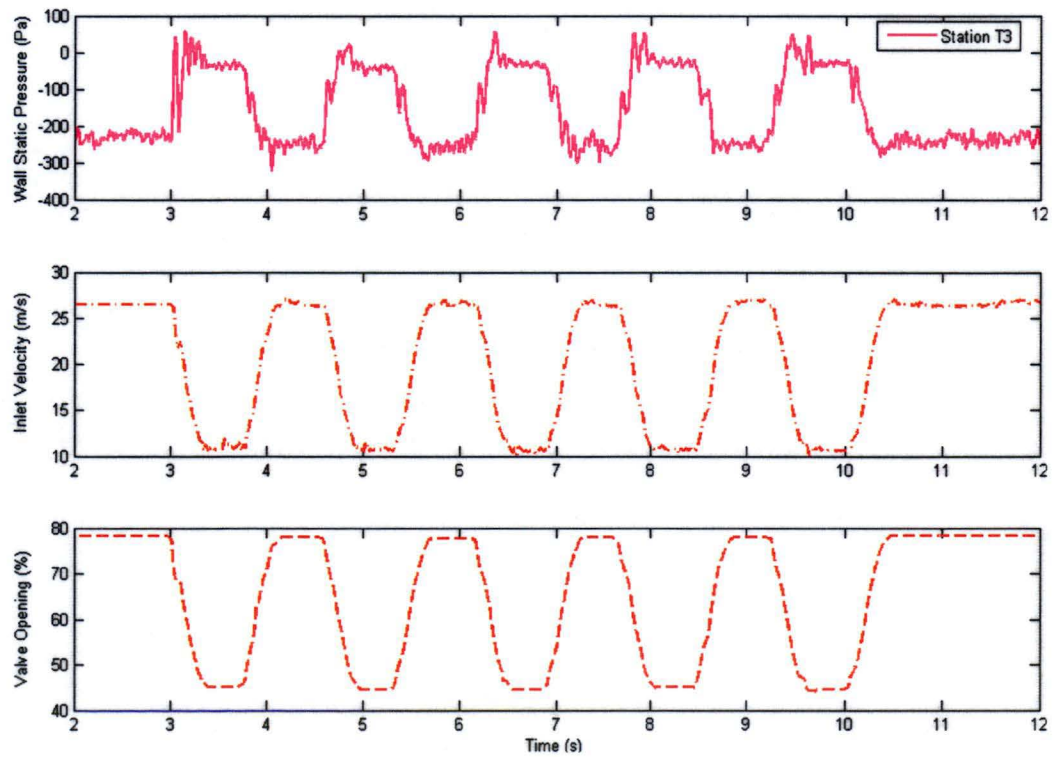

Figure 8.5: Experimental result of the transient flow in the draft tube following a sinusoidal valve movement (between 78% and 44% valve opening) conducted at the oscillation frequency of 0.6 Hz

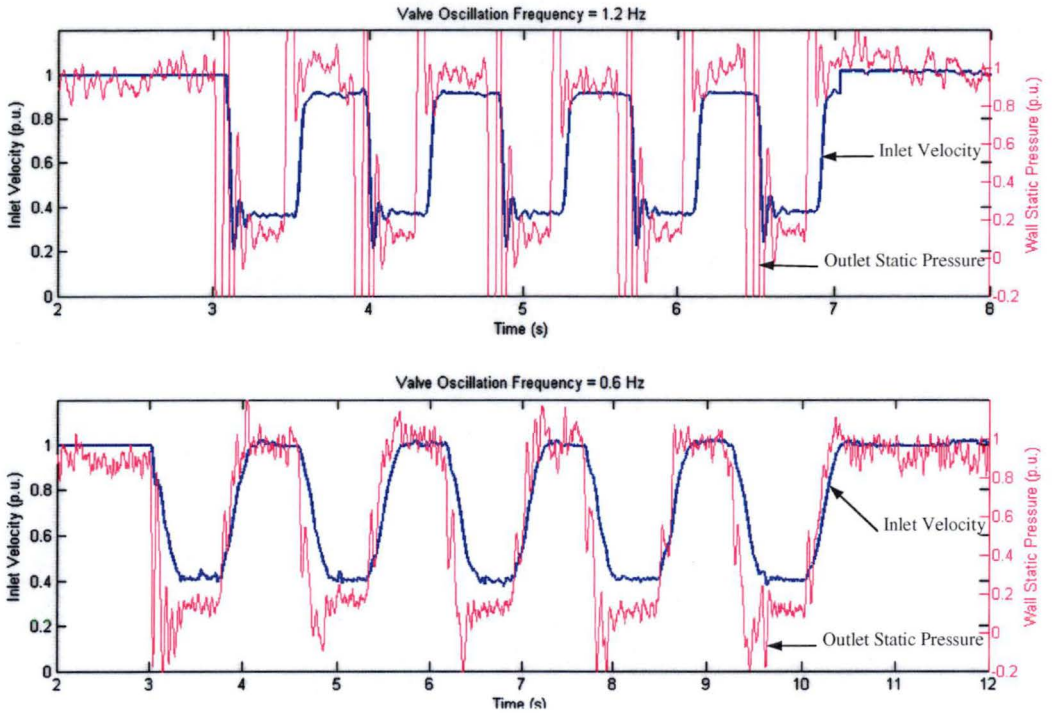

Figure 8.6: Comparisons between the inlet flow speed and outlet static pressure at two oscillation frequencies. Both transient static pressure and velocity are normalised with their initial values at 78% valve opening

Oscillation Frequency for the Model (Hz)	*Oscillation Frequency for the Prototype (Hz)*	*Gain (dB)*	*Phase Lag (°)*
0.6	0.013	3.94	– 24.8
1.2	0.027	5.83	– 39.9

Table 8.1: Phase lag and gain between the inlet flow speed and outlet static pressure of the draft tube model for two different oscillation frequencies: 0.6 and 1.2 Hz

8.3 Mathematical Flow Modelling

8.3.1 Three-dimensional CFD Model

The three-dimensional CFD code ANSYS CFX applied for the draft tube flow analyses have been described in some detail in Section 6.3. To examine the unsteady flow effects, the three-dimensional unsteady Navier-Stokes equations are solved in ANSYS CFX. The flow variables derived from this model are expressed in terms of time averages. Airflow in the draft tube model is assumed incompressible, but the actual pressure variation resulting from compressibility effects in the extension box is applied at the draft tube outlet as the outlet boundary condition. All transient simulations are conducted using the grid resolution of 1176000 nodes and the standard k-ε turbulence model. This arrangement is chosen as a compromise between the computational time and accuracy required. The steady-flow solutions presented in Chapter 7 are used as the

initial conditions in these simulations. Figure 8.7 shows the portion of the experimental pressure data used for the CFD outflow boundary condition. The total pressure profile used for the inflow boundary condition is kept unchanged during the simulations. A period of 0.3 second is simulated for the case of step increasing or decreasing the valve setting at the outlet.

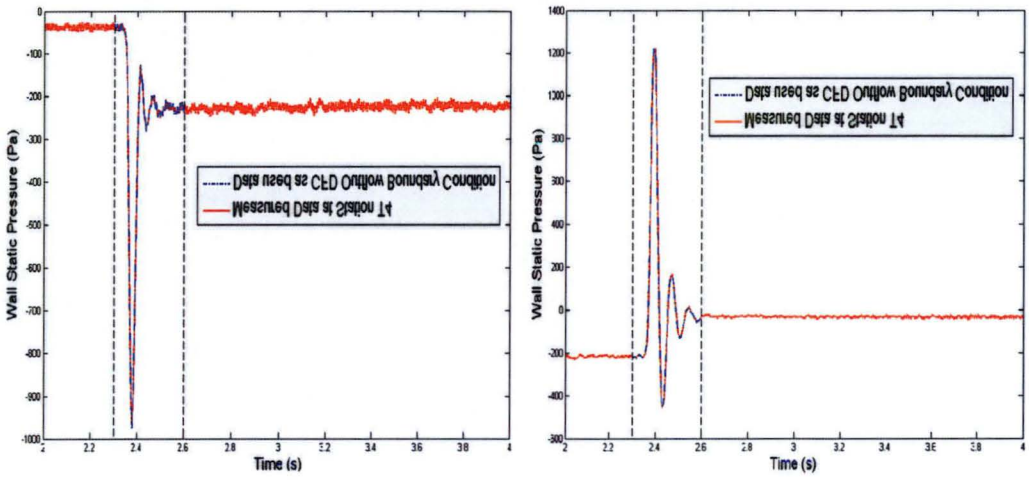

Figure 8.7: A portion of the experimental outlet static pressure (at Station T4) that will be used as the outflow boundary condition in ANSYS CFX (left: step increase in draft tube flow; Right: step decrease in draft tube flow)

The resulting CFD solutions will also be verified and validated in this Section. Verification and validation of the unsteady-flow solutions are not qualitatively different from those of the steady flow [103]. However, a thorough validation of the transient flow in the draft tube is impossible for the present study because of the paucity of data. Figures 8.8~8.9 show favourable comparisons between the CFD solutions generated by ANSYS CFX and the experimental data. Although the magnitude of the peak velocity is slightly underestimated by ANSYS CFX during the transients, the numerical solutions are well within the measurement uncertainties; this gives reasonable confidence in the unsteady CFD solution for the draft tube flow.

Figures 8.10~8.11 compare the numerical solutions of three different time steps, Δt = 0.0002 second, 0.001 second, and 0.005 second respectively. The maximum Courant number associated with the largest time step used is about 60.9. No obvious time dependency is observed for these calculations and so the time step of Δt = 0.001 second is currently used for the transient analysis of draft tube flow. A Helmholtz resonance frequency of around 20 Hz is clearly observed when the experimental pressure data are used for the outflow boundary condition. This complicates the analysis of the convective lag response that will be discussed in Section 8.4. To ease the analysis, an instantaneous step change in the outlet static pressure is used in the transient simulations,

as illustrated in Figures 8.12~8.13. CFD solutions for the sinusoidal oscillation of the draft tube flow will be presented later in Section 8.4.3.

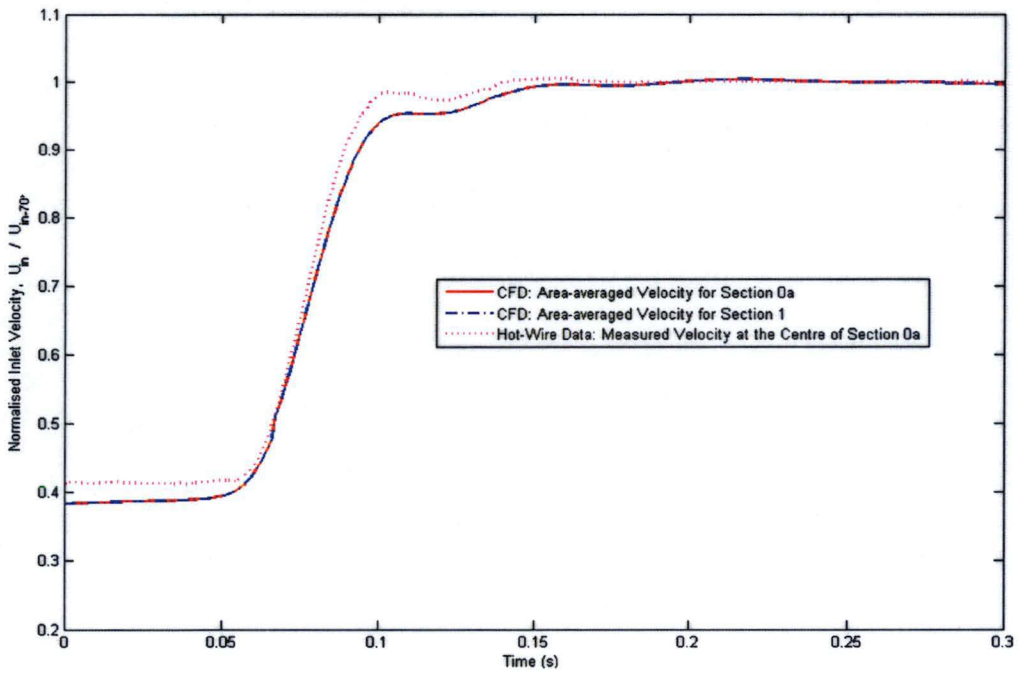

Figure 8.8: Comparisons between the CFD solution and experimental data for the velocity at the draft tube inlet when the valve is step-increased from 44% to 78% valve opening (Velocity is normalised with the steady-state value measured at 78% valve opening)

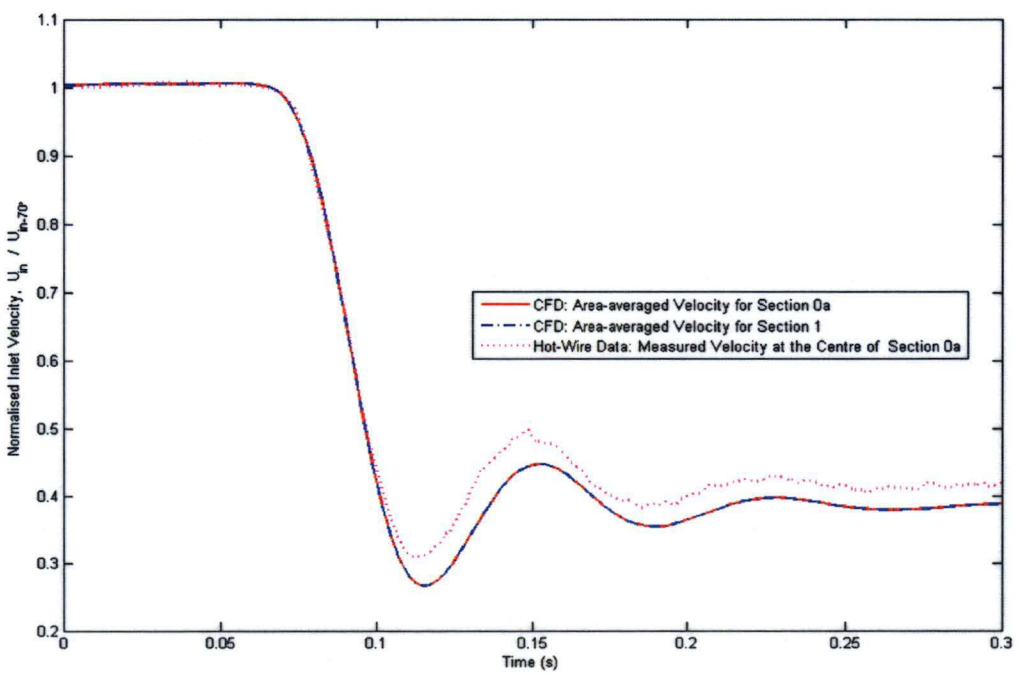

Figure 8.9: Comparisons between the CFD solution and experimental data for the velocity at the draft tube inlet when the valve is step-decreased from 78% to 44% valve opening (Velocity is normalised with the steady-state value measured at 78% valve opening)

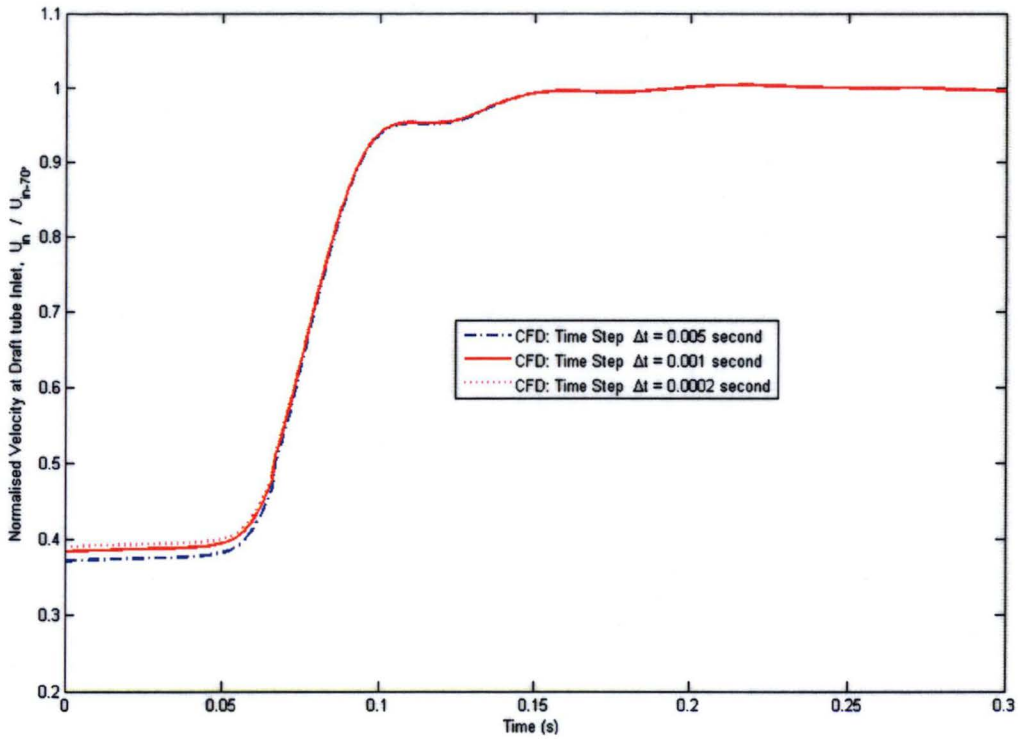

Figure 8.10: Comparisons of the CFD solutions performed at three different time steps for a step increase in the draft tube flow (Velocity is normalised with the steady-state value measured at 78% valve opening)

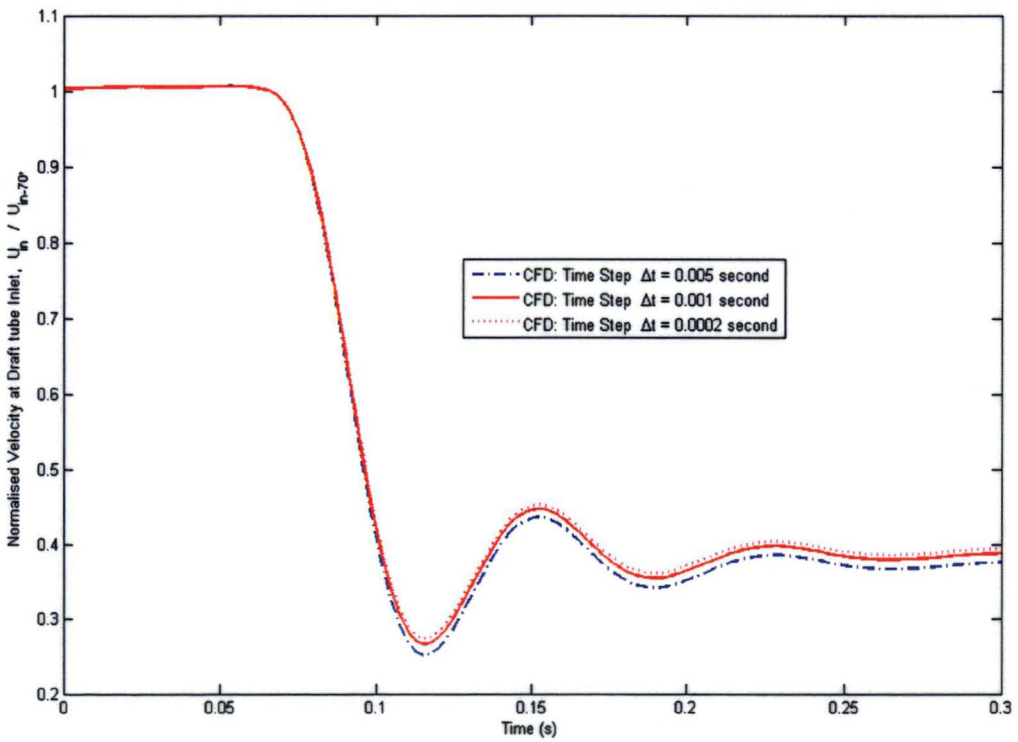

Figure 8.11: Comparisons of the CFD solutions performed at three different time steps for a step decrease in the draft tube flow (Velocity is normalised with the steady-state value measured at 78% valve opening)

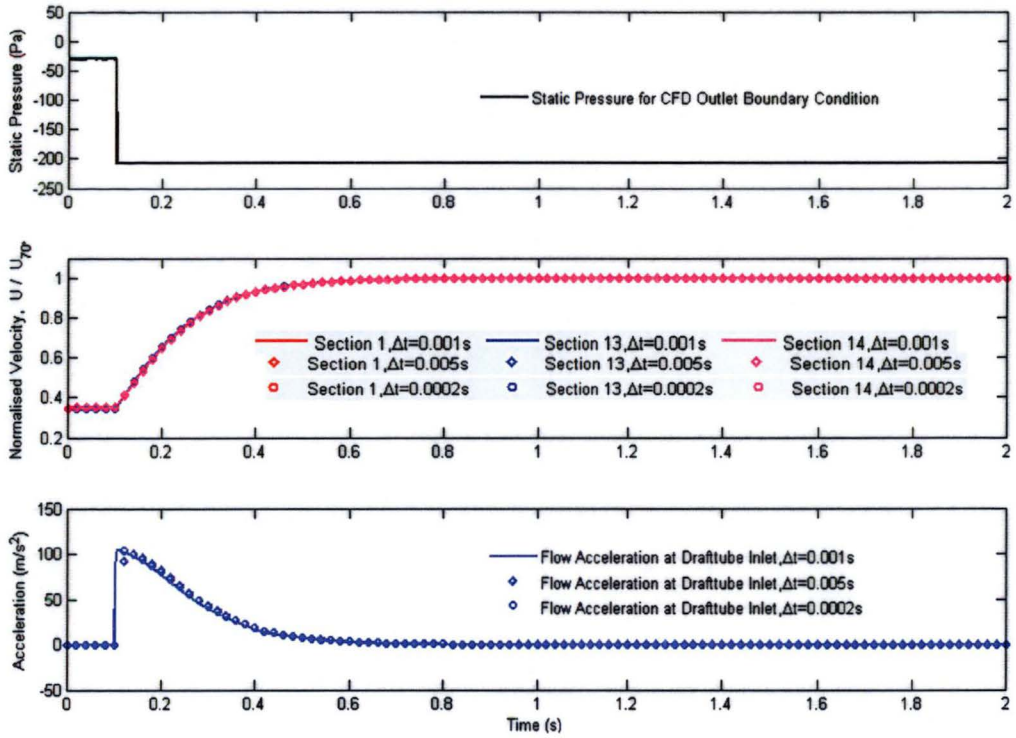

Figure 8.12: Comparisons of the CFD solutions performed at three different time steps for an instantaneous step increase in the draft tube flow (Velocity is normalised with the steady-state value measured at 78% valve opening)

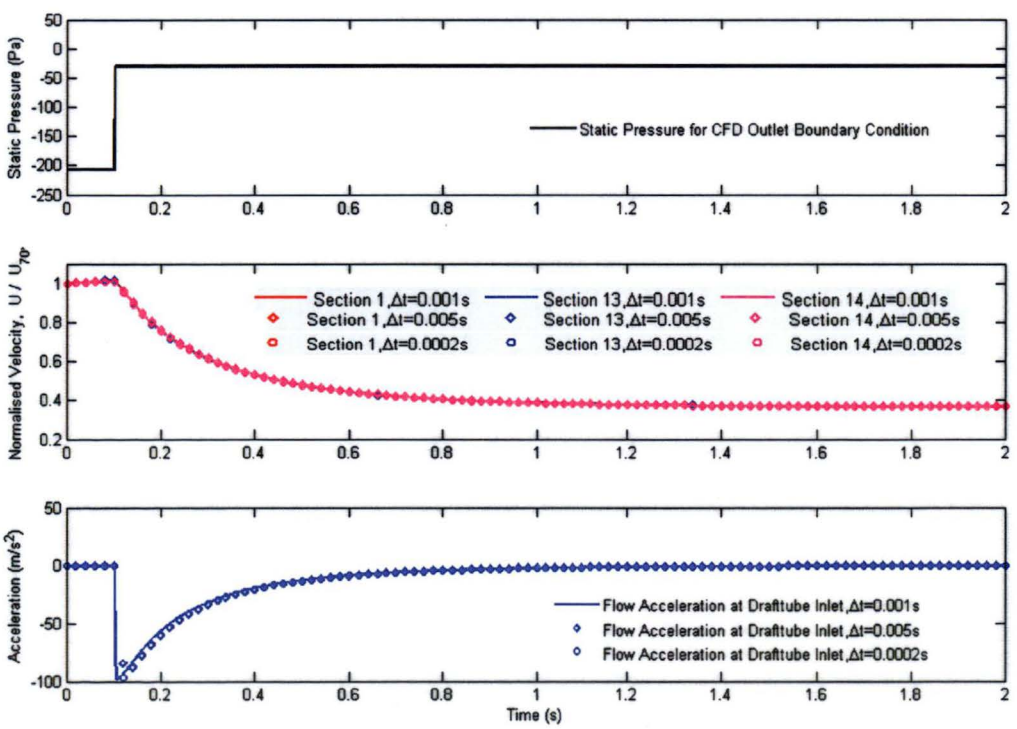

Figure 8.13: Comparisons of the CFD solutions performed at three different time steps for an instantaneous step decrease in the draft tube flow (Velocity is normalised with the steady-state value measured at 78% valve opening)

8.3.2 Two-dimensional Unsteady Stall Model

A two-dimensional unsteady stall model for the draft tube is developed here from the transitory stall analysis of Kwong and Dowling [61] for straight diffusers. Transitory stall usually occurs in the diffusing flow passage, where a large-scale flow separation is found. This separation zone is build up slowly and then suddenly swept out in a periodic way, causing an extensive area of unsteady reversed flow at the outlet and a large change of pressure recovery in the diffusing passage [81].

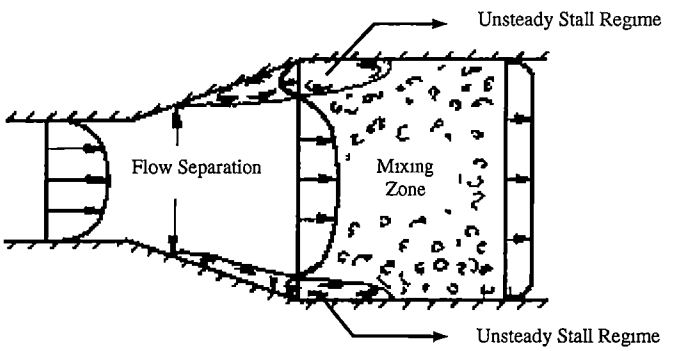

Figure 8.14: Transitory stall occurred in a typical diffusing flow passage (adapted from reference [81])

In this analysis, the inlet pipe and the draft tube model are so compact that the flow in them can be treated as incompressible. Hence, the unsteady Bernoulli equations along the streamlines from Section 0 (ambient conditions at pipe entrance) to Section 1 (draft tube inlet) and from Section 1 to Section 14 (draft tube outlet) of the model (see Figure 8.1) can be established:

$$p_1 + \tfrac{1}{2}\rho u_1^2 + \rho_a \frac{\partial}{\partial t}\int_0^1 u dl = P_a + \rho_a g \Delta z_{0\text{-}1} \tag{8.2}$$

$$p_{14} + \tfrac{1}{2}\rho_a u_{14}^2 + \rho_a \frac{\partial}{\partial t}\int_1^{14} u dx = p_1 + \tfrac{1}{2}\rho_a u_1^2 + \rho_a g \Delta z_{1\text{-}14} \tag{8.3}$$

where p = area-averaged static pressure at Sections 0, 1, or 14

P_a = ambient pressure at entrance of the inlet pipe

u = area-averaged velocity at Sections 0,1, or 14

l = average distance from Section 0 to Section 1

x = average distance from Section 1 to Section 14

$\Delta z_{0\text{-}1}$ = elevation head between Sections 0 and 1

$\Delta z_{1\text{-}14}$ = elevation head between Sections 1 and 14

On the other hand, the compressibility effects are thought to be quite significant inside the outlet extension box. The volume of the outlet extension box is relatively large and the flow inside the extension box may behave like a Helmholtz resonator. Applying the continuity equation from the draft tube entrance to the exit of the extension box yields:

$$\rho_a A_1 u_1 = V_{ext} \frac{\partial \rho_a}{\partial t} + \rho_a A_{ext} u_{ext-ss} \tag{8.4}$$

where A_1 = cross-sectional area at draft tube entrance

A_{ext} = cross-sectional area of the extension box

u_{ext-ss} = steady-state value of the velocity at the exit of the extension box

V_{ext} = volume of the outlet extension box ≈ 0.087 m^3

Flow Continuity between Section 1 and 14 gives:

$$\rho_a A_1 u_1 = \rho_a A_{14} u_{14-ss} = \rho_a \frac{A_1}{\left(1 - \overline{C_p}\right)^{0.5}} u_{14-ss} \tag{8.5}$$

where A_{14} = cross-sectional area at the draft tube outlet $= A_{ext}$

$u_{14\text{-}ss}$ = steady-state value of the velocity at the draft tube outlet $\approx u_{ext\text{-}ss}$

$\overline{C_p}$ = draft tube static pressure coefficient

Equation 8.5 applies to the section of flow that is inviscid (i.e. unstalled flow region) in the draft tube model.

The flow in the draft tube is highly unsteady and the fluctuations in the flow cannot be altered immediately. A first-order lag equation is established to account for the convective lag effect inside the draft tube model:

$$\tau_d \frac{du_{14}}{dt} = u_{14-ss} - u_{14} \tag{8.6}$$

where τ_d = convective time lag $= L / u_1$

u_{14} = instantaneous velocity at the draft tube outlet

Kwong and Dowling [61] apply a similar unsteady stall model to predict the frequency of oscillation inside a straight diffuser. For linear perturbation of frequency (ω), Equations 8.2~8.6 can be linearised to:

$$\hat{p}_1 + \rho_a \overline{u}_1 \hat{u}_1 = -\rho_a i\omega L_{in} \hat{u}_1 \tag{8.7}$$

$$\hat{p}_{14} = \frac{\rho_a A_1 c^2}{i\omega V_{ext}} \hat{u}_1 - \frac{\rho_a A_{14} c^2}{i\omega V_{ext}} \hat{u}_{14} \tag{8.8}$$

$$\hat{u}_{14} = \frac{A_1}{A_{14}(1 + i\omega\tau_d)} \hat{u}_1 = \frac{(1 - \overline{C}_P)^{0.5}}{(1 + i\omega\tau_d)} \hat{u}_1 \tag{8.9}$$

$$\hat{p}_{14} + \rho_a \overline{u}_{14} \hat{u}_{14} + \tfrac{1}{2} \rho_a i\omega L(\hat{u}_1 + \hat{u}_{14}) = \hat{p}_1 + \rho_a \overline{u}_1 \hat{u}_1 \tag{8.10}$$

where L = effective length of the draft tube model $= L_{dt} + 0.13\left(\frac{4A_1}{\pi(1-\overline{C}_P)^{0.5}}\right)^{0.5}$

L_{dt} = average length of the draft tube model

L_{in} = effective length of the inlet pipe = $l_p + 0.3D_p$

l_p = length of the inlet pipe

D_p = inlet pipe diameter

c = speed of sound at 20°C, 1atm ≈ 343.5 m/s

Substituting Equations 8.7~8.9 to 8.10 yields:

$$\tau_d(\tfrac{1}{2}L + L_{in})i\omega^3 + L_{eq}\omega^2 - \left(\frac{A_1 c^2 \tau_d}{V_{ext}} + \overline{u}_1(1-\overline{C}_P)\right)i\omega - \frac{A_1 c^2}{V_{ext}}\left[1-(1-\overline{C}_P)^{0.5}\right] = 0 \tag{8.11}$$

where L_{eq} = equivalent length of the inlet pipe and draft tube model

$= 0.5L \times [(1-\overline{C}_P)^{0.5} + 1] + L_{in}$

For a convective time lag of around 0.057 second (see Section 8.4.1 for details), the frequency of oscillation ($f = \omega / 2\pi$) is determined by solving Equation 8.11 in MATLAB. In general, the solution consists of three roots: one root of ω is purely imaginary and describes a decaying mode; the other two roots are complex. The real part of ω gives the frequency of oscillation, while the imaginary part of ω represents the damping [61]. The predicted frequency of oscillation for the current draft tube model is 19.3 Hz. This is much higher than the value of 3~5 Hz for Kwong and Dowling's straight diffuser tests; but this is expected, as the frequency of oscillation is highly geometry-dependent. The critical parameter influencing the solution is the volume of outlet extension box connected at the exit of the draft tube. Kwong and Dowling's diffuser model has a plenum volume of 2.66 m^3, which is 31 times larger than the volume of the outlet extension box used in the present analysis.

Figure 8.15 shows the power spectrum analysis of the instantaneous wall static pressure at 78% valve opening. As illustrated, the frequency of oscillation calculated from the unsteady stall model lies within the region of local spectral peak. However, the observed spectral peak is quite broad because of the relatively low divergence angle ($2\theta_{eq} \approx 9.4°$) for the current draft tube geometry. A similar trend was also found by Kwong and Dowling [61]. Hence, it is very difficult to say at this stage of whether the convective lag time calculated by the unsteady stall model is truly representative of the actual system behaviour.

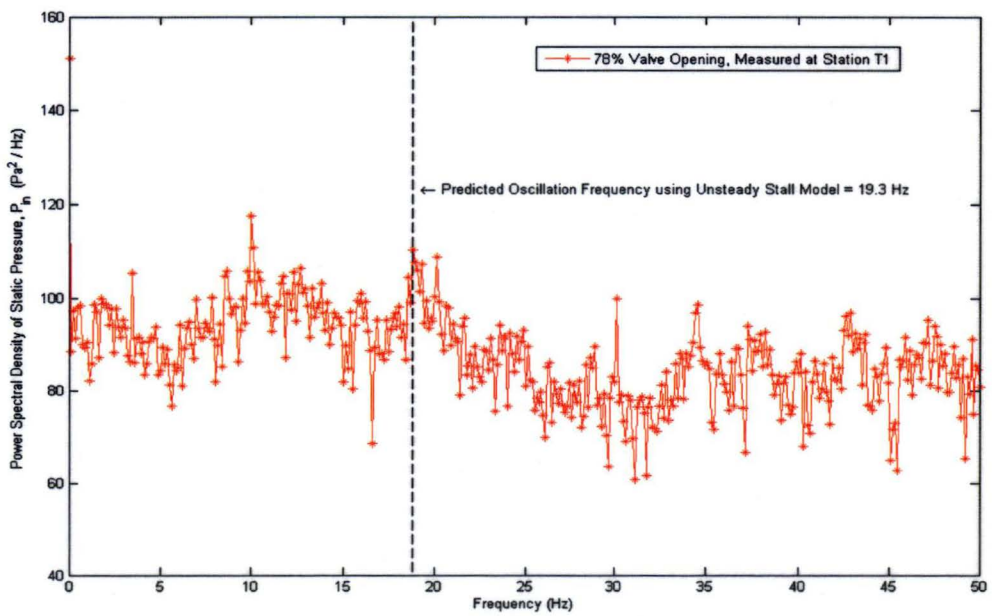

Figure 8.15: Power spectrum analysis of the wall static pressure at the inlet of the draft tube model. The oscillation frequency calculated from the unsteady stall model matches the local peak of the pressure spectrum

8.3.3 One-dimensional Momentum Theory

One-dimensional momentum theory does not take into account the lag time due to unsteady flow effects but it is useful for comparisons with the three-dimensional CFD model. The assumptions used in the inelastic waterway model of the power plant will also be applied in this analysis. The inlet pipe connected to the draft tube is treated like the waterway conduit of the power plant but the turbine runner is not included here. Applying the momentum equation between Sections 0 and 1 of the inlet pipe (see Figure 8.1) gives:

$$\begin{aligned} &\sum F = ma \\ &\Rightarrow \frac{p_0}{\rho_a g} - \frac{p_1}{\rho_a g} - h_f = \tau_{1D-p} \frac{du_0}{dt} \end{aligned} \tag{8.12}$$

where F = pressure force acting on the inlet pipe

m = mass of the air within the inlet pipe

a = flow acceleration

τ_{1D-p} = inertia time constant for the inlet pipe = l_p / g

l_p = inlet pipe length

h_f = head loss of the inlet pipe due to friction

For the draft tube model, the unsteady Bernoulli equation can be applied between Sections 1 and 14:

$$p_1 + \tfrac{1}{2} \rho_a u_1^2 = p_{14} + \tfrac{1}{2} \rho_a u_{14}^2 + \rho_a \frac{\partial}{\partial t} \int_1^{14} u dx \tag{8.13}$$

Flow continuity between Sections 0 and 1 as well as Sections 0 and 14 gives:

$$\begin{cases} u_1 = u_0 \\ u_{14} = \left(\dfrac{A_1}{A_{14}} \right) u_0 \end{cases} \tag{8.14}$$

Substituting Equation 8.14 in 8.13 and rearranging gives:

$$\frac{p_1}{\rho_a g} = \frac{1}{\rho_a g}\left[p_{14} + \tfrac{1}{2}\rho_a u_{14}^2 - \tfrac{1}{2}\rho_a u_1^2 + \rho_a \frac{\partial}{\partial t}\int_1^{14} u dx \right]$$

$$= \frac{p_{14}}{\rho_a g} - \left(1 - \frac{A_1^2}{A_{14}^2}\right)\frac{u_0^2}{2g} + \frac{A_1}{2g}\sum_{i=1}^{13} L_i \times \frac{A_i + A_{i+1}}{A_i \times A_{i+1}}\frac{du_0}{dt} \tag{8.15}$$

$$= \frac{p_{14}}{\rho_a g} - \overline{C}p_{ideal-dt}\frac{u_0^2}{2g} + \tau_{1D-dt}\frac{du_0}{dt}$$

where τ_{1D-dt} = inertia time constant for the draft tube model
$\overline{C}p_{ideal-dt}$ = ideal pressure recovery factor based on area ratio A_1/A_{14}

The static head term at the pipe entrance can be evaluated from the Bernoulli equation:

$$\frac{p_0}{\rho_a g} = \frac{P_a}{\rho_a g} - \frac{u_0^2}{2g} \tag{8.16}$$

The head loss due to friction (h_f) for the inlet pipe can be expressed as:

$$h_f = \frac{fl_p}{D_p}\frac{u_0^2}{2g} \tag{8.17}$$

The friction factor of $f = 0.015$ is assumed based on the Moody diagram with smooth pipe and a Reynolds number of $Re_D = 2.5\times10^5$. Substituting Equations 8.15~8.17 into 8.12 gives:

$$\frac{P_a}{\rho_a g} - \frac{u_0^2}{2g} - \frac{p_{14}}{\rho_a g} + \overline{C}p_{ideal-dt}\frac{u_0^2}{2g} - \tau_{1D-dt}\frac{du_0}{dt} - \frac{fl_p}{D_p}\frac{u_0^2}{2g} = \tau_{1D-p}\frac{du_0}{dt}$$

$$\Rightarrow u_0 = \frac{1}{\tau_{1D-dt} + \tau_{1D-p}}\int\left\{-\frac{p_3 - P_a}{\rho_a g} - \left[1 - \overline{C}p_{ideal} + \frac{f(L_{in} + L)}{D_p}\right]\frac{u_0^2}{2g}\right\}dt \tag{8.18}$$

Equation 8.18 is solved using the MATLAB Simulink. The time response of the flow subjected to an instantaneous step or a sinusoidal change in outlet static pressure is analysed and compared with the CFD model in Section 8.4.

8.4 Analysis of Convective Lag Response for the Draft tube Flow

8.4.1 Convective Time Lag

Analysis of unsteady flow in the draft tube is a complex problem that has not received sufficient attention. The convective time lag for transient operation is particularly important for accurate control and modelling of a power plant. This Section presents an initial stage of development for modelling transient flow behaviour in the draft tube. The flow responses of the draft tube will be examined in detail here. The convective lag time τ_d for the draft tube model is of the order of $L / \overline{u}_1$ where L is the average length of the draft tube and $\overline{u}_1$ is the average of the initial and final values of the transient velocities at the draft tube inlet. In the current simulations, the average inlet velocity $\overline{u}_1$ is about 20 m/s, while the average draft tube length is 1.1 m. This yields a convective lag time of $\tau_d = 0.057$ second.

Figures 8.16~8.17 show the time response of the inlet velocity subjected an instantaneous step increase or decrease in the outlet static pressure. As the draft tube is assumed to behave like a first-order system, the time response (t) of the draft tube flow when subjected to an instantaneous change in outlet static pressure can be determined using a dimensionless time scale t/τ such that:

$$\frac{U_{in}(t) - U_{in}(initial)}{U_{in}(final) - U_{in}(initial)} = e^{-t/\tau} \quad \text{where} \quad t/\tau = 1 \tag{8.19}$$

The time responses of the draft tube flow calculated by the three-dimensional CFD model and one-dimensional inertia model are summarised in Table 8.2. As illustrated, the time response for the load rejection is longer than for load acceptance (the time response of the flow on opening differs from that on closing). This is presumably caused by the differences in frictional damping in these two cases.

Case	*Time Response (second)*	
	3-D CFD Model	*1-D Inertia Model*
Load acceptance (Decrease in outlet static pressure)	0.14	0.10
Load rejection (Increase in outlet static pressure)	0.27	0.22

Table 8.2: Time response of the draft tube flow when subjected to an instantaneous change in outlet static pressure

The unphysical bump in the velocity calculated by the one-dimensional model (see Figures 8.16~8.17) at the start of the transient is mainly due to the rigid column assumption, which does not work well for the case of instantaneous changes in draft tube flow. Overall, the three-dimensional CFD model predicts a longer response time than the one-dimensional inertia model. The differences between the CFD model and inertia model are 20~30% lower than the expected lag time of 0.057 second. This can be partly explained by the assumption of flow uniformity in the one-dimensional inertia model, which will be discussed in more detail in Section 8.4.2.

Although the Francis turbine runner and guide vanes are not included in this analysis, the convective time lag for flow through these components is expected to be of the same order as the convective time lag of flow through the turbine draft tube. For the full-scale prototype, the convective time lag of the turbine draft tube is about 2.5~3.6 seconds for a given initial power output of 0.2 p.u.~ 0.9 p.u.

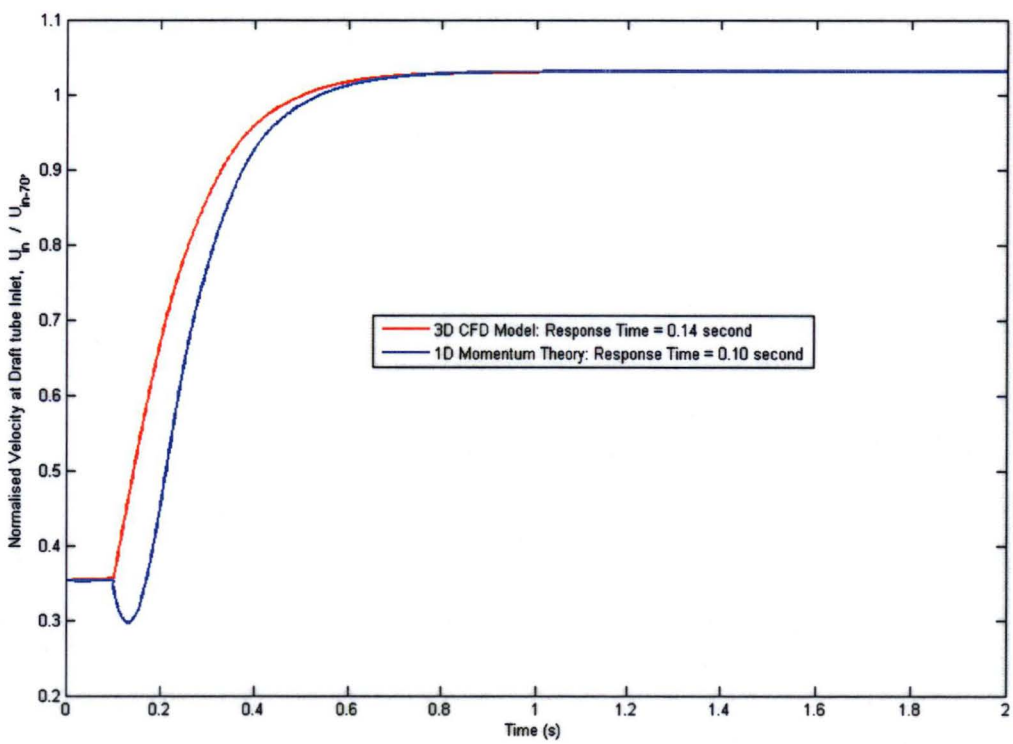

Figure 8.16: Comparisons between three-dimensional CFD model and one-dimensional momentum theory for the flow subjected to an instantaneous step decrease in outlet static pressure

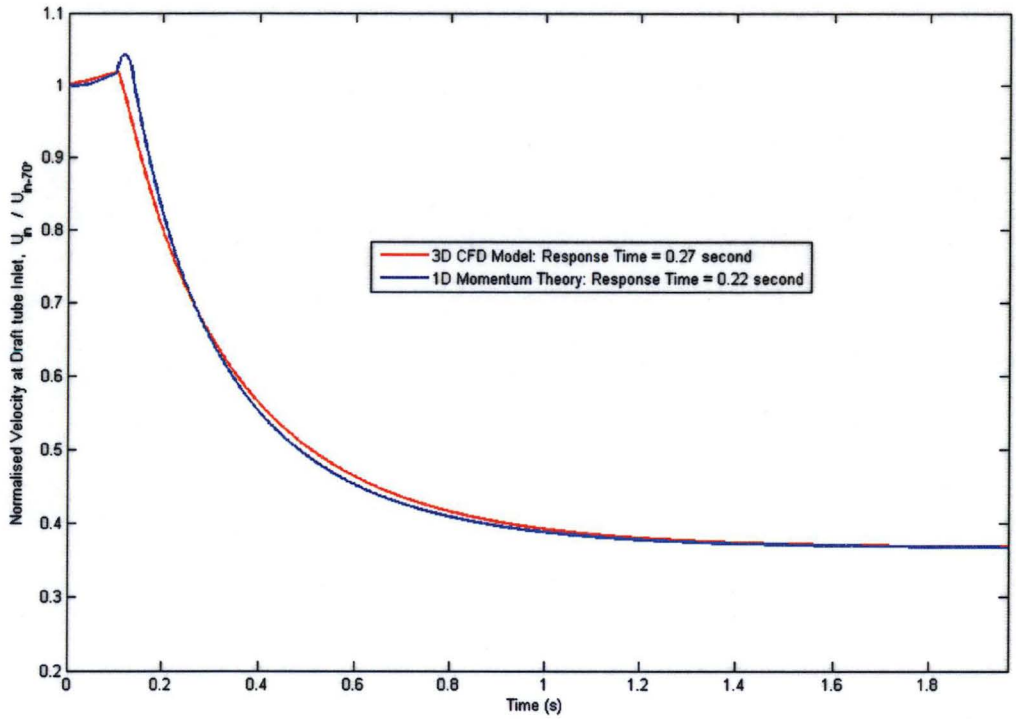

Figure 8.17: Comparisons between three-dimensional CFD model and one-dimensional momentum theory for the flow subjected to an instantaneous step increase in outlet static pressure

8.4.2 Influence of Flow Non-uniformity

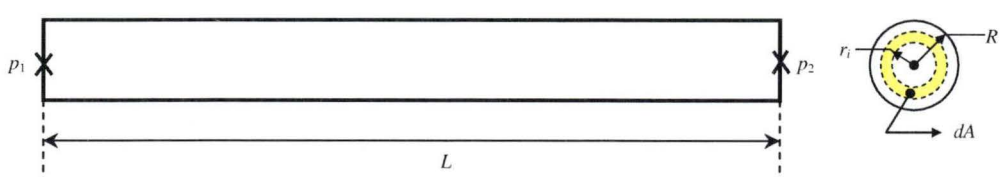

Figure 8.18: Geometry of a simple waterway conduit used to investigate the effect of flow non-uniformity

The effect of flow non-uniformity on transient operations of the waterway column is now analysed by considering the transient flow in a simple conduit with a constant cross-sectional area A and a conduit length L. A static pressure differential is applied at the end of the conduit to cause an acceleration or deceleration of the flow (du/dt). Conduit head losses are assumed negligible for simplicity.

Applying the one-dimensional momentum equation across the conduit (between Sections 1 and 2 as shown in Figure 8.18) gives:

$$\sum F = ma$$

$$\Rightarrow (p_1 - p_2)A = \rho_a AL\frac{du}{dt} \tag{8.20}$$

$$\Rightarrow \frac{du}{dt} = \frac{1}{\rho_a L}(p_1 - p_2)$$

The change of flow per unit time dq through an elemental area dA_i can be computed as follows:

$$dq = \sum dq_i = \sum \frac{dA_i}{\rho_a L}(p_1 - p_2) \tag{8.21}$$

The elemental area dA_i is defined as:

$$dA_i = \pi\left[\left(r_i + \frac{R}{2k}\right)^2 - \left(r_i - \frac{R}{2k}\right)^2\right] \tag{8.22}$$

where k = the number of equal elements of the pipe radius

R = radius of the conduit

r_i = radial distance of the element from the centre of the conduit

A power law is used to describe the initial non-uniform velocity distribution q_{ini}:

$$\frac{u_i}{U_{\max}} = \left(1 - \frac{r_i}{R}\right)^{1/n} \quad \text{where} \quad U_{\max} = \frac{(n+1)(2n+1)}{2n^2}u_{ini} \tag{8.23}$$

$$\therefore q_{ini-i} = u_i A = \left(1 - \frac{r_i}{R}\right)^{1/n}\frac{(n+1)(2n+1)}{2n^2}u_{ini}$$

For a non-uniform velocity distribution, the change of flow normalised by initial flow rate dq/q_{ini} is obtained as follows:

$$\frac{dq}{q_{ini}} = \sum \frac{dq_i}{q_{ini-i}}$$

$$= \frac{(p_1 - p_2)}{\rho_a L} \times \frac{2n^2}{(n+1)(2n+1)u_{ini}} \times \sum \left[\left(1 - \frac{r_i}{R}\right)^{-1/n} \times \frac{dA_i}{A} \right] \tag{8.24}$$

$$= \frac{(p_1 - p_2)}{\rho_a L} \times \frac{2n^2}{(n+1)(2n+1)u_{ini}} \times \sum \left(1 - \frac{r_i}{R}\right)^{-1/n} \times \left[\left(\frac{r_i}{R} + \frac{1}{2k}\right)^2 - \left(\frac{r_i}{R} - \frac{1}{2k}\right)^2 \right]$$

For a uniform flow distribution, the change of flow per initial flow rate dq/q_{ini} is calculated as:

$$\frac{dq}{q_{ini}} = \sum \frac{dq_i}{q_{ini-i}}$$

$$= \frac{(p_1 - p_2)}{\rho_a L u_{ini}} \times \frac{dA_i}{A} \tag{8.25}$$

$$= \frac{(p_1 - p_2)}{\rho_a L u_{ini}} \times \sum \left[\left(\frac{r_i}{R} + \frac{1}{2k}\right)^2 - \left(\frac{r_i}{R} - \frac{1}{2k}\right)^2 \right]$$

To show the effect of flow non-uniformity, the cross-sectional area of the conduit has been divided into 100,000 equal elements. For a conduit length of L = 1 m and a fluid density of ρ_a = 1.19 kg/m^3, a static pressure differential of 207 Pa is applied at the end of the conduit. The change of flow rate per initial flow is calculated and compared in Table 8.3. It is apparent that the flow responses are quicker in a non-uniform flow than in a uniform flow. About 3% difference is found between the computed flow accelerations using a uniform and a non-uniform velocity distribution. The effect will be more significant in the full-scale machine because the flow distribution is expected to be highly irregular in the real turbine draft tube. This partly explains the discrepancies observed in Section 8.4.1.

	Non-Uniform Flow / Uniform Flow				
n	7	8	9	10	11
dq/q_{ini} (u_{ini}=11 m/s)	1.026	1.019	1.016	1.013	1.010
dq/q_{ini} (u_{ini}=30 m/s)	1.025	1.019	1.015	1.013	1.010

Table 8.3: Effects of flow non-uniformity on the change of flow per initial flow rate. Flow is becoming more uniform with increasing value of *n*

8.4.3 Effect of Pressure Oscillation Frequency

The mechanism of the convective time lag in the draft tube with respect to the quasi-steady flow is assumed universal in the present study. This universality may originate from the wave propagation properties of the vortex flows. In general, the dynamic response of the draft tube flow is similar to that of a first-order system, and the lag time is assumed constant for all types of excitations. Figure 8.19 shows the variation of the inlet flow speed when subjected to a sinusoidally varying static pressure at the draft tube outlet. Three different oscillation frequencies are being simulated: 0.5 Hz, 4.5 Hz, and 8.5 Hz. Results show that the attenuation of the flow amplitude decreases with increasing frequency, whereas the phase lag between the velocity and the pressure increases with increasing frequency.

The gains and phase lags calculated by the three-dimensional CFD model and one-dimensional momentum theory are compared in Table 8.4. Although the predicted values do not vary significantly between the models, some frequency dependency can still be observed for phase lags between the pressure and the velocity. This difference cannot be accounted for by the inertia effects alone, which is currently observed in the modelling of the power plant. The frequency-dependent phase lag could be more significant when the turbine guide vanes are included in the simulations. More research must be carried out in the future to confirm this statement.

Oscillation Frequency for the Model (Hz)	*Oscillation Frequency for the Prototype (Hz)*	*Gain (dB)*		*Phase Lag (°)*	
		CFD	*Inertia*	*CFD*	*Inertia*
0.5	0.011	3.95	3.49	– 24.9	– 23.2
4.5	0.099	13.75	11.83	– 84.5	– 80.6
8.5	0.19	19.79	17.42	– 88.5	– 82.2

Table 8.4: Phase lag and gain between the inlet flow speed and outlet static pressure of the draft tube model calculated by the three-dimensional CFD model and one-dimensional inertia model

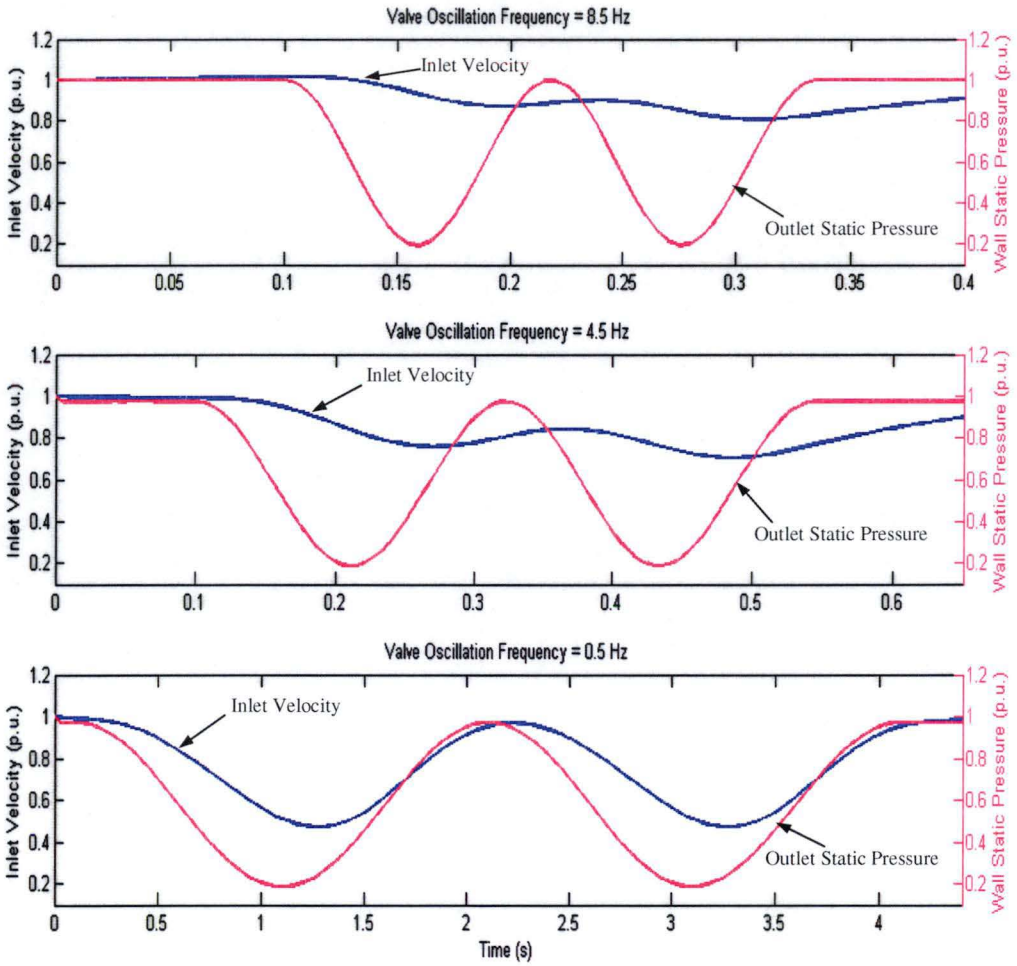

Figure 8.19: Comparisons between the inlet flow speed and outlet static pressure at three different oscillation frequencies. Both transient static pressure and velocity are normalised with their initial values

8.3.4 Effects of Inlet Swirl on the Transient Phenomena of a Draft tube

Nonoshita et al. [84] conducted a series of load rejection tests to investigate the effects of inlet swirl on the transient phenomena in a straight draft tube. The strength of initial swirl rate was found to greatly affect the transient behaviour associated with water column separation in the draft tube. A larger swirl rate generated a large amount of released air and caused a time delay of around 0.5 second in the first pressure peak and a longer period between these pressure peaks. However, their results also showed inlet swirl to have little impact on the development of the flow rate in the draft tube. Hence, a constant lag time may be sufficient to describe the convective lag effects of the draft tube flow in a Francis-turbine power plant. This increases confidence in the simplified zero-swirl analysis adopted in the present investigation.

8.5 Analysis of Transient Draft tube Forces and Loss Coefficient

CFD solutions are used here as a primary tool for investigating the transient draft tube forces and the unsteady pressure loss coefficient in this analysis. The draft tube flow subjected to an instantaneous step change in the outlet static pressure is examined here. The procedure used to compute the unsteady pressure losses is similar to the one used for steady-flow analyses. The total pressures are mass-flow-averaged over the entire inlet and outlet planes of the draft tube model. For the transient draft tube forces, the volume of the draft tube is divided into 13 smaller control volumes to ease the analysis. The conventional approach of treating the draft tube as a single component tends to overestimate the applied forces on the draft tube even at steady-flow conditions.

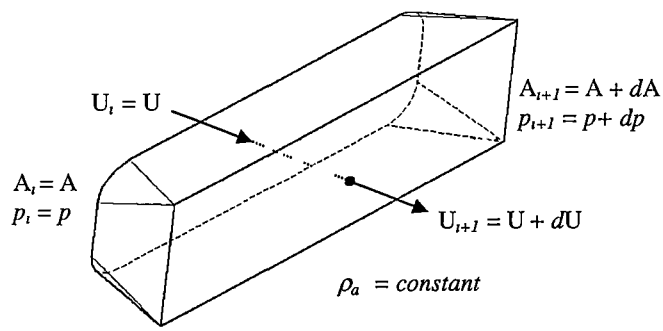

Figure 8.20: A portion of the draft tube model used for the analysis of draft tube forces

Figure 8.20 shows a portion of the draft tube model used for calculation of the draft tube forces. The force applied on the draft tube F_{dt} is the sum of the net static pressure forces acting on the boundaries of the control surface. The draft tube force coefficient $C_{F\text{-}dt}$ can then be expressed as follows:

$$C_{F-dt} = \sum_{i=1}^{14} \frac{F_i - F_{i+1} + F_{bs}}{0.5\rho_a U_{in}^2 A_{in}} = \sum_{i=1}^{14} \frac{(p_i - p_{i+1})}{0.5\rho_a U_{in}^2} \times \left(\frac{A_i + A_{i+1}}{2A_{in}} \right) \tag{8.26}$$

where F_i = pressure force acted at Section i = $p_i A_i = pA$

F_{i+1} = pressure force acted at Section i+1 = $p_{i+1} A_{i+1} = (p + dp)(A + dA)$

F_{bs} = pressure force acted at bounding surface = $\left(p + \frac{dp}{2} \right) dA$

Figures 8.21~8.22 show the time varying pressure loss coefficients of the draft tube model computed by the CFD model, while Figures 8.23~8.24 present the transient draft tube forces for an instantaneous step change in outlet static pressure. For a load acceptance, the time needed for the draft tube flow to reach its final steady-state values is about 0.5 second, which is equivalent to 9 times the convective time lag. On the other hand, the settling time (T_s) for the draft tube flow after a load rejection is approximately 1.2 second, which is equal to 21 times the convective time lag. These properties will be used for the power plant modelling presented in Section 8.4.1.

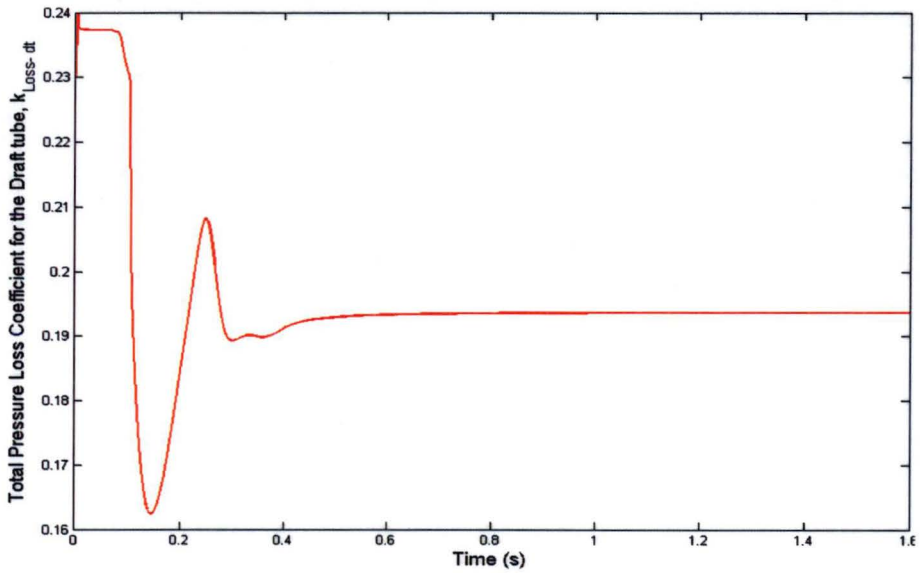

Figure 8.21: Computed unsteady pressure loss coefficient of the draft tube model following an instantaneous step decrease in the outlet static pressure (corresponds to load acceptance)

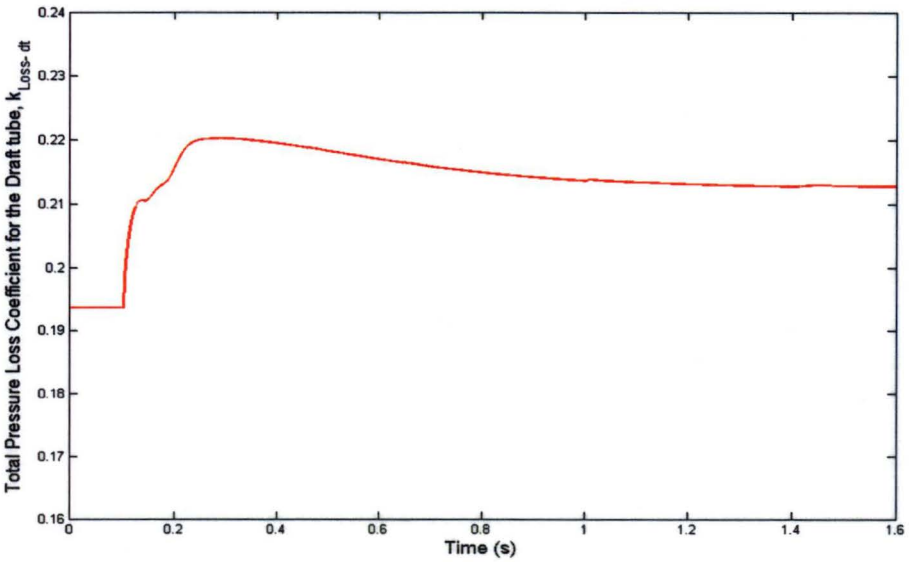

Figure 8.22: Computed unsteady pressure loss coefficient of the draft tube model following an instantaneous step increase in the outlet static pressure (corresponds to load rejection)

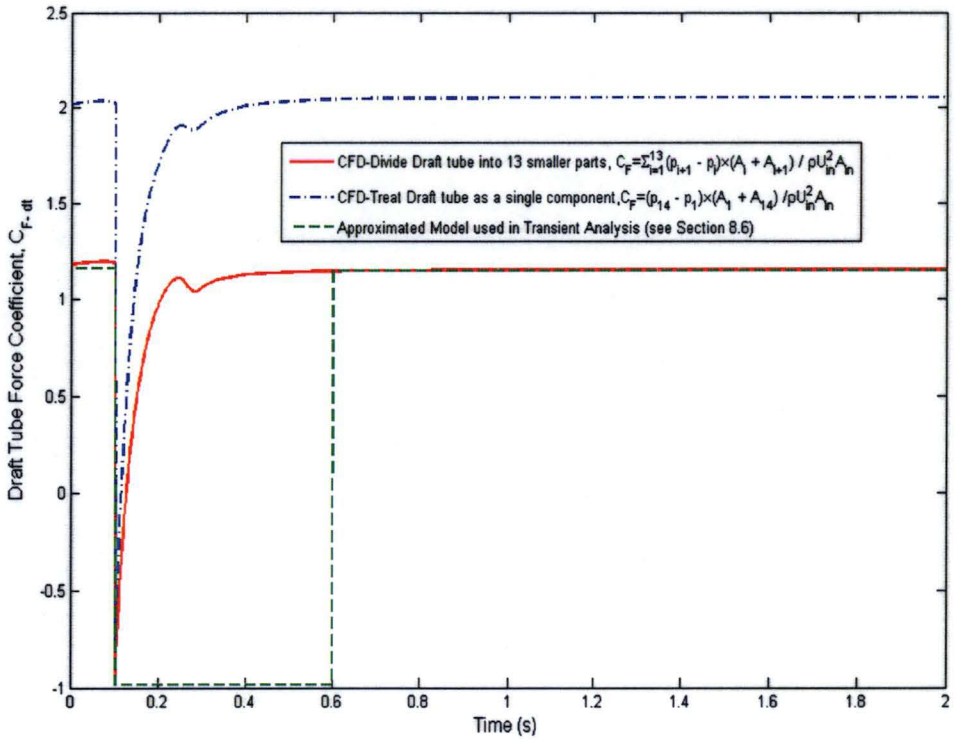

Figure 8.23: Computed transient pressure force coefficient for the draft tube model following an instantaneous step decrease in the outlet static pressure (corresponds to load acceptance)

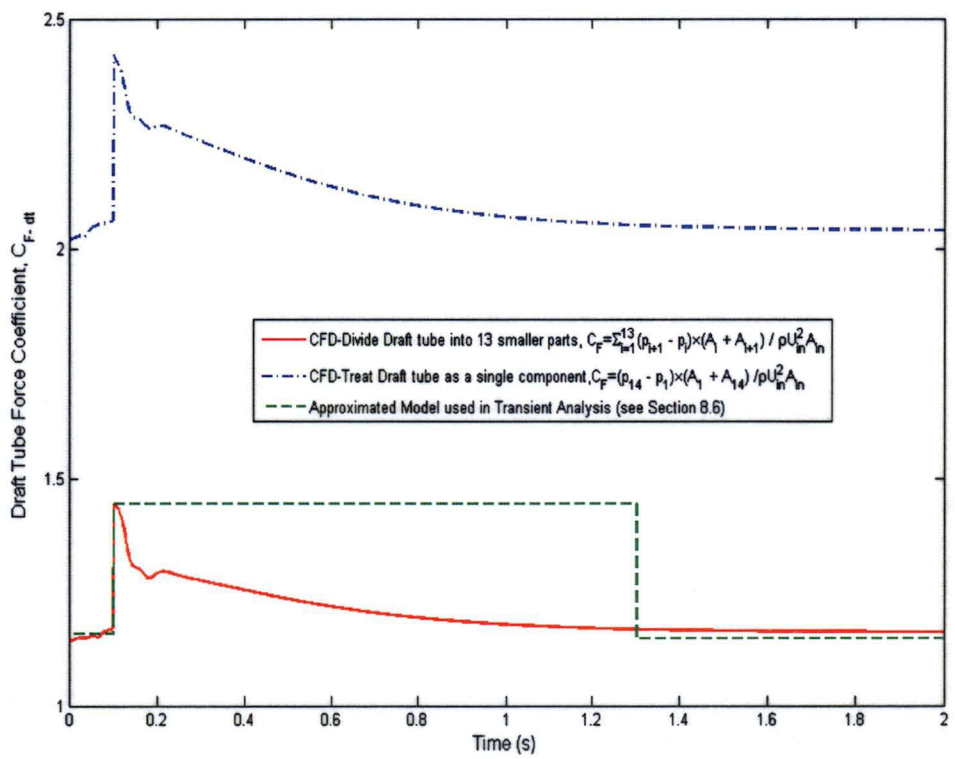

Figure 8.24: Computed transient pressure force coefficient for the draft tube model following an instantaneous step increase in the outlet static pressure (corresponds to load rejection)

8.6 Practical Application of Transient Analysis for Power Plant Modelling

To allow for the unsteady flow effects, the transient force coefficients of the draft tube ($C_{F\text{-}dt}$) are now included in the Simulink model for the Mackintosh power plant (see Figure 8.25). The peak values of the $C_{F\text{-}dt}$ calculated in Section 8.3.3 are used to limit the values of the transient static pressure force coefficient K_{dt} used in the power plant model (see Equation 4.23 in Section 4.6.2.6 for calculation of K_{dt}). As mentioned in Section 8.3.3, the settling time (T_s) for the transient forces can be related to the convective lag time of the draft tube while the convective time lag (τ_d) depends on the initial and final steady-state values of the operating flow.

$$\begin{cases} T_{s-up} = 9 \times \tau_d \\ \\ T_{s-down} = 21 \times \tau_d \end{cases} \tag{8.27}$$

where $T_{s\text{-}up}$ = settling time for load acceptance

$T_{s\text{-}down}$ = settling time for load rejection

τ_d = convective time lag for load acceptance= $\dfrac{A_{in-dt} L}{\overline{Q} \times Q_{rated}}$

$A_{in\text{-}dt}$ = cross-sectional area at the draft tube inlet ≈ 13 m^2

L = average length of the draft tube ≈ 30 m

Q_{rated} = rated flow rate of the Francis turbine ≈ 150 m^3/s

$\overline{Q}$ = per-unit flow rate for a load acceptance/rejection ≈ $\frac{1}{2}\left(\overline{Q}_{initial} + \overline{Q}_{final}\right)$

The settling time for the transient draft tube forces are found to be around 23~32 seconds when the load is increased and 50~72 seconds when the load is rejected. The simulated results are presented in Figures 8.26~8.30 (flow non-uniformity effects are included in both models). As illustrated, the inclusion of the transient draft tube force coefficient has better modelled the magnitude of the transient power output fluctuations for the Mackintosh power station.

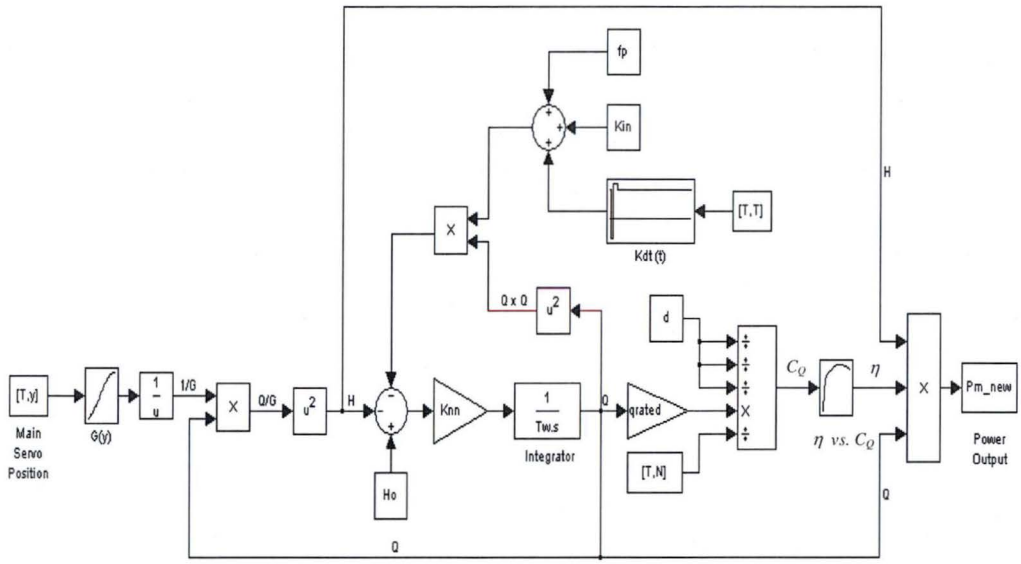

Figure 8.25: Simulink block diagram showing the nonlinear turbine & inelastic waterway model for Mackintosh power plant. The effects transient draft tube forces are included in this model (Compared with Figure 4.4)

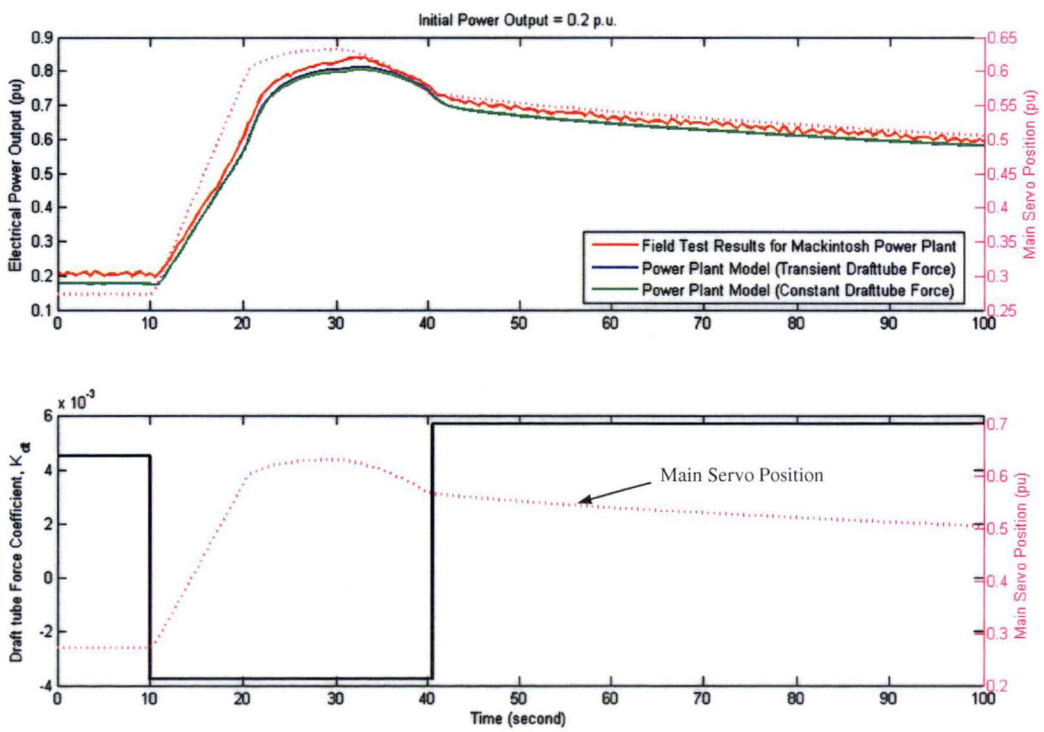

Figure 8.26: Comparison of the simulated and measured power outputs for load acceptance when the machine is operated at an initial load of 0.2 p.u. (Dotted line indicates main servo position)

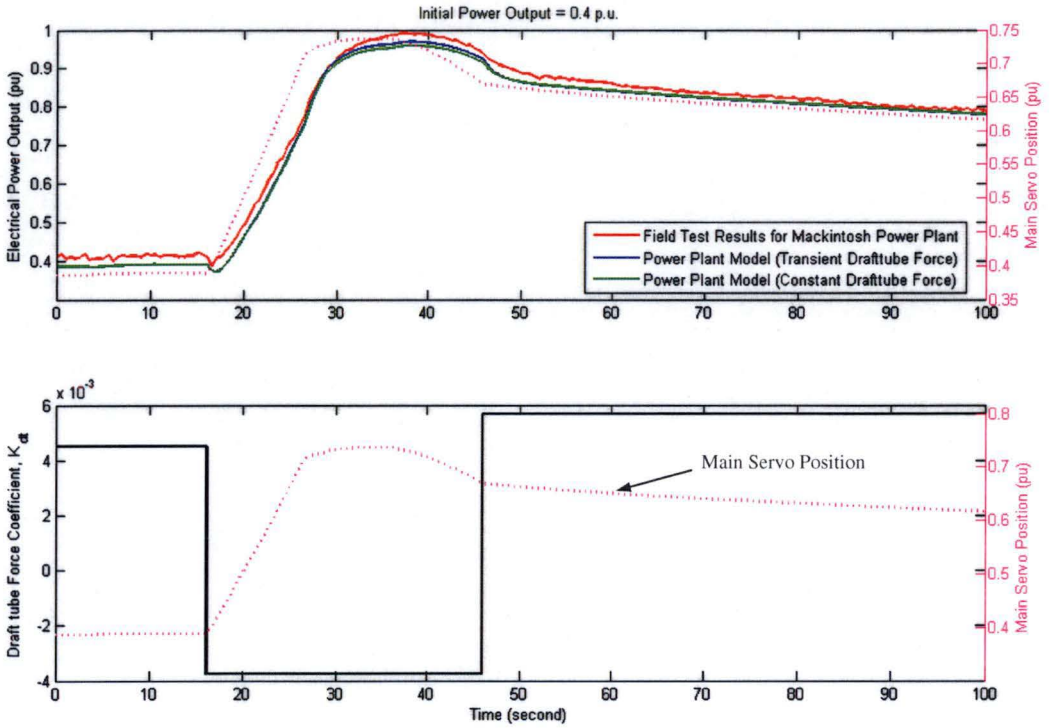

Figure 8.27: Comparison of the simulated and measured power outputs for load acceptance when the machine is operated at an initial load of 0.4 p.u. (Dotted line indicates main servo position)

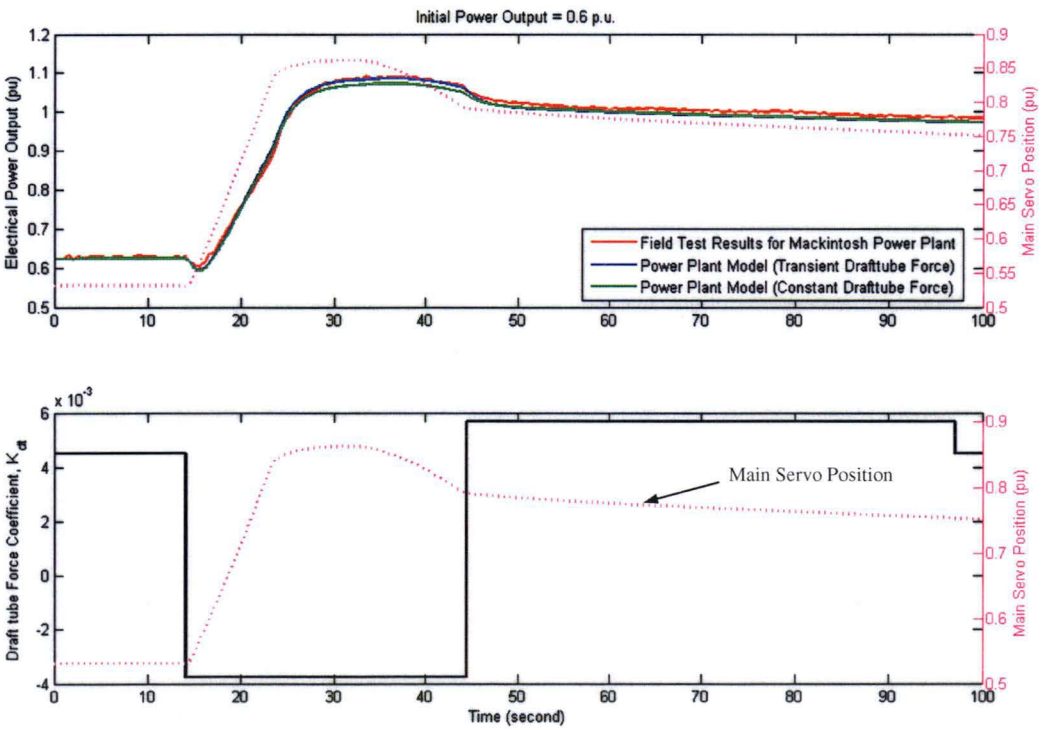

Figure 8.28: Comparison of the simulated and measured power outputs for load acceptance when the machine is operated at an initial load of 0.6 p.u. (Dotted line indicates main servo position)

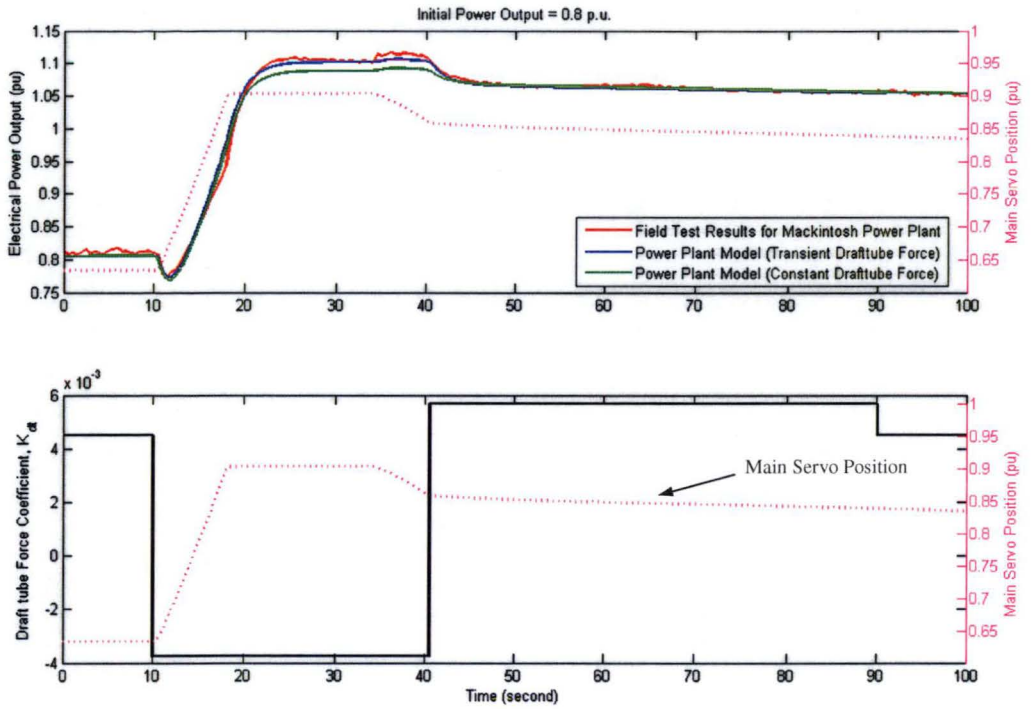

Figure 8.29: Comparison of the simulated and measured power outputs for load acceptance when the machine is operated at an initial load of 0.8 p.u. (Dotted line indicates main servo position)

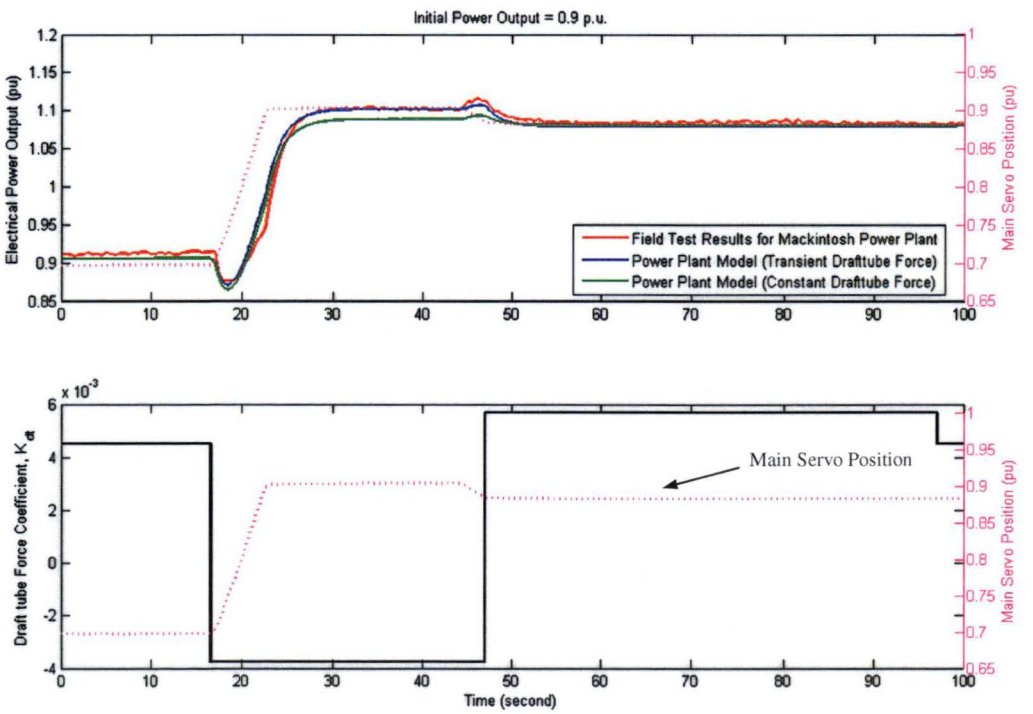

Figure 8.30: Comparison of the simulated and measured power outputs for load acceptance when the machine is operated at an initial load of 0.9 p.u. (Dotted line indicates main servo position)

8.7 Conclusions

Unsteady flow effects in the model draft tube following a sudden change in discharge have been studied computationally using mathematical models of various complexities. The CFD solutions were validated against the thermal anemometry measurements. The three-dimensional CFD numerical analysis was shown to predict a longer response time than the one-dimensional hydraulic model currently used for simulating the operations of the Mackintosh power station. The inclusion of transient draft tube forces in the power plant model improved the simulation accuracy for the Mackintosh station. Convective lag effects and fluctuations in the draft tube pressure force or loss coefficients were shown to largely explain the remaining discrepancies in current quasi-steady predictions of transient hydro power plant operation.

CHAPTER 9

CONCLUSIONS

9.1 Summary

The specific objectives of this thesis were to:

- develop and validate nonlinear quasi-steady flow models for the Francis turbine and waterway systems of single- and multiple-machine hydroelectric power plants;
- verify and validate the steady- and transient-flow solutions of CFD models for the turbine draft tube flows using the experimental model tests; and
- evaluate convective lag effects in the draft tube flow as well as the influence of transient draft tube force and loss coefficient variations during unsteady operation of a Francis turbine.

These objectives have been carefully investigated and it has been found that nonlinear modelling of the Francis turbine and waterway systems significantly improves the simulation accuracy of the power plants. The nonlinear computer models were developed in MATLAB Simulink for transient stability analysis of power stations subjected to a large frequency disturbance. Inelastic waterway models that take into account the inertia effect of the water column were found to perform satisfactorily in the current simulations. These results also showed that linearised models will underestimate the magnitude of power fluctuations during a large system disturbance. Overall, the improved hydraulic models presented in this thesis possess several important characteristics that can overcome the deficiencies of the existing industry models. These features include:

- introduction of a nonlinear guide vane function to account for the nonlinear relation between the turbine flow and gate opening;
- use of the dimensionless turbine performance curves to properly represent the nonlinear characteristics of the Francis turbine;

- application of a flow non-uniformity factor to correct for the effects of non-uniform velocity distribution in the hydraulic conduits;
- inclusion of the inlet dynamic pressure and draft tube static pressure force terms in the unsteady momentum equation for the waterway column;
- detailed calculations of the hydraulic model parameters such as water starting time and pressure loss coefficients for the entire waterway column; and
- consideration of the hydraulic coupling effects for multiple-turbine plant.

Favourable comparisons have been obtained between simulations and full-scale test results collected at Hydro Tasmania's Mackintosh and Trevallyn power stations. For the Mackintosh power plant, a noticeable phase lag between the measured and simulated power outputs, which increases in magnitude with guide vane oscillation frequency, was observed for this short penstock installation. The well-tested electro-mechanical model for the governor operation was unlikely to have been a significant cause of error. The remaining discrepancies were most likely due to the unsteady flow effects in the Francis turbine. The flow pattern in the Francis turbine does not change instantaneously with the guide vane movement and thus a time lag in flow establishment through the runner and draft tube may occur. For the Trevallyn power station, this unsteady flow effect was found to be relatively insignificant, as this power plant has a relatively long waterway conduit and high water inertia. The inertia effect of the water column in such cases is expected to dominate any unsteady flow effects of the Francis turbine operation.

To further examine these effects, the flow in a typical Francis-turbine draft tube without swirl has been studied experimentally and computationally. The 1:27.1 scale model draft tube used for these analyses was geometrically similar to the one employed in Hydro Tasmania's Mackintosh station. Extensive verification and validation of the simulations using ANSYS CFX were performed. The three-dimensional Reynolds-Averaged Navier-Stokes equations were solved by the code. Grid resolution, turbulence model, and boundary conditions were identified as the major factors affecting the accuracy of the numerical solution. Although a mesh-independent solution was not achieved in these simulations, a mesh size of 1176000 nodes was found to provide a

good compromise between computational time and the accuracy required. No firm conclusions can be drawn at this stage about the accuracy of the turbulence models used, due to the scarcity of experimental data for validating the CFD solutions. Preliminary investigations indicated that simulations using a standard k-ε turbulence model produced reasonably accurate results. The more advanced turbulence models such as Reynolds stress models did capture the self-excited unsteadiness of the draft tube flow but they did not seem to improve agreement with steady-state experiments.

Great care was taken in the selection of suitable boundary conditions for the CFD analysis: experimentally derived boundary conditions were used whenever possible; this is especially true for the inflow boundary condition. The inlet boundary layer properties were checked to ensure that the simulations would reflect the actual flow situations. The outflow boundary of the draft tube was extended to a distance of five times the outlet height to improve the convergence rate of the solution. Computational studies indicated that the inlet swirl of the draft tube would greatly affect the flow distribution inside the draft tube (see Section 7.4.3).

For transient-flow operations, the validated steady-flow solutions were used as the initial conditions in the unsteady simulations. Three different time steps were used to check for the time dependency of the solutions. The calculations were found insensitive to the Courant number of the flow and a time step of 0.001 second was applied for all transient simulations. Favourable comparisons were obtained between CFD solutions and thermal anemometry measurements. These provide some confidence for use of CFD in the transient analysis of the draft tube flow.

Unsteady flow effects in the turbine draft tube were evaluated using a three-dimensional CFD model, a two-dimensional unsteady stall model, and one-dimensional momentum theory. The convective time lag of the draft tube depended on the initial and final steady-state values of the flow. The predicted oscillation frequency using unsteady stall model seemed to match the experimental data, but the exact determination of convective lag time using this approach was difficult due to the relatively broad power spectrum of the experimental static pressure.

The time responses of the draft tube flow when subjected to an instantaneous step change in outlet static pressure were determined using Equation 8.19. The time response for the load rejection is longer than for load acceptance. This is presumably caused by the differences in frictional damping in these two cases. The three-dimensional CFD analysis was shown to predict a longer response time than the one-dimensional hydraulic model currently used as the power industry standard. The above difference was lower than the expected convective time lage of 0.057 second for the draft tube model. This can be partly explained by the assumption of uniform velocity distribution used in one-dimensional momentum theory.

The pressure oscillation frequency was found to greatly affect the flow response in the laboratory model tests. Although frequency dependence of the flow was clearly seen, it was still very difficult to quantify the impact of the oscillation frequency on the convective lag time of the flow. The Helmholtz resonance present in the experimental model tests further complicated the analysis of the frequency-dependent lag between the outlet static pressure and inlet flow speed. In general, the gain and phase lag between the inlet flow speed and outlet static pressure of the draft tube both increased with increasing oscillation frequency.

Transient behaviour was also observed in the calculated static pressure force and loss coefficients. The settling times of these coefficients when subjected to an instantaneous step increase and decrease of the flow were about 9 and 21 times the convective time lag, respectively. Inclusion of the unsteady draft tube forces into the power plant model of Mackintosh station produced favourable improvements in predicting the magnitude of power fluctuations. Overall, the convective lag effects as well as the fluctuations in draft tube pressure force and loss coefficients were shown to largely explain the remaining discrepancies in current quasi-steady predictions of the transient hydro power plant operation.

9.2 Recommendations for Future Study

9.2.1 Full-Scale Field Testings of the Francis-Turbine Power Plants

Acoustic methods should be used to measure the full-scale turbine flow during transient operations. These should provide valuable information for validation of the hydraulic models and evaluation of the nonlinear guide vane function.

Turbine and generator efficiency should be measured on every full-scale machine before the dynamic tests are carried out. The ages of the hydraulic components in the Francis turbine installations were found to influence the efficiency of an individual machine. A current efficiency test would greatly reduce the uncertainty involved in the parameter identification process, and increase the modelling accuracy.

The power outputs, guide vane positions, flow rates, speed variations, and static pressures should be measured and recorded on every machine under test in multiple-machine stations. Effects of simultaneously changing the operating conditions of turbines sharing a common waterway conduit should be thoroughly investigated to confirm the effects of hydraulic coupling on the transient stability of a power plant. Frequency response tests should be carried out at different load levels so that a complete safe operating zone can be established for the Francis turbine operations.

A continuous data acquisition system should be developed to build the database needed for validating power plant models. This would provide increased modelling fidelity and control accuracy of a power plant.

9.2.2 Hydraulic Modelling of Francis-Turbine Power Plants

Simulated results should be verified using different simulation programs. The hydraulic model should also be validated for power plants possessing a long waterway conduit. Comparisons with an elastic waterway models would be interesting in this case. The methods of characteristics commonly used in solving equations for elastic waterways would provide some flexibility in adding extra equations to account for unsteady friction losses in the conduits (see Equation 4.27).

Modelling and control strategies based on the concepts of Artificial Intelligence (AI) should be considered. This approach is now becoming feasible, as Hydro Tasmania has recently begun its program to continuously acquire the data from its power plants. The AI modelling procedure is based primarily on the principle of pattern recognition and the predictive capabilities of the neural networks implemented through a cluster-wise segmented associative memory scheme. Exhaustive system identification processes can be eliminated using this approach. Neural-network based controllers should be tried in the Francis-turbine power plants because they are found to give better damping effects for the generator oscillations over a wide range of operating conditions [29].

9.2.3 Experimental Model Testings of the Turbine Draft Tube

The use of a water model would be beneficial in determining the magnitude of scale effects and eliminating the Helmholtz resonance effects presented in the aerodynamic model. Two-phase flow studies for the turbine draft tube would also be informative in the transient analysis associated with the water column separation. The effects of inlet swirl could be examined by adding a ring of guide vanes at the draft tube inlet. A complete model of the Francis turbine runner and guide vanes would be even more desirable, as the time lag due to the movement of turbine guide vanes is thought to be of the same order as the convective time lag of the draft tube.

Due to the extreme combination of streamline curvature, adverse pressure gradients and secondary flows, experimental measurements of all Reynolds stresses would be valuable. This information would be particularly useful for the assessment of turbulence models used in the CFD simulations of draft tube flow. Laser Doppler Anemometry (LDA) should be used to check for the hot wire measurements, as the hot wire is incapable of sensing the flow direction in the highly unsteady and recirculating flow regimes.

Surface flow visualisation should be performed in order to aid the analyses of draft tube flow. This technique provides a visual image of the skin friction distribution on the surface and helps better understanding of the unsteady flow phenomena inherent in the flow. Fluorescent mini-tuft and oil-film methods are most suitable techniques currently

available. While detailed boundary-layer information is not obtainable, general patterns of flow separation and reattachment are recognisable with surface flow visualisation.

9.2.4 CFD Simulations of Turbine Draft Tube

Impacts of inlet boundary conditions for the draft tube should be carefully examined. In particular, the effects of swirl on either steady- or unsteady-flow operations of the draft tube should be thoroughly investigated. The current model is probably unable to correctly account for all the imposed information. The problems with inlet boundary condition underline the need to include the whole Francis turbine runner and guide vanes in the calculations of draft tube flow. This would require millions of additional nodes for computations. Although an unsteady rotor-stator interface can be easily modelled in ANSYS CFX, the limitations of turbulence models are still present. Detached Eddy Simulation (DES) and Large Eddy Simulation (LES) are becoming feasible with increasing computer power, and it would be interesting to verify the current RANS approach for the transient prediction of the draft tube flow against these more realistic models.

Simulation of the transient flow effects due to the movements of turbine guide vanes would be interesting. Flow modelling for variable guide vane motion is still challenging, as the moving-mesh techniques developed in ANSYS CFX can only account for very simple motion such as translation or rotation of a circular cylinder.

APPENDIX

DRAWINGS FOR THE EXPERIMENTAL MODEL TESTS

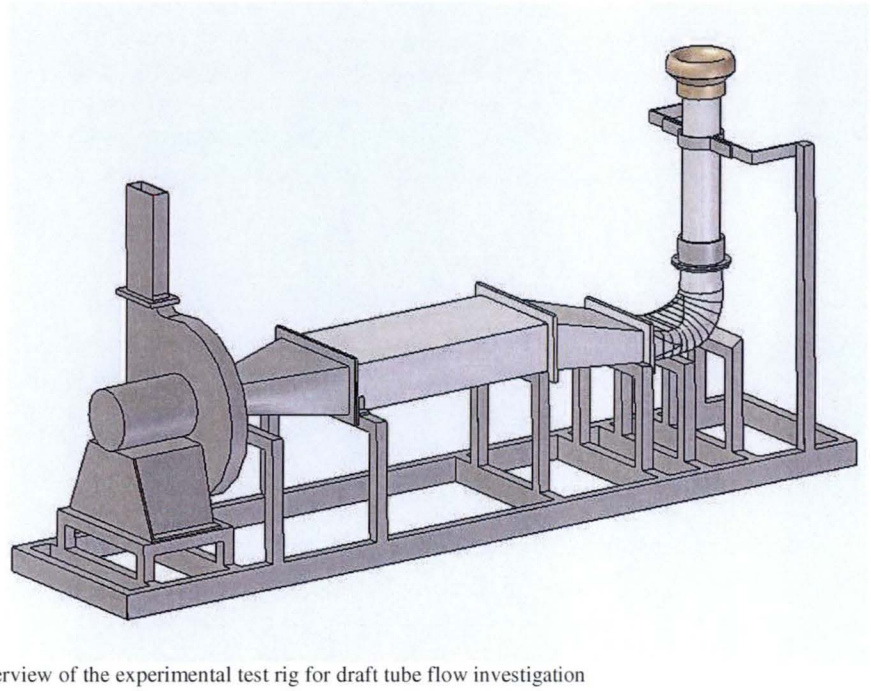

Figure A.1: Overview of the experimental test rig for draft tube flow investigation

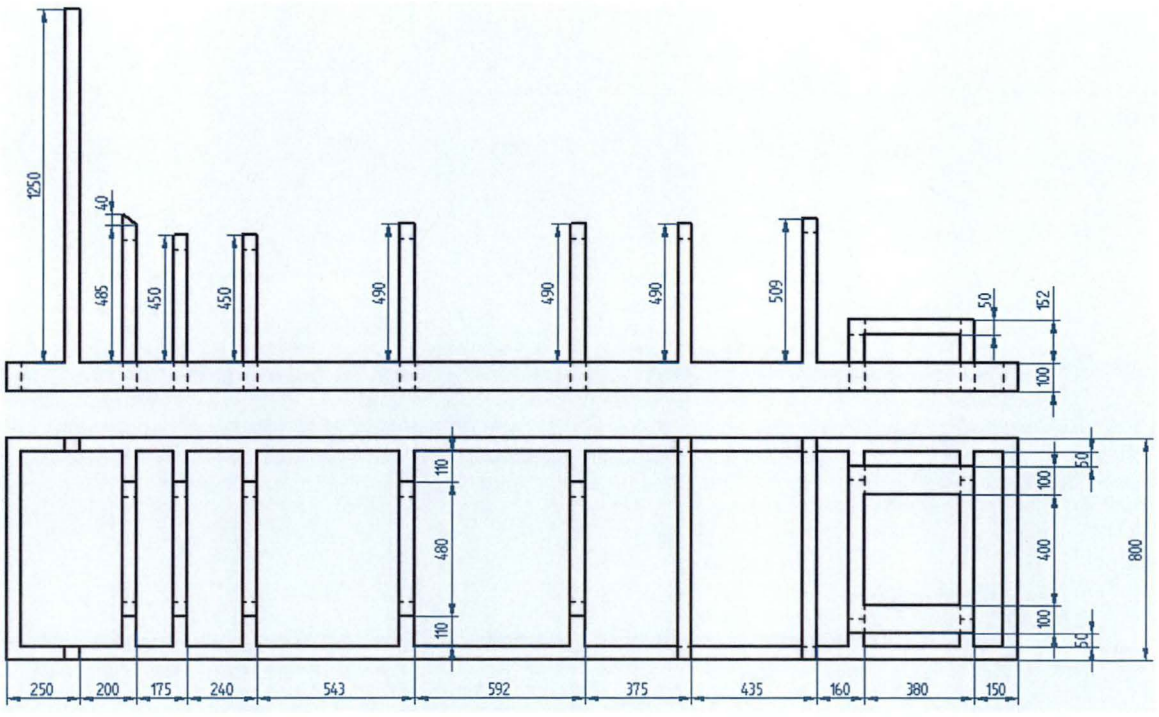

Figure A.2: Steel support frame for the experimental draft tube model (All dimensions in mm)

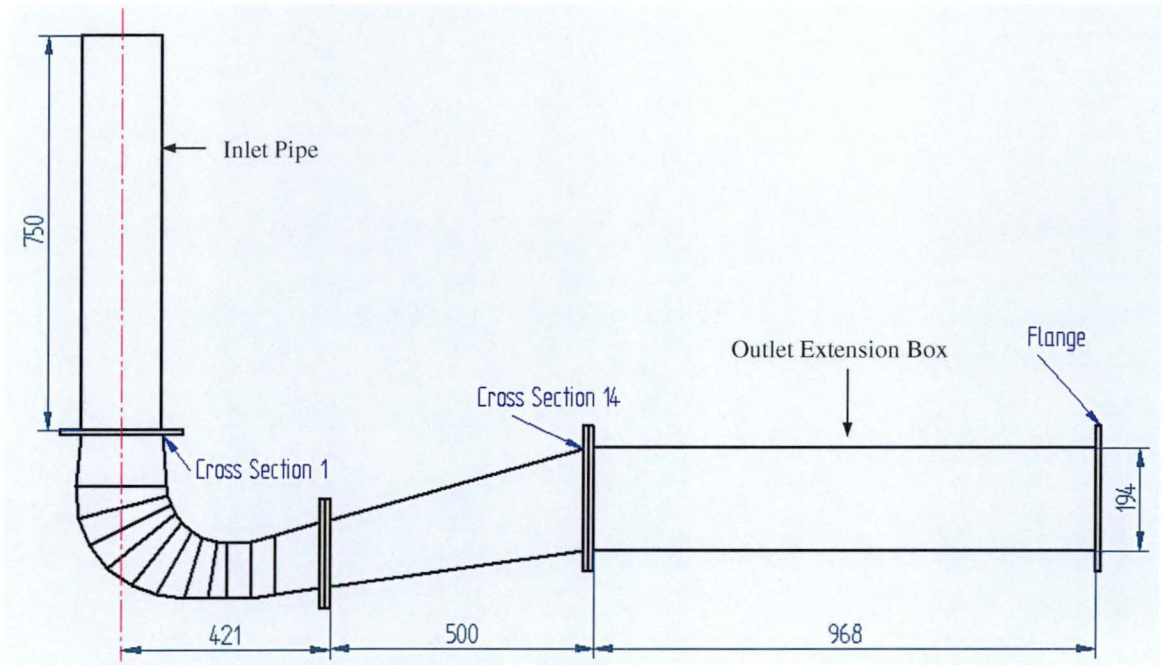

Figure A.3: Details of the experimental model used for draft tube flow investigation (All dimensions in mm)

Section i	*Top Surface Distance between Sections i & i+1*	*Bottom Surface Distance between Sections i & i+1*	*Radius for the corner fillet* R_i	*Section Height* H_i	*Section Width* W_i
1	100	100	–	75	75
2	17	59	–	84	84
3	17	56	86	172	181
4	20	54	85	171	196
5	20	57	82	164	218
6	24	50	76	152	248
7	24	52	68	136	274
8	29	45	59	118	295
9	21	37	53	107	310
10	46	45	52	104	318
11	48	47	41	106	327
12	97	94	29	112	337
13	518	504	–	125	357
14	–	–	–	194	465

Table A.1: Geometry details (from draft tube inlet to outlet) of the 1:27.1 scale model draft tube (All dimensions in mm)

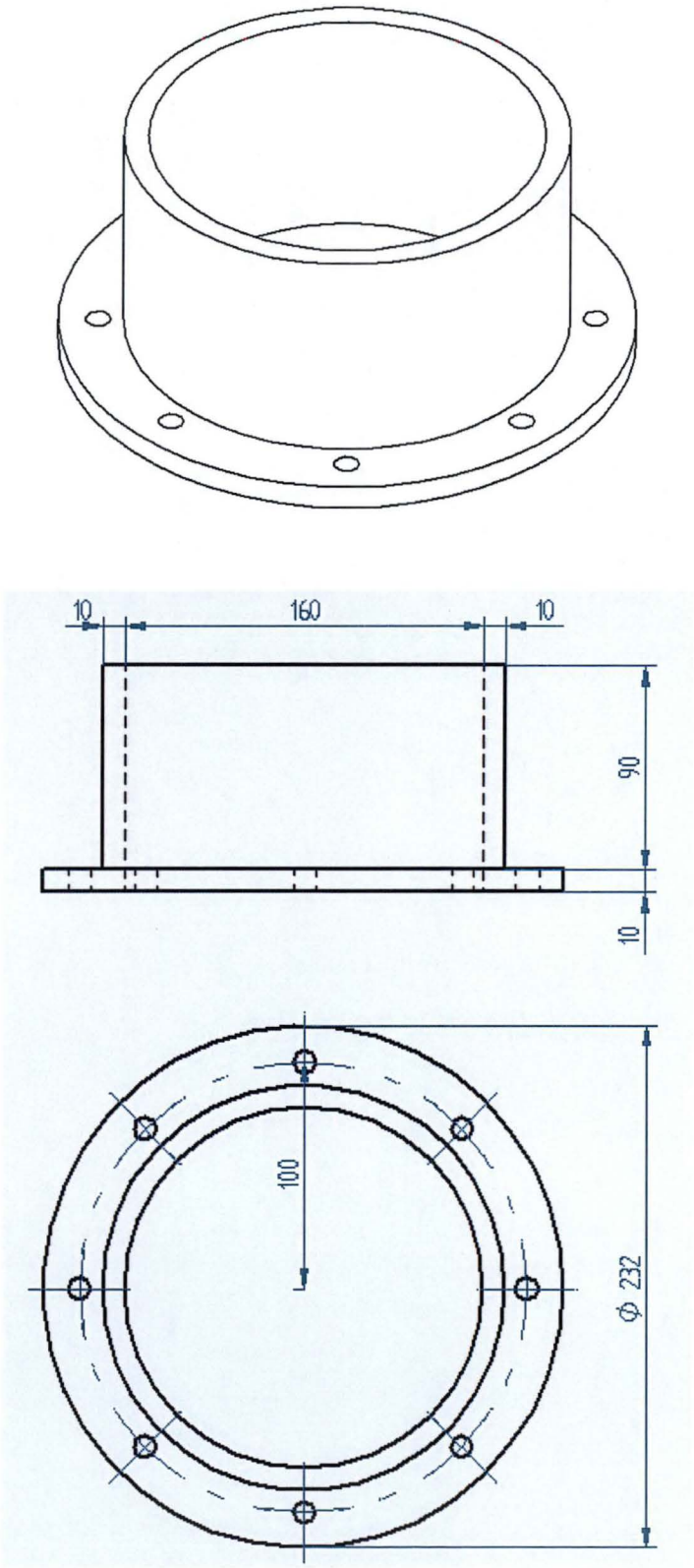

Figure A.4: Inlet pipe holder connecting the 750mm pipe and the draft tube model (All dimensions in mm)

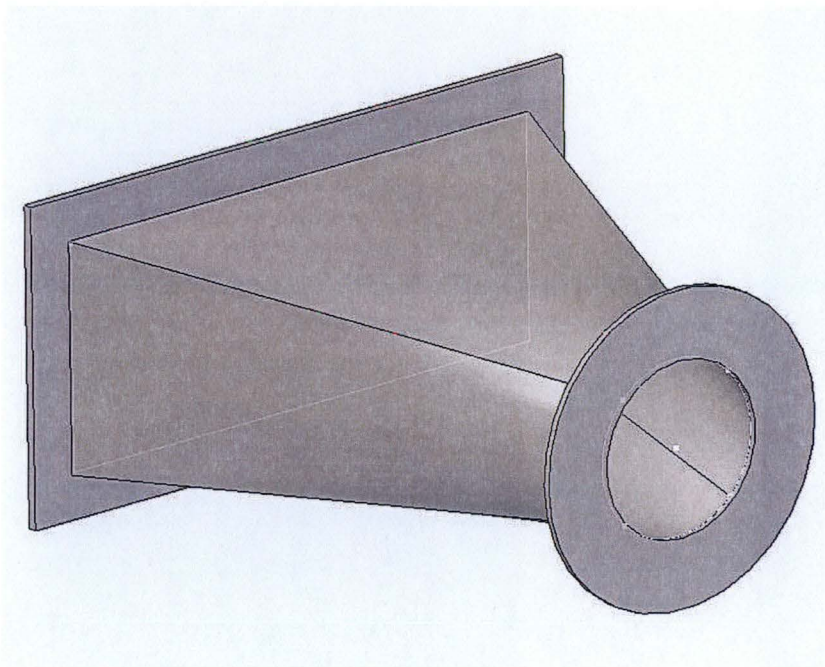

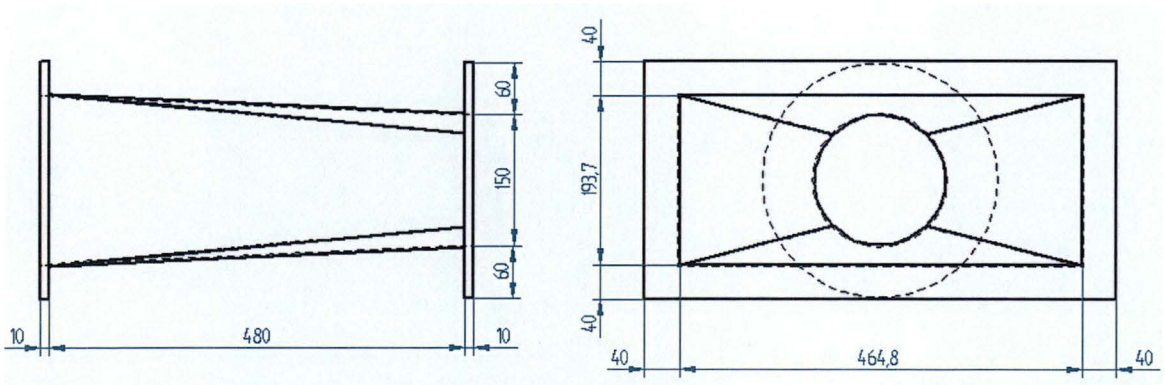

Figure A.5: Contraction cone at the outlet of the extension box (All dimensions in mm)

BIBLIOGRAPHY

[1] Aeschliman, D.P. & Oberkampf, W.L. "Experimental methodology for computational fluid dynamics code validation", AIAA Journal, 1997.

[2] Andersson, U. & Karlsson, R., "Quality aspects of the turbine 99 draft tube experiment", Proceedings of Turbine 99 – workshop on draft tube flow, Porjus, Sweden, June 20–23 1999.

[3] Andersson, U., "Turbine 99 – experiments on draft tube flow (test case T)", Proceedings of Turbine 99 – workshop on draft tube flow, Porjus, Sweden, June 20–23 1999.

[4] ANSYS CFX Inc., "ANSYS CFX release 10.0 user's manual", Waterloo, Ontario, Canada, 2005.

[5] Apsley, D.D., "Lecture notes for computational hydraulics", School of Mechanical, Aerospace and Civil Engineering, University of Manchester, 2005.

[6] Arpe, J.A. & Avellan, F., "Pressure wall measurements in the whole draft tube: steady and unsteady analysis", Proceedings of the XXI IAHR Symposium on Hydraulic Machinery and Systems, Lausanne, September 9–12 2002.

[7] Arpe, J.A., "Experimental investigation of unsteady pressure and velocity field in a draft tube of Francis turbine", PhD Thesis, Department De Génie Mécanique, École Polytechnique Fédérale De Lausanne, Switzerland, 2003.

[8] Arts, T., Boerrigter, H., Carbonaro, M., Charbonnier, J.M., Degrez, G., Olivari, D., Riethmuller, M.L., & Van den Braembussche, R.A., "Measurement techniques in fluid dynamics: an introduction", von Karman Institute for Fluid Dynamics, 1997.

[9] Avellan, F., "Flow investigation in a Francis draft tube: the Flindt project", Proceedings of the Hydraulic Machinery and Systems 20th IAHR Symposium, Charlotte, August 7–9, 2000.

[10] Bauer, D., Peikert, R., Sato, M. & Sick, M., "A case study in selective visualisation of unsteady 3D flow", Proceedings of the conference on Visualisation, Boston, Massachusetts, USA, 2002, pp. 525–528.

[11] Bélanger, A., "Simulation of the ERCOFTAC draft tube using PowerFlow", Proceedings of Turbine 99 workshop 2, Älvkarleby, Sweden, June 18–20, 2001.

[12] Berca, E.L., Ciocan, G.D. & Avellan, F., "Wall friction and boundary layer development in the cone of a Francis turbine scale model", 22nd IAHR Symposium on Hydraulic Machinery and Systems, Stockholm, Sweden, June 29 – July 2 2004.

[13] Bergant, A., Simpson, A.R. & Vítkovský, J., "Developments in unsteady pipe flow friction modeling", Journal of Hydraulic Research, Vol. 39, No. 3, 2001.

[14] Bergström, J. & Gebart, R., "Estimation of numerical accuracy for the flow field in a draft tube", International Journal of Numerical Methods for Heat and Fluid Flow, Vol. 9, No. 4, 1999, pp. 472–486.

[15] Bergström, J., "Modelling and numerical simulation of hydro power flows", PhD Thesis, Department of Mechanical Engineering, Division of Fluid Mechanics, LuLea University of Technology, Sweden, 2000.

[16] Binsfeld Engineering Inc., "TorqueTrak 9000 digital telemetry system users manual", MacFarlane Road, Maple City, MI, USA.

[17] Bonsor, K., "How Hydropower Plants Work", retrieved March 4 2006, from internet website: http://people.howstuffworks.com/hydropower-plant1.htm

[18] Brekke, H. & Li, X.X., "The structure matrix method for stability analysis of hydroelectric power plants", Proceedings of 6th International Conference on Pressure Surges, British Hydromechanics Research Association, Cranfield, Bedford, UK, 1990, pp. 297–308.

[19] Buttsworth, D.R., Elston, S.J. & Jones, T.V., "Directional sensitivity of skin friction measurements using nematic liquid crystal", Measurement Science Technology, No. 9, 1998, pp. 1856–1865.

[20] Cervantes, M.J. & Engström, T.F., "Influence of boundary conditions using factorial design", Proceedings of Turbine 99 workshop 2, Älvkarleby, Sweden, June 18–20, 2001.

[21] Chaudhry, M.H., "A nonlinear mathematical model for analysis of transients caused by a governed Francis turbine", Proceedings of 3rd International Conference on Pressure Surges, British Hydro-mechanics Research Association, Canterbury, UK, 1980, pp. 301–314.

[22] Clerides, D. & Jones, P.M., "Flow prediction in a hydroturbine draft tube", Proceedings of Turbine 99 – workshop on draft tube flow, Porjus, Sweden, June 20–23 1999.

[23] Ciocan, G.D., Avellan, F., & Berca, E.L., "Wall friction measurements: application in a Francis turbine cone", Proceedings of 2002 Joint US ASME-European Fluids Engineering Summer Conference, Montreal, Quebec, Canada, July 14–18 2002.

[24] Coldrick, M., Ivey, P., & Wells, R., "Considerations for using 3-D pneumatic probes in high speed axial compressors", ASME Journal of Turbomachinery, Vol. 125, January 2003, pp. 149–154.

[25] Collis, D.C. & Williams, M.J., "Two-dimensional convection from heated wires at low Reynolds number", Journal of Fluid Mechanics, No. 6, 1959, pp. 357–384.

[26] De Jaeger, E., Janssens, N., Malfliet, B. & Van De Meulebrooke, F., "Hydro turbine model for system dynamic studies", IEEE Transactions on Power Systems, Vol. 9, No. 4, November 1994, pp. 1709–1715.

[27] DeSiervo, F. & Deleva, F., "Modern trends in selecting and designing Francis turbines", Water Power and Dam Construction, Vol. 28, No. 8, 1976.

[28] DISA Elektronik A/S, "Description of the DISA 55M Sytem", Herlev, Denmark, October 1971 (Reg. No. 9150A4211).

[29] Djukanovic, M., Novicevic, M., Dobrijevic, D.J. & Babic, B., "Neural-net based coordinated stabilising control for the exciter and governor loops of low head hydropower plants", IEEE Transactions on Energy Conversion, Vol. 10, No. 4, December 1995, pp. 760–767.

[30] Dörfler, P., "Mathematical model of the pulsations in Francis turbines caused by the vortex core at part load", Escher Wyss News, 1980, pp. 101–106.

[31] Drtina, P., Göde, E. & Schachenmann, A., "Three-dimensional turbulent flow simulation for two different hydraulic turbine draft tube", Proceedings of the First European Computational Fluid Dynamics Conference, September 7–11 1992, Brussels, Belgium.

[32] Dubé, L. & Martin, C., "Hydro-QUÉBEC's experience in on-site testing of hydraulic-turbine efficiency", 14th Inter-Ram Conference for the electric power industry, 1986.

[33] Engström, T.F., Gustavsson, L.H. & Karlsson, R.I., "The second ERCOFTAC workshop on draft tube flow", Proceedings of Turbine 99 – Workshop 2, Älvkarleby, Sweden, June 18–20 2001.

[34] Feltes, J.W., Orero, S., Fardanesh, B., Uzunovic, E., Zelingher, S. & Abi-Samra N., "Deriving model parameters from field test measurements", IEEE Computer Applications in Power, Vol.15, No. 4, October 2002, pp. 30–36.

[35] Fox, R.W. & Kline, S.J., "Flow regimes in curved subsonic diffusers", Journal of Basic Engineering, Vol.84, 1962, pp. 303–316.

[36] Friedman, D. & Westphal, W.R., "Experimental investigation of a 90° cascade diffusing bend with an area ratio of 1.45:1 and with several inlet boundary layers", NACA technical note 2668, Washington, USA, April 1952.

[37] Gebart, B.R., Gustavsson, L.H. & Karlsson, R.I., "Proceedings of turbine – 99 workshop on draft tube flow in Porjus Sweden", Luleå University of Technology, Technical Report 2000:11, Sweden 2000.

[38] Gordon, J.L., "Hydraulic turbine efficiency", Canadian Journal of Civil Engineering, Vol. 28, No. 2, April 2001, pp. 238–252.

[39] Grotjans, H., "Higher order turbulence modelling for draft tube applications", Proceedings of Turbine 99 – workshop on draft tube flow, Porjus, Sweden, June 20–23 1999.

[40] Gyllenram, W., "Modelling of swirling flow in a conical diffuser", Diploma Thesis, Division of Thermo and Fluid Dynamics, Chalmers University of Technology, Göteborg, Sweden, 2003.

[41] Haimes, R., Connell, S.D. & Vermeersch, S.A., "Visual grid quality assessment for 3D unstructured meshes", AIAA Journal 93-3352, Orlando FL, July 1993.

[42] Hannett, L.N., Feltes, J.W., Fardanesh, B. & Crean, W., "Modelling and control tuning of a hydro station with units sharing a common penstock section" IEEE Transactions on Power Systems, Vol. 14, No.4, November 1999, pp. 1407–1414.

[43] Hellström, I.G.J., "Redesign of an existing hydropower draft tube", MSc Thesis, Department of Applied Physics and Mechanical Engineering, Luleå University of Technology, Sweden, 2005.

[44] Hosio, Y., "Contributions to model tests of draft tube surges of Francis turbine", Proceedings, Joint Symposium on Design and Operation of Fluid Machinery, Fort Collins, Colorado, June 1978, pp. 141–150.

[45] Hydro Tasmania Inc., "Devils Gate power station: ASEA Electro-hydraulic turbine governors – Description and operating instruction", Hydro Tasmania Reference No. F025692.

[46] Idelchik, I.E., "Handbook of hydraulic resistance", 2nd edition, Hemisphere Publishing Corporation, Washington, USA, 1986. ISBN: 0891162844.

[47] IEEE committee, "Dynamic models for steam and hydro turbines in power system studies," *IEEE* Transactions on Power Apparatus and Systems, Vol. PAS-92, No. 6, 1973, pp. 1904–1915.

[48] Iliescu, M.S. & Ciocan, G.D., "3D PIV and LDV measurements at the outlet of a Francis turbine draft tube", Proceedings of 2002 joint US ASEM-European Fluids Engineering Summer Conference, Montreal, Quebec, Canada, July 14–18 2002.

[49] Iliescu, M.S. & Ciocan, "2 phase PIV measurements at the runner outlet in a Francis turbine", Proceedings of 4th ASME_JSME Joint Fluids Engineering Conference, Honolulu, Hawaii, USA, July 6–11 2003.

[50] Jonzén, S., Hemström, B. & Andersson, U., "Turbine 99 – accuracy in CFD simulations on draft tube flow", Proceedings of Turbine 99 workshop 2, Älvkarleby, Sweden, June 18–20, 2001.

[51] Jones, D I., "Multivariable control analysis of a hydraulic turbine" Transactions of Institute of Measurement and Control, Vol. 21, No. 2/3, 1999, pp. 122–136.

[52] Jørgensen, F.E., "How to measure turbulence with hot-wire anemometers – a practical guide", DANTEC Dynamics, Skovlunde, Denmark, 2002. (Publication no. 9040U6151)

[53] Jošt, D., Lipej, A. & Schweiger, V., "Flow in draft tube and tunnel of high head Francis turbine", 11th IAHR International Meeting of the Work Group on the Behaviour of Hydraulic Machinery under Steady Oscillatory Conditions, Stuttgart, Germany, October 8–10 2003.

[54] Kim, S.E., Malan, P., Lai, Y.G. & Patel, V.C., "CFD prediction of turbulent flow through a draft tube", Proceedings of Turbine 99 – workshop on draft tube flow, Porjus, Sweden, June 20–23 1999.

[55] Klein, A., "Review: Effects of Inlet Conditions on Conical-Diffuser Performance", ASME Journal of Fluids Engineering, Vol. 103, 1981, pp. 250–257.

[56] Knoblauch, H., Klasinc, R., Heigerth, G. & Sattler, W., "Scale model test for a distributing piping". Proceedings of the XXVII IAHR Congress, 22/8/1999. Graz.

[57] Komminaho, J. & Bard, A., "Calculations on a draft tube with Fluent", Proceedings of Turbine 99 – workshop on draft tube flow, Porjus, Sweden, June 20–23 1999.

[58] Kornilov, V.I., Litvinenko, Yu.A. & Pavlov, A.A., "Skin-friction measurements in an incompressible pressure-gradient turbulent boundary layer", 11th International Conference on Methods of Aerophysical Research, Novosibirsk, Russia, 1–7 July 2002.

[59] Kundur, P., "Power system stability and control", McGraw-Hill, USA, 1994.

[60] Kurosawa, S., Nagafuji, T., Tezuka, K. & Biswas, D., "Navier-stokes simulations with a non-linear eddy viscosity model for the draft tube of a Kaplan turbine", Proceedings of Turbine 99 – workshop on draft tube flow, Porjus, Sweden, June 20–23 1999.

[61] Kwong, A.H.M & Dowling, A.P., "Unsteady flow in diffusers", ASME Journal of Fluid Engineering, Vol. 116, December 1994, pp. 842–847.

[62] Lai, Y.G. & Patel, V.C., "CFD simulation and assessment of the draft tube flow", Proceedings of Turbine 99 – workshop on draft tube flow, Porjus, Sweden, June 20–23 1999.

[63] Launder, B.E., Reece, G.J. & Rodi, W., "Progress in the developments of a Reynolds-stress turbulence closure", Journal of Fluid Mechanics, Vol. 68, 1975, pp. 537–566

[64] Laurence, D., "Limitations of current RANS models & progress perspectives", QNET CFD, 2nd workshop, Lucerne, May 22, 2002.

[65] Lindenmeyer, D., Moshref, A., Schaeffer, C. & Benge, A., "Simulation of the start-up of a hydro power plant for the emergency power supply of a nuclear power station", IEEE Transactions on Power Systems, Vol. 16, No. 1, February 2001, pp. 163–169.

[66] Liseikin, V.D., "Grid generation methods", Springer-Verlag, Berlin, Heidelberg, New York, 1999.

[67] Longatte, F., Kueny, J.L. & Avellan, F., "Three-dimensional analysis of the flow in the ERCOFTAC draft tube with N3S and Fluent softwares", Proceedings of Turbine 99 – workshop on draft tube flow, Porjus, Sweden, June 20–23 1999.

[68] Lörstad, D. & Fuchs, L., "LES of turbulent flow in a draft tube of a water turbine", Proceedings of Turbine 99 – workshop on draft tube flow, Porjus, Sweden, June 20–23 1999.

[69] Ma, Z.Y., Nishi, M. & Yoshida, K., "Numerical flow analysis for elbow draft tubes by finite element method", Proceedings of Turbine 99 – workshop on draft tube flow, Porjus, Sweden, June 20–23 1999.

[70] Mansoor, S.P., "Behaviour and operation of pumped storage hydro plants" PhD Thesis, University of Wales, Bangor, UK, July 2000.

[71] Malik, O., Hope, G., Hancock, G., Li, Z.H., Ye, L.Q. & Wei, S.P., "Frequency measurement for use with a microprocessor-based water turbine governor", *IEEE* Transactions on Energy Conversion, Vol. 6, No. 3, September 1991, pp. 361–366.

[72] Mauri, S., Kueny, J.L. & Avellan, F., "Numerical prediction of the flow in a turbine draft tube influence of the boundary conditions", Proceedings of ASME 2000 Fluids Engineering Division Summer Meeting, Boston, Massachusetts, USA, June 11–15 2000.

[73] Mauri, S., Kueny, J.L. & Avellan, F., "Werlé-Legendre separation in a hydraulic machine draft tube", Proceedings of ASME 2002 Fluids Engineering Division Summer Meeting, Montreal, Quebec, Canada, July 14–18 2002.

[74] Mauri, S., Kueny, J.L. & Avellan, F., "Flow simulation in an elbow diffuser: verification and validation", Proceedings of XXI IAHR Symposium on Hydraulic Machinery and Systems, Lausanne, September 9–12 2002.

[75] Mauri, S., "Numerical simulation and flow analysis of an elbow diffuser", PhD Thesis, Département De Génie Mécanique, École Polytechnique Fédérale De Lausanne, Switzerland, 2002.

[76] McPheat, J., "Integrated dynamic modelling of hydro-electric power systems", MEngSci Thesis, University of Adelaide, Australia, November 1997.

[77] Mehta, U., "Guide to credible computational fluid dynamics simulations", AIAA Journal of Propulsion and Power, Vol. 12, No. 5, October 1996, pp. 940–948.

[78] Menter, F.R., "Two-equation eddy-viscosity turbulence models for engineering applications", AIAA Journal, Vol. 32 No. 8, 1994.

[79] Menter, F.R., Kuntz, M. & Langtry, R., "Ten years of industrial experience with the SST turbulence model", Proceedings of the 4th International Symposium on Turbulence, Heat and Mass Transfer, 2003, pp. 625–632.

[80] Mikhail, A.F. & Knowlton, R.J., "Performance testing of the St. Lawrence power project using current meters", International Group on Hydraulic Efficiency Measurements, July 2000.

[81] Miller, D.S., "Internal flow systems". BHRA Fluid Engineering, Vol. 5, 1978. ISBN 0 900983787.

[82] Monsonyi, E. & Seth H.B.S., "The surge tank – a device for controlling water hammer", Water Power & Dam Construction, February 1975, pp. 69–74.

[83] Mosonyi, E., "Water power development – low head power plants", Volume 1, Akadémiai Kiadó, Budapest, Hungary, 1987, ISBN 9630542714.

[84] Nanoshita, T., Matsumoto, Y., Ohashi, H. & Kubota, T., "Water column separation in a straight draft tube", Proceedings of the 3rd ASME/JSME Joint Fluids Engineering Conference, San Francisco, California, USA, July 18–22, 1999.

[85] Nicolet, C., Arpe, J & Avellan, F., "Identification and modelling of pressure fluctuations of a Francis turbine scale model at part load operation", 22nd IAHR Symposium on Hydraulic Machinery and Systems, Stockholm, Sweden, June 29–July 2 2004.

[86] Nilsson, H., "Numerical investigations of turbulent flow in water turbines", PhD Thesis, Division of Thermo and Fluid Dynamics, Chalmers University of Technology, Göteborg, Sweden, 2002. ISBN 9172911875.

[87] Ng, T.B., "Waterjet intake flows", Honours Thesis, Department of Civil & Mechanical Engineering, University of Tasmania, Australia, 2001.

[88] Oberkampf, W.L. & Blottner, F.G. & Aeschliman, D.P., "Methodology for computational fluid dynamics code verification/validation", 26th AIAA Fluid Dynamics Conference, San Diego, California, USA, June 19–22 June 1995.

[89] Orfanidis, S.J., "Introduction to signal processing", Prentice-Hall, Englewood Cliffs, NJ, 1996.

[90] Owen, S., "A survey of unstructured mesh generation technology", retrieved March 4 2005, from Carnegie Mellon University, department of Civil & Environ. Eng. website: http://www.andrew.cmu.edu/user/sowen/survey/index.html.

[91] Page, M. & Giroux, A.M., "Turbine 99 draft tube flow computation with FIDAP and TASCflow", Proceedings of Turbine 99 – workshop on draft tube flow, Porjus, Sweden, June 20–23 1999.

[92] Paik, J, Sotiropoulos, F., & Sale, M.J., "Numerical simulation of swirling flow in complex hydroturbine draft tube using unsteady statistical turbulence models", Journal of Hydraulic Engineering, Vol.131, 2005, pp. 441–456.

[93] Parsons, D.J. & Hill, P.G., "Effects of curvature on two-dimensional diffuser flow", ASME Journal of Fluid Engineering, Vol. 95, 1973, pp. 349–360.

[94] Patel, V.C., "Calibration of the Preston tube and limitations of its use in pressure gradients", Journal of Fluid Mechanics, Vol. 23, No. 1, 1965, pp. 185–208.

[95] Phillipson, S.J., "Comparison of accuracy for various element types: laminar flow", ANSYS CFX validation report, CFX-VAL11/0404, 28 October 2002.

[96] Ramey, D. & Skooglund, J., "Detailed hydrogovernor representation for system stability studies", *IEEE* Transactions on Power Apparatus and Systems, Vol. PAS–89, January 1970, pp. 106–112.

[97] Ramos, H. & Almeida, A.B., "Parametric analysis of water-hammer effects in small hydro schemes", Journal of Hydraulic Engineering, July 2002, pp. 689–696.

[98] Rayner, P. & Ho, S., "Devils Gate power station – dynamic modelling and Tasmanian electricity code compliance assessment", Hydro Electric Corporation Internal Report, 18/8/2003. (Report No. 112475 – Report 1).

[99] Rayner, P., "GEN-109168-TP-01: Trevallyn power station – testing to verify penstock hydraulic model" Hydro Tasmania Consulting Division, May 2003.

[100] Reddy, H., Seshadri, V. & Kothari, D.P., "Effect of draft tube size on the performance of a cross-flow turbine", Energy Sources, Vol.18, 1996, pp. 143–149.

[101] Resiga, R.S., Ciocan, G.D., Anton, I. & Avellan, F., "Analysis of the swirling flow downstream of a Francis turbine runner", ASME Journal of Fluids Engineering, Vol. 128, January 2006, pp. 177–189.

[102] Ripley, R.C., Whitehouse, D.R., & Lien, F.S., "Effect of mesh topology on shock wave loading computations", Proceedings 11th Annual Conference of the CFD Society of Canada, Vancouver, Canada, 2003.

[103] Roache, P.J., "Verification and validation in computational science and engineering", Hermosa Publishers, New Mexico, USA, 1998.

[104] Rokni, M. & Sundén, B., "Calculation of turbulent fluid flow and heat transfer in ducts by a full Reynolds stress model", International Journal for Numerical Methods in Fluids, Vol. 42, 2003, pp. 147–162.

[105] Rudolf, P. & Skotak, A., "Unsteady flow in the draft tube with elbow part B – numerical investigation", Symposium of the Behaviour of Hydraulic Machines under Steady Oscillatory Conditions, Trondheim, Norway, June 2001.

[106] Rumsey, C.L. & Vatsa, V.N., "A comparison of the predictive capabilities of several turbulence models using upwind and central-difference computer codes", AIAA Journal 93–0192, Reno, NV, January 1993.

[107] Ruprecht, A., Heitele, M., Helmrich, T., Moser, W. & Aschenbrenner, T., "Numerical simulation of a complete Francis turbine including unsteady rotor/stator interactions", 20th IAHR Symposium on Hydraulic Machinery and Systems, Charlotte, August 2000.

[108] Ruprecht, A., Helmrich, T., Aschenbrenner, T. & Scherer, T., "Simulation of vortex rope in a turbine draft tube", Proceedings of the Hydraulic Machinery and Systems 21st IAHR Symposium, Lausanne, September 9–12 2002.

[109] Ruprecht, A., "Unsteady flow simulation in hydraulic machinery", Task Quarterly, Vol. 6, No. 1, 2002, pp. 187–208.

[110] Sagi, C.J. & Johnston, J.P., "The design and performance of two-dimensional, curved diffusers", ASME Journal of Basic Engineering, Vol. 89, 1967, pp. 715–731.

[111] Sanathanan, C.K., "Accurate low order model for hydraulic turbine-penstock", IEEE Transactions on Energy Conservation, Vol. EC-2, 1987, pp. 196–200.

[112] Scanlon, A., "Water power", 2nd edition, HEC, Tasmania, Australia 1995, ISBN 0724642315.

[113] Shewchuk, J.R., "Mesh generation for domains with small angles", Proceedings of the Sixteenth Annual Symposium on Computational Geometry, Clear Water Bay, Kowloon, Hong Kong, June 12–14, 2000.

[114] Shyy, W. & Braaten, M.E., "Three-dimensional analysis of the flow in a curved hydraulic turbine draft tube", International Journal for Numerical Methods in Fluids, Vol. 6, 1986, pp. 861–882.

[115] Shimmei, K., Ishii, T. & Niikura, K., "Numerical simulations of flow in Kaplan draft tube Turbine 99 ERCOFTAC workshop on draft tube flows", Proceedings of Turbine 99 workshop 2, Älvkarleby, Sweden, June 18–20, 2001.

[116] Skåre, P.E., Dahlhaug, O.G. & Kjeldsen, M., "CFD calculation of a draft tube flow", Proceedings of Turbine 99 – workshop on draft tube flow, Porjus, Sweden, June 20–23 1999.

[117] Skotak, A., "Draft tube flow simulation state-of-the-art approach application", Proceedings of Turbine 99 – workshop on draft tube flow, Porjus, Sweden, June 20–23 1999.

[118] Skotak, A., "Unsteady flow in the draft tube with elbow Part A – Experimental investigation", 10th IAHR International Meeting of the Work Group on the Behaviour of Hydraulic Machinery under Steady Oscillatory Conditions, Tronheim, Norway, June 26–28 2001.

[119] Simonsen, A.J., "Experimental and numerical investigation of a bend-diffuser configuration", PhD Thesis, Department of Energy and Process Engineering, The Norwegian University of Science and Technology, Norway, October 2003.

[120] Sotiropoulos, F. & Ventikos, Y., "The three-dimensional structure of confined swirling flows with vortex breakdown", Journal of Fluid Mechanics, Vol. 426, 2000, pp. 155–175.

[121] Speziale, C.G., Sarkar, S. & Gatski, T.B., "Modelling the pressure-strain correlation of turbulence: an invariant dynamical systems approach", Journal of Fluid Mechanics, Vol. 277, 1991, pp. 245–272.

[122] Staubli, T. & Meyer, D., "Draft tube calculations", Proceedings of Turbine 99 – workshop on draft tube flow, Porjus, Sweden, June 20–23 1999.

[123] Streeter, V.L. & Wylie, E.B., "Fluid mechanics", McGraw-Hill, Toronto, Canada, 1981.

[124] The MathWorks Inc., "MATLAB release 14 user's guide", MA, USA, 2004.

[125] Thakur, S., Vu, T., Shyy, W. & Laprise, C., "Computation of fluid flow in a model draft tube", Proceedings of Turbine 99 – workshop on draft tube flow, Porjus, Sweden, June 20–23 1999.

[126] Thompson, J.F., Warsi, Z.U.A. & Mastin, C.W., "Numerical grid generation: Foundations and applications", North-Holland, New York, USA, 1985.

[127] Tsang, C.L.P & Oldfield, M.L.G., "Oxford 4-hole pressure probe (Probe h3)", user manual, University of Oxford, UK, January 1 2003.

[128] Ueda, T. & Kubota, T., "Model test report of hydraulic turbine for Mackintosh & Bastyan power station", Fuji Electric Corporation, Kawasaki, Japan, December 7 1976. (Hydro Tasmania Reference No. 568870)

[129] Van Wie, D.M. & Rice, T., "Quantification of data uncertainties and validation of CFD results in the development of hypersonic airbreathing engines", 27th AIAA Fluid Dynamics conference, New Orleans, Louisiana, June 17–20 1996.

[130] Vaughan, P., "Bastyan and Mackintosh turbine/ waterway simulations", Memorandum, Hydro Tasmania, 2001.

[131] Versteeg, H.K. & Malalasekera, W., "An introduction to computational fluid dynamics", Prentice Hall, London, 1995, ISBN 0582218845.

[132] Vu, T.C., Nennemann, B., Ciocan, G.D., Iliescu, M.S., Braun, O. & Avellan, F., "Experimental study and unsteady simulation of the Flindt draft tube rotating vortex rope", Proceedings of the Hydro 2004 Conference, Porto, Portugal, October 16–18, 2004.

[133] Wahl, T.L., "Draft tube surging hydraulic model study", MEngSci Thesis, Department of Civil Engineering, Colorado State University, USA, 1990.

[134] Walker, G.J., "An investigation of the boundary layer behaviour on the blading of a single-stage axial-flow compressors", PhD Thesis, University of Tasmania, 1971.

[135] Walker, G.J. & Sargison, J.E., "Turbine and waterway modelling: investigation and development of improved models stage 1 report", School of Engineering, University of Tasmania, 5/4/2002. (HT Professional Service Contract No. 900831).

[136] Warnick, C.C., Mayo, H.A., Carson, J.L. & Sheldon, L.H., "Hydropower engineering", Prentice Hall, Englewood, NJ, 1984, ISBN 0134484983.

[137] Watters, G.Z., "Modern analysis and control of unsteady flow in pipelines", Ann Arbor Science Publishers Inc., Michigan, USA, 1980, ISBN 0250402289.

[138] Weber, H.W., Prillwitz, F., Hladky, M. & Asal H.P., "Reality oriented simulation models of power plants for restoration studies", Control Engineering Practice 9, 2001, pp. 805–811.

[139] White, F.M., "Viscous fluid flow", McGraw-Hill, USA, 1974. ISBN 0070697108.

[140] Wilcox, D.C., "Turbulence modelling for CFD", DCW Industries Inc., LA Canada, CA, 1993.

[141] Working Group on Prime Mover & Energy Supply Models for System Dynamic Performance Studies, "Hydraulic turbine and turbine control models for system dynamic performance studies", IEEE Transactions on Power System, Vol.7, No.1, February 1992, pp. 167–179.

[142] Wylie, E.B. & Streeter, V.L., "Fluid transients in systems", Prentice Hall, Englewood Cliffs, NJ, 1993.

[143] Wyler, J.S., "Probe blockage effects in free jets and closed tunnels", ASME Journal of Engineering Power, Vol. 97, No. 4, 1975, pp. 509–515.

[144] Yang, J.M., Liu, W.J. & Wu, Y.L., "The large eddy simulation method for computation of 3-D unsteady periodic turbulent flow in draft tube", ShuiLi XueBao, No. 8, August 2001, pp. 79–84 (in Chinese).

[145] Yaras, M.I., "Effects of inlet conditions on the flow in a fishtail curved diffuser with strong curvature", ASME Journal of Fluids Engineering, Vol. 118 No. 4, 1996, pp. 772–778.

[146] Yaras, M.I., "Flow measurements in a fishtail diffuser with strong curvature," ASME Journal of Fluids Engineering, Vol. 121, No. 2, 1999, pp. 410–417.

[147] Yaras, M.I. & Orsi, P., "Measurements of the effects of periodic inflow unsteadiness on the aerodynamics of a fishtail diffuser," ASME Paper GT-2002-30455, 47th ASME-IGTI Turbomachinery Conference Proceedings, 2002.

[148] Yaras, M.I. & Grosvenor, A.D., "Evaluation of one- and two-equation turbulence models part I- axisymmetric separating and swirling flows," International Journal for Numerical Methods in Fluids, Vol. 42, 2003, pp. 1293–1319.

[149] Yaras, M.I. & Orsi, P., "Measurements of the transient velocity field in a strongly curved diffusing bend with periodic inflow unsteadiness", Experiments in Fluids, Vol.36, 2004, pp. 363–372.

[150] Ye, L.Q., Wei, S.P., Malik, O. & Hope, G., "Variable structure and time-varying parameter control for hydroelectric generating unit", *IEEE* Transactions on Energy Conversion, Vol.4, No. 3, September 1989, pp. 293–299.

[151] Yuan, W.X. & Schilling, R., "Numerical simulation of the draft tube and tailwater flow interaction", Journal of Hydraulic Research, Vol.40, No. 1, 2002, pp. 73–81.

[152] Zhu, B., Chi, X. & Shih, T.I-P., "Computing aerodynamic performance of 2D iced airfoils: blocking strategy and convergence rate", 20th Applied Aerodynamics Conference, St. Louis, Missouri, USA, June 24–26 2002.

[153] www.ntf.flinders.edu.au (Tidal Information by National Tidal Facility Australia), retrieved in November 2003.

[154] Hydro Tasmania's Trevallyn Plant Drawings: Reference No. A-00818, A-02153, A-01349, A-01395, A-01402, A-01470, A-01529, B-02218, O-08371, O-08768, O-08769, retrieved in November 2003.

[155] Canann, S.A., Saigal, S. & Owen, S.J., "Special edition on unstructured mesh generation", International Journal for Numerical Methods in Engineering, Vol. 1, No. 49, 2000.

[156] Rhie, C.M. & Chow, W.L., "Numerical study of the turbulent flow past an airfoil with trailing edge separation", Journal of AIAA, Vol. 21, No. 11, 1983, pp. 1525–1532.